frontiers | Research Topics

Biogeochemistry and genomics of silicification and silicifiers, volume II

Edited by
Brivaela Moriceau, Shilin Liu, Lihua Ran, Jeffrey William Krause, Paul J. Tréguer and Su Mei Liu

Published in
Frontiers in Marine Science

ISSN 1664-8714
ISBN 978-2-8325-5378-7
DOI 10.3389/978-2-8325-5378-7

About Frontiers

Frontiers is more than just an open access publisher of scholarly articles: it is a pioneering approach to the world of academia, radically improving the way scholarly research is managed. The grand vision of Frontiers is a world where all people have an equal opportunity to seek, share and generate knowledge. Frontiers provides immediate and permanent online open access to all its publications, but this alone is not enough to realize our grand goals.

Frontiers journal series

The Frontiers journal series is a multi-tier and interdisciplinary set of open-access, online journals, promising a paradigm shift from the current review, selection and dissemination processes in academic publishing. All Frontiers journals are driven by researchers for researchers; therefore, they constitute a service to the scholarly community. At the same time, the *Frontiers journal series* operates on a revolutionary invention, the tiered publishing system, initially addressing specific communities of scholars, and gradually climbing up to broader public understanding, thus serving the interests of the lay society, too.

Dedication to quality

Each Frontiers article is a landmark of the highest quality, thanks to genuinely collaborative interactions between authors and review editors, who include some of the world's best academicians. Research must be certified by peers before entering a stream of knowledge that may eventually reach the public - and shape society; therefore, Frontiers only applies the most rigorous and unbiased reviews. Frontiers revolutionizes research publishing by freely delivering the most outstanding research, evaluated with no bias from both the academic and social point of view. By applying the most advanced information technologies, Frontiers is catapulting scholarly publishing into a new generation.

What are Frontiers Research Topics?

Frontiers Research Topics are very popular trademarks of the *Frontiers journals series*: they are collections of at least ten articles, all centered on a particular subject. With their unique mix of varied contributions from Original Research to Review Articles, Frontiers Research Topics unify the most influential researchers, the latest key findings and historical advances in a hot research area.

Find out more on how to host your own Frontiers Research Topic or contribute to one as an author by contacting the Frontiers editorial office: frontiersin.org/about/contact

Biogeochemistry and genomics of silicification and silicifiers, volume II

Topic editors

Brivaela Moriceau — UMR6539 Laboratoire des Sciences de L'environnement Marin (LEMAR), France

Shilin Liu — Huazhong Agricultural University, China

Lihua Ran — Second Institute of Oceanography, Ministry of Natural Resources, China

Jeffrey William Krause — Dauphin Island Sea Lab, United States

Paul J. Tréguer — Université de Bretagne Occidentale, France

Su Mei Liu — Ocean University of China, China

Citation

Moriceau, B., Liu, S., Ran, L., Krause, J. W., Tréguer, P. J., Liu, S. M., eds. (2024). *Biogeochemistry and genomics of silicification and silicifiers, volume II*. Lausanne: Frontiers Media SA. doi: 10.3389/978-2-8325-5378-7

Table of contents

frontiers | Frontiers in Marine Science

TYPE Original Research
PUBLISHED 27 July 2022
DOI 10.3389/fmars.2022.924452

OPEN ACCESS

EDITED BY
Brivaela Moriceau,
UMR6539 Laboratoire des Sciences de L'environnement Marin (LEMAR), France

REVIEWED BY
Anne Willem Omta,
Massachusetts Institute of Technology, United States
Shanying Tong,
Ludong University, China

*CORRESPONDENCE
Alessandra Norici
a.norici@univpm.it

SPECIALTY SECTION
This article was submitted to Marine Biogeochemistry, a section of the journal Frontiers in Marine Science

RECEIVED 20 April 2022
ACCEPTED 01 July 2022
PUBLISHED 27 July 2022

CITATION
Petrucciani A, Knoll AH and Norici A (2022) Si decline and diatom evolution: insights from physiological experiments. *Front. Mar. Sci.* 9:924452. doi: 10.3389/fmars.2022.924452

Si decline and diatom evolution: Insights from physiological experiments

Alessandra Petrucciani[1], Andrew H. Knoll[2] and Alessandra Norici[1,3]*

[1]Laboratory of Algal and Plant Physiology, Dipartimento di Scienze della Vita e dell'Ambiente, Università Politecnica delle Marche, Ancona, Italy, [2]Department of Organismic and Evolutionary Biology, Harvard University, Cambridge, MA, United States, [3]Faculty of Sciences, Shantou University-Università Politecnica delle Marche (STU-UNIVPM) Joint Algal Research Center, Shantou University, Shantou, China

In today's oceans, diatoms are abundant and diverse primary producers distinguished by their silica shells. Although molecular clocks suggest that diatoms arose as much as 250 million years ago (Ma), the earliest known diatom fossils date from 190 Ma, leading to the suggestion that early diatoms were at best lightly silicified. By the Cretaceous Period, large circular (in cross section) diatoms with highly silicified frustules thrived in surface oceans, only later to be joined by species with elongated and thinner frustules, as well as lower SiO_2 content. Decreased Si availability in surface oceans has been proposed as a principal driver of diatom evolution. Here, we investigate this through physiological experiments assessing the functional acclimation response of diatoms to reconstructed paleo-seawater. Four diatom species, differing in size and shape, were acclimated to reconstructed paleoenvironments mimicking Mesozoic/Cenozoic concentrations of nutrients in the presence of different Si regimes. When exposed to 500 µM Si, all populations, save for that of *Conticribra weissflogii*, became more highly silicified; the higher Si content per cell at 500 µM Si coincided with slower growth in small-sized cells. All species except *C. weissflogii* also showed lower photosynthetic efficiency as well as greater cell volume in comparison with diatoms acclimated to 205 or 25 µM Si. Average cell stoichiometry correlates with cell shape, but not size; pennates, in particular *Phaeodactylum tricornutum*, showed an acclimatory response to Si regimes, modulating Si use efficiency (the lower the external Si concentrations, the higher the C and N quotas per Si).

Experimental data suggest that in the densely silicified and bigger *C. weissflogii* grown at higher Si, diffusion of silicic acid across membranes made a larger contribution to Si uptake, saving energy which could be reallocated into growth. In contrast, for less highly silicified and smaller species, high energy costs of Si homeostasis needed to prevent the overaccumulation of

intracellular Si limited growth. While our experimental species reacted individualistically to changing silica availability, with distinct levels of plasticity, selective pressure associated with the temporal decline in Si availability may well have favored elongated shapes. Modern, less silicified species are unable to exploit high Si concentrations.

KEYWORDS

Si decline, diatom, paleo-reconstructed environments, algal physiology, selective pressure

Introduction

In the modern ocean, diatoms are abundant and diverse primary producers, distinguished by their silica shells, or frustules. Accounting for some 20% of primary production on Earth, diatoms sustain the global food web while being responsible for 240 Tmol of biogenic silica precipitation annually (Loucaides et al., 2012; Vallina et al., 2014; Malviya et al., 2016; Sutton et al., 2018; Vincent and Bowler, 2020; Tréguer et al., 2021). The oldest known diatom fossils occurred in Late Jurassic (ca. 165 million years old, Ma) amber (Girard et al., 2020), and since that time, diatoms have diversified to play a crucial role in ocean ecology (Armbrust, 2009); indeed, their radiation has molded marine ecosystems through time (Finkel and Kotrc, 2010; Kotrc and Knoll, 2015; Cermeño et al., 2015; Medlin, 2015; Knoll and Follows, 2016; Benoiston et al., 2017), affecting both the carbon and silica cycles (Siever, 1992; Ragueneau et al., 2006; Renaudie, 2016; Conley et al., 2017; Tréguer et al., 2018).

In Precambrian oceans, before the evolution of organisms with biomineralized skeletons, the concentration of dissolved silica (DSi) in seawater must have been much higher than today (Siever, 1992; Conley and Carey, 2015; Conley et al., 2017). The Ediacaran/Cambrian radiations of siliceous sponges and radiolarians established biology as a major component of the silica cycle, demonstrably changing the depositional dynamics of silica in the oceans (Maliva et al., 1989; Kidder and Tomescu, 2016) and probably decreasing the seawater DSi concentration (Conley et al., 2017). New biological influences emerged during the Mesozoic Era, as multiple clades of silica biomineralizing protists spread through the oceans (Kotrc and Knoll, 2015; Marron et al., 2016). Diatoms, in particular, are thought to have further drawn down DSi in surface seawater, leading to the low concentration (<30 μM) observed today (Racki and Cordey, 2000; Conley et al., 2017). Changes in hydrothermal fluxes and continental weathering can also have influenced DSi through time (Frings et al., 2016; Conley et al., 2017), but independent perspectives on orogenesis and seafloor spreading suggest that the Mesozoic-Cenozoic DSi decline was largely mediated by biology.

Within diatoms, the diversification of specialized transporters (silicon transporters, SIT) helped to make them the dominant marine DSi utilizers in Cenozoic oceans (Durkin et al., 2016; Fontorbe et al., 2017). As a consequence, competitors for this resource, principally radiolarians and sponges, show declines in test mass and/or environmental distribution (Harper and Knoll, 1975; Maldonado et al., 1999; Lazarus et al., 2009; Hendry et al., 2018). Diatoms themselves show a change in skeletal morphology through time, with a trend toward smaller, more elongated, and less highly silicified frustules toward the present (Finkel et al., 2005; Armbrust, 2009; Finkel and Kotrc, 2010). It is worth noting that factors other than DSi availability may have influenced the evolution of silicifiers (e.g., Finkel et al., 2005; Hendry et al., 2018) and that changing selectivity of preservation may also influence the observed record (Westacott et al., 2021). That noted, could changes in DSi availability have influenced the observed shifts in the fossil record? We hypothesize that decreasing DSi favored smaller and less silicified diatom cells in marine environments. To test this hypothesis, four morphologically distinct modern diatoms (*Chaetoceros muelleri*, *Conticribra weissflogii*, *Phaeodactylum tricornutum*, *Cylindrotheca fusiformis*) were acclimated to paleo-reconstructed environments according to Ratti et al. (2011), modified to mimic Mesozoic to modern changes in DSi concentration. As nutrient limitation is known to affect silica deposition and dissolution in diatoms (Takeda, 1998; Hutchins and Bruland, 1998; Boyle, 1998; De La Rocha et al., 2000; Mosseri et al., 2008; Finkel et al., 2010; Bucciarelli et al., 2010; Cohen et al., 2017; Meyerink et al., 2017; Panagiotopoulos et al., 2020), experiments using reconstructed seawater that include interpreted variation in the bioavailability of N, Fe, Zn, and Mo (Ratti et al., 2011; Giordano et al., 2018) better approximate ancient marine environments and their interactions with organisms. Growth, photosynthetic efficiency, organic and inorganic composition, and frustule morphology were assessed.

Material and methods

Algal cultures

Two centric diatom species, *Chaetoceros muelleri* (CCAP 1010/3, https://www.ccap.ac.uk/) and *Conticribra weissflogii* (*Thalassiosira weissflogii* in earlier literature; DCG 0320, https://bccm.belspo.be/about-us/bccm-dcg), and two raphid pennate diatoms characterized by thin frustules, *Cylindrotheca fusiformis* (NEPCC417) and *Phaeodactylum tricornutum* (DCG 0981), were acclimated for at least 10 generations to three newly designed growth media combining the Mesozoic/Cenozoic concentration of nutrients (as already published by Ratti et al., 2011; Table 1) and the presence of different Si regimes (Table 2) in AMCONA medium (Fanesi et al., 2014) buffered with 10 mM Tris–HCl, pH 8.0.

There are varying estimates for DSi levels in ancient oceans. Siever (1992) proposed that diatom evolution gradually reduced seawater DSi from some 1000 µM to its present level of<30 µM in most surface waters. In contrast, Conley et al. (2017) estimated that DSi concentrations of 500 µM in pre-diatom oceans fell rapidly to near-modern levels as diatoms began their radiation. Most recently, Trower et al. (2021) used Si isotope ratios to argue that DSi levels could have been as low as 150 µM in Paleozoic oceans. Regardless of the starting point, all conclude that diatom radiation reduced DSi concentrations in surface seawater. The DSi values used in our experiments were chosen to explore this range of estimated changes through time.

Acclimated batch cultures were established in 500ml flasks filled with 200 ml of medium and maintained in a culture chamber at 18°C, illuminated with cool white fluorescent lamps at 60 µmol m^{-2} s^{-1} and 12:12-h light–dark cycles. All experiments were carried out in the exponential growth phase.

Specific growth rate and cell volume

Cell number was measured using a CASY TT Cell Counter (Innovatis AG, Reutlingen, Germany). Aliquots of 100 µl of culture were diluted in 10 ml of an electrolyte solution (CASY TON; Innovatis AG). Cells were pumped into the cell counter through a 150µm capillary at a constant flow, and the number of cells was determined through the enumeration of events measured as change in conductivity. The same instrument was also used to measure the cellular size as the volume of electrolyte solution displaced by the passage of cells through a measuring pore (Palmucci et al., 2011). All determinations were carried out on samples from three distinct cultures. Specific growth rates, µ (1), were derived from daily counts of exponentially growing cells, carried out on a minimum of three distinct cultures for each treatment.

TABLE 1 Mesozoic/Cenozoic concentration of nutrients. Ratti et al., 2011.

Nutrient	Final concentration
NaNO3	10 µM
$FeCl_3 \cdot 6H_2O$	50 nM
$ZnSO_4 \cdot 7H_2O$	100 nM
$Na_2MoO_4 \cdot 2H_2O$	105 nM

TABLE 2 Silicic acid concentrations added to the Mesozoic/Cenozoic medium to mimic the progressive DSi depletion through geologic time.

Treatment	Si concentration
Pre- to early diatoms	500 µM
Intermediate	205 µM
Modern	25 µM

$$\mu = \frac{ln(N_t/N_0)}{t} \text{ Monod, J. (1949)} \quad (1)$$

where t is time (d), N_0 is the initial cell density (cell· ml^{-1}) at time 0, and N_t is the cell density at the considered time t.

Pigment quantification and photosynthetic efficiency

Algae were centrifuged at 1500 g for 5 min. Then, pigments were extracted from the pellet in 2 ml of 100% (v/v) methanol (Ritchie, 2006); the extracts were stored in the dark, at -20°C overnight. The colorless pellet was then separated from the supernatant by centrifugation at 13,000 g for 5 min. The absorbance of the supernatant was evaluated spectrophotometrically (Beckman DU 640 Spectrophotometer, Beckman Coulter) in a range from 750 to 350 nm (scan speed 0.5 nm). The absorbance (Abs) at wavelengths of 664, 630, and 470 nm was used for pigment quantification of chlorophyll *a*, chlorophyll c_1 + c_2, and carotenoids, respectively. Methanol absorbance was used as blank, and absorbance at 730 nm was subtracted to all measurements.

Chlorophyll (Chl) concentrations were calculated according to Ritchie, 2006 equations:

$$\text{Chl a}\left(\mu g\ ml^{-1}\right) = 13.2654 \cdot Abs_{664nm} - 2.6839 \cdot Abs_{630nm} \quad (2)$$

$$\text{Chl } C_1 + C_2\ \left(\mu g\ ml^{-1}\right) = 28.8191 \cdot Abs_{630nm} - 6.0138 \cdot Abs_{630nm} \quad (3)$$

$$Total\ \text{Chl}\ \left(\mu g \cdot mL^{-1}\right) = \text{Chl } a + \text{Chl } C_1 + C_2 \quad (4)$$

Carotenoids' concentrations were calculated according to Wellburn, 1994 equations:

$$Total\ carotenoids\ \left(\mu g \cdot ml^{-1}\right) = \left(1000 \cdot Abs_{470nm} - 1.63 \cdot Chla - 104.96 \cdot Ch\,C_1 + C_2\right)/221 \quad (5)$$

All results were expressed as pg of pigment per cell (Figure S2).

In vivo variable fluorescence of photosystem II (PSII) chlorophyll *a* (P_{680}) was analyzed using a Dual Pulse Amplitude Modulation (PAM) 100 fluorimeter (Heinz Walz GmbH, Effeltrich, Germany). Samples of 10^7 cells were collected by centrifugation at 1500 g for 5 min, resuspended in 2 ml of fresh growth medium, and dark-adapted for 10 min. Subsequently, samples were transferred into a glass cuvette for the PAM analysis under continuous stirring. The measuring light (40 µmol photons m^{-2} s^{-1}) was turned on to determine the F_0 value, the minimum value for chlorophyll fluorescence. Then, a saturation pulse (10,000 µmol photons m^{-2} s^{-1}, 600 ms) was applied to saturate all centers and allowed to measure the F_m value, the maximum value of fluorescence. The maximum quantum efficiency of PSII, F_v/F_m, was then calculated as follows:

$$\frac{F_V}{F_m} = \frac{(F_m - F_0)}{F_m} \quad (6)$$

F_v/F_m represents a robust indicator of the maximum quantum yield of PSII photochemistry (Misra et al., 2012). All parameters were obtained using the Dual PAM v1.8 software (Walz GmbH, Effeltrich, Germany).

Elemental composition

Cellular C and N contents were determined using an elemental analyzer (ECS 4010, Costech Italy) from 0.1 to 1 mg of dry cells washed twice with an ammonium formate solution isosmotic to the culturing media and dried at 80°C (Giordano et al., 2018). Sulfanilamide (C:N:S = 6:2:1) was used in a standard curve for quantification (Giordano et al., 2018). Data acquisition and analysis were performed with the software EAS Clarity (Costech Analytical Technologies Inc., Milano, Italy; organic composition). All measurements were carried out on three biological replicas.

Similarly prepared samples (0.5–1 mg of dry weight) were analyzed by an elemental analyzer (ECS 4010, Costech Italy) connected to the ID Micro EA isotope ratio mass spectrometer (Compact Science Systems, Lymedale Business Centre, Newcastle-Under-Lyme, United Kingdom) to obtain carbon and nitrogen stable isotope ($\delta^{13}C$ and $\delta^{15}N$) ratios. Urea was the isotopic standard reference showing $\delta^{13}C$ = −36.6‰ and $\delta^{15}N$ = -2.2‰; its replicates were used to normalize isotopic values of algal biomass. Two blank samples (empty aluminum capsules) were analyzed at the start of each analysis to verify that the CO_2 and N_2 backgrounds were low, and urea standards were also analyzed after every six samples to monitor instrument performance. Data acquisition and analysis were performed with the software EA IsoDelta (Compact Science Systems, Lymedale Business Centre, Newcastle-Under-Lyme, United Kingdom). All the measurements were carried out on three biological replicas.

The absolute abundance of silicon and elements other than C and N was measured using a total reflection X-ray fluorescence spectrometer (S2 PICOFOX, Bruker AXS Microanalysis GmbH, Berlin, Germany) according to Giordano et al. (2018). Sampled diatoms were washed twice with an ammonium formate solution isosmotic to the culturing media and resuspended in 250 µl of dH_2O. A solution of 0.1 g l^{-1} Ga (Sigma-Aldrich, St. Luis, MO, USA) in 5% HNO_3 was added as internal standard to a final concentration of 0.5 µl l^{-1}. The suspension was carefully vortexed, and an aliquot of 10 µl was deposed on a plastic sample holder, dried on a heating plate, and measured for 1,000 s. Spectral deconvolution and quantification of elemental abundances were performed by the Spectra 6.1 software (Bruker AXS Microanalysis GmbH, Berlin, Germany).

Organic composition

Diatoms collected during the exponential phase were washed twice with a 0.5M solution of ammonium formate and used to prepare samples for analysis of FTIR spectroscopy. Aliquots of 50 µl of cell suspension were transferred to a silicon window and dried at 80°C (Domenighini and Giordano, 2009). FTIR spectra on whole cells were acquired with a Tensor 27 FTIR spectrometer (Bruker Optics, Ettlingen, Germany). Bands were assigned to cellular pools as described by Giordano et al. (2001), and the relative abundances of lipids, carbohydrates, proteins, and silica were calculated *via* band integrals of deconvolved spectra, with OPUS 6.5 software (Bruker Optics GmbH, Ettlingen, Germany). Considering that silica absorbance (~1,075 cm^{-1}) masks some of the typical carbohydrate bands in diatoms, only the integrated value at ~1,150 cm^{-1} was used as proxy for carbohydrates (Palmucci et al., 2011). Semiquantification of carbohydrates and lipids was obtained by comparing the total protein content measured by a quantitative method (see below) with the FTIR absorbance ratio between the pool of interest and that of proteins according to Palmucci et al. (2011); the three macromolecular pools expressed in arbitrary units were normalized to the corresponding 500 µM of Si pool.

Protein content was measured according to the Lowry method described by Peterson (1977) on diatoms collected by centrifugation (13,000 g for 5 min) during the exponential phase. A volume of 500 µl 1% sodium dodecyl sulfate (SDS) and 0.1 mol l^{-1} of NaOH were added to the pellet to facilitate membrane disruption and solubilization of proteins. The tubes were vortexed and then incubated at room temperature for 10 min. A volume of 500 µl of reagent A (25% H_2O, 25% SDS 10%, 25%

NaOH 0.8M, 25% CTC reagent) was added, and the samples were vortexed and let to sit at room temperature for 10 min. A volume of 250 µl of reagent B (83.3% H_2O, 16.7% Folin and Cicalteau's phenol reagent) was then added, and samples were immediately vortexed vigorously; finally, they were incubated in the dark for 30 min. Afterward, the sample absorbance was measured in a Beckman DU 640 Spectrophotometer (Beckman Coulter) at 750 nm. Protein contents were calculated by interpolating absorbance data in a standard curve constructed with known concentrations of bovine serum albumin (BSA). All the measurements were carried out on three biological replicas, and results were expressed as pg of proteins per cell (Figure S4).

Frustule characterization through scanning electron microscopy

Diatom frustules were obtained through oxidation of the organic material using hydrogen peroxide, H_2O_2. Salts of the culture medium were washed out from the cells for three times with deionized water, then 30% H_2O_2 was added to the cell suspension to a final concentration of about 15%. Samples were dried in oven at 60°C for 1 day (less silicified species, *P. tricornutum* and *C. fusiformis*) or three days (more silicified species, *C. muelleri* and *C. weissflogii*). Finally, the material was washed four times with deionized water to carefully remove H_2O_2. Drops of cleaned material were then poured on a cellulose acetate and cellulose nitrate mixture filter (MF-Millipore™, mesh size 0,45 µm) fixed on conductive carbon adhesive discs pasted on the stub and left to dry completely at 50°C. The stub was then sputter-coated with a thin layer of gold–palladium in a Balzer Union evaporator and analyzed by SEM (High Resolution ZEISS – SUPRA 40). Images were obtained at different magnifications to make morphometric measurements of frustule details (raphe and fibulae in *C. fusiformis*, Reimann et al., 1965; setae and punctae in *C. muelleri*, Reinke, 1984) from at least 10 frustules per each of the three biological replicas.

Statistical analysis

Significant differences among the means of dependent variables in different paleoenvironments (independent variable) were tested with a one-way analysis of variance (ANOVA), followed by Tukey's *post-hoc* test. Macromolecular pools as dependent variables in response to paleoenvironments and according to diatom species (independent variables) were analyzed by two-way ANOVA, followed by Tukey's *post-hoc* test. Comparison of treatment pairs (morphological parameters at 500 and 25 µM Si, Table S2) was achieved with a two-tailed *t*-test. The level of significance was set at 0.05. GraphPad Prism 8.0.2.263 was used to carry out the tests (GraphPad Software, San Diego, CA, USA).

Results

Growth, cell volume, and photosynthetic efficiency

The four diatom populations were acclimated to reconstructed paleoenvironments. Growth of the smaller species *C. muelleri* and *P. tricornutum* was deeply affected by Si availability in the medium (Figure S1); specifically, the higher the DSi concentration, the lower the growth rate (Table 3). In fact, *C. muelleri* cells grew very slowly when DSi was 500 µM. The decrease in growth rate of these species was accompanied by an increase in cell volume (Table 3). Growth rates of the larger species *C. weissflogii* and *C. fusiformis* were similar among the three DSi treatments. High concentrations of silicic acid

TABLE 3 Average ± SD of specific growth rate (µ), cell volume, and *Fv/Fm* in the four diatoms acclimated to different paleoenvironments (n ≥ 3).

		500 µM Si	205 µM Si	25 µM Si
Specific growth rate (µ, day^{-1})	*C. muelleri*	0.13 ± 0.04^{a}	0.48 ± 0.08^{b}	0.54 ± 0.08^{b}
	C. weissflogii	0.28 ± 0.03	0.28 ± 0.01	0.25 ± 0.03
	P. tricornutum	0.29 ± 0.01^{a}	0.36 ± 0.02^{a}	0.58 ± 0.04^{b}
	C. fusiformis	0.41 ± 0.09	0.52 ± 0.05	0.47 ± 0.15
Cell volume (μm^3)	*C. muelleri*	581 ± 93^{a}	470 ± 55^{ab}	439 ± 56^{b}
	C. weissflogii	1352 ± 229^{a}	1713 ± 209^{b}	1459 ± 160^{ab}
	P. tricornutum	266 ± 50^{a}	143 ± 20^{b}	134 ± 50^{b}
	C. fusiformis	474 ± 64^{a}	363 ± 28^{b}	381 ± 75^{b}
Fv/Fm	*C. muelleri*	0.10 ± 0.05^{a}	0.41 ± 0.06^{b}	0.45 ± 0.08^{b}
	C. weissflogii	0.61 ± 0.14	0.72 ± 0.02	0.74 ± 0.03
	P. tricornutum	0.49 ± 0.04^{a}	0.67 ± 0.03^{b}	0.66 ± 0.02^{b}
	C. fusiformis	0.25 ± 0.05^{a}	0.60 ± 0.03^{b}	0.65 ± 0.01^{b}

Different letters indicate significant differences among conditions in the same species ($p > 0.05$, one-way ANOVA followed by Tukey's *post-hoc* test, results in Table S3).

mimicking a pre-diatom regime resulted in a lower maximum PSII Quantum Yield in dark-adapted cells, F_v/F_m, of *C. muelleri*, *P. tricornutum*, and *C. fusiformis*. In contrast, *C. weissflogii* did not show any change in photosynthetic efficiency (Table 3).

Elemental composition

When cells were subjected to different Si regimes during growth, all diatoms grown in the highest DSi condition except for *C. weissflogii* accumulated more Si per volume unit (Figure 1). The largest variation was observed in pennate diatoms, *C. fusiformis* and *P. tricornutum*, showing twice the content when the concentration of external silicic acid reached 500 µM as compared to contents in the other conditions. The same was true when the Si content was expressed on a per cell basis (Table S1).

The P cell quota had a similar trend to that of the Si cell quota (Table S1). Only *P. tricornutum* also showed significantly higher C, N, and Fe contents in the highest DSi condition (Table S1). In general, the C:N:P:S:Si ratio of the cells was inversely related to the concentration of silicic acid in the growth medium: lower amounts of assimilated C, N, P, and S per unit of cell Si with higher DSi availability (Table 4). Furthermore, the P cell quota increased with increasing DSi availability (Table S1). Only *P. tricornutum* also showed significantly higher C, N, and Fe contents in the highest DSi condition (Table S1), with the Fe : Si ratio remaining approximately constant across the different Si treatments (Table 4).

Interestingly, our centric and pennate diatoms show divergent trends in carbon isotopic fractionation across treatments (Figure 2). Centric diatoms significantly increased observed fractionation (more negative $\delta^{13}C$) as DSi decreased, just the opposite of observed trends in our pennate species. Also, a strong correlation (Pearson r = -0.99 in *P. tricornutum* and -0.96 in *C. fusiformis*, Figure S3) between the $\delta^{13}C$ and intracellular Si content was observed in pennate cells, but not in our centric species.

Organic composition

In cells of *C. muelleri*, *C. fusiformis*, and *P. tricornutum*, proteins were more abundant in response to higher silicic acid concentrations in the growth medium (Figure 3 and Figure S4). In pennate diatoms, the same trend was observed for the carbohydrate pool. Save for *C. weissflogii*, all diatoms did not significantly change the lipid pool in response to DSi treatment. Regarding macromolecular ratios, the cellular carbohydrate/lipid ratio showed C reallocation in all species (Table 5). In centric diatoms, the protein-to-carbohydrate ratio was not affected while the protein-to-lipid ratio was significantly higher in response to higher DSi availability (Table 5).

Frustule characterization through scanning electron microscopy

Frustule structure shows only limited variation as a function of treatment. In *C. muelleri*, setae were thicker when grown at high DSi, but not significantly (Figures 4C, D; Table S2). Neither

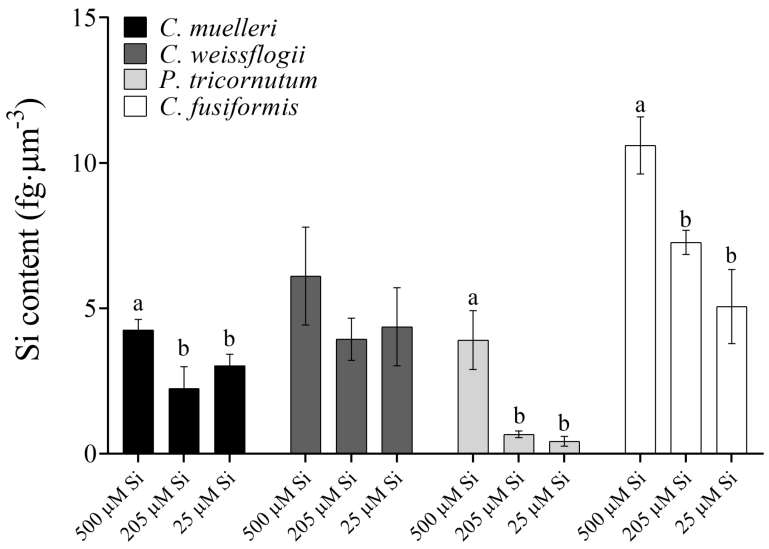

FIGURE 1
Si content per volume (fg·µm^{-3}) in the four diatoms acclimated to different paleoenvironments. Data are means of three biological replicas. Error bars show SD. Different letters represent significant differences among conditions in the same species ($p < 0.05$, one-way ANOVA followed by Tukey's *post-hoc* test, results in Table S3).

10.3389/fmars.2022.924452

TABLE 4 Cell stoichiometry in relation to Si content (pg·cell^{-1}) of the four diatoms acclimated to different paleoenvironments.

		C : Si	N : Si	P : Si	S : Si	Fe : Si
	500 µM Si	13.56 ± 3.14	2.66 ± 0.97	0.58 ± 0.03	0.18 ± 0.07	0.018 ± 0.007
C. muelleri	205 µM Si	11.23 ± 1.90	2.44 ± 0.39	0.47 ± 0.13	0.33 ± 0.09	0.144 ± 0.099
	25 µM Si	16.13 ± 6.65	3.30 ± 1.52	0.28 ± 0.17	0.26 ± 0.07	0.022 ± 0.002
	500 µM Si	2.38 ± 1.90	0.58 ± 0.57	0.013 ± 0.002	0.04 ± 0.01	0.001 ± 0.001
C. weissflogii	205 µM Si	1.22 ± 0.38	0.19 ± 0.08	0.021 ± 0.001	0.06 ± 0.02	0.006 ± 0.002
	25 µM Si	1.60 ± 0.84	0.19 ± 0.09	0.012 ± 0.007	0.10 ± 0.09	0.004 ± 0.001
	500 µM Si	20.90 ± 7.26^{a}	4.34 ± 0.54^{a}	0.50 ± 0.07^{a}	0.42 ± 0.06^{a}	0.083 ± 0.006
P. tricornutum	205 µM Si	78.01 ± 31.42^{b}	11.94 ± 4.36^{b}	2.67 ± 0.53^{b}	3.01 ± 0.42^{b}	0.078 ± 0.013
	25 µM Si	93.77 ± 14.44^{b}	12.93 ± 2.19^{b}	3.47 ± 0.62^{b}	4.27 ± 0.73^{c}	0.076 ± 0.006
	500 µM Si	3.57 ± 1.60^{a}	0.68 ± 0.29^{a}	0.16 ± 0.02	0.11 ± 0.08	0.034 ± 0.009^{ab}
C. fusiformis	205 µM Si	9.13 ± 1.09^{b}	1.74 ± 0.23^{b}	0.15 ± 0.01	0.11 ± 0.01	0.005 ± 0.001^{a}
	25 µM Si	5.29 ± 1.66^{ab}	0.66 ± 0.16^{ab}	0.15 ± 0.03	0.35 ± 0.29	0.016 ± 0.009^{b}

Data are means of three replicates ± SD. Different letters indicate significant differences among conditions in the same species ($p > 0.05$, one-way ANOVA followed by Tukey's *post-hoc* test, results in Table S3).

did *C. weissflogii* show any significant difference in frustule morphology as a function of treatment (Figure 4B). By contrast, the pennate species both showed a significant difference between frustules grown at high versus low DSi (Figure 5 and Table S2). Under high DSi, *P. tricornutum* frustules were significantly wider and raphes significantly thicker (Figures 5A, C, D), while the raphe in *C. fusiformis* was significantly wider (Figures 5B, E, F and Table S2).

Discussion

Paleontological and geochemical data support the hypothesis that diatom radiation drove a decline in the DSi of surface seawater that influenced the subsequent evolution of both diatoms and other organisms that form skeletons of silica (Finkel et al., 2005; Rabosky and Sorhannus, 2009; Conley et al., 2017; Hendry et al., 2018). At the same time, other factors, including climate change, orogenesis, and

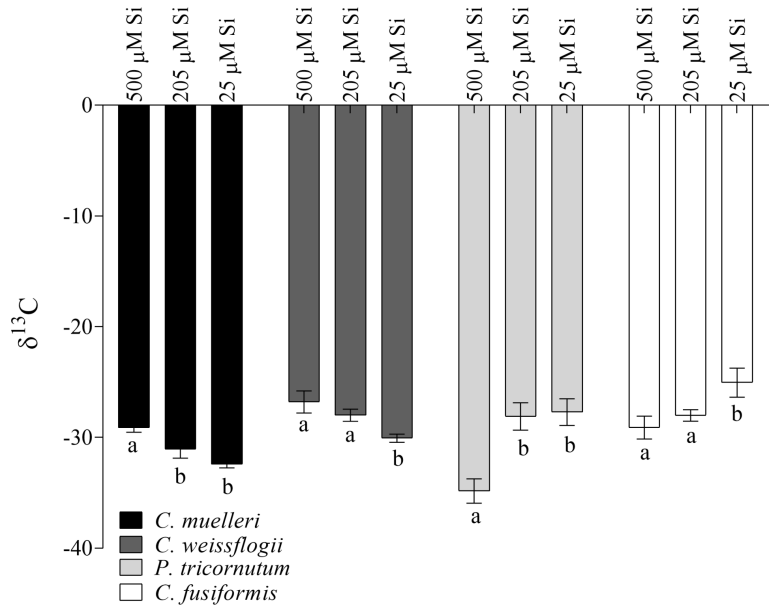

FIGURE 2
$\delta^{13}C$ values in the four diatoms acclimated to different paleoenvironments. Data are means of three biological replicas. Error bars show SD. Different letters represent significant differences among conditions in the same species ($p < 0.05$, one-way ANOVA followed by Tukey's *post hoc* test, results in Table S3).

10.3389/fmars.2022.924452

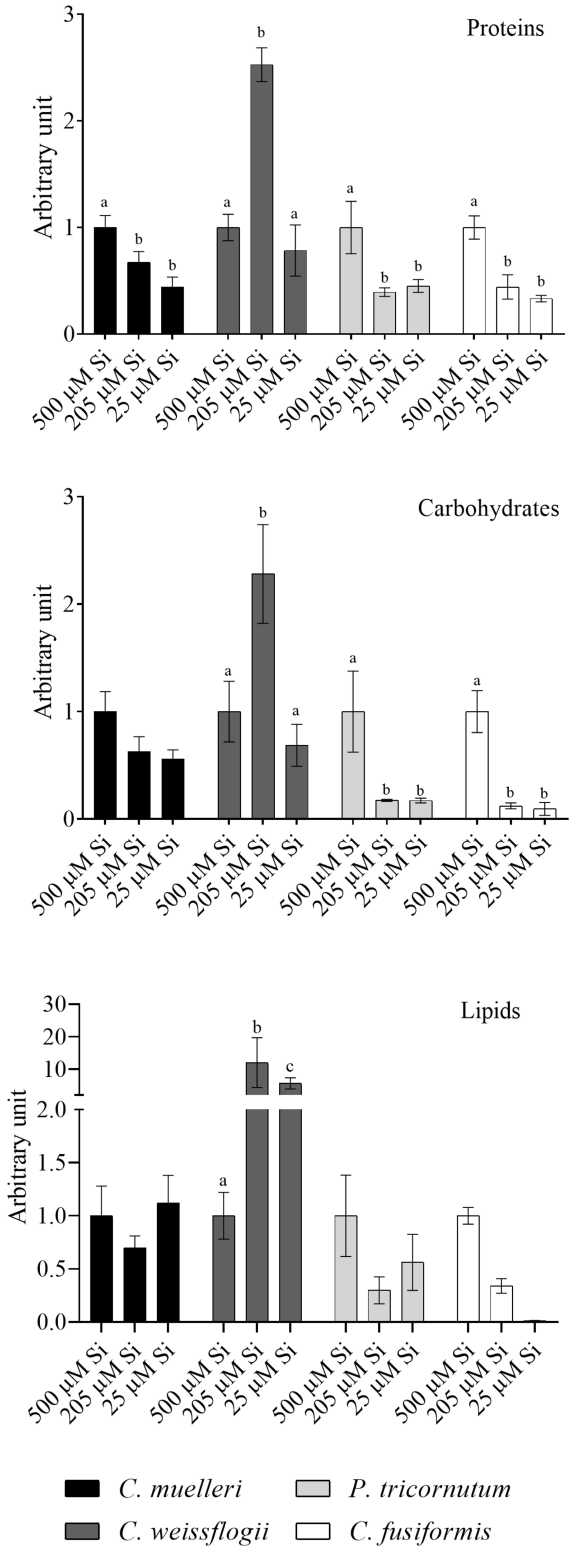

FIGURE 3
Protein, carbohydrates, and lipid pools in the four diatoms acclimated to different paleoenvironments. Data are means of three replicates. Error bars show SD. Different letters represent significant differences among conditions in the same species ($p < 0.05$, two-way ANOVA followed by Tukey's *post-hoc* test, results in **Table S3**).

TABLE 5 Macromolecular pool ratios (arbitrary unit) for the four diatoms acclimated to different paleoenvironments.

		500 µM Si	205 µM Si	25 µM Si
Proteins/carbohydrates	*C. muelleri*	0.89 ± 0.10	0.98 ± 0.22	0.72 ± 0.24
	C. weissflogii	0.31 ± 0.03	0.34 ± 0.08	0.34 ± 0.02
	P. tricornutum	0.79 ± 0.14^{a}	1.84 ± 0.66^{ab}	2.18 ± 0.65^{b}
	C. fusiformis	0.51 ± 0.11^{a}	1.79 ± 0.07^{ab}	2.24 ± 1.18^{b}
Proteins/lipids	*C. muelleri*	13.42 ± 2.46^{a}	12.57 ± 1.61^{a}	5.50 ± 2.60^{b}
	C. weissflogii	51.17 ± 11.46^{a}	6.80 ± 0.44^{b}	6.09 ± 0.26^{b}
	P. tricornutum	9.37 ± 1.70	12.83 ± 3.83	7.88 ± 2.25
	C. fusiformis	6.63 ± 0.61^{a}	8.73 ± 1.81^{a}	231 ± 72^{b}
Carbohydrates/lipids	*C. muelleri*	14.96 ± 3.01^{a}	13.21 ± 1.36^{a}	7.45 ± 0.96^{b}
	C. weissflogii	169 ± 57	36.77 ± 23.97	18.04 ± 1.47
	P. tricornutum	11.92 ± 0.13^{a}	7.79 ± 3.67^{ab}	3.63 ± 0.05^{b}
	C. fusiformis	13.26 ± 1.72^{a}	5.01 ± 0.99^{a}	57.12 ± 47.48^{b}

Data are means of three replicates ± SD. Letters represent significant differences among conditions in the same species ($p < 0.05$, one-way ANOVA followed by Tukey's *post-hoc* test, results in Table S3).

predation pressure, may have influenced both observed paleontological patterns and inferred temporal variation in seawater composition (Falkowski et al., 2004; Zachos et al., 2008; Ratti et al., 2013; Lazarus et al., 2014; Conley et al., 2017; Giordano et al., 2018; Petrucciani et al., 2022). The experiments reported here confirm that whatever other factors inform our understanding of Mesozoic–Cenozoic diatom evolution, declining DSi could have had a direct influence on diatom growth, physiology, and morphogenesis.

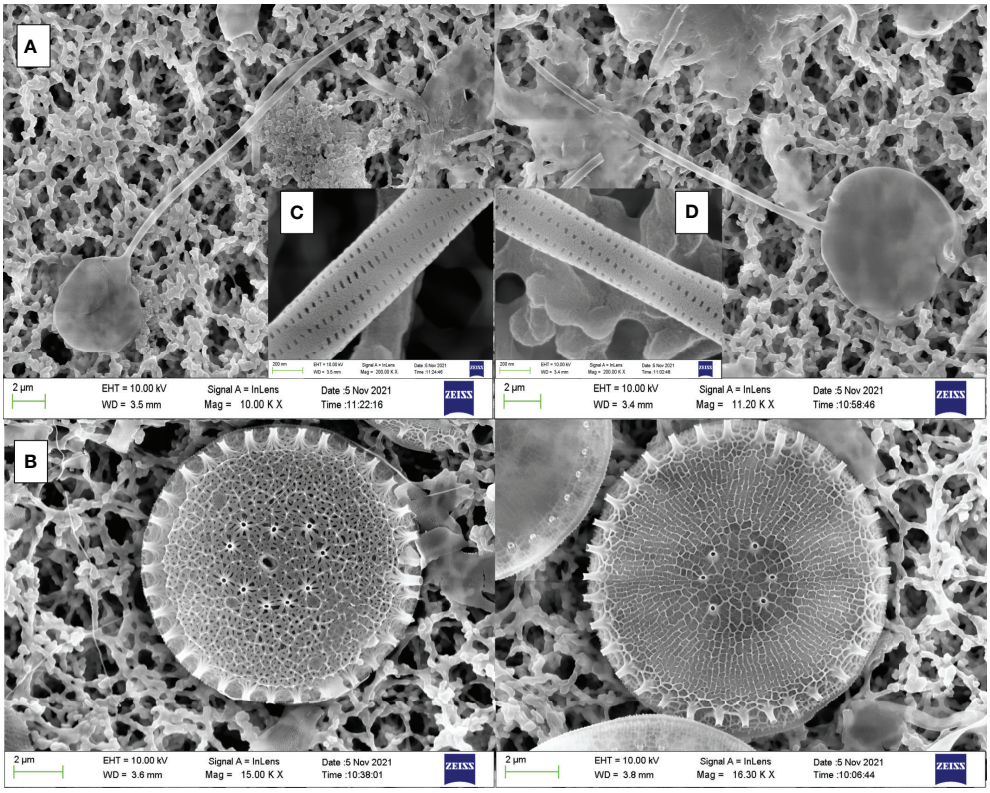

FIGURE 4
SEM images of frustules from *C. muelleri* **(A)** and *C. weissflogii* **(B)** acclimated to 500 µM Si (left images) and 25 µM Si (right images). Details of *C. muelleri* setae at 500 µM Si **(C)** and 25 µM Si **(D)** are shown.

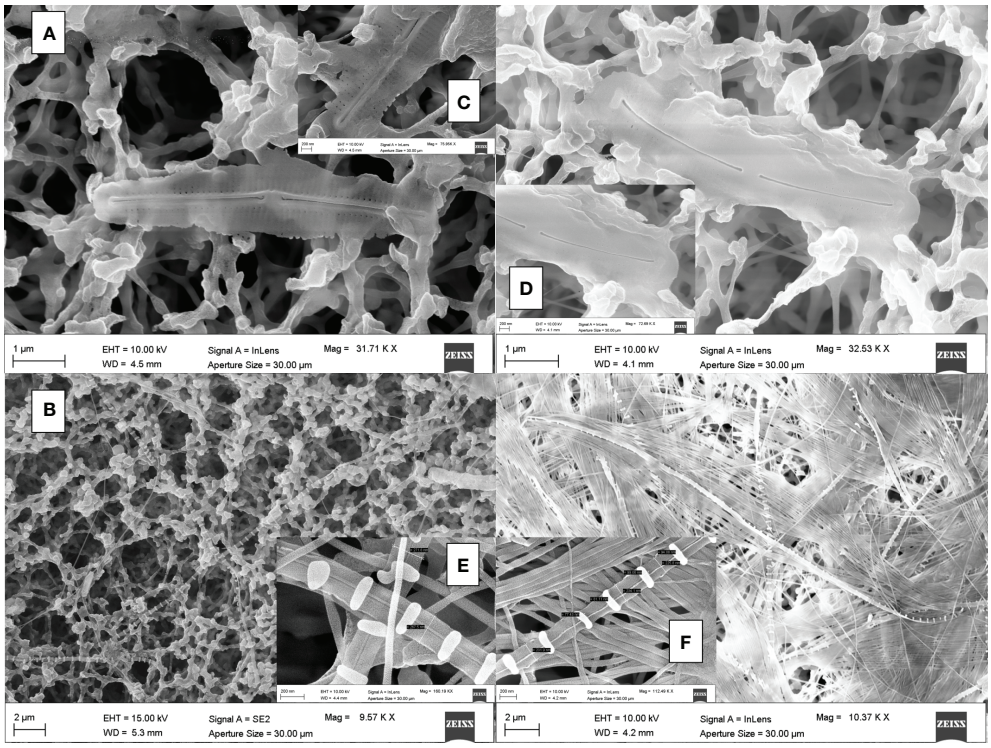

FIGURE 5
SEM images of frustules from *P. tricornutum* **(A)** and *C. fusiformis* **(B)** acclimated to 500 µM Si (left images) and 25 µM Si (right images). Details of *P. tricornutum* and *C. fusiformis* raphe at 500 µM Si (**(C, E)** respectively) and 25 µM Si (**(D, F)** respectively) are shown.

Growth in reconstructed paleoenvironments: facing high [DSi]

Perhaps counterintuitively, our experimental species did not grow better at high DSi concentrations; indeed, just the opposite occurred. All the diatoms in our experiments thrived at the low concentrations of N, Fe, Zn, Mo, and Si characteristic of modern oceans (Table 3 and Figure S1). In modern oceans, regional and seasonal Si limitation (i.e., in the Southern Ocean) is known to downregulate Si uptake and silicification in DSi users, including diatoms (Pinkerton et al., 2021). Nevertheless, diatoms maintain nearly maximal division rates (Olsen and Paasche, 1986). Our data underscore that different species show distinct responses to Si availability. In fact, although growth of the two smaller species, *C. muelleri* and *P. tricornutum*, was significantly lower at the highest DSi concentration (Table 3), the acclimation of *C. muelleri* to 500µM DSi concentration was strongly hampered (Figure S1) as the pennate species reached a stationary phase growth (Figure S1). The drastic reduction in photosynthetic efficiency was consistent with growth limitation (Table 3). It has been suggested that a high silicic acid concentration in the external medium can lead to cytotoxic effects (Marron et al., 2016) through auto-polymerization of intracellular soluble Si which then overaccumulates (Milligan et al., 2004).

Why a high external concentration of DSi should result in a high intracellular Si concentration is unclear. It is known that Si influx makes use of i) energy-dependent transporters for Si uptake (SIT), which have acquired the influx function in response to the scarce availability of Si in oceans, and ii) diffusion (Thamatrakoln et al., 2006; Thamatrakoln and Hildebrand, 2008; Hildebrand et al., 2018). On the other hand, Si efflux is an overlooked and poorly understood process in diatom metabolism. These originally utilized ancestral SITs requiring energy have been hypothesized, as do currently utilized SITs (Martin-Jezequel et al., 2000; Milligan et al., 2004; Thamatrakoln and Hildebrand, 2008; Shrestha and Hildebrand, 2015; Hildebrand et al., 2018). Our data (Table 3 and Figure S1) likely indicate that DSi uptake was not turned off by algal cells; direct damage due to intracellular Si polymerization and/or energy-dependent mechanisms to avoid it (i.e., counterbalancing Si influx with Si efflux) might affect growth as observed for *C. muelleri* and *P. tricornutum*. The effect was observed in less silicified and smaller species characterized by a higher S/V ratio and thus incurring a higher cost to maintain Si homeostasis than bigger cells (Table 3, Figure S1). It is particularly intriguing that in *P. tricornutum*, Fe : Si was the only ratio not modulated by Si availability in the external medium (Table 4). Nevertheless, when DSi was 500 µM, both Si and Fe cell quotas were higher (roughly 17 and 14 times, respectively) than those in modern Si-treated algae

(Table S1). This finding may add nuance to the observation that Fe deficiency leads to enhanced Si content (De La Rocha et al., 2000), suggesting that Fe is strongly involved in Si homeostasis. Further studies are needed to clarify how Fe interacts with Si influx/efflux/biomineralization.

The densely silicified and larger (hence, lower S/V ratio, Table 3 and Figure 1) cells of *C. weissflogii* had a different fate when grown under high DSi conditions (Table 3 and Figure S1). In the presence of higher environmental DSi concentrations, diffusion of silicic acid across membranes is supposed to make a bigger contribution to the Si uptake than it does in lower DSi growth conditions. This could explain why energy is saved and reallocated into *C. weissflogii* growth, assuming that DSi influx through SITs is less relevant and the efflux is not needed due to the high Si requirement for thicker *C. weissflogii* frustules. Only in this species did the photosynthetic efficiency remain unchanged by varying DSi levels (Table 3).

Cell composition in reconstructed paleoenvironments: facing high [DSi]

Cell composition in terms of macromolecular pools varied among treatments and in a shape-dependent manner. At high [DSi], our pre- to early diatom Si treatment cells of pennate diatoms were most costly (in terms of energy investment associated with the observed organic composition; Gerotto et al., 2020) and palatable (Palmucci et al., 2011; Ratti et al., 2013), preferentially allocating fixed C into carbohydrates and proteins (Figure 3, Table 5) as compared to the same species acclimated to modern Si treatment.

Data suggest that over geologic time, DSi availability has affected the overall C allocation pattern of diatoms (in particular pennates) and, therefore, predation pressure *via* its influence on palatability for predators. Thus, DSi decline has favored the evolution of energy-saving, less palatable cells, which are more competitive in intraspecific and interspecific interactions (Petrucciani et al., 2022).

Interestingly, Si availability also affected C isotopic fractionation: when DSi concentration was higher, pennate diatoms increased C fractionation (more negative $\delta^{13}C$) (Figure 2). This could be explained by a change in availability of intracellular inorganic carbon among growth regimes: in fact, a lower contribution of inorganic C mobilized from HCO_3^- to the fixed C in pennates grown in high DSi conditions results in increased discrimination against $^{13}CO_2$ (Korb et al., 1996; Keller and Morel, 1999; Vuorio et al., 2006). This may well reflect to a downregulation in pennates of CCM (Riebesell et al., 2000) in favor of other mandatory energy-dependent mechanisms such as Si deposition and Si efflux under high DSi conditions (Giordano et al., 2005; Giordano et al., 2017). Therefore, lower photosynthetic efficiencies were reported (Table 3). In any event, the correlation between silicon content and C fractionation observed in these species underscores the deep interaction between the two elements as well as between biomineralization and C fixation (Figure S3). This is somewhat unexpected, since in centric diatoms the uncoupling of silicon compared with carbon and nitrogen metabolisms was reported (Claquin et al., 2002; Suroy et al., 2015). The observed variations in isotopic fractionation also add further nuance to physiological and paleoenvironmental interpretations of organic carbon isotopes in Mesozoic and Cenozoic marine sediments (Hayes et al., 1999).

Greater availability of DSi was associated, as well, with a greater accumulation of Si in both cells (Figure 1, Table S1) and frustules (Figures 4 and 5), as also evident in the literature compilation of Finkel et al (2010). The high Si content was not simply a function of greater cell volume since Si content expressed on a per-volume basis was also higher in the 500µM Si treatment (Figure 1). In addition, a higher Si quota per cell in diatoms is known to be induced by a slower growth rate (Brzezinski et al., 1990; Friedrichs et al., 2013). Both factors (high DSi and low growth rate) were present when *C. muelleri* and *P. tricornutum* showed the highest Si content (Table 3 and Figure S1). The change in Si quota was striking in pennate diatoms (Figure 1 and Table S1), as shown by raphe thickening in *P. tricornutum* frustules (Figures 5A, B). The entire cellular stoichiometry was overturned (Table 4). *C. fusiformis* showed a similar trend, suggesting that the pennate diatoms acclimated to changing growth conditions by modulating Si use efficiency: the higher the available DSi in the environment, the lower the efficiency in its use (Table 4). In contrast, centric diatoms had a homeostatic behavior regarding their elemental stoichiometry: such strategy did not allow growth in *C. muelleri* and limited maximal cell density in *C. weissflogii* (Table 4 and Figure S1).

In conclusion, even with our small sample size, it becomes clear that diatom responses to changing silica bioavailability are commonly individualistic; that is, there may be few parameters for which diatoms universally respond in the same way. The centric and pennate species in our experiments commonly responded in different ways or to different degrees, suggesting that centrics and pennates may show broad and consistent differences in their physiological responses to changing DSi levels.

While we cannot discount climate change and changing preservational selectivity as influences on the observed fossil record of diatoms, the experimental approach used here acclimating algal species to reconstructed paleoenvironments bolsters the case that decreasing [DSi] had an important influence on diatom biomineralization through time. In particular, the observed physiological responses of pennate species may have helped to drive their differential diversification, governing reduced size and silica usage in diatoms as a group.

Data availability statement

The original contributions presented in the study are included in the article/supplementary material. Further inquiries can be directed to the corresponding author.

Author contributions

AP carried out all the experiments and analyzed the data. AHK designed the paleo-reconstructed media and provided a geological perspective to the manuscript. AN conceived and designed the project. AP, AHK, and AN wrote the paper. All authors contributed to the article and approved the submitted version.

Funding

Research for AP PhD project was partially funded by Cariverona Foundation, Italy.

Acknowledgments

Special gratitude goes to the late Mario Giordano who encouraged experiments to test geologically inspired hypotheses for observed patterns.

Conflict of interest

The authors declare that the research was conducted in the absence of any commercial or financial relationships that could be construed as a potential conflict of interest.

Publisher's note

Supplementary material

The Supplementary Material for this article can be found online at: https://www.frontiersin.org/articles/10.3389/fmars.2022.924452/full#supplementary-material.

References

Armbrust, E. V. (2009). The life of diatoms in the world's oceans. *Nature* 459, 185–192. doi: 10.1038/nature08057

Benoiston, A. S., Ibarbalz, F. M., Bittner, L., Guidi, L., Jahn, O., Dutkiewicz, S., et al. (2017). The evolution of diatoms and their biogeochemical functions. *Phil. Trans. R. Soc B* 372, 20160397. doi: 10.1098/rstb.2016.0397

Boyle, E. (1998). Pumping iron makes thinner diatoms. *Nature* 393, 733–734. doi: 10.1038/31585

Brzezinski, M., Olson, R., and Chisholm, S. (1990). Silicon availability and cell-cycle progression in marine diatoms. *Mar. Ecol. Prog. Ser.* 67, 83–96. doi: 10.3354/meps067083

Bucciarelli, E., Pondaven, P., and Sarthou, G. (2010). Effects of an iron-light co-limitation on the elemental composition (Si, c, n) of the marine diatoms *Thalassiosira oceanica* and *Ditylum brightwellii*. *Biogeosciences* 7 (2), 657–669. doi: 10.5194/bg-7-657-2010

Cermeño, P., Falkowski, P. G., Romero, O. E., Schaller, M. F., and Vallina, S. M. (2015). Continental erosion and the Cenozoic rise of marine diatoms. *Proc. Natl. Acad. Sci. U.S.A.* 112, 4239–4244. doi: 10.1073/pnas.1412883112

Claquin, P., Martin-Jézéquel, V., Kromkamp, J. C., Veldhuis, M. J. W., and Kraay, G. W. (2002). Uncoupling of silicon compared with carbon and nitrogen metabolisms and the role of the cell cycle in continuous cultures of thalassiosira pseudonana (bacillariophyceae) under light, nitrogen, and phosphorus control. *J. Phycology* 38, 922–930. doi: 10.1046/j.1529-8817.2002.t01-1-01220.x

Cohen, N. R., Ellis, K. A., Lampe, R. H., McNair, H., Twining, B. S., Maldonado, M. T., et al. (2017). Diatom transcriptional and physiological responses to changes in iron bioavailability across ocean provinces. *Front. Mar. Sci.* 4. doi: 10.3389/fmars.2017.00360

Conley, D. J., and Carey, J. C. (2015). Silica cycling over geologic time. *Nat. Geosci* 8, 431–432. doi: 10.1038/ngeo2454

Conley, D. J., Frings, P. J., Fontorbe, G., Clymans, W., Stadmark, J., Hendry, K. R., et al. (2017). Biosilicification drives a decline of dissolved si in the oceans through geologic time. *Front. Mar. Sci.* 4. doi: 10.3389/fmars.2017.00397

De La Rocha, C., Hutchins, D., Brzezinski, M., and Zhang, Y. (2000). Effects of iron and zinc deficiency on elemental composition and silica production by diatoms. *Mar. Ecol. Prog. Ser.* 195, 71–79. doi: 10.3354/meps195071

Domenighini, A., and Giordano, M. (2009). Fourier Transform infrared spectroscopy of microalgae as a novel tool for biodiversity studies, species identification, and the assessment of water quality 1. *J. phycology* 45 (2), 522–531. doi: 10.1111/j.1529-8817.2009.00662.x

Durkin, C. A., Koester, J. A., Bender, S. J., and Armbrust, E. V. (2016). The evolution of silicon transporters in diatoms. *J. phycology* 52, 716–731. doi: 10.1111/jpy.12441

Falkowski, P. G., Katz, M. E., Knoll, A. H., Quigg, A., Raven, J. A., Schofield, O., et al. (2004). The evolution of modern eukaryotic phytoplankton. *Science* 305, 354–360. doi: 10.1126/science.1095964

Fanesi, A., Raven, J. A., and Giordano, M. (2014). Growth rate affects the responses in the green alga *Tretaselmis suecica* to the external perturbation. *Plant Cell Environ.* 37 (2), 512–519. doi: 10.1111/pce.12176

Finkel, Z. V., Katz, M. E., Wright, J. D., Schofield, O. M. E., and Falkowski, P. G. (2005). Climatically driven macroevolutionary patterns in the size of marine diatoms over the Cenozoic. *Proc. Natl. Acad. Sci.* 102, 8927–8932. doi: 10.1073/pnas.0409907102

Finkel, Z. V., and Kotrc, B. (2010). Silica use through time: macroevolutionary change in the morphology of the diatom fustule. *Geomicrobiology J.* 27, 596–608. doi: 10.1080/01490451003702941

Finkel, Z. V., Matheson, K. A., Regan, K. S., and Irwin, A. J. (2010). Genotypic and phenotypic variation in diatom silicification under paleo-oceanographic conditions: Diatom silicification. *Geobiology* 8, 433–445. doi: 10.1111/j.1472-4669.2010.00250.x

Fontorbe, G., Frings, P. J., de la Rocha, C. L., Hendry, K. R., Carstensen, J., and Conley, D. J. (2017). Enrichment of dissolved silica in the deep equatorial pacific during the Eocene-oligocene: Equatorial pacific DSi enrichment. *Paleoceanography* 32, 848–863. doi: 10.1002/2017PA003090

Friedrichs, L., Hörnig, M., Schulze, L., Bertram, A., Jansen, S., and Hamm, C. (2013). Size and biomechanic properties of diatom frustules influence food uptake by copepods. *Mar. Ecol. Prog. Ser.* 481, 41–51. doi: 10.3354/meps10227

Frings, P. J., Clymans, W., Fontorbe, G., de la Rocha, C. L., and Conley, D. J. (2016). The continental Si cycle and its impact on the ocean Si isotope budget. *Chem. Geology* 425, 12–36. doi: 10.1016/j.chemgeo.2016.01.020

Gerotto, C., Norici, A., and Giordano, M. (2020). Toward enhanced fixation of CO2 in aquatic biomass: Focus on microalgae. *Front. Energy Res.* 8. doi: 10.3389/fenrg.2020.00213

Giordano, M., Beardall, J., and Raven, J. A. (2005). CO_2 concentrating mechanisms in algae: mechanisms, environmental modulation, and evolution. *Annu. Rev. Plant Biol.* 56, 99–131. doi: 10.1146/annurev.arplant.56.032604.144052

Giordano, M., Kansiz, M., Heraud, P., Beardall, J., Wood, B., and McNaughton, D. (2001). Fourier Transform infrared spectroscopy as a novel tool to investigate

changes in intracellular macromolecular pools in the marine microalga chaetoceros muellerii (bacillariophyceae). *J. Phycology* 37, 271–279. doi: 10.1046/j.1529-8817.2001.037002271.x

Giordano, M., Norici, A., and Beardall, J. (2017). Impact of inhibitors of amino acid, protein, and RNA synthesis on c allocation in the diatom *Chaetoceros muellerii*: a FTIR approach. *ALGAE* 32, 161–170. doi: 10.4490/algae.2017.32.6.6

Giordano, M., Olivieri, C., Ratti, S., Norici, A., Raven, J. A., and Knoll, A. H. (2018). A tale of two eras: Phytoplankton composition influenced by oceanic paleochemistry. *Geobiology* 16, 498–506. doi: 10.1111/gbi.12290

Girard, V., Saint Martin, S., Buffetaut, E., Saint Martin, J. P., Néraudeau, D., Peyrot, D., et al. (2020). Thai Amber: insights into early diatom history? *Bull. la Société Géologique France* 2020 191 (1), 23. doi: 10.1051/bsgf/2020028

Harper, H. E., and Knoll, A. H. (1975). Silica, diatoms, and Cenozoic radiolarian evolution. *Geol* 3, 175. doi: 10.1130/0091-7613(1975)3<175:SDACRE>2.0.CO;2

Hayes, J. M., Strauss, H., and Kaufman, A. J. (1999). The abundance of ^{13}C in marine organic matter and isotopic fractionation in the global biogeochemical cycle of carbon during the past 800 ma. *Chem. Geology* 161, 103–125. doi: 10.2475/ajs.289.4.436

Hendry, K. R., Marron, A. O., Vincent, F., Conley, D. J., Gehlen, M., Ibarbalz, F. M., et al. (2018). Competition between silicifiers and non-silicifiers in the past and present ocean and its evolutionary impacts. *Front. Mar. Sci.* 5. doi: 10.3389/fmars.2018.00022

Hildebrand, M., Lerch, S. J. L., and Shrestha, R. P. (2018). Understanding diatom cell wall silicification-moving forward. *Front. Mar. Sci.* 5. doi: 10.3389/fmars.2018.00125

Hutchins, D. A., and Bruland, K. W. (1998). Iron-limited diatom growth and Si: N uptake ratios in a coastal upwelling regime. *Nature* 393, 561–564. doi: 10.1038/31203

Keller, K., and Morel, F. (1999). A model of carbon isotopic fractionation and active carbon uptake in phytoplankton. *Mar. Ecol. Prog. Ser.* 182, 295–298. doi: 10.3354/meps182295

Kidder, D. L., and Tomescu, I. (2016). Biogenic chert and the Ordovician silica cycle. *Palaeogeography Palaeoclimatology Palaeoecol.* 458, 29–38. doi: 10.1016/j.palaeo.2015.10.013

Knoll, A. H., and Follows, M. J. (2016). A bottom-up perspective on ecosystem changes in mesozoic oceans. *Proc. R. Soc B.* 283, 20161755. doi: 10.1098/rspb.2016.1755

Korb, R., Raven, J., Johnston, A., and Leftley, J. (1996). Effects of cell size and specific growth rate on stable carbon isotope discrimination by two species of marine diatom. *Mar. Ecol. Prog. Ser.* 143, 283–288. doi: 10.3354/meps143283

Kotrc, B., and Knoll, A. H. (2015). A morphospace of planktonic marine diatoms. i. two views of disparity through time. *Paleobiology* 41, 45–67. doi: 10.1017/pab.2014.4

Lazarus, D., Barron, J., Renaudie, J., Diver, P., and Türke, A. (2014). Cenozoic Planktonic marine diatom diversity and correlation to climate change. *PloS One* 9, e84857. doi: 10.1371/journal.pone.0084857

Lazarus, D. B., Kotrc, B., Wulf, G., and Schmidt, D. N. (2009). Radiolarians decreased silicification as an evolutionary response to reduced Cenozoic ocean silica availability. *Proc. Natl. Acad. Sci.* 106, 9333–9338. doi: 10.1073/pnas.0812979106

Loucaides, S., Van Cappellen, P., Roubeix, V., Moriceau, B., and Ragueneau, O. (2012). Controls on the recycling and preservation of biogenic silica from biomineralization to burial. *Silicon* 4, 7–22. doi: 10.1007/s12633-011-9092-9

Maldonado, M., Carmona, M. C., Uriz, M. J., and Cruzado, A. (1999). Decline in mesozoic reef-building sponges explained by silicon limitation. *Nature* 401, 785–788. doi: 10.1038/44560

Maliva, R. G., Knoll, A. H., and Siever, R. (1989). Secular change in chert distribution: a reflection of evolving biological participation in the silica cycle. *PALAIOS* 4, 519. doi: 10.2307/3514743

Malviya, S., Scalco, E., Audic, S., Vincent, F., Veluchamy, A., Poulain, J., et al. (2016). Insights into global diatom distribution and diversity in the world's ocean. *Proc. Natl. Acad. Sci. U.S.A.* 113, E1516–E1525. doi: 10.1073/pnas.1509523113

Marron, A. O., Ratcliffe, S., Wheeler, G. L., Goldstein, R. E., King, N., Not, F., et al. (2016). The evolution of silicon transport in eukaryotes. *Mol. Biol. Evol.* 33, 3226–3248. doi: 10.1093/molbev/msw209

Martin-Jezequel, V., Hildebrand, M., and Brzezinski, M. A. (2000). Silicon metabolism in diatoms: implications for growth. *J. Phycol* 36, 821–840. doi: 10.1046/j.1529-8817.2000.00019.x

Medlin, L. K. (2015). A timescale for diatom evolution based on four molecular markers: reassessment of ghost lineages and major steps defining diatom evolution. *Vie Milieu* 65 (4), 821–840.

Meyerink, S., Ellwood, M. J., Maher, W. A., and Strzepek, R. (2017). Iron availability influences silicon isotope fractionation in two southern ocean diatoms (*Proboscia inermis* and *Eucampia antarctica*) and a coastal diatom (*Thalassiosira pseudonana*). *Front. Mar. Sci.* 4, 217. doi: 10.3389/fmars.2017.00217

Milligan, A. J., Varela, D. E., Brzezinski, M. A., and Morel, F. M. M. (2004). Dynamics of silicon metabolism and silicon isotopic discrimination in a marine diatomas a function of pCO_2. *Limnol. Oceanogr.* 49, 322–329. doi: 10.4319/lo.2004.49.2.0322

Misra, A. N., Misra, M., and Singh, R. (2012). Chlorophyll fluorescence in plant biology. *Biophysics.* 49, 322–329. doi: 10.4319/lo.2004.49.2.0322

Monod, J. (1949). The growth of bacterial cultures. *Annu. Rev. Microbiol.* 3, 371–394. doi: 10.1146/annurev.mi.03.100149.002103

Mosseri, J., Quéguiner, B., Armand, L., and Cornet-Barthaux, V. (2008). Impact of iron on silicon utilization by diatoms in the southern ocean: A case study of Si/N cycle decoupling in a naturally iron-enriched area. *Deep Sea Res. Part II: Topical Stud. Oceanography* 55, 801–819. doi: 10.1016/j.dsr2.2007.12.003

Olsen, S., and Paasche, E. (1986). Variable kinetics of silicon-limited growth in *Thalassiosira pseudonana* (Bacillariophyceae) in response to changed chemical composition of the growth medium. *Br. Phycological J.* 21, 183–190. doi: 10.1080/00071618600650211

Palmucci, M., Ratti, S., and Giordano, M. (2011). Ecological and evolutionary implications of carbon allocation in marine phytoplankton as a function of nitrogen availability: a fourier transform infrared spectroscopy approach1: c allocation as a function of n availability. *J. Phycology* 47, 313–323. doi: 10.1111/j.1529-8817.2011.00963.x

Panagiotopoulos, C., Goutx, M., Suroy, M., and Moriceau, B. (2020). Phosphorus limitation affects the molecular composition of *Thalassiosira weissflogii* leading to increased biogenic silica dissolution and high degradation rates of cellular carbohydrates. *Organic Geochemistry* 148, 104068. doi: 10.1016/j.orggeochem.2020.104068

Peterson, G. L. (1977). A simplification of the protein assay method of lowry et al. which is more generally applicable. *Analytical Biochem. 83* 2, 346–356. doi: 10.1016/0003-2697(77)90043-4

Petrucciani, A., Chaerle, P., and Norici, A. (2022). Diatoms versus copepods: could frustule traits have a role in avoiding predation? *Front. Mar. Sci.* 8. doi: 10.3389/fmars.2021.804960

Pinkerton, M. H., Boyd, P. W., Deppeler, S., Hayward, A., Höfer, J., and Moreau, S. (2021). Evidence for the impact of climate change on primary producers in the southern ocean. *Front. Ecol. Evol.* 9, 592027. doi: 10.3389/fevo.2021.592027

Rabosky, D. L., and Sorhannus, U. (2009). Diversity dynamics of marine planktonic diatoms across the Cenozoic. *Nature* 457, 183–186. doi: 10.1038/nature07435

Racki, G., and Cordey, F. (2000). Radiolarian palaeoecology and radiolarites: is the present the key to the past? *Earth-Science Rev.* 52, 83–120. doi: 10.1016/S0012-8252(00)00024-6

Ragueneau, O., Schultes, S., Bidle, K., Claquin, P., and Moriceau, B. (2006). Si And c interactions in the world ocean: Importance of ecological processes and implications for the role of diatoms in the biological pump: Si and c interactions in the ocean. *Global Biogeochem. Cycles* 20, n/a–n/a. doi: 10.1029/2006GB002688

Ratti, S., Knoll, A. H., and Giordano, M. (2011). Did sulfate availability facilitate the evolutionary expansion of chlorophyll a+c phytoplankton in the oceans? sulfate and evolution of chlorophyll a+c phytoplankton. *Geobiology* 9, 301–312. doi: 10.1111/j.1472-4669.2011.00284.x

Ratti, S., Knoll, A. H., and Giordano, M. (2013). Grazers and phytoplankton growth in the oceans: an experimental and evolutionary perspective. *PloS One* 8, e77349. doi: 10.1371/journal.pone.0077349

Reimann, B. E. F., Lewin, J. C., and Volcani, B. E. (1965). Studies on the biochemistry and fine structure of silica shell formation in diatoms: I. the structure of the cell wall of *Cylindrotheca fusiformis*. *J. Cell Biol.* 24, 39–55. doi: 10.1083/jcb.24.1.39

Reinke, D. C. (1984). Ultrastructure of *Chaetoceros muelleri* (bacillariophyceae): auxospore, resting spore and vegetative cell morphology. *J. Phycology* 20, 153–155. doi: 10.1111/j.0022-3646.1984.00153.x

Renaudie, J. (2016). Quantifying the Cenozoic marine diatom deposition history: links to the c and Si cycles. *Biogeosciences* 13, 6003–6014. doi: 10.5194/bg-13-6003

Riebesell, U., Burkhardt, S., Dauelsberg, A., and Kroon, B. (2000). Carbon isotope fractionation by a marine diatom: dependence on the growth-rate-limiting resource. *Mar. Ecol. Prog. Ser.* 193, 295–303. doi: 10.3354/meps193295

Ritchie, R. J. (2006). Consistent sets of spectrophotometric chlorophyll equation for acetone, methanol, and ethanol solvents. *Photosynthesis Res.* 89, 27–41. doi: 10.1007/s11100-006-9065-9

Shrestha, R. P., and Hildebrand, M. (2015). Evidence for a regulatory role of diatom silicon transporters in cellular silicon responses. *Eukaryot Cell* 14, 29–40. doi: 10.1128/EC.00209-14

Siever, R. (1992). The silica cycle in the precambrian. *Geochimica Cosmochimica Acta* 56, 3265–3272. doi: 10.1016/0016-7037(92)90303-Z

Suroy, M., Panagiotopoulos, C., Boutorh, J., Goutx, M., and Moriceau, B. (2015). Degradation of diatom carbohydrates: A case study with n- and Si-stressed thalassiosira weissflogii. *J. Exp. Mar. Biol. Ecol.* 470, 1–11. doi: 10.1016/j.jembe.2015.04.018

Sutton, J. N., André, L., Cardinal, D., Conley, D. J., de Souza, G. F., Dean, J., et al. (2018). A review of the stable isotope bio-geochemistry of the global silicon cycle and its associated trace elements. *Front. Earth Sci.* 5, 112. doi: 10.3389/feart.2017.00112

Takeda, S. (1998). Influence of iron availability on nutrient consumption ratio of diatoms in oceanic waters. *Nature* 393, 774–777. doi: 10.1038/31674

Thamatrakoln, K., Alverson, A. J., and Hildebrand, M. (2006). Comparative sequence analysis of diatom silicon transporters: toward a mechanistic model of silicon transport. *J. Phycology* 42, 822–834. doi: 10.1111/j.1529-8817.2006.00233.x

Thamatrakoln, K., and Hildebrand, M. (2008). Silicon uptake in diatoms revisited: a model for saturable and nonsaturable uptake kinetics and the role of silicon transporters. *Plant Physiol.* 146, 1397–1407. doi: 10.1104/pp.107.107094

Tréguer, P., Bowler, C., Moriceau, B., Dutkiewicz, S., Gehlen, M., Aumont, O., et al. (2018). Influence of diatom diversity on the ocean biological carbon pump. *Nat. Geosci* 11, 27–37. doi: 10.1038/s41561-017-0028-x

Tréguer, P. J., Sutton, J. N., Brzezinski, M., Charette, M. A., Devries, T., Dutkiewicz, S., et al. (2021). Reviews and syntheses: The biogeochemical cycle of silicon in the modern ocean. *Biogeosciences* 18, 1269–1289. doi: 10.5194/bg-18-1269-2021

Trower, E. J., Strauss, J. V., Sperling, E. A., and Fischer, W. W. (2021). Isotopic analyses of Ordovician–Silurian siliceous skeletons indicate silica-depleted Palaeozoic oceans. *Geobiology* 19, 460–472. doi: 10.1111/gbi.12449

Vallina, S. M., Follows, M. J., Dutkiewicz, S., Montoya, J. M., Cermeno, P., and Loreau, M. (2014). Global relationship between phytoplankton diversity and productivity in the ocean. *Nat. Commun.* 5, 4299. doi: 10.1038/ncomms5299

Vincent, F., and Bowler, C. (2020). Diatoms are selective segregators in global ocean planktonic communities. *mSystems* 5 (1), e00444–19. doi: 10.1128/mSystems.00444-19

Vuorio, K., Meili, M., and Sarvala, J. (2006). Taxon-specific variation in the stable isotopic signatures ($\delta^{13}C$ and $\delta^{15}N$) of lake phytoplankton. *Freshw. Biol.* 51, 807–822. doi: 10.1111/j.1365-2427.2006.01529.x

Wellburn, A. R. (1994). The spectral determination of chlorophylls a and b, as well as total carotenoids, using various solvents with spectrophotometers of different resolution. *J. Plant Physiol.* 1443, 307–313. doi: 10.1016/S0176-1617(11)81192-2

Westacott, S., Planavsky, N. J., Zhao, M. Y., and Hull, P. M. (2021). Revisiting the sedimentary record of the rise of diatoms. *PNAS* 118 (27), e2103517118. doi: 10.1073/pnas.2103517118

Zachos, J. C., Dickens, G. R., and Zeebe, R. E. (2008). An early Cenozoic perspective on greenhouse warming and carbon-cycle dynamics. *Nature* 451, 279–283. doi: 10.1038/nature06588

frontiers | Frontiers in Marine Science

TYPE Original Research
PUBLISHED 12 August 2022
DOI 10.3389/fmars.2022.875415

OPEN ACCESS

EDITED BY
Ludvig Löwemark,
National Taiwan University, Taiwan

REVIEWED BY
Zhifei Liu,
Tongji University, China
Xiangbin Ran,
Ministry of Natural Resources, China
Shaily Rahman,
University of Colorado Boulder, United States

*CORRESPONDENCE
Lihua Ran
lihuaran@sio.org.cn
Jianfang Chen
jfchen@sio.org.cn

SPECIALTY SECTION
This article was submitted to Marine Biogeochemistry, a section of the journal Frontiers in Marine Science

RECEIVED 14 February 2022
ACCEPTED 28 July 2022
PUBLISHED 12 August 2022

CITATION
Liang W, Ran L, Yang Z, Wiesner MG, Liang Y, Sun L and Chen J (2022) Underestimation of biogenic silica sinking flux due to dissolution in sediment traps: A case study in the South China Sea.
Front. Mar. Sci. 9:875415.
doi: 10.3389/fmars.2022.875415

Underestimation of biogenic silica sinking flux due to dissolution in sediment traps: A case study in the South China Sea

Wen Liang[1,2], Lihua Ran[1,3,4]*, Zhi Yang[1], Martin G. Wiesner[3], Yuzhao Liang[1,5], Lin Sun[1] and Jianfang Chen[1,3]*

[1]Key Laboratory of Marine Ecosystem Dynamics (MED), Second Institute of Oceanography, Ministry of Natural Resources, Hangzhou, China, [2]Frontiers Science Center for Deep Ocean Multispheres and Earth System, and Key Laboratory of Marine Chemistry Theory and Technology, Ministry of Education, Ocean University of China, Qingdao, China, [3]State Key Laboratory of Satellite Ocean Environment Dynamics (SOED), Second Institute of Oceanography, Ministry of Natural Resources, Hangzhou, China, [4]Southern Marine Science and Engineering Guangdong Laboratory (Zhuhai), Zhuhai, China, [5]South China Sea Marine Survey Technology Center, State Oceanic Administration, Guangzhou, China

The dissolved silicate concentrations in the supernatant of sediment trap sampling bottles retrieved from deep water (1000-3000 m) at four stations in the South China Sea (SCS) were measured to calculate the underestimated flux of biogenic silica (bSi) in sinking particles due to bSi dissolution. High dissolved silicate concentrations in the supernatant, ranging from 122.6 to 1365.8 µmol/L, indicated significant dissolution of particulate bSi in the sampling bottles. Underestimation of the bSi flux in the SCS by ~2% to ~34% (average: ~10%) due to bSi dissolution was revealed, and the degree of underestimation increased with decreasing total bSi flux. The amount of bSi dissolved within the sampling series at each station was generally positively correlated with dissolution time and to a certain extent influenced by the bSi amount collected by the sampling bottles under a low bSi sinking flux. Apparently stronger bSi dissolution was found at two of the four stations due to relatively high bSi dissolution rates, which were possibly related to a higher reactive surface area of the bSi or bacterial activity. Overall, our results demonstrated that the considerable bSi dissolution in sediment trap sampling bottles should not be ignored, especially in the low-productivity oligotrophic ocean, and bSi flux calibration *via* measurement of the dissolved silicate in sampling bottles is necessary. To reduce bSi flux underestimation due to the deployment of time-series sediment traps, larger-volume sampling bottles should be avoided in the oligotrophic open ocean, and sinking particle samples should be analyzed as soon as the sediment traps are recovered.

KEYWORDS

sediment trap, biogenic silica, dissolution, underestimation, South China Sea

Introduction

Biogenic silica (bSi), also referred to as biogenic opal, comprises the skeletons or cell walls of siliceous organisms, such as diatoms, silicoflagellates, sponge spicules, siliceous rhizarians and several species of choanoflagellates in marine environments (Biard et al., 2018; Maldonado et al., 2019; Puppe, 2020; Llopis Monferrer et al., 2020; Tréguer et al., 2021). Silicate is an essential nutrient supporting the growth of siliceous organisms and the picocyanobacteria *Synechococcus* (Baines et al., 2012; Ohnemus et al., 2016). The biogeochemical cycle of silicon, including assimilation by phytoplankton, remineralization from organic organisms, dissolution and burial of siliceous organisms in sediments, controls silicate bioavailability in the global ocean (Struyf et al., 2009; Tréguer et al., 2021). In addition, as one of the main ballast minerals transporting particulate organic carbon to the deep ocean, bSi plays an important role in the global biogeochemical cycles of carbon (Ragueneau et al., 2006; Honjo et al., 2008; Street-Perrott and Barker, 2008; Lampitt et al., 2009; Guidi et al., 2016; Tréguer et al., 2018).

Sediment traps are widely implemented as an effective tool to observe marine biogeochemical processes and marine biological carbon export by collecting sinking particles over time in the deep ocean. The sinking particles are analyzed in the laboratory to obtain detailed information on biogeochemical fluxes, and bSi, as one of the main components in sinking particles, is measured to estimate the silicon export flux and the coupled relation between silicon and carbon (Ran et al., 2015; Li et al., 2017; Tan et al., 2020). The mole ratio of bSi to $CaCO_3$, another major ballast material of particulate organic carbon attributed to coccoliths and foraminifer tests (Schiebel, 2002; Poulton et al., 2007), in sinking particles is an important indicator of different marine biogeochemical provinces (Ragueneau et al., 2002). Oceanic regions with higher bSi/$CaCO_3$ ratios (>1.0) are normally referred to as silica oceans, and regions with ratios<1.0 constitute carbonate oceans (Honjo et al., 2008). Therefore, accurate measurement of bSi in sinking particles is essential for research on marine silicon and carbon cycles.

It is acknowledged that the bSi of dead organisms begins to dissolve in the water column due to the high-undersaturated concentration of silicate in marine environments (Hurd, 1973; Tréguer and Rocha, 2013). It is foreseeable that the dissolution of bSi will also inevitably occur in a sediment trap because the sampling bottles are generally filled with seawater that is highly undersaturated in silicate. Continuous bSi dissolution in sediment trap sampling bottles could result in significant underestimation of the bSi sinking flux by more than 80% under low bSi fluxes and by 60% under the annual average flux in high-latitude seas, such as the Greenland Sea, Norwegian Sea and Baltic Sea (Bauerfeind and Bodungen, 2006). Nevertheless, few follow-up studies on bSi dissolution in sediment traps during the sampling period and the effect on bSi flux measurements have been reported. This may result in substantial underestimation of the silicon biogeochemical flux in the current global marine silicon cycle budget (Tréguer and Rocha, 2013; Tréguer et al., 2021) and corresponding misunderstanding of the marine biogeochemical carbon cycle and marine biological carbon pump (Honjo et al., 2008).

The South China Sea (SCS), as the largest marginal sea in the tropical northwestern Pacific, is under the control of the East Asian monsoon, and therefore has significant seasonal variation in the marine environment and biogeochemical processes in the upper ocean. It is generally considered oligotrophic water with relatively low surface biomass (Du et al., 2013; Du et al., 2017). Nevertheless, diatoms are important contributors to phytoplankton communities in this oligotrophic water, especially during winter monsoon period (Ning et al., 2004). Long-term time-series observations by sediment traps in the SCS since the 1980s have indicated significant seasonal and interannual variations and spatial differences in the bSi export flux to the deep ocean, related to variations in diatom productivity (Wiesner et al., 1996; Lahajnar et al., 2007; Ran et al., 2015; Li et al., 2017; Zhang et al., 2019; Tan et al., 2020; Li et al., 2022). The bSi/$CaCO_3$ ratio in the sinking particles is generally<1.0 in the northern SCS except in the period of highest productivity (Zhang et al., 2019; Tan et al., 2020), and >1.0 in the central SCS except in the period of lowest productivity (Li et al., 2017; Li et al., 2022), indicating a variable export mechanism of POC in this relatively small semienclosed and oligotrophic ocean basin. However, the measurement of the bSi sinking flux in previous works did not consider dissolution of bSi in the sampling bottles of sediment traps and its effect on the bSi flux measurements.

In the present work, the SCS was selected to investigate bSi dissolution in sediment traps and its impact on bSi flux estimation in this low-latitude oligotrophic marginal sea. Both the bSi in sinking particles and the silicate in the supernatant of the sediment trap sampling bottles were analyzed to evaluate the degree of bSi dissolution in the sediment trap bottles during the sampling period and calculate the underestimation of the bSi sinking flux. The results also provide valuable clues for further study of the dissolution kinetics of bSi in dark, cryogenic and high-pressure deep ocean environments.

Materials and methods

Time-series sediment trap mooring

Time-series sinking particle samples collected at 4 stations in the northern SCS (Figure 1 and Table 1) were used in this study.

They were collected from July 2012 to April 2013 at station SCS-NW, from May 2015 to April 2016 at station SCS-N, and from May 2017 to May 2018 at station SCS-B and SCS-C at water depths ranging from 1000 or 3000 m. The sediment traps used in this study were the PARFLUX Mark 78H-21 from Mclane Research Laboratories, Inc. The sea water temperature ranged from 2.4°C to 4°C at the depth of the deployed sediment traps (Chen et al., 2001; Tian and Wei, 2005; Wang et al., 2011).

Before the sediment traps were deployed, the adopted polyethylene sampling bottles (250 ml for SCS-N and 500 ml for SCS-NW, SCS-B and SCS-C) were filled with a filtered surface seawater-based solution of sodium chloride (NaCl, 35 $g{\cdot}L^{-1}$) and mercury chloride ($HgCl_2$, 3.3 $g{\cdot}L^{-1}$) to minimize microbial activity and diffusive processes (Wiesner et al., 1996; Li et al., 2017). The surface seawater retrieved from the open ocean where the sediment traps were deployed was nearly depleted in silicate (silicate concentration = 0.8~1.4 $\mu mol{\cdot}L^{-1}$). After recovery of the sediment traps, the collected samples were stored in a refrigerator at 4°C. Approximately 30 mL of the supernatant in each sampling bottle was filtered through a polycarbonate filter (0.45-μm pore size) for silicate analysis. Wet particle samples were passed through a 1-mm mesh nylon sieve to remove zooplankton, and the <1-mm component was divided into ten equal parts with a high-precision rotary splitter (McLane WSD-10). Each subsample for bSi analysis was filtered through preweighed polycarbonate filters and dried at 45°C for 72 h before being precisely weighed.

Measurement of silicate in the supernatant of the sediment trap sampling bottles

Each supernatant sample for silicate analysis was diluted 10–30 times with silicate-depleted sea surface water. The diluted sample was then acidified and mixed with an ammonium heptamolybdate solution to form molybdosilicic acid. The resulting acid was reduced with a reducing agent (L (+) ascorbic acid or a mixed reagent of H_2SO_4, metol and Na_2SO_3) into a blue dye, which was measured at 810 nm with spectrophotometer. Oxalic acid was added to the reducing agent to avoid phosphate interference. For the supernatant samples from station SCS-N, the silicate concentrations were measured by a Skalar San++ nutrient automatic analyzer, with the chemical treatments of samples embedded in the analyzer.

The silicate concentration in the supernatant was considered to originate from the dissolution of biogenic silica (bSi_D), as the filtered surface seawater-based solution used to fill the sampling bottles was generally silicate depleted. The absolute amount of bSi_D was calculated with equation (1):

$$M(bSi_D) = 67.29 \times V \times C \quad (1)$$

TABLE 1 Site location and sampling information of the sediment traps deployed in the northern SCS.

Station	Sampling period	Longitude (°E)	Latitude (°N)	Deployment depth (m)	Water depth (m)	Number of valid sampling bottles	Volume of the sampling bottles (L)	Collecting area S_0 (m^2)	Sampling interval Δt (day)	Supernatant separation time	Dissolution time** (day)
SCS-NW	2012–2013	110.50	17.50	1000	1500	16	0.50	0.51	7, 15 or 30	No records	–
SCS-N	2015–2016	116.00	18.50	1000	3736	20	0.25	0.51	17	2016/05/19	52-375
	2015–2016	116.00	18.50	3000	3736	20	0.25	0.51	17	2016/05/19	52-375
SCS-B	2017–2018	113.17	17.96	1000	1650	10*	0.50	0.51	18	2018/07/07	241-421
SCS-C	2017–2018	119.21	21.13	1000	1730	17	0.50	0.51	18	2018/07/07	69-411

*No sinking particle samples were collected due to uncontrollable factors during the second half of the sampling year.
** The dissolution time of bSi started from the sampling time of each bottle to the supernatant separation time in the laboratory.

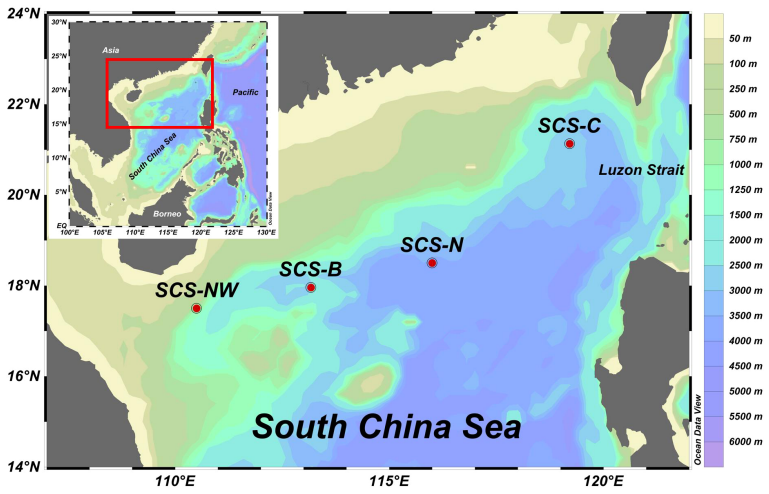

FIGURE 1
Site locations of the sediment trap moorings in the SCS.

where $M(bSi_D)$ is the amount of bSi_D (mg), 67.29 is the molar mass ($g{\cdot}mol^{-1}$) of bSi [$SiO_2{\cdot}0.4\ H_2O$; Mortlock and Froelich (1989)], V is the volume of the sampling bottle (L), and C is the silicate concentration in the supernatant ($\mu mol{\cdot}L^{-1}$).

Then, the underestimated bSi flux due to bSi dissolution was calculated with equation (2):

$$F(bSi_D) = \frac{M(bSi_D)}{S_0 \times \Delta t} \quad (2)$$

where $F(bSi_D)$ is the bSi_D flux ($mg{\cdot}m^{-2}{\cdot}d^{-1}$), S_0 is the collecting area of the sediment trap (m^2), and Δt is the sampling interval (day).

Measurement of biogenic silica in sinking particles

The flux of particulate bSi (bSi_P) was measured following Mortlock and Froelich (1989): 20–50 mg of a dry sinking particle sample was ground and transferred to a 50-mL polypropylene centrifuge tube. Then, 5 mL of 2% H_2O_2 and 5 mL of 1 mol/L HCl were added to remove impurities such as organics and carbonate, respectively. The sample was centrifuged, and the supernatant was removed with a pipette. Then, Milli-Q water was mixed with the sample and centrifuged again to remove the supernatant. This process was repeated three times to remove the residual reaction liquid. After the resultant sample was dried at 60°C, 40 mL of a 2 M Na_2CO_3 solution was added, and the obtained sample was heated in a water bath at 85°C for 5 h. The sample was then centrifuged, and 20 mL of the supernatant was employed for silicate measurement with the silicomolybdenum blue method *via* spectrophotometry.

The amount of bSi_P was calculated with equation (3):

$$M(bSi_P) = 67.29 \times V_{Na_2CO_3} \times C_{extract} \times \frac{m}{M} \quad (3)$$

where $M(bSi_P)$ is the amount of bSi_P (mg), 67.29 is the molar mass ($g{\cdot}mol^{-1}$) of bSi [$SiO_2{\cdot}0.4\ H_2O$; Mortlock and Froelich (1989)], V_{Na2CO3} is the volume of the Na_2CO_3 solution (L), $C_{extract}$ is the silicate concentration in the supernatant of the extraction solution ($\mu mol{\cdot}L^{-1}$), m is the total amount of sinking particles (mg), and M is the amount of sinking particles considered for silicate analysis (mg).

Then, the bSi_P flux was calculated with equation (4):

$$F(bSi_P) = \frac{M(bSi_P)}{S_0 \times \Delta t} \quad (4)$$

where $F(bSi_P)$ is the bSi_P flux ($mg{\cdot}m^{-2}{\cdot}d^{-1}$), S_0 is the collecting area of the sediment trap (m^2), and Δt is the sampling interval (day).

Revising the total biogenic silica fluxes

The total bSi (bSi_T) flux was revised by adding the bSi_D flux and the bSi_P flux based on equation (5):

$$F(bSi_T) = F(bSi_D) + F(bSi_P) \quad (5)$$

The ratio of bSi_D to bSi_T ($bSi_D\%$) was calculated based on equation (6):

$$bSi_D\,\% = \frac{F(bSi_D)}{F(bSi_T)} \times 100\,\% \quad (6)$$

Results

Dissolved biogenic silica in the sediment trap sampling bottles

The silicate concentration in the supernatant of the sediment traps deployed in different areas of the SCS is shown in Figure 2 and Table 2. The silicate concentration in the sampling bottles at stations SCS-N and SCS-NW was much higher than that in the sampling bottles at stations SCS-B and SCS-C. At stations SCS-N and SCS-NW, the silicate concentration decreased gradually over time from the beginning to the end of the sampling year. The highest concentration varied within the range of 1200–1400 μmol·L^{-1}, normally found in the first or second sampling bottle. The silicate concentration in the supernatant at stations SCS-B and SCS-C was generally lower than 400 μmol·L^{-1}, which is lower than the lower limit of the silicate concentration (564.7 μmol·L^{-1}) at stations SCS-NW and SCS-N. Nevertheless, a gradual decreasing trend in silicate in the sampling bottles from the beginning to the end of the sampling year was also observed at stations SCS-B and SCS-C.

The amount of bSi_D was calculated based on the silicate concentration in the supernatant of each sampling bottle [equation (1)], and the flux of bSi_D was further calculated [equation (2)]. The bSi_D amount and flux at station SCS-NW were much higher than those at stations SCS-N, SCS-B and SCS-C (Figure 3). Although an apparent higher silicate concentration in the supernatant was found at station SCS-N

TABLE 2 Silicate concentration in the supernatant of the sampling bottles, bSi_D flux, bSi_P flux and bSi_T flux at the different sediment trap stations in the SCS.

Station	Depth of the sediment trap (m)	Silicate concentration (μmol·L^{-1})		bSi_D flux (mg·m^{-2}·d^{-1})		bSi_P flux (mg·m^{-2}·d^{-1})		bSi_T flux (mg·m^{-2}·d^{-1})	
		Range	Mean	Range	Mean	Range	Mean	Range	Mean
SCS-N	1000	768.2-1186.0	984.5	1.5-2.3	1.9	7.5-48.4	24.3	9.0-50.6	26.3
	3000	683.8-1107.0	949.1	1.3-2.2	1.8	2.9-33.3	22.4	4.2-35.4	24.3
SCS-NW	1000	564.7-1365.8	1015.5	2.1-6.0	4.2	10.3-152.7	45.2	15.6-157.7	50.8
SCS-B	1000	161.4-377.3	304.2	0.6-1.4	1.1	3.0-18.6	10.0	4.3-19.8	11.2
SCS-C	1000	122.6-435.6	223.8	0.5-1.6	0.8	1.4-37.7	14.1	2.0-38.2	14.9

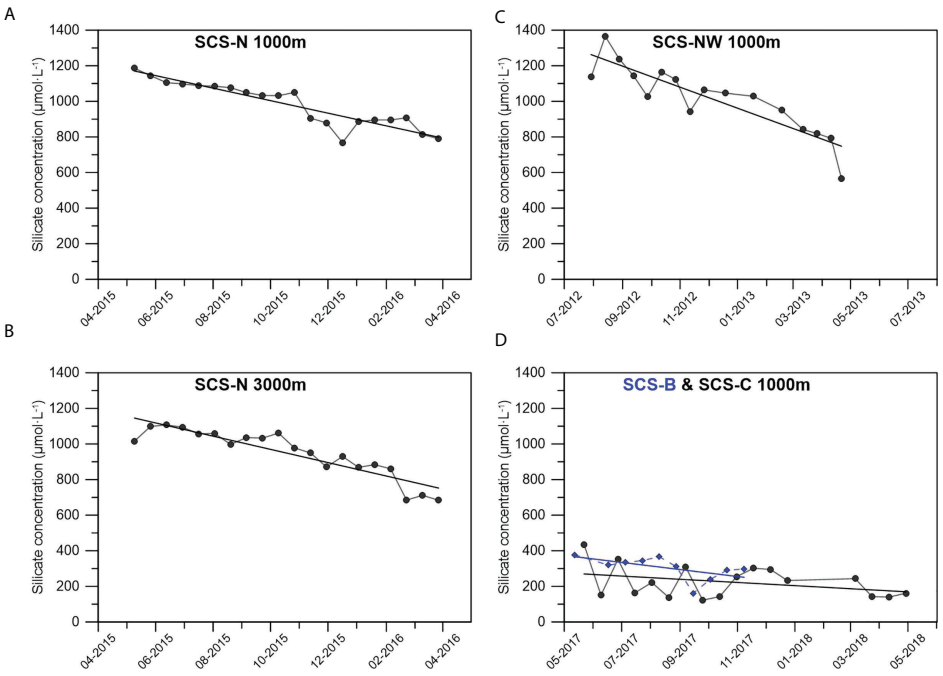

FIGURE 2
Silicate concentration in the supernatant of the sediment trap sampling bottles at 1000 m of stationSCS-N **(A)**, 3000 m of station SCS-N **(B)**, 1000 m of station SCS-NW **(C)** and 1000 m of station B & C with the blueish diamonds representing the data of SCS-B **(D)**.

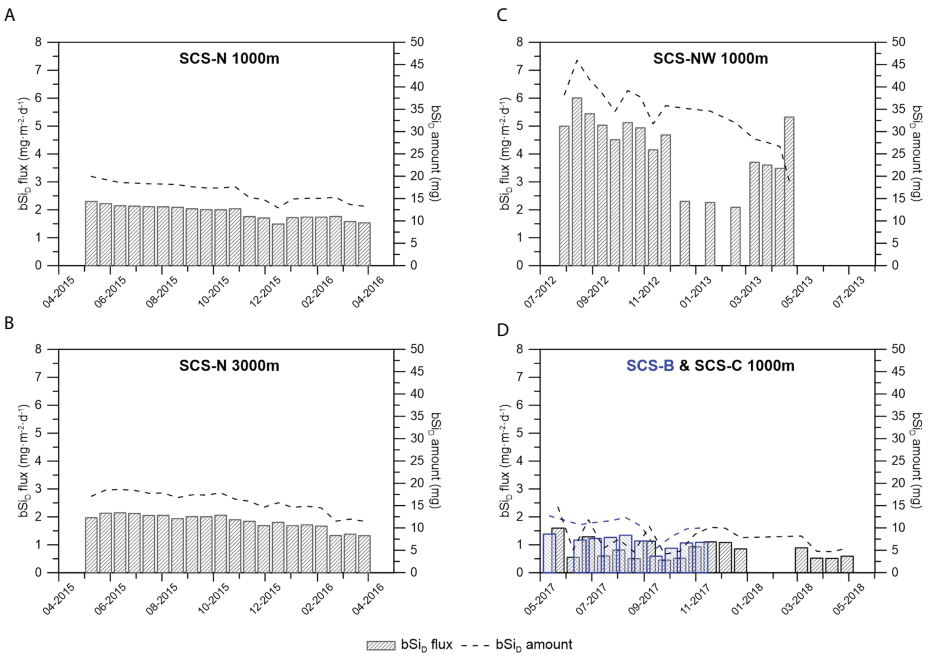

FIGURE 3
The bSi_D flux and amount calculated based on the silicate concentration in the sediment trap sampling bottles at 1000 m of station SCS-N **(A)**, 3000 m of station SCS-N **(B)**, 1000 m of station SCS-NW **(C)** and 1000 m of station B & C with the blueish bars and blueish dotted line representing the data of SCS-B **(D)**.

than at stations SCS-B and SCS-C, the differences in the bSi_D amount and flux at these stations were not as significant as the difference in the silicate concentration.

Particulate biogenic silica fluxes observed by sediment traps

Variations in the bSi_P flux at the four stations in the deep SCS are shown in Figure 4 and Table 2. The bSi_P flux at stations SCS-B and SCS-C from 2017–2018 was slightly lower than that at station SCS-N from 2015-2016 and much lower than that at station SCS-NW from 2012-2013. Seasonal variations in the bSi_P flux were found at all stations; for example, a higher bSi_P flux was found in winter than in summer at station SCS-C, and three remarkable peaks in the bSi_P flux were observed at station SCS-NW. However, no significant correlation was found between the variation in bSi_P and the change pattern of bSi_D.

Revised total biogenic silica fluxes

Significant dissolution of bSi, indicated by the high silicate concentrations in the sediment trap sampling bottles at all stations in the SCS (Figure 2), is bound to result in underestimation of the bSi sinking flux. Based on equations (5) and (6), the bSi_T flux and bSi_D% were calculated and are shown in Figure 5 and Table 2. The variation in the bSi_T flux generally followed the variation in the bSi_P flux, and the contribution of bSi_D to the bSi_T was lower than that of bSi_P. Nevertheless, an apparent change in bSi_D% was found. It ranged from 4.4% to 16.6% (average: 8.3%) at 1000 m at station SCS-N, from 5.8% to 31.2% (average: 8.9%) at 3000 m at station SCS-N, from 2.8% to 34.0% (average: 13.3%) at 1000 m at station SCS-NW, from 6.4% to 31.9% (average: 12.3%) at 1000 m at station SCS-B and from 1.3% to 33.2% (average: 9.7%) at 1000 m at station SCS-C. In general, the bSi_D% value at station SCS-N was lower than that at stations SCS-NW, SCS-B and SCS-C, except for one outlier at 3000 m at station SCS-N.

Discussion

Potential factors influencing bSi dissolution in sediment trap sampling bottles

As shown in Figures 2 and 3, a general decreasing trend in silicate concentration and bSi_D flux and amount from the beginning of the sampling period to the end was found at all studied stations, implying a positive correlation between the degree of bSi dissolution and the time for bSi dissolution. This is

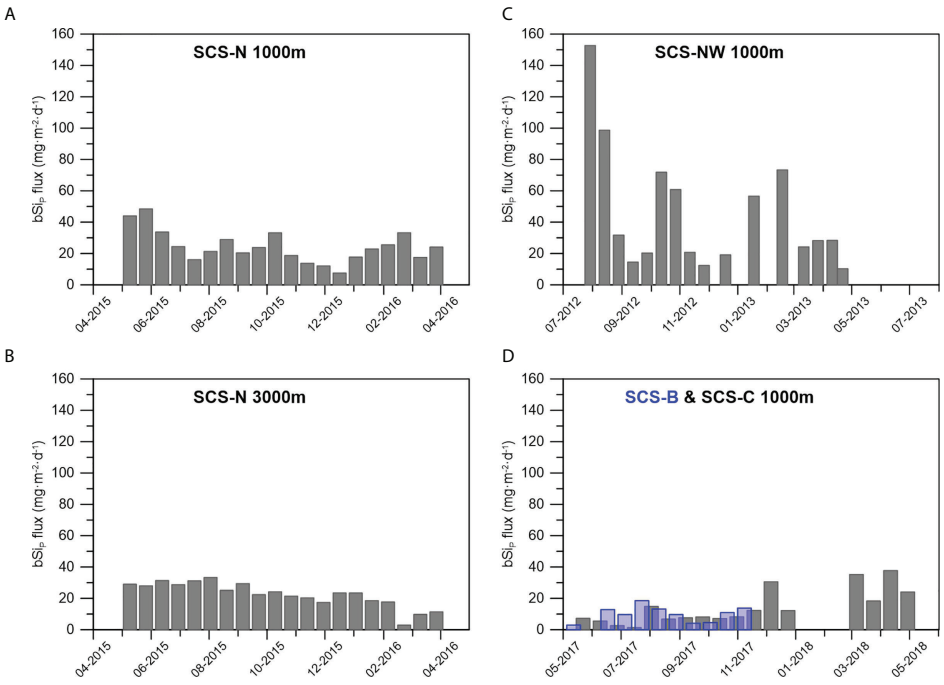

FIGURE 4
The bSi_P flux at different stations at 1000m of station SCS-N **(A)**, 3000 m of station SCS-N **(B)**,1000m of station SCS-NW **(C)** and 1000 m of station B & C with the blueish bars representing the data of SCS-B **(D)**.

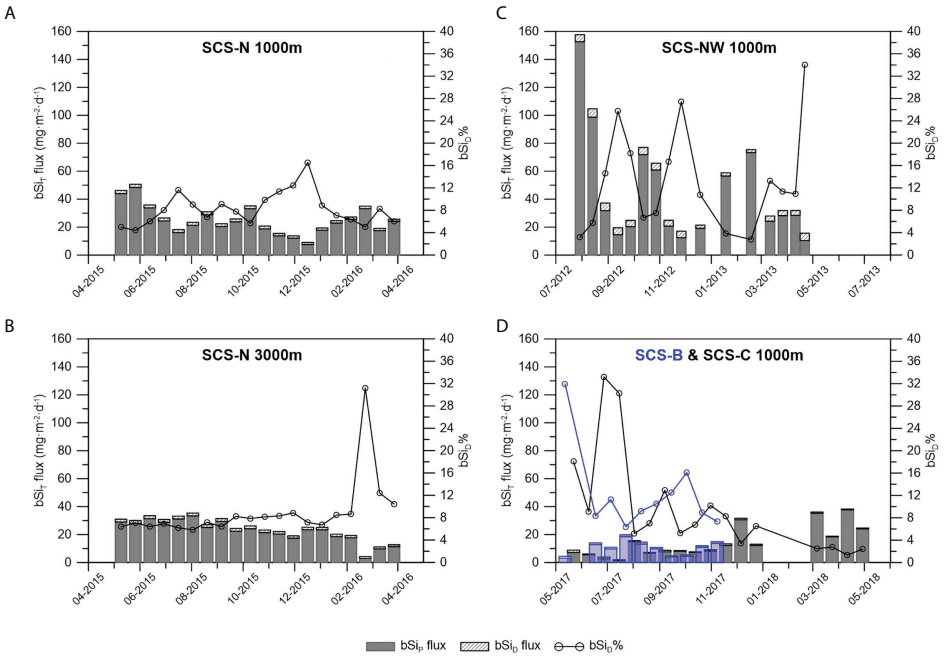

FIGURE 5
Revision of the bSi flux and contribution of bSi_D to bSi_T (bSi_D%) at 1000m of station SCS-N **(A)**, 3000 m of station SCS-N **(B)**, 1000 m of station SCS-NW **(C)** and 1000m of station B & C with the blueish bars and blueish circles representing the data of SCS-B **(D)**.

understandable, as the dissolution amount of bSi is determined by the dissolution rate (mol·g^{-1}·h^{-1}), the mass of solute bSi (g), and the time for dissolution (h). As shown in Figure 6, this positive correlation between the bSi_D amount and the time for dissolution was significant at stations SCS-NW, SCS-N and SCS-B, with the exception of station SCS-C.

Another obvious phenomenon is the remarkably different degrees of bSi dissolution among stations in the study area. Much stronger bSi dissolution occurred at stations SCS-NW and SCS-N, as indicated by the much higher silicate concentrations (Figure 2). Because there was no significant difference in the dissolution time among the stations, the different degrees of dissolution among the stations were either due to different dissolution rates or differences in bSi amounts. As the average bSi flux at stations SCS-NW and SCS-N was higher than that at stations SCS-B and SCS-C, it is easy to conclude that the stronger dissolution of bSi at stations SCS-NW and SCS-N was due to the higher bSi amount. Coincidently, a drop in the silicate concentration from November to December 2015 interrupting the gradually decreasing trend of the silicate concentration at 1000 m at station SCS-N (Figure 2) corresponded well to a decline in the bSi flux (Figures 4, 5). Another sudden decline in the silicate concentration found in the last sampling bottle of station SCS-NW (Figure 2) also corresponded to the lowest bSi amount due to the shortest sampling interval (only 1 week).

However, we also found that the bSi_T flux in the sampling bottles from the end of 2017 to 2018 at station SCS-C was comparable to and sometimes even higher than the bSi_T flux at the end of station SCS-N (Figures 4, 5), but the silicate concentration and bSi_D amount in these sampling bottles from station SCS-C were still apparently lower (Figures 2, 3). As shown in Figure 7, the correlation between the bSi_D amount and the bSi_T amount was generally poor, except at 3000 m at station SCS-N. It should be noted that this close relationship between the bSi_D and the bSi_T at 3000 m at station SCS-N is most likely attributable to the general decreasing trend of both the bSi_D amount and the bSi_T amount over time (Figures 2 and 5, respectively). Therefore, the bSi amount in the sampling bottles was not the determining factor for the different degrees of bSi dissolution among sites, although it could function as a limiting factor under a low bSi amount, and the difference in dissolution rate may explain the different degrees of bSi dissolution among the stations.

The degree of environmental silicate unsaturation ($1\text{-}C/C_{eq}$) is one of the key factors determining the dissolution rate of bSi (Loucaides et al., 2012a). As the water prefilled in the sampling bottles was almost entirely depleted in silicate ($C \approx 0$), the degree of silicate unsaturation in all sampling bottles was close to 1 at the very beginning of the dissolution process. This inevitably resulted in the highest average bSi dissolution rate in each sampling series occurring in the last sampling bottles of each station (Figure 2). On the other hand, apparent differences in silicate concentrations in the last sampling bottles of each station indicated that significant differences in bSi dissolution rates among stations started from the initial stage of bSi dissolution (Figures 2 and 3). As dissolution proceeded, the degree of silicate unsaturation decreased gradually because the silicate concentration (C) in the sampling bottles increased. It is worth noting that the silicate concentration in the bottles is also determined by the volume of the sampling bottles. As the same amount of bSi dissolved, the silicate concentration

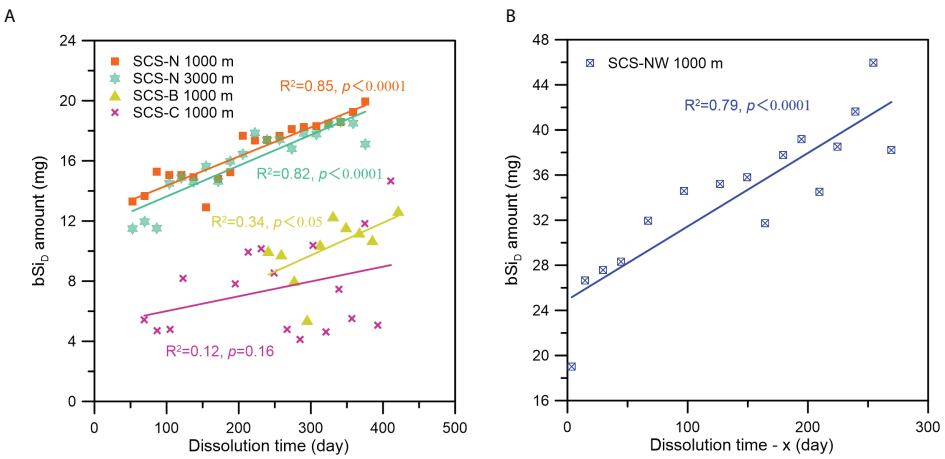

FIGURE 6
Relationship between the bSi_D amount and the dissolution time at the different stations **(A**. station SCS-N, SCS-B and SCS-C; **(B)** station SCS-NW) in the SCS. Note: Because the time when the supernatant taken in the laboratory for station SCS-NW samples was not recorded exactly, we defined a constant x as the time period from the recovery time of the sediment trap to the time when the supernatant was taken in the laboratory, and the "Dissolution time - x" is the time period from the sampling time of each bottle to the recovery time of the sediment trap.

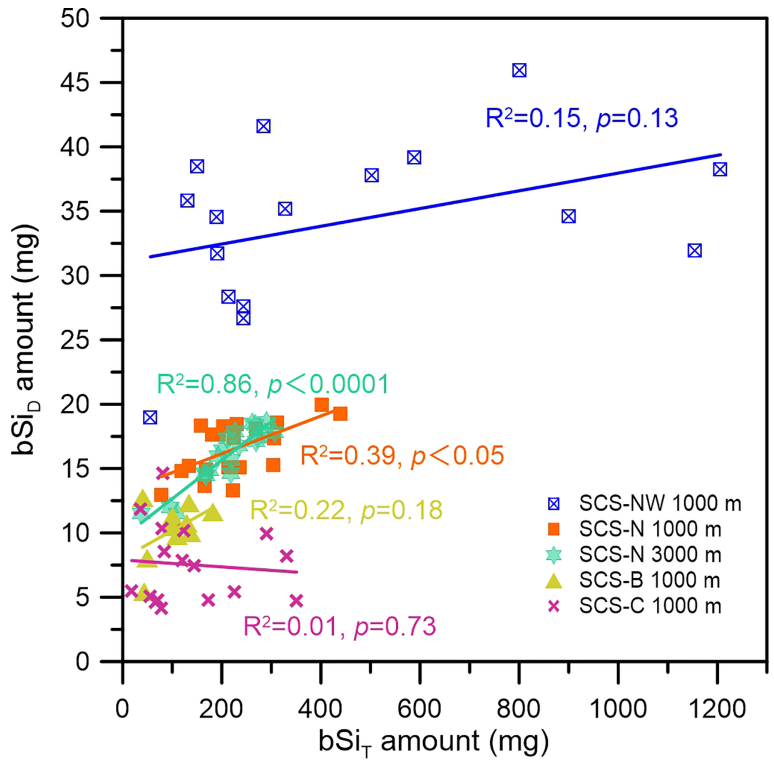

FIGURE 7
Relationship between the bSi_D amount and bSi_T amount in the sampling bottles at the different stations in the SCS.

increased less in the 500 ml sampling bottle than in the 250 ml sampling bottle, which in turn influenced the silicate unsaturation and the bSi dissolution rate. However, the difference in the volume of sampling bottles between SCS-NW, SCS-B, SCS-C (500 ml) and SCS-N (250 ml) could not explain the apparent lower bSi dissolution rate at stations SCS-B and SCS-C.

In addition to the environmental silicate concentration (*C*), the equilibrium solubility of bSi (C_{eq}) is another determining factor of the degree of environmental silicate unsaturation ($1-C/C_{eq}$). The apparently higher bSi dissolution rate at stations SCS-NW and SCS-N than at stations SCS-B and SCS-C might be due to the higher bSi solubility of bSi particles at stations SCS-NW and SCS-N. The highest silicate concentration in the supernatant at the beginning of the sampling period reached ~1300 μmol·L^{-1} at station SCS-NW and ~1100 μmol·L^{-1} at station SCS-N (Figure 2). This value was comparable to the solubility of bSi at 2°C measured in stirred flow-through experiments (1000~1200 μmol·L^{-1}) by Rickert et al. (2002) and higher than that observed in the field (800~1000 μmol/L) *via* batch reactors in the deep (> 1000 m) Mozambique Channel (Loucaides et al., 2012b). However, we are not sure whether the silicate in the sampling bottle with the highest silicate concentration reached saturation. Therefore, we could only approximately estimate that the equilibrium solubility of the sinking bSi particles in the deep northern SCS was at least 1100 μmol·L^{-1}. On the other hand, the highest silicate concentration in the supernatant at stations SCS-B and SCS-C was ~400 μmol·L^{-1} (Figure 2), which is much lower than 1100 μmol·L^{-1}. Whether it is limited by bSi solubility or attributed to other factors determining a low dissolution rate remains unknown.

Previous works have demonstrated that water temperature, pressure, and pH are potential environmental factors determining bSi solubility (Hurd, 1973; Lawson et al., 1978; Kamatani et al., 1980; Van Cappellen and Qiu, 1997; Rickert et al., 2002), in which a higher water temperature usually yields enhanced solubility. However, the sea water temperature at the depths of the deployed sediment traps, both at 1000 and 3000 m, in the deep SCS generally remained constant, ranging from 2.4°C to 4°C (Tian and Wei, 2005; Wang et al., 2011), and the samples were stored in a refrigerator at 4°C after recovery, indicating that the environmental temperature could not result in a large difference in bSi solubility among stations. The bSi solubility has been estimated to increase with pressure based on experiments with synthetic amorphous silica (Loucaides et al., 2012a and references therein), but there was no large difference between the silicate concentration at 3000 m at station SCS-N and that at 1000 m, indicating that pressure was not the key

factor influencing bSi solubility in the deep SCS. The pH of the supernatant in the sampling bottles was approximately measured with a pH meter (Mettler Toledo S210K) before sample splitting *via* a McLane WSD-10 rotary splitter, which revealed that the pH ranged from 7.4 to 7.8 at room temperature for the supernatant at stations SCS-B and SCS-C and reached approximately 6.0 for that at station SCS-NW. The relatively high pH at stations SCS-B and SCS-C could result in lower resistance of bSi and higher bSi solubility (Hurd, 1973; Van Cappellen and Qiu, 1997; Taucher et al., 2022), which is against our assumption that the lower bSi dissolution rate at stations SCS-B and SCS-C was due to lower bSi solubility. Therefore, the possibly different bSi solubilities as a result of differences in ambient physical and chemical conditions cannot explain the notably different bSi dissolution rates among the stations.

In addition to ambient physical and chemical conditions, some of the internal characteristics of bSi, e.g., reactive surface area (A_s), degree of aging and diagenesis, are other important controlling factors for bSi solubility (Loucaides et al., 2012a). As the settling velocity of sinking particles in the open ocean is dozens to hundreds of meters per day (Giering et al., 2020) and the settling velocity of sinking particles in the northern SCS was estimated to be 30-50 m per day (Ran et al., 2015), the degree of aging and diagenesis of bSi in sinking particles at 1000 m may not be a key factor in differentiating bSi solubility among sites. The difference in the A_s of the bSi seems to be the only possibility to explain the possible difference in bSi solubility and bSi dissolution rate among sites. However, this speculation needs more detailed study, including research on the siliceous organism compositions and the nanostructure of different bSi components at each station.

Another possible explanation of the difference in the bSi dissolution rate among stations could be the effect of bacterial activity. The silica cell walls of diatoms while alive are protected from dissolution by an organic film (Hecky et al., 1973), but bacteria can decompose this organic matter after diatom death (Bidle and Azam, 1999), thus accelerating bSi dissolution (Bidle and Azam, 2001). The relatively low pH value at station SCS-NW could probably be attributed to the notable degradation of sinking organic matter, which was indicated by the high concentrations of dissolved organic carbon and dissolved inorganic nitrogen in the sediment trap (Sun et al., 2015). The relatively high pH value of the supernatant at stations SCS-B and SCS-C could indicate lower degradation of organic matter and lower microbial activity, which could probably result in less bSi exposure in the solution. However, this possibility should be confirmed or modified through further research, and more microbiological work should be involved.

In summary, except for the decreasing trend in the bSi dissolution amount in the sampling bottles over time, a significant difference in bSi dissolution among stations was found in the study area. This significant difference could not be explained by the difference in bSi flux among stations, although the bSi_D amount is influenced by the total bSi amount in the sampling bottles. The main reason for the difference in the degree of bSi dissolution at the different stations was likely due to the difference in the dissolution rate, which was presumably related to the different A_s of bSi or bacterial activity. Studying the dissolution kinetics of bSi from different stations with flow-through experiments (Van Cappellen and Qiu, 1997; Rickert et al., 2002), together with microbiological analysis, siliceous organism identification and measurement of the bSi nanostructure, will help identify the exact controlling factor causing the differences in dissolution rates in future work. It should be noted that the volume of the sampling bottle not only influences the silicate concentration in the bottles but also modifies the dissolution rate by impacting the silicate unsaturation and eventually influencing the degree of bSi dissolution.

Underestimation of the bSi flux due to bSi dissolution

As shown in Figures 2 and 3, although the silicate concentration at stations SCS-B and SCS-C, respectively, were much lower than that at station SCS-N, the discrepancy in the calculated bSi_D flux between these stations was not as significant as that in the silicate concentration (Figure 3), mainly because the volume of the sampling bottles deployed at stations SCS-B and SCS-C (500 ml) was twice that of the sampling bottles deployed at station SCS-N (250 ml) (Table 1). On the one hand, the high silicate concentration in the supernatant and the large-volume sampling bottles employed at station SCS-NW resulted in much higher bSi_D fluxes (Figure 3 and Table 2). It should also be noted that the bSi_D flux in several samples collected from November 2012 to February 2013 at station SCS-NW decreased suddenly (Figure 3), which was likely due to the longer sampling interval (1 month) during this period. On the other hand, the sudden increase in the bSi_D flux and bSi_D% for the last SCS-NW sample occurred due to the shorter sampling interval (only 1 week, Figure 3). This indicated that the bSi_D flux was determined not only by the bSi_D amount in the sampling bottles but also by the volume of the sampling bottles and the preset sampling intervals.

A clear negative correlation between bSi_D% and the bSi_T flux was found at all stations (Figure 8). In some of the samples, the bSi_D% value was higher than 30%, suggesting that approximately 1/3 of the contained bSi was dissolved in the sampling bottles. This negative relationship between bSi_D% and the bSi_T flux has also been reported in similar work in the North Atlantic Ocean (Gallinari et al., 2002), but a much higher bSi_D% (4.6–66.1%) has been found in the deep North Atlantic Ocean (Figure 8). This result indicated that bSi could be significantly underestimated when the bSi_T flux was relatively low, which normally occurs when the productivity of siliceous organisms, e.g., diatoms, is relatively low in the oligotrophic open ocean or in the ocean with

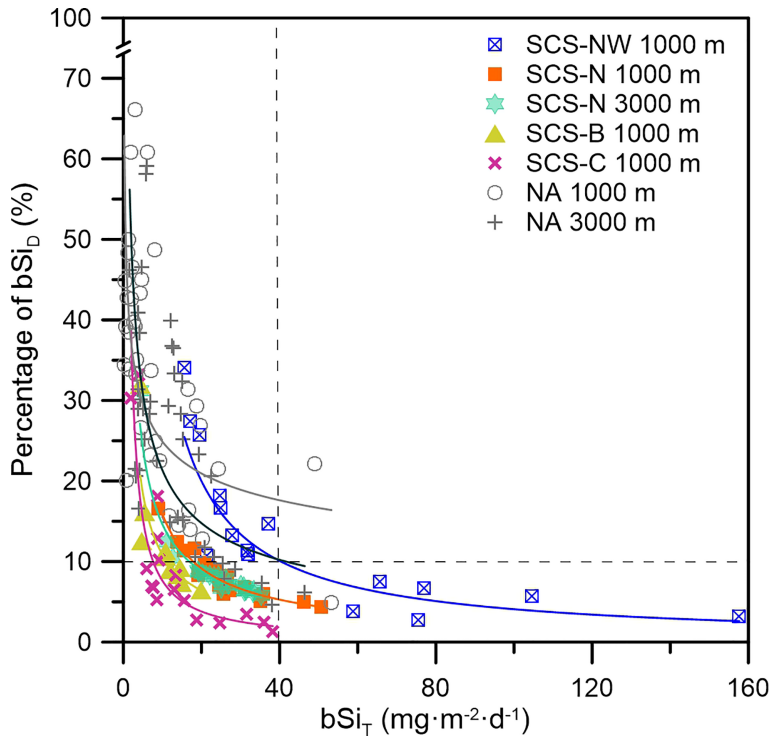

FIGURE 8
Percentage of the bSi_D as a function of the bSi_T flux at the different stations in the SCS and North Atlantic Ocean [NA, North Atlantic; data retrieved from Gallinari et al. (2002)].

a notable seasonal variation in primary productivity. Generally, the underestimation could exceed 10% when the bSi_T flux was lower than 40 mg·m^{-2}·d^{-1} (Figure 8), which suggests that the global export flux of bSi to the deep ocean has generally been underestimated, probably by more than 10%, and correspondingly, bSi recycling in the deep ocean might be overestimated (Tréguer et al., 2021). It is therefore strongly suggested that the bSi_D fraction in sediment trap sampling bottles should be measured to better understand sinking particles of bSi, which is important for quantitative research on the biogeochemical process of silicon in the ocean and the global marine silicon cycle.

Conclusion

In this work, we studied the influence of bSi dissolution on bSi sinking flux estimation *via* sediment traps in the northern SCS. The results indicated apparent bSi dissolution in the sediment trap sampling bottles, which resulted in an underestimation of the bSi sinking flux of 2~34% (average: ~10%) in the northern SCS. The impact of bSi dissolution on bSi flux estimation became increasingly notable with decreasing total bSi flux, especially when the total bSi flux was lower than 40 mg·m^{-2}·d^{-1}. Therefore, to better quantify the biogeochemical flux of silicon in the deep ocean, the collected samples should be split and analyzed in the laboratory as soon as possible after trap recovery, and it is necessary to measure the dissolved bSi in the supernatant to revise the particulate bSi flux, especially when the bSi flux is inherently low. The degree of bSi dissolution in the sediment trap sampling bottles at each station was mainly controlled by the dissolution time but influenced by the total bSi amount in the sampling bottles if the bSi sinking flux was extremely low. Apparent differences in the degree of bSi dissolution in the sampling bottles among stations were found. However, neither the dissolution time difference nor the bSi amount difference could explain such a large discrepancy in the degree of bSi dissolution, and the difference in the bSi dissolution rate might be the only possible reason, but more experiments are needed to better understand the controlling factors of the bSi dissolution rate in sediment traps in the future. It is worth noting that the volume of the sampling bottles adopted could influence the dissolution amount of bSi and result in greater underestimation of the bSi flux. Thus, smaller-volume sampling bottles are recommended for application in sediment traps, especially in oligotrophic open ocean settings.

Data availability statement

The raw data supporting the conclusions of this article will be made available by the authors, without undue reservation.

Author contributions

WL and LR: conception and design of study. JC: financial support. WL: drafting the manuscript. LR, ZY and MW: revising the manuscript. WL, YL and LS: acquisition of data. WL, MW, YL and LS: interpretation of data. All authors contributed to the article and approved the submitted version.

Funding

This work was funded by the State Key R&D Project of China (2016YFC0304105), the Project of the State Key Laboratory of Satellite Ocean Environment Dynamics, Second Institute of Oceanography, MNR (SOEDZZ2104), and the National Natural Science Foundation of China (91128212, 41006034, and 41876123). We acknowledge the support of SML311019006/311020006.

Conflict of interest

The authors declare that the research was conducted in the absence of any commercial or financial relationships that could be construed as a potential conflict of interest.

Publisher's note

All claims expressed in this article are solely those of the authors and do not necessarily represent those of their affiliated organizations, or those of the publisher, the editors and the reviewers. Any product that may be evaluated in this article, or claim that may be made by its manufacturer, is not guaranteed or endorsed by the publisher.

References

Baines, S. B., Twining, B. S., Brzezinski, M. A., Krause, J. W., Vogt, S., Assael, D., et al. (2012). Significant silicon accumulation by marine picocyanobacteria. *Nat. Geosci.* 5, 886–891. doi: 10.1038/ngeo1641

Bauerfeind, E., and Bodungen, B. V. (2006). Underestimation of biogenic silicon flux due to dissolution in sediment trap samples. *Mar. Geol.* 226, 297–306. doi: 10.1016/j.margeo.2005.11.001

Biard, T., Krause, J. W., Stukel, M. R., and Ohman, M. D. (2018). The significance of giant phaeodarians (Rhizaria) to biogenic silica export in the California current ecosystem. *Glob. Biogeochem Cycle* 32, 987–1004. doi: 10.1029/2018GB005877

Bidle, K. D., and Azam, F. (1999). Accelerated dissolution of diatom silica by marine bacterial assemblages. *Nature* 397, 508–512. doi: 10.1038/17351

Bidle, K. D., and Azam, F. (2001). Bacterial control of silicon regeneration from diatom detritus: Significance of bacterial ectohydrolases and species identity. *Limnol Oceanogr* 46, 1606–1623. doi: 10.2307/3069085

Chen, C., Wang, S., Wang, B., and Pai, S. (2001). Nutrient budgets for the south China Sea basin. *Mar. Chem.* 75, 281–300. doi: 10.1016/S0304-4203(01)00041-X

Du, C., Liu, Z., Dai, M., Kao, S., Cao, Z., Zhang, Y., et al. (2013). Impact of the kuroshio intrusion on the nutrient inventory in the upper Northern South China Sea: insights from an isopycnal mixing model. *Biogeosciences* 10, 6419–6432. doi: 10.5194/bg-10-6419-2013

Du, C., Liu, Z., Kao, S., and Dai, M. (2017). Diapycnal fluxes of nutrients in an oligotrophic oceanic regime: The south China Sea. *Geophys. Res. Lett.* 44, 11510–11518. doi: 10.1002/2017GL074921

Gallinari, M., Ragueneau, O., Corrin, L., Demaster, D., and Tréguer, P. (2002). The importance of water column processes on the dissolution properties of biogenic silica in deep-sea sediments i. solubility. *Geochim Cosmochim Acta* 66, 2701–2717. doi: 10.1016/S0016-7037(02)00874-8

Giering, S., Cavan, E. L., Basedow, S. L., Briggs, N., Burd, A. B., Darroch, L. J., et al. (2020). Sinking organic particles in the ocean–flux estimates from *in situ* optical devices. *Front. Mar. Sci.* 6. doi: 10.3389/fmars.2019.00834

Guidi, L., Chaffron, S., Bittner, L., Eveillard, D., Larhlimi, A., Roux, S., et al. (2016). Plankton networks driving carbon export in the oligotrophic ocean. *Nature* 532, 465–470. doi: 10.1038/nature16942

Hecky, R. E., Mopper, K., Kilham, P., and Degens, E. T. (1973). The amino acid and sugar composition of diatom cell-walls. *Mar. Biol.* 19, 323–331. doi: 10.1007/BF00348902

Honjo, S., Manganini, S. J., Krishfield, R. A., and Francois, R. (2008). Particulate organic carbon fluxes to the ocean interior and factors controlling the biological pump: A synthesis of global sediment trap programs since 1983. *Prog. Oceanogr* 76, 217–285. doi: 10.1016/j.pocean.2007.11.003

Hurd, D. C. (1973). Interactions of biogenic opal, sediment and seawater in the central equatorial pacific. *Geochim Cosmochim Acta* 37, 2257–2282. doi: 10.1016/0016-7037(73)90103-8

Kamatani, A., Riley, J. P., and Skirrow, G. (1980). The dissolution of opaline silica of diatom tests in sea water. *J. Oceanogr* 36, 201–208. doi: 10.1007/BF02070333

Lahajnar, N., Wiesner, M. G., and Gaye, B. (2007). Fluxes of amino acids and hexosamines to the deep South China Sea. *Deep Sea Res. Part I* 54, 2120–2144. doi: 10.1016/j.dsr.2007.08.009

Lampitt, R. S., Salter, I., and Johns, D. (2009). Radiolaria: major exporters of organic carbon to the deep ocean. *Glob. Biogeochem Cycle* 23, GB1010. doi: 10.1029/2008GB003221

Lawson, D. S., Hurd, D. C., and Pankratz, H. S. (1978). Silica dissolution rates of decomposing phytoplankton assemblages at various temperatures. *Am. J. Sci.* 278, 1373–1393. doi: 10.2475/ajs.278.10.1373

Li, H., Wiesner, M. G., Chen, J., Zheng, L., Zhang, J., and Ran, L. (2017). Long term variation of mesopelagic biogenic flux in the central South China Sea: Impact of monsoonal seasonality and mesoscale eddy. *Deep Sea Res. Part I* 126, 62–72. doi: 10.1016/j.dsr.2017.05.012

Li, H., Zhang, J., Xuan, J., Wu, Z., Ran, L., Wiesner, M. G., et al. (2022). Asymmetric response of the biological carbon pump to the ENSO in the south China Sea. *Geophys. Res. Lett.* 49, e2021GL095254. doi: 10.1029/2021GL095254

Llopis Monferrer, N., Boltovskoy, D., Tréguer, P., Sandin, M., Not, F., and Leynaert, A. (2020). Estimating biogenic silica production of rhizaria in the global ocean. *Glob. Biogeochem Cycle* 34, e2019GB006286. doi: 10.1029/2019GB006286

Loucaides, S., Koningc, E., and Van Cappellen, P. (2012b). Effect of pressure on silica solubility of diatom frustules in the oceans: Results from long-term laboratory and field incubations. *Mar. Chem.*. 136, 1–6. doi: 10.1016/j.marchem.2012.04.003

Loucaides, S., Van Cappellen, P., Roubeix, V., Moriceau, B., and Ragueneau, O. (2012a). Controls on the recycling and preservation of biogenic silica from biomineralization to burial. *Silicon* 4, 7–22. doi: 10.1007/s12633-011-9092-9

Maldonado, M., López-Acosta, M., Sitjà, C., García-Puig, M., Galobart, C., and Ercilla, G. (2019). Sponge skeletons as an important sink of silicon in the global oceans. *Nat. Geosci.* 12, 815–822. doi: 10.1038/s41561-019-0430-7

Mortlock, R. A., and Froelich, P. N. (1989). A simple method for the rapid determination of biogenic opal in pelagic marine sediments. *Deep Sea Res.* 36, 1415–1426. doi: 10.1016/0198-0149(89)90092-7

Ning, X., Chai, F., Xue, H., Cai, Y., Liu, C., and Shi, J. (2004). Physical-biological oceanographic coupling influencing phytoplankton and primary production in the south China Sea. *J. Geophys. Res.* 109, C10. doi: 10.1029/2004JC002365

Ohnemus, D. C., Rauschenberg, S., Krause, J. W., Brzezinski, M. A., Collier, J. L., Geraci-Yee, S., et al. (2016). Silicon content of individual cells of synechococcus from the north Atlantic ocean. *Mar. Chem.* 187, 16–24. doi: 10.1016/j.marchem.2016.10.003

Poulton, A. J., Adey, T. R., Balch, W. M., and Holligan, P. M. (2007). Relating coccolithophore calcification rates to phytoplankton community dynamics: regional differences and implications for carbon export. *Deep Sea Res. Part II* 54, 538–557. doi: 10.1016/j.dsr2.2006.12.003

Puppe, D. (2020). Review on protozoic silica and its role in silicon cycling. *Geoderma* 365, 114224. doi: 10.1016/j.geoderma.2020.114224

Ragueneau, O., Dittert, N., Pondaven, P., Tréguer, P., and Corrin, L. (2002). Si/C decoupling in the southern ocean different? *Deep Sea Res. Part II* 49, 3127–3154. doi: 10.1016/s0967-0645(02)00075-9

Ragueneau, O., Schultes, S., Bidle, K., Claquin, P., and Moriceau, B. (2006). Si And c interactions in the world ocean: importance of ecological processes and implications for the role of diatoms in the biological pump. *Glob. Biogeochem Cycle* 20, GB4S02. doi: 10.1029/2006GB002688

Ran, L., Chen, J., Wiesner, M. G., Ling, Z., Lahajnar, N., Yang, Z., et al. (2015). Variability in the abundance and species composition of diatoms in sinking particles in the northern south China Sea: Results from time-series moored sediment traps. *Deep Sea Res. Part II* 122, 15–24. doi: 10.1016/j.dsr2.2015.07.004

Rickert, D., Schlüter, M., and Wallmann, K. (2002). Dissolution kinetics of biogenic silica from the water column to the sediments. *Geochim Cosmochim Acta* 66, 439–455. doi: 10.1016/S0016-7037(01)00757-8

Schiebel, R. (2002). Planktic foraminiferal sedimentation and the marine calcite budget. *Glob. Biogeochem Cycle* 16, 1065. doi: 10.1029/2001gb001459

Street-Perrott, F. A., and Barker, P. A. (2008). Biogenic silica: a neglected component of the coupled global continental biogeochemical cycles of carbon and silicon. *Earth Surf Process Landf: J. Br. Geomorphological Res. Group* 33, 1436–1457. doi: 10.1002/esp.1712

Struyf, E., Smis, A., Damme, S. V., Meire, P., and Conley, D. J. (2009). The global biogeochemical silicon cycle. *Silicon* 1, 207–213. doi: 10.1007/s12633-010-9035-x

Sun, L., Li, H., Jennerjahn, T., Ran, L., Jin, H., Zhang, J., et al. (2015). Underestimation of C and N flux in the Northern South China Sea due to dissolution in sediment trap samples. *Acta Oceanol Sin.* 37, 19–26. doi: 10.3969/j.issn.0253-4193.2015.12.003

Tan, S., Zhang, J., Li, H., Sun, L., Wu, Z., Wiesner, M. G., et al. (2020). Deep ocean particle flux in the northern south China Sea: Variability on intra-seasonal to seasonal timescales. *Front. Earth Sci.* 8. doi: 10.3389/feart.2020.00074

Taucher, J., Bach, L. T., Prowe, A. E. F., Boxhammer, T., Kvale, K., and Riebesell, U. (2022). Enhanced silica export in a future ocean triggers global diatom decline. *Nature* 605, 696–700. doi: 10.1038/s41586-022-04687-0

Tian, T., and Wei, H. (2005). Analysis of water masses in the northern south China Sea and bashi channel. *Periodical Ocean Univ. China* 35, 9–12. doi: 10.16441/j.cnki.hdxb.2005.01.002

Tréguer, P. J., Bowler, C., Moriceau, B., Dutkiewicz, S., Gehlen, M., Aumont, O., et al. (2018). Influence of diatom diversity on the ocean biological carbon pump. *Nat. Geosci.* 11, 27–37. doi: 10.1038/s41561-017-0028-x

Tréguer, P. J., and Rocha, C. (2013). The world ocean silica cycle. *Annu. Rev. Mar. Sci.* 5, 477–501. doi: 10.1146/annurev-marine-121211-172346

Tréguer, P. J., Sutton, J. N., Brzezinski, M., Charette, M. A., Devries, T., Dutkiewicz, S., et al. (2021). Reviews and syntheses: the biogeochemical cycle of silicon in the modern ocean. *Biogeosciences* 18, 1269–1289. doi: 10.5194/bg-18-1269-2021

Van Cappellen, P., and Qiu, L. (1997). Biogenic silica dissolution in sediments of the southern ocean. i. solubility. *Deep Sea Res. Part II* 44, 1129–1149. doi: 10.1016/S0967-0645(96)00113-0

Wang, G., Xie, S., Qu, T., and Hang, R. (2011). Deep south China Sea circulation. *Geophys. Res. Lett.* 38, L05601. doi: 10.1029/2010gl046626

Wiesner, M. G., Zheng, L., Wong, H. K., Wang, Y., and Chen, W. (1996). "Fluxes of particulate matter in the South China sea," in *Particle Flux in the Ocean*. Eds. V. Ittekkot, P. Schäfer, P. Depetris and S. Honjo (Chichester: John Wiley & Sons Ltd), 293–299.

Zhang, J., Li, H., Xuan, J., Wu, Z., Yang, Z., Wiesner, M. G., et al. (2019). Enhancement of mesopelagic sinking particle fluxes due to upwelling, aerosol deposition, and monsoonal influences in the northwestern south China Sea. *J. Geophys. Res.* 124, 99–112. doi: 10.1029/2018JC014704

frontiers | Frontiers in Marine Science

TYPE Original Research
PUBLISHED 10 October 2022
DOI 10.3389/fmars.2022.895995

OPEN ACCESS

EDITED BY
Alex J. Poulton,
Heriot-Watt University,
United Kingdom

REVIEWED BY
Akira Kuwata,
Tohoku National Fisheries Research Institute, Japan
Ian Salter,
Alfred Wegener Institute Helmholtz Centre for Polar and Marine Research (AWI), Germany

*CORRESPONDENCE
Natalia Llopis Monferrer
nataliallopis90@gmail.com

SPECIALTY SECTION
This article was submitted to Marine Biogeochemistry, a section of the journal Frontiers in Marine Science

RECEIVED 14 March 2022
ACCEPTED 16 September 2022
PUBLISHED 10 October 2022

CITATION
Llopis Monferrer N, Biard T, Sandin MM, Lombard F, Picheral M, Elineau A, Guidi L, Leynaert A, Tréguer PJ and Not F (2022) Siliceous Rhizaria abundances and diversity in the Mediterranean Sea assessed by combined imaging and metabarcoding approaches. *Front. Mar. Sci.* 9:895995. doi: 10.3389/fmars.2022.895995

Siliceous Rhizaria abundances and diversity in the Mediterranean Sea assessed by combined imaging and metabarcoding approaches

Natalia Llopis Monferrer[1,2*], Tristan Biard[3], Miguel M. Sandin[2,4], Fabien Lombard[5,6], Marc Picheral[5], Amanda Elineau[5], Lionel Guidi[5], Aude Leynaert[1], Paul J. Tréguer[1] and Fabrice Not[2]

[1]Univ Brest, CNRS, IRD, Ifremer, LEMAR, Plouzane, France, [2]Sorbonne University, CNRS, UMR7144 Adaptation and Diversity in Marine Environment (AD2M) Laboratory, Ecology of Marine Plankton team, Station Biologique de Roscoff, Place Georges Teissier, Roscoff, France, [3]LOG, Laboratoire d'Océanologie et de Géosciences, Univ. Littoral Côte d'Opale, Univ. Lille, CNRS, UMR 8187, Wimereux, France, [4]Department of Organismal Biology (Systematic Biology), Uppsala University, Uppsala, Sweden, [5]Sorbonne Université, CNRS, Laboratoire d'Océanographie de Villefranche, Villefranche-sur-Mer, France, [6]Institut Universitaire de France, Paris, France

Siliceous Rhizaria (polycystine radiolarians and phaeodarians) are significant contributors to carbon and silicon biogeochemical cycles. Considering their broad taxonomic diversity and their wide size range (from a few micrometres up to several millimetres), a comprehensive evaluation of the entire community to carbon and silicon cycles is challenging. Here, we assess the diversity and contribution of silicified Rhizaria to the global biogenic silica stocks in the upper 500 m of the oligotrophic North-Western Mediterranean Sea using both imaging (FlowCAM, Zooscan and Underwater Vision Profiler) and molecular tools and data. While imaging data (cells m^{-3}) revealed that the most abundant organisms were the smallest, molecular results (number of reads) showed that the largest Rhizaria had the highest relative abundances. While this seems contradictory, relative abundance data obtained with molecular methods appear to be closer to the total biovolume data than to the total abundance data of the organisms. This result reflects a potential link between gene copies number and the volume of a given cell allowing reconciling molecular and imaging data. Using abundance data from imaging methods we estimate that siliceous Rhizaria accounted for up to 6% of the total biogenic silica biomass of the siliceous planktonic community in the upper 500m of the water column.

KEYWORDS

Rhizaria, Phaeodaria, polycystine, imaging technologies, metabarcoding, silicon cycle

1. Introduction

Marine environments represent the largest ecosystem on Earth, housing a broad variety of planktonic organisms, from viruses and bacteria to unicellular and small multicellular eukaryotes. These organisms, which span more than six orders of magnitude in size, form complex ecological networks that sustain major biogeochemical cycles (Edwards et al., 2013). While phytoplankton forms the base of marine food webs, zooplankton occupy numerous trophic levels and can contribute to carbon export through mechanisms such as vertical migration and production of fecal pellets (Stukel et al., 2013; Toullec et al., 2019). To date, studies of phytoplankton assemblages have focused mostly on diatoms, dinoflagellates, and cyanobacteria (Alves-de-Souza et al., 2008), while the role of zooplankton in the ocean has been assessed through the study of copepods and euphausiids (e.g., Buitenhuis et al., 2006), mainly because of their high abundances and good preservation in formaline. These are however very specific compartments, only representing limited aspects of the functional diversity of plankton (Le Queré et al., 2005), omitting the potential role of other organisms when developing biogeochemical models.

In recent years, automated sampling devices, image analysis technologies, and machine learning algorithms have been developed to quantify abundances of marine organisms (Gorsky et al., 2010; Picheral et al., 2010; Irisson et al., 2022) and to accelerate the analysis of planktonic samples which are generally time-consuming (Benfield et al., 2007). These methods have been fundamental in revealing the occurrence and potential impact of previously neglected organisms in biogeochemical cycles (Biard et al., 2016). In addition to imaging systems, DNA-metabarcoding, allowing an extensive taxonomic coverage, has become a powerful alternative to morphological observation, being largely used in high-throughput exploration of the diversity of microbial communities (de Vargas et al., 2015; Faure et al., 2019).

Despite the benefits of either method, these come with inherent uncertainties. Imaging tools do not cover all the size spectra of plankton (Lombard et al., 2019), and several tools/instruments need to be used simultaneously to study all components of the marine ecosystem. On the other end, molecular approaches produce relative-abundance and compositional data. Abundances of specific groups are inherently influenced by the abundances of other groups, thus biasing conclusions (Gloor et al., 2017).

In the modern ocean, Rhizaria, a group of unicellular eukaryotic organisms that span a wide range of sizes, from tens to hundreds of micrometres, are known to play important roles in food webs and biogeochemical cycles (Biard, 2022). In the last decade, this group has been highlighted as a critical source of carbon export (Lampitt et al., 2009; Guidi et al., 2016; Gutierrez-Rodriguez et al., 2018), silica cycling (Biard et al., 2018; Llopis Monferrer et al., 2020), and a significant component of ocean biomass (Biard et al., 2016). While some rhizarians build their skeletons of calcium carbonate (Foraminifera) or strontium sulfate (Acantharia), numerous marine rhizarians form siliceous skeletons (Nassellaria, Spumellaria, Collodaria and Phaeodaria) (Takahashi et al., 1983). Considering their large taxonomic diversity, broad size spectrum and extended range of vertical niches (Biard and Ohman, 2020) as well as various trophic modes (Suzuki and Not, 2015), Rhizaria lack a characterisation of their full size range and quantification of their contribution to biogeochemical cycles.

Historically, living Rhizaria, have been collected using plankton nets and Niskin bottles (Boltovskoy et al., 1993; Boltovskoy, 2003; Ishitani and Takahashi, 2007). These conventional sampling methods collect more efficiently smaller specimens, which are also numerically more abundant (e.g., Boltovskoy et al., 2010). So far, large individuals have seldom been taken into account, mainly due to the fragility of their skeletons and only fragments are generally found in the nets. The development of *in-situ* imaging techniques has enabled the first characterizations and estimates of these organisms in the pelagic realm (Biard et al., 2016; Biard and Ohman, 2020). Despite their recent confirmed relevance to current marine biogeochemical cycles (*e.g.*, Biard et al., 2016; Guidi et al., 2016; Llopis Monferrer et al., 2020), knowledge about the distribution and abundances of living Rhizaria is still highly fragmented due to the scarcity of the data and heterogeneity between collection methods and sample analyses. These protists have been patchily sampled and their distribution and role in the biogeochemical cycles, especially in the silicon cycle, are not yet fully understood.

In September 2017, we participated in the Mediterranean Ocean Observing System for the Environment – *Grande Echelle* (MOOSE-GE) cruise. During this cruise, three imaging technologies, FlowCAM, ZooScan and Underwater Vision Profiler, were employed in combination along with DNA metabarcoding sampled at the same locations. We used this integrative approach to describe the broad size spectrum of Rhizaria, their abundance and diversity. Using the data obtained with the imaging instruments and the existing allometry between silica content and rhizarians' biovolume (Llopis Monferrer et al., 2020), we assess the contribution of rhizarian biogenic silica standing stock and potential taxa specific contribution to the silicon cycle on a regional scale.

2. Material and methods

2.1. Study area

Sampling was conducted at 16 sites during the MOOSE-GE 2017 expedition (30/08/2017-24/09/2017) on board R/V Atalante in the North-Western basin of the Mediterranean Sea (Figure 1). This area is characterized by oligotrophic conditions with patchy

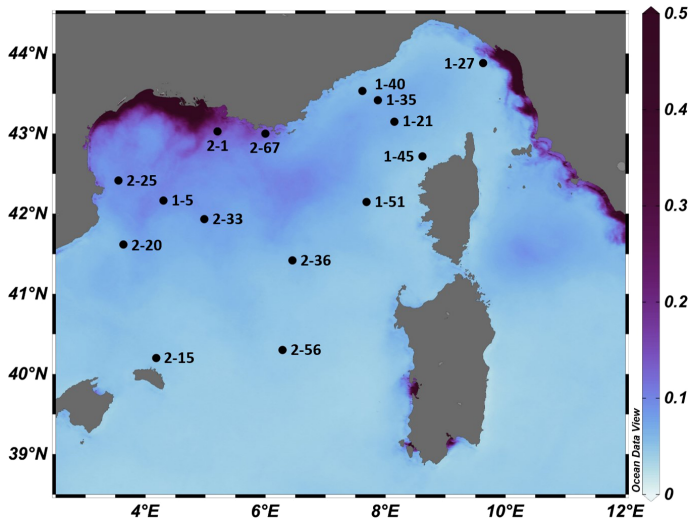

FIGURE 1
Map of the study area (North-Western Mediterranean basin) of the MOOSE-GE expedition with positions of the sampling stations (LEG-Station) that were analysed in this study. Axis colour represents average chlorophyll values in mg m^{-3} during September 2017, the study period. Data was collected using E.U. Copernicus Marine Service Information (https://doi.org/10.48670/moi-00114).

productivity regions (Mayot et al., 2017). The Gulf of Lion is an important area of deep water formation (Donoso et al., 2017), with intense mesoscale activity along with the coastal current and mid-sea eddies present along the basin (Robinson et al., 2001).

2.2. Environmental and biogeochemical data

At each station, a rosette carrying 12 Niskin bottles (12 L) and equipped with a CTD (Seabird Electronics) to measure temperature and salinity was deployed. Samples were taken according to the requirements of biogeochemical parameters. Chlorophyll-a concentration was estimated from bottle water samples using HPLC (Uitz et al., 2009). To measure biogenic silica concentrations, 1 L of seawater sampled at 3 depths distributed between the surface and the deep chlorophyll maximum (DCM), which was calculated according to maximum values of fluorescence, was filtered onto 0.6 µm, 47 mm isopore polycarbonate filters (GE Healthcare Whatman). After filtration, filters were kept in petri dishes and stored at room temperature. Analyses were performed using the double digestion method according to Brzezinski and Nelson (1989).

2.3. Plankton collection

A triple net, with 64, 200, and 500 µm mesh sizes was deployed in a vertical haul mode at the constant speed of 0.8 m s^{-1} in the upper 500 m. A flowmeter was attached to the mouth of each net to quantify the amount of water passing through the net. Once the net was on board the ship, samples concentrated in each cod-end were diluted in 4 L of 0.2-µm filtered seawater and divided into several subsamples.

For the 64 µm cod-end, a subsample of 1.5 L was concentrated on a 50 µm mesh sieve. The concentrated sample was carefully removed from the sieve using a squeeze bottle and preserved with acidic Lugol's solution (2% final concentration) in a 250 mL dark plastic bottle to avoid light and stored at 4°C for later analysis with the FlowCAM (Fluid Imaging Inc.) (Sieracki et al., 1998).

For the 200 µm cod-end, a subsample of 1.5 L was concentrated using a 180 µm sieve. The content of the sieve was poured into a 250-mL plastic bottle with 25 – 30 mL tetraborax buffered formaldehyde (4%v/v) and stored at room temperature for later analysis with the Zooscan imaging system (Hydroptic; Gorsky et al., 2010).

For genetic analyses, 1 L of each cod-end (64, 200 and 500 µm), was filtered through a 10 µm polycarbonate filter. Filters from the different size fractions were flash-frozen in liquid nitrogen and stored independently at -80°C until DNA extraction.

2.4. Image acquisition and processing

2.4.1. FlowCAM analyses

The FlowCAM is an imaging system for measuring and classifying organisms and particles (size from 3 to 5000 µm,

depending on the objective chosen) present in a liquid medium. Samples from the 64 µm cod-end and fixed with Lugol's solution were analysed using a FlowCAM at the Villefranche Platform for Quantitative imaging (PIQv). Before the analysis, samples were filtered through a 200 µm sieve to remove large particles and avoid clogging of the FlowCAM chamber. Plankton organisms were counted using the "auto-trigger mode" of the FlowCAM. Samples were examined under a 4x objective lens and pumped through a 3mm x 0.3mm chamber for 45 minutes or until reaching 30 000 images (volume varied 0.6883 ml to 8.88707 ml). Raw images were saved to analyse them using the Zooprocess software (Gorsky et al., 2010).

2.4.2. Zooscan analyses

The Zooscan is a plankton scanner that takes high-resolution images of planktonic samples (Gorsky et al., 2010). Samples in tetraborax-formaldehyde 4%v/v were digitized at 4800 dpi using the Zooscan at the PIQv. Each of the samples collected were first divided into two size fractions using 1000 µm sieves: d1 for the organisms larger than 1 mm and d2, for the organisms smaller than 1 mm. Each of the two size fractions (d1, d2) was subsampled using a Motoda splitter to reach aliquots containing nearly 500 to 1000 objects and imaged with the Zooscan (Gorsky et al., 2010).

2.4.3. *In situ* imaging – UVP analyses

The Underwater Vision Profiler (UVP5; Hydroptic) was integrated on the CTD-rosette. The UVP5 allows the acquisition of particles and zooplankton images larger than >700 µm and to quantify them in a known volume of water. The UVP operates a 4 MPix camera imaging a field of view of approximately 180 x 180 mm^2 about 200mm in front of the camera. Vertical profiles exceeded 500 m except Station 27 (Leg1), but only data from the upper 500 m of the water column was used in this study in order to compare with results from the plankton nets.

2.4.4. Metabarcoding sequencing

DNA was extracted using the MasterPure Complete DNA and RNA Purification Kit (Epicentre) following the manufacturer's instructions. This particular extraction method was used because it has been proven to be appropriate for cells with robust skeletons, such as Rhizaria (Pernice et al., 2016). Polymerase chain reaction (PCR) amplification was performed with the general eukaryotic primer pair TAReuk454FWD1 (5'-CCAGCASCYGCGGTAATTCC-3') and TAReukREV3 (5'-ACTTTCGTTCTTGATYRA-3') targeting the V4 hypervariable region of the 18S rDNA (Stoeck et al., 2010). Sequencing was performed using the Illumina MiSeq platform (2x250 bp) for over 50000 reads per sample.

2.5. Data analysis

2.5.1. Imaging

All raw images generated by FlowCAM, Zooscan, and UVP were analysed and processed using the Zooprocess software (Gorsky et al., 2010). Extracted images were uploaded to Ecotaxa, an online collaborative software dedicated to the visual exploration and taxonomic annotation of planktonic images (Picheral et al., 2017). The Random Forest algorithm (Breiman, 2001) was used to classify all objects into major plankton categories. The automatic classification was visually inspected to ensure the quality of the sorting. Only images corresponding to siliceous Rhizaria were picked out for subsequent analyses. For each instrument, abundances (ind. m^{-3}) of each rhizarian category were calculated at every station and morphological measurements associated with each vignette, such as body length and width, were used to obtain biovolumes (Supplementary Tables 1–3).

2.5.2. Metabarcoding data curation and analysis

Raw reads obtained from sequencing were processed and clustered following DADA2 (Callahan et al., 2016). The resulting amplicons sequence variants (ASVs) were taxonomically assigned using global search implemented in Vsearch (Rognes et al., 2016) against PR2 v4.14.0 database (Guillou et al., 2012) updated with Radiolaria sequences from (Méndez-Sandín, 2019). ASVs were considered for further analyses as long as they were present in at least 2 of the 48 samples examined and had more than 10 total reads in those samples and assigned to Phaeodaria and polycystine radiolarians (Spumellaria and Nassellaria, excluding Collodaria). Different size fractions were pooled together. The final dataset was composed of a total of 48 ASVs, normalized by sample to relative abundance.

2.6. Rhizaria biovolume and biogenic silica content

Area of the imaged specimen were computed according to Picheral et al. (2017). From the area, we calculated the equivalent spherical diameter (ESD; Equation1) to prevent overestimation of the individual's biovolume, since in some cases, the skeleton can have complex shapes, including long and irregular spines.

$$ESD = 2 \sqrt{\frac{Area}{\pi}} \quad (1)$$

where *ESD* (in µm) is the equivalent spherical diameter and *Area* is the pixel area of the imaged organism.

Then, we calculated the biovolume (μm^3) using the following equation:

$$Volume = \frac{4}{3}\ \pi\ \left(\frac{ESD}{2}\right)^3 \quad (2)$$

where ESD is the spherical diameter calculated with equation 1.

After calculating the biovolume (equation 2), we calculated the individual silica content of Rhizaria by using the log-linear relationship established by Llopis Monferrer et al. (2020), which relates silica content to biovolume ($R^2 = 0.86$):

$$log_{10}(Q_{bSi}) = [-4.05 \pm 0.18] + [0.52 \pm 0.02] log_{10}(biovolume) \quad (3)$$

where Q_{bSi} is the biogenic silica content of the specimen (µg-Si $cell^{-1}$).

3. Results

3.1. Environmental data

Surface temperature during the cruise ranged from 16.0°C to 22.2°C. Integrated Chlorophyll *a* (Chl *a*) values over the 0-150 m layer, varied between 2 and 45 mg m^{-2}. The depth of deep chlorophyll maximum (DCM) varied from 42 to 95 m. Biogenic silica concentrations, integrated over the surface to DCM layer ranged from 1.7 to 6.8 mmol-Si m^{-2} (Table 1).

3.2. Size spectra of the organisms captured by the different imaging technologies

A total of 753 rhizarians specimens were imaged using different imaging devices: either the FlowCAM (195 vignettes; 64-200 µm), the Zooscan (341, 200-1000 µm), or the UVP (217; >1000 µm). The overall size of the analysed organisms ranges from 45 to 3663 µm in equivalent spherical diameter (ESD; Figure 2). In the present study, the FlowCAM recorded the smallest individuals, with an ESD ranging from 45 to 176 µm (mean ± standard deviation; 103 ± 26 µm). Among the three instruments, the FlowCAM was the only one able to capture some of the polycystine radiolarians (*i.e.*, Spumellaria and Nassellaria) and phaeodarians of the genus *Challengeria*. The Zooscan captured individuals with ESD ranging from 365 to 1244 µm (799 ± 146 µm), which all belonged to the family Aulacanthidae (Phaeodaria). The UVP imaged the largest individuals, starting with an ESD of 945 µm up to 3662 µm (1279 ± 429 µm), with the smallest individuals belonging to the Aulacanthidae family and the largest cells to the Coelodendridae family (Phaeodaria).

We observed a discontinuity between the size class captured by the FlowCAM and the Zooscan. No specimen was observed between 176 µm (largest individual imaged by the FlowCAM) and 365 µm (*i.e.*, the smallest individual collected by the 200 µm mesh-size and imaged by the Zooscan). However, there was a size (ESD) overlap for organisms of about 1000 µm (essentially Aulacanthidae individuals) that were captured by both, the

TABLE 1 Study sites location and collection date. Chlorophyll a (Chl *a*) and biogenic silica (bSi) values were integrated over the 0-DCM layer.

Station	Date YYYYMMDD	Latitude (°N)	Longitude (°E)	Distance to the coast km	DCM m	Chl *a* mg m^{-2}	Bottom depth m	Sea Temp. °C	bSi mmol-Si m^{-2}
1-5	20170901	42.17	4.30	96	57	45	1909	21.8	1.7
1-21	20170905	43.15	8.15	78	71	17	2582	22.4	2.0
1-27	20170906	43.88	9.63	23	84	16	405	24.5	2.4
1-35	20170907	43.42	7.88	49	80	31	2330	23.0	2.3
1-40	20170908	43.53	7.62	28	70	22	2237	23.3	2.0
1-45	20170909	42.72	8.62	19	83	16	1558	23.8	3.5
1-51	20170910	42.15	7.68	76	83	11	2768	21.5	2.3
2-1	20170912	43.03	5.20	36	48	2	1109	16.1	1.7
2-15	20170914	40.20	4.18	14	95	20	839	25.4	2.7
2-20	20170915	41.62	3.63	50	86	29	954	23.8	2.8
2-25	20170916	42.42	3.55	33	68	30	897	18.3	6.8
2-33	20170917	41.93	4.98	146	68	22.3	2352	19.3	5.5
2-36	20170918	41.42	6.45	189	76	20	2690	21.6	4.3
2-45	20170919	40.00	8.03	29	90	20	1153	23.6	5.5
2-56	20170920	40.30	6.28	179	80	15.5	2828	23.1	5.6
2-67	20170921	43.00	6.00	13	42	NA	1005	18.7	2.2

NA, non available data.

10.3389/fmars.2022.895995

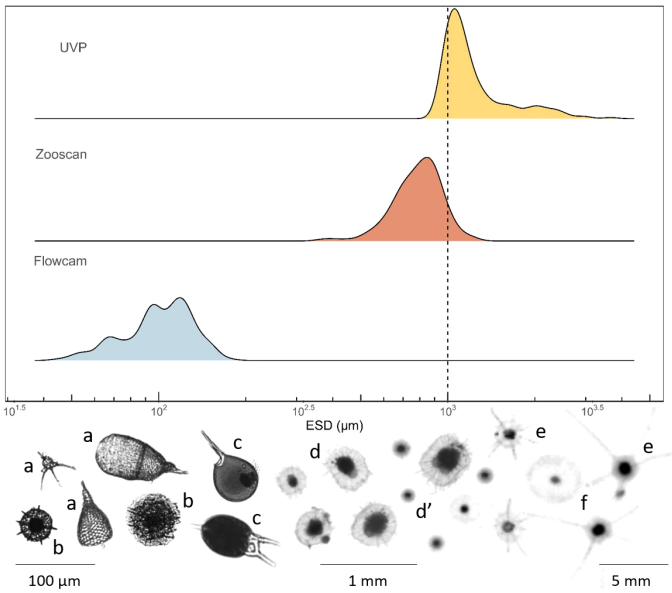

FIGURE 2
Density plot comparing the total size range of Rhizaria (in equivalent spherical diameter; ESD) captured by the three imaging tools used in this study (FlowCAM, Zooscan and UVP). The area under the curve represents the probability of getting an x value between a range of x values. The dashed line represents the upper limit of the Zooscan data considered and the lower limit of the UVP data, which was established to avoid overlap between these two instruments. **(A)** FlowCam images of Nassellaria, **(B)** Spumellaria, **(C)** FlowCam images of phaeodarians of the family Challengeridae, **(D, D')** Zooscan and UVP images of phaeodarians of the family Aulacanthidae respectively, **(E)** UVP images of phaeodarians of the family Coelodendridae and, **(F)** UVP images of phaeodarians of the family Aulosphaeridae.

Zooscan and the UVP. In order to avoid overestimation of the Rhizaria abundances (*i.e.*, counting twice the same size fraction), we excluded the specimens with an ESD larger than 1000 µm from the Zooscan data, and specimens with an ESD equal or smaller than 1000 µm from the UVP data.

3.3. Rhizaria diversity and abundance

The abundances of specimen (i.e., cells m^{-3}) were established based on quantitative methods (imaging tools) (Supplementary Tables 1–3). The smallest size range investigated in this study (Nassellaria, Spumellaria and Phaeodaria of the genus *Challengeria*), the 64-200 µm (FlowCAM) showed the highest abundance values at all stations, ranging from 5.0 to 61.1 cell m^{-3} (Table 2). The small size fraction was mainly dominated by nassellarians in all stations. Phaeodaria of the genus *Challengeria* were observed in lower proportions (in 12 of the 16 stations studied; Table 3). Regarding the 200-1000 µm size fraction, which corresponded to data obtained with the Zooscan, abundances of specimens identified as Aulacanthidae, the only category imaged with this instrument, had a maximum of 3.4 cells m^{-3}. Rhizarian abundances in the largest size fraction (>1000 µm), imaged by the UVP were generally slightly lower than those found for the 200-1000 µm size fraction (from 0.3 to

TABLE 2 The abundance of siliceous Rhizaria collected using three different devices corresponding a different size ranges.

Station	Size sampled		
Leg-Stn	64-200 µm	>200 µm Rhizaria concentration (cell m^{-3})	>1000 µm
1-5	5.1	0.3	1.7
1-21	10.2	0.4	1.3
1-27	17.2	1.1	1.8
1-35	42.5	0.3	1.0
1-40	41.7	1.1	1.9
1-45	15.5	1.2	1.3
1-51	19.8	1.8	1.4
2-1	26.2	1.0	0.7
2-15	13.0	0.2	1.9
2-20	53.9	1.3	1.9
2-25	5.0	1.1	0.6
2-33	19.4	0.5	0.7
2-36	61.1	0.2	1.4
2-45	10.1	0.0	0.3
2-56	40.8	0.1	0.7
2-67	16.9	3.4	1.5

FlowCAM corresponds to 64-200 µm, Zooscan to >200 µm and UVP to individuals >1000 µm.

TABLE 3 The presence and absence of the different taxonomic groups for the entire size spectra studied using imaging (I) and metabarcoding (M) methods.

Taxonomic groups	Nassellaria		Spumellaria		Challengeridare		Aulacanthidae		Coelodendridae		Aulosphaeridae		Other Phaeodaria	
Method	**I**	**M**	**I**	**M**	**I**	**M**	**I**	**M**	**I**	**M**	**I**	**M**	**I**	**M**
Leg-Stn														
1-5	x					x	x	x	x	x	x		x	x
1-21	x		x	x	x	x	x	x	x	x				x
1-27	x	x		x	x	x	x	x		x		x	x	x
1-35	x		x	x	x		x	x	x	x	x			
1-40	x	x	x		x		x	x	x	x	x			x
1-45	x			x	x		x	x	x	x			x	x
1-51	x				x		x	x	x	x			x	x
2-1	x		x	x	x		x	x		x		x		x
2-15	x				x		x		x		x			
2-20	x		x	x	x		x	x	x	x	x			x
2-25	x						x	x	x	x				
2-33	x		x		x		x	x	x	x				x
2-36	x		x		x		x	x	x	x	x			x
2-45	x	x	x	x		x	x	x	x	x				x
2-56	x		x	x	x	x	x	x	x	x	x	x		x
2-67	x			x		x	x	x	x	x	x	x		x

No metabarcoding data was available for stations leg2-05. For the imaging methods, Other Phaeodaria includes the groups Castanellidae and Cannosphaeridae, for metabarcoding it comprises other non-identified groups.

1.9 cells m^{-3}), except some stations (Table 2). The Phaeodaria groups found during this cruise belong to the families Aulacanthidae, Castanellidae, Coelodendridae, Aulosphaeridae and Cannosphaeridae (Figure 3).

When we examine the biovolume, we encounter an opposite trend to abundance (Figure 3B). The biovolume values of the individuals captured by Zooscan or UVP (> 200 µm) are higher than the ones obtained for individuals imaged by the FlowCAM and bring composition closer to metabarcoding than abundance values.

In the metabarcoding data, organisms belonging to the largest families (*i.e.*, Coelodendridae and Aulacanthidae) contributed the most to the relative sequence abundance (Figure 3C). When analysing the contribution of the various groups of organisms in terms of biovolume, we find that Aulacanthidae and Coelodendridae are the most represented taxa in each site while organisms belonging to smaller taxonomic groups are scarcely represented (Figure 3B).

From molecular techniques, we estimated that Rhizaria belonging to the >64 µm size class represented a total of 4.53% (± 3.49) of the eukaryotic community reads, while the fraction > 200 represented 11.3% (± 7.80), and the largest fraction, > 500 µm represented the highest percentage, 15.8% (± 13.90) in all samples. When comparing the relative abundances obtained by both methods (imaging and molecular), on the same size fraction sampled, we observed that the taxonomic groups determined by each method were not the same. Consequently, the computed relative abundances differed for the two methods (Table 3; Figure 3). A difference between the different taxonomic groups is observed when calculating the corresponding percentage of occurrence, ranging from 0.1% (Aulosphaeridae) and 0.9% (Aulacanthidae). However, when comparing relative abundances obtained through molecular tools and relative biovolume from imaging techniques, the results are closer at most of the stations investigated (Figure 3).

3.4. Contribution of Rhizaria to bSi standing stock

We examined the contribution of the different size ranges to the total silica biomass of Rhizaria. When converted to biomass using the allometric relationship (Equation 3), we found that the largest individuals (>1000 µm) contributed the most to the total Si stock in the water column, from 5.2 to 70.3 µmol-Si m^{-2}. Overall, the small and medium-sized individuals (>64 – 1000 µm) contributed equally to the largest individuals at all stations, except at offshore stations leg2-36, leg2-56, where small-sized individuals dominated. These stations presented the deepest bottom depths (Figure 4). Small Rhizaria (<200 µm) contributed to the biogenic silica standing stock from 2 to 50% depending on the sampling stations, contributing from 1.1 to 39.9 µmol-Si m^{-2} (Table 4).

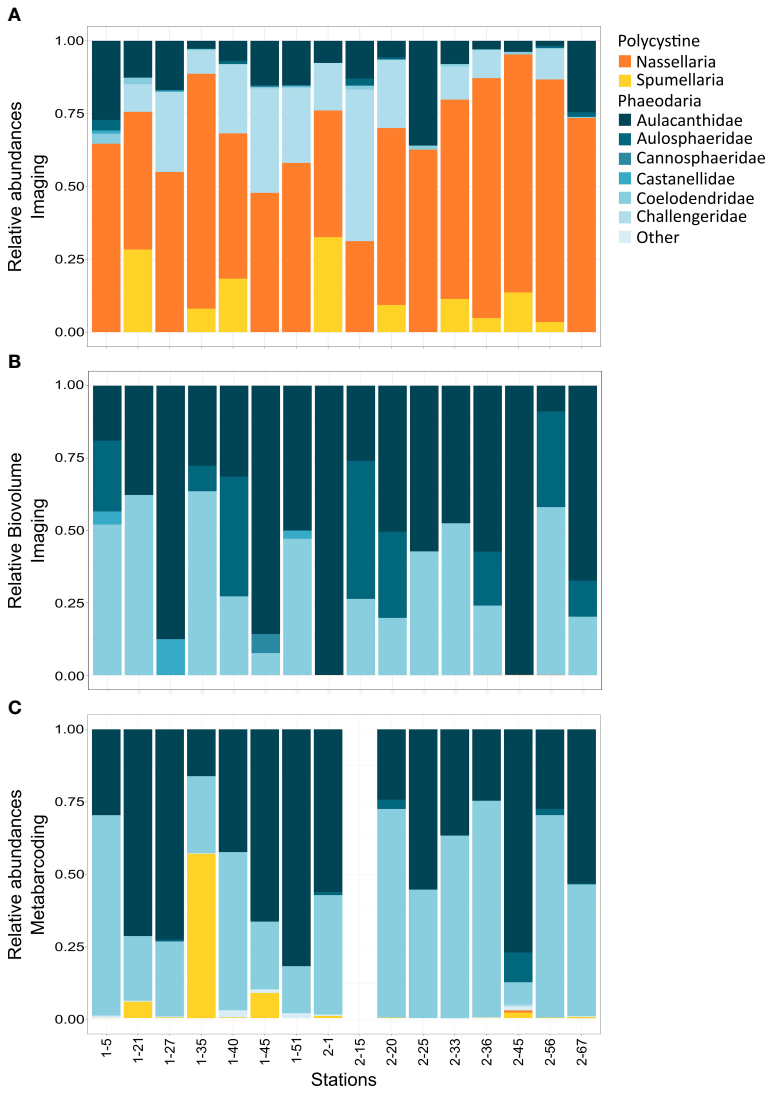

FIGURE 3
(A) Imaging technologies data. Relative abundances of the main rhizarians taxonomic groups cumulated from the different size fractions (> 64-200, 200-1000, > 1000 µm), from data obtained using the FlowCAM, Zooscan and UVP. **(B)** Imaging technologies data. Relative biovolume of the main rhizarians taxonomic groups cumulated from the different size fractions (> 64-200, 200-1000, > 1000 µm), from data obtained using the FlowCAM, Zooscan and UVP. **(C)** Molecular metabarcoding data. Relative abundance reads of the main rhizarian taxonomic groups in the different size fractions cumulated (> 64, > 200, > 500µm) of the V4 rDNA from vertical tow nets. No metabarcoding data was available for stations leg2-05.

4. Discussion

4.1. Rhizaria abundances and diversity: Imaging

This study is one of the few that simultaneously analyses a planktonic compartment covering a wide size spectrum using a wide array of instruments and methods. We used three imaging methods and genetic analyses to investigate a broad section of the Rhizaria size range. We found that these organisms are present at every station. In the North-Western basin of the Mediterranean Sea, Rhizaria abundances reached 61.1 cells m^{-3} in 0-500 m water depth, with small cells being largely dominant (from 5.0 to 61.1 cells m^{-3}) over larger ones (up to 3.4 cells m^{-3}). These abundances are consistent with the size distribution of organisms reported in previous studies where small rhizarians are generally more abundant than larger ones in the upper water column of the ocean (Boltovskoy et al., 1993; Llopis Monferrer et al., 2020). Yet, abundances observed here fall in the lower range of estimates from a worldwide compilation from

10.3389/fmars.2022.895995

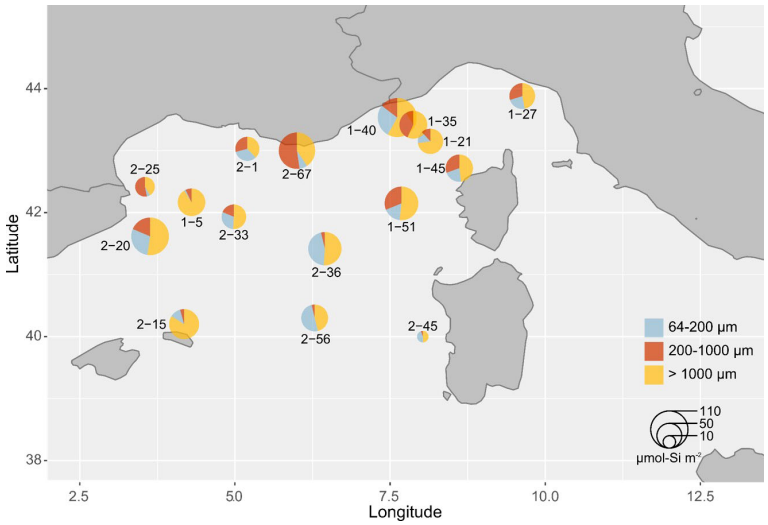

FIGURE 4
Overview of the bSi biomass of Rhizaria integrated into the upper 500 m of the water column (µmol-Si m^{-2}) in the Mediterranean Sea. Piecharts indicate relative contributions of the three size classes studied to the total bSi at each station and their size is proportional to their Si contribution.

microscopic observations of net samples deployed the 0-200 m water layer of the tropical and subtropical waters (40°N/S), which stated that small Rhizaria cell abundances ranged from 79 to 892 cells m^{-3} for polycystine radiolarians and from 5 to 20 cells m^{-3} for larger phaeodarians (Llopis Monferrer et al., 2020). Low cell densities observed in this study could be due to the integration of abundance values to 500 m instead of 200 m. Also, the different techniques used to obtain abundance values

TABLE 4 Biogenic silica integrated over the 0 – 500 m layer for Rhizaria collected using three different devices corresponding to different size ranges.

Station	bSi Rhizaria (µmol-Si m^{-2})			bSi Rhizaria (mmol-Si m^{-2})	bSi water column (mmol-Si m^{-2})	%
Leg-Stn	64-200 µm	>200 µm	>1000 µm	Total		
1-5	1.1	4.3	55.4	0.1	1.7	3.7
1-21	7.9	6.1	37.3	0.1	2.0	2.6
1-27	12.4	15.9	24.8	0.1	2.4	2.2
1-35	21.0	5.7	35.3	0.1	2.3	2.8
1-40	33.0	17.7	70.3	0.1	2.0	6.2
1-45	12.7	18.1	28.4	0.1	3.5	1.7
1-51	15.4	28.2	46.8	0.1	2.3	3.9
2-1	15.4	13.4	17.5	0.0	1.7	2.7
2-15	8.4	3.1	60.0	0.1	2.7	2.7
2-20	32.8	21.0	59.0	0.1	2.8	4.0
2-25	1.6	16.4	12.8	0.0	6.8	0.5
2-33	14.6	9.1	24.7	0.0	5.5	0.9
2-36	39.9	3.3	44.9	0.1	4.3	2.1
2-45	4.8	0.5	5.2	0.0	5.5	0.2
2-56	28.9	2.1	26.3	0.1	5.6	1.0
2-67	7.4	55.2	42.9	0.1	2.2	4.8

FlowCAM corresponds to 64-200 µm, Zooscan to >200 µm and UVP to individuals >1000 µm. Biogenic silica (bSi) values integrated over the 0-DCM layer and the potential impact (%) of Rhizaria to the total bSi bulk (net bSi/seawater bSi).

(microscopy versus FlowCAM) as well as the seasonality patterns in rhizarians communities. Analysis of plankton time series on the Northern coast of the Mediterranean Sea shows the highest biovolume of Rhizaria (including the non-silicified) in August, and quite low numbers the rest of the year (Romagnan et al., 2015).

Low cell densities could also be explained by the caveats associated with the use of imaging instruments. Although the combined use of the three instruments covered a broad size spectrum, we observed a size gap between the FlowCAM and Zooscan. From 176 µm to 365 µm no specimens were observed (Figure 2), which corresponds to the size class in which we may find many specimens of polycystines and phaeodarians (e.g., genus *Challengeria*; Llopis Monferrer et al., 2020). Their absence in the results could be explained by the handling of FlowCAM samples before the analysis, since these are sieved onto a 200 µm mesh size to prevent instrument clogging. To avoid the underestimation of larger cells, samples could be divided into different size fractions and analysed using smaller or larger flow cells. Moreover, many siliceous Rhizaria specimens can exhibit a size smaller than 64 µm which was the smallest plankton mesh used (e.g., small size species, juvenile forms), leading to an underestimation of total siliceous Rhizaria abundances. Finally, fixatives used classically (e.g., Lugol's iodine or formaldehyde) are known to affect organisms leading to potentially underestimated cell counts (Choi and Stoecker, 1989; Beers and Stewart, 1970).

Regarding the Zooscan (200–1000 µm), its operational size range starts at 240 µm. This instrument may limit the enumeration of small individuals whose sizes are close to the detection limit. Although all observations reported in this study lie within the range in which reliable quantitative results can be obtained, not all the operational size range is efficient to obtain quantitative results. The Zooscan captured the smallest individuals of the family Aulacanthidae and therefore it was necessary to avoid an even higher gap between different instruments (e.g., between the FlowCAM and the UVP).

The UVP has the advantage of determining *in situ* abundances of organisms in in the water column without damaging the organisms, along with their size distribution. However, despite this instrument has been designed to study large (>100 µm) particles, it is impossible to reliably identify Rhizaria groups when the size of the specimen is below 700 µm. Furthermore, the largest organisms are the least abundant and taxa with few representatives are likely to be overlooked.

4.2. Comparison of imaging and metabarcoding results

Molecular methods provide insights into the relative abundances and diversity of organisms but results are not quantitative. Molecular data can attempt to be compared to quantitative imaging technologies. In this study, the results of the imaging and metabarcoding comparisons do not match, neither in terms of relative abundances nor in terms of taxonomic diversity. However, when we analyse the biovolume obtained using imaging techniques, results are comparable and closer to metabarcoding data.

Molecular results show that siliceous Rhizaria were present in every sample among the different stations and size fractions and that the largest individuals had the highest relative abundances when comparing to data obtained through imaging approaches. It is well known that genes copies vary among protists and correlation exists between size and number of rDNA copies (Zhu et al., 2005; Godhe et al., 2008, Biard et al., 2017) which might bias their representativeness in an ecosystem leading to an overrepresentation of large specimens in metabarcoding data compared to morphologically cell counting. If we examine the biovolume results, they support the hypothesis that larger individuals usually present higher genome size and more gene copies, being more proportional to biomass than quantitative abundances (*i.e.*, number of cells). In the present study, larger organisms, despite being less abundant in the water column, may have an important impact on the total biomass because of their large size.

On the other hand, in terms of diversity, Nassellaria, which is the dominant group in abundance with imaging techniques, rarely appear in metabarcoding data. Nassellaria possess robust skeletons (Takahashi et al., 1983) and cell breakage may affect DNA extraction and amplification (Not et al., 2007; Méndez-Sandín, 2019). In addition, metabarcoding analyses rely on the reference database. Since sequences obtained from the environment will be compared to the closest related sequence, taxa not yet included in the database may lead to an underestimation of the relative abundances found in the metabarcoding data.

Although a correlation between rDNA copy number per cell and cell length was established across eukaryotic marine Collodaria (Biard et al., 2017), the comparison of relative abundances and diversity measured by imaging methods and molecular tools (Supplementary Figure S1) is complex and must be made cautiously. In this study, we excluded Collodaria specimen because they can include colonies composed by tens to thousands of cells, number which is complicated to determine with imagine methods and therefore, biogenic silica estimations cannot be conducted. Also, Collodaria can be naked (e.g., *Collozoum* sp.) or provided with siliceous spines (e.g., *Sphaerozoum* sp.), feature that cannot always be confirmed with imaging methods.

Imaging and metabarcoding methods have great potential and allow a rapid analysis and processing of samples. All these approaches for plankton enumeration have, however, uncertainties when estimating the actual composition and abundance of the community, and a thorough interpretation of the results requires assessment of the limits of each method.

To provide reliable comparisons between imaging and molecular methods, sampling protocols must be homogeneous (*e.g.*, sample the same size class, analysing the same water sample using both methods). Single-cell sequencing may help to avoid the mismatch between the taxonomic groups as it will enrich the database.

4.3. Use of imaging data to assess the relative contribution of Rhizaria to the bSi stock in the NW Mediterranean Sea

Rhizaria are important contributors to biogenic silica production in the global ocean (Takahashi et al., 1983; Biard et al., 2018; Llopis Monferrer et al., 2020). They span a wide size range and occupy a variety of ecosystems which makes it difficult to achieve an integrated perspective on their specific contribution to biogeochemical cycles (Suzuki and Not, 2015; Biard and Ohman, 2020).

The North-Western Mediterranean basin is characterised by oligotrophic conditions. During Fall (September-early November), surface waters are nutrient-depleted, and microphytoplankton is generally dominated by non-siliceous organisms (Leblanc et al., 2003). Leblanc et al. (2003) reported biogenic silica integrated stocks from 3.1 to 21.5 mmol-Si m^{-2} in the first 150 m of the water column at a station located in the North-Western Mediterranean basin with the lowest values of diatom biogenic silica corresponding to autumn. Values of diatom biogenic silica are close to 0 below 150 m throughout the year (Leblanc et al., 2003). During MOOSE-GE 17 cruise, biogenic silica values integrated over the 0-DCM layer ranged between 1.7 and 6.8 mmol-Si m^{-2}, which are concordant to those found by Leblanc et al. (2003) at a similar period of the year.

Using data obtained from the imaging tools along with the allometric relationship previously established (Llopis Monferrer et al., 2020), we provide the first attempt to determine the contribution of siliceous Rhizaria, across a broad size spectrum, to the biogenic silica standing stock in the Mediterranean Sea. Assuming that phytoplankton biogenic silica under the DCM was null (Leblanc et al., 2003), we compared Rhizaria biogenic silica values from the first 500 m of the water column to biogenic silica values of the water column. Therefore, we found that siliceous Rhizaria contributed up to 6% (2.6 ± 1.6) of the total biogenic silica in the water column (Table 4),

The contribution of Rhizaria to the biogenic silica biomass can be highly variable. For example, in productive areas of the World Ocean, where Rhizaria are less abundant and diatoms concentrations are much higher, the impact of these protists on the biogenic silica biomass in surface waters is much lower, as in the case of the Ross Sea in Antarctica, where Rhizaria account for only 0.1% at most of the total biogenic silica (Llopis Monferrer et al., 2021).

In this study, the smallest size class was collected with a plankton net over the first 500 m. With this sampling method, there is no detailed information on the vertical distribution of small Rhizaria, and it is difficult to know if they mainly thrive in the euphotic layer, where phytoplankton grow. We investigated metabarcoding from the Niskin bottles (Supplementary Figure S2), where the small phytoplankton community was represented. We observed that Rhizaria were relatively more abundant than diatoms in most of the stations, most likely due to the fact that larger organisms present more gene copies. For larger individuals, imaged *in-situ* with the UVP, the highest abundances were found at approximately 100 m depth (Supplementary Figure S3), below the maximum of diatom biogenic silica found in this area (Leblanc et al., 2003). There is evidence that the vertical distribution of some groups of Rhizaria can be associated with hydrographic features, such as the DCM (Kling and Boltovskoy, 1995; Dennett, 2002). A wider depth coverage, including the depth preferences of each taxonomic group, would be needed to study in detail the effect of these features on the rhizarians community.

Different Rhizaria species have different depth preferences (Boltovskoy et al., 2017; Biard and Ohman, 2020). According to this information, Rhizaria living in deeper layers, have been omitted in our estimates. This uneven distribution of organisms would affect the contribution of Rhizaria to the global biogenic silica standing stocks, especially in the waters below the euphotic layer, where they can be very abundant contributing to the biogenic silica fluxes to the deep ocean (Nakamura et al., 2013).

According to Llopis Monferrer et al. (2020), in tropical and subtropical waters (0-40°N/S) the contribution of Rhizaria to the standing stock of silicifiers in the 0-200 m water layer is of the same order of magnitude as their contribution estimated for the 200-1000 m layer. The impact of deeper-living organisms on the silica cycle has not been considered here, as we only analysed rhizarians found in the 0-500 m layer, but it could significantly increase their contribution to the total biomass.

Our results highlight that the study of the entire size spectrum and vertical distribution of Rhizaria is essential to fully understand the role of these protists in the biogeochemical cycle of silicon. Despite the possible underestimation of cell concentrations due to the sample manipulation (in FLowCAM and Zooscan protocols), small specimen accounted for up to 50% of the biogenic silica standing stock at some stations, showing that the small size class cannot be ignored. The biogenic silica content was certainly influenced by the taxonomic groups present at each station and their different cell sizes. Small Rhizaria, represented by polycystine (Nassellaria and Spumellaria) possess solid skeletons and are generally denser (up to 530 µg-Si mm^{-3}) than large phaeodarians (10

μg-Si mm^{-3}) (Llopis Monferrer et al., 2020), whose skeletons are instead porous (Nakamura et al., 2018).

Despite the uncertainties associated with each method employed, results showed that both, small and large Rhizaria are non-negligible contributors to the biogenic silica biomass in this oligotrophic region. To better understand the global significance of these organisms and to be able to include them in the biogeochemical models, the full extent of siliceous rhizarians must be considered.

4.4. Prospects to better characterize the entire Rhizaria community

Silicified Rhizaria vary widely in size, and studying them simultaneously is a challenging task. Furthermore, collecting enough individuals to get a fair representation of its abundance and diversity is a difficult task (Cortese, 2004). To sample both, large and small organisms concurrently, bongo nets can be used, as is the case of the present study. Sampling Rhizaria specimens can be also done by filtering water (Boltovskoy et al., 1993). For example, the entire content of a Niskin bottle could be analysed by imaging and/or molecular tools. By sampling with Niskin bottles, small collected Rhizaria could be associated with a given depth and physicochemical parameters, providing valuable information on the ecology of each specimen. Larger plankton could be sampled by traditional closing nets (*e.g.*, Multinet) to take into account different water layers. Alternatively, the Bottle-Net could be used as an alternative to the traditional plankton net. The Bottle-Net is an oceanographic device designed specifically for the Malaspina 2010 Circumnavigation (Agustí et al., 2020) to improve the collection of microplankton and particles (Leblanc et al., 2021). This instrument is designed to be mounted on a standard rosette and it consists of an external PVC and stainless-steel frame, with a 20 μm mesh size inside it. One of the major assets of this device is that it can sample a delimited water layer and it does not concentrate as many organisms as the plankton net, avoiding damage to the organisms.

To investigate large Rhizaria, the UVP appears as the most adequate instrument. This *in-situ* device is attached to the CTD, no extra time is needed for its deployment and environmental parameters can be associated with the organisms imaged. With this information, their ecological preferences and vertical niches can be characterized (Biard and Ohman, 2020). Its depth range is 6000 m, therefore, it can study the vertical distribution of Rhizaria up to zones where other tools cannot reach. The size of the resulting dataset is vast, resulting in a complex and time-consuming task to manually classify all the images.

Molecular tools, in turn, are a promising alternative to morphological observation for diversity determination but still many concepts are yet to be understood, such as cellular architecture and cellular size, copy number and intragenomic variability (Sandin et al., 2021). Another limitation of molecular methods is that DNA is capable of remaining available even when cells are dead (environmental DNA). This makes it difficult to know whether organisms found at a certain depth inhabit that same depth or are simply organisms sedimented from surface waters, making it impossible to know whether the DNA comes from a metabolically active cell, a dead cell, or the remnant of a cell (Brisbin et al., 2020).

The combination of imaging and molecular tools may lead to a better understanding of Rhizaria biology and ecology as it offers extensive coverage of the size spectrum.

Data availability statement

The datasets presented in this study can be found in online repositories. The names of the repository/repositories and accession number(s) can be found below: https://doi.org/10.6084/m9.figshare.19362374.v1.

Author contributions

NL, FL, MP, AE, LG, AL, PT, and FN participated to the conceptualisation of the manuscript. NL, TB, and FL worked on the quantitative data. MS provided and worked on the metabarcoding data. All authors have reviewed and provided input on the manuscript.

Funding

This work was supported by the ROSI project from the French National program LEFE (Les Enveloppes Fluides et l'Environnement) and ANR RadiCal (ANR-18-CE01-0011).

Acknowledgments

The authors are grateful to the MOOSE observation national network (funded by CNRS-INSU and Research Infrastructure ILICO), which supports the annual ship-based hydrographic sections in the northwestern Mediterranean Sea (MOOSE-GE). We also thank the science team and crew of the RV Atalante and Pierre Testor (CNRS, LOCEAN) as head of the MOOSE GE-2017 mission cruise. We thank the EMBRC platform PIQv for image analysis and the CCPv for access to samples. This work was supported by EMBRC-France, whose French state funds are managed by the ANR within the Investments of the Future program under reference ANR-10-INBS-02. This work was supported by the ROSI project from the French National program LEFE (Les Enveloppes Fluides et l'Environnement) and ANR RadiCal (ANR-18-CE01-0011). We are grateful to C. Dambrine and H. Whitby for their comments and help. We also thank the reviewers of this manuscript for their valuable comments.

Conflict of interest

The authors declare that the research was conducted in the absence of any commercial or financial relationships that could be construed as a potential conflict of interest.

Publisher's note

All claims expressed in this article are solely those of the authors and do not necessarily represent those of their affiliated organizations, or those of the publisher, the editors and the reviewers. Any product that may be evaluated in this article, or claim that may be made by its manufacturer, is not guaranteed or endorsed by the publisher.

Supplementary material

The Supplementary Material for this article can be found online at: https://www.frontiersin.org/articles/10.3389/fmars.2022.895995/full#supplementary-material

References

Agustí, S., Krause, J. W., Marquez, I. A., Wassmann, P., Kristiansen, S., and Duarte, C. M. (2020). Arctic (Svalbard islands) active and exported diatom stocks and cell health status. *Biogeosciences* 17, 35–45. doi: 10.5194/bg-17-35-2020

Alves-de-Souza, C., Gonzalez, M. T., and Iriarte, J. L. (2008). Functional groups in marine phytoplankton assemblages dominated by diatoms in fjords of southern Chile. *J. Plankton Res.* 30, 1233–1243. doi: 10.1093/plankt/fbn079

Beers, J. R., and Stewart, G. L. (1970). Numerical abundance and estimated biomass of microzooplankton. *Bulletin of the Scripps Institute of Oceanography* 17, 67–87.

Benfield, M., Grosjean, P., Culverhouse, P., Irigolen, X., Sieracki, M., Lopez-Urrutia, A., et al. (2007). RAPID: Research on automated plankton identification. *Oceanog.* 20, 172–187. doi: 10.5670/oceanog.2007.63

Biard, T. (2022) *Rhizaria. eLs*. Available at: https://doi.org/in.press.

Biard, T., Bigeard, E., Audic, S., Poulain, J., Gutierrez-Rodriguez, A., Pesant, S., et al. (2017). Biogeography and diversity of collodaria (Radiolaria) in the global ocean. *ISME J.* 11, 1331–1344. doi: 10.1038/ismej.2017.12

Biard, T., Krause, J. W., Stukel, M. R., and Ohman, M. D. (2018). The significance of giant phaeodarians (Rhizaria) to biogenic silica export in the California current ecosystem. *Global Biogeochem. Cycles* 32, 987–1004. doi: 10.1029/2018GB005877

Biard, T., and Ohman, M. D. (2020). Vertical niche definition of test-bearing protists (Rhizaria) into the twilight zone revealed by *in situ* imaging. *Limnol. Oceanogr. lno*. 11472, 2583–2602. doi: 10.1002/lno.11472

Biard, T., Stemmann, L., Picheral, M., Mayot, N., Vandromme, P., Hauss, H., et al. (2016). *In situ* imaging reveals the biomass of giant protists in the global ocean. *Nature* 532, 504–507. doi: 10.1038/nature17652

Boltovskoy, (2003). First record of a brackish radiolarian (Polycystina): Lophophaena rioplatensis n. sp. in the Rio de la plata estuary. *J. Plankton Res.* 25, 1551–1559. doi: 10.1093/plankt/fbg107

Boltovskoy, D., Alder, V. A., and Abelmann, A. (1993). Annual flux of radiolaria and other shelled plankters in the eastern equatorial atlantic at 853 m: Seasonal variations and polycystine species-specific responses. *Deep Sea Res. Part I: Oceanogr. Res. Pap.* 40, 1863–1895. doi: 10.1016/0967-0637(93)90036-3

Boltovskoy, D., Anderson, O. R., and Correa, N. (2017). *Handbook of the protists, springer*. Eds. J. M. Archibald, A. G. B. Simpson and C. H. Slamovits (Cham, Switzerland: Springer).

Boltovskoy, D., Kling, S. A., Takahashi, K., and Bjørklund, K. (2010). World atlas of distribution of recent polycystina (Radiolaria). *Palaeontologia Electronica* 13 (3).

Breiman, L. (2001). Random forests. *Mach. Learn.* 45, 5–32. doi: 10.1023/A:1010933404324

Brisbin, M. M., Brunner, O. D., Grossmann, M. M., and Mitarai, S. (2020). Paired high-throughput, *in-situ* imaging and high-throughput sequencing illuminate acantharian abundance and vertical distribution (preprint). *Limnol. Oceanogr*. 65 (12), 2953–2965. doi: 10.1101/2020.02.27.967349

Brzezinski, M. A., and Nelson, D. M. (1989). Seasonal changes in the silicon cycle within a gulf stream warm-core ring. *Deep Sea Res. Part A. Oceanogr. Res. Pap.* 36, 1009–1030. doi: 10.1016/0198-0149(89)90075-7

Buitenhuis, E., Le Quéré, C., Aumont, O., Beaugrand, G., Bunker, A., Hirst, A., et al. (2006). Biogeochemical fluxes through mesozooplankton: Biogiochemical fluxes through mesozooplankton. *Global Biogeochem. Cycles* 20. doi: 10.1029/2005GB002511

Callahan, B. J., McMurdie, P. J., Rosen, M. J., Han, A. W., Johnson, A. J. A., and Holmes, S. P. (2016). DADA2: High-resolution sample inference from illumina amplicon data. *Nat. Methods* 13, 581–583. doi: 10.1038/nmeth.3869

Choi, J. W., and Stoecker, D. K. (1989). Effects of fixation on cell volume of marine planktonic pro- tozoa. *Appl. Environ. Microbial.* 55, 1761–65.

Cortese, G. (2004). *The 300 specimens problem*. Radiolaria: Newsletter of the international association of radiolarian paleontologists. 22, 13–18.

Dennett, M. R. (2002). Video plankton recorder reveals high abundances of colonial radiolaria in surface waters of the central north pacific. *J. Plankton Res.* 24, 797–805. doi: 10.1093/plankt/24.8.797

de Vargas, C., Audic, S., Henry, N., Decelle, J., Mahe, F., Logares, R., et al. (2015). Eukaryotic plankton diversity in the sunlit ocean. *Science* 348, 1261605–1261605. doi: 10.1126/science.1261605

Donoso, K., Carlotti, F., Pagano, M., Hunt, B. P. V., Escribano, R., and Berline, L. (2017). Zooplankton community response to the winter 2013 deep convection process in the NWMediterranean Sea: Zooplankton and winter deep convection. *J. Geophys. Res. Ocean.* 122, 2319–2338. doi: 10.1002/2016JC012176

Edwards, M., Beaugrand, G., Helaouët, P., Alheit, J., and Coombs, S. (2013). Marine ecosystem response to the Atlantic multidecadal oscillation. *PloS One* 8, e57212. doi: 10.1371/journal.pone.0057212

Faure, E., Not, F., Benoiston, A.-S., Labadie, K., Bittner, L., and Ayata, S.-D. (2019). Mixotrophic protists display contrasted biogeographies in the global ocean. *ISME J.* 13, 1072–1083. doi: 10.1038/s41396-018-0340-5

Gloor, G. B., Macklaim, J. M., Pawlowsky-Glahn, V., and Egozcue, J. J. (2017). Microbiome datasets are compositional: And this is not optional. *Front. Microbiol.* 8. doi: 10.3389/fmicb.2017.02224

Godhe, A., Asplund, M. E., Härnström, K., Saravanan, V., Tyagi, A., and Karunasagar, I. (2008). Quantification of diatom and dinoflagellate biomasses in coastal marine seawater samples by real-time PCR. *Appl. Environ. Microbiol.* 74, 7174–7182.

Gorsky, G., Ohman, M. D., Picheral, M., Gasparini, S., Stemmann, L., Romagnan, J.-B., et al. (2010). Digital zooplankton image analysis using the ZooScan integrated system. *J. Plankton Res.* 32, 285–303. doi: 10.1093/plankt/fbp124

Guidi, L., Chaffron, S., Bittner, L., Eveillard, D., Larhlimi, A., Roux, S., et al. (2016). Plankton networks driving carbon export in the oligotrophic ocean. *Nature* 532, 465–470. doi: 10.1038/nature16942

Guillou, L., Bachar, D., Audic, S., Bass, D., Berney, C., Bittner, L., et al. (2012). The protist ribosomal reference database (PR2): A catalog of unicellular eukaryote small Sub-unit rRNA sequences with curated taxonomy. *Nucleic Acids Res.* 41, D597–D604. doi: 10.1093/nar/gks1160

Gutierrez-Rodriguez, A., Stukel, M. R., Lopes dos Santos, A., Biard, T., Scharek, R., Vaulot, D., et al. (2018). High contribution of rhizaria (Radiolaria) to vertical export in the California current ecosystem revealed by DNA metabarcoding. *ISME J.* 13, 964–976. doi: 10.1038/s41396-018-0322-7

Irisson, J.-O., Ayata, S.-D., Lindsay, D. J., Karp-Boss, L., and Stemmann, L. (2022). Machine learning for the study of plankton and marine snow from images. *Annu. Rev. Mar. Sci.* 14, 277–301. doi: 10.1146/annurev-marine-041921-013023

Ishitani, Y., and Takahashi, K. (2007). The vertical distribution of radiolaria in the waters surrounding Japan. *Mar. Micropaleontol.* 65, 113–136. doi: 10.1016/j.marmicro.2007.06.002

Kling, S. A., and Boltovskoy, D. (1995). Radiolarian vertical distribution patterns across the southern California current. *Deep Sea Res. Part I: Oceanogr. Res. Pap.* 42, 191–231. doi: 10.1016/0967-0637(94)00038-T

Lampitt, R. S., Salter, I., and Johns, D. (2009). Radiolaria: Major exporters of organic carbon to the deep ocean: Radiolaria export carbon to the deep ocean. *Global Biogeochem. Cycles* 23. doi: 10.1029/2008GB003221. n/a-n/a.

Leblanc, K., Lafond, A., Cornet, V., Legras, J., Marie, B., and Quéguiner, B. (2021). Deep particle stocks following the summer bloom around the kerguelen islands: Insights into diatoms physiological state, community structure and mortality modes. *J. Mar. Syst.* 222, 103609. doi: 10.1016/j.jmarsys.2021.103609

Leblanc, K., Quéguiner, B., Garcia, N., Rimmelin, P., and Raimbault, P. (2003). Silicon cycle in the NW Mediterranean Sea: Seasonal study of a coastal oligotrophic site. *Oceanol. Acta* 26, 339–355. doi: 10.1016/S0399-1784(03)00035-5

Le Queré, C., Harrison, S. P., Colin Prentice, I., Buitenhuis, E. T., Aumont, O., Bopp, L., et al. (2005). Ecosystem dynamics based on plankton functional types for global ocean biogeochemistry models. *Global Change Biol.* 11 (1), 2016–2040. doi: 10.1111/j.1365-2486.2005.1004.x

Llopis Monferrer, N., Boltovskoy, D., Tréguer, P., Sandin, M. M., Not, F., and Leynaert, A. (2020). Estimating biogenic silica production of rhizaria in the global ocean. *Global Biogeochem. Cycles* 34. doi: 10.1029/2019GB006286

Llopis Monferrer, N., Leynaert, A., Tréguer, P., Gutiérrez-Rodríguez, A., Moriceau, B., Gallinari, M., et al. (2021). Role of small rhizaria and diatoms in the pelagic silica production of the southern ocean. *Limnol. Oceanogr.* 66 (6), 2187–2202. doi: 10.1002/lno.11743

Lombard, F., Boss, E., Waite, A. M., Vogt, M., Uitz, J., Stemmann, L., et al. (2019). Globally consistent quantitative observations of planktonic ecosystems. *Front. Mar. Sci.* 6. doi: 10.3389/fmars.2019.00196

Mayot, N., D'Ortenzio, F., Taillandier, V., Prieur, L., de Fommervault, O. P. , Claustre, H., et al. (2017). Physical and biogeochemical controls of the phytoplankton blooms in north Western Mediterranean Sea: A multiplatform approach over a complete annual cycle, (2012–2013 DEWEX experiment). *J. Geophys. Res. Ocean.* 122, 9999–10019. doi: 10.1002/2016JC012052

Méndez-Sandín, M. (2019). Diversité et évolution des nassellaires et spumellaires (radiolaires). *Station Biol. Roscoff*. Available at: https://hal.archives-ouvertes.fr/tel-03137926v1

Nakamura, Y., Imai, I., Yamaguchi, A., Tuji, A., and Suzuki, N. (2013). Aulographis japonica sp. nov. (Phaeodaria, aulacanthida, aulacanthidae), an abundant zooplankton in the deep sea of the Sea of Japan. *Plankton Benthos Res.* 8, 107–115. doi: 10.3800/pbr.8.107

Nakamura, Y., Iwata, I., Hori, R. S., Uchiyama, N., Tuji, A., Fujita, M. J., et al. (2018). Elemental composition and ultrafine structure of the skeleton in shell-bearing protists–a case study of phaeodarians and radiolarians. *J. Struct. Biol.* 204, 45–51. doi: 10.1016/j.jsb.2018.06.008

Not, F., Gausling, R., Azam, F., Heidelberg, J. F., and Worden, A. Z. (2007). Vertical distribution of picoeukaryotic diversity in the Sargasso Sea. *Environ. Microbiol.* 9, 1233–1252. doi: 10.1111/j.1462-2920.2007.01247.x

Pernice, M. C., Giner, C. R., Logares, R., Perera-Bel, J., Acinas, S. G., Duarte, C. M., et al. (2016). Large Variability of bathypelagic microbial eukaryotic communities across the world's oceans. *ISME J.* 10, 945–958. doi: 10.1038/ismej.2015.170

Picheral, M., Colin, S., and Irisson, J.-O. (2017) *EcoTaxa [WWW document]*. Available at: http://ecotaxa.obs-vlfr.fr/ (Accessed 6.29.20).

Picheral, M., Guidi, L., Stemmann, L., Karl, D. M., Iddaoud, G., and Gorsky, G. (2010). The underwater vision profiler 5: An advanced instrument for high spatial resolution studies of particle size spectra and zooplankton: Underwater vision profiler. *Limnol. Oceanogr. Methods* 8, 462–473. doi: 10.4319/lom.2010.8.462

Robinson, A. R., Leslie, W. G., Theocharis, A., and Lascaratos, A. (2001). Mediterranean Sea Circulation, in: Encyclopedia of ocean sciences. *Elsevier*, 1689–1705. doi: 10.1006/rwos.2001.0376

Rognes, T., Flouri, T., Nichols, B., Quince, C., and Mahé, F. (2016). VSEARCH: A versatile open source tool for metagenomics. *PeerJ* 4, e2584. doi: 10.7717/peerj.2584

Romagnan, J.-B., Legendre, L., Guidi, L., Jamet, J.-L., Jamet, D., Mousseau, L., et al. (2015). Comprehensive model of annual plankton succession based on the whole-plankton time series approach. *PloS One* 10, e0119219. doi: 10.1371/journal.pone.0119219

Sandin, M. M., Romac, S., and Not, F. (2021). Intra-genomic rDNA gene variability of nassellaria and spumellaria (Rhizaria, radiolaria) assessed by Sanger, MinION and illumina sequencing. *Environ. Microbio.* 24 (7), 2979–2293. doi: 10.1101/2021.10.05.463214

Sieracki, C., Sieracki, M., and Yentsch, C. (1998). An imaging-in-flow system for automated analysis of marine microplankton. *Mar. Ecol. Prog. Ser.* 168, 285–296. doi: 10.3354/meps168285

Stoeck, T., Bass, D., Nebel, M., Christen, R., Jones, M. D. M., Breiner, H.-W., et al. (2010). Multiple marker parallel tag environmental DNA sequencing reveals a highly complex eukaryotic community in marine anoxic water. *Mol. Ecol.* 19, 21–31. doi: 10.1111/j.1365-294X.2009.04480.x

Stukel, M., Ohman, M., Benitez-Nelson, C., and Landry, M. (2013). Contributions of mesozooplankton to vertical carbon export in a coastal upwelling system. *Mar. Ecol. Prog. Ser.* 491, 47–65. doi: 10.3354/meps10453

Suzuki, N., and Not, F. (2015). "Biology and ecology of radiolaria," in *Marine protists: Diversity and dynamics* (New York: Springer, Tokyo), 179–222.

Takahashi, K., Hurd, D. C., and Honjo, S. (1983). Phaeodarian skeletons: Their role in silica transport to the deep Sea. *Science* 222, 616–618. doi: 10.1126/science.222.4624.616

Toullec, J., Vincent, D., Frohn, L., Miner, P., Le Goff, M., Devesa, J., et al. (2019). Copepod grazing influences diatom aggregation and particle dynamics. *Front. Mar. Sci.* 6. doi: 10.3389/fmars.2019.00751

Uitz, J., Claustre, H., Griffiths, F. B., Ras, J., Garcia, N., and Sandroni, V. (2009). A phytoplankton class-specific primary production model applied to the kerguelen islands region (Southern ocean). *Deep Sea Res. Part I: Oceanogr. Res. Pap.* 56, 541–560. doi: 10.1016/j.dsr.2008.11.006

Zhu, F., Massana, R., Not, F., Marie, D., and Vaulot, D. (2005). Mapping of picoeucaryotes in marine ecosystems with quantitative PCR of the 18S rRNA gene. *FEMS Microbiol. Ecol.* 52, 79–92.

frontiers | Frontiers in Marine Science

TYPE Original Research
PUBLISHED 09 December 2022
DOI 10.3389/fmars.2022.1005068

OPEN ACCESS

EDITED BY
Brivaela Moriceau,
UMR6539 Laboratoire des Sciences de L'environnement Marin (LEMAR), France

REVIEWED BY
Jun-ichi Kadokawa,
Kagoshima University, Japan
Bernard Moussian,
Université Côte d'Azur, France
Xiangbin Ran,
Ministry of Natural Resources, China

*CORRESPONDENCE
Manuel Maldonado
maldonado@ceab.csic.es

SPECIALTY SECTION
This article was submitted to Marine Biogeochemistry, a section of the journal Frontiers in Marine Science

RECEIVED 27 July 2022
ACCEPTED 16 November 2022
PUBLISHED 09 December 2022

CITATION
Maldonado M, López-Acosta M, Abalde S, Martos I, Ehrlich H and Leynaert A (2022) On the dissolution of sponge silica: Assessing variability and biogeochemical implications. *Front. Mar. Sci.* 9:1005068. doi: 10.3389/fmars.2022.1005068

On the dissolution of sponge silica: Assessing variability and biogeochemical implications

Manuel Maldonado[1]*, María López-Acosta[1,2], Samuel Abalde[1,3], Isabel Martos[1], Hermann Ehrlich[4,5] and Aude Leynaert[6]

[1]Centro de Estudios Avanzados de Blanes (CEAB), CSIC, Blanes, Spain, [2]Instituto de Investigaciones Marinas (IIM), CSIC, Vigo, Spain, [3]Department of Zoology, Swedish Museum of Natural History, Stockholm, Sweden, [4]Institute of Electronic and Sensor Materials, TU Bergakademie Freiberg, Freiberg, Germany, [5]Center for Advanced Technology, Adam Mickiewicz University, Poznan, Poland, [6]Institut Univeresitaire Européen de la Mer. LEMAR UMR, Pluozané, France

The dissolution of the biogenic silica that constitutes the skeletons of silicifying organisms is an important mechanism for regenerating dissolved silicon in the ocean. The silica skeletons deposited to the seafloor after the organisms die keep dissolving until becoming definitively buried. The low dissolution rate of sponge skeletons compared to that of diatom skeletons favors their burial and makes sponges (Phylum Porifera) to function as important silicon sinks in the oceans. However, it remains poorly understood whether the large variety of siliceous skeletons existing in the Porifera involves similar variability in their dissolution rates, which would affect the general conceptualization of these organisms as silicon sinks. Herein we investigated kinetics of silica dissolution for major types of skeletons in the three siliceous lineages of Porifera, following standardized digestion conditions in 1% sodium carbonate with orbital agitation at 85°C. The results are compared with those of a previous study conducted under identical conditions, which considered diatom silica, sponge silica, and lithogenic silica. Unexpectedly, the silica of homoscleromorph sponges dissolved only a bit slower than that of freshly cultured diatoms and as fast as diatom earth. However, the rest of sponge skeletons were far more resistant, although with some differences: the isolated spicules of hexactinellid sponges dissolved slightly faster than when forming frameworks of fused spicules, being hexactinellid frameworks as resistant to dissolution as the silica of demosponges, irrespective of occurring in the form of isolated spicules or frameworks. The experiments also indicated that the complexation of sponge silica with aluminum and with chitin does not increase its resistance to dissolution. Because the rapidly-dissolving homoscleromorph sponges represent less than 1% of extant sponges, the sponge skeletons are still conceptualized as important silicon sinks due to their comparative resistance to dissolution. Yet, the turnover of silica into dissolved silicon will always be faster in environments dominated by hexactinellids with isolated spicules than in environments dominated by other hexactinellids and/or demosponges. We

discuss whether the time required for a given silica type to completely dissolve in 1% sodium carbonate could be a predictor of its preservation ratio in marine sediments.

KEYWORDS

sponge silica, silica turnover, silicate regeneration, sediment digestion, chitin, aluminum, total biogenic silica, silicon cycling

Introduction

In the marine biogeochemical cycle of silicon (Si), siliceous sponges are recognized as distinctive players (Maldonado et al., 2012; Tréguer and De La Rocha, 2013; Tréguer et al., 2021). They are slow consumers compared to diatoms and their main effects are mediated through long-term accumulation of impressive Si standing stocks in the form of silica skeletons in the living populations. Those skeletons are deposited to the sediments once the sponges die. Deposited skeletal pieces feed a fossil record dating back to the Early Cambrian, 525 mya (Tang et al., 2019). More questionable proposals suggest some Precambrian fossil vestiges to be sponge silica skeletons (Muscente et al., 2015). The sponge skeletons accumulated in marine sediments make important local to regional silica reservoirs (Rützler and Macintyre, 1978; Bavestrello et al., 1996; Chu et al., 2011; Gutt et al., 2013; Murillo et al., 2016; Maldonado et al., 2021; López-Acosta et al., 2022). A first quantification of the deposition and burial of sponge skeletons, which occurs more markedly on continental margins and around seamounts, revealed that these processes lead to a substantial Si sink in the global ocean (Maldonado et al., 2019). Burial of sponge silica is favored by its high resistance to dissolution compared to that of the silica of other common marine silicifiers, such as radiolarians and diatoms. For instance, about 45.2% (on average) of the sponge silica deposited to the sediments per year is estimated to become buried permanently (Maldonado et al., 2019), while the ratio for diatom silica is only about 7.5% (Tréguer et al., 2021), being the rest recycled as silicic acid (DSi= dissolved silica) that escapes from the sediments to the bottom water. Thus, the resistance to dissolution of the biogenic silica (BSi) produced by the various marine silicifiers has important implications to the recycling of DSi, which is, in turn, a pivotal nutrient sustaining primary marine productivity (Nelson et al., 1995).

The approximately 9,500 extant species of sponges described taxonomically (de Voogd et al., 2022) are distributed into four major lineages, three of them characterized by having siliceous skeletons: Demospongiae (84%), Hexactinellida (7%), and Homoscleromorpha (1%); sponges with a calcareous skeleton make the remaining 8% of species. Since the 1970's, a variety of experimental studies have consistently concluded that the silica constituting the skeletons of sponges is more resistant to dissolution than diatom silica, in both seawater and alkaline solutions (Kamatani, 1971; Kamatani and Oku, 2000; Maldonado et al., 2005; Chu et al., 2011; Maldonado et al., 2019), for reasons that are not yet well understood. However, a study by Bertolino et al. (2017) proposed that the resistance to dissolution of the silica of some hexactinellid sponges could be not that strong, since relatively large spicules of hexactinellids (particularly those in the family Rosellidae) appeared to dissolve almost entirely in the course of an 8 month experiment. This view was contested by a subsequent study investigating the Si cycle in an aggregation of rosellid hexactinellids (Maldonado et al., 2021), which documented that superficial silica layers of the spicules of rosellid hexactinellids progressively peel off and detach (i.e., silica delamination). Thus, the "high silica dissolution rate" reported by Bertolino et al. (2017) mostly accounted for unnoticed mechanical BSi delamination rather than for actual chemical BSi dissolution. To further investigate the potential differences in the dissolution dynamics of the sponge silica between major sponge lineages, we have conducted the present study. To understand the between-group variability of the dissolution properties of the BSi is important, because such property affects the general conceptualization of siliceous sponges as a relevant Si sink in the global ocean. It also affects the assumptions underlying the quantification of Si cycling through sponges. Thus, we examine herein whether there are marked differences in the resistance to dissolution between different types of siliceous skeletons in the phylum Porifera, by conducting comparative laboratory dissolution experiments based on standard methodology.

Likewise, there is no mechanistic understanding about the reasons of the comparatively high resistance of sponge silica to dissolution. Two main hypotheses have been postulated (Maldonado et al., 2012), but never tested experimentally: 1) the molecular network of the sponge silica would incorporate aluminum (Al) in larger quantities than diatom silica. Aluminum is known to stabilize covalently the silica matrix of diatoms (Machill et al., 2013), lowering its solubility by as much as 25% when one out of every 70 Si atoms is substituted by an Al (III) ion (Van Bennekom et al., 1991; Dixit et al., 2001; Van Cappellen et al., 2002); 2) the spicules of some hexactinellid

10.3389/fmars.2022.1005068

sponges are known to incorporate chitin layers intercalated between the concentric silica layers (Ehrlich et al., 2007b; (Ehrlich et al., 2016). Since chitin is a skeletal amino polysaccharide highly resistant to degradation, its presence could hamper the chemical attack to the most accessible sites of the BSi molecular structure, decreasing solubility. These two hypotheses are herein tested experimentally in an attempt to improve our understanding of the processes governing the dissolution and recycling of the sponge silica.

Materials and methods

Digestion of sponge silica

The dissolution kinetics of the skeletal BSi of a variety of sponge species were compared using a 1% solution of sodium carbonate as standard dissolution medium (DeMaster, 1991). Representatives of the main skeletal types in the three phylogenetic lineages of siliceous sponges were selected for the experiment. For the demosponge lineage, we selected 2 skeleton types: 1) millimeters long oxeas and anchor-like spicules (anatriaenes) that are naturally exposed to the seawater because they protrude out of the sponge body to form the rootlets that anchor the sponge *Geodia hentscheli* to the bottom (Figure 1A), 2) pieces of the hypersilicified skeletal framework of fused desmas in the lithistid demosponge *Leiodermatium pfeifferae* (Figure 1B). For the homoscleromorph lineage, we selected the combination of small isolated monaxonic triaxonic, and tetraxonic spicules of the species *Corticium candelabrum* (Figure 1C). For the hexactinellid lineage, we also selected two skeleton types: 1) the skeleton of *Aphrocallistes vastus* (Figure 1D) in which a variety of isolated hexactinal spicules and a massive dictyonal skeletal framework of fused skeletal pieces co-occur; 2) the skeleton of only isolated spicules from the body wall of three rosellids, *Schaudinnia rosea* (Figure 1E), *Asconema setubalense* (Figure 1F), and *Vazella pourtalesii* (Figure 1G). The group of rosellid hexactinellids included 3 species in order to facilitate a within-group assessment of variability in the dissolution rate and compare the results with a previous study suggesting that the resistance to dissolution of the silica of rosellid hexactinellids

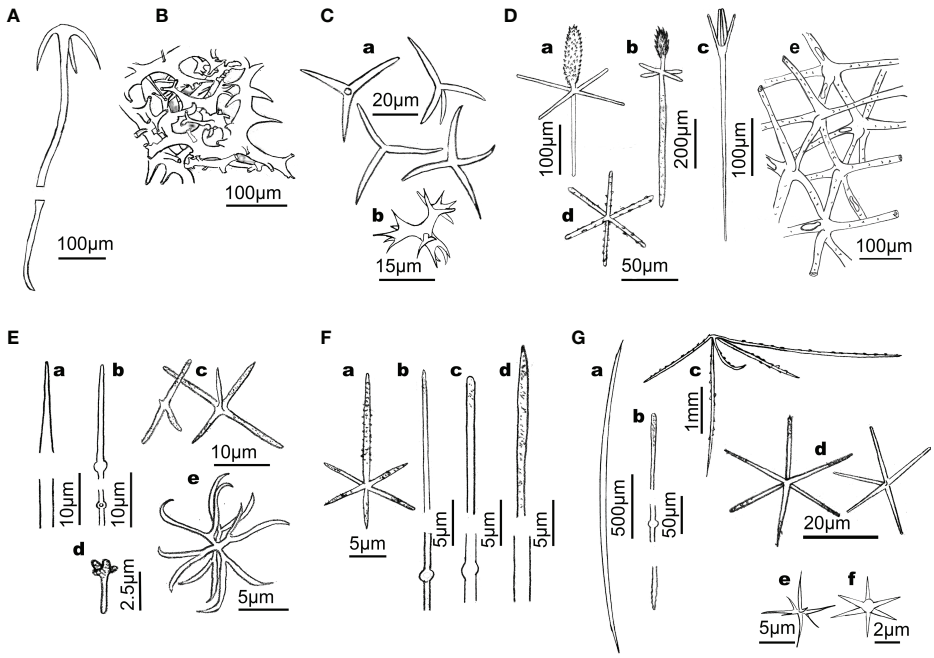

FIGURE 1
Line drawings summarizing the main types of siliceous skeletons involved in the dissolution experiment. **(A)** Anatriaene from the rootlets of the astrophorid demosponge *Geodia hentscheli*. **(B)** Skeletal framework of fused desmas of the lithistid demosponge *Leiodermatium pfeifferae*. **(C)** Microtriactines and microtetractines (a) along with candelabra (b) of the homoscleromorph *Corticium candelabrum*. **(D)** Skeleton of hexactinellid hexactinosid *Aphrocallistes vastus*, where a variety of hexactinal spicules (e.g., a, b: dermal pinnule; c: dermal scopule; d: parenchymal hexactine) and a skeletal dictyonal framework (e) co-occur. **(E)** Skeleton of the hexactinellid rosellid *Schaudinnia rosea*, which lacks skeletal framework and contains, among other skeletal pieces, a variety of diactinal spicules (a, b) within the body wall, dermal triactines and pentactines (c, d), and hexasters (e). **(F)** Skeleton of the hexactinellid rosellid *Asconema setubalense*, containing, among other skeletal pieces, atrial hexactines **(A)** and diactines of several sizes (b–d). **(G)** Skeleton of the hexactinellid rosellid *Vazella pourtalesii*, containing, among other skeletal pieces, diactinal (a, b) and pentactinal (c) spicules that reinforce the body wall and project out of the body, along with smaller pentactines and hexactines (d), and a variety of hexasters (e) and microhexactines (f).

might be much lower than that of other sponges (Bertolino et al., 2017). In addition to the sponge skeletons, we also dissolved aged frustules of diatoms in the form of diatomaceous earth from a Miocene deposit (Castalia diatom earth; https://www.naturitas.es/p/hogar-y-huerto/huerto/abonos-sustratos-y-fertilizantes/tierra-de-diatomeas-250-g-castalia).

Digestions were based on 5 silica subsamples of each skeleton type. Each subsample consisted of ~2.997 mg of acid-cleaned, dried BSi, which is equivalent to ~1.4 mg Si (Supplementary Data File S1). To obtain the silica, pieces of sponge tissue were boiled for a few minutes in concentrated nitric acid, then rinsed in distilled water, and finally in ethanol, prior to dry them to constant weight in an oven to 60°C for several days. Digestions of cleaned BSi were conducted in 50 mL, hermetically-closed Teflon bombs immersed in distilled water at 85°C with orbital agitation, using a 50L SBS TBA-30 bath that was user-modified for agitation and temperature control (Supplementary Video S1). Digestion Teflon bombs were sampled at 0, 2, 3, 4, 5, 6, 8, 12, 24, 48, 60, 72, and 84 h. At each sampling time, 1 mL of digesting solution was pipetted out after gently centrifugation of bombs at 1500 rpm for 3 min. The sampled digesting solution was added to 19 mL of 0.021N HCl solution for buffering and blocking the digestion reaction, bringing the pH of the resulting mix down to 6, an optimal value for colorimetric determination of Si concentration (± 5%) using an Alliance Futura autoanalyzer. Finally, the % of Si released during digestions was plotted against time for depicting between-material differences in dissolution kinetics. Additionally, two spare Teflon tubes from each material were poured on a 0.45 cm polycarbonate filter of 1µm pore at 6h and 24h. The retained particulate BSi material was subsequently coated and examined under a high resolution Jeol Field Emission J1700S SEM (University of Barcelona, Spain).

Results are presented as percentage of dissolved Si over time rather than just mere changes in DSi concentration in the digestion bombs. Unlike the raw values of DSi concentrations, the percentages of dissolved Si overtime incorporate three corrections that make their comparison straightforward, as it follows: 1) At every sampling time, 1mL is extracted from the bombs for analysis. Consequently, the volume is decreasing overtime and the DSi concentration is increasing at a higher pace than it would be expected by mere silica dissolution. 2) Although we used equivalent amounts of Si (approx. 1.4 mg Si) in each sample replicate across materials, the process of weighing always involves a small weight variation (± 1.5%) across samples. Such variation, if not corrected, becomes an additional confounding factor complicating the interpretation of DSi concentrations. 3) Not all sponge silicas have the same purity, due to their different levels of complexation of the silica with organic components (chitin, actin, other proteins embedded in the silica, etc.). The purity levels, which are indicated in the Supplementary Data Files S1, S2, can only be calculated after the 84h digestion. Again, the DSi concentration need to be corrected by this factor to yield the correct percentage of BSi dissolution.

For comparative purposes and to generate a more general pattern for the resistance to dissolution of the various types of sponge BSi, we plotted together the results obtained here and those obtained from an experiment previously conducted under identical experimental conditions by our team and published elsewhere (Maldonado et al., 2019). In that previous study, we processed two additional types of demosponge skeletons: small needle-like (oxea) spicules of *Petrosia ficiformis*, and small star-like spicules (cortical spherasters) of *Chondrilla caribensis*. Frustules of freshly cultured diatoms (*Thalassiosira weissflogii*) were also processed as representative of diatom BSi. Two aluminosilicates (benthonite and kaolinite) were used as representatives of the lithogenic silica (LSi). The only methodological difference between the previous digestion study and the current one is that we used eight replicates per material in the former versus five replicates in the current one. All together, the global comparative analysis included fresh and subfossil diatom skeletons, four types of demosponge skeletons, four types of hexactinellid skeletons, one type of homoscleromorph skeleton, and two aluminosilicates.

In addition, we examined statistically the quantitative differences in the resistance to dissolution between 8 main silica types, according to lineage and previously known dissolution behavior: i) frustules of freshly cultured *T. weissflogii* (labelled as *Thalassiosira* BSi, N= 8), ii) diatom earth (diatomite BSi, N= 8), iii) isolated spicules of the homoscleromorph sponge *C. candelabrum* (Homos BSi; N= 5), iv) isolated, delaminating spicules of hexactinellids (Hexact-iso BSi; N= 15), v) dictyonal frameworks of hexactinellids (Hexact-fus BSi; N= 5), vi) isolated spicules of demosponges (Demosp-iso BSi; N= 21), vii) desma frameworks of lithistid demosponges (Demosp-fus BSi; N= 5), viii) kaolinite and bentonite aluminosilicates (Lithogenic silica; N= 16). We calculated the average dissolution percentage per silica type after 5 h in 1% sodium carbonate at 85°C and examined statistically between-type differences using a one-way ANOVA. A period of 5 h was selected for such comparison, because according to the initial postulates of the 1% sodium carbonate approach designed to estimate total biogenic silica in sediments, nearly all biogenic silica should have been dissolved after 5 h (DeMaster, 1991). However, it was recently demonstrated that the approach underestimates the resistance to dissolution of the sponge silica, which at 5-6 hours only shows incipient to moderate signs of dissolution (Maldonado et al., 2019). Initial non-normal dissolution percentages became normally distributed and homoscedastic after an arcsin-square root transformation prior to the ANOVA. "A posteriori" pairwise comparisons to identify the groups of silica types responsible for the differences followed the Holm-Sidak test.

Aluminum effects on silica dissolution

The content of Al of the skeletal silica was determined in the demosponges *Petrosia ficiformis* (needle-like spicules) and *C. caribensis* (aster-like spicules), and in diatomaceous earth. Then, it was used to interpret differences among the three types of siliceous skeletons in the resistance to dissolution. For Al determination, replicates (1 mg BSi each) of acid-cleaned, dried spicules of *P. ficiformis* and *C. caribensis*, and diatomaceous earth were dissolved in 5 mL of 10% HF. Standard solutions of known concentrations were prepared in the same medium as the samples. Al and Si were determined at the PSO/IUEM (Pôle Spectrométrie Océan, Institut Universitaire Européen de la Mer, Brest, France) by inductively coupled plasma-atomic emission spectrometry (ICP-AES) using a Horiba Jobin Yvon® Ultima 2 spectrometer. Statistically significant differences in the Al : Si ratios of *P.ficiformis* (n=7), *C. caribensis* (n=3), and diatomaceous earth (n=4) were examined using a Kruskal-Wallis one-way ANOVA on ranks followed by a posteriori Dunn's tests, given unequal sampling size and departure from normality. The differences in Al content were assessed versus the dissolution pattern of the three BSi types.

Chitin effects on silica dissolution

To test the role of chitin in the resistance of the sponge BSi to dissolution, acid-cleaned spicules of the hexactinellid sponge *Ijimalophus hawaiicus* (containing 15.3 ± 1.3 µg chitin mg^{-1} BSi; Ehrlich et al., 2016) and the demosponge *Petrosia ficiformis* (lacking chitin; this study) were digested in 1% sodium carbonate and their dissolution kinetics compared. As the assayed spicules of *I. hawaiicus* are the ones making the 30-40 cm long, external stalk that anchors the sponge to the soft bottom (Maldonado et al., 2005), we expected these spicules to have developed special mechanisms (e.g., chitin-silica complexing) to prevent their dissolution when being exposed to a continuous flow of passing-by silicon-desaturated seawater. In contrast, the spicule of *P. ficiformis*, which occur "protected" within the sponge mesohyl, would not need such a defense against dissolution. A comparison of the spicules of *I. hawaiicus* with equivalent spicules from other hexactinellid but lacking chitin would have also been a relevant test. However, such a silica was not available to us when conducting this study.

To determine the presence/absence of chitin in the spicules of *P. ficiformis*, we used three analytical techniques: i) Calcofluor White (CFW) staining, ii) chitinase test, and iii) electrospray ionization mass spectrometry ESI-MS. Calcofluor White (Fluorescent Brightener M2R, Sigma-Aldrich, Taufkirchen, Germany) shows enhanced fluorescence after binding to chitin (Tsurkan et al., 2021). This staining method was applied to purified organic matter obtained after demineralization of *P. ficiformis* spicules. The material was soaked in 0.1 M KOH-glycerine-water solution and few drops of the 0.1% CFW solution were added. This mixture was incubated for 3 h in darkness, washed several times with demineralized water, dried at room temperature and examined using BZ-9000 microscope (Keyence, Osaka, Japan) in both light-microscopy and fluorescent microscopy modes. The highly sensitive CFW staining showed no positive results, indicating the absence of chitin (Supplementary Figure S1). Likewise, the chitinase digestion test (Ehrlich et al., 2010), based on light-microscopy detection of enzymatic dissolution of chitin-containing structures confirmed the absence of chitin. Finally, for the electrospray ionization mass spectrometry ESI-MS, samples obtained after final isolation step were hydrolyzed in 6 M HCl for 24 h at 50°C. After the HCl hydrolysis, samples were filtrated through a 0.4 µm filter and freeze-dried in order to remove excess HCl. The remaining solid was dissolved in water for ESI-MS analysis. D-glucosamine (Sigma-Aldrich, Taufkirchen, Germany) was used as standard. The ESI-MS analytical measurements were performed using an Agilent Technologies 6230 TOF LC/MS spectrometer (Applied Biosystems, Santa Clara, CA, USA). Nitrogen was used as the nebulizing and desolvation gas. Graphs were generated using Origin 8.5 for PC (Originlab Corporation, Northampton, MA, USA). Again, the results of ESI-MS analysis showed the absence of the mass spectrum of d-glucosamine, which should consist of three main signals with mw/z=162, 180 and 359, corresponding respectively to the species [M − H_2O^+ H^+], [M + H^+] and [2 M + H^+]. Together, these results provide strong evidence that the biological material isolated from the spicules of *P. ficiformis* contains no chitin.

To test whether the presence of chitin has an effect on the dissolution rate of the silica, two spicule batches were prepared for each of the two sponge species. One batch was treated with the enzyme chitinase for 72 h, the other batch consisted of chitinase-untreated BSi. As chitin occurs internally between the concentric BSi layers, acid-cleaned spicules were grinded to gross dust to facilitate chitinase to reach the chitin embedded in the silica. Each batch contained 5 replicates of 3 mg BSi each, which were deposited in 2 mL Eppendorf vials. In the vials of one of the batches, 0.8 mL of a chitinase solution (1 mg mL^{-1}) was added, being the mix incubated with gentle orbital agitation at 25°C for 72 h. To avoid that some of the silica-associated chitin could not be broken down because of saturation of the chitinase enzyme over the long incubation period, the added amount of chitinase (1.5 units) was about 27-fold that required to digest the amount of chitin expected within the sponge spicules (i.e., 15.3 ± 1.3 µg chitin per mg BSi). The chitinase solution was prepared by adding dust of *Trichoderma viridae* (Sigma; CAS-No 90001-06-3) to potassium phosphate buffer (pH= 6.1). The other half of the vials were incubated without chitinase, adding just the phosphate buffer solution.

After the incubation with chitinase, we did not quantified how much chitin had exactly been dissolved, because of obvious

difficulties. It was just assumed that most of the chitin exposed at the grinded silica had been degraded and that those differences in chitin abundance should be enough to have an effect on the subsequent silica dissolution rate. After the incubation period, the Eppendorf vials were centrifuged and the incubation medium removed by pipetting. Then, we rinsed in ethanol 96% and centrifuged three more times. The ethanol was finally evaporated at 40 °C and the bottom of the vial containing the sample was cut using a scalpel to be dropped into a 50 mL teflon test tube for digestion in 1% sodium carbonate at 85°C (as indicated in the section "Digestion of sponge silica"). 1mL samples from test tubes were taken at times 2, 3, 4, 5, 6, 8, 12, 24, 36, and 48 h.

Results

Comparative dissolution of sponge silica

The digestion in 1% sodium carbonate at 85°C is a method typically used to estimate the amount of biogenic silica in sediments. For correct functioning, the method needs all biogenic silica be completely dissolved before 5 h. However, our experiment shows that, after 5 h, 6 h and 24 h in treatment, a large amount of undissolved sponge silica still persisted (Figures 2–5; Supplementary Data Files S1, S2). At 5 h, the skeletons of the class Demospongiae had dissolved very little, irrespective of being in the form of the hypersilicified desma framework of *Leiodermatium pfeifferae* (12.5 ± 1.8% dissolution; Figures 2A, 3A–C) or the long, isolated spicules of *Geodia hentscheli* rootlets (9.9 ± 0.7% dissolution; Figures 2A, 3D–F). The silica of the class Hexactinellida dissolved a bit more than that of demosponges, but always less than 40% in 5 h. Specifically, the silica of the hexactinellid with the spicules fused in a dictyonal framework (*Aphrocallistes vastus*: 14.4 ± 1.9%; Figures 2A, 3G–O) dissolved more slowly than that of the three rosellid species with isolated, delaminating spicules (*Vazella pourtalesii:* 37.5 ± 5.9%; *Schaudinnia rosea*: 32.8 ± 3.8%; *Asconema setubalense*: 27.9 ± 1.8). The only sponge silica dissolving substantially (74.4 ± 3.9%) in 5 h was that of the class Homoscleromorpha, a small lineage of siliceous sponges represented in the experiment by the tiny isolated spicules of *Corticium candelabrum*. Yet, a virtually complete dissolution (98.6 ± 4.3%) of the BSi of *C. candelabrum* required at least 24 h in treatment.

A qualitative SEM study of the skeletons after 6 h and 24 h in treatment (Figures 3–5) corroborated the quantitative dissolution data. The desma skeleton of demosponge *L. pfeifferae* was only incipiently dissolved (Figure 3A) at 6 h. Its resistance to dissolution caused that even after 24 h in treatment, many desmas were still poorly dissolved (Figure 3B), with not much etching on their surface (Figure 3C). Likewise, many of the spicules of the rootlets of demosponge *G. henstcheli* remained largely undissolved after both 6 h (Figures 3D, E) and 24 h (Figure 3F). The dictyonal framework of the hexactinellid *A. vastus* showed only incipient digestion at 6h (Figures 3G, H), but extensive digestion of the internal silica occurred at 24 h (Figure 3I). Most of the isolated spicules of this species dissolved faster than its dictyonal framework, with, for instance, hexactines (Figures 3H, I), scopula (Figures 3J, K), and pinnules (Figures 3L, M), showing evident signs of dissolution at 6 h and being completely dissolved in the 24 h sample. However, the tiny asters arrived at 6h with only few dissolution cavities on their surface (Figures 3N, O). After 6 h, the spicules of the three rosellid sponges (Figure 4) were a little bit more dissolved than those of *A. setubalense*. Yet, at 6h many of the diactines of *S. rosea* showed only incipient signs of dissolution at their surface (Figure 4A), with the axial canal being relatively well preserved (Figures 4B, C). However, after 24 h, most of the diactines had extensively dissolved from the inside (Figures 4D–F) and some had also delaminated silica layers (Figure 4G, arrow). However, as it also happened for *A. vastus*, the tiny asters were comparatively resistant to dissolution at both 6 h (Figures 4G, H) and 24 h (Figure 4I). In *A. setubalense*, the hexactines (Figures 4J, K) and diactines (Figures 4J, L) showed obvious signs of dissolution at 6 h. The dissolution was more evident in the hexactines, with both more pronounced etching at the surface (Figure 4K) and inside the tips of the actines (arrows in Figure 4J). In *V. pourtalesii*, a combination of dermal and choanosomal diactines, along with a tiny aster (a), remained all largely undissolved after 6h, with obvious signs of silica delamination, rather than silica digestion (Figure 4M). Likewise, the hexactines of this species remained largely undissolved at 6h (Figure 4N), though with evidence that the most peripheral silica layer (arrows) had been partially dissolved (Figure 4O, arrows). Surprisingly, many of the micro-spicules of *C. candelabrum* were still present after 6h (Figure 5A). However, detailed inspection revealed that those spicules had experienced substantial dissolution at their tips and inside (Figures 5A–C, arrows), as well as on their surface (Figure 5D), showing a surface etching pattern different from that in demosponges and hexactinellids. After 24 h, most of these micro-spicules had been entirely dissolved. Yet, some were still undissolved after 24 h (Figures 5E, F), remaining unclear the reasons for the resistance to dissolution of only some spicules, given than they are similar in shape and structure to their dissolved counterparts.

When previously published data for several kinds of silica digested in 1% sodium carbonate in a fully comparable experimental setup (Maldonado et al., 2019) were plotted together with the data of the current study, a wider context of reference emerges (Figure 2B) to better assess within-group and between-group patterns of sponge silica dissolution. It can be seen that the dissolution of the diatom earth at 5 h (75.4 ± 6.6%) is nearly identical to that of the homoscleromorph sponge *C. candelabrum*, but less than that of freshly cultured diatoms (99.2 ± 2.9%; Figure 2B). It can also be noticed that at 5h, the

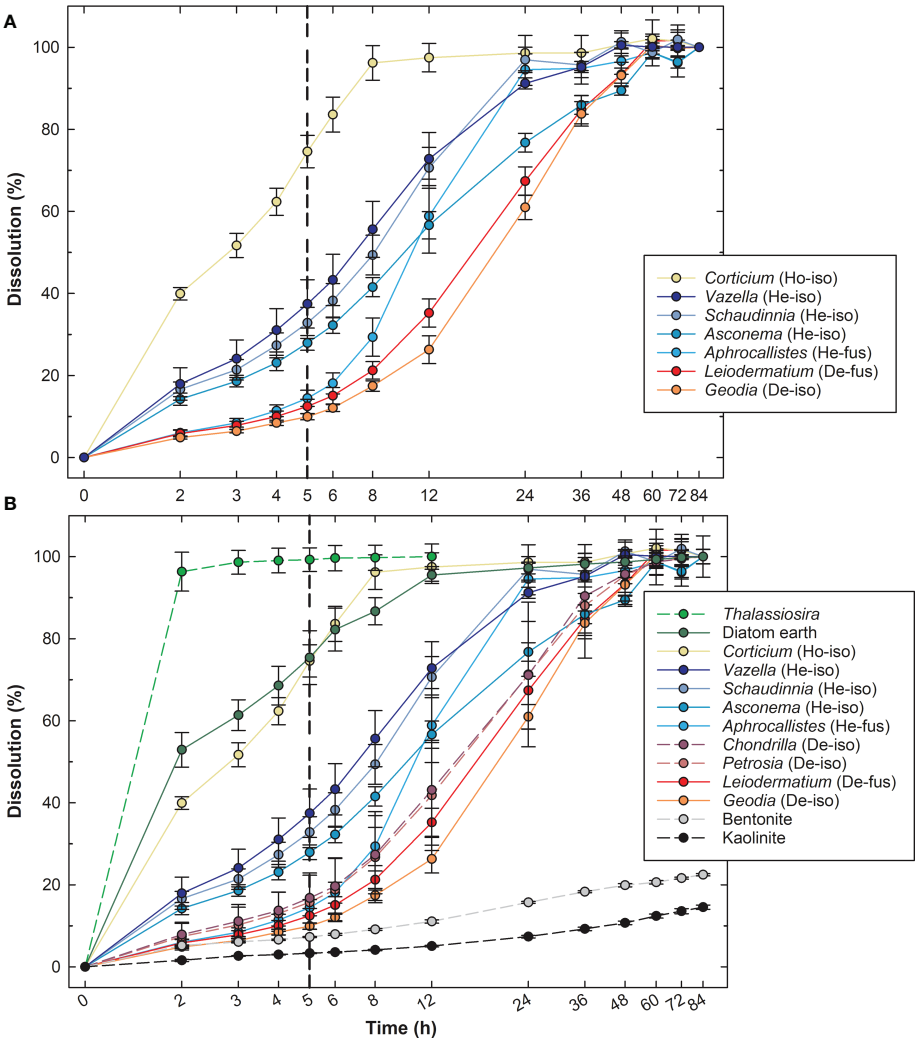

FIGURE 2
Dissolution (%; average ± SD) dynamics of various siliceous materials in 1% sodium carbonate in gentle agitation during 84 h. **(A)** Comparative dissolution of major types of sponge siliceous skeletons assayed in the current study: small isolated spicules of *Corticium candelabrum* in the Class Homoscleroemorpha (Ho-iso); delaminating, isolated spicules of three rosellids species, *Vazella pourtalesii*, *Schaudinnia rosea*, *Asconema setubalense* in the Class Hexactinellida (He-iso); spicules of *Aphocallistes vastus* fused in a dictyonal silica framework (He-fus); desmas of *Leiodermatium pfeifferae* fused in a silica framework in the Class Demospongiae (De-fus); isolated spicules from the rootlets of *Geodia hentscheli* in the Class Demospongiae (De-iso). **(B)** Comparison of the dissolution dynamics of the above described sponge skeleton types in comparison with those of diatom *Thalassiosira weissflogii*, diatom earth, isolated aster-like spicules of demosponge *Chondrilla caribensis* (De-iso), isolated needle-like spicules of desmosponge *Petrosia ficiformis* (De-iso), and aluminosilicates bentonite and kaolinite, as detailed in Maldonado et al. (2019), and herein represented by dashed lines. Note that the representation of the dissolution line of *T. weissflogii* and *C. candelabrum* ends at 12 h and 60 h, respectively, because silica dissolution is virtually completed.

lithogenic silica has dissolved between 3% and 8% on average, the demosponge silica between 9% and 14%, and the hexactinellid silica between 14% and 37%. Differences in the resistance to dissolution were further examined quantitatively (Figure 6) by grouping the various digested materials by main silica type, as it follows: frustules of freshly cultured *T. weissflogii* (*Thalassiosira* BSi), diatom earth (diatomite BSi), isolated spicules of the homoscleromorph sponge *C. candelabrum* (Homos BSi), isolated, delaminating spicules of hexactinellids (Hexact-iso BSi), dictyonal frameworks of hexactinellids (Hexact-fus BSi), isolated spicules of demosponges (Demosp-iso BSi), desma frameworks of lithistid demosponges (Demosp-fus BSi), kaolinite and bentonite aluminosilicates (Lithogenica silica). The one-way ANOVA comparing average dissolution percentage (arcsin-sqroot transformed) per silica type after 5 h hours found significant between-type differences ($F= 380.6$, $P < 0.001$; see extended statistics of analysis in Supplementary Results S1). The "a posteriori" comparisons are graphically

10.3389/fmars.2022.1005068

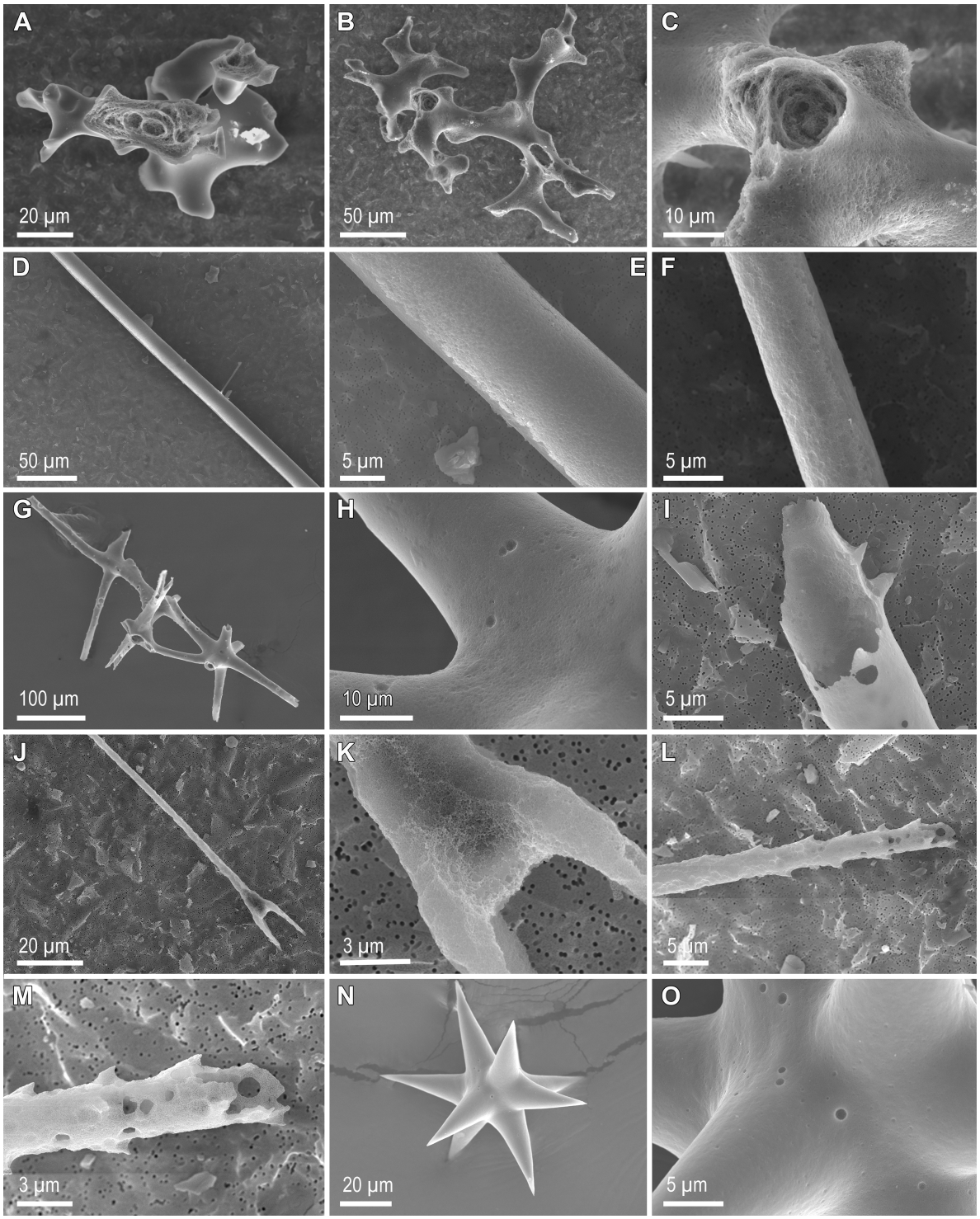

FIGURE 3
Scanning electron microscopy images of sponge skeletal pieces after 6 h and 24 h in 1% sodium carbonate at 85°C. Desmas of demosponge *Leiodermatium pfeffeirae* have largely resisted dissolution after 6 h **(A)** and also after 24 h **(B)**, when only incipient signs of etching at the spicule surface occur **(C)**. Spicules from the rootlets of demosponge *Geodia henstcheli*, which remain largely undissolved and with only incipient etching of their silica surface after 6 h **(D, E)** and 24 h **(F)** in treatment. Dictyonal framework of hexactinellid *Aphrocallistes vastus* remaining largely undissolved after 6 h **(G, H)**, but largely dissolved from the inside after 24 h **(I)**. In contrast to the framework, some of the isolated spicules from *A vastus*, such as the scopula **(J, K)** and the pinnules **(L, M)**, were largely dissolved at 6 h, but other, such as the small asters **(N)**, showed only incipient signs of dissolution at this time **(O)**.

10.3389/fmars.2022.1005068

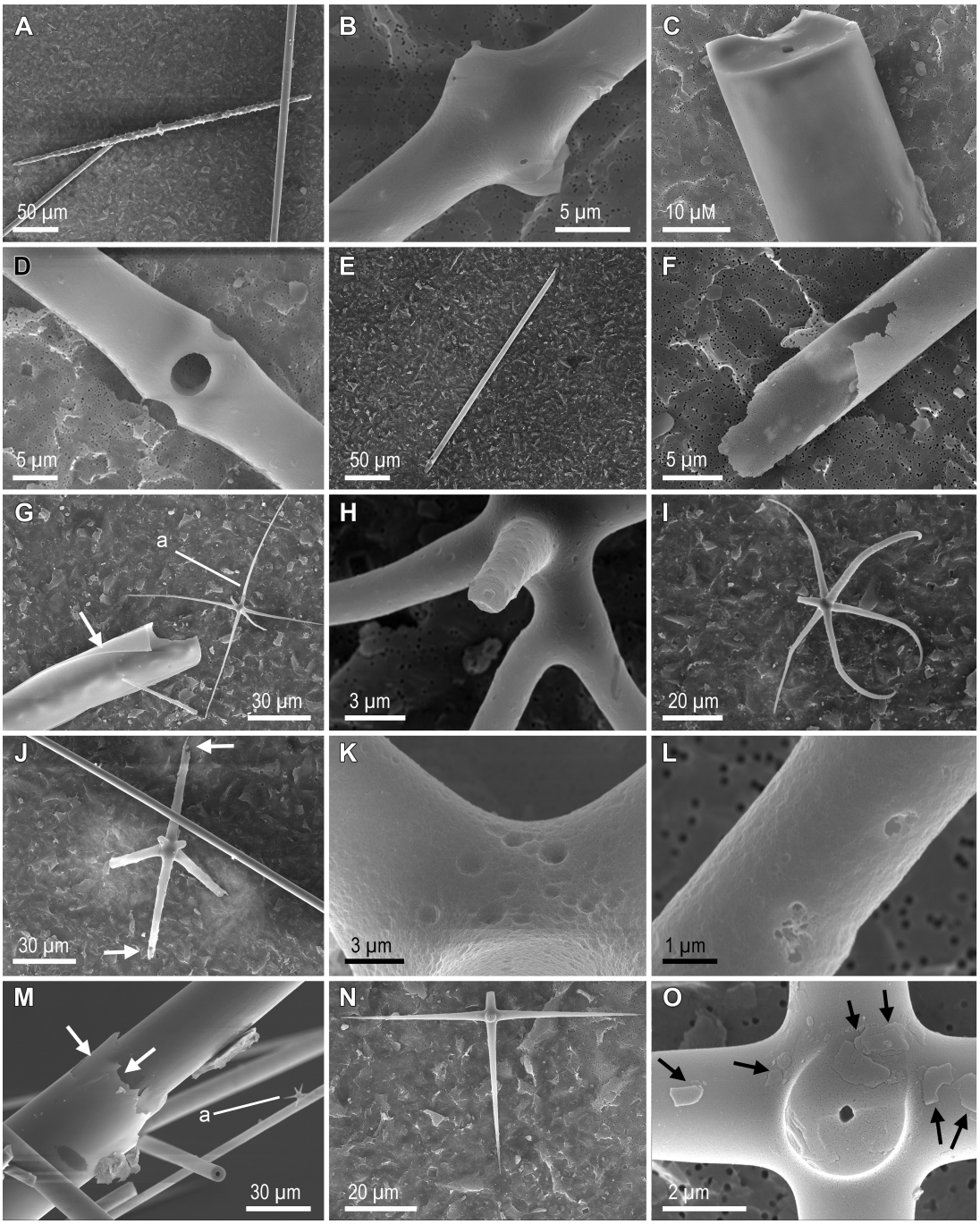

FIGURE 4
Scanning electron microscopy images of sponge skeletal pieces after 6 h and 24 h in 1% sodium carbonate at 85°C. Dermal **(A, B)** and choanosomal **(A, C)** diactines of hexactinellid *Schaudinnia rosea* showing weak dissolution at 6 h, but more extensive dissolution after 24 h **(D–F)**. Unlike the large spicules, the tiny asters **(A)** remained largely un dissolved after both 6h **(G, H)** and 24 h **(I)**. Note in G the occurrence of an undissolved peripheral layer (arrow) delaminated from a large choanosomal diactine. Hexactine **(J, K)** and diactine **(J, L)** of hexactinellid *Asconema setubalense*, showing moderate signs of dissolution at 6 h. The dissolution is more evident in the hexactine, with both more pronounced etching at the surface **(K)** and also inside the tips of the actines (arrows in J). **(M)** A combination of dermal and choanosomal diactines of hexactinellid *Vazella pourtalesii*, along with a tiny aster (a), all remaining largely undissolved after 6 h. Note signs of delamination of the peripheral silica layers (arrows). **(N)** Hexactine of *V. pourtalesii* remaining largely undissolved at 6 h, although with evidence **(O)** that the most peripheral silica layer (arrows) has been partially dissolved.

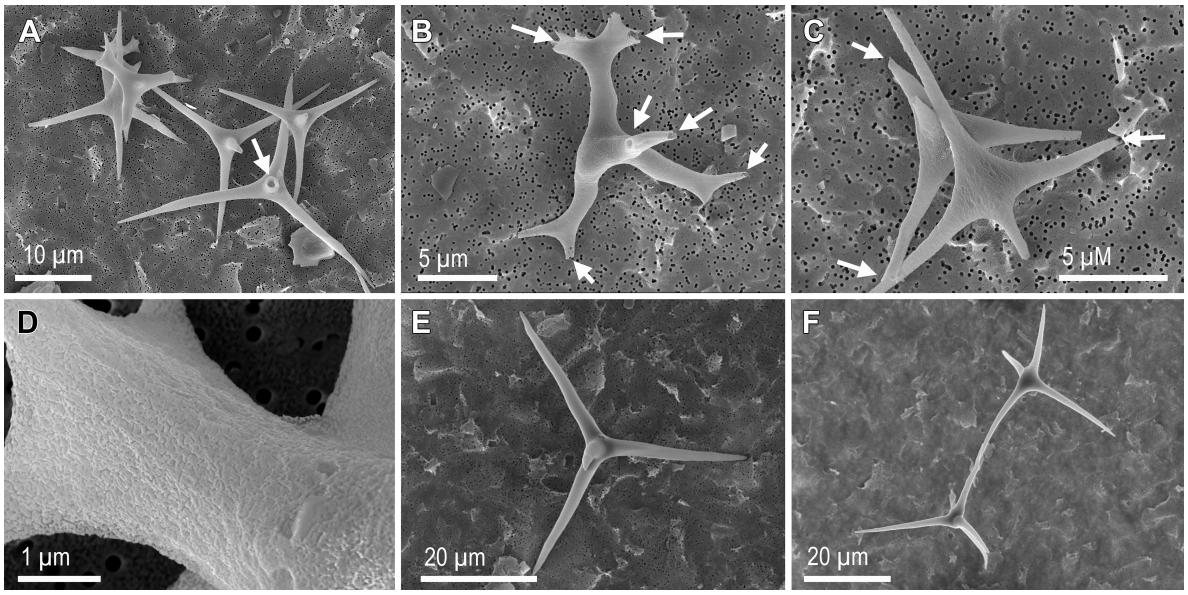

FIGURE 5
Scanning electron microscopy images of sponge skeletal pieces of the homoscleromorph *Corticium candelabrum* after 6 h and 24 h in 1% sodium carbonate at 85°C. Many of the microspicules were still present after 6 h **(A–C)**. However, they all showed substantial dissolution at their tips and inside (arrows), as well as at their surface **(D)**, revealing a surface etching pattern different from that in demosponges and hexactinellids. After 24 h, very few spicules remained undissolved **(E, F)**, being unclear the reasons for the resistance of such few spicules, given than they are similar in shape and structure to their dissolved counterparts.

summarized in Figure 6. They show that fresh frustules (99.3 ± 2.9%), diatomite (75.4 ± 6.6%) and the tiny spicules of homosclerophorid sponges (74.6 ± 3.9%) dissolved at relatively high rates, which —in the conceptual frame of these multiple comparisons— were not significantly different from each other. The isolated, delaminating spicules of rosellid hexactinellids (32.7 ± 5.6%) dissolved significantly slower than the former BSi types, but they still did it about twice faster than the dictyonal frameworks of hexactinellids (14.4 ± 2.0%), the isolated spicules of demosponges (14.8 ± 6.0%), and the desmas frameworks of demosponges (12.5 ± 1.8%), the three of which did not dissolve significantly different from each other. All types of biogenic silica assayed dissolved significantly faster than the lithogenic silica (5.3 ± 2.0%). In terms of magnitude, the most important difference occurs between the group made by diatom frustules (fresh and aged) plus spicules of homoscleromorph sponges (84.3 ± 12.9%) versus the group made by the silica of the remaining sponge skeletons (20.3 ± 10.1%).

Effects of aluminum and chitin on silica dissolution

To test the role of aluminum (Al) in explaining the patterns of resistance to dissolution of the sponge BSi, the spicules of two sponge species (*Chondrilla caribensis* and *Petrosia ficiformis*) and diatomaceous earth were analyzed for their Al/Si atom:atom ratio. The average (± SD) Al/Si ratio in the diatomaceous earth ($2.07x10^{-2} \pm 1.45x\ 10^{-2}$) was significantly higher than those of the two spicules ($1.60x10^{-3} \pm 0.92x10^{-3}$ in *C. caribensis* and $2.65x10^{-3} \pm 1.6x10^{-3}$ in *P. ficiformis*), which in turn were not significantly different from each other (Figure 7 and Supplementary Results S2).

Because the concentration of dissolved Al in most marine environments is very low, the Al/Si ratio in frustules of diatoms either living in the wild or cultured in non-Al-enriched media often falls in the range of 10^{-4} to10^{-3} (Gehlen et al., 2002; Van Cappellen et al., 2002), and we assumed it to be so (not measured) in our cultured diatoms. While the larger Al content of the diatomaceous earth could account for its larger resistance to dissolution relative to freshly cultured diatoms (Figure 2B), it cannot explain the differences in dissolution rate between diatom earth and sponge BSi. The Al/Si ratios of sponge spicules were an order of magnitude smaller than that of diatomaceous earth, but spicules dissolved significantly more slowly (Figure 6). The Al content can neither explain differences in dissolution rate between "types" of sponge silica: the Al/Si ratio in *C. caribensis* is about 1.65 times lower than in *P. ficiformis*, but the dissolution kinetics of both types of sponge skeletons are nearly identical (Figure 2B).

To test whether the presence of chitin increases the resistance to dissolution of the sponge silica, grinded, chitinase-treated and untreated spicules of the hexactinellid

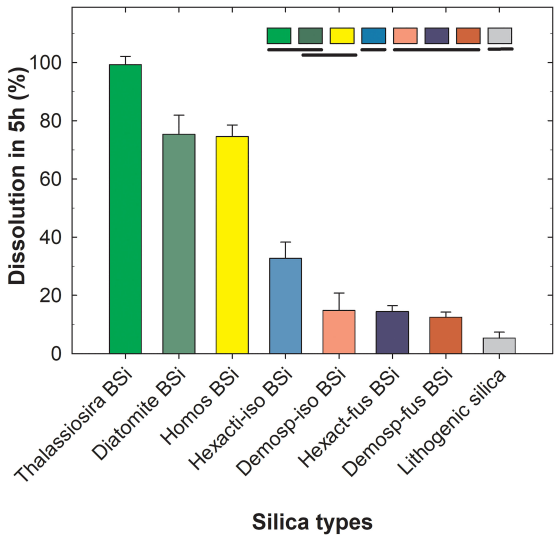

FIGURE 6
Percentage dissolution (avg ± SD) of the various silica types after 5 h in 1% sodium carbonate at 85 °C, ordered in decreasing magnitude: biogeneic silica (BSi) in the form of frustules of diatom *Thalassiosira weissflogii*, diatom earth (diatomite BSi), spicules of homosclerophorid sponge *Corticium candelabrum* (Homos BSi), isolated, delaminating spicules of rosellid hexactinellid sponges (Hexact-iso BSi), isolated spicules of several shapes of demosponges (Demosp-iso BSi), spicules fused in skeletal framework of hexactinellids (Hexact-fus BSi), desmas fused in skeletal framework of demosponges (Demosp-fus BSi), and lithogenic silica represented by aluminosilicates bentonite and kaolinite. A one-way ANOVA detected significant between-type differences in average dissolution (see Supplementary Results S1 for extended statistics). "A posteriori" pairwise comparisons (Holm-Sidak test) are summarized graphically at the top of the graph. Silica types are ordered by decreasing magnitude in average dissolution (%) at 5 h and types that are not statistically different from each other are underlined by the same line. The graph summarizes that fresh frustules, diatomite and spicules of a homoscleromorph sponge dissolve at comparatively higher rates than the rest of assayed BSi, but with no significantly difference from each other. The isolated spicules of hexactinellids dissolve more slowly than the former BSi types, but they still do it two fold faster than the frameworks of fused spicules of hexactinellids, the isolated spicules of demosponges, and the desmas frameworks of demosponges, the three of which do not dissolve differently from each other. All assayed types of biogenic silica dissolved faster than the lithogenic silica.

Ijimalophus hawaiicus (containing chitin) and the demosponge *P. ficiformis* (lacking chitin) were digested in 1% sodium carbonate. Chitinase-treated and untreated replicates of grinded BSi were digested to 100% dissolution, which occurred from 12 h to 24 h (Figure 8), a digestion period shorter than required for entire (not grinded) spicules, which took place in about 60 h (Figure 2B). For both species, dissolution dynamics of chitinase-treated and untreated samples were virtually undistinguishable (Figure 8). Importantly, the silica of *I. hawaiicus* (containing chitin) dissolved even faster during the first 12 h than the silica of *P. ficiformis* (lacking chitin). This pattern is consistent with previous reports that hexactinellid BSi dissolves in seawater faster than demosponge silica (Maldonado et al., 2005; Bertolino et al., 2017). In summary, Al and chitin cannot explain by themselves the distinct resistance to dissolution of the silica of demosponges and hexactinellids.

Discussion

Ecological significance of laboratory dissolution rates

Several compounds, such as sodium carbonate, sodium hydroxide, potassium hydroxide, and hydrofluoric acid, are available for dissolving biogenic silica and extracting it from sediments (Hurd, 1973; Paasche, 1973; Eggimann et al., 1980; Mortlock and Froelich, 1989; Müller and Schneider, 1993; Kamatani and Oku, 2000; Bossert et al., 2019; Maldonado et al., 2019). The most widespread method is the utilization of 1% sodium carbonate (DeMaster, 1981; Conley, 1998). Thus, such a method provides a standardized approach to accurately compare the resistance to dissolution of the main types of sponge BSi skeletons. However, a major challenge remains posed on whether the different dissolution rates in 1% sodium carbonate measured in this study could be translated into some ranking of dissolution rates in the natural environment. To that aim, we are tentatively proposing a simple model that may predict annual dissolution/preservation (%) of the sponge silica relative to its deposition rate to the sediments. Our proposal is here initially formulated after combining some data available in the literature with new data from this study. Though we are aware that our proposal will need additional testing with future data sets, the available arguments for the proposed model are as it follows:

1) The average preservation rate of diatom frustules in sediments (9.2 Tmol y^{-1}) relative to their deposition as silica rain (84 Tmol y^{-1}) is about 10.9% (Tréguer et al., 2021) and such diatom silica is dissolved entirely in 1% sodium carbonate in about 2 h to 3 h (DeMaster, 1991; Figure 2B).
2) In a study of 17 marine sediment cores, the preservation of the sponge silica —in broad sense, that is, combining all spicule types— in marine sediments was estimated at about 45.2 ± 27.4%, relative to its annual deposition (Maldonado et al., 2019). If only the 12 cores dominated by demosponge spicules in that study are considered (i.e., cores 1, 2, 4, 6, 7, 9-15), the average preservation for demosponge skeletons can be recalculated as 46.1 ± 28.4%. The present study shows that such a BSi is completely dissolved in 1% sodium carbonate only after 72 h (Figure 2B).

10.3389/fmars.2022.1005068

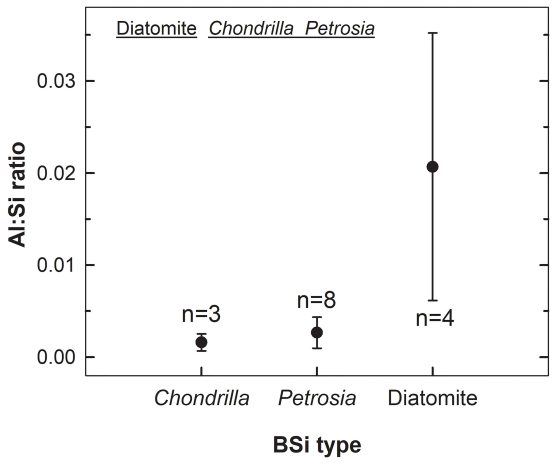

FIGURE 7
Comparison of Al : Si ratios in the BSi of the spicules of the sponges *Chondrilla caribensis* and *Petrosia ficiformis*, and Miocenic diatomaceous earth. A Kruskal-Wallis one-way ANOVA on ranks found significant between-group differences (H= 8.823, *P*= 0.012). The "a posteriori" Dunn's test revealed that the ratio in the diatomaceous earth is significantly larger than that in the spicules of the two sponges (*P*= 0.022, *P*= 0.036), which were not significantly different from each other (*P* > 0.50), as graphically indicated in the upper zone of the graph (i.e., BSi types with Al : Si ratios not significantly different are underlined by the same line). See extended statistics in Supplementary Results S2. "n" refers to the number of replicates analyzed, which varied depending on sample availability.

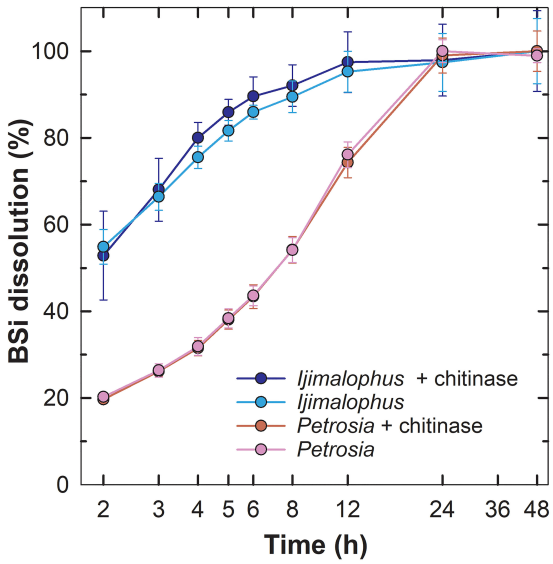

FIGURE 8
Chitinase effects on sponge BSi dissolution. Dissolution kinetics in 1% sodium carbonatate of grinded chitinase-treated and untreated spicules of the hexactinellid *Ijimalophus hawaiicus* and the demosponge *Petrosia ficiformis*. Time (h) is presented in logarithmic scale.

3) The study of sediments in an aggregation of the rosellid hexactinellid *Vazella pourtalesii* estimated that sponge silica preservation by burial relative to its annual deposition rate is about 35.1 ± 10.1% (Maldonado et al., 2021). Such a silica is completely dissolved in 1% sodium carbonate after 48 h (Figure 2B).

When these three datasets are plotted (Figure 9), the model best fitting the relationship between BSi preservation (% relative to deposition) in the sediments and time (h) to total BSi dissolution in 1% sodium carbonate is a linear regression $Y = y_0 + (a \times X)$ (Supplementary Results S3). Such a regression predicts the silica of homosclerophorid spicules to have a comparatively poor average preservation in marine sediments of 22.12 ± 1.38% (Figure 6). Indeed, such a predicted poor preservation is consistent with the rapid dissolution in 1% sodium carbonate detected for the spicules of *C. candelabrum* (Figures 2A, 5). The comparatively rapid dissolution of these spicules may also be the reason why the fossil record of the class Homoscleromorpha is surprisingly poor (Botting and Muir, 2018).

Thus, the proposed model may provide a tentative proxy to estimate natural BSi preservation as a function of time to total dissolution in 1% sodium carbonate. If so, it would save considerable amounts of time in sediment analyses. Yet, a general applicability of this tentative proposal needs to be corroborated in future studies incorporating additional types of BSi, such as radiolarians, benthic diatoms, choanoflagellates, etc. Conducting a dissolution process based on continuous monitoring (e.g., Barão et al., 2015) rather than monitoring at given time steps would also increase accuracy when further testing and/or refining this proxy.

Dissolution patterns and their causes

A mechanistic understanding on how biogenic silica dissolves has proven elusive because the amorphous organic nature of such silica lacks structural order and prevents application of classical techniques used for crystals (Dove et al., 2008). Regarding the BSi of sponges, the experiments indicate that the silica of homoscleromorph sponges dissolved significantly faster than that of the other sponges, following a pattern nearly identical to that of the aged silica of diatom earth. The homoscleromorphs make a small class of sponges, which harbors only nine taxonomic genera and 118 species, that is, it represents less than 1% of extant sponge species. A few of those species (i.e., 21 spp.) do not even have a siliceous skeleton. Therefore, although these sponges may be common at some specific shallow-water tropical and subtropical habitats (typically coral reefs and caves), the magnitude of their global contribution to the Si fluxes in sediments is expected to be negligible.

10.3389/fmars.2022.1005068

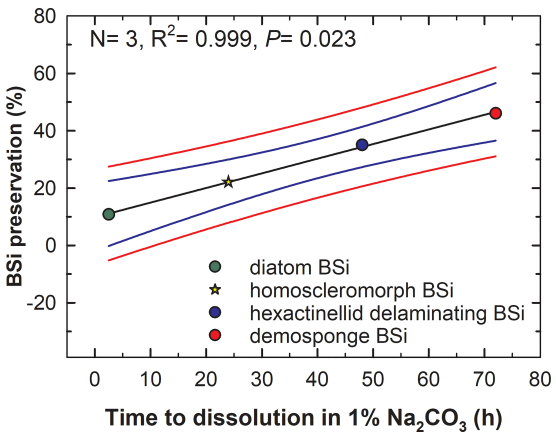

FIGURE 9
Relationship between the time (h) required by the various types of BSi (diatoms, rosellid hexactinellids, demosponges) to dissolve completely in 1% sodium carbonate at 85°C and their respective preservation (%) in the marine sediments. The relationship is best fitted by a linear regression model (black line) in the form of "Preservation (%) = 10.04 + (0.5×dissolution time)", which is statistically significant (see extended statistics in Supplementary Results S3). Blue and red lines indicate the 95% confidence band and the 95% prediction band of model, respectively. The preservation of the silica of homoscleromorph sponges relative to its deposition is predicted to be around 22.12 ± 1.38% (yellow start) as a function of its resistance to dissolution in sodium carbonate (Figure 2).

In contrast to homosclerophorids, the demosponges make the bulk of the sponge fauna on continental shelves, showing also great abundance at bathyal depths. The skeletons of demosponges are found in abundance in sediments from continental margins and around seamounts (Bavestrello et al., 1996; Bertolino et al., 2012; Murillo et al., 2016; Maldonado et al., 2019; Costa et al., 2021). Our results agree with the general notion that the skeletal pieces of demosponges are relatively resistant to dissolution in seawater and alkaline digesters. For instance, (Kamatani 1971), using siliceous spicules of an unidentified demosponge, demonstrated that the spicules dissolved only 0.3% after 24 days in seawater, while the frustules of *Thalassiosira decipiens* did it in 90.1%. Kamatani also reported that appreciable differences occurred between sponge spicules and diatom frustules that were not geologically aged regarding the infra-red spectra of their silica, both in the absorption pattern near 980 cm^{-1} and the ratio of absorption intensities (D2/D1 and D3/D1). Consequently, Kamatani concluded that it "seemed reasonable to assume that the difference in solubility between diatom and sponge silica would be due not only to the thickness and specific surface area, but also to the internal structure suggested by the infra-red spectrum". Thirty years later, (Kamatani and Oku, 2000) reported again large differences in dissolution between the silica of an unidentified demosponge and the silica of the diatoms *Skeletonema costatum* and *Rhizosolenia hebetata* in both NaOH and Na_2CO_3 solutions. In 2005, an 8-month dissolution experiment in sterile seawater reported that needle-like spicules of the hexactinellid *Ijimalophus hawaiicus* dissolved 5%, while dissolution of needle-like and aster-like spicules of demosponges *Petrosia ficiformis* and *Chondrilla caribensis*, respectively, was undetectable (Maldonado et al., 2005). The experiments by Kamatani (1971) along with those by (Maldonado et al., 2005; Maldonado et al., 2019) also provide strong support to the idea that differences in specific surface area are not a major responsible for the comparative resistance of the sponge silica to dissolution. Spicules with drastically different surface areas dissolve at similar slow rates. In some cases, the shapes expected to have lower surface area dissolve even more rapidly than the ones with higher specific surface area, in a clear demonstration that the specific surface area is not a major driver of the differences in the resistance to dissolution between the different types of sponge silica. For instance, the 30µm, star-like sterrasters of the demosponge *Geodia* dissolve more slowly than the 50-cm long, needle-like spicules of the hexactinellid *Ijimalophus* (Maldonado et al., 2005). However, the opposite pattern would be expected if specific surface area was the main responsible for the resistance to dissolution in these sponge silicas. Likewise, the 30µm, star-like oxyasters of the demosponge *Chondrilla* dissolve at identical rate than the 150 µm long, needle-like oxeas of the demosponge *Petrosia* (Figure 2B), despite large predicted differences in their specific surface area.

Sediment studies also provide indirect evidence of the high resistance of sponge silica to dissolution. Extant aggregations of *Geodia* spp. are known to have built a continuous reservoir of well-preserved, aster-like spicules (sterrasters) in the sediments, dating 130,000 years BP (Murillo et al., 2016). In agreement with such a long-term preservation of *Geodia* sterrasters, our experiments indicate that spicules of *Geodia hentscheli* (Figures 2, 3D–F) are among the most resistant to dissolution. It appears that in the many cases in which the function of the sponge skeletons requires direct exposure of the silica to the seawater (e.g., spicules of the attachment rootlets of *G. hentcheli*), mechanisms have been developed through evolution to avoid dissolution and preserve spicule functionality. A paradigmatic example would be the giant siliceous spicule of the hexactinellid *Monorhaphis chuni* that serves as anchoring stalk for the sponge during more than 15,000 years (Jochum et al., 2017), while showing no evident external signs of dissolution during that long period. It remains unclear which are the mechanisms that prevent or slow down sponge silica dissolution, but the Al and chitin contents of the silica do not appear to be major drivers of such a resistance (Figures 7, 8).

Initially, we hypothesized that complexation of the sponge silica with chitin could be a factor slowing dissolution, but it appears to be the opposite, according to our experimental results (Figure 8). To date, chitin has been identified in a variety of 21 marine and three fresh-water sponge species (Talevski et al.,

2020), though rarely incorporated into the silica. It occurs incorporated into the silica of only some hexactinellid sponges (Ehrlich and Worch, 2007; Ehrlich et al., 2007a; Elrich et al., 2008; Tabachnick et al., 2011; Elrich et al., 2016), but it has never been found in the silica of demosponges and homoscleromorphs to date. The microscopic organization of the silica of the hexactinellid *I. hawaiicus*, which contains chitin and dissolves comparatively faster than the chitin-lacking silica of the demosponge *P. ficiformis*, comes into some general agreement with the organization of the silica of the other skeleton type experiencing relative fast dissolution, the spicules of the homosclerophorid *C. candelabrum*. Transmission electron microscopy revealed occurrence of relative thick layers of organic components (of undetermined nature) between the silica layers (Maldonado and Riesgo, 2007). Thus, it appears that complexation with organic materials makes the silica matrix less dense and it could explain the comparatively rapid dissolution detected in homosclerophorids and hexactinellids with delaminating spicules. It is likely that, in the sponge skeletons with a marked concentric layering of the silica due to intercalation sheets of chitin, collagen or other organic compounds, the alkaline digesters may infiltrate more easily between the concentric silica layers, multiplying the surface area exposed to digestion and accelerating the process, relative to other types of sponge silica where silica layers are closely fused to each other. This general pattern may also held at some point for diatom silica, since some experiments have suggested that dissolved protease from environmental bacteria appear to digest by enzymatic hydrolysis some of the proteins embedded in the silica matrix, accelerating the dissolution of the frustules (Roubeix et al., 2008). This effect would be different from the better known hydrolytic attack to the exopolysaccharides and other organic layers that externally cover the frustules of diatoms and that avoid a direct contact with the seawater that otherwise would cause their rapid dissolution (Bidle and Azam, 1999; Toullec and Moriceau, 2018). Such external organic covers have never been reported from sponge silica, despite most sponges having part of their spicules directly exposed to the seawater and despite those spicules not dissolving during the lifetime of the sponges. Thus, the effects of the external organic layer on the dissolution of diatom silica are not directly comparable to the effect of the organic components truly embedded within the silica matrix of the sponge spicules (Maldonado and Riesgo, 2007; Ehrlich et al., 2016).

We also hypothesized that incorporation of Al within the silica matrix could be other of the mechanisms responsible for the slow dissolution of the sponge silica. However, the Al/Si ratios in the sponge silica were an order of magnitude smaller than in diatomaceous earth (Figure 7), but still the sponge spicules dissolved more slowly (Figure 2B). The Al content can neither explain differences in dissolution rate between "types" of sponge silica: the Al/Si ratio in *C. caribensis* was about 1.75 times lower than in *P. ficiformis* (Figure 7), but their dissolution kinetics in the 1% Na_2CO_3 solution were extremely similar (Figure 2B). The effects of other elements (e.g., incorporation of Ge and/or Zn: Sim-Smith et al., 2017; leaching effect of Na^+, K^+, Li^+ ions: Crundwell, 2017) in the general control of BSi dissolution rate need to be addressed in future studies. In the case of spicules that are continuously exposed to seawater to accomplish their ecological function, it cannot be discarded physico-chemical mechanisms — which remain elusive— to favor values of surface free energy that may increase passivation of the external surface of silica to solvents.

Before we can reach a mechanistic understanding of the dissolution of biogenic silica, further characterization of the BSi behavior in seawater and Si-desaturated solutions rich in ions is required. Likewise, a recent surprising report of actin deeply embedded in the silica of demosponges and hexactinellids (Ehrlich et al., 2022) emphasizes the need of deepening into the atom-level characterization of the complexation of BSi with organic elements, which may significantly determine dissolution patterns. The persisting lack of knowledge in this sense is relevant because the dissolution kinetics of the biogenic silica reservoirs in the water column and the sediments are one of the main controls of the biogeochemical cycling of silicon in the ocean.

Conclusions

The main conclusions of this study are several. First, the dissolution properties of the biogenic silica vary not only across organismal phyla, but also within sponges, where differences occur between the main siliceous lineages (i. e., Demospongiae, Hexactinellida, Homoscleromorpha). Second, the bulk of sponge silica still dissolves very slowly compared to diatom silica, except for the microspicules of homosclerophorid sponges. Third, the complexation of the sponge silica with aluminum and chitin does not explain the comparatively higher resistance to dissolution of sponge silica. The intercalation of chitin or other organic elements between concentric silica layers in some hexactinellid and homoscleromorph sponges, if any, facilitates spicule dissolution rather than preventing it. Fourth, the spicules of hexactinellids in the family Rosellidae, which drop off their peripheral silica layers, dissolve about twice faster than the silica of the rest of hexactinellids and demosponges, but still substantially slower than diatom skeletons. Fifth, a chemical digestion of sediments rich in sponge spicules is little appropriate to obtain accurate determinations of total BSi in them, due to large differences in resistance to dissolution between the various types of biogenic silica. Sixth, developing a methodology to easily quantify the amount of sponge silica and its preservation in marine sediments remains as a major future challenge. Seventh, we propose herein a tentative proxy to be

further explored, suggesting that preservation of sponge silica in marine sediments may be grossly estimated as a function of time to its total dissolution in 1% sodium carbonate.

Data availability statement

The original contributions presented in the study are included in the article/Supplementary Material. Further inquiries can be directed to the corresponding author.

Author contributions

MM designed the study and wrote the first manuscript version. Dissolution experiments were conducted by MM, SA, ML-A, and AL. AL analyzed Al contents. HE analyzed chitin contents. MM and IM conducted the SEM study. All authors contributed to the article and approved the submitted version.

Funding

This research has been funded by projects "Dark-Si" (Spanish Ministry of Science, Innovation and Universities: PID2019-108627RB-I00) and "SIFS" (Spanish Council for Scientific Research: PIE-202130E034) awarded to MM. HE was partially supported by OPUS 19 grant from the National Science Centre, Poland (2020/37/B/ST5/01909) and by Alexander von Humboldt Polish Honorary Research Scholarship (FNP, Poland).

Acknowledgments

Celia Sitjá, Erik García, and Marta García are thanked for helping at different steps of the experiments, Morgane Galliniari for conducting ICP-AES analyses, and Maravillas Abad for autoanalyzer silicate determinations.

Conflict of interest

The authors declare that the research was conducted in the absence of any commercial or financial relationships that could be construed as a potential conflict of interest.

Publisher's note

All claims expressed in this article are solely those of the authors and do not necessarily represent those of their affiliated organizations, or those of the publisher, the editors and the reviewers. Any product that may be evaluated in this article, or claim that may be made by its manufacturer, is not guaranteed or endorsed by the publisher.

Supplementary material

The Supplementary Material for this article can be found online at: https://www.frontiersin.org/articles/10.3389/fmars.2022.1005068/full#supplementary-material

References

Barão, L., Vandevenne, F., Clymans, W., Frings, P., Ragueneau, O., Meire, P., et al. (2015). Alkaline-extractable silicon from land to ocean: A challenge for biogenic silicon determination. *Limnol. Oceanogr. Methods* 13, 329–344. doi: 10.1002/LOM3.10028

Bavestrello, G., Cattaneo-Vietti, R., Cerrano, C., Cerutti, S., and Sarà, M. (1996). Contribution of sponge spicules to the composition of biogenic silica in the ligurian Sea. *Pubbl. della Stn. Zool. di Napoli Mar. Ecol.* 17, 41–50. doi: 10.1111/j.1439-0485.1996.tb00488.x

Bertolino, M., Calcinai, B., Capellacci, S., Cerrano, C., Lafratta, A., Pansini, M., et al. (2012). *Posidonia oceanica* meadows as sponge spicule traps. *Ital. J. Zool.* 79, 231–238. doi: 10.1080/11250003.2011.614641

Bertolino, M., Cattaneo-Vietti, R., Pansini, M., Santini, C., and Bavestrello, G. (2017). Siliceous sponge spicule dissolution: In field experimental evidences from temperate and tropical waters. *Estuar. Coast. Shelf Sci.* 184, 46–53. doi: 10.1016/j.ecss.2016.10.044

Bidle, K. D., and Azam, F. (1999). Accelerated dissolution of diatom silica by marine bacterial assemblages. *Nature* 397, 508–512. doi: 10.1038/17351

Bossert, D., Urban, D. A., Maceroni, M., Ackermann-Hirschi, L., Haeni, L., Yajan, P., et al. (2019). A hydrofluoric acid-free method to dissolve and quantify silica nanoparticles in aqueous and solid matrices. *Sci. Rep. 2019 91* 9, 1–12. doi: 10.1038/s41598-019-44128-z

Botting, J. P., and Muir, L. A. (2018). Early sponge evolution: A review and phylogenetic framework. *Palaeoworld* 27, 1–29. doi: 10.1016/J.PALWOR.2017.07.001

Chu, J. W. F., Maldonado, M., Yahel, G., and Leys, S. P. (2011). Glass sponge reefs as a silicon sink. *Mar. Ecol. Prog. Ser.* 441, 1–14. doi: 10.3354/meps09381

Conley, D. J. (1998). An interlaboratory comparison for the measurements of biogenic silica in sediments. *Mar. Chem.* 63, 39–48.

Costa, G., Bavestrello, G., Cattaneo-Vietti, R., Dela Pierre, F., Lozar, F., Natalicchio, M., et al. (2021). Palaeoenvironmental significance of sponge spicules in pre-messinian crisis sediments, northern Italy. *Facies* 67, 9. doi: 10.1007/s10347-020-00619-4

Crundwell, F. K. (2017). On the mechanism of the dissolution of quartz and silica in aqueous solutions. *ACS Omega* 2, 1116–1127. doi: 10.1021/acsomega.7b00019

DeMaster, D. J. (1981). The supply and accumulation of silica in the marine environment. *Geochim. Cosmochim. Acta* 45, 1715–1732. doi: 10.1016/0016-7037(81)90006-5

DeMaster, D. J. (1991). "Measuring biogenic silica in marine sediments and suspended matter," in *Marine particles: Analysis and characterization*, vol. 363–367 . Eds. D. C. Hurd and D. W. Spenser (Washington: American Geophysical Union).

de Voogd, N. J., Alvarez, B., Boury-Esnault, N., Carballo, J. L., Cárdenas, P., Díaz, M.-C., et al. (2022) *World Porifera database*. Available at: https://www.marinespecies.org/porifera/.

Dixit, S., Van Cappellen, P., and van Bennekom, A. J. (2001). Processes controlling solubility of biogenic silica and pore water build-up of silicic acid in marine sediments. *Mar. Chem.* 73, 333–352. doi: 10.1016/S0304-4203(00)00118-3

Dove, P. M., Han, N., Wallace, A. F., and De Yoreo, J. J. (2008). Kinetics of amorphous silica dissolution and the paradox of the silica polymorphs. *Proc. Natl. Acad. Sci. U. S. A.* 105, 9903–9908. doi: 10.1073/PNAS.0803798105/ASSET/8D42F9F4-68B8-421C-AA9E-BF0BC38C3C8D/ASSETS/GRAPHIC/ZPQ9990836760004.JPEG

Eggimann, D. W., Manheim, F. T., and Betzer, P. R. (1980). Dissolution and analysis of amorphous silica in marine sediments. *J. Sediment. Petrol.* 50, 215–225. doi: 10.1306/212F79AF-2B24-11D7-8648000102C1865D

Ehrlich, H., Ilan, M., Maldonado, M., Muricy, G., Bavestrello, G., Kljajic, Z., et al. (2010). Three-dimensional chitin-based scaffolds from verongida sponges (Demospongiae: Porifera). part i. isolation and identification of chitin. *Int. J. Biol. Macromol.* 47, 132–140. doi: 10.1016/j.ijbiomac.2010.05.007

Ehrlich, H., Janussen, D., Simon, P., Bazhenov, V. V., Shapkin, N. P., Erler, C., et al. (2008). Nanostructural organization of naturally occurring composites-part II: Silica-chitin-based biocomposites. *J. Nanomater.* 2008, 1-18. doi: 10.1155/2008/670235

Ehrlich, H., Krautter, M., Hanke, T., Simon, P., Knieb, C., Heinemann, S., et al. (2007a). First evidence of the presence of chitin in skeletons of marine sponges. part II. glass sponges (Hexactinellida: Porifera). *J. Exp. Zool. Part B Mol. Dev. Evol.* 308, 473–483. doi: 10.1002/jez.b.21174

Ehrlich, H., Luczak, M., Ziganshin, R., Mikšík, I., Wysokowski, M., Simon, P., et al. (2022). Arrested in lass: Actin within sophisticated architectures of biosilica in sponges. *Adv. Sci.*, 9 (11), 2105059. doi: 10.1002/advs.202105059

Ehrlich, H., Maldonado, M., Parker, A. R., Kulchin, Y. N., Schilling, J., Köhler, B., et al. (2016). Supercontinuum generation in naturally occurring glass sponges spicules. *Adv. Opt. Mater.* 4, 1608–1613. doi: 10.1002/adom.201600454

Ehrlich, H., Maldonado, M., Spindler, K.-D. D., Eckert, C., Hanke, T., Born, R., et al. (2007b). Evidence of chitin as a component of the skeletal fibers of marine sponges. part i. verongidae (Demospongiae: Porifera). *J. Exp. Zool. (Molecular Dev. Evol.* 308B, 347–356. doi: 10.1002/jez.b.21156

Ehrlich, H., and Worch, H. (2007). "Sponges as natural composites: from biomimetic potential to development of new biomaterials," in *Porifera Research. biodiversity, innovation and sustainability*. Eds. M. R. Custódio, G. Lôbo-Hajdu, E. Hajdu and G. Muricy (Rio de Janeiro: Rio de Janeiro: Museu Nacional), 303–312.

Gehlen, M., Beck, L., Calas, G., Flank, A. M., Van Bennekom, A. J., and Van Beusekom, J. E. E. (2002). Unraveling the atomic structure of biogenic silica: Evidence of the structural association of Al and Si in diatom frustules. *Geochim. Cosmochim. Acta* 66, 1601–1609. doi: 10.1016/S0016-7037(01)00877-8

Gutt, J., Böhmer, A., and Dimmler, W. (2013). Antarctic Sponge spicule mats shape macrobenthic diversity and act as a silicon trap. *Mar. Ecol. Prog. Ser.* 480, 57–71. doi: 10.3354/meps10226

Hurd, D. C. (1973). Interactions of biogenic opal, sediment and seawater in the central equatorial pacific. *Geochim. Cosmochim. Acta* 37, 2257–2282. doi: 10.1016/0016-7037(73)90103-8

Jochum, K. P., Schuessler, J. A., Wang, X.-H., Stoll, B., Weis, U., Müller, W. E. G., et al. (2017). Whole-ocean changes in silica and Ge/Si ratios during the last deglacial deduced from long-lived giant glass sponges. *Geophys. Res. Lett.* 44, 11555–11564. doi: 10.1002/2017gl073897

Kamatani, A. (1971). Physical and chemical characteristics of biogenous silica. *Mar. Biol.* 8, 89–95. doi: 10.1007/BF00350922

Kamatani, A., and Oku, O. (2000). Measuring biogenic silica in marine sediments. *Mar. Chem.* 68, 219–229. doi: 10.1016/S0304-4203(99)00079-1

López-Acosta, M., Maldonado, M., Grall, J., Ehrhold, A., Sitjà, C., Galobart, C., et al. (2022). Sponge contribution to the silicon cycle of a diatom-rich shallow bay. *Limnol. Oceanogr.* 67, 2431–2447. doi: 10.1002/LNO.12211

Machill, S., Kohler, L., Ueberlein, S., Hedrich, R., Kunaschk, M., Paasch, S., et al. (2013). Analytical studies on the incorporation of aluminium in the cell walls of the marine diatom stephanopyxis turris. *BioMetals* 26, 141–150. doi: 10.1007/s10534-012-9601-3

Maldonado, M., Beazley, L., López-Acosta, M., Kenchington, E., Casault, B., Hanz, U., et al. (2021). Massive silicon utilization facilitated by a benthic-pelagic coupled feedback sustains deep-sea sponge aggregations. *Limnol. Oceanogr.* 66, 366–391. doi: 10.1002/lno.11610

Maldonado, M., Carmona, M. C., Velásquez, Z., Puig, A., Cruzado, A., López, A., et al. (2005). Siliceous sponges as a silicon sink: An overlooked aspect of benthopelagic coupling in the marine silicon cycle. *Limnol. Oceanogr.* 50, 799–809. doi: 10.4319/lo.2005.50.3.0799

Maldonado, M., López-Acosta, M., Sitjà, C., García-Puig, M., Galobart, C., Ercilla, G., et al. (2019). Sponge skeletons as an important sink of silicon in the global oceans. *Nat. Geosci.* 12, 815–822. doi: 10.1038/s41561-019-0430-7

Maldonado, M., Ribes, M., and van Duyl, F. C. (2012). Nutrient fluxes through sponges. biology, budgets, and ecological implications. *Adv. Mar. Biol.* 62, 113–182. doi: 10.1016/B978-0-12-394283-8.00003-5

Maldonado, M., and Riesgo, A. (2007). Intra-epithelial spicules in a homosclerophorid sponge. *Cell Tissue Res.* 328, 639–650. doi: 10.1007/s00441-007-0385-7

Mortlock, R. A., and Froelich, P. N. (1989). A simple method for the rapid determination of biogenic opal in pelagic marine sediments. *Deep. Res. (Part I Oceanogr. Res. Pap.* 36, 1415–1426. doi: 10.1016/0198-0149(89)90092-7

Müller, P. J., and Schneider, R. (1993). An automated leaching method for the determination of opal in sediments and particulate matter. *Deep. Res. Part I Oceanogr. Res. Pap.* 40, 425–444. doi: 10.1016/0967-0637(93)90140-X

Murillo, F. J., Kenchington, E., Lawson, J. M., Li, G., and Piper, D. J. W. (2016). Ancient deep-sea sponge grounds on the Flemish cap and grand bank, northwest Atlantic. *Mar. Biol.* 163, 1–11. doi: 10.1007/s00227-016-2839-5

Muscente, A. D., Marc Michel, F., Dale, J. G., and Xiao, S. (2015). Assessing the veracity of precambrian 'sponge' fossils using *in situ* nanoscale analytical techniques. *Precambrian Res.* 263, 142–156. doi: 10.1016/j.precamres.2015.03.010

Nelson, D. M., Tréguer, P., Brzezinski, M. A., Leynaert, A., and Quéguiner, B. (1995). Production and dissolution of biogenic silica in the ocean: revised global estimates, comparison with regional data and relationship to biogenic sedimentation. *Global Biogeochem. Cycles* 9, 359–372. doi: 10.1029/95GB01070

Paasche, E. (1973). Silicon and the ecology of marine plankton diatoms. II. silicate-uptake kinetics in five diatom species. *Mar. Biol.* 19, 262–269. doi: 10.1007/bf02097147

Roubeix, V., Becquevort, S., and Lancelot, C. (2008). Influence of bacteria and salinity on diatom biogenic silica dissolution in estuarine systems. *Biogeochemistry* 88, 47–62. doi: 10.1007/s10533-008-9193-8

Rützler, K., and Macintyre, I. G. (1978). Siliceous sponge spicules in coral reefs sediments. *Mar. Biol.* 49, 147–159. doi: 10.1007/BF00387114

Sim-Smith, C., Ellwood, M., and Kelly, M. (2017). "Sponges as proxies for past climate change events," in *Climate change, ocean acidification and sponges*. Eds. J. C. and J. B. (Berlin: Springer, Cham), 49–78. doi: 10.1007/978-3-319-59008-0_3

Tabachnick, K. R., Menshenina, L. L., Pisera, A., and Ehrlich, H. (2011). Revision of *Aspidoscopulia* reiswig 2002 (Porifera: Hexactinellida: Farreidae) with description of two new species. *Zootaxa* 2883, 1–22. doi: 10.11646/zootaxa.2883.1.1

Talevski, T., Talevska Leshoska, A., Pejoski, E., Pejin, B., Machałowski, T., Wysokowski, M., et al. (2020). Identification and first insights into the structure of chitin from the endemic freshwater demosponge ochridaspongia rotunda (Arndt 1937). *Int. J. Biol. Macromol.* 162, 1187–1194. doi: 10.1016/J.IJBIOMAC.2020.06.247

Tang, Q., Wan, B., Yuan, X., Muscente, A. D., and Xiao, S. (2019). Spiculogenesis and biomineralization in early sponge animals. *Nat. Commun.* 10, 3348. doi: 10.1038/s41467-019-11297-4

Toullec, J., and Moriceau, B. (2018). Transparent exopolymeric particles (TEP) selectively increase biogenic silica dissolution from fossil diatoms as compared to fresh diatoms. *Front. Mar. Sci.* 5. doi: 10.3389/FMARS.2018.00102/BIBTEX

Tréguer, P. J., and de la Rocha, C. L. (2013). The world ocean silica cycle. *Ann. Rev. Mar. Sci.* 5, 477–501. doi: 10.1146/annurev-marine-121211-172346

Tréguer, P. J., Sutton, J. N., Brzezinski, M., Charette, M. A., Devries, T., Dutkiewicz, S., et al. (2021). Reviews and syntheses: The biogeochemical cycle of silicon in the modern ocean. *Biogeosciences* 18, 1269–1289. doi: 10.5194/bg-18-1269-2021

Tsurkan, M. V., Voronkina, A., Khrunyk, Y., Wysokowski, M., Petrenko, I., and Ehrlich, H. (2021). Progress in Chitin Analytics. *Carb. Pol.* 252, 117204. doi: 10.1016/j.carbpol.2020.117204

Van Bennekom, A. J., Buma, A. G. J., and Nolting, R. F. (1991). Dissolved aluminium in the weddell-Scotia confluence and effect of Al on the dissolution kinetics of biogenic silica. *Mar. Chem.* 35, 423–434. doi: 10.1016/S0304-4203(09)90034-2

Van Cappellen, P., Dixit, S., and van Beusekom, J. (2002). Biogenic silica dissolution in the oceans: Reconciling experimental and field-based dissolution rates. *Global Biogeochem. Cycles* 16, 23-1-23–10. doi: 10.1029/2001gb001431

frontiers | Frontiers in Marine Science

TYPE Original Research
PUBLISHED 13 January 2023
DOI 10.3389/fmars.2022.1058730

OPEN ACCESS

EDITED BY
Martin F. Soto-Jimenez,
Institute of Marine Science and Limnology, National Autonomous University of Mexico, Mexico

REVIEWED BY
Tom Trull,
Commonwealth Scientific and Industrial Research Organisation (CSIRO), Australia
Ramanathan Alagappan,
Jawaharlal Nehru University, India
Shahab Varkouhi,
University College London, United Kingdom

*CORRESPONDENCE
Jill N. Sutton
jill.sutton@univ-brest.fr
Su Mei Liu
sumeiliu@ouc.edu.cn

SPECIALTY SECTION
This article was submitted to Marine Biogeochemistry, a section of the journal Frontiers in Marine Science

RECEIVED 30 September 2022
ACCEPTED 28 December 2022
PUBLISHED 13 January 2023

CITATION
Zhu D, Sutton JN, Leynaert A, Tréguer PJ, Schoelynck J, Gallinari M, Ma Y and Liu SM (2023) Revisiting the biogenic silica burial flux determinations: A case study for the East China seas.
Front. Mar. Sci. 9:1058730.
doi: 10.3389/fmars.2022.1058730

Revisiting the biogenic silica burial flux determinations: A case study for the East China seas

Dongdong Zhu[1,2,3], Jill N. Sutton[3]*, Aude Leynaert[3], Paul J. Tréguer[3], Jonas Schoelynck[4], Morgane Gallinari[3], Yuwei Ma[1,2] and Su Mei Liu[1,2]*

[1]Frontiers Science Center for Deep Ocean Multi-spheres and Earth System, Key Laboratory of Marine Chemistry Theory and Technology, Ministry of Education, Ocean University of China, Qingdao, China, [2]Laboratory for Marine Ecology and Environmental Science, Qingdao National Laboratory for Marine Science and Technology, Qingdao, China, [3]University of Brest, Centre national de la recherche scientifique, L'Institut de recherche pour le développement, Ifremer, Institut Universitaire Européen de la Mer, Plouzané, France, [4]Department of Biology, Ecosphere Research Group, University of Antwerp, Universiteitsplein 1, Wilrijk, Belgium

The Coastal and Continental Margin Zones (CCMZs) contribute to 40% of the total burial flux of biogenic silica (bSi) of the world ocean. However, the accurate determination of the bSi content ($bSiO_2$%) in marine sediments remains a challenge. The alkaline methods commonly used to quantitatively determine $bSiO_2$% can completely digest the amorphous silica of diatoms but are less effective at digesting radiolarians and sponge spicules. In addition, the lithogenic silica (lSi) found in sediments is partly digested during these alkaline extractions, which can bias the accuracy of the determined $bSiO_2$%. This is of importance in CCMZs where the lSi:bSi ratio is high. In this study, we examined sediments collected in the CCMZs of East China seas, an environment of peculiar interest given the large amount of lSi deposited by the Yellow River and the Yangtze River. The results show that alkaline digestions using stronger solutions and pretreatment steps resulted in an overestimate of the $bSiO_2$% due to increased leaching of silica mainly from authigenic silicates and clays, whereas weak digestions underestimated the $bSiO_2$% owing to incomplete digestion of sponge spicules. We found that the use of the Si/Al method accurately corrects for the lSi fraction in marine sediments, and thereby improves the determinations of $bSiO_2$% in the sediments of East China seas CCMZs. Ensuring full digestion of all bSi remains challenging, in particular for sponge spicules, motivating both verifications via microscopy and longer extraction times. To emphasize the influence of these methodological

differences, we revised the bSi burial flux in the East China seas and provide a new estimate of 253 (± 286) Gmol-SiO_2 yr^{-1}, which is one third of the previous estimates. We discuss the potential contribution from radiolarian and sponges and we propose a new general protocol for the determination of bSi in sediments that minimizes the methodological bias in bSi determination.

KEYWORDS

biogenic silica, alkaline digestion, analytical methods, burial flux, coastal and continental margin zones, East China seas, marine silicon cycle

1 Introduction

Coastal and Continental Margin Zones (CCMZs) are distinct settings for the interrogation of global marine biogeochemical cycling of silica (Si), climate change and marine ecological processes (Jeandel and Oelkers, 2015; Jeandel, 2016; Tréguer et al., 2018; Rahman et al., 2019). The CCMZs represent approximately 10% of the global marine surface area (3.61×10^8 km^2) (Costello et al., 2010), and account for 40% of the total biogenic silica (bSi) burial (~9.2 Tmol-Si yr^{-1}) in the global ocean (DeMaster, 2019; Tréguer et al., 2021). This estimate was based solely on the burial of diatom bSi. However, marine Si is also removed through reverse weathering in major tropical and subtropical deltas (Rahman et al., 2016; Rahman et al., 2017), the burial of siliceous sponges spicules predominantly on the continental shelf and margins (DeMaster, 2019; Maldonado et al., 2019), and the burial of radiolarian tests (Maldonado et al., 2019). Recent work estimated that if all of these processes are taken into account, the burial flux of Si that occurs mainly within the CCMZs, removes 5.0 to 10.1 Tmol-Si yr^{-1} (DeMaster, 2019; Tréguer et al., 2021), which is equivalent to roughly one to two-thirds of the global Si output flux (15.6 Tmol-Si yr^{-1}) from the marine environment (DeMaster, 2019; Tréguer et al., 2021).

The calculation of the marine Si budget at the global or local level is dependent on the precision and accuracy of the bSi measurements (DeMaster, 1991). Within the CCMZs, the combination of lSi with bSi decreases the reactive surface area of biogenic opal and lowers its solubility (Dixit and Van Cappellen, 2003; Varkouhi et al., 2020a; Varkouhi and Wells, 2020), which enhances the bSi burial efficiency. However, high precipitation rates of terrestrial lSi dilute the bSi and result in an opal-depleted coastal sediment (DeMaster, 2002; Wu et al., 2017; Wu and Liu, 2020). Therefore, accurate determination of the bSi content ($bSiO_2$%) in the CCMZs sediment is particularly challenging owing to its characteristically low $bSiO_2$%, high lithogenic silica (lSi; clay mineral, authigenic aluminosilicate, quartz) content (DeMaster, 1991), and complexity of bSi types (e.g. diatoms, phytolith, radiolarians, sponge spicules; Figure 1A) (DeMaster, 1991; Maldonado et al., 2019). Among several different techniques (e.g., X-ray Diffraction (Goldberg, 1958; Eisma and van der Gaast, 1971), point counts of siliceous microfossil (Pudsey, 1993; Varkouhi et al., 2020b), infrared analysis (Fröhlich, 1989), normative calculation technique (Leinen, 1977), wet chemical method (DeMaster, 1981; Mortlock and Froelich, 1989; Müller and Schneider, 1993)), wet chemical method is the most commonly used method for determining the $bSiO_2$% in marine sediments (Conley, 1998). Considering the complex sediment composition of CCMZs sediments, a mild alkaline leach (0.1 M Na_2CO_3) is recommended to minimize the interference of lSi in bSi determination when using the wet chemical method (DeMaster, 1981). However, a mild alkaline leach underestimates the quantity of bSi due to an incomplete extraction of more resistant bSi (Figure 1A), such as radiolarians (Mortlock and Froelich, 1989; Müller and Schneider, 1993) and siliceous sponge spicules (Maldonado et al., 2019). Nonetheless, complete digestion of resistant bSi using a strong alkaline solution can introduce additional bias due to the inevitable attack on lSi. To accurately determine $bSiO_2$% in sediment from different marine environments, various kinds of wet alkaline methods with different digestion conditions (i.e., alkaline solution, sample to solution ratio, extraction temperature, duration of extraction and pre-treatment of sediment by HCl and H_2O_2 prior to alkaline digestion) have been proposed and applied in the literature (DeMaster, 1981; Mortlock and Froelich, 1989; Müller and Schneider, 1993; Kamatani and Oku, 2000; Conley and Schelske, 2001; Koning et al., 2002; Liu et al., 2002; Olivarez Lyle and Lyle, 2002). These methods were grouped into two different types: (1) Si/time alkaline digestion and (2) Si/Al alkaline digestion (Swann, 2010). The Si/time method (Figure 1B), which is the conventional wet alkaline method, requires the measurement of alkaline extracted Si concentration and corrects the lSi fraction based on the assumption of the difference in dissolution kinetics between bSi (non-linear dissolution) and lSi (linear dissolution) (DeMaster, 1981). The Si/Al alkaline digestion method (Figure 1B) requires the measurement of alkaline extracted Si and Al concentrations,

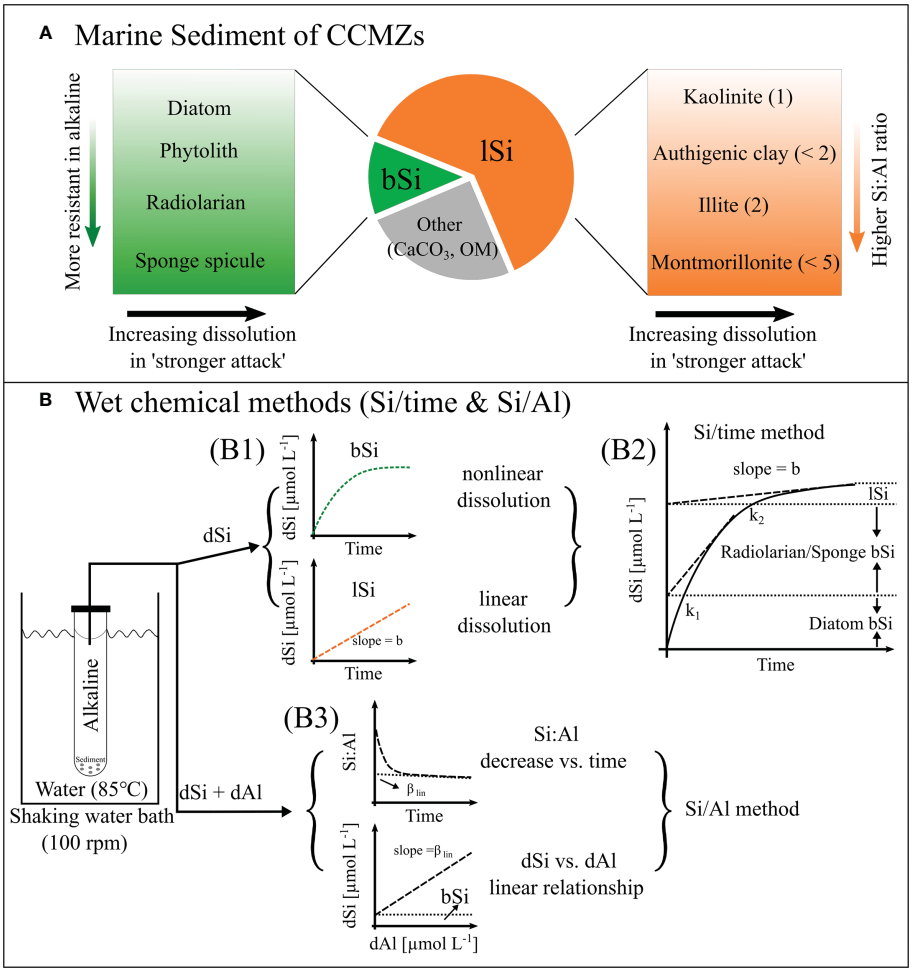

FIGURE 1
The schematic diagram shows the: **(A)** components in the sediment of CCMZs and **(B)** Wet chemical methods (B1: Si/time method; B2: Si/Al method). **(A)** shows the types of bSi in sediment and their dissolution capability: diatom< phytolith< radiolarian< sponge spicule (Mortlock and Froelich, 1989; Müller and Schneider, 1993; Meunier et al., 2014) and types of lSi in sediment and their Si:Al ratio: authigenic clay: Si:Al< 2 (Mackin, 1989; Michalopoulos and Aller, 1995); Kaolinite: Si:Al = 1, Illite: Si:Al = 2, Montmorillonite: Si:Al< 5 (Koning et al., 2002). The 'stronger attack' represents high alkaline concentration/pH, longer extraction time and sample pretreatment with acid (e.g. HCl) and/or oxidizing agents (e.g. H_2O_2). **(B)** shows the alkaline digestion (85°C) of bSi and correction of lSi using the Si/time method (B1) modified from DeMaster (1981), the Si/time method (B2) modified from Conley and Schelske (2001) and the Si/Al method (B3) modified from Kamatani and Oku (2000). The Si/time method (B1 and B2) assumes the bSi dissolves non-linearly through time whereas the lSi dissolves linearly (the slope equals to dissolution rate 'b') through time, the different types of bSi (diatom, radiolarian and sponge spicules) can be quantified based on their dissolution rate (*k1*, and *k2*). The Si/Al method (B3) assumes that the ratio of alkaline extractable Si vs. Al is constant, and the alkaline extractable Al is mainly lSi origin, the Si:Al ratio of bSi is higher (> 5) than lSi (< 5) (Koning et al., 2002). The Si: Al vs. time plot shows a decrease of Si:Al ratios to constant value after a complete digestion of bSi.

and corrects the lSi fraction based on the assumption that the Si:Al ratio of lSi is low (Si:Al< 5, Figure 1A) and the extracted Al is mainly lSi origin (Kamatani and Oku, 2000; Koning et al., 2002). Previous studies found methodological differences in the $bSiO_2$% between Si/time and Si/Al methods in both lacustrine (Swann, 2010) and marine sediments (Barão et al., 2015). It has been noted that major biases in the $bSiO_2$% can be generated among different wet alkaline methods (DeMaster, 1991; Gehlen and van Raaphorst, 1993; Schlüter and Rickert, 1998; Kamatani and Oku, 2000; Barão et al., 2015), influencing the estimation of the bSi burial flux especially in the opal-depleted ($bSiO_2$-depleted) sediment of the CCMZs (DeMaster, 1991; DeMaster, 2002; Tréguer et al., 2021).

The East China seas, which consists of the Bohai Sea (BH), the Yellow Sea (YS), and the East China Sea (ECS), is one of the largest CCMZs in the Northwest Pacific Ocean. The East China seas are characterized by high sedimentation rates (Qiao et al., 2017), low $bSiO_2$% (< 3%) and high lithogenic material content (> 70%) (Liu et al., 2002; Wu et al., 2017; Wu and Liu, 2020). Previous studies demonstrated that the burial of bSi in the East China seas is 924 (± 693) Gmol-SiO_2 yr^{-1} (Liu et al., 2016; Wu et al., 2017; Wu and Liu, 2020), accounting for ~5% of the bSi

burial in the global ocean. These estimations were based on the $bSiO_2$% determined using several alkaline digestion techniques, such as using different concentrations of alkaline solution (0.1 M Na_2CO_3, 2% Na_2CO_3, 2.0 M Na_2CO_3), duration of the alkaline digestion (5 h, 8 h) and pre-treatment process (with HCl and H_2O_2 prior to alkaline extraction) that may underestimate or overestimate the bSi content due to the incomplete digestion of bSi or the interference of lSi in bSi determination (Kamatani and Oku, 2000; Barão et al., 2015) and leaching of authigenic silicates activated by acid treatment (Michalopoulos and Aller, 2004; Rahman et al., 2016; Pickering et al., 2020). Such an under- or overestimate of the bSi content will influence the magnitude of the burial flux of bSi determined for the CCMZs where the sediment load is high and the bSi content is low. In addition, diatoms, radiolarians (Liu et al., 2017; Qu et al., 2020a; Qu et al., 2020b), sponge spicules (Chou et al., 2012) and living siliceous sponges (Zhang et al., 2003) were observed in the sediment of the East China seas. However, the influence of their presence on the determination of bSi content and consequent role in marine Si cycling for this region, is still not defined. The radiolarians and siliceous sponge spicules are more resistant to alkaline attacks than diatoms (DeMaster, 1981; Müller and Schneider, 1993), thus the types of bSi need to be considered when characterizing the bSi content of sediments (DeMaster, 1991).

This study aims to provide an accurate determination of the burial flux of the East China seas CCMZs by conducting a thorough evaluation of the potential methodological biases influencing the determination of bSi. To evaluate these methodological biases, multiple samples of characteristically diverse marine sediment from the East China seas were measured for $bSiO_2$% using different alkaline solution concentrations (0.1 M, 0.2 M, 2.0 M Na_2CO_3), with and without pretreatment. In addition, the types of marine bio-siliceous structures (diatoms, radiolarian tests, and sponge spicules) and their abundances in the different sediment samples were quantified to select an appropriate wet alkaline method. Further, the $bSiO_2$% determined using the Si/time method (20 h digestion in 0.1 M Na_2CO_3) and the Si/Al method (1 h digestion in 0.5 M NaOH) were compared for an accurate evaluation of the alkaline extracted Si (bSi and lSi) from sediments of the CCMZs. The detailed evaluation of these methodological biases resulted in the production of a revised evaluation of the burial flux of bSi for the East China seas CCMZ and a discussion on the implementation of a standardized method for the determination of $bSiO_2$% in similar depositional environments.

2 Materials and methods

2.1 Study area and sample locations

The East China seas (Figure 2) consists of the BH (surface area: 7.73×10^4 km^2), the YS (surface area: 38×10^4 km^2), and the ECS (surface area: 77×10^4 km^2) (Qiao et al., 2017). The semi-enclosed BH and YS are shallow water bodies with an average water depth of 18 m (maximum 85 m) and 44 m (maximum 140 m) respectively. About 21 large rivers (length of mainstream > 100 km) deliver 782.2×10^9 kg yr^{-1} of sediment to the BH, with more than 90% delivered by the Yellow River. Roughly 30 rivers discharge 13.0×10^9 kg yr^{-1} of sediment into the YS (Qiao et al., 2017). However, up to 90% of its total sediment burial flux (414.6×10^9 kg yr^{-1}) is transported from the BH and 5.7% is eroded sediment from the old Yellow River (Qiao et al., 2017). The ECS consists of a broad continental shelf and the Okinawa Trough, with an average water depth of 349 m (maximum 2700 m). About 18 rivers deliver 490.5×10^9 kg yr^{-1} of sediment into the ECS, of which approximately 80% is delivered from the Yangtze River (Qiao et al., 2017). The $bSiO_2$% in surface sediments of the BH, YS and ECS were 0.92 ± 0.24% (Liu et al., 2002), 2.20 ± 0.79% (Wu et al., 2017) and 1.97 ± 0.53% (Wu and Liu, 2020), respectively, and are considered to be relatively low values (< 3% is considered a threshold value for bSi concentrations) and requires an accurate determination (Koning et al., 2002; Liu et al., 2002; DeMaster, 2019; Trégueur et al., 2021).

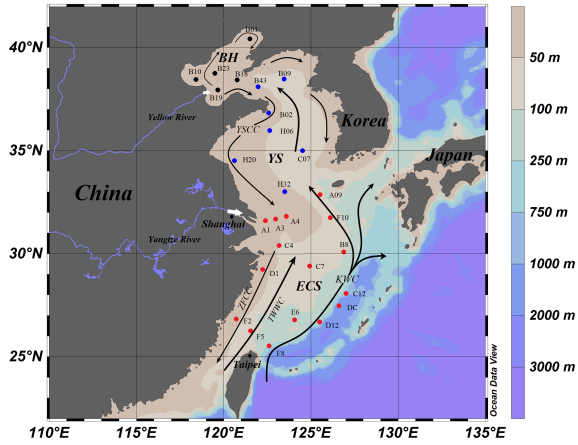

FIGURE 2
Map of the study area indicating the sampling stations. The location of samples are grouped in different colors at the Bohai Sea (black dots •), Yellow Sea (blue dots •), and the East China Sea (red dots •). The surface sediment samples (0 – 2 cm) were obtained during several research cruises during 2008-2013. The distributions of currents are based on Liu et al. (2007) and Qin et al. (1996). White arrows represent the Yellow River and Yangtze River discharge. (YSCC: Yellow Sea Coastal Current; ZFCC: Zhejiang Fujian Coastal Current; TWWC: Taiwan Warm Current; KWC: Kuroshio Warm Current). The map is created using Ocean Data View (ODV) software (Schlitzer, Reiner, Ocean Data View, https://odv.awi.de, 2021).

Field observations were conducted in the East China seas from 2008 to 2013. The sampling sites are shown in Figure 2. At each sampling site, surface sediment samples (0 – 2 cm) were collected using a stainless-steel box sampler and subsequently packed in sealed plastic bags at -20°C on board. Frozen samples were then freeze-dried in the laboratory and stored at room

temperature (~20°C) until analysis. Two sediment samples for interlaboratory comparison (sample code: Still Pond, R-64) were also measured using the Si/time (0.1 M Na_2CO_3, 20 h digestion) and the Si/Al (0.5 M NaOH, 1 h digestion) alkaline digestion method. The location of these sampled sediments and their descriptions are given in Conley (1998).

2.2 Analytical methods

2.2.1 The biogenic silica types and abundance

The different types of bSi and their abundance in the sediment of the East China seas were determined using an inverted microscope (Zeiss Axio Observer A1) at 10X magnification. The abundance (numbers per gram: 10^3 g^{-1} dry sediments) of different marine bSi organisms in samples A3, C4, C7, C12, and F2 were examined optically (see Figure 2 for sample locations). The samples were selected based on their water depth and sediment type (A3, F2: silty-clay; C4, C7: sandy; C12: clay-silt). In order to prepare the samples for microscopic observation, ca. 5 – 10 mg of homogenized dry sediment was pretreated using 1.0 M HCl (10 mL) and 10% H_2O_2 (10 mL) and heated at 60°C for 2 h. The solution was subsequently discarded after centrifugation (4000 rpm, 5 min) and the residual sediment was rinsed three times using Milli-Q water (18.2 MΩ). The decarbonated sediment samples were homogenized in Milli-Q water (1 mL) and the samples were put on a glass microscope slide for optical observation. The abundance of individuals for different types of bSi (i.e., diatom frustules, radiolarian skeletons and siliceous sponge spicules) was counted and normalized as the number of individuals per gram of dry sediment (10^3 g^{-1}).

2.2.2 Biogenic silica

The content of bSi found in the sediments in this study is expressed as $bSiO_2$% (molar mass of $bSiO_2$: 60 g mol^{-1}) to avoid potential errors associated with the difference in bond water content of different types of bSi and/or ages of siliceous organisms.

Two wet chemical methods were used to quantify the $bSiO_2$%: the Si/time method (DeMaster, 1981; Conley and Schelske, 1993; Conley and Schelske, 2001; Liu et al., 2002) and the Si/Al method (Koning et al., 2002; Barão et al., 2014; Barão et al., 2015). For the Si/time alkaline digestion, samples were digested using a 0.1 M Na_2CO_3 solution for 20 h. Before wet-alkaline digestion, freeze-dried marine sediment was gently ground using an agate pestle and mortar. The grinding process aims to homogenize the sediment. Sediment (~100 mg) was then weighed into a 50 mL polypropylene copolymer centrifuge tube (Nalgene no. 3119-0050; Caps no. DS3132-0024) or 50 mL fluorinated ethylene propylene (FEP) centrifuge tube (Nalgene no. 3114-0050; Caps no. DS3131-0024). An alkaline solution (40 mL, 0.1 M Na_2CO_3) was added to the centrifuge tube using a calibrated 10 mL pipette (10 ± 0.01 mL, Eppendorf). The sample to liquid ratio (S/L) was ca. 2.5 g/L. The tubes were tightly capped after the addition of the alkaline solution and the sediments were well mixed using a Vortex. Samples were immediately placed into a shaking water bath (Julabo SW22) pre-heated to 85 °C with an oscillation frequency of 100 rpm. An aliquot of 200 µL clear centrifugation supernatant was taken from the extraction solution at each time interval and neutralized using 1.0 M HCl solution. Later, the neutralized samples were diluted by Milli-Q water (18.2 MΩ cm^{-1}) to 10 mL, then the dissolved silicic acid (dSi) was measured following the molybdate-blue method (Grasshoff et al., 1983) using a spectrometer as described in Mortlock and Froelich (1989). Determination of the blanks during each extraction experiment showed the Si from both the reagent and tube were negligible. Additionally, alkaline digestion of pre-treated (P; pretreating the sediment using 1.0 M HCl and 10% H_2O_2) and non-pretreated (NP) sediment were performed using 0.1 M, 0.2 M, 2.0 M Na_2CO_3 solutions to determine the effect of the concentration of Na_2CO_3 and pretreatment process (P vs. NP) on bSi determination.

In this study, the $bSiO_2$% was determined following the calculation method described by Liu et al. (2002) where sediments undergo an 8 h digestion. In addition, the $bSiO_2$% was also calculated following the method described in DeMaster (1981); Liu et al. (2002) and Conley and Schelske (1993, 2001) when sediment was digested in a 0.1 M Na_2CO_3 solution for 20 h. The method described in Conley and Schelske (1993, 2001) was applied for quantifying the diatom bSi, radiolarian and/or sponge bSi (Figure 1B). Moreover, the $bSiO_2$% analyzed according to the method described by Mortlock and Froelich (1989) was also performed.

The Si/Al method refers to the continuous analysis of Si and Al concentrations in the alkaline digestion at a high sampling resolution time (Figure S1). In this study, $bSiO_2$% was measured following the continuous analysis method (Koning et al., 2002; Barão et al., 2015) at the University of Antwerp (Belgium). The dSi and dissolved Al (dAl) in alkaline solution (0.5 M NaOH) were measured continuously at 1 second (s) resolution (Müller and Schneider, 1993). Freeze-dried sediment samples (~100 mg) were added into a stainless-steel vessel with an initial 180 mL of 0.5 M NaOH pre-heated to 85 °C. The S/L ratios of all the analyses range from 0.56 to 0.89 g/L. The closed vessel (to avoid evaporation) is directly connected to a continuous analyzer (Skalar®, The Netherlands) and a rotating motor continuously homogenizes the sample in the extraction liquid, maintaining a constant S/L ratio. The dSi concentration is determined according to the molybdate-blue method (Grasshoff et al., 1983), while dAl is determined according to the fluorometric method (Hydes and Liss, 1976). Standard samples of dSi and dAl with concentrations of 1 mg L^{-1}, 2 mg L^{-1}, 4 mg L^{-1}, 6 mg L^{-1}, 8 mg L^{-1}, 10 mg L^{-1}, 20 mg L^{-1}, 30 mg L^{-1}, and 40 mg L^{-1} were used for calibration, and only the linear regression curves with

correlation coefficients ≥ 0.999 were accepted according to previous studies (Barão et al., 2015). Two independent reference solutions (with concentrations of 3 mg L^{-1}, and 9 mg L^{-1} of dSi and dAl) were tested before and after the continuous alkaline extractions to guarantee an analytical error below 5%. The stock standard solutions for Si and Al were made using $Na_2SiO_3{\cdot}9H_2O$ (Sigma-Aldrich S4392) and $KAl(SO_4)_2{\cdot}12H_2O$ (Merck 101047).

2.2.3 Scanning Electron Microscopy (SEM)

The observed siliceous organisms in the sediment samples were imaged using Scanning Electron Microscopy (SEM; FEI Quanta 200, and Hitachi TM4000). To chemically characterize the bSi and its associated authigenic aluminosilicate 'coating', the Scanning Electron Microscopy was coupled with an Energy Dispersive Spectrometer (SEM-EDS) analysis using FEI Quanta 200 and OXFORD X-MAX Silicon Drift Detector (detector size: 80 mm) at Ifremer-LCG (France). Typically, the bio-siliceous structures were handpicked under a stereomicroscope and mounted on an adhesive carbon tab (Leit) using a brush. The carbon tab was pasted on pin stubs and coated with gold (Cheize et al., 2019). The major elements were quantitatively determined under a high vacuum at 20 kV.

2.3 Analytical procedures for Si/Al data

Each extraction in the continuous analysis procedure provides Si and Al concentrations through time at a one-second resolution (Figure S1), and the unit of parameter t in the models (Eq. 1 – 3) was normalized into minutes (min). Determination of the $bSiO_2$% follows the procedure that assumes the presence of two discrete phases: (1) a linear phase indicating lithogenic silicate (lSi) dissolution and (2) a nonlinear phase indicating bSi and/or non-bSi dissolution (DeMaster, 1981; Koning et al., 2002). The $bSiO_2$% was calculated following the 4 models (Eq.1 = Model 1; Eq.2 = Model 2 and Model 3; Eq.3 = Model 4) described by Koning et al. (2002) using the Origin 2021b software.

Model 1 demonstrates the first-order dissolution of a single Si phase (Si_{extr}) as shown in Eq.1:

$$\begin{aligned} Si_{aq} &= [Si_{extr}]_0\left(1-e^{-kt}\right)+bt \\ Al_{aq} &= \frac{1}{\beta_1}\,[Si_{extr}]_0\left(1-e^{-kt}\right)+\frac{1}{\beta_{lin}}\,bt \end{aligned} \quad (1)$$

Here, Si_{aq} and Al_{aq} are the concentrations of silicic acid and aluminum in mg L^{-1}, in the reaction vessel at time t (min). $[Si_{extr}]_0$ is the initial extractable silica present in the vessel in mg L^{-1}, equivalent to the final concentration of Si_{aq} reached when all extractable silica (bSi and lSi) has dissolved, k is the reactivity constant (min^{-1}) and β_1 is the atomic ratio of Si and Al released during the dissolution of extractable silica fraction. b (mg L^{-1} min^{-1}) represents the constant dissolution rate of Si from clay minerals and β_{lin} is the Si:Al ratio in the lithogenic fraction.

Natural sediment samples may consist of several types of extractable bSi. For natural samples containing two Si_{extr} fractions ($Si_{extr}1 = ExtrSi_1$, $Si_{extr}2 = ExtrSi_2$; $n = 2$), the increases of the silicic acid concentration in the reaction vessel with time can be as the sum of two first-order dissolution processes (Model 2, Eq. 2), using the same parameters as described in Eq.1. For natural samples containing three Si_{extr} fractions ($n = 3$), the increase in silicic acid concentration with time can be the sum of three first-order dissolution processes (described as Model 3). $[Si_{extr}]_{0,i}$ is the initial extractable silica present in the extractable silica fraction i, k_i is the reactivity constant and β_i is the Si:Al ratio for fraction i.

$$\begin{aligned} Si_{aq} &= \sum_i^n [Si_{extr}]_{0,i}\,(1-e^{-k_i t}) + bt \\ Al_{aq} &= \sum_i^n \frac{1}{\beta_i}[Si_{extr}]_{0,i}\,(1-e^{-k_i t}) + \frac{1}{\beta_{lin}}\,bt \end{aligned} \quad (2)$$

Model 4 demonstrates the reactive continuum dissolution of the infinite number of fractions (i) (Eq. 3) (Koning et al., 1997) and can be described as:

$$\begin{aligned} Si_{aq} &= [Si_{extr}]_0\left(1-\left(\tfrac{\alpha}{\alpha+t}\right)^{\nu}\right)+bt \\ Al_{aq} &= \tfrac{1}{\beta_1}\,[Si_{extr}]_0\left(1-\left(\tfrac{\alpha}{\alpha+t}\right)^{\nu}\right)+\tfrac{1}{\beta_{lin}}\,bt \end{aligned} \quad (3)$$

Where the parameter α represents the average lifetime of the alkaline extractable components in sediment and ν represents a non-dimensional parameter solely related to the shape of the distribution curve. Model 4 allows a continuum of reactivity of bSi and lSi and assumes one Si:Al ratio for all the bSi components, it is not justified by data fitting in this study. The highest number of bSi components justified by model fitting was model 2, in agreement with Barão et al. (2015) and Raimonet et al. (2015).

The alkaline extractable Si (AlkExSi) may contain several non-linear fractions, based on the Si:Al ratio and reactivity constant (k). The origin of different extractable Si fractions (bSi, lSi) can be evaluated (Koning et al., 2002). The lSi fraction (Figure 1A) is normally characterized by low reactivity (Koning et al., 2002) and small Si:Al ratios (authigenic silicates: Si:Al< 2, Mackin, 1989; Michalopoulos and Aller, 1995; Kaolinite: Si:Al = 1, Illite: Si:Al = 2, Montmorillonite, Si:Al< 5, Koning et al., 2002), the bSi fraction is characterized by high reactivity ($k > 0.1$ min^{-1} and $\beta_i > \beta_{lin}$) and high Si:Al ratios ($\beta_i >$ 5) (Koning et al., 2002; Barão et al., 2015). Moreover, chemically altered bSi structures were characterized by a nonlinear dissolution with low reactivity ($k< 0.1$ min^{-1}) and low Si:Al ratio (< 5) (Koning et al., 2002).

For the fitted results from the above-mentioned models, optimization was carried out by maximizing the likelihood statistic log(L) (Armstrong et al., 2002; Moriceau et al., 2009) as described as follows:

$$\log(L) = -\frac{N}{2}\log\left(\frac{\sum\left(\log(\hat{C}_j) - \log(C_j)\right)^2}{N}\right) \quad (4)$$

Where N is the total number of data points, C_j is the measured concentration (mg L^{-1}) for data point *j*. and the $\hat{C}_j$ is the corresponding model prediction. The difference in log(*L*) (Δ log(*L*)) between fits of different models to the same data gives the goodness of fit of one model compared to the other (Figure S1). As described in Moriceau et al., 2009, if the log(*L*) of one model is at least two points higher per added parameter than another, it is considered a better model (Hilborn and Mangel, 1997). In this study, the results from the fitted model were used for methodology comparison. A non-parametric Aligned Ranks Transformation (ART) Analysis of Variance (ANOVA) was performed using R. studio software to test for significant differences between methods.

2.4 Burial flux of $bSiO_2$ in the CCMZs of East China seas

The burial flux (F_b) of $bSiO_2$ in sediment can be expressed as follows (Ingall and Jahnke, 1994):

$$F_b = C * w \quad (5)$$

Where *C* (mol g^{-1}) is the concentration of $bSiO_2$, and is calculated from the $bSiO_2$% determined in dry sediment (in g of SiO_2 g^{-1}), and converted to mol g^{-1} by dividing it by the molecular weight of SiO_2 (6×10^{-3} g mol^{-1}), *w* (g cm^{-2} yr^{-1}) is the mass accumulation rate. The *w* used in this study is averaged sediment accumulation rate at BH (0.50 g cm^{-2} yr^{-1}), YS (0.37 g cm^{-2} yr^{-1}) and ECS (0.26 g cm^{-2} yr^{-1}) reported previously (Qiao et al., 2017). Note, a primary objective of this study was to determine the potential influence that methodological biases can have on the bSi burial flux Therefore, an average sedimentation rate of the study area was applied. The F_b was then multiplied by the respective area of the BH, the YS and the ECS to calculate the burial flux of bSi of each region and the East China seas.

3 Results

3.1 Biogenic silica types and their abundances

Table 1 shows the abundance of the three types of marine bSi in sediment obtained from the East China seas (see Figure 2 for sample sites). All of the samples used in this study were examined under a microscope to determine the relative composition of different bSi types. Among the three major types of marine bSi (i.e., diatoms, radiolarians, sponge spicules), diatoms and sponge spicules were observed in the sediments of BH, YS, and ECS. Radiolarian skeletons were only observed in the sediment of YS and ECS. The abundance of sponge spicules and their size (length) and the number of radiolarian tests varied between samples from the BH, the YS

TABLE 1 Different types of marine bSi (diatoms, radiolarians, sponge spicules) and their abundances (10^3 g^{-1} dry sediments) in the surface sediment of East China seas.

Region		Biogenic silica types/abundance			
		Diatom	Radiolarians	Sponge spicules	
Bohai Sea (n=5)		++	–	+[a]	This study
		13.0[1]	no data	no data	Other studies
Yellow Sea (n=7)		++	–	+[b]	This study
		17.0[2]	~0[5]	no data	Other studies
East China Sea (n=16)		++	+	+++[c]	This study
		11.3-19.9[3,4]	0.02-7.3[5,6]	no data	Other studies
	A3	3.8	0	5.2	This study
	F2	6.1	0.4	17.6	This study
	C4	2.2	0	3.3	This study
	C7	5.2	0.1	8.4	This study
	C12	14.8	12.4	231.7	This study

the numbers in the table are references. 1: Li et al., 2020; 2: Wang et al., 2016; 3: Chen et al., 2014; 4: Li et al., 2018; 5: Qu et al., 2020a; 6: Liu et al., 2017; n represents the number of samples used for evaluating the types of bSi of each region.
"+", "++", "+++": observation of bSi from low to high abundance; "–": not observed; [a]: observation of low abundance of small sponge spicules (length: 10 – 40 μm) of BH; [b]: observation of low abundance of sponge spicules with intermediate size (length: 50 – 300 μm) of YS; [c]: observation of high abundance of sponge spicules (length: 100 – 500 μm).Note that phytolith and siliceous dinoflagellate are not counted in this study.

and the ECS. Microscopic observations indicated that radiolarian skeletons were rare in the sediment of the YS, whereas more radiolarian tests were found in the sediment samples of ECS. Although sponge spicules were found in all sediment samples (Table 1), the size of sponge spicules in the sediment of the BH (length: 10 – 40 μm), and YS (length: 50 – 300 μm) are smaller than that of the ECS (100 – 500 μm). The abundance of sponge spicules in the sediment of BH and YS is less than what was observed for diatoms. In contrast, the abundance of sponge spicules was greater than diatoms in ECS sediment samples (Table 1).

We found that radiolarians and sponge spicules were more abundant in the sediment of the ECS than the BH and the YS from the microscopic observations. Therefore, five samples (C4, C7, C12, F2, and A3) were selected from the ECS for determining the abundance of different types of bSi. The radiolarians and sponge spicules are more abundant in the offshore sediment (C7, C12) than in nearshore sediment (A3, F2, C4). The abundance of sponge spicules is greater than that of diatom tests in the 5 samples (C4, C7, C12, F2, A3) from ECS, especially in sample C12 where the abundance of sponge spicules (231.7×10^3 g^{-1}) is ca. 15 times greater than that of diatoms (14.8×10^3 g^{-1}). The abundance of diatoms is similar for the BH, YS and ECS, which is in agreement with previous research (Chen et al., 2014; Wang et al., 2016; Li et al., 2018; Li et al., 2020). However, radiolarians and sponge spicules are more abundant in the ECS, especially in the sediment of the outer shelf of the ECS.

3.2 Wet alkaline digestions

3.2.1 Evaluation of reference samples

Two interlaboratory comparison sediment samples (Still Pond, R-64) were measured using Si/time (Figure S2) and Si/Al (Figure S3) alkaline digestion to assess the accuracy of the biogenic silica measurement. Similar results were obtained to previous works (Table 2), but also showed dependence on the extraction method. The $bSiO_2$% applying a 0.5 M NaOH digestion (Still Pond: 2.74%; R-64: 7.23%) and a 0.1 M Na_2CO_3 digestion (Still Pond: 2.00 ± 0.05%; R-64: 5.50 ± 0.10%) are within the acceptable range of $bSiO_2$% values (Still Pond: 2.82 ± 1.17%; R-64: 6.49 ± 2.09%) reported in Conley (1998) (Table 2). The wide range of data presented in Conley (1998) is likely due to the influence of methodological differences applied (alkaline solution concentration and/or chemical pretreatment), the act of crushing the sediment prior to the alkaline attack, and the existence of sponge spicules in Still Pond and R-64 which was not previously reported in Conley (1998), because siliceous sponge spicules were observed in both reference samples. The coefficient of variability (i.e., relative standard deviation) for five parallel extractions was< 3%, indicating good reproducibility.

3.2.2 Comparation of the extraction methods

The results presented here compare the analysis of $bSiO_2$% determined using different Si/time methods. Triplicate digestion of the pre-treated (P) and non-pretreated (NP) sediment (Figure 3) was performed to determine the influence of the pre-treatment process on bSi determination. As expected, stronger solutions and pretreatment of sediment led to a greater release of silica (Table 3, Figures 3, 4). According to the different alkaline digestion and microscopic observation, this is mainly due to the extraction of lSi rather than bSi (e.g., sponge spicules). The pre-treatment of sediment using HCl (1.0 M) and H_2O_2 (10%) as described by Mortlock and Froelich (1989) will activate the authigenic silicate phases and the clay minerals, thus cause an overestimation of the $bSiO_2$%.

Figure 3 shows a continuous increase of the SiO_2% over time. The alkaline extracted silica (AlkExSi) content is higher for the pretreated sediments than the non-pretreated sediments. Similar result was obtained for the total amount of alkaline extracted silica (TAlkExSi) after the 8 h digestion (0.1 M Na_2CO_3, P > 0.1

TABLE 2 The $bSiO_2$% of interlaboratory comparison sediment samples (Still Pond and R-64). The location of the two samples is described in Conley (1998).

Still Pond		R-64		Alkaline	Digestion time (h)	References
$bSiO_2$	std	$bSiO_2$	std			
2.00	0.05	5.50	0.10	0.1 M Na_2CO_3[a]	5	This study
2.74	–	7.23	–	0.5 M NaOH[a]	1	This study
1.84	–	7.80	–	0.5 M NaOH[a]	0.5	Barão et al. (2015)
2.68	0.06	–	–	2% Na_2CO_3[b]	8	Wu et al. (2015)
3.88	0.19	7.50	0.13	2.0 M Na_2CO_3[b]	8	Liu et al. (2002)
2.82	1.17	6.49	2.09	Na_2CO_3/NaOH	NA	Conley (1998)

[a]no pre-treatment before the wet alkaline digestion; [b]pre-treatment of sediment using HCl (1.0 M) and H_2O_2 (10%) before the alkaline digestion.
Note that sponge spicules were observed in the two sediment samples. NA represents not available.

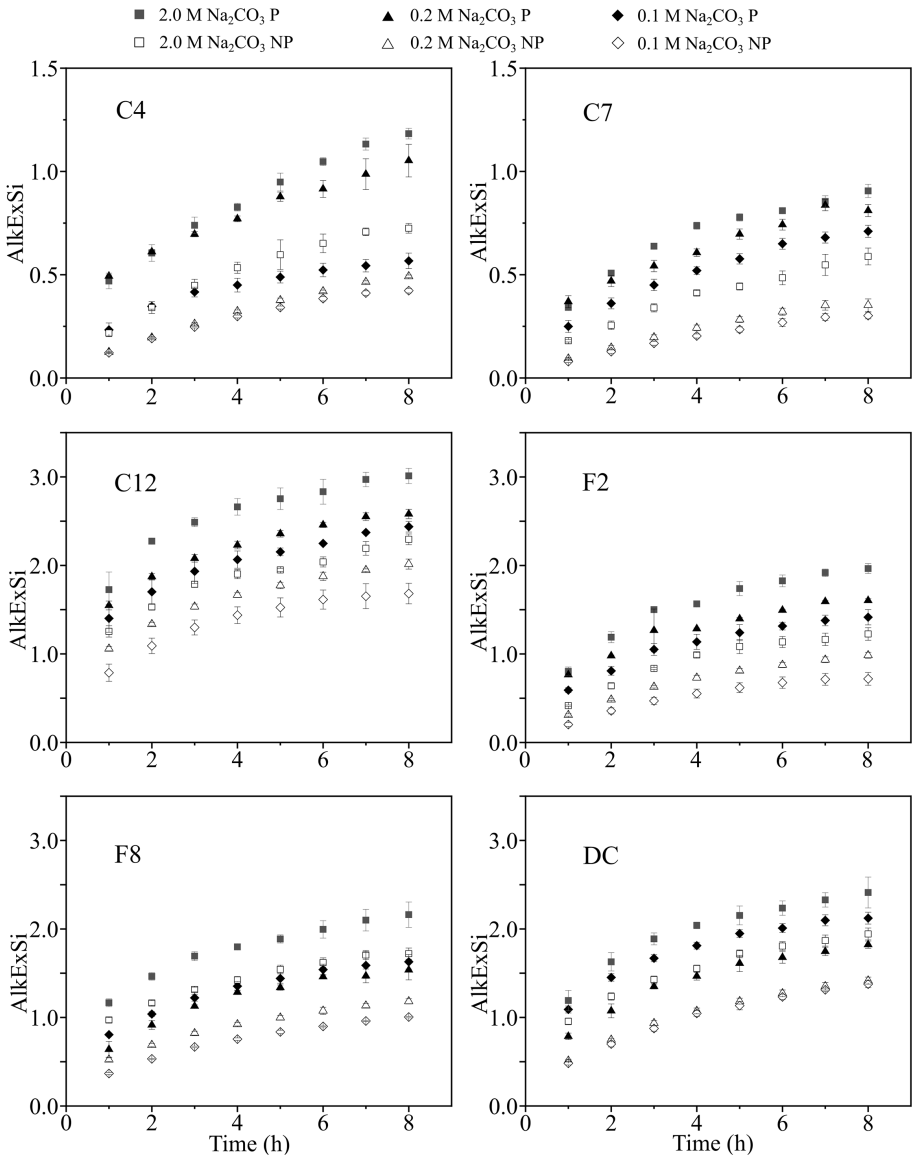

FIGURE 3
Conventional wet alkaline digestion using Na_2CO_3 (0.1 M, 0.2 M and 2.0 M; P vs. NP) solution. A subsample was removed at each 1 h with a total extraction of 8 h. The alkaline extracted silica content (SiO_2%) was normalized into the dry weight of the sediment. P represents pretreatment of sediment using HCl (1.0 M) and H_2O_2 (10%) before digestion; NP represents no pretreatment before alkaline digestion. The error bars were averaged from triplicate digestions. The locations of samples C4, C7, C12, F2, F8, and DC are shown in Figure 1.

M Na_2CO_3, NP; 0.2 M Na_2CO_3, P > 0.2 M Na_2CO_3, NP; 2.0 M Na_2CO_3, P > 2.0 M Na_2CO_3, NP; Figure 4). As shown in Figure S4 and Figure S5, most of the SiO_2 was leached from sediments during the first 4 h ($AlkExSi_{(1-4)}$) and less SiO_2 was extracted during the 5 h to 8 h digestion ($AlkExSi_{(5-8)}$). The quantity of $AlkExSi_{(1-4)}$ and $AlkExSi_{(5-8)}$ correspond to 66% – 86% and 14% – 34% of total amount of silica (TAlkExSi; TAlkExSi = $AlkExSi_{(1-4)}$ + $AlkExSi_{(5-8)}$) extracted during the 8 h alkaline digestion (Figure S5). In addition, the $AlkExSi_{(1-4)}$ leached from the pre-treated sediment was higher than from the non-pretreated sediment (Figures S4, S5), and the amount of the $AlkExSi_{(5-8)}$ was low (< 0.2%SiO_2) and showed small variations when digested under different alkaline solutions (0.1 M, 0.2 M and 2.0 M Na_2CO_3, P vs. NP). Moreover, more silica ($AlkExSi_{(1-4)}$ and $AlkExSi_{(5-8)}$) can be leached in stronger alkaline, but the proportion of $AlkExSi_{(1-4)}$ and $AlkExSi_{(5-8)}$ to TAlkExSi does not change much (Figure S5).

Table 3 and Figure S6 showed the $bSiO_2$% calculated from the 8 h digestion experiment. Through ART ANOVA analysis, a significant difference between different alkaline digestions was identified (Table S1). ART ANOVA analysis showed the increase of $bSiO_2$% between 0.1 M Na_2CO_3 (P vs. NP), 0.2 M

TABLE 3 The $bSiO_2$% was determined using 0.1 M, 0.2 M and 2.0 M Na_2CO_3 (P vs. NP).

Station	0.1 M Na_2CO_3				0.2 M Na_2CO_3				2.0 M Na_2CO_3				2.0 M Na_2CO_3 MF 1989	
	NP		P		NP		P		NP		P		P	
	$bSiO_2$	std	$bSiO_2$	std	$bSiO_2$	std	$bSiO_2$	std	$bSiO_2$	std	$bSiO_2$	std	$bSiO_2$	std
C4	0.27	0.02	0.39	0.03	0.21	0.01	0.51	0.18	0.44	0.13	0.65	0.09	0.95	0.04
C7	0.17	0.03	0.47	0.03	0.14	0.05	0.56	0.02	0.18	0.03	0.52	0.10	0.78	0.02
C12	1.41	0.09	1.40	0.16	1.46	0.03	2.10	0.07	1.28	0.22	2.31	0.34	2.75	0.12
F2	0.55	0.04	0.72	0.13	0.55	0.03	1.18	0.07	0.86	0.05	1.42	0.23	1.74	0.08
F8	0.41	0.01	0.79	0.08	0.76	0.10	1.33	0.03	1.22	0.27	1.50	0.10	1.89	0.05
DC	0.80	0.04	1.35	0.07	0.84	0.04	1.39	0.07	1.24	0.34	1.71	0.29	2.15	0.11
Ave.	0.56	0.42	0.90	0.49	0.66	0.45	1.17	0.56	0.84	0.46	1.35	0.67	1.72	0.71

The standard deviations were based on triplicate digestion. Detailed information on the digestion conditions (S/L, temperature, concentration of alkaline solution) and pretreatment process was described in section 3 (i.e., Materials and methods). The averaged $bSiO_2$% of C4 (0.49 ± 0.25%), C7 (0.40 ± 0.23%), C12 (1.82 ± 0.56%), F2 (1.00 ± 0.44%), F8 (1.13 ± 0.49%), DC (1.34 ± 0.57%) determined using different concentrations of alkaline solution (0.1 M, 0.2 M, 2.0 M Na_2CO_3, P vs. NP), showed a large variation of standard deviation (30 – 60%), which was also reported previously in Conley (1998). ART ANOVA analysis showed a significant difference ($p < 0.0001$) of the $bSiO_2$% determined using different concentrations of Na_2CO_3 (P and NP). MF 1989 represents the $bSiO_2$% determined following the method described by Mortlock and Froelich (1989), this method (no mineral correction) is presented for comparison with the 2.0 M Na_2CO_3 digestion that applied a mineral correction.

Na_2CO_3 (P vs. NP) and 2.0 M Na_2CO_3 (P vs. NP) were significant ($p< 0.0001$); Noymer (2008) (Table S1). The yield, expressed as $bSiO_2$%, between the P and the NP alkaline digestions are: 0.1 M Na_2CO_3 (P) = 194% 0.1 M Na_2CO_3 (NP), 0.2 M Na_2CO_3 (P) = 226% 0.2 M Na_2CO_3 (NP) and 2.0 M Na_2CO_3 (P) = 185% 2.0 M Na_2CO_3 (NP) in average (calculated from Table 3). Besides the pre-treatment process, a higher concentration of Na_2CO_3 can extract more silica significantly ($p< 0.0001$) than a lower concentration of Na_2CO_3 (C7, F2, F8 and DC; Figure S6), except for the $bSiO_2$% determined using a 0.2 M Na_2CO_3 (P) and the 2.0 M Na_2CO_3 (P) digestion ($p = 0.0726$). For the non-pretreated (NP) digestion experiment, the average $bSiO_2$% extracted using 2.0 M Na_2CO_3 solution is 49% and 69% higher than the 0.2 M Na_2CO_3 and 0.1 M Na_2CO_3 digestion, respectively. However, the $bSiO_2$% of samples C7 and C12 was approximately the same when the sample was digested using different concentrations of Na_2CO_3 (0.1, 0.2, 2.0 M), and the $bSiO_2$% of samples C4, F2, F8, and DC was higher when using a higher concentration of Na_2CO_3 solution (Figure S6). Compared to the alkaline concentration, the pretreatment process has a more important influence on bSi determination. The $bSiO_2$% determined following the single-step alkaline digestion method proposed for abyssal deposits (Mortlock and Froelich, 1989) generated much higher $bSiO_2$% values ($p< 0.0001$) than all other digestions. Moreover, the $bSiO_2$% determined using 0.1 M Na_2CO_3 (NP; DeMaster, 1981) was not significantly different ($p = 0.0726$) compared to the $bSiO_2$% determined using 0.5 M NaOH (NP; Koning et al., 2002) (Table S1). The $bSiO_2$% determined by 2.0 M Na_2CO_3 (P) is about 2.6 times of the $bSiO_2$% determined by 0.1 M Na_2CO_3 (NP). The average $bSiO_2$% of samples C4, C7, C12, F2, F8 and DC determined using different methods (0.1 M, 0.2 M, 2.0 M Na_2CO_3, P vs. NP; Table 3) were 0.49 ± 0.25%, 0.40 ± 0.23%, 1.82 ± 0.56%, 1.00 ± 0.44%, 1.13 ± 0.49% and 1.34 ± 0.57% respectively, showed a large variation (31 – 57%) of the standard deviation. The proportion of standard deviation to the averaged $bSiO_2$% was large for low $bSiO_2$% samples (C4: 51%, C7: 57%) than other samples. After the alkaline digestions, microscopic observations (10X; Zeiss Axio Observer A1) showed complete digestion of diatoms and radiolarians, whereas sponge spicules remain present.

3.2.3 Separation of bSi from lSi using dissolution rates

A 20 h-alkaline digestion (Figure S7) was performed for separating different bSi (diatom, radiolarian and sponge) from lSi using the Si dissolution rate (Conley and Schelske, 2001). Microscopic observations of the sediment residual indicated that diatoms and radiolarian skeletons were digested completely while sponge spicules were not fully extracted. The time-dependent methods (e.g., 5 h, DeMaster (1981); 8 h, Liu et al. (2002); 20 h, Conley and Schelske (2001)) all showed variations which emphasize that the fixed duration approach (Mortlock and Froelich, 1989) is insufficient in the study area. The time-dependent methods yield different $bSiO_2$% estimates, that accord with the duration of digestion, i.e., the 5 h digestion with the shortest time showed the least $bSiO_2$% (0.22 ± 0.18%), the moderate duration (8 h) of the attack gave an intermediate $bSiO_2$% (0.40 ± 0.29%), and the longest duration of digestion produce the highest $bSiO_2$% (0.52 ± 0.34%) (Table 4). The ART

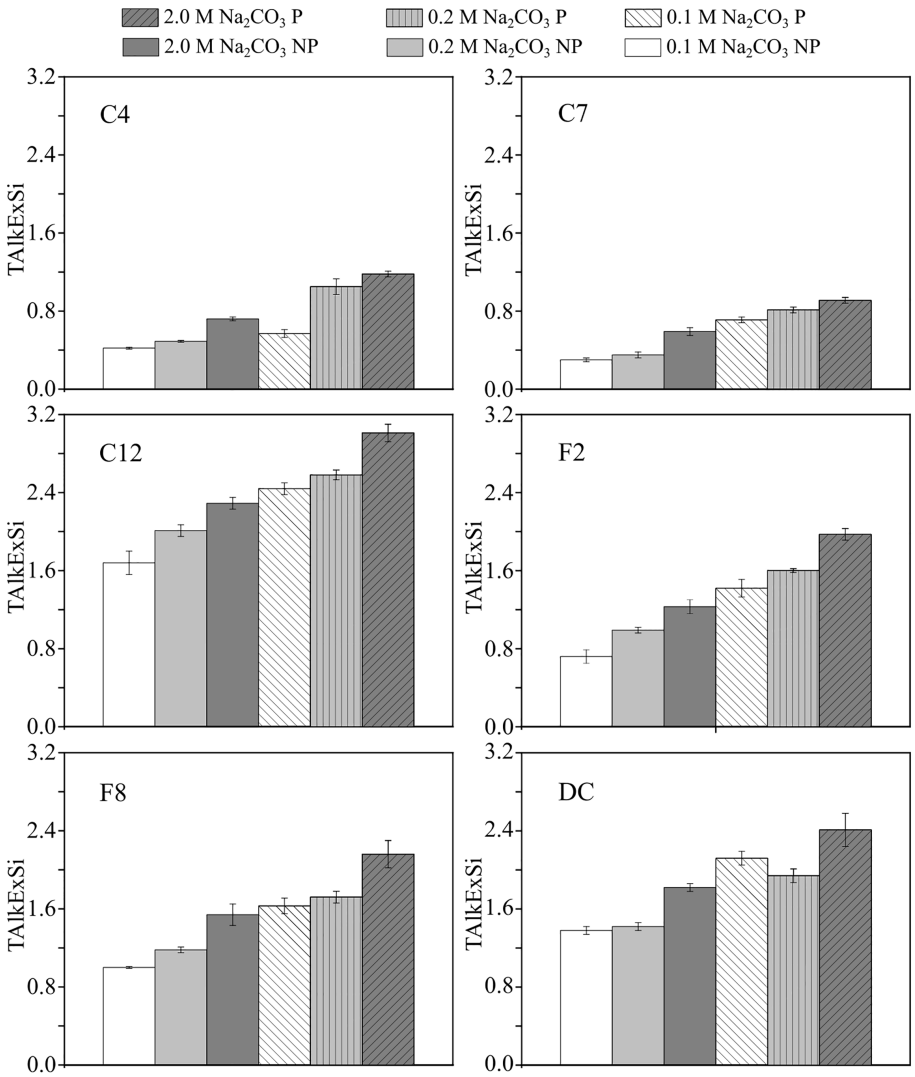

FIGURE 4
The total alkaline extracted silica content (TAlkExSi) of sample C4, C7, C12, F2, F8, DC using 0.1 M, 0.2 M, 2.0 M Na_2CO_3 solution (P vs. NP). The results presented are the SiO_2% extracted after 8 h. More SiO_2% was extracted in a high concentration of the alkaline solution and after the pre-treatment process.

ANOVA analysis indicated a significant ($p < 0.0001$) difference in the $bSiO_2$% among the three different time intervals.

According to the method described in Conley and Schelske (2001), the diatom $bSiO_2$%, radiolarian and sponge $bSiO_2$% were calculated at a 5 h and 20 h digestion interval, respectively (Table 4, Figure S8). The diatom $bSiO_2$%, radiolarian and sponge $bSiO_2$% and total $bSiO_2$% in sediment used in this study averaged 0.25 ± 0.22% (0.003 – 0.97%), 0.27 ± 0.15% (0.03 – 0.52%) and 0.52 ± 0.34% (0.04 – 1.49%), respectively (Table 4). The amount of diatom $bSiO_2$% is approximately equal to the amount of radiolarian and sponge $bSiO_2$% (Figure S8). ART ANOVA analysis showed a significant difference ($p < 0.0001$) between diatom $bSiO_2$%, radiolarian and sponge $bSiO_2$% and the total $bSiO_2$%. Detailed calculations of the averaged $bSiO_2$% of the BH, YS and ECS were also presented (Table 4).

3.2.4 Separation of bSi form lSi using Si/Al ratios

The Si/Al method is proposed based on the assumption that Si is extracted continuously from bSi and lSi whereas the Al is extracted mainly from lSi (Koning et al., 1997; Kamatani and Oku, 2000; Koning et al., 2002), therefore the quantity of bSi and lSi can be corrected using the Si:Al ratio (Kamatani and Oku, 2000). The purpose of determining the $bSiO_2$% using the Si/Al method is to fully digest bSi and correct the lSi properly. It should be noted that after 1 h digestion using 0.5 M NaOH,

10.3389/fmars.2022.1058730

TABLE 4 The $bSiO_2$% in sediments of the East China seas (BH, YS, ECS) was determined using the Si/time alkaline digestion method (0.1 M Na_2CO_3; NP).

Region	Methods	DeMaster (1981)		Conley and Schelske (2001)						Liu et al. (2002)	
		Total $bSiO_2$		Diatom $bSiO_2$		Sponge $bSiO_2$		Total $bSiO_2$		Total $bSiO_2$	
	digestion time (h)	5		5		20		20		8	
	Station	$bSiO_2$	std	$bSiO_2$	std	$bSiO_2$	std	$bSiO_2$	std	$bSiO_2$	std
Bohai Sea (n=5)	B01	0.22	0.02	0.25	0.02	0.27	0.01	0.52	0.01	0.43	0.01
	B10	0.24	0.02	0.27	0.03	0.27	0.01	0.54	0.03	0.43	0.04
	B19	0.25	0.005	0.28	0.02	0.26	0.02	0.54	0.03	0.42	0.02
	B23	0.37	0.01	0.42	0.01	0.39	0.01	0.80	0.03	0.67	0.03
	B18	0.13	0.02	0.15	0.003	0.11	0.01	0.26	0.01	0.21	0.03
	Ave.	**0.24**	**0.08**	**0.27**	**0.09**	**0.26**	**0.09**	**0.53**	**0.18**	**0.43**	**0.15**
Yellow Sea (n=7)	B43	0.51	0.03	0.60	0.02	0.37	0.02	0.97	0.03	0.79	0.07
	H20	0.13	0.03	0.15	0.00	0.25	0.03	0.40	0.03	0.28	0.03
	B09	0.11	0.04	0.11	0.01	0.05	0.04	0.15	0.01	0.12	0.04
	B02	0.29	0.01	0.34	0.02	0.38	0.01	0.72	0.03	0.57	0.03
	H06	0.20	0.05	0.21	0.08	0.50	0.01	0.71	0.07	0.47	0.07
	H32	0.19	0.02	0.22	0.02	0.30	0.01	0.51	0.03	0.33	0.02
	C07	0.19	0.01	0.23	0.01	0.34	0.02	0.57	0.01	0.40	0.02
	Ave.	**0.23**	**0.13**	**0.26**	**0.16**	**0.31**	**0.14**	**0.58**	**0.25**	**0.41**	**0.11**
East China Sea (n=12)	A09	0.09	0.01	0.09	0.01	0.16	0.002	0.26	0.01	0.13	0.01
	F10	0.13	0.05	0.17	0.02	0.39	0.02	0.57	0.04	0.34	0.02
	E6	0.02	0.01	0.003	0.01	0.03	0.01	0.04	0.01	0.01	0.02
	D1	0.20	0.02	0.27	0.02	0.41	0.01	0.68	0.01	0.41	0.01
	D12	0.51	0.03	0.59	0.03	0.48	0.02	1.07	0.03	0.73	0.05
	A3	0.12	0.01	0.13	0.01	0.17	0.01	0.29	0.02	0.24	0.02
	C4	0.09	0.01	0.11	0.01	0.20	0.01	0.31	0.01	0.27	0.02
	C7	0.06	0.01	0.07	0.01	0.11	0.01	0.18	0.01	0.17	0.03
	C12	0.83	0.07	0.97	0.06	0.52	0.03	1.49	0.09	1.41	0.09
	B8	0.04	0.01	0.05	0.01	0.11	0.00	0.16	0.01	0.14	0.01
	F2	0.20	0.03	0.25	0.03	0.33	0.02	0.58	0.05	0.55	0.04
	F5	0.06	0.02	0.06	0.02	0.06	0.01	0.12	0.02	0.13	0.04
	Ave.	**0.19**	**0.23**	**0.23**	**0.27**	**0.25**	**0.17**	**0.48**	**0.42**	**0.38**	**0.37**
East China seas (n=24)	**Ave.**	**0.22**	**0.18**	**0.25**	**0.22**	**0.27**	**0.15**	**0.52**	**0.34**	**0.40**	**0.29**
Interlaboratory comparison sample	Still Pond	1.31	0.09	1.55	0.10	0.43	0.13	1.98	0.10	2.00	0.05
	R-64	4.06	0.07	4.30	0.03	1.57	0.43	5.87	0.44	5.50	0.10

The locations of the samples are shown in Figure 1. The different types of bSi determined (diatom, sponge and total $bSiO_2$) are specified according to the digestion time or method used. The "n" represents the total amount of samples used for bSi determination. ART ANOVA analysis showed a significant difference ($p< 0.0001$) between the $bSiO_2$% calculated at 5 h intervals [DeMaster, 1981; Diatom $bSiO_2$, Conley and Schelske (2001)], 8 h intervals (Liu et al., 2002) and 20 h intervals (Conley and Schelske, 2001).
The bold values represent the average $bSiO_2$% (Ave.) and the standard deviation (Std) of the $bSiO_2$% at each region.

diatoms were not observed whereas a few radiolarian skeletons and some sponge spicules were observed within the residual sediment of ECS samples (Figure S9). Therefore, the Si/Al alkaline digestion method determines mostly diatom bSi and radiolarian bSi and partly sponge bSi, instead of the total $bSiO_2$%.

The measured dSi and dAl results and the best fit models were shown in Figure S3. After the likelihood statistic (Eq. 4) analysis, we found most samples (27/30 samples including sample Still Pond and R-64) were fitted better with 2 components (Model 2) than 1 component (Model 1), and the time evolution of release rates and Si:Al ratios were never sufficient to justify higher component models (Models 3 or 4). Generally, Si and Al were released non-linearly during the first 20 minutes and followed by a linear dissolution, and the AlkExSi was always higher than the AlkExAl (Figure S3). The bulk Si:Al ratios (2< Si:Al< 20) were high at the beginning of digestion and decreased to a relatively constant value (2< Si:Al< 5 for most samples, except D12 and C12) after 30 min (Figure 5), showing a rapid bSi dissolution during the< 30 min and complete extraction of bSi after > 50 min. The TAlkExSi ranged from 0.65 mg-Si g^{-1} to 24.0 mg-Si g^{-1}, whereas the total alkaline extracted Al content (TAlkExAl) ranged from 0.14 mg-Si g^{-1} to 6.0 mg-Si g^{-1}, with a relative constant β_{lin} (2.71 ± 0.63, Table 5).

The reactivity constant (k) of the first non-linear fraction (average k_1 = 1.96 min^{-1}) was greater than the second fraction (average k_2 = 0.084 min^{-1}) (Figure 6), and the β_1 is higher than the β_2 (except for D1, Table 5). Figure 6 showed a wide range of Si:Al ratios for β_1 ($2<\beta_1< 25$) and k_1 ($0.5< k_1< 5$), and small ranges of β_2 ($2<\beta_2< 8$) and k_1 ($0< k_2< 0.2$). In addition, β_2 has similar Si:Al ratios compare to β_{lin}, and β_1 is always higher than the β_{lin} (Figure 6). The $ExtrSi_1$, $ExtrSi_2$ and the linear lSi fraction account for 19.3 ± 9.9%, 27.4 ± 12.6% and 53.3 ± 10.1% of the TAlkExSi, respectively (Table S2). Based on Si:Al ratio (β_i) and the reactivity (k_i), the calculated $bSiO_2$% (dry weight) and $lSiO_2$% (linear lSi fraction + non-linear lSi fraction) in sediments of East China seas were 1.82 ± 2.28 mg-Si g^{-1} (0.39 ± 0.49%$bSiO_2$) and 5.95 ± 4.69 mg-Si g^{-1} (1.28 ± 1.00% $bSiO_2$), respectively (calculated from Table 5). However, the definition of bSi ($\beta_i > 5$ or $\beta_{lin}< \beta_i< 5$ & $k > 0.1$ min^{-1}) and lSi ($1< Si/Al< 4$) (Koning et al., 2002; Barão et al., 2015) based on Si/Al ratios and reactivity may limit our understanding of the different Si fractions. Our results showed that sometimes $\beta_2< \beta_{lin}$ (B01, H32, A3, E6, F2; Table 5), suggest that the $ExtrSi_2$ is lSi origin. However, whether this fraction is authigenic silicate is not clear, because the Si:Al ratio of authigenic silicates (< 2, Mackin (1989); Michalopoulos and Aller (1995)) and clay mineral (1- 4, Koning et al. (2002)) are both below 5. Barão et al. (2015) found the non-

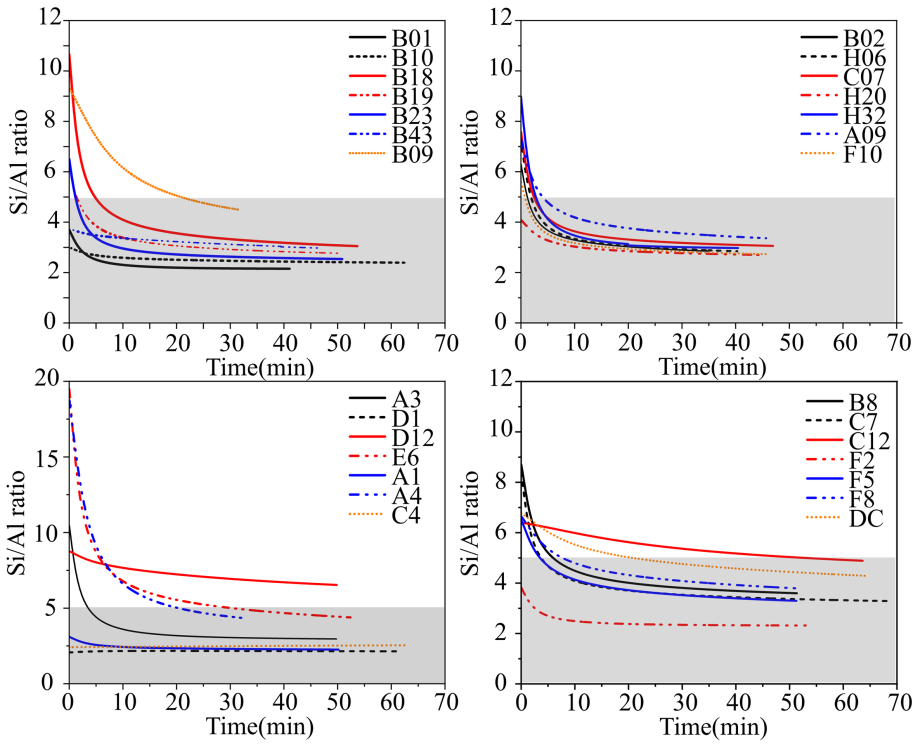

FIGURE 5
The Si:Al ratio during alkaline digestion. Sediments were digested following the method described in Koning et al. (2002) and Barão et al. (2015). The grey area represents the Si:Al below 5, indicating the extraction of lSi.

10.3389/fmars.2022.1058730

TABLE 5 Parameters from the Si and Al continuous dissolution (Si/Al method) with 0.5 M NaOH (1 h digestion).

Station	Optimum model	$ExtrSi_1$ (mg-Si g^{-1})	$ExtrSi_2$ (mg-Si g^{-1})	TAlkExSi (mg-Si g^{-1})	TAlkExAl (mg-Si g^{-1})	k_1 (min^{-1})	k_2 (min^{-1})	β_1	β_2	b (mg-Si g^{-1} min^{-1})	β_{lin}	$bSiO_2$%
B01	Model 2	0.82	2.34	6.13	2.89	1.90	0.08	4.40	1.83	0.07	2.13	0.18
B10	Model 2	1.26	3.73	12.25	5.14	1.45	0.07	3.16	2.53	0.12	1.95	0.27
B19	Model 2	0.96	1.97	6.16	2.24	1.63	0.08	7.14	2.81	0.07	2.32	0.21
B23	Model 2	1.64	4.91	14.88	5.79	1.66	0.08	10.44	2.36	0.16	2.30	0.35
B18	Model 2	0.58	0.83	3.22	1.01	3.10	0.09	12.83	3.08	0.03	2.45	0.12
B43	Model 2	1.49	6.01	15.29	5.18	1.52	0.08	3.86	3.86	0.16	2.45	0.32
H20	Model 2	0.73	1.56	4.21	1.56	1.84	0.06	4.36	2.64	0.04	2.40	0.16
B09	Model 1	0.66	NA	1.58	0.36	0.69	NA	10.71	NA	0.03	3.23	0.14
B02	Model 2	1.40	3.80	10.83	3.77	2.46	0.10	7.83	3.06	0.17	2.38	1.11
H06	Model 2	1.46	4.50	12.21	4.26	1.64	0.08	11.89	2.81	0.16	2.45	0.31
H32	Model 2	1.10	1.69	5.83	1.94	2.23	0.09	12.15	2.13	0.07	2.82	0.24
C07	Model 2	1.04	2.48	7.00	2.29	2.79	0.08	9.01	2.88	0.08	2.65	0.22
A09	Model 2	0.46	0.68	2.19	0.65	2.46	0.09	8.05	3.44	0.02	2.66	0.10
F10	Model 2	0.88	1.74	7.50	2.72	2.17	0.11	6.75	2.81	0.11	2.45	0.56
A3	Model 2	0.66	0.64	2.92	1.02	2.50	0.10	13.83	1.83	0.03	2.74	0.28
D1	Model 2	0.89	4.08	10.59	4.95	0.99	0.07	2.00	2.29	0.09	2.07	0.19
D12	Model 2	2.47	2.63	23.31	3.73	1.89	0.12	8.94	7.84	0.08	5.07	1.09
DC	Model 2	4.99	5.88	17.82	3.72	1.32	0.05	7.91	5.44	0.15	3.60	2.33
E6	Model2	0.40	0.16	0.97	0.24	3.32	0.13	22.44	2.72	0.01	2.82	0.12
B8	Model 2	0.39	0.39	2.02	0.56	3.57	0.10	9.47	3.22	0.02	3.12	0.17
C4	Model 1	1.14	NA	2.97	1.20	0.06	NA	2.31	NA	0.03	2.71	0.24
C7	Model 2	0.25	0.39	2.25	0.68	4.50	0.09	9.21	3.35	0.02	2.98	0.05
C12	Model 2	5.29	5.67	17.10	3.54	1.17	0.06	7.86	4.79	0.10	3.80	1.13
F2	Model 2	0.90	3.52	9.15	3.93	1.52	0.07	4.80	2.09	0.09	2.27	0.19
F5	Model 2	0.39	0.44	1.68	0.51	2.56	0.08	6.92	3.26	0.02	2.69	0.08
F8	Model 2	2.50	4.62	10.69	2.77	1.06	0.05	7.35	4.15	0.08	2.70	0.54
A1	Model 2	0.81	2.72	6.35	2.84	1.46	0.08	3.44	2.22	0.06	2.09	0.17
A4	Model 1	0.21	NA	0.65	0.14	1.34	NA	25.02	NA	0.01	3.14	0.05
SP-1	Model 2	6.53	6.45	18.73	4.42	1.49	0.13	9.96	4.50	0.10	2.47	2.78
SP-2	Model 2	7.44	5.18	17.11	4.81	0.50	0.05	5.88	5.18	0.09	1.79	2.70
R-64-1	Model 2	19.20	15.32	46.09	7.97	0.64	0.15	20.39	6.37	0.19	2.49	7.40
R-64-2	Model 2	15.16	17.76	43.65	11.26	1.26	0.18	22.06	11.00	0.18	2.96	7.05

$ExtrSi_i$ (mg-Si g^{-1}) is the concentration of each Si fraction dissolving nonlinearly, k_i (min^{-1}) is their respective reactivity and Si: Al_i ratio. Parameter b refers to the slope of the fraction dissolving linearly. SP-1, SP-2 and R-64-1, R-64-2 represent duplicate digestions of sample Still Pond and R-64. TAlkExSi and TAlkExAl represent the total alkaline extracted Si and Al. The $bSiO_2$% presented here is the bSi content in dry weight. NA represents data that is not available.

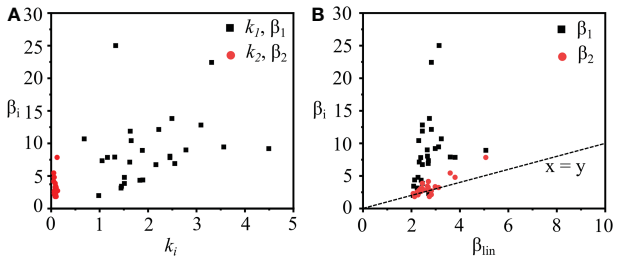

FIGURE 6
The plots show parameters (β_i, β_{lin}, k_i) from the modeling results. **(A)** shows the relationship between the Si:Al ratio (β_i) and the reactivity (k_i) of the nonlinear dissolution Si fractions, the reactivity of the first nonlinear fraction (k_1) is higher than the second nonlinear fraction (k_2). The range of β_1 ($1 < \beta_1 < 25$) is bigger than β_2 ($2 < \beta_2 < 10$). **(B)** shows the relationship of the Si:Al ratio between the two non-linear dissolving fractions (β_1, β_2) and lSi (β_{lin}). β_1 is bigger than β_2 and β_{lin} and β_2 is approximately equal to β_{lin}.

linear Si fractions (*ExtrSi*$_1$, *ExtrSi*$_2$) obtained using the Si/Al alkaline digestion method is higher than the $bSiO_2$% examined using the Si/time method (0.1 M Na_2CO_3). However, the *ExtrSi*$_1$ is approximately equal to diatom $bSiO_2$% (Barão et al., 2015). Implies the reactive non-linear fraction originates from the diatom bSi and the less reactive non-linear fraction originates from less soluble Si fractions (implicating resistant bSi, such as radiolarians, sponge spicules and/or altered diatoms, or lSi). So far, we cannot differentiate the less soluble Si fractions. A future study looking at the alkaline digestion of diatoms, radiolarian skeletons, sponge spicules and synthesized sediment using both Si/Al method and Si/time method would improve our understanding of the definition of different Si fractions.

3.3 SEM and SEM-EDS analysis

The existence of a clay mineral "coating" on the surface of the siliceous organism was observed by SEM (Figure 7, Figure S10) in samples before alkaline digestion. Generally, the diatoms and radiolarian tests were coated with more clay minerals than the siliceous sponge spicules. Diatom frustules in sample A1 were pre-treated using HCl (1.0 M) and H_2O_2 (10%), showing the partial removal of the coated clay minerals after the pre-treatment process. Additionally, Si, Al, K, Mg, Ca, Fe, Ti, S and As were detected from the diatom tests in sample A1 (Figure S10), indicating incomplete removal of clay materials (authigenic and/or allogenic clays) after pre-treatment. Besides Si and O, the major metal elements from reaction products of the reverse weathering process, such as Al, Mg, K and Fe (Michalopoulos and Aller, 2004), were commonly detected through EDS-SEM analysis (Figure S10).

In addition, diatoms and radiolarian tests were not observed in sediment residuals after the alkaline digestions (0.1 M, 0.2 M, 2.0 M Na_2CO_3, 8 h digestion, P vs. NP; 0.5 M NaOH, 1 h digestion, NP), whereas sponge spicules were found in the sediment residuals (post-digestion), especially in sediment from the outer shelf and slope of ECS. The digestion and destruction of the sponge spicule structures by the alkaline solution are visible from the SEM image (Figure 8). Different types of sponge spicules (i.e., *strongyle, acanthostyle, tignule*) were observed and picked from sediment residuals of sample C12, which was previously extracted in a 2.0 M Na_2CO_3 (P, 85° C) solution for 8 h. Nevertheless, the degree of destruction of the different shapes/types of sponge spicules by alkaline solution is variable. For example, the *strongyle* sponge spicules (Figures 8G–I) are more heavily digested than the *acanthostyle* sponge spicules (Figures 8A–C) and the *tignule* sponge spicules (Figures 8D–F).

4 Discussion

This study determined the $bSiO_2$% in sediment from the CCMZs of the East China seas using both the Si/time and the Si/Al methods and estimated the abundance of different types of bSi in sediment. The results show that the commonly used pretreatment step and different alkaline digestion methods inherently bias the accurate determination of $bSiO_2$%. For example, this study found that strong alkaline digestion can overestimate bSi content and does not completely digest sponge bSi, in agreement with Maldonado et al. (2019), which are important factors to consider when evaluating total bSi fluxes in the marine environment. These technical biases are important to understand since pretreatment procedures (e.g., HCl and H_2O_2) can overestimate the burial flux of bSi in CCMZs. To emphasize the influence of these methodological differences, we present a revised bSi burial flux for the East China seas. The causes of the methodological biases are discussed below (section 5.1) and the importance of resistant bSi in the East China seas is presented (section 5.2). Finally, a general procedure (section 5.3) is proposed to ensure that determination of bSi burial flux is supported by an accurate quantification of $bSiO_2$% in coastal sediments.

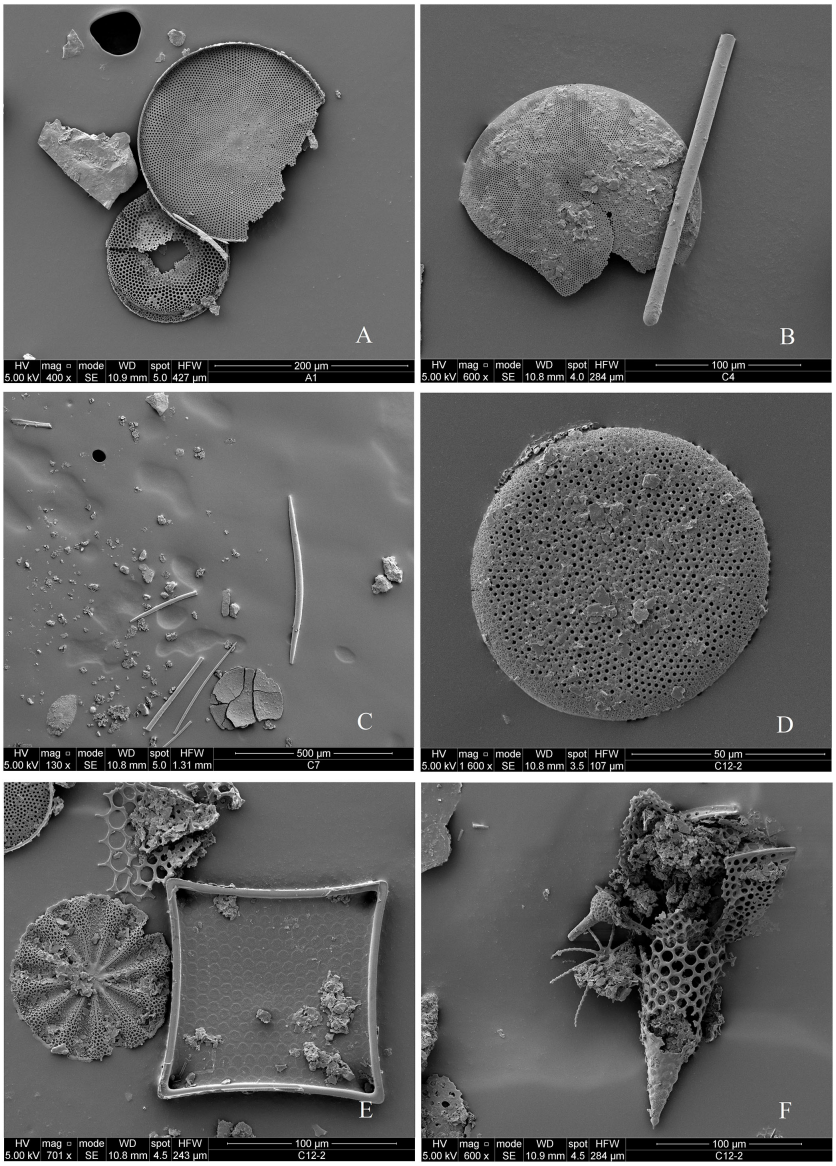

FIGURE 7
SEM images show different siliceous organisms found in sediment samples (A1, C4, C7, and C12) before alkaline digestion. **(A)** diatom frustule in sample A1, **(B)** diatom frustule and sponge spicule in sample C4, **(C)** diatom frustule and sponge spicule in sample C7, **(D-F)** diatom frustules and radiolarian skeletons in sample C12. Sample A1 was pretreated using HCl (1.0 M) and H_2O_2 (10%) for 1 h, sample C4, C7, and C12 were not pretreated.

4.1 Re-evaluated burial flux of bSi in the CCMZs of East China seas

Considering the complex bSi types (diatoms, radiolarians and sponge spicules) (Table 1) and high AlkExSi from lSi from East China seas sediments (Table 5), an accurate determination of the bSi content is challenging due to the technical problems highlighted by Maldonado et al. (2019) and Koning et al. (2002) for coastal sediments. In this study, we assessed the Si/time and Si/Al methods in order to define the optimal method for the determination of the bSi content. This information is necessary to accurately evaluate bSi burial in the CCMZs of East China seas.

This study found two major limitations for the Si/time method: 1) insufficient correction of the lSi phase and 2) inadequate digestion of the resistant bSi (mainly sponge spicules). Applying a weak alkaline digestion completely digests the diatoms but cannot fully digest sponge spicules (Figure 8), whereas a strong alkaline digestion extracts more lSi from the sediment and resulting in an overestimation of the bSi content. In addition, the AlkExSi concentration continues to increase during an alkaline extraction (Figure 3, Figure S7,

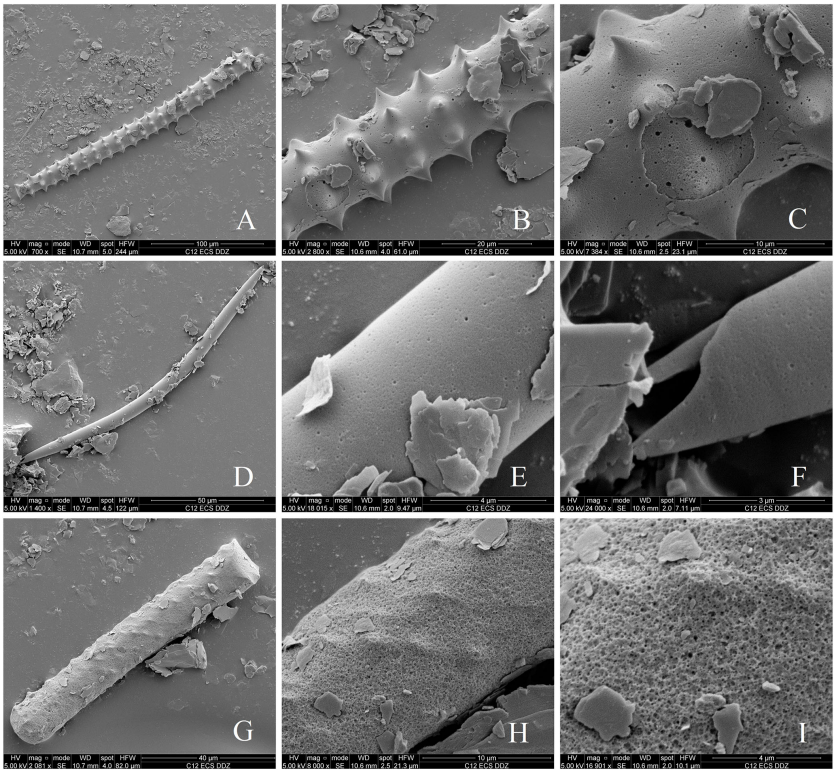

FIGURE 8
SEM images of three types of siliceous sponge spicule structures observed in the residual sediment of sample C12 after 8 h digestion using 2.0 M Na_2CO_3 (P). **(A-C)** *acanthostyle* sponge spicule, **(D-F)** *tignule* sponge spicule, **(G-I)**: *strongyle* sponge spicule. **(B, C, E)** and **(F, G, I)** are zoom-in views of images **(A, D, G)**, respectively.

Figure S11) and a flat "plateau" as shown in Figure S2 is never reached, suggesting a continuous dissolution of resistant bSi (e.g., sponge spicules) and lSi. Therefore, a complete digestion of the bSi using the Si/time method cannot be defined for the sediment of East China seas, and the use of a simple tangent line to calculate bSi content (DeMaster, 1981) is insufficient.

Furthermore, authigenic silicates precipitate on the structure of bSi (Figure 7, Figure S10) can decrease the reactive surface area of bSi and decrease its solubility (Williams et al., 1985; Varkouhi and Wells, 2020). Applying an acid and peroxide pretreatment procedure can remove the authigenic silicates and enhance the reactivity of bSi (Mortlock and Froelich, 1989; Saad et al., 2020). However, our results showed the $bSiO_2$% increased by more than 100% after the pretreatment (Table 3, Figure S6), a significant ($p < 0.0001$) statistical increase (Table S1), which is not in agreement with our microscopic observations (Table 1, Figure 8). Ohlendorf and Sturm (2008) and Dai et al. (2017) found that using a pretreatment step increased the bSi yield and they suggested that more bSi was being digested after the removal of the mineral coating. We argue that this observed increase bSi yield is mainly due to an enlarged amount of Si extracted from authigenic silicate and clay minerals. This argument is supported by observations made by Michalopoulos and Aller (2004), who concluded that a mild acid pretreatment step (0.1 M HCl) can activate the authigenic silicate in the Amazon delta sediment. They also suggested that the mild acid pre-treatment can activate the neo-formed reverse weathering product (authigenic silicates) without changing the structure of crystallized clay minerals. However, applying a stronger acid (1.0 M HCl) and peroxide (10% H_2O_2) pretreatment can weaken the structure of clay minerals (Komadel and Madejová, 2006; Hu et al., 2022), therefore, enhancing the solubility of the clay mineral. The chemical composition differences between bSi and authigenic silicates suggest that they are two different marine Si pools (Michalopoulos and Aller, 2004; Rahman et al., 2016; Pickering et al., 2020). Applying pre-treatment can cause an overestimation of the bSi pool, therefore, further studies on disentangling the different Si pools are required (DeMaster, 1991; Michalopoulos and Aller, 2004; Frings et al., 2014; Ehlert et al., 2016; Rahman et al., 2016; Pickering et al., 2020; Frings et al., 2021a; Frings et al., 2021b).

Although the Si/time method determines the bSi content based on a simple Si vs. time tangent line, the mineral interference still needs to be corrected. This is typically done with the Si/Al method for CCMZs sediment (Koning et al., 2002;

Barão et al., 2015). However, the quantification of the bSi content by Si/Al method is underestimated since the sponge bSi is not completely digested (Figure S9). Previous studies concluded that all sponge spicules and most (> 70%) of radiolarians were digested after 1 h continuous alkaline digestion using 0.5 M NaOH (Müller and Schneider, 1993). Maldonado et al. (2019) found that only 10% to 20% of fresh sponge spicules were dissolved after 1.5 h of alkaline digestion using 0.5 M NaOH. The sponge spicules used by Müller and Schneider (1993) were treated in acid solution and 10% H_2O_2 for removing the organic matter and then ground, thus can be digested completely. However, the sponge spicules used by Maldonado et al. (2019) were not crushed, and were therefore harder to be digested completely. Thus, 30 to 90% of the sponge spicules may not be determined by the Si/Al method. Moreover, crushing the sediment or pre-treating the samples would enhance the digestion efficiency of the sponge bSi, but inevitably increase the surface area of lSi and bring out an overestimation of the bSi content. Therefore, pretreatment of sediment should be applied with caution, and we suggest applying a Si/Al method with an extension of extraction time to > 12 h (Maldonado et al., 2019). Unfortunately, this is not currently possible for the Si/Al method proposed by Koning et al. (2002).

The burial flux of bSi ($F_b = C * w$) in the CCMZs of the East China seas was re-evaluated, considering the sediment mass accumulation rate (w) from previously published studies and the concentration of $bSiO_2$ in sediments (C). The variations of the estimated bSi burial flux are dependent on the determination of the bSi content of the study area. The total bSi burial flux of the East China seas thus re-evaluated varied from 132 (± 112) Gmol-SiO_2 yr^{-1}, 249 (± 158) Gmol-SiO_2 yr^{-1} and 329 (± 209) Gmol-SiO_2 yr^{-1} using the $bSiO_2$% determined at 5 h, 8 h and 20 h digestion interval, respectively. And the estimated bSi burial flux is 253 (± 286) Gmol-SiO_2 yr^{-1} based on the Si/Al method (Table 6). Given the presence of high lSi content in the sediment samples of the East China seas, a well-known opal-depleted CCMZs influenced by the terrestrial input delivered from the Yellow River and the Yangtze River, we opted for the Si/Al (1 h digestion in 0.5 M NaOH) method as the optimal method for the determination of the bSi content in the East China seas. Our best estimate of the burial flux of $bSiO_2$ (253 ± 286 Gmol-SiO_2 yr^{-1}) in the East China seas is about one third of the previous studies (924 ± 693 Gmol-SiO_2 yr^{-1}; Wu et al., 2017; Wu and Liu, 2020). This is mainly due to the methodological bias, because the previous studies determined the $bSiO_2$% with a pre-treatment (with HCl and H_2O_2) process (Wu et al., 2017; Wu and Liu, 2020) that overestimate the $bSiO_2$%, subsequently, the bSi burial flux is over-estimated. The Si/Al method can correct the lSi properly, but still digest the sponge spicules insufficiently. Therefore, our estimation of the bSi burial flux is an underestimate.

Notably, the difference in bSi burial flux is also influenced by the sampling technique (sampling at different locations and seasons) and the calculation of sediment mass accumulation rate. We adopted an average mass accumulation rate for the BH, YS and ECS (see section 3.4) and the potential factors (such as riverine sediment input, resuspension of sediment by currents and primary production) that influence the sediment mass accumulation rate were not discussed in this study but are necessary for future works. The substantial decrease in the estimation of Si burial flux in the East China seas raises the question of whether it can have an impact on the global scale and on the balance of the silica cycle in the ocean.

TABLE 6 Burial flux of $bSiO_2$ (Gmol-SiO_2 yr^{-1}) of the BH, the YS, and the ECS.

Methods	Time interval of digestion		BH	YS	ECS	Total burial flux (Gmol-SiO_2 yr^{-1})
Si/time (0.1 M Na_2CO_3)	5 h	$bSiO_2$%	0.24 ± 0.08	0.23 ± 0.13	0.19 ± 0.23	132 ± 112
		burial flux (Gmol-SiO_2 yr^{-1})	15.46 ± 5.15	54.03 ± 30.54	62.76 ± 75.98	
	8 h	$bSiO_2$%	0.43 ± 0.15	0.41 ± 0.11	0.38 ± 0.37	249 ± 158
		burial flux (Gmol-SiO_2 yr^{-1})	27.70 ± 9.66	96.31 ± 25.84	125.53 ± 122.22	
	20 h	$bSiO_2$%	0.53 ± 0.18	0.58 ± 0.25	0.48 ± 0.42	329 ± 209
		burial flux (Gmol-SiO_2 yr^{-1})	34.14 ± 11.60	136.24 ± 58.73	158.56 ± 138.74	
Si/Al (0.5 M NaOH)	1 h	$bSiO_2$%	0.23 ± 0.09	0.36 ± 0.34	0.46 ± 0.60	253 ± 286
		burial flux (Gmol-SiO_2 yr^{-1})	14.82 ± 5.80	84.36 ± 79.67	153.49 ± 200.20	

The total $bSiO_2$ burial flux of the East China seas equals the sum of the burial flux of the BH, YS, and ECS. The Si/time method (0.1 M Na_2CO_3, NP) and the Si/Al method (0.5 M NaOH, NP) was displayed for the determination of $bSiO_2$%. The Si/Al method was defined as an optimum method due to an accurate correction of lSi.

4.2 Contribution of radiolarian and sponge in bSi burial of the East China seas

Our findings emphasize that radiolarian and sponge bSi are important sinks of marine Si for the East China seas, especially the ECS. Microscopic observations indicate the sediment of BH is composed principally of diatoms (Li et al., 2020), YS is composed of diatoms (Wang et al., 2016), and the ECS is composed of diatoms (Chen et al., 2014; Li et al., 2018), radiolarians (Liu et al., 2017; Qu et al., 2020b) and sponge spicules (Table 1). No significant differences were observed in the average abundance of diatoms in the surface sediment of BH, YS and ECS. However, the abundance of sponge spicules is of the same magnitude as diatoms in the sediment of ECS (Table 1), and the abundance of radiolarians is of the same magnitude as diatoms in the outer shelf and slope of ECS (Qu et al., 2020a). Besides the observational data, our alkaline digestion results confirm the quantity of the less soluble bSi fraction (i.e., sponge spicules and radiolarians) is approximately equivalent to diatom $bSiO_2$% (Table 4). Our data showed the abundance of radiolarians and sponge spicules was not as important as diatoms in the BH and YS (Table 1), thus the origin of the less soluble bSi in BH and YS may be partly due to phytolith discharged from rivers. Since phytoliths are less soluble than diatoms (Meunier et al., 2014) and can contribute 14% – 64% of bSi in estuaries and coastal sediment (Ran et al., 2017).

Although little is known about the quantity of radiolarian and sponge bSi in the East China seas (Zhang et al., 2003; Liang et al., 2021), the current results imply that the burial of "dark bSi" (radiolarian skeleton and sponge spicules, as defined by Maldonado et al. (2019)) is possibly as important as diatoms in East China seas. The burial of silicon associated with siliceous sponges was mainly found on continental slopes/margins (Maldonado et al., 2019), as one of the largest CCMZs in the Northwest Pacific, the Si burial through siliceous sponges would be more important than previously expected (Chou et al., 2012; Ran et al., 2017).

4.3 General protocol for the determination of bSi in coastal sediments

Our findings emphasize that besides diatoms, the less soluble types of bSi (i.e., radiolarians and sponge spicules) also act as an important marine Si sink in the CCMZs of the East China seas. However, the accurate determination of the magnitude of these marine Si sinks is complicated by different types of methods to determine the bSi content in sediments. The following is a brief summary of the different wet alkaline methods employed in this study and their technical limitations:

(1) The Si/time alkaline method (0.1 M Na_2CO_3, NP, 5 h digestion) (DeMaster, 1981), which is commonly used to quantitatively determine $bSiO_2$% in the sediment of CCMZs, incompletely digests the skeletal structures of radiolarians and sponge spicules and partly digests lSi, similar to the findings from Maldonado et al. (2019). A 20 h extraction in 0.1 M Na_2CO_3 solution can digest the diatom and radiolarian bSi and ca. 80% of sponge bSi. The determination of the $bSiO_2$% using a 2.0 M Na_2CO_3 solution overestimates the $bSiO_2$% because silica is digested from clay minerals, which biases the accuracy of the method.

(2) The one-hour Si/Al method (0.5 M NaOH, NP) (Koning et al., 2002) underestimate the $bSiO_2$% due to incomplete digestion of radiolarian skeleton and sponge spicules. Therefore, an extension of the digestion time is necessary.

(3) The pre-treatment of sediment using HCl (1.0 M) and H_2O_2 (10%) prior to alkaline digestion can cause an overestimation of the $bSiO_2$% due to the digestion of authigenic silicates and/or clay minerals. Thus, a pre-treatment procedure should be avoided.

To resolve these technical problems, we propose the following general wet alkaline digestion procedure for the appropriate determination of bSi content in the sediments of CCMZs:

(1) Determine the types of bSi in sediment using a microscope.

(2) Selecting an appropriate alkaline solution according to the type of sediments.

- For sediment samples containing mainly diatoms, a 5 h alkaline digestion using 0.1 M Na_2CO_3 solution is capable of extracting bSi.

- For sediment samples containing diatoms, sponge spicules and/or radiolarian skeletons, alkaline digestion > 2 h in 0.5 M – 1.0 M NaOH (Si/Al method) solution is suggested.

(3) Checking the residue sediment (post-digestion) using a microscope to observe if there are no more radiolarian tests and/or sponge spicules.

5 Conclusion

Our results showed that alkaline extractions of CCMZs sediments using 2.0 M Na_2CO_3 solution resulted in an overestimation of the $bSiO_2$% owing to silica being digested

from clay minerals. Applying a 0.1 M Na_2CO_3 digestion (20 h) can minimize the lSi interference on bSi determination, but can cause at least 20% of underestimation of the $bSiO_2$% owing to incomplete digestion of sponge spicules. Our results also show that alkaline extractions that apply a pretreatment procedure overestimate the determined $bSiO_2$% due to the digestion of the authigenic silicate phases and clays and subsequently overestimate the bSi burial flux. Consequently, we propose the general alkaline digestion protocol to accurately determine $bSiO_2$% in marine sediments of CCMZs using the Si/Al method by either applying the continuous analysis method (Koning et al., 2002) or the time-series digestion method (Kamatani and Oku, 2000). Based on these new results and the application of the Si/Al method in order to produce accurate $bSiO_2$% results, we revised the current estimate of bSi burial flux to 253 ± 286 Gmol-SiO_2 yr^{-1}, which is one third of the previously reported (924 ± 693 Gmol-SiO_2 yr^{-1}). Our estimate still underestimates the bSi burial flux of the East China seas, and further work on examining the resistant bSi (i.e., phytolith, radiolarian and sponge spicule) content is still required. We argue that the pre-treatment process (with HCl and H_2O_2) applied in previous estimates is the main reason that bSi burial flux was previously over-estimated. In order to ensure the accurate determination of bSi from different depositional settings in the future, we strongly suggest the development of an international intercalibration exercise.

Data availability statement

The original contributions presented in the study are included in the article/Supplementary Material. Further inquiries can be directed to the corresponding authors.

Author contributions

DZ, JNS, SL, AL, and PT designed this study. DZ conducted the experiments, did the analysis and wrote the first manuscript. DZ, JNS, SL, AL, PT, JS, MG, and YM edited the manuscript. All authors contributed to the article and approved the submitted version.

Funding

This study was funded by the Natural Sciences Foundation of China (NSFC: U1806211, 42176040), the Taishan Scholars Program of Shandong Province, Aoshan Talents Program Supported by the Qingdao National Laboratory for Marine Science and Technology (No. 2015ASTP-OS08), by the French National Research Agency (18-CEO1-0011-01), and the University of Antwerp Bijzonder Onderzoeksfonds (Project ID: 43171). This work was supported by ISblue project, Interdisciplinary graduate school for the blue planet (ANR-17-EURE-0015) and co-funded by a grant from the French government under the program "Investissements d'Avenir" embedded in France 2030.

Acknowledgments

This study represents partial fulfillment of the requirements for the Ph.D. thesis of DDZ at the Ph.D. course of the Ocean University of China (OUC) and the Université de Bretagne Occidentale (UBO). DDZ would like to thank the doctoral mobility grants from the ISblue, UBO and CHIBIDO LAB (LEMAR: Laboratory of Environmental Marine Sciences). DDZ also would like to thank Dr. Eric Struyf, Mrs. Anne Cools, Mrs. Anke De Boeck and Mr. Tom Van der Spiet for their help and assistance during the alkaline digestion experiment at the Department of Biology, University of Antwerp. Thanks to the interlaboratory sediment samples kindly provided by Prof. Daniel Conley (Lund University).

Conflict of interest

The authors declare that the research was conducted in the absence of any commercial or financial relationships that could be construed as a potential conflict of interest.

Publisher's note

Supplementary material

The Supplementary Material for this article can be found online at: https://www.frontiersin.org/articles/10.3389/fmars.2022.1058730/full#supplementary-material

References

Armstrong, R. A., Lee, C., Hedges, J. I., Honjo, S., and Wakeham, S. G. (2002). A new, mechanistic model for organic carbon fluxes in the ocean based on the quantitative association of POC with ballast minerals. *Deep. Res. Part II Top. Stud. Oceanogr.* 49, 219–236. doi: 10.1016/S0967-0645(01)00101-1

Barão, L., Clymans, W., Vandevenne, F., Meire, P., Conley, D. J., and Struyf, E. (2014). Pedogenic and biogenic alkaline-extracted silicon distributions along a temperate land-use gradient. *Eur. J. Soil Sci.* 65, 693–705. doi: 10.1111/ejss.12161

Barão, L., Vandevenne, F., Clymans, W., Frings, P., Ragueneau, O., Meire, P., et al. (2015). Alkaline-extractable silicon from land to ocean: A challenge for biogenic silicon determination. *Limnol. Oceanogr. Methods* 13, 329–344. doi: 10.1002/lom3.10028

Cheize, M., Planquette, H. F., Fitzsimmons, J. N., Pelleter, E., Sherrell, R. M., Lambert, C., et al. (2019). Contribution of resuspended sedimentary particles to dissolved iron and manganese in the ocean: An experimental study. *Chem. Geol.* 511, 389–415. doi: 10.1016/j.chemgeo.2018.10.003

Chen, C., Zhao, G., Chen, M., Lan, D., and Lan, B. (2014). Diatom distribution in surface sediments from Chinese inshore waters and the relationship to modern environmental variables. *Chin. J. Oceanol. Limnol.* 32, 828–844. doi: 10.1007/s00343-014-3194-3

Chou, Y., Lou, J. Y., Chen, C. T. A., and Liu, L. L. (2012). Spatial distribution of sponge spicules in sediments around Taiwan and the sunda shelf. *J. Oceanogr.* 68, 905–912. doi: 10.1007/s10872-012-0143-7

Conley, D. J. (1998). An interlaboratory comparison for the measurement of biogenic silica in sediments. *Mar. Chem.* 63, 39–48. doi: 10.1016/S0304-4203(98)00049-8

Conley, D. J., and Schelske, C. L. (1993). Potential role of sponge spicules in influencing the silicon biogeochemistry of Florida lakes. *Can. J. Fish. Aquat. Sci.* 50, 296–302. doi: 10.1139/f93-034

Conley, D. J., and Schelske, C. L. (2001). ""Biogenic silica," in biogenic silica," in *Tracking environmental change using lake sediments*. Eds. L. W. Smol JP and B. HJB (Dordrecht,The Netherlands: KluwerAcademic Publishers), 281–293. doi: 10.1007/0-306-47668-1_14

Costello, M. J., Cheung, A., and De Hauwere, N. (2010). Surface area and the seabed area, volume, depth, slope, and topographic variation for the world's seas, oceans, and countries. *Environ. Sci. Technol.* 44, 8821–8828. doi: 10.1021/es1012752

Dai, Z., Xue, Y., Zhang, H., Tu, C., and Luo, Y. (2017). Biogenic silica in the surface sediment of the bohai Sea. *Mar. Sci.* 41, 42–49. doi: 10.11759/hykx20160917002

DeMaster, D. J. (1981). The supply and accumulation of silica in the marine environment. *Geochim. Cosmochim. Acta* 45, 1715–1732. doi: 10.1016/0016-7037(81)90006-5

DeMaster, D. J. (2002). The accumulation and cycling of biogenic silica in the southern ocean: Revisiting the marine silica budget. *Deep. Res. Part II Top. Stud. Oceanogr.* 49, 3155–3167. doi: 10.1016/S0967-0645(02)00076-0

DeMaster, D. J. (2019). "The Global Marine Silica Budget: Sources and Sinks" in the *Encyclopedia of Ocean Sciences*, ed J. K. Cochran, H. J. Bokuniewicz and P. L. Yager, (Academic Press), 473–483. doi: 10.1016/B978-0-12-409548-9.10799-7

DeMaster, D. J. (1991). "Measuring biogenic silica in marine sediments and suspended matter," in *Marine Particles: Analysis and Characterization*, ed. D. C. Hurd and D. W. Spencer (American Geophysical Union), 363–367. doi: 10.1029/GM063p0363

Dixit, S., and Van Cappellen, P. (2003). Predicting benthic fluxes of silicic acid from deep-sea sediments. *J. Geophys. Res. Ocean.* 108, 1–10. doi: 10.1029/2002jc001309

Ehlert, C., Doering, K., Wallmann, K., Scholz, F., Sommer, S., Grasse, P., et al. (2016). Stable silicon isotope signatures of marine pore waters – biogenic opal dissolution versus authigenic clay mineral formation. *Geochim. Cosmochim. Acta* 191, 102–117. doi: 10.1016/j.gca.2016.07.022

Eisma, D., and van der Gaast, S. J. (1971). Determination of opal in marine sediments by X-ray diffraction. *Netherlands J. Sea Res.* 5, 382–389. doi: 10.1016/0077-7579(71)90019-6

Frings, P. J., de la Rocha, C., Struyf, E., van Pelt, D., Schoelynck, J., Hudson, M. M., et al. (2014). Tracing silicon cycling in the okavango delta, a sub-tropical flood-pulse wetland using silicon isotopes. *Geochim. Cosmochim. Acta* 142, 132–148. doi: 10.1016/j.gca.2014.07.007

Frings, P. J., Oelze, M., Schubring, F., Frick, D. A., and von Blanckenburg, F. (2021a). Interpreting silicon isotopes in the critical zone. *Am. J. Sci.* 321, 1164–1203. doi: 10.2475/08.2021.02

Frings, P. J., Schubring, F., Oelze, M., and von Blanckenburg, F. (2021b). Quantifying biotic and abiotic Si fluxes in the critical zone with Ge/Si ratios along a gradient of erosion rates. *Am. J. Sci.* 321, 1204–1245. doi: 10.2475/08.2021.03

Fröhlich, F. (1989). Deep-sea biogenic silica: new structural and analytical data from infrared analysis - geological implications. *Terra Nova* 1, 267–273. doi: 10.1111/j.1365-3121.1989.tb00368.x

Gehlen, M., and van Raaphorst, W. (1993). Early diagenesis of silica in sandy north sea sediments: quantification of the solid phase. *Mar. Chem.* 42, 71–83. doi: 10.1016/0304-4203(93)90238-J

Goldberg, E. D. (1958). Determination of opal in marine sediments. *J. Mar. Res.* 17, 178–182.

Grasshoff, K., Ehrhardt, M., and Kremling, K. (1983). *Methods of seawater analysis. 2nd Edition* Vol. 419 (Weinheim: WILEY-VCH Verlag Chemie GmbH).

Hilborn, R., and Mangel, M. (1997). "The ecological detective: confronting models with data," in *Monographs in population biology no. 28*. Eds. S. A. Levin and H. S. Horn (NJ, USA: Princeton University Press), 315.

Hu, B., Zhang, C., and Zhang, X. (2022). The effects of hydrochloric acid pretreatment on different types of clay minerals. minerals. *Minerals*. 12, 1167–1185. doi: 10.3390/min12091167

Hydes, D. J., and Liss, P. S. (1976). Fluorimetric method for the determination of low concentrations of dissolved aluminium in natural waters. *Analyst* 101, 922–931. doi: 10.1039/an9760100922

Ingall, E., and Jahnke, R. (1994). Evidence for enhanced phosphorus regeneration from marine sediments overlain by oxygen depleted waters. *Geochim. Cosmochim. Acta* 58, 2571–2575. doi: 10.1016/0016-7037(94)90033-7

Jeandel, C. (2016). Overview of the mechanisms that could explain the "Boundary exchange" at the land-ocean contact. *Philos. Trans. R. Soc A Math. Phys. Eng. Sci.* 374, 287–300. doi: 10.1098/rsta.2015.0287

Jeandel, C., and Oelkers, E. H. (2015). The influence of terrigenous particulate material dissolution on ocean chemistry and global element cycles. *Chem. Geol.* 395, 50–66. doi: 10.1016/j.chemgeo.2014.12.001

Kamatani, A., and Oku, O. (2000). Measuring biogenic silica in marine sediments. *Mar. Chem.* 68, 219–229. doi: 10.1016/S0304-4203(99)00079-1

Komadel, P., and Madejová, J. (2006). Chapter 7.1 acid activation of clay minerals. *Dev. Clay Sci.* 1, 263–287. doi: 10.1016/S1572-4352(05)01008-1

Koning, E., Brummer, G. J., Van Raaphorst, W., Van Bennekom, J., Helder, W., and Van Iperen, J. (1997). Settling, dissolution and burial of biogenic silica in the sediments off Somalia (northwestern Indian ocean). *Deep. Res. Part II Top. Stud. Oceanogr.* 44, 1341–1360. doi: 10.1016/S0967-0645(97)00018-0

Koning, E., Epping, E., and Van Raaphorst, W. (2002). Determining biogenic silica in marine samples by tracking silicate and aluminium concentrations in alkaline leaching solutions. *Aquat. Geochemistry* 8, 37–67. doi: 10.1023/A:1020318610178

Leinen, M. (1977). A normative calculation technique for determining opal in deep-sea sediments. *Geochim. Cosmochim. Acta* 41, 671–676. doi: 10.1016/0016-7037(77)90304-0

Liang, Y., Ran, L., and Zhang, L. (2021). The spatial distribution of biogenic silica content and diatom abundance in the surface sediment of the China seas. *Acta Micropaleontol. Sin.* 38, 112–130. doi: 10.16087/j.cnki.1000-0674.2021.01.010

Li, Y., Fang, J., Tian, L. Z., Wang, F., and Chen, Y. S. (2020). Diatom assemblages in surface sediments and their reflection on the water migration pathway from the inshore waters of western bohai bay, china. *Appl. Ecol. Environ. Res.* 18, 2179–2196. doi: 10.15666/aeer/1802_21792196

Liu, J. P., Xu, K. H., Li, A. C., Milliman, J. D., Velozzi, D. M., Xiao, S. B., et al. (2007). Flux and fate of Yangtze river sediment delivered to the East China Sea. *Geomorphology* 85 (3–4), 208–224. doi: 10.1016/j.geomorph.2006.03.023

Liu, S. M., Ye, X. W., Zhang, J., and Zhao, Y. F. (2002). Problems with biogenic silica measurement in marginal seas. *Mar. Geol.* 192, 383–392. doi: 10.1016/S0025-3227(02)00531-5

Liu, J., Zang, J., Bouwman, L., Liu, S., Yu, Z., and Ran, X. (2016). Distribution and budget of dissolved and biogenic silica in the bohai Sea and yellow Sea. *Biogeochemistry* 130, 85–101. doi: 10.1007/s10533-016-0244-2

Liu, L., Zhang, Q., Chen, M. H., Zhang, L. L., and Xiang, R. (2017). Radiolarian biogeography in surface sediments of the Northwest pacific marginal seas. *Sci. China Earth Sci.* 60, 517–530. doi: 10.1007/s11430-016-5179-4

Li, Y., Wang, L., Fan, D., Chen, M., and Lin, Y. (2018). Distribution of biogenic silica in seafloor sediments on the East China Sea inner shelf: Seasonal variations

and typhoon impact. *Estuar. Coast. Shelf Sci.* 212, 353–364. doi: 10.1016/j.ecss.2018.07.023

Lyle, A. O., and Lyle, M. W. (2002). Determination of biogenic opal in pelagic marine sediments: A simple method revisited. *Proc. Ocean Drill. Program* 199, 1215–1222. doi: 10.2973/odp.proc.ir.199.106.2002

Mackin, J. E. (1989). Relationships between Si, Al, and fe deposited on filter-covered glass substrates in marine sediments and in suspensions of sediments and standard clays. *Mar. Chem.* 26, 101–117. doi: 10.1016/0304-4203(89)90055-8

Maldonado, M., López-Acosta, M., Sitjà, C., García-Puig, M., Galobart, C., Ercilla, G., et al. (2019). Sponge skeletons as an important sink of silicon in the global oceans. *Nat. Geosci.* 12, 815–822. doi: 10.1038/s41561-019-0430-7

Meunier, J. D., Keller, C., Guntzer, F., Riotte, J., Braun, J. J., and Anupama, K. (2014). Assessment of the 1% Na2CO3 technique to quantify the phytolith pool. *Geoderma* 216, 30–35. doi: 10.1016/j.geoderma.2013.10.014

Michalopoulos, P., and Aller, R. C. (1995). Rapid clay mineral formation in Amazon delta sediments: Reverse weathering and oceanic elemental cycles. *Science* 270, 614–617. doi: 10.1126/science.270.5236.614

Michalopoulos, P., and Aller, R. C. (2004). Early diagenesis of biogenic silica in the Amazon delta: Alteration, authigenic clay formation, and storage. *Geochim. Cosmochim. Acta* 68, 1061–1085. doi: 10.1016/j.gca.2003.07.018

Moriceau, B., Goutx, M., Guigue, C., Lee, C., Armstrong, R., Duflos, M., et al. (2009). Si-C interactions during degradation of the diatom skeletonema marinoi. *Deep. Res. Part II Top. Stud. Oceanogr.* 56, 1381–1395. doi: 10.1016/j.dsr2.2008.11.026

Mortlock, R. A., and Froelich, P. N. (1989). A simple method for the rapid determination of biogenic opal in pelagic marine sediments. deep Sea res. *Part A Oceanogr. Res. Pap.* 36, 1415–1426. doi: 10.1016/0198-0149(89)90092-7

Müller, P. J., and Schneider, R. (1993). An automated leaching method for the determination of opal in sediments and particulate matter. *Deep. Res. Part I* 40, 425–444. doi: 10.1016/0967-0637(93)90140-X

Noymer, A. (2008). "Alpha, significance level of test," in *Encyclopedia of survey research methods: Thousand oaks*. Ed. P. J. Lavrakas (Sage Publications), 18–18.

Ohlendorf, C., and Sturm, M. (2008). A modified method for biogenic silica determination. *J. Paleolimnol.* 39, 137–142. doi: 10.1007/s10933-007-9100-7

Pickering, R. A., Cassarino, L., Hendry, K. R., Wang, X. L., Maiti, K., and Krause, J. W. (2020). Using stable isotopes to disentangle marine sedimentary signals in reactive silicon pools. *Geophys. Res. Lett.* 47, 1–11. doi: 10.1029/2020GL087877

Pudsey, C. J. (1993). Calibration of a point-counting technique for estimation of biogenic silica in marine sediments. *J. Sediment. Res.* 63, 760–762. doi: 10.2110/jsr.63.760

Qiao, S., Shi, X., Wang, G., Zhou, L., Hu, B., Hu, L., et al. (2017). Sediment accumulation and budget in the bohai Sea, yellow Sea and East China Sea. *Mar. Geol.* 390, 270–281. doi: 10.1016/j.margeo.2017.06.004

Qin, Y. S., Zhao, Y. Y., Chen, L. R., and Zhao, S. L. (1996). *Geology of the East China sea. a series of solid earth sciences research in China*. Beijing: Science Press.

Qu, H., Wang, J., Xu, Y., and Li, X. (2020b). Radiolarian assemblage as an indicator of environmental conditions in the marginal seas of the Western north pacific. *Mar. Micropaleontol.* 157, 101859. doi: 10.1016/j.marmicro.2020.101859

Qu, H., Xu, Y., Wang, J., and Li, X. Z. (2020a). Radiolarian assemblages in the shelf area of the East China Sea and yellow Sea and their ecological indication of the kuroshio current derivative branches. *PeerJ* 8, 1–19. doi: 10.7717/peerj.9976

Rahman, S., Aller, R. C., and Cochran, J. K. (2016). Cosmogenic 32Si as a tracer of biogenic silica burial and diagenesis: Major deltaic sinks in the silica cycle. *Geophys. Res. Lett.* 43, 7124–7132. doi: 10.1002/2016GL069929

Rahman, S., Aller, R. C., and Cochran, J. K. (2017). The missing silica sink: Revisiting the marine sedimentary Si cycle using cosmogenic 32Si. *Global Biogeochem. Cycles* 31, 1559–1578. doi: 10.1002/2017GB005746

Rahman, S., Tamborski, J. J., Charette, M. A., and Cochran, J. K. (2019). Dissolved silica in the subterranean estuary and the impact of submarine groundwater discharge on the global marine silica budget. *Mar. Chem.* 208, 29–42. doi: 10.1016/j.marchem.2018.11.006

Raimonet, M., Ragueneau, O., Jacques, V., Corvaisier, R., Moriceau, B., Khripounoff, A., et al. (2015). Rapid transport and high accumulation of amorphous silica in the Congo deep-sea fan: A preliminary budget. *J. Mar. Syst.* 141, 71–79. doi: 10.1016/j.jmarsys.2014.07.010

Ran, X., Xu, B., Liu, J., Zhao, C., Liu, S., and Zang, J. (2017). Biogenic silica composition and δ13C abundance in the changjiang (Yangtze) and huanghe (Yellow) rivers with implications for the silicon cycle. *Sci. Total Environ.* 579, 1541–1549. doi: 10.1016/j.scitotenv.2016.11.161

Saad, E. M., Pickering, R. A., Shoji, K., Hossain, M. I., Glover, T. G., Krause, J. W., et al. (2020). Effect of cleaning methods on the dissolution of diatom frustules. *Mar. Chem.* 224, 103826. doi: 10.1016/j.marchem.2020.103826

Schlüter, M., and Rickert, D. (1998). Effect of pH on the measurement of biogenic silica. *Mar. Chem.* 63, 81–92. doi: 10.1016/S0304-4203(98)00052-8

Swann, G. E. A. (2010). A comparison of the Si/Al and si/time wet-alkaline digestion methods for measurement of biogenic silica in lake sediments. *J. Paleolimnol.* 44, 375–385. doi: 10.1007/s10933-009-9308-9

Tréguer, P. J., Bowler, C., Moriceau, B., Dutkiewicz, S., Gehlen, M., Aumont, O., et al. (2018). Influence of diatom diversity on the ocean biological carbon pump. *Nat. Geosci.* 11, 27–37. doi: 10.1038/s41561-017-0028-x

Tréguer, P. J., Sutton, J., Brzezinski, M., Charette, M., Devries, T., Dutkiewicz, S., et al. (2021). Reviews and syntheses: The biogeochemical cycle of silicon in the modern ocean. *Biogeosciences Discuss.* 18, 1269–1289. doi: 10.5194/bg-2020-274

Varkouhi, S., Cartwright, J. A., and Tosca, N. J. (2020a). Anomalous compaction due to silica diagenesis — textural and mineralogical evidence from hemipelagic deep-sea sediments of the Japan Sea. *Mar. Geol.* 426, 106204. doi: 10.1016/j.margeo.2020.106204

Varkouhi, S., Tosca, N. J., and Cartwright, J. A. (2020b). Pore-water chemistry: A proxy for tracking the signature of ongoing silica diagenesis. *Journal of Sedimentary Research*. 90, 1037–1067. doi: 10.2110/JSR.2020.56

Varkouhi, S., and Wells, J. (2020). The relation between temperature and silica benthic exchange rates and implications for near-seabed formation of diagenetic opal. *Results Geophys. Sci.* 1–4, 100002. doi: 10.1016/j.ringps.2020.100002

Wang, Y., Liu, D., Di, B., Shi, Y., and Wang, Y. (2016). Distribution of diatoms and silicoflagellates in surface sediments of the yellow Sea and offshore from the changjiang river, China. *Chin. J. Oceanol. Limnol.* 34, 44–58. doi: 10.1007/s00343-015-4237-0

Williams, L. A., Parks, G. A., and Crerar, D. A. (1985). Silica diagenesis: I. solubility controls. *J. Sediment. Petrol.* 55, 301–311. doi: 10.1306/212f86ac-2b24-11d7-8648000102c1865d

Wu, B., and Liu, S. M. (2020). Dissolution kinetics of biogenic silica and the recalculated silicon balance of the East China Sea. *Sci. Total Environ.* 743, 140552. doi: 10.1016/j.scitotenv.2020.140552

Wu, B., Liu, S. M., and Ren, J. L. (2017). Dissolution kinetics of biogenic silica and tentative silicon balance in the yellow Sea. *Limnol. Oceanogr.* 62, 1512–1525. doi: 10.1002/lno.10514

Wu, B., Lu, C., and Liu, S. M. (2015). Dynamics of biogenic silica dissolution in Jiaozhou Bay, western Yellow Sea. Marine Chemistry. *Mar. Chem.* 174, 58–66. doi: 10.1016/j.marchem.2015.05.004

Zhang, W., Xue, S., Zhao, Q., Zhang, X., Li, J., Jin, M., et al. (2003). Biopotentials of marine sponges from China oceans: Past and future. *Biomol. Eng.* 20, 413–419. doi: 10.1016/S1389-0344(03)00066-2

frontiers | Frontiers in Marine Science

TYPE Original Research
PUBLISHED 23 March 2023
DOI 10.3389/fmars.2023.1141448

OPEN ACCESS

EDITED BY
Selvaraj Kandasamy,
Xiamen University, China

REVIEWED BY
Paul J. Tréguer,
Université de Bretagne Occidentale, France
Oscar E. Romero,
University of Bremen, Germany

*CORRESPONDENCE
Timo Spiegel
tspiegel@geomar.de

SPECIALTY SECTION
This article was submitted to Marine Biogeochemistry, a section of the journal Frontiers in Marine Science

RECEIVED 10 January 2023
ACCEPTED 01 March 2023
PUBLISHED 23 March 2023

CITATION
Spiegel T, Dale AW, Lenz N, Schmidt M, Sommer S, Kalapurakkal HT, Przibilla A, Lindhorst S and Wallmann K (2023) Biogenic silica cycling in the Skagerrak. *Front. Mar. Sci.* 10:1141448. doi: 10.3389/fmars.2023.1141448

Biogenic silica cycling in the Skagerrak

Timo Spiegel[1]*, Andrew W. Dale[1], Nina Lenz[2], Mark Schmidt[1], Stefan Sommer[1], Habeeb Thanveer Kalapurakkal[1], Anna Przibilla[3], Sebastian Lindhorst[4] and Klaus Wallmann[1]

[1]Marine Biogeochemistry, GEOMAR Helmholtz Centre for Ocean Research Kiel, Kiel, Germany, [2]Ocean Circulation and Climate Dynamics, GEOMAR Helmholtz Centre for Ocean Research Kiel, Kiel, Germany, [3]Inorganic Environmental Chemistry, Helmholtz-Zentrum Hereon, Geesthacht, Germany, [4]Earth System Sciences, Universität Hamburg, Hamburg, Germany

Dissolved silicate (H_4SiO_4) is essential for the formation of the opaline skeletal structures of diatoms and other siliceous plankton. A fraction of particulate biogenic silica (bSi) formed in surface waters sinks to the seabed, where it either dissolves and returns to the water column or is permanently buried. Global silica budgets are still poorly constrained since data on benthic bSi cycling are lacking, especially on continental margins. This study describes benthic bSi cycling in the Skagerrak, a sedimentary depocenter for particles from the North Sea. Biogenic silica burial fluxes, benthic H_4SiO_4 fluxes to the water column and bSi burial efficiencies are reported for nine stations by evaluating data from in-situ benthic landers and sediment cores with a diagenetic reaction-transport model. The model simulates bSi contents and H_4SiO_4 concentrations at all sites using a novel power law to describe bSi dissolution kinetics with a small number of adjustable parameters. Our results show that, on average, 1100 mmol m^{-2} yr^{-1} of bSi rains down to the Skagerrak basin seafloor, of which 50% is released back to overlying waters, with the remainder being buried. Biogenic silica cycling in the Skagerrak is generally consistent with previously reported global trends, showing higher Si fluxes and burial efficiencies than deep-sea sites and similar values compared to other continental margins. A significant finding of this work is a molar bSi-to-organic carbon burial ratio of 0.22 in Skagerrak sediments, which is distinctively lower compared to other continental margins. We suggest that the continuous dissolution of bSi in suspended sediments transported over long distances from the North Sea leads to the apparent decoupling between bSi and organic carbon in Skagerrak sediments.

KEYWORDS

biogenic silica, dissolved silicate, *in situ* measurement, burial, marine cycling, diagenetic model, sedimentation rate, Skagerrak

1 Introduction

Global marine biogeochemical cycling of dissolved silicate (H_4SiO_4) and biogenic silica (bSi) is mainly controlled by riverine inputs and by outputs by burial at the seafloor (Wollast, 1974; DeMaster, 1981; Nelson et al., 1995; Tréguer et al., 1995; Ragueneau et al., 2000; DeMaster, 2002; Tréguer and de la Rocha, 2013; Rahman et al., 2017; DeMaster, 2019). Silicon (Si) is an essential nutrient in the ocean for a number of siliceous organisms such as diatoms, silicoflagellates, siliceous sponges and radiolaria (DeMaster, 2002). The bSi and carbon (C) cycles are coupled *via* biomineralization in the surface ocean and subsequent dissolution of detritus in the water column and burial in sediments. The tightness of this coupling is thus important for the sequestration of atmospheric CO_2 (Dugdale et al., 1995; Ragueneau et al., 2006; Tréguer and de la Rocha, 2013; Tréguer et al., 2018; Tréguer et al., 2021).

The global ocean is undersaturated with respect to bSi (Hurd, 1973; Nelson et al., 1995; Ragueneau et al., 2000; Tréguer and de la Rocha, 2013). Biogenic siliceous material dissolves as it sinks through the water column and only a fraction of the bSi exported from the surface ocean reaches the seafloor (Nelson and Gordon, 1982; Wollast and Mackenzie, 1981; Nelson et al., 1991; Nelson et al., 1995; Tréguer et al., 1995). Upon sedimentation, bSi is subject to further dissolution, although the regenerated dissolved H_4SiO_4 can reprecipitate into authigenic minerals (Mackenzie et al., 1981; Mackenzie and Kump, 1995; Michalopoulos and Aller, 1995; Loucaides et al., 2010; Ehlert et al., 2016) or adsorb to mineral surfaces (Huang, 1975; Sigg and Stumm, 1981; Swedlund, 1999; Davis et al., 2001; Davis et al., 2002). The competition between these processes determines the proportion of bSi that is reintroduced to the water column as a benthic flux of H_4SiO_4 and the proportion that is permanently buried. Tréguer and de la Rocha (2013) underlined the importance of the benthic bSi cycle by showing that most of the marine bSi dissolves at the sediment-water interface rather than during the sinking of silica particles.

Based on molar bSi:C ratios and particulate organic carbon (POC) burial rates, DeMaster (2002) updated global estimates of bSi burial on continental margins and demonstrated that the contribution of these regions to the global Si budget is more important than previously thought. Since then, more studies have focused on the margins, e.g. in the North Atlantic (Schlüter and Sauter, 2000; Schmidt et al., 2001; Oehler et al., 2015b). Yet, current global Si budgets still lack sufficient data, especially with regard to benthic fluxes and burial efficiencies, to accurately constrain bSi burial and dissolution on continental margins.

To our knowledge, no comprehensive study on bSi cycling has been published for the Skagerrak; a continental margin representing the largest depocenter for sediments transported from the North Sea (Eisma and Kalf, 1987; Van Weering et al., 1987; Van Weering et al., 1993). Here, we present a dataset on bSi cycling for the Skagerrak and quantify benthic fluxes of H_4SiO_4, bSi rain rates to the seafloor, burial fluxes and burial efficiencies using a combination of geochemical observations and modelling. We propose a novel model for bSi cycling in Skagerrak sediments with potential broader applicability. We compare our results with other regions to highlight bSi cycling in the Skagerrak in a global context.

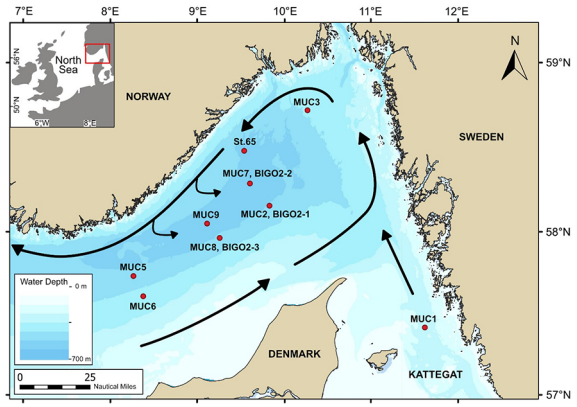

FIGURE 1
Study area and sampling sites of MUCs and BIGOs within the Skagerrak. Black arrows indicate the surface water circulation.

2 Study area

The Skagerrak strait is located between Denmark, Norway and Sweden and links the North Sea and the Kattegat with maximum water depths of approximately 700 m (Figure 1). Surface waters in the Skagerrak circulate anticlockwise. Water from the North Sea enters the Skagerrak through the Jutland Current from the south, which, together with the Baltic Current, results in the outflowing Norwegian Coastal Current leaving the Skagerrak to the north (Van Weering et al., 1987; Otto et al., 1990). Annual total sediment deposition in the Skagerrak is $46 \cdot 10^6$ tons yr^{-1} (De Haas and Van Weering, 1997). Sediment composition varies between sand (<40% clay), mainly along the Danish coast, and fine-grained silt and clay sediments in the deeper parts (Stevens et al., 1996). Substantial animal burrows are present in the upper 10 - 20 cm in the fine-grained areas (Canfield et al., 1993a; Kristensen et al., 2018). Skagerrak sediments are characterized by a large lateral input of mostly lithogenic material from the North Sea (Van Weering et al., 1993; De Haas and Van Weering, 1997). Nutrient supply from external waters and local rivers support an annual primary productivity of 130 g C_{org} m^{-2} yr^{-1} (Beckmann and Liebezeit, 1988). Both siliceous (diatoms) and carbonaceous (haptophytes) frustule-building phytoplankton are present in the Skagerrak, with diatoms being dominant during the early bloom in February-March and a second bloom in May-June (Gran-Stadniczeñko et al., 2019).

3 Materials and methods

Data are presented from nine stations (65 to 677 m water depth) visited over two sampling campaigns, AL557 and AL561, with R/V Alkor in June and August 2021, respectively (Schmidt, 2021, Thomas et al., 2022). Only data from St. 65 are from June 2021 (Figure 1; Table 1). At each station, a short sediment core was recovered (<50cm) using a multiple-corer (MUC). Sediments at these sites were dominated by fine-grained material except MUC6, which was taken from a more sandy area (Table 1). At three stations during AL561, autonomous benthic landers (Biogeochemical

TABLE 1 Summary of sampling sites and general information on multicorer (MUC) and biogeochemical observatory (BIGO) stations.

Station	Latitude N	Longitude E	Water depth (m)	Porosity [a]	Grain sizes [b] D_{50} (µm)	bSi [a] (%)	TOC [a] (%)	$CaCO_3$ [a] (%)	Lithogenic [c] material (%)
MUC1	57° 27.030'	11° 30.480'	65	0.75	11	3.2	1.7	12.0	80
MUC6	57° 38.086'	08° 23.998'	185	0.50	94	0.6	0.6	6.3	91
MUC3	58° 44.876'	10° 13.437'	215	0.77	11	2.5	2.0	14.1	78
MUC5	57° 45.191'	08° 17.173'	434	0.77	9	2.6	2.1	13.8	78
MUC8	57° 59.286'	09° 14.305'	490	0.77	14	2.0	2.5	14.0	77
MUC2	58° 10.884'	09° 47.624'	500	0.78	9	2.5	2.5	13.4	77
St. 65	58° 30.068'	09° 29.887'	530	0.79		2.1	2.2	12.5	79
MUC9	58° 04.352'	09° 05.736'	604	0.80	8	2.2	2.1	11.4	80
MUC7	58° 18.785'	09° 34.335'	677	0.82	7	2.3	2.1	11.4	81
BIGO-2-1	58° 10.969'	09° 47.423'	502						
BIGO-2-2	58° 18.778'	09° 34.362'	678						
BIGO-2-3	57° 59.220'	09° 14.300'	490						

[a]Porosity, and contents of bSi (as wt% SiO_2), total organic carbon (TOC) and $CaCO_3$ represent mean values for the whole core.
[b]Grain sizes are given as D_{50} (50% of particles are smaller than this value), provided as average of all samples from the core.
[c]Lithogenic material was calculated as: Lithogenic material = 100 – (bSi + $CaCO_3$ + 2.8 · TOC), where the factor 2.8 converts the mass of TOC to total particulate organic matter (Sayles et al., 2001).

Observatories, BIGO) were deployed to determine benthic H_4SiO_4 fluxes.

3.1 Sampling

Sediment samples for porosity and solid phase analyses from the MUC were taken every centimetre and subsequently stored refrigerated at 4°C. An additional core from each station was subsampled at the same resolution for ^{210}Pb radionuclide and grain size analyses. From a third core, sediment for porewater analysis was sampled in an argon-filled glove bag in a refrigerated laboratory adjusted to bottom water temperatures (ca. 7°C). The samples were centrifuged at 4000 rpm at 8°C for 20 min to separate porewater from the solid phase. Subsequently, the supernatant water was filtered through a 0.2 µm cellulose-acetate syringe filter inside the glove bag. Porewater from St. 65 (AL557) was sampled with syringes and rhizones (0.15 µm pore size).

3.2 *In-situ* flux measurements

For the measurement of total solute fluxes, the GEOMAR BIGO type lander (Biogeochemical Observatory) was deployed as described in detail by (Sommer et al. (2009). BIGO-2 contained two circular flux chambers (internal diameter 28.8 cm area 651.4 cm^2). A TV-guided launching system allowed smooth placement of the observatory on the sea floor. Approximately 2 hours (BIGO-2-1) or 4 hours (BIGO-2-2 & -3) after the observatories were placed on the seabed, the chambers were slowly driven into the sediment (~30 cm h^{-1}). During this initial period, where the bottom of the chambers was not closed by the sediment, the water inside the flux chamber was periodically replaced with ambient bottom water. The water body inside the chamber was replaced once more with ambient bottom water after the chamber had been driven into the sediment to flush out solutes that might have been released from the sediment during chamber insertion. To determine fluxes of H_4SiO_4, eight sequential water samples were removed with glass syringes (volume ~ 47 ml) using syringe water samplers. The syringes were connected to the chamber using 1 m long Vygon tubes with a dead volume of 5.2 ml. Prior to deployment, these tubes were filled with distilled water.

3.3 Analytical methods

Porewater H_4SiO_4 analysis was done onboard immediately after filtering using standard methods (Grasshoff et al., 1999) with a Hitachi U-2001 spectrophotometer. The analytical precision of the analysis was better than 2 µmol L^{-1}. The porewater samples from St. 65 (AL557) were stored frozen until they were analyzed for H_4SiO_4 six months after sampling with a TECAN infinite 200 plate reader at 810 nm according to the method by Ringuet et al. (2011). Porewater sub-samples for total dissolved iron (Fe), potassium (K) and lithium (Li) were acidified with 10 µL of suprapure concentrated HNO_3 per mL of sample and stored refrigerated at 4°C in the dark for later analyses at GEOMAR by inductively coupled plasma optical emission spectroscopy (ICP-OES, Varian ICP 720-ES). A seawater standard (IAPSO) was used for quality control. The analytical accuracy was better than 2%.

Porosity was determined from the loss of water after freeze-drying. Biogenic silica contents were analyzed on freeze-dried and homogenized sediment by a wet-leaching procedure based on the method of Müller and Schneider (1993) using 1 M NaOH as the leaching solution. An internal sediment standard was used for quality control and the analytical accuracy was better than 7%.

The presented bSi contents are given as wt% SiO_2. This method may underestimate bSi content if particles are coated with metal oxides that protect bSi from dissolution or if bSi is incorporated into authigenic clay minerals (Michalopoulos and Aller, 2004; Rahman et al., 2017). Biogenic silica may also be overestimated if coexisting non-biogenic compounds are extracted by the alkaline leach (DeMaster, 1991; Kamatani and Oku, 2000). In particular, for sediments with high contents of lithogenic silica, alkaline leaching of lithogenic silica can interfere with the measured bSi content (Ragueneau and Tréguer, 1994; Zhu et al., 2023). Total carbon (TC) and total organic carbon (TOC) were analyzed on freeze-dried and homogenized sediment using a EuroEA 3000 element analyzer. For TOC analysis, sediments were first decarbonized with 0.25 N HCl on a hotplate at ~70°C. Total inorganic carbon (TIC) was calculated by subtracting TOC from TC. TIC values are reported as weight percent $CaCO_3$ assuming that all TIC occurs as calcium carbonate. The analytical accuracy was better than 5% for TOC and TC based on repeated analyses of certified reference material BSTD1 (soil standard).

Analysis of ^{210}Pb was carried out at stations MUC1, MUC3, MUC5, MUC9 and St.65. Freeze-dried and homogenized sediment was embedded into containers sealed with a two-component epoxy resin. Samples were left standing for two weeks to ensure steady state equilibration between ^{226}Ra and ^{214}Bi. Activities of total ^{210}Pb were measured *via* its peak intensity at 46.5 keV by gamma spectrometry on n-type planar or coaxial Canberra Ge-detectors at GEOMAR (MUC5), Göttingen (St.65) and IAF Dresden (MUC1, MUC3, MUC9). Total ^{210}Pb activities were corrected for the natural background decay of ^{226}Ra at 295 keV in marine sediments to obtain excess ^{210}Pb ($^{210}Pb_{ex}$) values.

3.4 Grain size determination

Bulk grain size distributions were determined for each station except St. 65. Samples were treated with 10% - 30% hydrogen peroxide and 60% acetic acid to dissolve organic and carbonate compounds. Subsequently, samples were dispersed in water using tetra-sodium diphosphate decahydrate. Grain size distributions were determined at the CEN, University of Hamburg, with a laser-diffraction particle-sizer (Sympatec HELOS/KF Magic; range 0.5/18 to 3500 µm). Accuracy of measurements and absence of a long-term instrumental drift was ensured by regular analysis of an in-house standard (standard deviation for mean grain size and D_{50} over the analysis period was < 1.1 µm). Statistical evaluation of the grain size distribution was based on the graphical method (Folk and Ward, 1957), calculated using GRADISTAT software (Blott and Pye, 2001).

3.5 Steady-state calculations

Biogenic silica burial fluxes (bSi_{bur}) were calculated as follows:

$$bSi_{bur} = ds\,(1-\phi)\,SR\,bSi \quad (1)$$

Where ds is the density of dry solids, ϕ is the mean porosity of the whole sediment core, bSi is the mean bSi content of each sediment core in wt% SiO_2 and SR is the sediment accumulation or sedimentation rate in compacted sediments. Mean bSi contents were used due to scattering of bSi and an absence of clear trends with sediment depth. SR was either determined from $^{210}Pb_{ex}$ data (Eq. 7) or taken from literature values close to the station (Table 2).

At BIGO stations, benthic fluxes of H_4SiO_4 (J_{Si}) were calculated from least-square linear regression fits of concentration versus time plots of the data obtained by benthic chamber in-situ measurements and the height of overlying water in the benthic chamber (Dale et al., 2021). The H_4SiO_4 benthic fluxes represent the mean flux of both benthic chambers at each station. At non-BIGO stations, porewater gradients of H_4SiO_4 were used to calculate H_4SiO_4 benthic fluxes by applying Fick's First Law. This approach only considers diffusive transport and does not account for additional non-local transport by bioirrigation, in contrast to in-situ BIGO measurements that provide the total flux. The enhancement of solute transport by bioturbation and bioirrigation was obtained by calculating a correction factor, α (Ståhl et al., 2004). The factor (mean α = 2.2) was calculated as the ratio between benthic fluxes determined from in-situ measurements and porewater gradients at the three BIGO stations. The correction factor was then applied to the diffusive flux at non-BIGO stations to obtain total H_4SiO_4 benthic fluxes:

$$J_{Si} = -\phi\, D_{sed}\, \frac{d[C]}{dx}\, \alpha \quad (2)$$

Where J_{Si} is the H_4SiO_4 benthic flux, ϕ is porosity, d[C]/dx is the concentration gradient between porewater (taken at 0.5cm) and bottom water (taken from overlying water of the MUCs), and D_{sed} is the molecular diffusion coefficient of H_4SiO_4 corrected for tortuosity ($0.58 \cdot 10^{-5}$ cm^2 s^{-1}) and bottom water temperatures (7° C) taken from Rebreanu et al. (2008). H_4SiO_4 fluxes were always directed out of the sediment. In this study, they are reported as positive numbers.

Rain rates of bSi (bSi_{rr}) were then calculated as the sum of bSi burial fluxes and H_4SiO_4 benthic fluxes:

$$bSi_{rr} = bSi_{bur} + J_{Si} \quad (3)$$

The percent bSi burial efficiency (bSi_{be}) was then calculated as follows:

$$bSi_{be} = \frac{bSi_{bur}}{bSi_{rr}}\, 100\% \quad (4)$$

3.6 Model description

To simulate bSi turnover, we used a steady-state numerical transport-reaction model for dissolved H_4SiO_4 and particulate bSi and $^{210}Pb_{ex}$. The following one-dimensional partial differential equations (Berner, 1980) were applied to solve for the concentration profiles of H_4SiO_4 and bSi:

TABLE 2 Measured and modelled results for bSi cycling.

Measured and modelled data	MUC1 65m	MUC6 185m	MUC3 215m	MUC5 434m	MUC8 490m	MUC2 500m	St.65 530m	MUC9 604m	MUC7 677m
H_4SiO_4 bottom water (µmol L^{-1})	7.5	0.0	7.1	15.0	12.5	10.5	22.6 [a]	20.2	22.6
bSi content (wt%) [b]	3.2	0.6	2.5	2.6	2	2.5	2.1	2.2	2.3
Sedimentation rate, SR (cm yr^{-1})	0.14	0.12 [c]	0.14	0.32	0.21 [c]	0.38 [c]	0.26	0.19	0.24 [c]
bSi burial flux (mmol m^{-2} yr^{-1})	460	150	340	790	390	850	490	360	410
H_4SiO_4 benthic flux (mmol m^{-2} yr^{-1})	670 [d]	30 [d]	600 [d]	500 [d]	660	420	510 [d]	450 [d]	590
Bioirrigation (%) [e]	43	33	43	42	45	43	41	49	42
bSi rain rate, bSi_{rr} (mmol m^{-2} yr^{-1}) [f]	1130	180	940	1290	1060	1270	1070	1000	1000
bSi burial efficiency, bSi_{be} (%) [f]	41	83	36	61	37	67	49	44	41
Integrated bSi dissolution (mmol m^{-2} yr^{-1}) [f]	670	30	600	500	660	420	510	450	590
Kinetic constant, B_0 (mmol $cm^{-3\text{-}B2}$ yr^{-1})	0.40	0.06	0.28	0.26	0.35	0.26	0.32	0.27	0.42
Kinetic constant, B_1 (cm)	2.3	2.7	2.3	2.3	2.3	2.3	2.4	2.5	2.4
Kinetic constant, B_2 (-)	-2.6	-1.5	-2.4	-2.5	-2.5	-2.3	-2.4	-2.5	-2.6
Bioturbation coefficient, D_{B0} (cm^2 yr^{-1})	50	26	52	6	20	25	5	13	15
Bioturbation coefficient, x_B (cm)	20.0	4.0	19.5	3.0	2.5	2.3	1.5	3.0	3.0
Bioirrigation coefficient, D_{I0} (yr^{-1})	39	24	33	22	33	19	17	32	23
Bioirrigation coefficient, x_I (cm)	4.1	1.5	4.3	6.0	5.7	6.3	6.9	6.9	8.0
Porosity at sediment-water interface, ϕ_0 (-)	0.85	0.50	0.86	0.87	0.89	0.89	0.90	0.88	0.89
Porosity in compacted sediment, ϕ_c (-)	0.73	0.49	0.76	0.74	0.75	0.77	0.76	0.78	0.80
Attenuation coefficient, px (cm)	0.12	0.10	0.11	0.10	0.14	0.17	0.15	0.13	0.11

[a]Bottom water H_4SiO_4 concentration at St. 65 was taken from the adjacent station MUC7.
[b]Biogenic silica contents are given as mean values for the whole sediment core.
[c]Sedimentation rates were taken from reported values measured in cores close to our stations: MUC2: Van Weering et al. (1993); MUC6: Van Weering et al. (1987); MUC7: Paetzel et al. (1994); MUC8: Erlenkeuser and Pederstad (1984).
[d]H_4SiO_4 benthic fluxes were calculated by the diffusive fluxes and the correction factor α (Eq. 2).
[e]Bioirrigation contribution to total H_4SiO_4 benthic fluxes.
[f]In the model, bSi rain rates and burial efficiencies were prescribed using field data (Eq. 14, 15). Consequently, depth-integrated net bSi dissolution rates were also predefined and equal to the H_4SiO_4 benthic flux.
Stations are arranged with increasing water depth. Si fluxes in the table are rounded to two significant figures.

$$ds\,(1-\phi)\,\frac{\delta bSi}{\delta t} = \frac{\delta}{\delta x}\left(ds\,(1-\phi)\,D_B\frac{\delta BSi}{\delta x} - ds\,(1-\phi)\,us\,BSi\right) - ds\,(1-\phi)\,RbSi \quad (5)$$

$$\phi\,\frac{\delta H_4SiO_4}{\delta t} = \frac{\delta}{\delta x}\left(\phi\,D_s\frac{\delta H_4SiO_4}{\delta x} - \phi\,upw\,H_4SiO_4\right) + \phi\,D_I\,(BW - H_4SiO_4) + \phi\,RbSi \quad (6)$$

where x is sediment depth, t is time, ds is the density of dry solids (= 2.5 g cm^{-3}), ϕ is porosity, D_s is the tortuosity-corrected molecular diffusion coefficient, D_B is the bioturbation coefficient, D_I is the bioirrigation coefficient, BW denotes the concentration of H_4SiO_4 in ambient bottom water, us and upw are burial velocities for solids and porewater, respectively, and RbSi is the rate of bSi dissolution.

The following equation was used to simulate particle-bound $^{210}Pb_{ex}$ and derive burial velocities and bioturbation rates:

$$ds\,(1-\phi)\frac{\delta\,Pb_{ex}}{\delta t} = \frac{\delta}{\delta x}\,(ds\,(1-\phi)\,D_B\frac{\delta\,Pb_{ex}}{\delta x} - ds\,(1-\phi)\,us\,Pb_{ex}) - ds\,(1-\phi)\,\lambda\,Pb_{ex} \quad (7)$$

where Pb_{ex} is the excess activity of ^{210}Pb in sediments and λ is the ^{210}Pb decay constant (0.031 yr^{-1}).

Sediment compaction was considered in the model by fitting the following function to the porosity data at each station:

$$\phi = \phi_c + (\phi_0 - \phi_c)^{\left(-\frac{x}{px}\right)} \quad (8)$$

where ϕ_0 is the porosity at the sediment surface, ϕ_c is the porosity in compacted sediment and px is the attenuation coefficient. Burial velocities of solids and solutes were then described as:

$$us = \frac{SR\,(1-\phi_c)}{(1-\phi)} \quad (9)$$

$$upw = \frac{SR\,\phi_c}{\phi} \quad (10)$$

The distribution of $^{210}Pb_{ex}$ in surface sediments was used to constrain bioturbation rates:

$$D_B = D_{B0}\ \exp\left(-\frac{x^2}{2\,x_B{}^2}\right) \quad (11)$$

where D_{B0} is the bioturbation coefficient at the sediment-water interface and x_B controls the bioturbation mixing depth.

Flushing of animal burrows by bioirrigation was mathematically described as:

$$D_I = D_{I0}\ \exp\left(-\frac{x^2}{2\,x_I^2}\right) \quad (12)$$

where D_{I0} is the bioirrigation coefficient at the sediment-water interface and x_I controls the bioirrigation depth. Bioirrigation rates were constrained from porewater H_4SiO_4 concentrations.

Most models that simulate bSi dissolution use a rate that decreases rapidly with sediment depth to simulate porewater H_4SiO_4 concentrations (e.g. McManus et al., 1995; Rabouille et al., 1997; Khalil et al., 2007). Three different explanations have been put forward to explain the decrease in bSi dissolution; (i) saturation control by high porewater H_4SiO_4 levels (McManus et al., 1995; Rabouille et al., 1997), (ii) different phases of bSi undergoing dissolution, each with its own reactivity (Boudreau, 1990, Archer et al., 1993, McManus et al., 1995), and (iii) retardance of dissolution due to progressive coating of particle surfaces by Al-containing minerals (Kamatani et al., 1988; McManus et al., 1995). Since the underlying mechanisms are unknown in Skagerrak sediments, we made no attempt to resolve the different factors controlling the rate decline with depth. Instead, we applied an empirical power law model to simulate the combined effect of these processes, which implicitly includes dissolution, reprecipitation and adsorption, and which we refer to as the depth-dependent net bSi dissolution rate (RbSi). Thus, true bSi dissolution rates may be higher if large amounts of H_4SiO_4 are removed from porewaters by adsorption or reprecipitation.

Based on previous modelling work (Middelburg, 1989; Boudreau and Ruddick, 1991; Boudreau et al., 2008), Stolpovsky et al. (2015) proposed a depth-dependent power function to simulate POC degradation in bioturbated sediments:

$$RPOC = B_0\,(x + B_1)^{B_2} \quad (13)$$

where RPOC is the rate of POC degradation with sediment depth (mmol cm^{-3} yr^{-1}) and B_0 (mmol cm^{-3-B2} yr^{-1}), B_1 (cm) and B_2 (dimensionless) are parameters defining the decrease in POC degradation rate. Given that the rates of both bSi dissolution and POC degradation decrease with sediment depth, we assumed that the power law from Stolpovsky et al. (2015) is applicable to describe bSi dissolution kinetics:

$$RbSi = B_0\,(x + B_1)^{B_2} \quad (14)$$

where RbSi is the depth-dependent net rate of bSi dissolution (mmol cm^{-3} yr^{-1}). The values of B_0, B_1 and B_2 for bSi dissolution are expected to be different to those for POC degradation that were constrained from a global database of benthic oxygen and nitrate fluxes (Stolpovsky et al., 2015). Following Stolpovsky et al. (2015), we assume that the rain rate of bSi to the seafloor provides an upper limit of the total amount of bSi available for dissolution and that its burial efficiency describes the limit of bSi preservation. Consequently, bSi rain rates and burial efficiencies are model input parameters. If bSi_{rr} and bSi_{be} are known, the value of one of the parameters B_0, B_1 or B_2 can be determined from the other two, i.e. for B_0:

$$B_0 = \frac{((1+B_2)\,(-100 + bSi_{be})\,bSi_{rr})}{(100\,(B_2^{1+B_2} - B_1\,(B_1+L)^{B_2} - L\,(B_1+L)^{B_2}))} \quad (15)$$

where L is the depth at which bSi no longer dissolves. Since the depth profiles of bSi and H_4SiO_4 indicate that bSi dissolution stops near the bottom of the sediment core, we assumed L to be 50 cm.

Two adjustable parameters, B_1 and B_2, are required to simulate net bSi dissolution. These were constrained from the measured bSi and H_4SiO_4 data. In total, 10 parameters (B_1, B_2, SR, ϕ_0, ϕ_c, px, D_{I0}, x_I, D_{B0}, x_B) were adjusted to fit the porosity, $^{210}Pb_{ex}$, H_4SiO_4 and bSi data. The parameters SR, D_{B0} and x_B were evaluated by a Monte Carlo procedure (2000 runs) after Dale et al. (2021). For each model run, the parameters were randomly varied from 0.05 to 4 cm yr^{-1} for SR, 1 to 30 cm^2 yr^{-1} for D_{B0} and 1 to 3 cm for x_B. These ranges were chosen based on literature values and visual identification of the bioturbation layer in the $^{210}Pb_{ex}$ data. At stations MUC1 and MUC3, no clear bioturbation layer was observed. Here, ranges of D_{B0} and x_B for the Monte Carlo runs were extended to 1 - 150 cm^2 yr^{-1} and 1 - 30 cm, respectively.

Upper boundary conditions were set as constant concentrations for H_4SiO_4 and constant particulate fluxes to the seafloor for bSi. For $^{210}Pb_{ex}$, a constant rate of supply was set at the upper boundary from the measured integrated $^{210}Pb_{ex}$ activity in the sediment and the decay constant λ:

$$FPb_{ex} = \lambda\ ds\ (1-\phi_0) \int_0^{\infty} Pb_{ex}\ dx \quad (16)$$

where FPb_{ex} is the flux of $^{210}Pb_{ex}$ to the seafloor. At the lower boundary at 50 cm, a zero gradient condition was imposed for all model variables.

Model input data for each station are summarized in Table 2. The model was run to steady-state using the partial differential equation solver implemented in Mathematica 12.2. Mass conservation > 99% was achieved in all model runs. Mean deviations between the model and measured H_4SiO_4, bSi and $^{210}Pb_{ex}$ data, expressed as root mean square errors, were 27 µmol L^{-1}, 0.4 wt% and 0.6 dpm g^{-1}, respectively.

4 Results

4.1 $^{210}Pb_{ex}$ activities, sedimentation rates and mixing

At stations MUC5, MUC9 and St.65, $^{210}Pb_{ex}$ activities decreased exponentially below the upper centimetres where $^{210}Pb_{ex}$ activities tended to be more constant (Figure 2). In contrast, stations MUC1 and MUC3 showed an almost linear $^{210}Pb_{ex}$ decrease throughout

the whole core. Sedimentation rates determined by the model ranged from 0.14 to 0.32 cm yr^{-1} (Table 2) and varied with water depth, but no clear trend was observed.

Sediment mixing by bioturbation was limited to the upper 5 - 10 cm at most sites (Figure 3C, Eq. 11) with bioturbation coefficients (D_{B0}) and mixing coefficients (x_B) of 5 - 26 cm^2 yr^{-1} and 1.5 - 4.0 cm, respectively (Table 2). In contrast, bioturbation was predicted to proceed throughout the whole sediment core at stations MUC1 and MUC3. At these sites, extreme DB_0 and x_B values in the range of 50 cm^2 yr^{-1} and 20 cm, respectively, were required to simulate the measured $^{210}Pb_{ex}$ data. Bioirrigation was most intense in the upper layers and extended up to 5 - 20 cm depth, with deeper bioirrigation observed with increasing water depth (Figure 3C).

4.2 Dissolved and solid phase geochemistry

Sediments were generally fine-grained with mean D_{50} values ranging from 7 to 14 µm (Table 1). MUC6 contained a higher proportion of sand with a D_{50} of 94 µm. Solid phase bSi contents varied between 1 and 5 wt%, except for the sandy station MUC6, where lower values of 0.4 - 0.9 wt% were observed (Figure 3A). Biogenic silica showed no clear trend with sediment depth. $CaCO_3$ varied from ca. 6 – 13% and lithogenic material from 77 - 91% (Table 1).

H_4SiO_4 concentrations in the Skagerrak generally increased with sediment depth up to asymptotic concentrations of 300 - 660 µmol L^{-1} (Figure 3B). Although asymptotic values were not reached at every station, the data indicate that the maximum asymptotic concentrations decreased with water depth. Furthermore, concentration plateaus, or local minima, were observed between 2 - 15 cm and were most pronounced at the deeper stations (>400 m). Total dissolved Fe concentrations were below the detection limit in the upper 5 - 10 cm, followed by an increase up to a maximum concentration of 40 - 135 µmol L^{-1} (Figure 4A). Thereafter, dissolved Fe concentrations tended to decrease. The zone of increasing dissolved Fe concentrations coincided with the concentration plateaus of H_4SiO_4 at the deeper sites. Dissolved K and Li concentrations showed near-constant concentrations with sediment depth, ranging between 10 and 12 mmol L^{-1} and 24 and 36 µmol L^{-1}, respectively, across the different sites (Figure 4B).

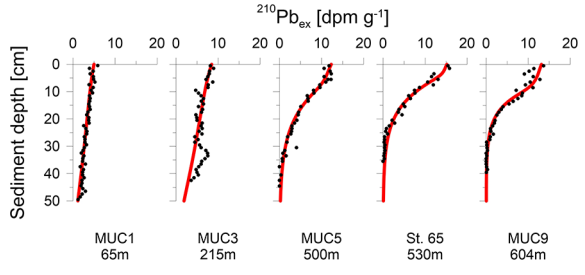

FIGURE 2
Measured data (symbols) and model simulations (curves) of $^{210}Pb_{ex}$.

4.3 Si fluxes and burial efficiencies

Burial fluxes varied between 150 and 850 mmol m^{-2} yr^{-1}. (Table 2). H_4SiO_4 fluxes at the three BIGO stations ranged between 420 and 660 mmol m^{-2} yr^{-1}, which is similar to reported in-situ flux measurements of 360 - 609 mmol m^{-2} yr^{-1} in the Skagerrak basin between 411 - 682 m water depth (Hall et al., 1996). Benthic fluxes at stations that were calculated based on porewater gradients and the correction factor α for non-diffusive transport (Eq. 2) were between 450 - 670 mmol m^{-2} yr^{-1}, except for the sandy station MUC6 that showed a lower rate of 30 mmol m^{-2} yr^{-1}. Bioirrigation accounted for 33 - 49% of the total benthic H_4SiO_4 flux. Biogenic silica rain rates varied between 180 and 1290 mmol m^{-2} yr^{-1} with burial efficiencies of 36 - 83%. Fluxes and burial efficiencies varied between the different stations, but no clear trend was observed with water depth (Figure 5).

4.4 Modelled bSi dissolution

The model predicted that most of the net bSi dissolution takes place within the top sediment layer (Figure 3C). The adjustable parameters B_1 and B_2 that describe bSi dissolution varied between 2.3 and 2.5 cm, and -2.3 and -2.6 (dimensionless), respectively, excluding sandy station MUC6 (Table 2). At this station, B_1 and B_2 were 2.7 and -1.5, respectively. There were no clear trends in B_0, B_1 and B_2 across different sites.

5 Discussion

5.1 Biogenic silica cycling

The major fluxes of bSi in Skagerrak sediments are investigated in this study through numerical interpretation of the geochemical data. In our approach, the down-core decrease in net bSi dissolution, bioirrigation and bioturbation can be quantified with our novel kinetic bSi dissolution model with reasonable confidence. The two adjustable parameters needed to describe bSi dissolution, B_1 and B_2, show consistent values across the stations with fine-grained material, demonstrating the potential to apply the model elsewhere in comparable environments. Our kinetic description of bSi dissolution represents an alternative to previous approaches. It is especially applicable for regions where bSi dissolution rates and underlying mechanisms that control dissolution rates are unknown but where data for bSi rain rate and burial are available.

Biogenic silica burial fluxes were calculated based on ^{210}Pb derived sedimentation rates that are in the range of reported values from nearby locations (Erlenkeuser and Pederstad, 1984; Van Weering et al., 1993; Deng et al., 2020). A mean bSi burial efficiency of 50% in fine-grained sediments in the Skagerrak basin indicates that about half of the annual bSi raining onto the seafloor,

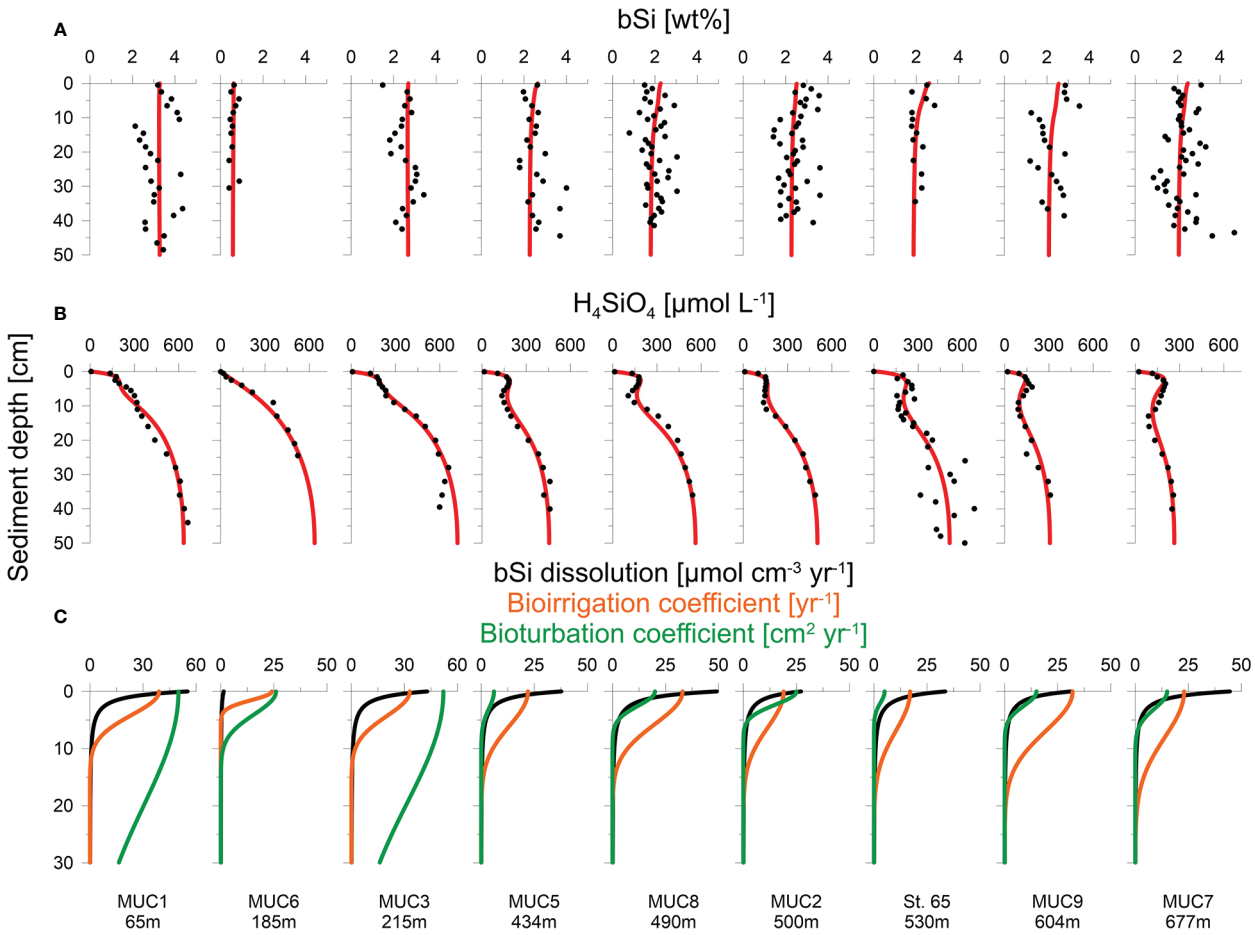

FIGURE 3
Measured data (symbols) and model simulations (curves) of **(A)** H_4SiO_4 concentration, **(B)** bSi content and **(C)** net bSi dissolution rates (black), bioirrigation coefficient (orange) and bioturbation (green). Note different depth scale in **(C)**.

on average ca. 1100 mmol m^{-2} yr^{-1}, is buried in the sediment. The other half dissolves and is subsequently returned to the water column. This calculation excludes the sandy station MUC6 and shallow stations MUC1 and MUC3, where non-exponential $^{210}Pb_{ex}$ profiles indicate substantial sediment mixing and more uncertainty in calculated bSi rain rates. The unusually intense and deep mixing rates required to simulate the data at MUC1 and MUC3 compared to other sites could be attributed to bottom trawling, which is frequent in the MUC1 region at water depths<200 m (Sköld et al., 2018). Piles of sediment alongside furrows created by dragging trawl doors through the sediment can reach 1 to 2 dm in height (Bradshaw et al., 2021) and it may be that sediment cores taken at stations MUC1 and MUC3 penetrated such sediment piles during sampling. We find this explanation more convincing than deep bioturbation since no visual evidence of macrofauna was observed below ca. 10 cm depth during the slicing of the sediment cores. Furthermore, if the bioturbation parameters were set to values similar to those predicted for the undisturbed sites, sedimentation rates of 1 to 2 cm yr^{-1} would be required to fit the $^{210}Pb_{ex}$ data (results not shown); a magnitude that seems unlikely for the Skagerrak. For a seafloor surface area of the Skagerrak basin below 200 m of about 10700 km^2, and assuming a mean bSi burial flux of 550 mmol m^{-2} yr^{-1}, we calculated a mean annual bSi burial flux of $6 \cdot 10^9$ mol yr^{-1}.

Ongoing dissolution of bSi leads to the accumulation of H_4SiO_4 in porewaters and drives H_4SiO_4 fluxes to the bottom water. Scanning electron micrographs have revealed evidence of chemical erosion of bSi in Skagerrak sediments (Meyenburg and Liebezeit, 1993). According to our model, the bulk of net bSi dissolution occurs in the upper 5 centimetres (Figure 3C). A steep down-core decline in the dissolution rate is mirrored by the steep increase in H_4SiO_4 concentrations below the sediment-water interface. This is not evident in the bSi profiles that show high variability, possibly due to interannual changes in bulk sediment supply and/or bSi rain rate. Our bSi contents are lower than ca. 6 wt % measured in a single sediment sample from the top 50 cm at 325 m water depth in the Skagerrak (Bohrmann, 1986). Meyenburg and Liebezeit (1993) and Fengler et al. (1994) reported 0.1 - 0.6 wt% bSi at water depths of 80 and 183 m, which is similar to the sandy station MUC6, although the sediment type in their data was not reported.

No obvious trends between Si fluxes and individual environmental factors were observed at our stations, despite sizeable differences in water depth. Aside from H_4SiO_4 concentration and temperature in the

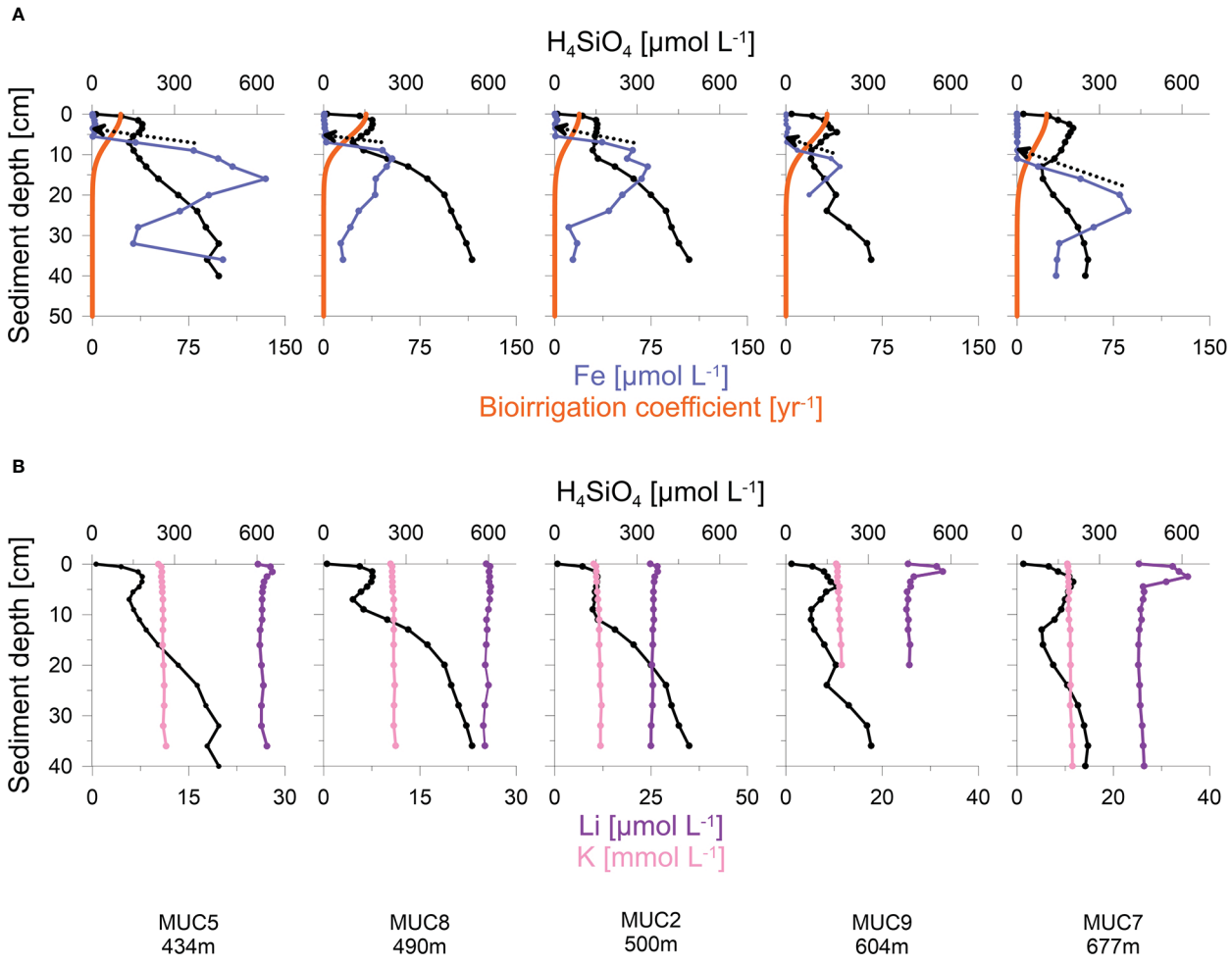

FIGURE 4
(A) Porewater concentrations of H_4SiO_4, total dissolved Fe and model simulations of bioirrigation (orange curves). Dashed arrows indicate the gradient used to calculate diffusive Fe fluxes; and **(B)** Porewater concentrations of H_4SiO_4, K and Li at deep-water stations with distinct H_4SiO_4-minima. Note different scales in Li and K concentrations.

water column, water depth typically controls the amount of bSi that reaches the seafloor (Nelson et al., 1995; Ragueneau et al., 2000; Tréguer and de la Rocha, 2013), with lower fluxes expected at deeper stations. However, apart from the sandy station MUC6, our data reveal relatively little variability in Si fluxes across stations (Figure 5; Table 2). Additional input of bSi to the deeper sites from the North Sea may partly explain this observation (see section 5.3). We observed a higher bSi burial efficiency at MUC6 where the sediment was coarser, which

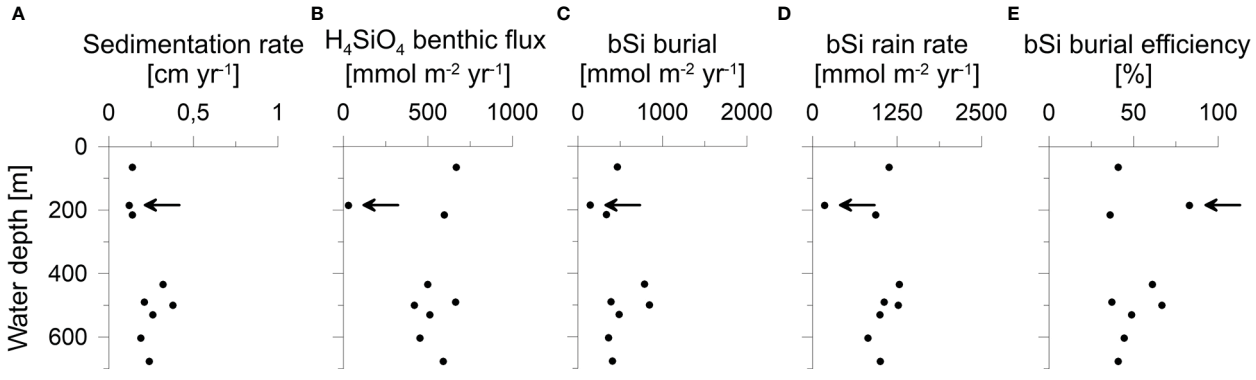

FIGURE 5
(A) Sedimentation rate, **(B)** H_4SiO_4 benthic flux, **(C)** bSi burial flux, **(D)** bSi rain rate and **(E)** burial efficiency plotted against water depth. Data at 185 m water depths correspond to the sandy station MUC6 (indicated by the arrow).

could point toward an additional control by grain size (Table 1; Figure 5E). Similar trends of burial efficiency and grain size were reported in sediments of the Helgoland mud area (Oehler et al., 2015b); a sedimentary depocenter in the southern North Sea.

To frame bSi cycling in the Skagerrak in a global context, we compared our bulk fluxes to sites compiled by Dale et al. (2021), most of which are from the deep-sea (>3000 m water depth). In general, the Skagerrak bSi burial data aligns well with the global trend (Figure 6) and extends the existing database towards continental margin sites of higher burial efficiencies and burial fluxes. The Skagerrak data is in the range of other continental margins, such as the Peru shelf (Froelich et al., 1988), the Helgoland mud area (Oehler et al., 2015b) and the Guaymas Basin (Geilert et al., 2020). Variations in bSi cycling among continental margins likely stem from a combination of different regional settings, i.e. water depth, surface productivity, sedimentation rates and sediment composition.

5.2 Controls on H_4SiO_4 porewater concentrations

The rapid downcore increase in H_4SiO_4 to a constant asymptotic concentration observed in the Skagerrak is typical for fine-grained marine sediments (Hurd, 1973; Schink et al., 1974; McManus et al., 1995; Rabouille et al., 1997; Khalil et al., 2007; Oehler et al., 2015b; Ehlert et al., 2016). The tendency for a decrease in the maximum concentration with increasing water depth has been attributed to the proportion of lithogenic material present in the sediment, whereby the release of dissolved aluminium from clay minerals and subsequent adsorption or incorporation into the particulate silica phase lowers bSi solubility (Van Beusekom et al., 1997; Van Cappellen and Qiu, 1997; Dixit et al., 2001; Dixit and Van Cappellen, 2003). At our sites, lithogenic material changed only slightly with water depth (Table 1). Consequently, inhibition of bSi dissolution by aluminium may not be a major control on H_4SiO_4 distributions in our sediment cores, although this conclusion would be strengthened with data on dissolved aluminium concentrations.

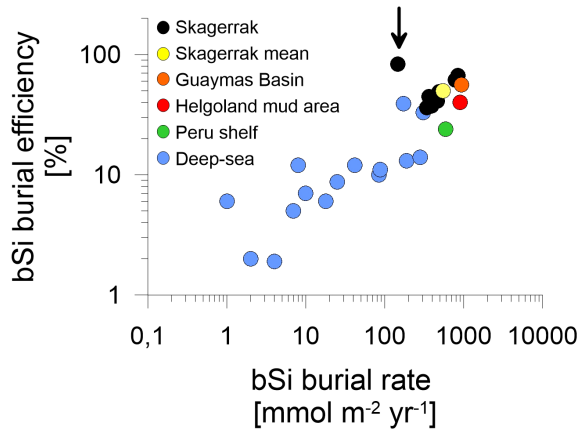

FIGURE 6
Log-log plot of regional mean bSi data adapted from the compiled dataset presented by Dale et al. (2021). Biogenic silica burial rates are plotted against bSi burial efficiencies. Individual Skagerrak stations (black) and a Skagerrak mean value of stations > 400 m water depth (yellow) are compared to deep-sea regions at >3000 m water depth (blue), the Peru shelf (green) by Froelich et al. (1988), the Helgoland mud area (red) by Oehler et al. (2015b) and the Guaymas Basin (orange) by Geilert et al. (2020). Data indicated by the arrow corresponds to sandy station MUC6.

Especially at the deeper stations (>400 m), H_4SiO_4 porewater profiles were characterized by decreases or local minima of H_4SiO_4 concentrations between 2 - 15 cm (Figure 3B). The model predicts that the H_4SiO_4 minima are caused by more intense removal of H_4SiO_4 in discrete sediment layers by bioirrigation versus H_4SiO_4 added by bSi dissolution. It further predicts more intense bioirrigation at the deeper stations where the minima are more pronounced (Figure 3C). This is supported by reports that deep-water Skagerrak sediments are preferably colonized by deeply penetrating deposit feeders, whereas suspension and interface feeders are more abundant at shallower depths (Rosenberg et al., 1996; Dauwe et al., 1998). However, our results differ from Kristensen et al. (2018), who observed decreasing bioirrigation intensity with water depth. In addition, our modelled bioirrigation extends deeper than the zone where dissolved Fe is below the detection limit (Figure 4A). Given that bioirrigation enhances the transport of oxidants into the sediment, and that dissolved Fe is rapidly oxidized, this may indicate that our model overestimates the depth of bioirrigation. Hence, it might be possible that the H_4SiO_4 minima observed at deeper sites are not caused by deep-reaching bioirrigation. Instead, high rates of H_4SiO_4 removal by adsorption or precipitation might lower H_4SiO_4 concentrations in distinct sediment layers.

High sedimentary manganese and iron oxide contents have been reported for the Skagerrak, especially in deep waters (Canfield et al., 1993a; Thamdrup et al., 1994). Experimental studies have demonstrated that H_4SiO_4 can adsorb to iron oxides (Huang, 1975; Sigg and Stumm, 1981; Swedlund, 1999; Davis et al., 2001; Davis et al., 2002), suggesting that this process is a potential sink for H_4SiO_4 in Skagerrak sediments. Since the depths of local H_4SiO_4 minima and dissolved iron removal coincide (Figure 4A), this sink may be relevant for the formation of observed H_4SiO_4 minima. In order to estimate the significance of this process, potential H_4SiO_4 adsorption fluxes were calculated from the diffusive flux of Fe and then compared to H_4SiO_4 removal by bioirrigation integrated over the depth interval centred on the H_4SiO_4 minima, typically spanning 5 cm (Figure 4A). Under the assumption that all dissolved Fe is consumed by iron oxide formation, the diffusive flux of Fe (Eq. 2) was calculated at the depth where Fe increases. With a diffusion coefficient (D_{sed}) of 121 $cm^2\ yr^{-1}$ (Schulz and Zabel, 2006), dissolved Fe removal fluxes of 6 - 14 mmol $m^{-2}\ yr^{-1}$ were calculated for the stations shown in Figure 4. Given mean H_4SiO_4 concentrations at the depth of H_4SiO_4 minima of ca. 150 µmol L^{-1} and assuming a pH value of 8, a molar Si/Fe sorption density on iron oxides of 0.2 is expected (Davis et al., 2002). Multiplying the Fe flux by the molar Si/Fe ratio yields potential H_4SiO_4 adsorption fluxes of 1 - 3 mmol $m^{-2}\ yr^{-1}$. This corresponds to only 2 - 6% of bioirrigation fluxes integrated over the depth of H_4SiO_4 minima. It illustrates that H_4SiO_4 adsorption to iron oxides may be a feasible but probably not a dominant pathway of local H_4SiO_4 removal in Skagerrak sediments.

During authigenic clay formation, H_4SiO_4 is consumed in the presence of dissolved cations (e.g. K and Li) and weathered clay

minerals, a process referred to as reverse weathering (Mackenzie et al., 1981; Mackenzie and Kump, 1995; Loucaides et al., 2010; Ehlert et al., 2016). Reverse weathering occurs in anoxic marine sediments rich in biogenic opal and metal hydroxides (Michalopoulos and Aller, 1995; Michalopoulos et al., 2000) but has not been investigated in the Skagerrak. Previous studies have demonstrated reverse weathering to be a dominant process altering H_4SiO_4 porewater profiles on continental margins (Michalopoulos and Aller, 1995; Michalopoulos and Aller, 2004; Wallmann et al., 2008; Ehlert et al., 2016; Spiegel et al., 2021). Furthermore, the competition between bSi dissolution and reprecipitation during reverse weathering can create features similar to the H_4SiO_4 minima in our dataset (Spiegel et al., 2021). Since dissolved cations are consumed during reverse weathering, we compared the porewater distribution of H_4SiO_4 to dissolved K and Li concentrations (Figure 4B). The concentration profiles of K and Li are near-constant with sediment depth and, thus, do not show obvious indications for reverse weathering, i.e. uptake in the same horizon as H_4SiO_4 minima. However, we note that the effect of reverse weathering on dissolved cation concentrations, especially for K (~10 mM), might be too low relative to bulk porewater concentrations to result in distinct porewater signatures.

Since our model describes a continuous decline in net bSi dissolution with sediment depth, we are currently unable to resolve processes that operate in narrow depth intervals where the H_4SiO_4 porewater plateaus are observed. Hence, explicitly describing adsorption, precipitation and aluminium inhibition could lead to a better fit to the data and consequently to a more detailed description of the benthic bSi cycle in the Skagerrak. A model that includes these additional sinks may also be able to reproduce the data using shallower penetration depths of bioirrigation that are more consistent with those that have been previously reported by Kristensen et al. (2018). Further empirical data on these processes in Skagerrak sediments and elsewhere would benefit future bSi model descriptions. Since their parameterization is uncertain on the basis of our dataset and yet to be investigated in the Skagerrak, we reiterate that our simple model currently only provides net bSi dissolution rates.

5.3 Effect of lateral sediment supply on bSi/TOC ratios

DeMaster (2002) calculated global bSi burial on continental margins of 1.8 - 2.8 · 10^{12} mol yr^{-1} based on organic carbon burial and a mean molar bSi/TOC burial ratio of 0.6. However, DeMaster (2002) and subsequent budgets (Tréguer and de la Rocha, 2013; DeMaster, 2019) excluded continental margins dominated by high lithogenic loads, such as the Skagerrak, in their calculations. Rahman et al. (2016) and Rahman et al. (2017) reported bSi burial fluxes based on ^{32}Si isotopes in tropical and subtropical deltaic regions dominated by significant lithogenic inputs. Their results, when incorporated into more recent global Si budgets, point toward a greater significance of margins in total bSi burial (Tréguer et al., 2021). Since we have no ^{32}Si data, we compared our findings to previous approaches utilizing sedimentary bSi/TOC molar ratios. Based on our field data (Table 1), we calculated a mean bSi/TOC molar ratio of 0.22 in Skagerrak sediments, which is distinctively lower than the mean ratio of 0.6 applied by DeMaster (2002). Other continental margin settings with high lithogenic inputs and where bSi was determined by the same method (Müller and Schneider, 1993) showed molar ratios of 1.0 for the Guaymas basin (Geilert et al., 2020), 0.52 for the Helgoland mud area (Oehler et al., 2015a; Oehler et al., 2015b) and 0.55 for the Amazon shelf (Spiegel et al., 2021). Dale et al. (2021) reported much lower ratios of 0.14 for the Peruvian oxygen minimum zone, which was attributed to a lack of bioturbation and enhanced bSi dissolution in undersaturated surface sediment layers. Tréguer et al. (2021) reported ratios between 2.4 and 11 in tropical and subtropical deltaic systems. The wide range in molar bSi/TOC ratios, presumably related to the differing diagenetic regimes, emphasizes the need to further study continental margins to better constrain global bSi burial.

Low bSi/TOC ratios in the Skagerrak may be confounded by the long transit time of sediments on the order of several months from the central North Sea and 1 - 2 years from the southern North Sea to the Skagerrak (Hainbucher et al., 1987; Dahlgaard et al., 1995; Salomon et al., 1995). Since seawater is undersaturated with respect to bSi, we hypothesize repeated resuspension and deposition during particle transport leads to more extensive bSi dissolution relative to POC. This may set the Skagerrak apart from most other continental margins with regard to the coupling between bSi and TOC. Similar regions need to be investigated in order to determine whether the Skagerrak is a unique environment with regards to bSi cycling or is emblematic of continental margins exhibiting protracted transport pathways.

6 Conclusions

In this study, we present bSi cycling in Skagerrak sediments based on geochemical data and modelling. Approximately 1100 mmol m^{-2} yr^{-1} of bSi annually rains onto the seafloor at the sites investigated, of which half dissolves in sediments and is reintroduced into the water column and half is permanently buried. Biogenic silica cycling shows some spatial variability across stations, which can probably be explained by differences in water depth, sedimentation rate and sediment grain size. At deep-water sites, we observed distinct minima or plateaus in the porewater profiles of H_4SiO_4 that are likely caused by deep-reaching bioirrigation rather than H_4SiO_4 removal by adsorption to iron oxide minerals. The contribution of reverse weathering to these minima remains uncertain. Biogenic silica cycling in the Skagerrak generally aligns with the global trends and shows comparable burial fluxes and burial efficiencies to other margins. However, Skagerrak sediments are characterized by distinctively lower molar bSi/TOC ratios compared to most other continental margins, which we suggest is due to decoupling between bSi and organic carbon during the long travel time of suspended matter transported from the North Sea. It is currently unclear whether Si cycling in the Skagerrak behaves similarly to other depocenters where sediment is first transported over large distances before it finally accumulates on the seafloor. The model presented here simulates bSi cycling and quantifies net bSi dissolution,

bioirrigation and bioturbation in Skagerrak sediments with few adjustable parameters but does not yet fully resolve the mechanisms behind H_4SiO_4 release and removal that operate in distinct and narrow depth intervals. Further work on the parameterization of bSi adsorption, reprecipitation and inhibition of bSi dissolution by aluminium would improve the predicted bSi kinetics. Our results contribute to the global dataset on bSi cycling and demonstrate the importance of continuing investigations in different regions, especially on continental margins, to better understand regional variability in bSi cycling and to constrain global Si budgets.

Data availability statement

The original contributions presented in the study are included in the article/Supplementary Material. Further inquiries can be directed to the corresponding author.

Author contributions

TS processed most of the samples in the laboratory and wrote the manuscript. TS, KW and AD developed the numerical model used in the study and contributed with discussions. NL helped with cruise planning, sample preparation in the laboratory and contributed with discussions. MS coordinated the research cruise Al561 and contributed with discussions. SS coordinated the biogeochemical observatory (BIGO) deployments and helped with evaluating the BIGO data. HK helped with the ^{210}Pb analyses and contributed with discussions. AP provided the porewater data for station 65. SL provided the grain-size data and helped with the interpretation. All authors contributed to the paper by drafting, reading, finalizing, and approving the text. All authors contributed to the article and approved the submitted version.

Funding

Funding for this study was provided by the Federal Ministry of Education and Research, Germany, *via* the APOC project (03F0874B) – “Anthropogenic impacts on particulate organic carbon cycling in the North Sea”. AP was funded by the Federal Ministry of Education and Research, Germany, *via* the CARBOSTORE project (03F0875A) – "Carbon Storage in German Coastal Seas.

Acknowledgments

We wish to thank the captain and crew of RV Alkor for supporting our research at sea, as well as our colleagues Regina Surberg, Bettina Domeyer, Anke Bleyer, Matthias Türk, Asmus Petersen and Christoph Böttner for their help onboard during the cruise and in the GEOMAR laboratories. We thank Andreas Neumann from the Helmholtz-Zentrum Hereon (Geesthacht, Germany) for providing sediment samples from RV Alkor cruise Al557. We would also like to acknowledge Bernd Kopka and Marvin Blaue from the Laboratory for Radioisotopes at the University of Göttingen and Christian Kunze and Robert Arndt from the IAF Dresden for the ^{210}Pb analyses.

Conflict of interest

The authors declare that the research was conducted in the absence of any commercial or financial relationships that could be construed as a potential conflict of interest.

Publisher’s note

Supplementary material

The Supplementary Material for this article can be found online at: https://www.frontiersin.org/articles/10.3389/fmars.2023.1141448/full#supplementary-material

References

Archer, D., Lyle, M., Rodgers, K., and Froelich, P. (1993). What Controls Opal Preservation in Tropical Deep-Sea Sediments? *Paleoceanography* 8, 7–21. doi: 10.1029/92PA02803

Beckmann, M., and Liebezeit, G. (1988). Organic carbon in the north Sea in May/June 1986: Distribution and controlling factors. *Mitt. Geol.-Palaontol. Inst. Univ. Hamburg* 65, 99–116.

Berner, R. A. (1980). *Early diagenesis: A theoretical approach, Princeton series in geochemistry* (Princeton, N.J: Princeton University Press).

Blott, S. J., and Pye, K. (2001). GRADISTAT: A grain size distribution and statistics package for the analysis of unconsolidated sediments. *Earth Surf. Process. Landf.* 26, 1237–1248. doi: 10.1002/esp.261

Bohrmann, G. (1986). Accumulation of biogenie silica and opal dissolution in upper quaternary skagerrak sediments. *Geo-Mar. Lett.* 6, 165–172. doi: 10.1007/BF02238088

Boudreau, B. P. (1990). Asymptotic forms and solutions of the model for silica-opal diagenesis in bioturbated sediments. *J. Geophys. Res.* 95, 7367. doi: 10.1029/JC095iC05p07367

Boudreau, B. P., Arnosti, C., Jørgensen, B. B., and Canfield, D. E. (2008). Comment on “Physical model for the decay and preservation of marine organic carbon.” *Science* 319, 1616–1616. doi: 10.1126/science.1148589

Boudreau, B. P., and Ruddick, B. R. (1991). On a reactive continuum representation of organic matter diagenesis. *Am. J. Sci.* 291, 507–538. doi: 10.2475/ajs.291.5.507

Bradshaw, C., Jakobsson, M., Brüchert, V., Bonaglia, S., Mörth, C.-M., Muchowski, J., et al. (2021). Physical disturbance by bottom trawling suspends particulate matter

and alters biogeochemical processes on and near the seafloor. *Front. Mar. Sci.* 8. doi: 10.3389/fmars.2021.683331

Canfield, D. E., Jørgensen, B. B., Fossing, H., Glud, R., Gundersen, J., Ramsing, N. B., et al. (1993a). Pathways of organic carbon oxidation in three continental margin sediments. *Mar. Geol.* 113, 27–40. doi: 10.1016/0025-3227(93)90147-N

Canfield, D. E., Thamdrup, B., and Hansen, J. W. (1993b). The anaerobic degradation of organic matter in Danish coastal sediments: Iron reduction, manganese reduction, and sulfate reduction. *Geochim. Cosmochim. Acta* 57, 3867–3883. doi: 10.1016/0016-7037(93)90340-3

Dahlgaard, H., Herrmann, J., and Salomon, J. C. (1995). A tracer study of the transport of coastal water from the English channel through the German bight to the kattegat. *J. Mar. Syst.* 6, 415–425. doi: 10.1016/0924-7963(95)00017-J

Dale, A. W., Paul, K. M., Clemens, D., Scholz, F., Schroller-Lomnitz, U., Wallmann, K., et al. (2021). Recycling and burial of biogenic silica in an open margin oxygen minimum zone. *Glob. Biogeochem. Cycles* 35, e2020GB006583. doi: 10.1029/2020GB006583

Dauwe, B., Herman, P., and Heip, C. (1998). Community structure and bioturbation potential of macrofauna at four north Sea stations with contrasting food supply. *Mar. Ecol. Prog. Ser.* 173, 67–83. doi: 10.3354/meps173067

Davis, C. C., Chen, H.-W., and Edwards, M. (2002). Modeling silica sorption to iron hydroxide. *Environ. Sci. Technol.* 36, 582–587. doi: 10.1021/es010996t

Davis, C. C., Knocke, W. R., and Edwards, M. (2001). Implications of aqueous silica sorption to iron hydroxide: Mobilization of iron colloids and interference with sorption of arsenate and humic substances. *Environ. Sci. Technol.* 35, 3158–3162. doi: 10.1021/es0018421

De Haas, H., and Van Weering, T. C. E. (1997). Recent sediment accumulation, organic carbon burial and transport in the northeastern north Sea. *Mar. Geol.* 136, 173–187. doi: 10.1016/S0025-3227(96)00072-2

DeMaster, D. J. (1981). The supply and accumulation of silica in the marine environment. *Geochim. Cosmochim. Acta* 45, 1715–1732. doi: 10.1016/0016-7037(81)90006-5

DeMaster, D. J. (1991). "Measuring biogenic silica in marine sediments and suspended matter," in *Geophysical monograph series*. Eds. D. C. Hurd and D. W. Spencer (Washington, D. C.: American Geophysical Union), 363–367. doi: 10.1029/GM063p0363

DeMaster, D. J. (2002). The accumulation and cycling of biogenic silica in the southern ocean: Revisiting the marine silica budget. *Deep Sea Res. Part II Top. Stud. Oceanogr.* 49, 3155–3167. doi: 10.1016/S0967-0645(02)00076-0

DeMaster, D. J. (2019). "The global marine silica budget: Sources and sinks," in *Encyclopedia of ocean sciences*, vol. 3 . Eds. K. Cochran, H. Bokuniewicz and P. Yager (Elsevier Academic Press), 473–483. doi: 10.1016/B978-0-12-409548-9.10799-7

Deng, L., Bölsterli, D., Kristensen, E., Meile, C., Su, C.-C., Bernasconi, S. M., et al. (2020). Macrofaunal control of microbial community structure in continental margin sediments. *Proc. Natl. Acad. Sci.* 117, 15911–15922. doi: 10.1073/pnas.1917494117

Dixit, S., and Van Cappellen, P. (2003). Predicting benthic fluxes of silicic acid from deep-sea sediments. *J. Geophys. Res.* 108, 3334. doi: 10.1029/2002JC001309

Dixit, S., Van Cappellen, P., and van Bennekom, A. J. (2001). Processes controlling solubility of biogenic silica and pore water build-up of silicic acid in marine sediments. *Mar. Chem.* 73, 333–352. doi: 10.1016/S0304-4203(00)00118-3

Dugdale, R. C., Wilkerson, F. P., and Minas, H. J. (1995). The role of a silicate pump in driving new production. *Deep Sea Res. Part Oceanogr. Res. Pap.* 42, 697–719. doi: 10.1016/0967-0637(95)00015-X

Ehlert, C., Doering, K., Wallmann, K., Scholz, F., Sommer, S., Grasse, P., et al. (2016). Stable silicon isotope signatures of marine pore waters – biogenic opal dissolution versus authigenic clay mineral formation. *Geochim. Cosmochim. Acta* 191, 102–117. doi: 10.1016/j.gca.2016.07.022

Eisma, D., and Kalf, J. (1987). Dispersal, concentration and deposition of suspended matter in the north Sea. *J. Geol. Soc* 144, 161–178. doi: 10.1144/gsjgs.144.1.0161

Erlenkeuser, H., and Pederstad, K. (1984). Recent sediment accumulation in skagerrak as depicted by 210pb-dating. *Nor. Geol. Tidsskr.* 64, 135–152.

Fengler, G., Grossman, D., Kersten, M., and Liebezeit, G. (1994). Trace metals in humic acids from recent skagerrak sediments. *Mar. pollut. Bull.* 28, 143–147. doi: 10.1016/0025-326X(94)90389-1

Folk, R. L., and Ward, W. C. (1957). Brazos river bar [Texas]; a study in the significance of grain size parameters. *J. Sediment. Res.* 27, 3–26. doi: 10.1306/74D70646-2B21-11D7-8648000102C1865D

Froelich, P. N., Arthur, M. A., Burnett, W. C., Deakin, M., Hensley, V., Jahnke, R., et al. (1988). Early diagenesis of organic matter in Peru continental margin sediments: Phosphorite precipitation. *Mar. Geol.* 80, 309–343. doi: 10.1016/0025-3227(88)90095-3

Geilert, S., Grasse, P., Doering, K., Wallmann, K., Ehlert, C., Scholz, F., et al. (2020). Impact of ambient conditions on the Si isotope fractionation in marine pore fluids during early diagenesis. *Biogeosciences* 17, 1745–1763. doi: 10.5194/bg-17-1745-2020

Gran-Stadniczeñko, S., Egge, E., Hostyeva, V., Logares, R., Eikrem, W., and Edvardsen, B. (2019). Protist diversity and seasonal dynamics in skagerrak plankton communities as revealed by metabarcoding and microscopy. *J. Eukaryot. Microbiol.* 66, 494–513. doi: 10.1111/jeu.12700

Hansen, H.P., and Koroleff, F. (1999). Determination of nutrients. In *Methods of seawater analysis. 1st ed*. Grasshoff, K., Kremling, K., and Ehrhardt, M. eds. doi: 10.1002/9783527613984.ch10

Hainbucher, D., Pohlmann, T., and Backhaus, J. (1987). Transport of conservative passive tracers in the north Sea: First results of a circulation and transport model. *Cont. Shelf Res.* 7, 1161–1179. doi: 10.1016/0278-4343(87)90083-5

Hall, P. O. J., Hulth, S., Hulthe, G., Landén, A., and Tengberg, A. (1996). Benthic nutrient fluxes on a basin-wide scale in the skagerrak (North-Eastern north Sea). *J. Sea Res.* 35, 123–137. doi: 10.1016/S1385-1101(96)90741-8

Huang, C. P. (1975). The removal of aqueous silica from dilute aqueous solution. *Earth Planet. Sci. Lett.* 27, 265–274. doi: 10.1016/0012-821X(75)90038-2

Hurd, D. C. (1973). Interactions of biogenic opal, sediment and seawater in the central equatorial pacific. *Geochim. Cosmochim. Acta* 37, 2257–2282. doi: 10.1016/0016-7037(73)90103-8

Kamatani, A., Ejiri, N., and Treguer, P. (1988). The dissolution kinetics of diatom ooze from the Antarctic area. *Deep Sea Res. Part Oceanogr. Res. Pap.* 35, 1195–1203. doi: 10.1016/0198-0149(88)90010-6

Kamatani, A., and Oku, O. (2000). Measuring biogenic silica in marine sediments. *Mar. Chem.* 68, 219–229. doi: 10.1016/S0304-4203(99)00079-1

Khalil, K., Rabouille, C., Gallinari, M., Soetaert, K., DeMaster, D. J., and Ragueneau, O. (2007). Constraining biogenic silica dissolution in marine sediments: A comparison between diagenetic models and experimental dissolution rates. *Mar. Chem.* 106, 223–238. doi: 10.1016/j.marchem.2006.12.004

Kristensen, E., Røy, H., Debrabant, K., and Valdemarsen, T. (2018). Carbon oxidation and bioirrigation in sediments along a skagerrak-Kattegat-Belt Sea depth transect. *Mar. Ecol. Prog. Ser.* 604, 33–50. doi: 10.3354/meps12734

Loucaides, S., Michalopoulos, P., Presti, M., Koning, E., Behrends, T., and Van Cappellen, P. (2010). Seawater-mediated interactions between diatomaceous silica and terrigenous sediments: Results from long-term incubation experiments. *Chem. Geol.* 270, 68–79. doi: 10.1016/j.chemgeo.2009.11.006

Mackenzie, F. T., and Kump, L. R. (1995). Reverse weathering, clay mineral formation, and oceanic element cycles. *Science* 270, 586–586. doi: 10.1126/science.270.5236.586

Mackenzie, F. T., Ristvet, B. L., Thorstenson, C. D., Lerman, A., and Leeper, R. H. (1981). "Reverse weathering and chemical mass balance in a coastal environment," In Martin, J. M., Burton, J. D., and Eisma, D. eds. *River inputs from ocean systems* (UNEP-UNESCO, Switzerland), 152–187.

McManus, J., Hammond, D. E., Berelson, W. M., Kilgore, T. E., Demaster, D. J., Ragueneau, O. G., et al. (1995). Early diagenesis of biogenic opal: Dissolution rates, kinetics, and paleoceanographic implications. *Deep Sea Res. Part II Top. Stud. Oceanogr.* 42, 871–903. doi: 10.1016/0967-0645(95)00035-O

Meyenburg, G., and Liebezeit, G. (1993). Mineralogy and geochemistry of a core from the Skagerrak/Kattegat boundary. *Mar. Geol.* 111, 337–344. doi: 10.1016/0025-3227(93)90139-M

Michalopoulos, P., and Aller, R. C. (1995). Rapid clay mineral formation in Amazon delta sediments: Reverse weathering and oceanic elemental cycles. *Sci. New Ser.* 270, 614–617. doi: 10.1126/science.270.5236.614

Michalopoulos, P., and Aller, R. C. (2004). Early diagenesis of biogenic silica in the Amazon delta: Alteration, authigenic clay formation, and storage. *Geochim. Cosmochim. Acta* 68, 1061–1085. doi: 10.1016/j.gca.2003.07.018

Michalopoulos, P., Aller, R. C., and Reeder, R. J. (2000). Conversion of diatoms to clays during early diagenesis in tropical, continental shelf muds. *Geology* 28, 1095. doi: 10.1130/0091-7613(2000)28<1095:CODTCD>2.0.CO;2

Middelburg, J. J. (1989). A simple rate model for organic matter decomposition in marine sediments. *Geochim. Cosmochim. Acta* 53, 1577–1581. doi: 10.1016/0016-7037(89)90239-1

Müller, P. J., and Schneider, R. (1993). An automated leaching method for the determination of opal in sediments and particulate matter. *Deep Sea Res. Part Oceanogr. Res. Pap.* 40, 425–444. doi: 10.1016/0967-0637(93)90140-X

Nelson, D. M., Ahern, J. A., and Herlihy, L. J. (1991). Cycling of biogenic silica within the upper water column of the Ross Sea. *Mar. Chem.* 35, 461–476. doi: 10.1016/S0304-4203(09)90037-8

Nelson, D. M., and Gordon, L. I. (1982). Production and pelagic dissolution of biogenic silica in the southern ocean. *Geochim. Cosmochim. Acta* 46, 491–501. doi: 10.1016/0016-7037(82)90153-3

Nelson, D. M., Tréguer, P., Brzezinski, M. A., Leynaert, A., and Quéguiner, B. (1995). Production and dissolution of biogenic silica in the ocean: Revised global estimates, comparison with regional data and relationship to biogenic sedimentation. *Glob. Biogeochem. Cycles* 9, 359–372. doi: 10.1029/95GB01070

Oehler, T., Martinez, R., Schückel, U., Winter, C., Kröncke, I., and Schlüter, M. (2015a). Seasonal and spatial variations of benthic oxygen and nitrogen fluxes in the helgoland mud area (southern north Sea). *Cont. Shelf Res.* 106, 118–129. doi: 10.1016/j.csr.2015.06.009

Oehler, T., Schlüter, M., and Schückel, U. (2015b). Seasonal dynamics of the biogenic silica cycle in surface sediments of the helgoland mud area (southern north Sea). *Cont. Shelf Res.* 107, 103–114. doi: 10.1016/j.csr.2015.07.016

Otto, L., Zimmerman, J. T. F., Furnes, G. K., Mork, M., Saetre, R., and Becker, G. (1990). Review of the physical oceanography of the north Sea. *Neth. J. Sea Res.* 26, 161–238. doi: 10.1016/0077-7579(90)90091-T

Paetzel, M., Schrader, H., and Bjerkli, K. (1994). Do decreased trace metal concentrations in surficial skagerrak sediments over the last 15–30 years indicate decreased pollution? *Environ. pollut.* 84, 213–226. doi: 10.1016/0269-7491(94)90132-5

Rabouille, C., Gaillard, J.-F., Tréguer, P., and Vincendeau, M.-A. (1997). Biogenic silica recycling in surficial sediments across the polar front of the southern ocean (Indian sector). *Deep Sea Res. Part II Top. Stud. Oceanogr.* 44, 1151–1176. doi: 10.1016/S0967-0645(96)00108-7

Ragueneau, O., Schultes, S., Bidle, K., Claquin, P., and Moriceau, B. (2006). Si And c interactions in the world ocean: Importance of ecological processes and implications for the role of diatoms in the biological pump: Si AND c INTERACTIONS IN THE OCEAN. *Glob. Biogeochem. Cycles* 20, GB4S02. doi: 10.1029/2006GB002688

Ragueneau, O., and Tréguer, P. (1994). Determination of biogenic silica in coastal waters: Applicability and limits of the alkaline digestion method. *Mar. Chem.* 45, 43–51. doi: 10.1016/0304-4203(94)90090-6

Ragueneau, O., Tréguer, P., Leynaert, A., Anderson, R. F., Brzezinski, M. A., DeMaster, D. J., et al. (2000). A review of the Si cycle in the modern ocean: Recent progress and missing gaps in the application of biogenic opal as a paleoproductivity proxy. *Glob. Planet. Change* 26, 317–365. doi: 10.1016/S0921-8181(00)00052-7

Rahman, S., Aller, R. C., and Cochran, J. K. (2016). Cosmogenic ^{32} Si as a tracer of biogenic silica burial and diagenesis: Major deltaic sinks in the silica cycle. *Geophys. Res. Lett.* 43, 7124–7132. doi: 10.1002/2016GL069929

Rahman, S., Aller, R. C., and Cochran, J. K. (2017). The missing silica sink: Revisiting the marine sedimentary Si cycle using cosmogenic ^{32} Si: The missing sedimentary silica sink. *Glob. Biogeochem. Cycles* 31, 1559–1578. doi: 10.1002/2017GB005746

Rebreanu, L., Vanderborght, J.-P., and Chou, L. (2008). The diffusion coefficient of dissolved silica revisited. *Mar. Chem.* 112, 230–233. doi: 10.1016/j.marchem.2008.08.004

Ringuet, S., Sassano, L., and Johnson, Z. I. (2011). A suite of microplate reader-based colorimetric methods to quantify ammonium, nitrate, orthophosphate and silicate concentrations for aquatic nutrient monitoring. *J. Env. Monit* 13, 370–376. doi: 10.1039/C0EM00290A

Rosenberg, R., Hellman, B., and Lundberg, A. (1996). Benthic macrofaunal community structure in the Norwegian trench, deep skagerrak. *J. Sea Res.* 35, 181–188. doi: 10.1016/S1385-1101(96)90745-5

Salomon, J. C., Breton, M., and Guegueniat, P. (1995). A 2D long term advection–dispersion model for the channel and southern north Sea part b: Transit time and transfer function from cap de la Hague. *J. Mar. Syst.* 6, 515–527. doi: 10.1016/0924-7963(95)00021-G

Sayles, F. L., Martin, W. R., Chase, Z., and Anderson, R. F. (2001). Benthic remineralization and burial of biogenic SiO2, CaCO3, organic carbon, and detrital material in the southern ocean along a transect at 170° West. *Deep Sea Res. Part II Top. Stud. Oceanogr.* 48, 4323–4383. doi: 10.1016/S0967-0645(01)00091-1

Schink, D. R., Fanning, K. A., and Pilson, M. E. Q. (1974). Dissolved silica in the upper pore waters of the Atlantic ocean floor. *J. Geophys. Res.* 79, 2243–2250. doi: 10.1029/JC079i015p02243

Schlüter, M., and Sauter, E. (2000). Biogenic silica cycle in surface sediments of the Greenland Sea. *J. Mar. Syst.* 23, 333–342. doi: 10.1016/S0924-7963(99)00070-6

Schmidt, M., Sommer, S., Böttner, C., Dale, A. W., Lenz, N., Spiegel, T., et al (2021). *Dynamics and variability of POC burial in depocenters of the North Sea (Skagerrak), Cruise No. AL561, 2.08.2021 – 13.08.2021, Kiel – Kiel, APOC, Alkor-Berichte, AL561* (Kiel, Germany: GEOMAR Helmholtz Centre for Ocean Research Kiel), 34 pp. doi: 10.3289/CR_AL561

Schmidt, M., Botz, R., Rickert, D., Bohrmann, G., Hall, S. R., and Mann, S. (2001). Oxygen isotopes of marine diatoms and relations to opal-a maturation. *Geochim. Cosmochim. Acta* 65, 201–211. doi: 10.1016/S0016-7037(00)00534-2

Schulz, H. D., and Zabel, M. (2006). *Marine geochemistry* (Berlin/Heidelberg: Springer-Verlag). doi: 10.1007/3-540-32144-6

Sigg, L., and Stumm, W. (1981). The interaction of anions and weak acids with the hydrous goethite (α-FeOOH) surface. *Colloids Surf.* 2, 101–117. doi: 10.1016/0166-6622(81)80001-7

Sköld, M., Göransson, P., Jonsson, P., Bastardie, F., Blomqvist, M., Agrenius, S., et al. (2018). Effects of chronic bottom trawling on soft-seafloor macrofauna in the kattegat. *Mar. Ecol. Prog. Ser.* 586, 41–55. doi: 10.3354/meps12434

Sommer, S., Linke, P., Pfannkuche, O., Schleicher, T., Schneider v. D, D., Reitz, A., et al. (2009). Seabed methane emissions and the habitat of frenulate tubeworms on the captain arutyunov mud volcano (Gulf of cadiz). *Mar. Ecol. Prog. Ser.* 382, 69–86. doi: 10.3354/meps07956

Spiegel, T., Vosteen, P., Wallmann, K., Paul, S. A. L., Gledhill, M., and Scholz, F. (2021). Updated estimates of sedimentary potassium sequestration and phosphorus release on the Amazon shelf. *Chem. Geol.* 560, 120017. doi: 10.1016/j.chemgeo.2020.120017

Ståhl, H., Tengberg, A., Brunnegård, J., Bjørnbom, E., Forbes, T. L., Josefson, A. B., et al. (2004). Factors influencing organic carbon recycling and burial in skagerrak sediments. *J. Mar. Res.* 62, 867–907. doi: 10.1357/0022240042880873

Stevens, R. L., Bengtsson, H., and Lepland, A. (1996). Textural provinces and transport interpretations with fine-grained sediments in the skagerrak. *J. Sea Res.* 35, 99–110. doi: 10.1016/S1385-1101(96)90739-X

Stolpovsky, K., Dale, A. W., and Wallmann, K. (2015). Toward a parameterization of global-scale organic carbon mineralization kinetics in surface marine sediments: Benthic carbon mineralization. *Glob. Biogeochem. Cycles* 29, 812–829. doi: 10.1002/2015GB005087

Swedlund, P. (1999). Adsorption and polymerisation of silicic acid on ferrihydrite, and its effect on arsenic adsorption. *Water Res.* 33, 3413–3422. doi: 10.1016/S0043-1354(99)00055-X

Thamdrup, B., Fossing, H., and Jørgensen, B. B. (1994). Manganese, iron and sulfur cycling in a coastal marine sediment, Aarhus bay, Denmark. *Geochim. Cosmochim. Acta* 58, 5115–5129. doi: 10.1016/0016-7037(94)90298-4

Thomas, H., Freund, W., Mears, C., Meckel, E., Minutolo, F., Nantke, C., et al. (2022). *ALKOR scientific cruise report. the ocean's alkalinity - connecting geological and metabolic processes and time-scales: mechanisms and magnitude of metabolic alkalinity generation in the north Sea cruise no. AL557* Vol. 22 (Kiel, Germany: GEOMAR Helmholtz-Zentrum für Ozeanforschung Kiel).

Tréguer, P., Bowler, C., Moriceau, B., Dutkiewicz, S., Gehlen, M., Aumont, O., et al. (2018). Influence of diatom diversity on the ocean biological carbon pump. *Nat. Geosci.* 11, 27–37. doi: 10.1038/s41561-017-0028-x

Tréguer, P. J., and de la Rocha, C. L. (2013). The world ocean silica cycle. *Annu. Rev. Mar. Sci.* 5, 477–501. doi: 10.1146/annurev-marine-121211-172346

Tréguer, P., Nelson, D. M., Van Bennekom, A. J., DeMaster, D. J., Leynaert, A., and Quéguiner, B. (1995). The silica balance in the world ocean: A reestimate. *Science* 268, 375–379. doi: 10.1126/science.268.5209.375

Tréguer, P. J., Sutton, J. N., Brzezinski, M., Charette, M. A., Devries, T., Dutkiewicz, S., et al. (2021). Reviews and syntheses: The biogeochemical cycle of silicon in the modern ocean. *Biogeosciences* 18, 1269–1289. doi: 10.5194/bg-18-1269-2021

Van Beusekom, J. E. E., Van Bennekom, A. J., Tréguer, P., and Morvan, J. (1997). Aluminium and silicic acid in water and sediments of the enderby and crozet basins. *Deep Sea Res. Part II Top. Stud. Oceanogr.* 44, 987–1003. doi: 10.1016/S0967-0645(96)00105-1

Van Weering, T. C. E., Berger, G. W., and Kalf, J. (1987). Recent sediment accumulation in the skagerrak, northeastern north Sea. *Neth. J. Sea Res.* 21, 177–189. doi: 10.1016/0077-7579(87)90011-1

Van Weering, T. C. E., Berger, G. W., and Okkels, E. (1993). Sediment transport, resuspension and accumulation rates in the northeastern skagerrak. *Mar. Geol.* 111, 269–285. doi: 10.1016/0025-3227(93)90135-I

Wallmann, K., Aloisi, G., Haeckel, M., Tishchenko, P., Pavlova, G., Greinert, J., et al. (2008). Silicate weathering in anoxic marine sediments. *Geochim. Cosmochim. Acta* 72, 2895–2918. doi: 10.1016/j.gca.2008.03.026

Wollast, R. (1974). "The silica problem," in *The Sea*, vol. 5 . Ed. E. D. Goldberg (New York: Wiley-Interscience), 365–381.

Wollast, R., and Mackenzie, F. T. (1983). "The global cycle of silica," in *Silicon geochemistry and biogeochemistry*. Ed. S. R. Aston (San Diego, Calif: Academic), 39–76.

Zhu, D., Sutton, J. N., Leynaert, A., Tréguer, P. J., Schoelynck, J., Gallinari, M., et al. (2023). Revisiting the biogenic silica burial flux determinations: A case study for the East China seas. *Front. Mar. Sci.* 9. doi: 10.3389/fmars.2022.1058730

frontiers | Frontiers in Marine Science

TYPE Original Research
PUBLISHED 14 April 2023
DOI 10.3389/fmars.2023.1083233

OPEN ACCESS

EDITED BY
Selvaraj Kandasamy,
Xiamen University, China

REVIEWED BY
Yanguang Liu,
Ministry of Natural Resources, China
Rebecca A Pickering,
Lund University, Sweden

*CORRESPONDENCE
Su Mei Liu
sumeiliu@ouc.edu.cn

SPECIALTY SECTION
This article was submitted to Marine Biogeochemistry, a section of the journal Frontiers in Marine Science

RECEIVED 28 October 2022
ACCEPTED 23 March 2023
PUBLISHED 14 April 2023

CITATION
Ma Y, Yang B, Zhou N, Huang J, Liu SM, Zhu D and Liang W (2023) Distribution and dissolution kinetics of biogenic silica in sediments of the northern South China Sea. *Front. Mar. Sci.* 10:1083233. doi: 10.3389/fmars.2023.1083233

Distribution and dissolution kinetics of biogenic silica in sediments of the northern South China Sea

Yuwei Ma [1,2], Bin Yang [3], Nan Zhou [1,2], Jin Huang [4,5], Su Mei Liu [1,2]*, Dongdong Zhu [1,2,6] and Wen Liang [1,2]

[1]Frontiers Science Center for Deep Ocean Multispheres and Earth System, and Key Laboratory of Marine Chemistry Theory and Technology, Ministry of Education, Ocean University of China, Qingdao, China, [2]Laboratory for Marine Ecology and Environmental Science, Qingdao National Laboratory for Marine Science and Technology, Qingdao, China, [3]Guangxi Key Laboratory of Marine Environmental Change and Disaster in Beibu Gulf, Beibu Gulf University, Qinzhou, China, [4]College of Chemistry, Chemical Engineering and Resource Utilization, Key Laboratory of Forest Plant Ecology Ministry of Education, Northeast Forestry University, Harbin, China, [5]School of Forestry, Northeast Forestry University, Harbin, China, [6]University of Brest, Centre national de la recherche scientifique (CNRS), L'Institut de recherche pour le développement (IRD), Ifremer, Institut Universitaire Européen de la Mer, Plouzané, France

The dissolution efficiency of sedssimentary biogenic silica ($bSiO_2$) dramatically affects the regeneration of dissolved silicic acid (dSi) at the sediment-water interface, which is a crucial pathway to maintain Si balance and silicic productivity growth in marine environments. We conducted wet alkaline leach and flow-through experiments to explore the dissolution behaviors of sedimentary $bSiO_2$ in the northern South China Sea (NSCS), one of the largest marginal sea continental shelves. The $bSiO_2$ contents of surface sediments were 0.64 - 2.06%, with an average of 1.04 ± 0.35%, varying with isobath water depth. The solubility of $bSiO_2$ in surface sediments ranged from 227 μmol L^{-1} to 519 μmol L^{-1}, and the dissolution rate constants varied from 0.67 to 1.53 yr^{-1} under specific conditions in lab incubation. The correlation between the biogenic materials ($bSiO_2$, OC, and TN) revealed a different preservation pattern of $bSiO_2$ in finer ($\Phi > \sim 5.5$) and coarser ($\Phi < \sim 5.5$) sediments. The high concentration of Al in sea water and "Al – detrital – $bSiO_2$" interactions in sediments significantly interfered with the apparent solubility and dissolution dynamics of $bSiO_2$. We combined the regional characteristics (primary production, bottom current, and resuspension-deposition) and the reconstructed dissolution kinetics of $bSiO_2$ explained the mismatch between the surface (diatom biomass)/(total phytoplankton biomass) ratio and the sedimentary $bSiO_2$/OC ratio, and the mismatch between the surface $bSiO_2$ primary productivity and the $bSiO_2$ sediment records in the NSCS. The resuspension-deposition, the higher reconstructed rate constants (0.94 ± 0.13 yr^{-1}), and the dissolution rate (0.20 ± 0.01 yr^{-1}) were responsible for the lower $bSiO_2$/OC ratio (0.45 ± 0.28) at the inner shelf, and the winnowing process at the outer shelf with the lower reconstructed reactivity (0.30 yr^{-1}) and dissolution rate (0.001 yr^{-1}) led to the good preservation of $bSiO_2$ in the upper

slope. Furthermore, through the comparison with other sea areas, the relatively lower reactivity (1.12 ± 0.3 yr^{-1}) of $bSiO_2$ in sediments supported the notion that the NSCS sediments may serve as an important silica sink in the world ocean silica cycle.

KEYWORDS

biogenic silica, dissolution, detrital, aluminum, silicon cycle, Northern South China Sea

1 Introduction

Biogenic silica ($bSiO_2$) is one of the most important components in marine sediments and believed to be a potentially powerful proxy to reconstruct paleoproductivity (Mortlock et al., 1991; Ragueneau et al., 2000). Diatoms are the dominant siliceous producers and responsible for nearly half of the oceanic uptake of CO_2 from the atmosphere (Nelson et al., 1995). Thus, the intimate coupling between the Si and C cycles have driven substantial studies in the last few decades in order to better understand the biogeochemical cycle of Si in marine systems (DeMaster et al., 1996; Nelson et al., 1996; Sayles et al., 2001; Ragueneau et al., 2006; Krause et al., 2011).

The idealized "silica pump", put forward by Dugdale et al. (1995), described a less efficient recycling of $bSiO_2$ than particulate organic matter in the euphotic zone, leading to more efficient export of $bSiO_2$ from upper to deep oceans and the potential limitation of dSi in a diatom-dominated system. Diatom frustules are readily dissolved in strongly undersaturated seawater when organisms die, and the "silica pump" efficiency largely depends on dissolution of $bSiO_2$ before it can be exported to the upper mixed layer in variable marine settings (Brzezinski and Nelson, 1989; Brzezinski and Nelson, 1995; Nelson et al., 1995; Nelson and Dortch, 1996; Bidle et al., 2003). Therefore, the dissolution of $bSiO_2$ is a vital process controlling the marine Si biogeochemical cycle. Particularly in sediments, ~ 89% of deposited $bSiO_2$ is regenerated back through dissolution and other processes (i.e., diffusion, advection, bioturbation, or bioirrigation) on a global ocean scale, which is an important channel to maintain silicic acid (dSi) in a relative steady state in surface oceans by diffusion and/or upwellings for silicic productivity growth (DeMaster, 2002; Tréguer et al., 2021). A considerable number of researches have been inspired to not only explore the temporal and spatial variability of sedimentary $bSiO_2$ dissolution kinetics in variable settings in open oceans (Hurd, 1973; Kamatani et al., 1988; Van Cappellen, 1996; Van Cappellen and Qiu, 1997a; Van Cappellen and Qiu, 1997b; Dixit et al., 2001; Ragueneau et al., 2001; Gallinari et al., 2002; Van Cappellen et al., 2002; Khalil et al., 2007; Gallinari et al., 2008; Cheng et al., 2009) and marginal seas (Van Bennekom et al., 1991; Rickert, 2000; Rickert et al., 2002; Gallinari et al., 2008; Wu et al., 2017; Wu and Liu, 2020), but also the factors ultimately controlling the fate of sedimentary Si, including ambient physical factors such as temperature (Lawson et al., 1978; Kamatani and Riley, 1979; Van Cappellen and Qiu, 1997a; Van Cappellen and Qiu, 1997b), pressure (Willey, 1974; Loucaides et al., 2012), pH (Van Cappellen and Qiu, 1997a; Van Cappellen and Qiu, 1997b; Loucaides et al., 2008), salinity (Loucaides et al., 2008), ionic composition (Loucaides et al., 2008), and its intrinsic nature such as surface chemical properties (Dixit and Van Cappellen, 2002; Fraysse et al., 2006; Loucaides et al., 2012), silicious organism species, and silicification degree (Loucaides et al., 2012). In addition, Rickert et al. (2002) addressed the removal of organic or inorganic coatings (that protect diatom frustules from dissolution by avoiding direct contact with seawater) will enhance the reactivity by at least an order of magnitude. Thus, the roles of aggregation, fecal pellets, or grazing must be considered (Moriceau et al., 2007). Bacterial ectoprotease action on marine diatom detritus strongly accelerates silica dissolution rates by removing the organic coating (Bidle and Azam, 1999; Bidle and Azam, 2001; Bidle et al., 2003), which also plays a significant role in regulating the "silica pump" and sedimentary $bSiO_2$. In addition, the interaction between Al (or K, Li, Na, Mg, Fe, and other reactive elements in porewater) and $bSiO_2$ during early diagenesis have been proposed as a special pathway to form authigenic clay, and have a profound impact on the burial of marine $bSiO_2$ (Rahman et al., 2017; Tréguer et al., 2021), especially in marginal seas with large estuaries (Michalopoulos and Aller, 2004).

The northern South China Sea (NSCS) is a semi-closed marginal sea with a broad shallow water shelf in the Western Pacific Ocean, and features relatively strong biological activity induced by river discharge, seasonal coastal upwelling, and monsoon winds (Chen et al., 2006; Hung et al., 2007). Accordingly, significant seasonal and spatial changes of primary production (Ning et al., 2004; Chen, 2005), particulate organic matter (Ho et al., 2010; Cai et al., 2015), and phytoplankton community structure (Cai et al., 2015) occurs in the NSCS. The second largest river in China, the Pearl River, empties an average freshwater discharge of 482 km^3 yr^{-1} and sediment load of 96 Mt yr^{-1} carrying ~ 53 Gmol-Si yr^{-1} into the NSCS (Liu et al., 2009; Ma et al., 2022), which results in relatively eutrophic conditions. These are benefits for the growth of micro-phytoplankton (> 20 μM in size), such as diatoms, which account for > 75% of the Chl-a concentration in NSCS coastal waters (Xiao et al., 2018). Large terrigenous input and oceanic current system lead to a complex sediments composition and transportation process. (Liu et al., 2016). All of these factors have a significant consequence on the "silica pump" and sedimentary $bSiO_2$. However, prior research on

sedimentary $bSiO_2$ in the South China Sea has mainly focused on distribution features (Zhou et al., 2010; Liu et al., 2012; Zhang et al., 2015) or burial fluxes (Ma et al., 2022). The dissolution and preservation mechanisms of sedimentary $bSiO_2$ is missing in this region. Here, we report the results of flow-through experiments using samples with different sediment components to study the characters influencing factors of the $bSiO_2$ dissolution and the implications for $bSiO_2$ preservation in the NSCS.

2 Materials and methods

2.1 Sample collection

Sampling expeditions were executed in the NSCS onboard the R/V "*Shi Yan 3*" during March and April 2014. In total, 40 surface sediment samples (0 – 2 cm) were collected using a stainless-steel box sampler. The sampling locations are indicated in Figure 1A. The collected sediments were sealed in polyethylene Ziploc bags, and the air removed at the same time. Then, they were immediately frozen at - 20 °C until further processing in the laboratory. Note that our sampling sites were mainly located in the northern continental shelf area of the South China Sea, and a few stations (i.e., 7, 8, 21, 34, and 88) were located in the NSCS shelf-break area (Figure 1A). A conductivity temperature depth (CTD) system was used to measure the bottom water temperature, salinity, and depth.

2.2 Flow-through experiments

Apparent solubility and dissolution kinetics of $bSiO_2$ of eight surface sediments with different sediment components (Figure 1A; Table 1) in the NSCS were measured using stirred flow-through reactors (Figure 2) (Van Cappellen and Qiu, 1997a; Gallinari et al., 2002; Rickert et al., 2002; Gallinari et al., 2008). Each reactor consisted of a cell with a suspended Teflon-coated magnetic stirring bar at the bottom, with a volume of 50 cm^3. Both cell ends were closed by nylon filters with a pore size of 0.45 μm, and the filters were supported by PTFE grids. The filters and grids were held in place by screw-on caps. The flowing solution could be pumped in or out of the headspaces without a barrier through narrow channels of the caps. The well-closed flow-through reactors sat on top of a multipoint magnetic stirrer, which were put into an accurately temperature-controlled incubator. All parts of the system were interconnected with PTFE pipes. In the experiments, up to 2 g of homogenized sediment sample with no pretreatment were added to the reactor (25°C) and an input solution of a well-characterized composition (0.7 M NaCl, buffered at pH 8.0 ± 0.1 using bicarbonate, with known different dSi concentrations) was pumped through the reactor at a constant flow rate until the dSi concentration in the reactor outflow stabilized. Because of the relatively low contents of $bSiO_2$ in the NSCS, the flow rates were maintained between 0.8 - 3.1 ml/h to ensure a measurable difference of dSi concentration between the inflow and outflow due to dissolution or precipitation. Lower flow rates were under higher degrees of undersaturation. The dSi concentration in the input solution was progressively decreased to produce a transition from a precipitation to a dissolution regime. In general, a group of experiments lasted 10 - 18 days according to flow rate and time to reach the steady-state. The dSi concentration and pH in the input solution were monitored throughout the whole course to ensure no influential fluctuations. All of the experiments were carried out under

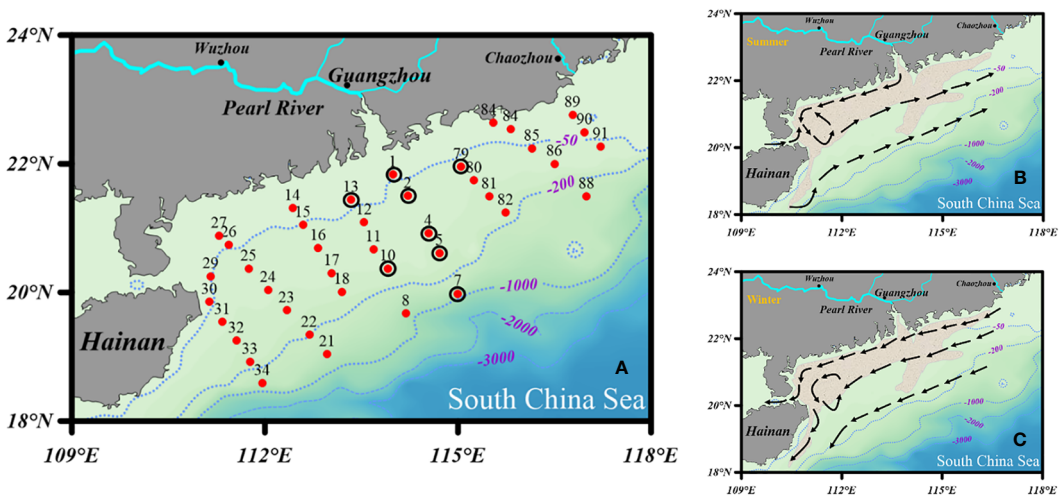

FIGURE 1
Sampling sites and patterns of surface coastal currents in **(B)** summer and **(C)** winter [modified from Wei et al. (2020)]. The khaki-shaded area represents the distribution of the Pearl River-derived mud belt based on Ge et al. (2014). The sediment samples were collected in April 2014. The red dots (*) and black circles (○) in **(A)** represent the grid stations and sediment locations for the flow-through experiments.

10.3389/fmars.2023.1083233

TABLE 1 Characterization of the sediment samples used for flow-through experiments.

Station	Depth (m)	Temperature (°C)	Sediment type[a]	SSA[b] (m^2/g)	Mean grain size (Φ)	$bSiO_2$ (%)	Organic matter[c] (%)	$CaCO_3$ (%)	Detritus[d] (%)
1	40	20.14	Clay - silt	11.634	6.52	1.23	2.58	3.4	92.8
2	54	19.46	Sand - silt	7.088	5.35	0.94	1.34	7.9	89.8
4	81	19.93	Silt - sand	2.280	3.42	0.64	0.78	9.6	89.0
5	107	18.62	Silt - sand	2.106	3.93	0.73	0.64	12.6	86.1
7	733	6.38	Silt	12.439	6.72	2.06	2.63	21.5	73.8
10	99	19.59	Silt - sand	–	6.91	0.7	0.64	13.5	85.2
13	36	20.51	Clay - silt	–	3.51	1.69	2.88	5.6	89.8
79	61	21.35	Sand - silt	–	5.86	1.4	2.27	4.9	91.4

[a]Shepard sediment classification.
[b]BET specific surface area.
[c]Assumes Redfield composition [Organic matter (%) = 2.8 × OC (%)] (Sayles et al., 2001).
[d]Detritus was the sample's remaining mineral percentage, including authigenic aluminosilicates, once $CaCO_3$, organic matter, and $bSiO_2$. Contents were extracted (Rickert et al., 2002).
"-" means no data.

ambient atmospheric pressure and sustained for about 80 days. It is worth noting that the homogeneous process perhaps enhances the reactivity of $bSiO_2$ by crushing the silicate minerals in the flow-through experiment like in wet alkaline digestion (DeMaster et al., 1983; Ward et al., 2021). Van Cappellen and Qiu (1997a) were the first to introduce flow-through experiments into the study of $bSiO_2$ dissolution in the Southern Ocean, however, the numerously subsequent studies followed the homogeneous process and not well quantified this influencing factor yet (Gallinari et al., 2002; Loucaides et al., 2008; Wu et al., 2017). Regardless, the sediment homogeneous process remains a commonly used method of sample preparation and we followed this procedure.

2.2.1 Solubility measurements

The reaction rate of $bSiO_2$ in various inflow solutions were calculated from the difference between each input dSi concentration and the corresponding steady-state output dSi concentration (Rickert et al., 2002):

$$R = \frac{V * \Delta[Si]}{m_{bSiO_2}} \quad (1)$$

where R (μmol g^{-1} h^{-1}) represents the reaction rate of $bSiO_2$; V (ml h^{-1}) donates the volume of flow rate; $\Delta[Si]$ (μmol L^{-1}) is the difference between outflow and inflow solution of concentration of dSi ($\Delta[Si] = [Si_{out}] - [Si_{in}]$); m_{bSiO_2} . (represents the mass of extractable $bSiO_2$ within the reactor. A positive rate indicates the dSi is undersaturated (dissolution) in the reactor, and a negative rate reflects oversaturation (precipitation). The solubility was estimated by linearly interpolating the two closest points from the equilibrium to obtain the value at which there was neither dissolution nor precipitation ($[Si_{out}] = [Si_{in}]$, or $R = 0$).

2.2.2 Dissolution rate constant and reaction order measurements

The flow-through reactor technique is particularly suitable for studying reaction kinetics as a function of the departure from equilibrium, which can provide important information

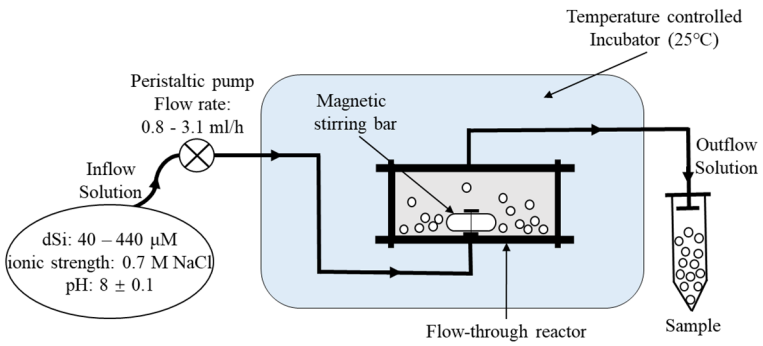

FIGURE 2
Schematic illustration of continuous flow-through experiments. Inflow solution with different dSi concentrations and given conditions were added to the reactor by a flow rate controlled peristaltic pump. PTFE pipes were used for interconnecting all parts of the system.

concerning the reactivity of the $bSiO_2$ (Van Cappellen, 1996; Gallinari et al., 2008). The non-linear dissolution kinetics law was proposed by several studies to model the experimental data (Van Cappellen and Qiu, 1997a; Van Cappellen and Qiu, 1997b; Rickert et al., 2002; Gallinari et al., 2008):

$$R = k_{diss}\left(1 - \frac{[Si]}{[Si]_{eq}}\right)^{m} \quad (2)$$

Here, R (μmol g^{-1} h^{-1}) is the reaction rate of $bSiO_2$; k_{diss} (μmol g^{-1} h^{-1}) donates the dissolution rate constant of $bSiO_2$, which reflect the apparent reactivity of the $bSiO_2$ particles; $[Si]$ (μM) is the dSi concentration; $[Si]_{eq}$ (μM) represents the apparent solubility of $bSiO_2$, and m is the reaction order that indicates the extent of deviation from the linear dissolution dynamics of $bSiO_2$.

2.3 Measurements of sedimentary $bSiO_2$, organic carbon, total nitrogen, and calcium carbonate

Sediment samples were freeze-dried in the laboratory. It is noteworthy that the grinding effect on the measurement of $bSiO_2$ by wet alkaline digestion could enhance the calculated $bSiO_2$ concentrations up to ~50% (DeMaster et al., 1983; Ward et al., 2021). Therefore, to improve the measurement reproducibility (< 2%) in low $bSiO_2$ content samples from marginal seas, the sediments were as gently as possible ground using an agate pestle and mortar (trying to avoid crushing the silicious structures and silicate minerals) for homogenization. The sedimentary $bSiO_2$ contents were analyzed using a modified alkaline leaching method (Liu et al., 2002) which combined the methods described in DeMaster (1981) and Mortlock and Froelich (1989). In detail, ~ 100 mg sediment samples were placed in 50 ml polypropylene centrifuge tubes after removing organics and carbonates with H_2O_2 and HCl. Exactly 40 ml of 2% Na_2CO_3 solution was added to the samples. The tubes were covered tightly and mixed homogenously using a vortex rotating machine, then incubated in a water bath preheated to 85 °C. After 1 h, the tubes were removed and centrifuged. Then, 125 μl of clear centrifugation supernatant was pipetted from each extraction solution for dSi analysis. This procedure was repeated for 1 – 8 h. Note that after each sampling, the tubes were stirred vigorously to resuspend the sediment then placed again in the water bath. All sampling steps were completed quickly to minimize dSi loss on solid surfaces. The concentrations of dSi in the leaching solution were determined using the molybdate blue spectrophotometric method (Mortlock and Froelich, 1989). The $bSiO_2$ content was calculated by a first order kinetic model, that is, the dSi we measured was a function of time t (Koning et al., 1997; Rickert et al., 2002):

$$[dSi\,\%]_t = [bSiO_2\,\%]_0 \times (1 - e^{-k_{Na_2CO_3}t}) + b_{Na_2CO_3}t \quad (3)$$

where $[bSiO_2\%]_0$ represents the content of $bSiO_2$ (wt.%) in the sediment sample; $[dSi\%]_t$ donates extracted content of SiO_2 at time t; $k_{Na_2CO_3}$. d $b_{Na_2CO_3}$. e apparent rate constants in Na_2CO_3 solution that summarize the influence of biogenic and detrital matrix on the dSi concentration, respectively (Koning et al., 1997; Rickert et al., 2002). The coefficient of variation (i.e., relative stand deviation) for five parallel extractions was< 2.00%, indicating good reproducibility. The result of inter-laboratory comparison through this method demonstrates good accuracy of $bSiO_2$ measurement (Liu et al., 2002; Wu et al., 2015).

The OC and TN contents were measured using a CHNOS Elemental Analyzer (Vario EL-III; Elementar Analysensysteme GmbH, Germany) after inorganic carbon was removed *via* acidification with 1 M HCl. The analytical precision of OC and TN was< 6% based on duplicate measurements (Liu et al., 2010). The data of OC contents have been published in Yang et al. (2018). The content of $CaCO_3$ was measured using acid-base titration (Müller, 1966), and the coefficient of variation was 1.0% for five parallel extractions. To calculate the detrital material contents, the OC was converted to organic matter contents assuming a multiplier of 2.8 g of organic matter per g of carbon (Redfield composition) (Sayles et al., 2001). Therefore, detritus % = 100 – ($bSiO_2$% + $CaCO_3$% + OC% × 2.8).

2.4 Specific surface area and grain size (Φ)

The specific surface area (SSA, m^2 g^{-1}) of the sediments were determined by the conventional N_2-BET method using an ASAP2460 full-automatic surface area analyzer (ASAP2460, Micromeritics, USA). Samples were heated overnight at 90 °C and for one hour at 150 °C prior to analysis. The multi-point BET surface area was calculated from the N_2 absorption isotherm. The sediment grain size was analyzed using a laser particle size analyzer (Mastersizer 2000; Malvern Instruments Ltd., Malvern, Worcestershire, UK) capable of analyzing grain sizes from 0.02 to 2000 μm. Three sediment size categories were distinguished: (1) clay: D< 4 μm; (2) silt: 4< D< 63 μm; and (3) sand: D > 63 μm. The samples were analyzed in duplicate, and the analytical precision was< 2%. The mean grain size was reported as Φ, where $\Phi = -\log_2 D$ (D unit: mm) (Krumbein, 1934). The data of grain size have been published in Yang et al. (2018).

3 Results

3.1 Distribution of biogenic ($bSiO_2$, OC, $CaCO_3$) matters and abiogenic detrital

The contents of $bSiO_2$ in surface sediments of the NSCS varied from 0.64% to 2.06%, with an average of 1.04% ± 0.35% (Figure 3A). As a whole, the $bSiO_2$ contents presented a strong zonal distribution tendency and varied with the water depth isobath, which decreased from the inner shelf (< 50 m) to the outer shelf (50 - 200 m), and then increased to the upper slope (> 200 m). Furthermore, higher levels were predominantly observed in the region with fine-grained (D< 63 μm) sediments and lower $bSiO_2$ concentrated in the sandy (D > 63 μm) sediments. The horizontal distribution of the OC

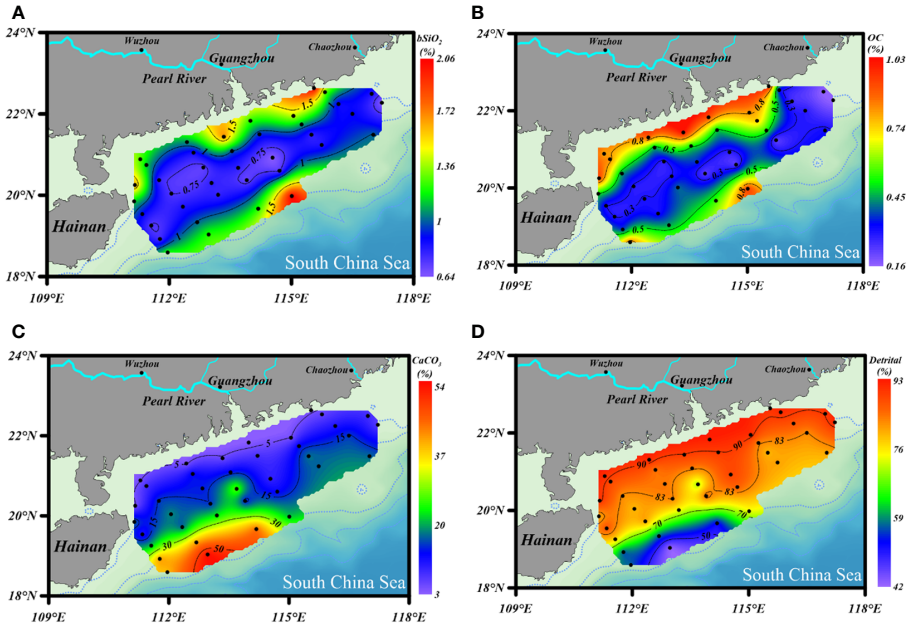

FIGURE 3
Distribution of **(A)** $bSiO_2$ (%), **(B)** OC (%), **(C)** $CaCO_3$ (%), and **(D)** detrital mineral (%) contents in surface sediments of the NSCS.

contents showed similar patterns with that of $bSiO_2$, which were 0.1% to 1.03%, with an average of 0.49% ± 0.27% (Figure 3B). The $bSiO_2$/OC mole ratios varied from 0.24 to 1.06, with lower values at the inner shelf (0.45 ± 0.28) and upper slope (0.42 ± 0.11) and higher values at the outer shelf (0.51 ± 0.14). The $CaCO_3$ and detrital contents were 16.6% ± 12.4% (3.4% - 54.8%) and 80.9% ± 12.4% (42.7% - 92.8%), respectively. The distribution trends of these two components were opposite, increasing gradually from the inner shelf to the upper slope for $CaCO_3$ and decreasing gradually for detritus (Figures 3C, D).

3.2 Apparent solubility and dissolution kinetics of $bSiO_2$

The dissolution rates of sedimentary $bSiO_2$ were plotted as a function of the outflow steady-state dSi concentrations (Figure 4). The uncertainties of the solubilities were calculated by the narrow fluctuation of $[Si_{out}]$ after steady state conditions were reached. The apparent solubility of $bSiO_2$ in surface sediments of the NSCS ranged from 227 to 519 μM with a mean value of 298 ± 94 μM, which is much lower than the solubility of the fresh diatom frustules (~ 1100, 0

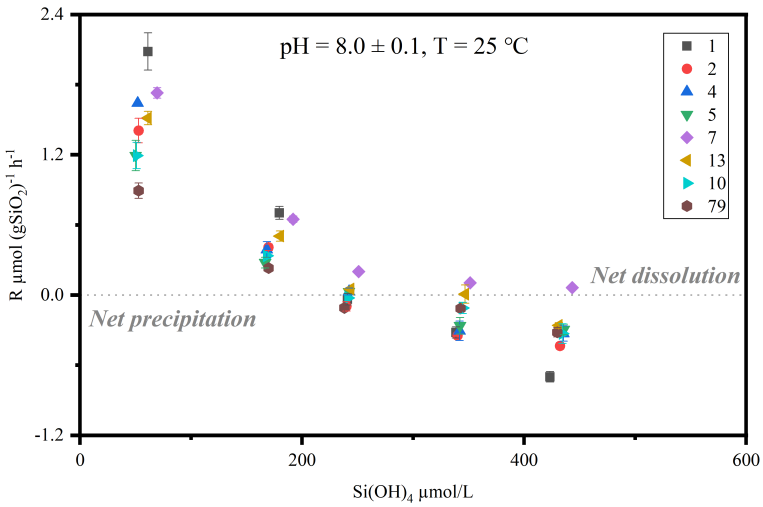

FIGURE 4
Steady state $bSiO_2$ dissolution-precipitation rates [μmol $(gSiO_2)^{-1}$ h^{-1}] are plotted as a function of dSi outflow concentrations (T = 25 °C, pH = 8.0 ± 0.1) in surface sediments of the NSCS. Positive rates indicate net dissolution, and negative rates indicate net precipitation. The legends and numbers in the upper right corner indicate different stations conducted flow-through experiments. The uncertainties are shown by error bars.

– 4 °C) (Hurd, 1973). In general, the solubility of the inner shelf and upper slope are higher than that of the outer shelf (except station 10). The highest solubility value was observed at station seven on the upper slope, where the $bSiO_2$ content was highest. The lowest value was recorded at station two on the outer shelf. The dissolution rate constant of the inner shelf and upper slope was higher than that of the outer shelf, which was from 0.67 to 1.53 yr^{-1}, with an average of 1.12 ± 0.3 yr^{-1} (Table 2). The east side (station 13) of the Pearl River estuary is evidently higher than the west side (station 79). Station one and 79 recorded the highest and lowest values, respectively. In addition, the reaction order (m >1) ranged from 1.1 to 3.42. A relative higher value was observed at station seven.

3.3 Grain size (Φ) and specific surface area character

The surface sediments in the NSCS were mainly composed of silt (4 - 63 μm) and sand (> 63 μm). Fine-grained sediments were found primarily in the Pearl River estuary and adjacent coastal region, and secondarily in the upper-slope area (station 7, 8, 21, and 34), whereas coarser sediments occurred mainly in the outer-shelf area (50 – 200 m), especially in the northeast (Figure 5). The highest values of specific surface area (SSA) were recorded at station one and seven, and the lowest values at station two, four, and five (Table 1).

4 Discussion

4.1 The distribution character of sedimentary $bSiO_2$

The distribution of $bSiO_2$ (Figure 3A) and $bSiO_2$/OC ratio (Figure 6) revealed a mismatch between the (diatom biomass)/(total phytoplankton biomass) ratio and the sedimentary $bSiO_2$/OC ratio at the inner shelf and outer shelf, and also a mismatch between the $bSiO_2$ primary productivity and the $bSiO_2$ sediment records at the upper slope of the NSCS. The sedimentary $bSiO_2$ record is believed to a good indicator for the surface $bSiO_2$ primary production (Schrader and Sorknes, 1991). The wide shelf of the NSCS receives a large discharge of terrigenous nutrients and results in overall enhanced biological productivity (Han et al., 2012). But the primary production presented distinct regional characteristics at the inner shelf (< 50 m), outer shelf (50 – 200 m), and upper slope (> 200 m). The satellite remote-sensed spatial distribution of Chl-a showed a gradient decrease from nearshore to offshore, and changes roughly along the 50 m isobath with concentrations of ~ 1 mg m^{-3} in all seasons. In addition, the total biomass of phytoplankton and the proportion of diatoms in the mixed layer also showed a gradient decrease from the nearshore to the offshore throughout the year (Xiao et al., 2018), which is consistent with the variation of surface primary productivity (< 40 m: 1.73 ± 0.12 g-C m^{-2} d^{-1}; 40 – 120 m: 0.67 ± 0.35 g-C m^{-2} d^{-1}; > 120 m: 0.43 ± 0.02 g-C m^{-2} d^{-1}) (Pan et al., 2015). This evidence indicated that even though there is no report of primary production of $bSiO_2$ in the NSCS at present, it can be speculated that the distribution of $bSiO_2$ primary production should be in a decreasing trend from nearshore to offshore. Therefore, the high sedimentary contents of $bSiO_2$ accumulated in the inner-shelf region (1.27% ± 0.39%) (Figure 3A) is mainly attributed to the enhanced $bSiO_2$ primary production by the large discharge of terrigenous nutrients, especially in the area affected by the perennial westward plume of the Pearl River (station 13). However, a mismatch between the $bSiO_2$ primary productivity and the $bSiO_2$ sediment records at the upper slope of the NSCS was observed. High contents of $bSiO_2$ (1.43% ± 0.42%) were recorded in the upper-slope region (0.71% ± 0.24%) (Figure 3A). It is obvious this was not related to the euphotic $bSiO_2$ primary production. Our flow-through experimental results showed a dissolution kinetics-controlled preservation of $bSiO_2$ in this area (discussed in section 4.4).

In addition to primary production, sediment grain size plays a role in the distribution of $bSiO_2$. As Figure 5 shows, the distribution of mean grain size (Φ) was similar with the distribution of $bSiO_2$ (%), and fine-grained sediments were mainly distributed in the inner-shelf and the upper-slope regions. The strong correlation between "Φ" values of mean grain size and $bSiO_2$ contents ($r = 0.71$, $p < 0.01$) indicated fine-textured particles (silt and clay) have greater physical protection for $bSiO_2$. Compared with different biogenic material (OC and TN) in different sediment types, we found a different preservation patterns of $bSiO_2$ in the sediments of the NSCS. As a

TABLE 2 Flow-through experimental results.

Station	Solubility (μmol/L)	k_{diss} 25°C (yr^{-1})	k_{diss} 25°C (μmol m^{-2} h^{-1})[a]	Situ-k_{diss} (yr^{-1})[b]	Situ-dSi Concentration[c]	Situ-dissolution rate [yr^{-1}][d]	Reaction order (m)
1	272 ± 6	1.53	0.25	1.02	191	0.21	1.32
2	227 ± 18	0.99	0.27	0.63	170	0.14	1.1
4	251 ± 1	1.26	1.05	0.83	125	0.27	1.64
5	252 ± 2	0.91	0.82	0.54	108	0.21	1.68
7	519 ± 1	1.49	0.22	0.3	419	0.001	3.42
10	283 ± 14	0.89		0.57	165	0.25	1.8
13	329 ± 29	1.22		0.85	103	0.2	2.08
79	252 ± 28	0.67		0.5	230	0.011	1.53

[a]Kinetic constant normalized by BET surface areas were calculated by using surface areas given in Table 1.
[b]k_{diss} kinetic constants were recalculated for situ-temperature assuming an activation energy of 60 kJ/mol by [Eq. (4)].
[c]Averaged of the dSi concentration in pore water at 0 - 2 cm. Note the situ-dSi concentration of station seven was sampled at the same site in June 2015.
[d]The situ-dSi dissolution rate was reconstructed from the situ-k_{diss} and situ-dSi concentrations using [Eq. (2)].

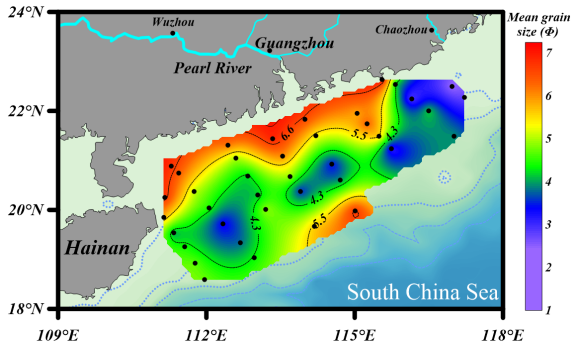

FIGURE 5
Distribution of $bSiO_2$/OC molar ratio in surface sediments of the NSCS.

part of organic matter, a great linear regression of TN versus OC in sediments with an intercept of zero demonstrates the two components are preserved in a well coupled manner, whether in finer or coarser sediments (Figure 7A). However, the positive linear relationship between OC (%) and $bSiO_2$ (%) has a higher slope (3.0) in fine-grained (Φ > ~ 5.5) sediments than in coarser (Φ< ~ 5.5) sediments (0.78) (Figure 7B), which suggests not only that fine-grained particles have better preservation performance for biogenic material, but also with each equal additional amount of OC stored, the fine-grained sediments will retain 2.8 times more $bSiO_2$ than coarser sediments in the NSCS. Furthermore, the average molar ratio of $bSiO_2$/OC in finer sediments (0.34 ± 0.07) (mainly at the inner shelf and upper slope) is lower than in coarser sediments (0.57 ± 0.17) (mainly at the outer shelf) (Figure 6). Therefore, there is a mismatch between the (diatom biomass)/(total phytoplankton biomass) ratio and the sedimentary $bSiO_2$/OC ratio in the inner shelf and outer shelf. The outer-shelf region with coarser sediments has been described as a sandy swath, and the sandy swath is the product of glacial sea level low stand and exposition to winnowing by strong bottom current recently (Wang and Li, 2009). The higher SiO_2/OC ratio, relative to the inner shelf and upper slope, could potentially be due to the higher energy level of this area. High-energy conditions could lead to more resuspension of sediments than low-energy environments and prompt longer oxygen exposure time, which in turn leads to lower OC contents through selective degradation of

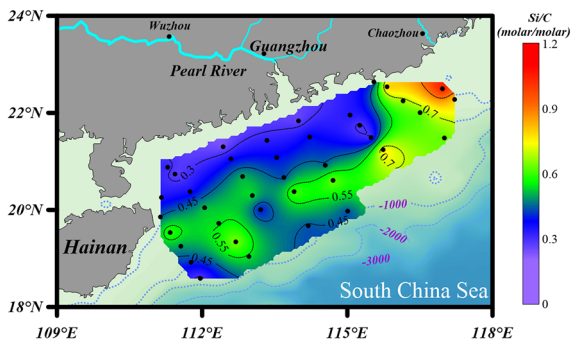

FIGURE 6
Distribution of mean grain size (Φ) in surface sediments of the NSCS.

labile young fractions and reduced TOC content (Van der Voort et al., 2018). Compared with the silicic acid degree of unsaturation, the demand of oxygen is much smaller for the dissolution of $bSiO_2$. The mismatch at the inner shelf is discussed in section 4.3.

4.2 The influence of aluminum and detrital material

The solubilities of $bSiO_2$ in the NSCS sediments (298 ± 94 μM) is seriously inhibited, which exhibits a low level compared with some marginal seas and open oceans (Figure 8). It has been proven that aluminum is probably the most significant factor affecting spatial variations in measured $bSiO_2$ solubility (Dixit et al., 2001). Field data and laboratory experiments reveal that the structural incorporation of Al into the silica framework by substituting Si atoms in the silica lattice reduces the solubility whether during the living diatom biomineralization process, settling after death, or deposited on the seafloor (Van Bennekom et al., 1991; Van Beueskom et al., 1997; Gehlen et al., 2002; Van Cappellen et al., 2002; Koning et al., 2007). The Pearl River delivers a high concentration of Al (360 – 690 nmol L^{-1}) to the NSCS and observes a shelf–to-slope transportation pattern (Zhang et al., 2020). Due to this severe terrigenous effect, the dissolved Al concentrations of seawater in the NSCS was reported to be at a high level (8 – 59 nmol L^{-1}, with an average of 30 ± 11 nmol L^{-1}) with a seaward decline (Guo, 2016), which is higher than some marginal seas, such as the Arabian Sea (3 – 15 nmol L^{-1}) and the Weddell-Scotia Seas (1 – 3 nmol L^{-1}) (Van Bennekom et al., 1991; Schüßler et al., 2005), and is much higher than some open oceans, such as the Pacific Ocean (0.3 – 5 nmol L^{-1}), the North Atlantic (6 – 25 nmol L^{-1}), and the Southern Ocean (0.33 – 0.8 nmol L^{-1}) (Orians and Bruland, 1986; Kramer et al., 2004; Middag et al., 2011). The scavenging proportion of the dissolved Al by phytoplankton was reported as up to 9.4 – 25.7% in summer (Zhang et al., 2020). Culture diatoms in Al-enriched solution exhibit a 20% lower solubility than in Al-depleted solution at 3 °C (Gallinari et al., 2002). The "primary uptake" of Al in the water column probably explains part of the reason why the solubility of the NSCS sediment is lower than some other sea areas. More important is the "Al – detrital – $bSiO_2$" interactions during early diagenesis of $bSiO_2$ in sediments. On one hand, the concentration of Al in pore water generally is several or tens of times (100 – 500 nmol L^{-1}) higher than seawater (Koning et al., 2007), which drives the "secondary uptake" of $bSiO_2$ debris. The well correlation between the dissolved Al concentration in pore water with the detrital/opal ratio in sediments confirms the detrital materials as an important source of Al (Dixit et al., 2001). The increase in Al levels often happens at the sediment-water interface (Van Cappellen and Qiu, 1997b). The high detrital matter content (80.9% ± 12.4%) in the NSCS sediments, which is higher than the Arabian Sea (30% – 50%), the Peru-Basin (66% ± 1%), and the Scotia Sea (36% - 66%) (Rickert, 2000), provides an abundance of Al to restrain the $bSiO_2$ dissolution and solubility. On the other hand, as the $bSiO_2$ deposited at the sediment-water interface, the continuously releasing Al (also including other ions, i.e., Mg^{2+}, K^+, and F^-) from detrital-rich sediments can induce

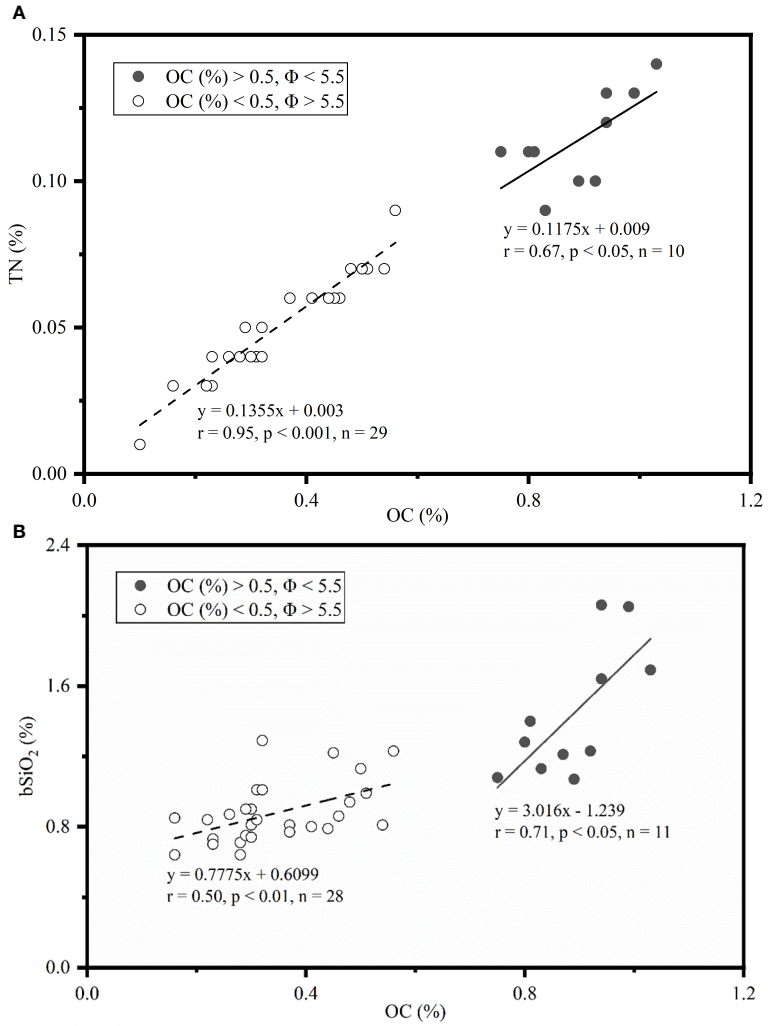

FIGURE 7
Correlations between **(A)** OC (%) and TN (%), and **(B)** OC (%) and $bSiO_2$ (%) contents in sediments with Pearson correlation coefficients (r) and regression curves. Solid and dashed lines denote the regression trends with OC > 0.5 and Φ< 5.5, and OC<0.5 and Φ > 5.5, respectively.

reprecipitation with dSi and $bSiO_2$ to form authigenic silicates or adsorb onto the surfaces of $bSiO_2$ to further reduce the solubility (Van Cappellen and Qiu, 1997b; Dixit et al., 2001; Michalopoulos and Aller, 2004; Loucaides et al., 2010), which is called reverse weathering. It has been proven a crucial pathway that can remove large amounts of silica from ocean within a short time (months to years) (Michalopoulos and Aller, 2004; Rahman et al., 2017; Tréguer et al., 2021). Rickert et al. (2002) used sediment samples pretreated with 10% HCl and H_2O_2 in the Scotia Sea and found that the solubility increased by 104% and the dissolution rate constant increased by 590% compared to unpretreated samples. The specific surface areas also increased by a factor of two to three times due to the pretreatment procedure (removing the organic coating and partially authigenic minerals). These results were attributed to the detrital minerals or authigenic aluminosilicates forming on the $bSiO_2$ surface, some of which could readily dissolve in mild HCl solution. Loucaides et al. (2010) reinforced the view by long-term incubation experiments (fresh diatom frustules were separated from the terrigenous sediments by a dialysis membrane, only allowing the exchange of dissolved species), and demonstrated the interaction between $bSiO_2$, seawater, and lithogenic minerals dramatically inhibits the solubility of $bSiO_2$ by forming new mineral precipitates on $bSiO_2$ surface. Our results showed that a strong correlation between solubility and detrital or detrital to $bSiO_2$ ratio (Figure 9). Gallinari et al. (2002) used different diatom species mixed with variable amounts of silicate minerals in a batch experiment, which presented a similar correlation between solubility and detrital to $bSiO_2$ ratios. This evidence supported our conclusion that the "Al – detrital – $bSiO_2$" interactions play important retarding roles in solubility space variation of $bSiO_2$ in the sediments of the NSCS.

4.3 The influence of specific surface area and particle size

Variations of specific surface area (SSA) must be considered when comparing the dissolution properties of sedimentary $bSiO_2$

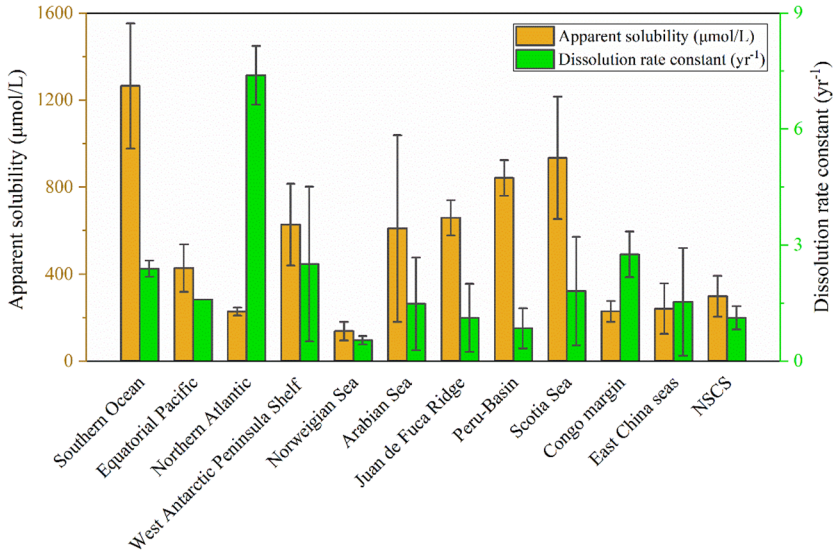

FIGURE 8
The solubilities and dissolution rate constants determined in this study for the NSCS sediments compared with other marginal seas or open oceans, including: the Southern Ocean (Van Cappellen and Qiu, 1997a; Van Cappellen and Qiu, 1997b), the Equatorial Pacific (Gallinari et al., 2002), the Northern Atlantic [averaged data from Gallinari et al. (2002); Gallinari et al. (2008) and Ragueneau et al. (2001)], the West Antarctic Peninsula Shelf (Gallinari et al., 2008), the Norweigian Sea (Rickert, 2000), the Arabian Sea (Rickert, 2000), the Juan de Fuca Ridge (Rickert, 2000), the Peru-Basin (Rickert, 2000), the Scotia Sea (Rickert, 2000), the Congo margin (Ragueneau et al., 2009), and east China seas (containing the Yellow Sea and the East China Sea) (Wu et al., 2017; Wu and Liu, 2020). Note that all the dissolution rate constants have been recalculated at 25°C using Eq. (4) for the purpose of comparison.

and siliceous plankton in marine surface waters (Van Cappellen et al., 2002). It is generally believed that the SSA can provide a reliable proxy to represent the availability of solid surface area for solution reaction (Hurd, 1973). The dissolution rate constant of freshly exposed diatom frustules measured in labs can be as high as ~16 yr^{-1}, and the SSA of diatom frustules varied from 16 to 260 m^2 g^{-1} (Van Cappellen et al., 2002), which are much higher than that in the NSCS sediments (~ 1.12 yr^{-1} and ~ 7.1 m^2 g^{-1}) (Table 1). In this regard, the lower rate constants and SSA values in sediments reflects that the preferential dissolution of the part with higher SSA in heterogeneous siliceous components, or the highly reactive part of $bSiO_2$ was regenerated during the settling process in the water column.

The reaction rate constants measured under the same conditions should reflect the relative differences of reactive surface areas (or reactive surface sites) (Rickert et al., 2002). However, it seems that sediment bulk SSA can be used as a proxy for the reactivity of $bSiO_2$ in the NSCS at some stations, such as station one and seven, which exhibit the highest dissolution rate constants corresponding to the highest SSA values. An abnormal phenomenon occurred at station four, which presented a relatively higher dissolution rate constant but very low SSA value. Our data overall presented a weak correlation between the dissolution rate constants and the sediment SSA, particle sizes, or $bSiO_2$ loadings (Tables 1, 2). Rickert et al. (2002) reported that the correlation of reaction rate constants and sediment SSA were only found in almost pure $bSiO_2$ samples (cultured phytoplankton or acid-cleaned samples from the water column), excluding pure siliceous oozes ($bSiO_2$ contents > 49%), whereas the adsorption capacity of the $bSiO_2$ for cobalt ions well corresponded to the reactivity changes (Van Cappellen and Qiu, 1997b). The BET surface area of siliceous ooze cores in the Southern Ocean basically remains unchanged with increasing depth, whereas the reaction rate constants still decrease by three times when the depth reaches 30 cm (Van Cappellen, 1996). However, elemental and microscopic analyses showed no changes in mineral composition or any diagenetic alterations throughout the sediment cores. This evidence implies that the reactivity of the $bSiO_2$ surface has altered but not the geometric surface area determined by nitrogen BET, which has been called a progressive "aging" process of the $bSiO_2$ surface (loss of reactive surface sites) (Van Cappellen, 1996). This "aging" process may be related to surface charge density (Dixit and Van Cappellen, 2002; Loucaides et al., 2010). It is worth noting that all of the FTIR (Fourier-transform infrared) spectroscopic evidence (Schmidt et al., 2001), the apparent reactivity rate constants obtained from leaching alkaline solution (Koning et al., 1997), and from flow-through experiment (Rickert et al., 2002) manifest that the loss of reactive surface sites has already begun as the $bSiO_2$ settles down in the water column. The sediment flux of the Pearl River is transported to the NSCS in the form of a plume, which presents distinct seasonal variations influenced by the East Asian monsoon: during summer, under the effect of weak southwest winds (~ 6 m s^{-1}), the water mass at the inner-shelf moves eastward, but the suspended particles of the Pearl River plume are still predominantly transported to the west due to the prevalent coastal current (Figure 1B); during winter, the coastal current is strengthened by the strong northeasterly winds (~ 9 m s^{-1}), which can resuspend sediments and keep them transporting westward (Figure 1C) (Liu et al., 2014). The dissolution rate constants of $bSiO_2$ on the east side of the Pearl River estuary (0.67 yr^{-1}, station 79) are distinctly lower than those

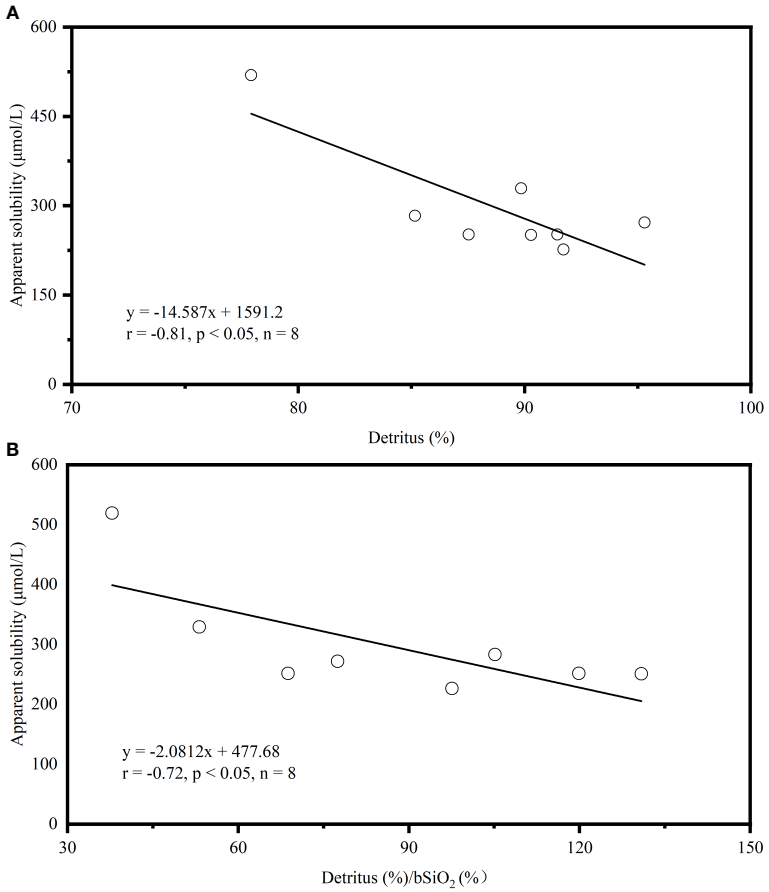

FIGURE 9
Correlations between **(A)** $bSiO_2$ apparent solubility (μmol/L) and detrital material content (%), and **(B)** $bSiO_2$ apparent solubility (μmol/L) and detrital material (%)/$bSiO_2$ (%) in sediments of the NSCS. The Pearson correlation coefficients (r) and regression curves are shown.

on the west side (1.22 yr^{-1}, station 13). Furthermore, the sedimentation rate on the west (~ 1cm yr^{-1}) side of the Pearl River estuary is much higher than on the east side (~ 0.5 cm yr^{-1}). We suggest that resuspension-deposition and higher sedimentation rate maintain the fresh $bSiO_2$ in the surface sediment on the west side of the Pearl River estuary and result in the high reactive of $bSiO_2$ in the surface sediments. It is completely different for the degradation of OC. Wei et al. (2020) reported older terrigenous OC on the west (1950 yr BP) side of the Pearl River estuary than on the east (1510 yr BP) due to resuspension-deposition. Repeated resuspension-deposition cycles could promote oxygen exposure time and accelerate the remineralization of fresh OC, and leave the refractory older OC, whereas redox oscillations have little impact on the dissolution of $bSiO_2$. This is probably also the reason why the highest (diatom biomass)/(total phytoplankton biomass) ratio in surface water but the lowest $bSiO_2$/OC ratio was recorded in the sediments of the west inner-shelf region (Figure 6). Besides the "aging" process, the vertical transport of $bSiO_2$ through the fast settling of aggregates or fecal pellets also play a role (Shi et al., 2019), trying to maintain the initial reactivity of $bSiO_2$ of the surface ocean, such as at station one with lower water depth and higher reactivity. In this case, the most important parameter could be the degree of coupling between surface waters and the seabed. For example, the formation of blooms and the rapid sedimentation of diatoms, either in the form of large aggregates or embedded within fecal pellets of large euphausiids (Nelson et al., 1995), could lead to the deposition of fresh diatoms with dissolution properties similar to those encountered in surface waters. Our sediment samples are located in a wide range of water depths (40 – 773 m), and subjected to intense turbulence by active water dynamics or sediment resuspension due to the buoyancy of river plumes, wind force, or terrigenous impact (Cao et al., 2020). The partly unsatisfactory agent of SSA for the reactivity surface of our samples presumably reflected the different "aging" or other water column processes (i.e., forming diatom aggregation or fecal pellets) of $bSiO_2$ particles when sinking in the water column.

4.4 Implications for the preservation of $bSiO_2$ in the NSCS sediments

The dissolution of $bSiO_2$ is very sensitive to temperature changes, and preservation status largely depends on the difference of *in situ* temperature (Kamatani and Riley, 1979; Van Cappellen and Qiu, 1997b). To further discuss the *in situ* preservation mechanism of $bSiO_2$ in the NSCS sediments, the measured

reaction rates were reconstructed under *in situ* conditions. We applied an average activation energy (E_{app}) of 60 kJ/mol to obtain the rate constants at *in situ* temperature using the equation (Rickert et al., 2002):

$$lnk_2 = lnk_1 + \frac{E_{app}}{R}\left[\frac{1}{T_1} - \frac{1}{T_2}\right] \quad (4)$$

where R = 8.314 J K^{-1} mol^{-1} and T (K) donates the temperature, k refers to the rate constant (yr^{-1}). The pressure was not considered because it has little influence within water depths of 800 m (Loucaides et al., 2012). The dissolution rate constants of $bSiO_2$ in the NSCS sediments at *in situ* temperature were 0.94 ± 0.13 yr^{-1}, 0.61 ± 0.13 yr^{-1}, and 0.30 yr^{-1} at the inner shelf, outer shelf, and upper slope, respectively (Table 2). The upper depth (2 cm) interval corresponds to the zone of net silica dissolution. Then, the net dissolution rate of $bSiO_2$ at the eight stations of the 2 cm surface sediments were reconstruct by combining the experimental derived non-linear dissolution law (Eq. (2), Figure 10) with the *in situ* pore water dSi concentration (averaged of 0 - 2 cm), which were 0.20 ± 0.01 yr^{-1}, 0.18 ± 0.11 yr^{-1}, and 0.001 yr^{-1} at the inner shelf, outer shelf, and upper slope, respectively (Table 2). The reconstructed *in situ* dissolution rate in the upper slope (station seven) is orders lower than that at the shelf. This suggests that the differences of $bSiO_2$ preservation between the inner shelf, outer shelf, and upper slope were the results of a wide range of *in situ* temperature-induced differences of dissolution rates constants and the departure from equilibrium-induced differences of *in situ* dissolution rates. These results showed dissolution kinetics-controlled evidence that explains the mismatch between the (diatom biomass)/(total phytoplankton biomass) ratio and the sedimentary $bSiO_2$/OC ratio in the inner shelf and outer shelf, and also a mismatch between the $bSiO_2$ primary productivity and the $bSiO_2$ sediment records in the upper slope of the NSCS. The mismatch of $bSiO_2$/OC ratio at the outer shelf is due to high-energy conditions and the mismatch at the inner shelf is attributed to the resuspension-deposition, which have been discussed in section 4.1 and section 4.3. The high reconstructed *in situ* rate constants (0.94 ± 0.13 yr^{-1}) and dissolution rate (0.20 ± 0.01 yr^{-1}) strengthened the fact of the lower $bSiO_2$/OC ratio observed at the inner shelf. Wei et al. (2020) suggested that surface sediments at the slope displayed a relatively higher terrigenous OC content and older terrigenous OC than that at the outer shelf, likely due to cross-shelf transport from the Pearl River and sediment winnowing on the outer shelf. Our results suggest that the lower *in situ* reactivity (0.30 yr^{-1}) and dissolution rate (0.001 yr^{-1}) allowed sedimentary $bSiO_2$ to be well preserved in this area.

The degree of undersaturation of the pore fluid represents the thermodynamic driving force for the dissolution process and is directly dependent on the solubility of the $bSiO_2$ (Van Cappellen and Qiu, 1997a). The dissolution rates were plotted against the departure from saturation state (Figure 10), which exhibits a non-linear dissolution kinetic, which was also observed in different deposition settings (Van Cappellen and Qiu, 1997a; Van Cappellen and Qiu, 1997b; Rickert et al., 2002; Ragueneau et al., 2009). The non-linear dissolution kinetics implied a higher dissolution rate in a highly unsaturated silicic solution, that is, more efficient recycling of $bSiO_2$ in dSi-depleted upper sediments compared with deep sediments, which is meaningful for benthic Si regeneration. However, the non-linear dissolution kinetics must be severely inhibited by the high contents of detritus in the NSCS sediments. The overall dissolution rate constants of $bSiO_2$ in the NSCS sediments was 1.12 ± 0.3 yr^{-1} at 25°C, which is lower than some marginal seas, such as the West Antarctic Peninsula Shelf [2.5 yr^{-1}, Gallinari et al. (2008)], the Arabian Sea [1.48 ± 1.4 yr^{-1}, Rickert (2000)], the Scotia Sea [1.81 ±

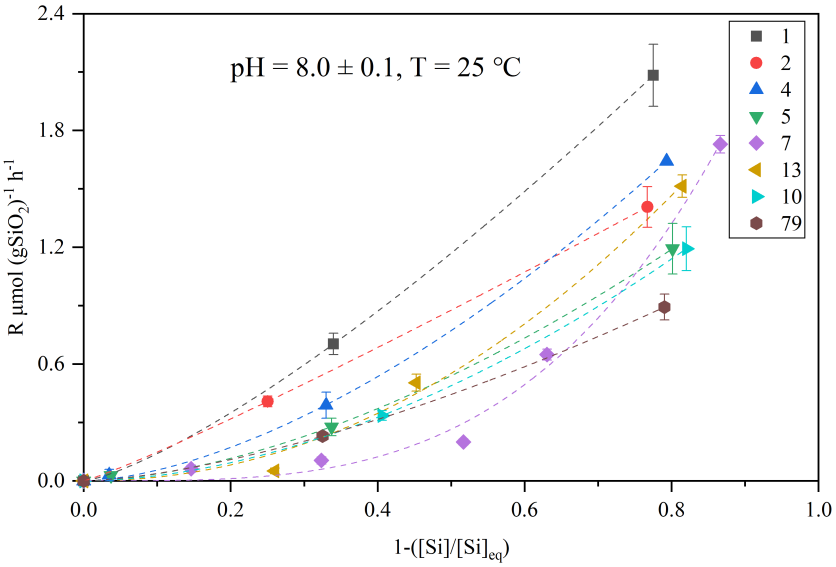

FIGURE 10
Experimental dissolution rates [μmol $(gSiO_2)^{-1}$ h^{-1}] plotted versus the departure from equilibrium. The dashed line is the curve fitted by the experimental data using Eq. (2). The legends ansssd numbers in the upper right corner indicate different stations conducted flow-through experiments. The uncertainties are shown by error bars.

1.4 yr^{-1}, Rickert (2000)], and the east China seas (containing the Yellow Sea and the East China Sea, 1.53 ± 1.39 yr^{-1} [Wu et al. (2017); Wu and Liu (2020)]; it is also lower than some open oceans, such as the Southern Ocean [2.39 ± 0.2 yr^{-1}, Van Cappellen and Qiu (1997b)], the equatorial Pacific [1.59 yr^{-1}, Gallinari et al. (2002)], and especially the North Atlantic [7.39 yr^{-1}, Ragueneau et al. (2001)] (Figure 8). The extremely high reaction rate constants of the $bSiO_2$ in sediments or the sediment trap of the North Atlantic Ocean are believed to be an important reason for the very low $bSiO_2$ contents (~1%) and poor preservation efficiency (12%) in the sediments compared with the Southern Ocean (Rickert, 2000; Ragueneau et al., 2001). Inversely, the relatively low reaction rate constants in the NSCS may be responsible for the well preservation efficiency of the $bSiO_2$ (27%) (Ma et al., 2022). Therefore, our results support the view that continental margin sediments play significant roles as silica sinks in the marine silica budget (DeMaster, 2002).

5 Conclusion

The $bSiO_2$ content in surface sediments of the NSCS ranged from 0.64% to 2.06%, with an average of 1.04% ± 0.35%. A strong zonal distribution tendency of the $bSiO_2$ distribution was observed, decreasing first and then increasing from the inner shelf to the upper slope. The excellent coupling accumulation of $bSiO_2$ and OC exhibits different preservation patterns in finer and coarser sediments compared with TN and OC. The solubility and dissolution kinetics in the NSCS sediments were at a relative low level (solubility: 298 ± 94 μM; dissolution rate constant: 1.12 ± 0.3 yr^{-1}) compared with other marginal seas and open oceans, likely due to the high Al concentration in the water column and the high content of lithogenic material in sediments. In addition, the distribution of satellite remote-sensed Chl-a, the proportion of diatoms in total biomass of phytoplankton, and the variation of surface primary productivity all point to a mismatch between the (diatom biomass)/(total phytoplankton biomass) ratio and the sedimentary $bSiO_2$/OC ratio at the inner shelf and outer shelf, and also a mismatch between the $bSiO_2$ primary productivity and the $bSiO_2$ sediment records at the upper slope of the NSCS. The resuspension-deposition and the higher reconstructed *in situ* rate constants (0.94 ± 0.13 yr^{-1}) and dissolution rate (0.20 ± 0.01 yr^{-1}) were responsible for the lower $bSiO_2$/OC ratio (0.45 ± 0.28) at the inner shelf, and the winnowing process at the outer shelf with a lower reconstructed *in situ* reactivity (0.30 yr^{-1}) and dissolution rate (0.001 yr^{-1}) led to the good preservation of $bSiO_2$ at the upper slope. The NSCS sediments may serve as an important silica sink in the global silicon cycle due to lower reactivity in comparison with other ocean areas.

Data availability statement

The raw data supporting the conclusions of this article will be made available by the authors, without undue reservation.

Author contributions

YM: conception and design of study. SML: financial support. YM: drafting the manuscript. SML, DZ and WL: revising the manuscript. YM, BY, NZ, and JH: acquisition of data. YM: interpretation of data. All authors contributed to the article and approved the submitted version.

Funding

This study was funded by the Natural Sciences Foundation of China (NSFC: 41376086), the Taishan Scholars Programme of Shandong Province, Aoshan Talents Program supported by the Qingdao National Laboratory for Marine Science and Technology (No. 2015ASTP-OS08). This study is a contribution to the IMBeR Program.

Acknowledgments

We thank the captain and crews of the R/V “Shi Yan 3” for their help during the sampling expeditions.

Conflict of interest

The authors declare that the research was conducted in the absence of any commercial or financial relationships that could be construed as a potential conflict of interest.

Publisher’s note

References

Bidle, K. D., and Azam, F. (1999). Accelerated dissolution of diatom silica by marine bacterial assemblages. *Nature* 397 (6719), 508–512. doi: 10.1038/17351

Bidle, K. D., and Azam, F. (2001). Bacterial control of silicon regeneration from diatom detritus: significance of bacterial ectohydrolases and species identity. *Limnology Oceanography* 46 (7), 1606–1623. doi: 10.4319/lo.2001.46.7.1606

Bidle, K. D., Brzezinski, M. A., Long, R. A., Jones, J. L., and Azam, F. (2003). Diminished efficiency in the oceanic silica pump caused by bacteria-mediated silica dissolution. *Limnology Oceanography* 48 (5), 1855–1868. doi: 10.4319/lo.2003.48.5.1855

Brzezinski, M. A., and Nelson, D. M. (1989). Seasonal changes in the silicon cycle within a gulf stream warm-core ring. *Deep Sea Res. Part A. Oceanographic Res. Papers* 36 (7), 1009–1030. doi: 10.1016/0198-0149(89)90075-7

Brzezinski, M. A., and Nelson, D. M. (1995). The annual silica cycle in the Sargasso Sea near Bermuda. *Deep Sea Res. Part I: Oceanographic Res. Papers* 42 (7), 1215–1237. doi: 10.1016/0967-0637(95)93592-3

Cai, P., Zhao, D., Wang, L., Huang, B., and Dai, M. (2015). Role of particle stock and phytoplankton community structure in regulating particulate organic carbon export in a large marginal sea. *J. Geophysical Research: Oceans* 120 (3), 2063–2095. doi: 10.1002/2014JC010432

Cao, Z., Wang, D., Zhang, Z., Zhou, K., Liu, X., Wang, L., et al. (2020). Seasonal dynamics and export of biogenic silica in the upper water column of a large marginal sea, the northern south China Sea. *Prog. Oceanography* 188, 102421. doi: 10.1016/j.pocean.2020.102421

Chen, Y.-L. L. (2005). Spatial and seasonal variations of nitrate-based new production and primary production in the south China Sea. *Deep Sea Res. Part I: Oceanographic Res. Papers* 52 (2), 319–340. doi: 10.1016/j.dsr.2004.11.001

Chen, C.-C., Shiah, F.-K., Chung, S.-W., and Liu, K.-K. (2006). Winter phytoplankton blooms in the shallow mixed layer of the south China Sea enhanced by upwelling. *J. Mar. Syst.* 59 (1-2), 97–110. doi: 10.1016/j.jmarsys.2005.09.002

Cheng, T., Hammond, D. E., Berelson, W. M., Hering, J. G., and Dixit, S. (2009). Dissolution kinetics of biogenic silica collected from the water column and sediments of three southern California borderland basins. *Mar. Chem.* 113 (1-2), 41–49. doi: 10.1016/j.marchem.2008.12.001

DeMaster, D. J. (1981). The supply and accumulation of silica in the marine environment. *Geochim. Cosmochim. Acta* 45 (10), 1715–1732. doi: 10.1016/0016-7037(81)90006-5

DeMaster, D. J. (2002). The accumulation and cycling of biogenic silica in the southern ocean: revisiting the marine silica budget. *Deep Sea Res. Part II: Topical Stud. Oceanography* 49 (16), 3155–3167. doi: 10.1016/S0967-0645(02)00076-0

DeMaster, D. J., Knapp, G. B., and Nittrouer, C. A. (1983). Biological uptake and accumulation of silica on the Amazon continental shelf. *Geochimica Cosmochimica Acta* 47 (10), 1713–1723. doi: 10.1016/0016-7037(83)90021-2

DeMaster, D. J., Ragueneau, O., and Nittrouer, C. A. (1996). Preservation efficiencies and accumulation rates for biogenic silica and organic c, n, and p in high-latitude sediments: The Ross Sea. *J. Geophysical Research: Oceans* 101 (C8), 18501–18518. doi: 10.1029/96JC01634

Dixit, S., and Van Cappellen, P. (2002). Surface chemistry and reactivity of biogenic silica. *Geochimica Cosmochimica Acta* 66 (14), 2559–2568. doi: 10.1016/S0016-7037(02)00854-2

Dixit, S., Van Cappellen, P., and Van Bennekom, A. J. (2001). Processes controlling solubility of biogenic silica and pore water build-up of silicic acid in marine sediments. *Mar. Chem.* 73 (3-4), 333–352. doi: 10.1016/S0304-4203(00)00118-3

Dugdale, R. C., Wilkerson, F. P., and Minas, H. J. (1995). The role of a silicate pump in driving new production. *Deep Sea Res. Part I: Oceanographic Res. Papers* 42 (5), 697–719. doi: 10.1016/0967-0637(95)00015-X

Fraysse, F., Pokrovsky, O. S., Schott, J., and Meunier, J.-D. (2006). Surface properties, solubility and dissolution kinetics of bamboo phytoliths. *Geochimica Cosmochimica Acta* 70 (8), 1939–1951. doi: 10.1016/j.gca.2005.12.025

Gallinari, M., Ragueneau, O., Corrin, L., DeMaster, D. J., and Tréguer, P. (2002). The importance of water column processes on the dissolution properties of biogenic silica in deep-sea sediments i. solubility. *Geochimica Cosmochimica Acta* 66 (15), 2701–2717. doi: 10.1016/S0016-7037(02)00874-8

Gallinari, M., Ragueneau, O., DeMaster, D., Hartnett, H., Rickert, D., and Thomas, C. (2008). Influence of seasonal phytodetritus deposition on biogenic silica dissolution in marine sediments–potential effects on preservation. *Deep Sea Res. Part II: Topical Stud. Oceanography* 55 (22-23), 2451–2464. doi: 10.1016/j.dsr2.2008.06.005

Ge, Q., Liu, J. P., Xue, Z., and Chu, F. (2014). Dispersal of the zhujiang river (Pearl river) derived sediment in the Holocene. *Acta Oceanologica Sinica.* 33, 1–9. doi: 10.1007/s13131-014-0407-8

Gehlen, M., Beck, L., Calas, G., Flank, A.-M., Van Bennekom, A. J., and Van Beusekom, J. E. E. (2002). Unraveling the atomic structure of biogenic silica: evidence of the structural association of Al and Si in diatom frustules. *Geochimica Cosmochimica Acta* 66 (9), 1601–1609. doi: 10.1016/S0016-7037(01)00877-8

Guo, Y. (2016). Distribution of dissolved aluminum in the northern south China Sea and its influence factors. (Qingdao: Ocean University of China). (in Chinese with English abstract)

Han, A., Dai, M., Kao, S.-J., Gan, J., Li, Q., Wang, L., et al. (2012). Nutrient dynamics and biological consumption in a large continental shelf system under the influence of both a river plume and coastal upwelling. *Limnology Oceanography* 57 (2), 486–502. doi: 10.4319/lo.2012.57.2.0486

Ho, T.-Y., Chou, W.-C., Wei, C.-L., Lin, F.-J., Wong, G. T., and Line, H.-L. (2010). Trace metal cycling in the surface water of the south China Sea: vertical fluxes, composition, and sources. *Limnology Oceanography* 55 (5), 1807–1820. doi: 10.4319/lo.2010.55.5.1807

Hung, J.-J., Wang, S.-M., and Chen, Y.-L. (2007). Biogeochemical controls on distributions and fluxes of dissolved and particulate organic carbon in the northern south China Sea. *Deep Sea Res. Part II: Topical Stud. Oceanography* 54 (14-15), 1486–1503. doi: 10.1016/j.dsr2.2007.05.006

Hurd, D. C. (1973). Interactions of biogenic opal, sediment and seawater in the central equatorial pacific. *Geochimica Cosmochimica Acta* 37 (10), 2257–2282. doi: 10.1016/0016-7037(73)90103-8

Kamatani, A., Ejiri, N., and Treguer, P. (1988). The dissolution kinetics of diatom ooze from the Antarctic area. *Deep Sea Res. Part A. Oceanographic Res. Papers* 35 (7), 1195–1203. doi: 10.1016/0198-0149(88)90010-6

Kamatani, A., and Riley, J. P. (1979). Rate of dissolution of diatom silica walls in seawater. *Mar. Biol.* 55 (1), 29–35. doi: 10.1007/BF00391714

Khalil, K., Rabouille, C., Gallinari, M., Soetaert, K., DeMaster, D., and Ragueneau, O. (2007). Constraining biogenic silica dissolution in marine sediments: a comparison between diagenetic models and experimental dissolution rates. *Mar. Chem.* 106 (1-2), 223–238. doi: 10.1016/j.marchem.2006.12.004

Koning, E., Brummer, G. J., Van Raaphorst, W., Van Bennekom, J., Helder, W., and Van Iperen, J. (1997). Settling, dissolution and burial of biogenic silica in the sediments off Somalia (northwestern Indian ocean). *Deep-Sea Res. Part Ii-Topical Stud. Oceanography* 44 (6-7), 1341–1360. doi: 10.1016/S0967-0645(97)00018-0

Koning, E., Gehlen, M., Flank, A.-M., Calas, G., and Epping, E. (2007). Rapid post-mortem incorporation of aluminum in diatom frustules: Evidence from chemical and structural analyses. *Mar. Chem.* 106 (1-2), 208–222. doi: 10.1016/j.marchem.2006.06.009

Kramer, J., Laan, P., Sarthou, G., Timmermans, K., and De Baar, H. (2004). Distribution of dissolved aluminium in the high atmospheric input region of the subtropical waters of the north Atlantic ocean. *Mar. Chem.* 88 (3-4), 85–101. doi: 10.1016/j.marchem.2004.03.009

Krause, J. W., Nelson, D. M., and Brzezinski, M. A. (2011). Biogenic silica production and the diatom contribution to primary production and nitrate uptake in the eastern equatorial pacific ocean. *Deep-Sea Res. Part Ii-Topical Stud. Oceanography* 58 (3-4), 434–448. doi: 10.1016/j.dsr2.2010.08.010

Krumbein, W. C. (1934). Size frequency distributions of sediments. *J. Sedimentary Res.* 4 (2), 65–77. doi: 10.1306/D4268EB9-2B26-11D7-8648000102C1865D

Lawson, D. S., Hurd, D. C., and Pankratz, H. S. (1978). Silica dissolution rates of decomposing phytoplankton assemblages at various temperatures. *Am. J. Sci.* 278 (10), 1373–1393. doi: 10.2475/ajs.278.10.1373

Liu, Y., Dai, M., Chen, W., and Cao, Z. (2012). "Distribution of biogenic silica in the upwelling zones in the south China Sea," in *Advances in geosciences*, vol. 28. (Atmospheric Science (AS) & Ocean Science (OS), 55–65.

Liu, S. M., De Zhu, B., Zhang, J., Wu, Y., Liu, G. S., Deng, B., et al. (2010). Environmental change in jiaozhou bay recorded by nutrient components in sediments. *Mar. pollut. Bull.* 60 (9), 1591–1599. doi: 10.1016/j.marpolbul.2010.04.003

Liu, Y., Gao, S., Wang, Y. P., Yang, Y., Long, J., Zhang, Y., et al. (2014). Distal mud deposits associated with the pearl river over the northwestern continental shelf of the south China Sea. *Mar. Geology.* 347, 43–57. doi: 10.1016/j.margeo.2013.10.012

Liu, S., Hong, G.-H., Zhang, J., Ye, X., and Jiang, X. (2009). Nutrient budgets for large Chinese estuaries. *Biogeosciences* 6 (10), 2245–2263. doi: 10.5194/bg-6-2245-2009

Liu, S., Ye, X., Zhang, J., and Zhao, Y. (2002). Problems with biogenic silica measurement in marginal seas. *Mar. Geology* 192 (4), 383–392. doi: 10.1016/S0025-3227(02)00531-5

Liu, Z., Zhao, Y., Colin, C., Stattegger, K., Wiesner, M. G., Huh, C.-A., et al. (2016). Source-to-sink transport processes of fluvial sediments in the south China Sea. *Earth-Science Rev.* 153, 238–273. doi: 10.1016/j.earscirev.2015.08.005

Loucaides, S., Behrends, T., and Van Cappellen, P. (2010). Reactivity of biogenic silica: Surface versus bulk charge density. *Geochimica Cosmochimica Acta* 74 (2), 517–530. doi: 10.1016/j.gca.2009.10.038

Loucaides, S., Koning, E., and Van Cappellen, P. (2012). Effect of pressure on silica solubility of diatom frustules in the oceans: Results from long-term laboratory and field incubations. *Mar. Chem.* 136, 1–6. doi: 10.1016/j.marchem.2012.04.003

Loucaides, S., Van Cappelle, P., and Behrends, T. (2008). Dissolution of biogenic silica from land to ocean: Role of salinity and pH. *LimOc* 53 (4), 1614–1621. doi: 10.4319/lo.2008.53.4.161

Ma, Y., Zhang, L., Liu, S., and Zhu, D. (2022). Silicon balance in the south China Sea. *Biogeochemistry*, 157, 327–353. doi: 10.1007/s10533-021-00879-4

Michalopoulos, P., and Aller, R. C. (2004). Early diagenesis of biogenic silica in the Amazon delta: Alteration, authigenic clay formation, and storage. *Geochimica Cosmochimica Acta* 68 (5), 1061–1085. doi: 10.1016/j.gca.2003.07.018

Middag, R., Van Slooten, C., De Baar, H., and Laan, P. (2011). Dissolved aluminium in the southern ocean. *Deep Sea Res. Part II: Topical Stud. Oceanography* 58 (25-26), 2647–2660. doi: 10.1016/j.dsr2.2011.03.001

Moriceau, B., Garvey, M., Ragueneau, O., and Passow, U. (2007). Evidence for reduced biogenic silica dissolution rates in diatom aggregates. *Mar. Ecol. Prog. Ser.* 333, 129–142. doi: 10.3354/meps333129

Mortlock, R., Charles, C., Froelich, P., Zibello, M., Saltzman, J., Hays, J., et al. (1991). Evidence for lower productivity in the Antarctic ocean during the last glaciation. *Nature* 351 (6323), 220–223. doi: 10.1038/351220a0

Mortlock, R. A., and Froelich, P. N. (1989). A simple method for the rapid determination of biogenic opal in pelagic marine sediments. *Deep Sea Res. Part A Oceanographic Res. Papers* 36 (9), 1415–1426. doi: 10.1016/0198-0149(89)90092-7

Müller, G. (1966). Grain size, carbonate content, and carbonate mineralogy of recent sediments of the Indian ocean off the eastern coast of Somalia. *Naturwissenschaften* 53 (21), 547–550. doi: 10.1007/BF00602953

Nelson, D. M., DeMaster, D. J., Dunbar, R. B., and Smith, W. O.Jr. (1996). Cycling of organic carbon and biogenic silica in the southern ocean: Estimates of water-column

and sedimentary fluxes on the Ross Sea continental shelf. *J. Geophysical Research: Oceans* 101 (C8), 18519–18532. doi: 10.1029/96JC01573

Nelson, D. M., and Dortch, Q. (1996). Silicic acid depletion and silicon limitation in the plume of the Mississippi river: evidence from kinetic studies in spring and summer. *Mar. Ecol. Prog. Ser.* 136, 163–178. doi: 10.3354/meps136163

Nelson, D. M., Tréguer, P., Brzezinski, M. A., Leynaert, A., and Quéguiner, B. (1995). Production and dissolution of biogenic silica in the ocean: Revised global estimates, comparison with regional data and relationship to biogenic sedimentation. *Global Biogeochemical Cycles* 9 (3), 359–372. doi: 10.1029/95GB01070

Ning, X. R., Chai, F., Xue, H., Cai, Y., Liu, C., and Shi, J. (2004). Physical-biological oceanographic coupling influencing phytoplankton and primary production in the South China Sea. *J. Geophys. Res.* 109, C10005. doi: 10.1029/2004JC002365

Orians, K. J., and Bruland, K. W. (1986). The biogeochemistry of aluminum in the pacific ocean. *Earth Planetary Sci. Lett.* 78 (4), 397–410. doi: 10.1016/0012-821X(86)90006-3

Pan, X., Wong, G. T., Tai, J.-H., and Ho, T. Y. (2015). Climatology of physical hydrographic and biological characteristics of the Northern South China Sea Shelf-sea (NoSoCS) and adjacent waters: Observations from satellite remote sensing. *Deep Sea Research Part II: Topical Studies in Oceanography* 117, 10–22. doi: 10.1016/j.dsr2.2015.02.022

Ragueneau, O., Gallinari, M., Corrin, L., Grandel, S., Hall, P., Hauvespre, A., et al. (2001). The benthic silica cycle in the northeast Atlantic: annual mass balance, seasonality, and importance of non-steady-state processes for the early diagenesis of biogenic opal in deep-sea sediments. *Prog. Oceanography* 50 (1-4), 171–200. doi: 10.1016/S0079-6611(01)00053-2

Ragueneau, O., Regaudie-de-Gioux, A., Moriceau, B., Gallinari, M., Vangriesheim, A., Baurand, F., et al. (2009). A benthic Si mass balance on the Congo margin: Origin of the 4000m DSi anomaly and implications for the transfer of Si from land to ocean. *Deep Sea Res. Part II: Topical Stud. Oceanography* 56 (23), 2197–2207. doi: 10.1016/j.dsr2.2009.04.003

Ragueneau, O., Schultes, S., Bidle, K., Claquin, P., and Moriceau, B. (2006). Si and C interactions in the world ocean: Importance of ecological processes and implications for the role of diatoms in the biological pump. *Global Biogeochemical Cycles* 20 (4), GB4502. doi: 10.1029/2006GB002688

Ragueneau, O., Tréguer, P., Leynaert, A., Anderson, R. F., Brzezinski, M. A., DeMaster, D. J., et al. (2000). A review of the Si cycle in the modern ocean: recent progress and missing gaps in the application of biogenic opal as a paleoproductivity proxy. *Global Planetary Change* 26 (4), 317–365. doi: 10.1016/S0921-8181(00)00052-7

Rahman, S., Aller, R. C., and Cochran, J. K. (2017). The missing silica sink: Revisiting the marine sedimentary Si cycle using cosmogenic 32Si. *Global Biogeochemical Cycles* 31 (10), 1559–1578. doi: 10.1002/2017GB005746

Rickert, D. (2000). Dissolution kinetics of biogenic silica in marine environments (German: Alfred Wegener Institute for Polar and Marine Research).

Rickert, D., Schlüter, M., and Wallmann, K. (2002). Dissolution kinetics of biogenic silica from the water column to the sediments. *Geochimica Cosmochimica Acta* 66 (3), 439–455. doi: 10.1016/S0016-7037(01)00757-8

Sayles, F., Martin, W., Chase, Z., and Anderson, R. (2001). Benthic remineralization and burial of biogenic SiO2, CaCO3, organic carbon, and detrital material in the southern ocean along a transect at 170 West. *Deep Sea Res. Part II: Topical Stud. Oceanography* 48 (19-20), 4323–4383. doi: 10.1016/S0967-0645(01)00091-1

Schmidt, M., Botz, R., Rickert, D., Bohrmann, G., Hall, S., and Mann, S. (2001). Oxygen isotopes of marine diatoms and relations to opal-a maturation. *Geochimica Cosmochimica Acta* 65 (2), 201–211. doi: 10.1016/S0016-7037(00)00534-2

Schrader, H., and Sorknes, R. (1991). Peruvian Coastal upwelling: Late quaternary productivity changes revealed by diatoms. *Mar. Geology* 97 (3-4), 233–249. doi: 10.1016/0025-3227(91)90118-N

Schüßler, U., Balzer, W., and Deeken, A. (2005). Dissolved Al distribution, particulate Al fluxes and coupling to atmospheric Al and dust deposition in the Arabian Sea. *Deep Sea Res. Part II: Topical Stud. Oceanography* 52 (14-15), 1862–1878. doi: 10.1016/j.dsr2.2005.06.005

Shi, Z., Liu, K., Zhang, S., Xu, H., and Liu, H. (2019). Spatial distributions of mesozooplankton biomass, community composition and grazing impact in association with hypoxia in the pearl river estuary. *Estuarine Coast. Shelf Sci.* 225, 106237. doi: 10.1016/j.ecss.2019.05.019

Tréguer, P., Sutton, J. N., Brzezinski, M., Charette, M. A., Devries, T., Dutkiewicz, S., et al. (2021). Reviews and syntheses: The biogeochemical cycle of silicon in the modern ocean. *Biogeosciences* 18, 1269–1289. doi: 10.5194/bg-18-1269-2021

Van Bennekom, A. J., Buma, A. G. J., and Nolting, R. F. (1991). Dissolved aluminium in the weddell-Scotia confluence and effect of Al on the dissolution kinetics of biogenic silica. *Mar. Chem.* 35 (1-4), 423–434. doi: 10.1016/S0304-4203(09)90034-2

Van Beueskom, J., Van Bennekom, A., Tréguer, P., and Morvan, J. (1997). Aluminium and silicic acid in water and sediments of the enderby and crozet basins. *Deep Sea Res. Part II: Topical Stud. Oceanography* 44 (5), 987–1003. doi: 10.1016/S0967-0645(96)00105-1

Van Cappellen, P. (1996). Reactive surface area control of the dissolution kinetics of biogenic silica in deep-sea sediments. *Chem. Geology* 132 (1-4), 125–130. doi: 10.1016/S0009-2541(96)00047-2

Van Cappellen, P., Dixit, S., and van Beusekom, J. (2002). Biogenic silica dissolution in the oceans: Reconciling experimental and field-based dissolution rates. *Global Biogeochemical Cycles* 16 (4), 23–21-23-10. doi: 10.1029/2001GB001431

Van Cappellen, P., and Qiu, L. (1997a). Biogenic silica dissolution in sediments of the southern ocean. i. solubility. *Deep Sea Res. Part II Topical Stud. Oceanography* 44 (5), 1109–1128. doi: 10.1016/S0967-0645(96)00113-0

Van Cappellen, P., and Qiu, L. (1997b). Biogenic silica dissolution in sediments of the southern ocean. II. kinetics. *Deep Sea Res. Part II: Topical Stud. Oceanography* 44 (5), 1129–1149. doi: 10.1016/S0967-0645(96)00112-9

Van der Voort, T. S., Mannu, U., Blattmann, T. M., Bao, R., Zhao, M., and Eglinton, T. I. (2018). Deconvolving the fate of carbon in coastal sediments. *Geophysical Res. Lett.* 45, 4134–4142. doi: 10.1029/2018GL077009

Wang, P., and Li, Q. (2009). *The south China Sea: Paleoceanography and sedimentology* (Netherlands: Springer), 506.

Ward, J., Hendry, K., Arndt, S., Faust, J. C., Freitas, F. S., Henley, S. F., et al. (2021). Stable silicon isotopes uncover a mineralogical control on the benthic silicon cycle in the Arctic barents Sea. *Geochimica et Cosmochimica Acta* 329, 206–230. doi: 10.1016/j.gca.2022.05.005

Wei, B., Mollenhauer, G., Hefter, J., Grotheer, H., and Jia, G. (2020). Dispersal and aging of terrigenous organic matter in the pearl river estuary and the northern south China Sea shelf. *Geochimica Cosmochimica Acta* 282, 324–339. doi: 10.1016/j.gca.2020.04.032

Willey, J. D. (1974). The effect of pressure on the solubility of amorphous silica in seawater at 0 c. *Mar. Chem.* 2 (4), 239–250. doi: 10.1016/0304-4203(74)90018-8

Wu, B., and Liu, S. M. (2020). Dissolution kinetics of biogenic silica and the recalculated silicon balance of the East China Sea. *Sci. Total Environ.* 743, 140552. doi: 10.1016/j.scitotenv.2020.140552

Wu, B., Liu, S. M., and Ren, J. L. (2017). Dissolution kinetics of biogenic silica and tentative silicon balance in the yellow Sea. *Limnology Oceanography* 62 (4), 1512–1525. doi: 10.1002/lno.10514

Wu, B., Lu, C., and Liu, S. (2015). Dynamics of biogenic silica dissolution in jiaozhou bay, western yellow Sea. *Mar. Chem.* 174, 58–66. doi: 10.1016/j.marchem.2015.05.004

Xiao, W., Wang, L., Laws, E., Xie, Y., Chen, J., Liu, X., et al. (2018). Realized niches explain spatial gradients in seasonal abundance of phytoplankton groups in the south China Sea. *Prog. Oceanography* 162, 223–239. doi: 10.1016/j.pocean.2018.03.008

Yang, B., Liu, S.-M., and Zhang, G.-L. (2018). Geochemical characteristics of phosphorus in surface sediments from the continental shelf region of the northern south China Sea. *Mar. Chem.* 198, 44–55. doi: 10.1016/j.marchem.2017.11.001

Zhang, X., Ren, J., Guo, Y., Li, L., and Zhang, R. (2020). Distributions and influencing factors of dissolved aluminum in the zhujiang river estuary,continental slope of the northern south China Sea in autumn and summer. *Haiyang Xuebao* 42 (02), 10–21. (in Chinese with English abstract)

Zhang, L. L., Wang, R. J., Chen, M. H., Liu, J. G., Zeng, L. L., Xiang, R., et al. (2015). Biogenic silica in surface sediments of the south China Sea: Controlling factors and paleoenvironmental implications. *Deep-Sea Res. Part Ii-Topical Stud. Oceanography* 122, 142–152. doi: 10.1016/j.dsr2.2015.11.008

Zhou, P., Li, D., Liu, G., Men, W., and Ji, L. (2010). Biogenic silica in surface sediments of the northeastern and southern south China Sea. *J. Trop. Oceanography* 29 (04), 40–47. (in Chinese with English abstract)

frontiers | Frontiers in Marine Science

TYPE Original Research
PUBLISHED 05 July 2023
DOI 10.3389/fmars.2023.1162685

OPEN ACCESS

EDITED BY
Alex J. Poulton,
Heriot-Watt University, United Kingdom

REVIEWED BY
Wei Liu,
Wenzhou Vocational College of Science and Technology, China
Arnaud Laurent,
Dalhousie University, Canada

*CORRESPONDENCE
Jeffrey W. Krause
jkrause@disl.edu

†PRESENT ADDRESSES
Adam D. Boyette,
Naval Oceanographic Office, Stennis Space Center, MS, United States
Rebecca A. Pickering,
Department of Geology, Lund University, Lund, Sweden

RECEIVED 09 February 2023
ACCEPTED 31 May 2023
PUBLISHED 05 July 2023

CITATION
Krause JW, Boyette AD, Marquez IA, Pickering RA and Maiti K (2023) Drivers of diatom production and the legacy of eutrophication in two river plume regions of the northern Gulf of Mexico.
Front. Mar. Sci. 10:1162685.
doi: 10.3389/fmars.2023.1162685

Drivers of diatom production and the legacy of eutrophication in two river plume regions of the northern Gulf of Mexico

Jeffrey W. Krause[1,2]*, Adam D. Boyette[3†], Israel A. Marquez[1,2], Rebecca A. Pickering[1,2†] and Kanchan Maiti[4]

[1]Dauphin Island Sea Lab, Dauphin Island, AL, United States, [2]School of Marine and Environmental Sciences, University of South Alabama, Mobile, AL, United States, [3]Division of Marine Science, School of Ocean Science and Engineering, University of Southern Mississippi, Stennis Space Center, MS, United States, [4]Department of Oceanography and Coastal Studies, Louisiana State University, Baton Rouge, LA, United States

In the northern Gulf of Mexico (nGoM), the Louisiana Shelf (LS) and Mississippi Bight (MB) subregions are influenced by eutrophication to varying degrees. Despite recognition that dissolved silicon may regulate diatom productivity in the nGoM, there is only one published data set reporting biogenic silica ($bSiO_2$) production rates for each subregion. We report that $bSiO_2$ production rates on the LS and MB are high and appear to be controlled by different nutrients among seasons. Despite exceptional upper trophic level biomass regionally, which suggests significant primary production by diatoms (as in other systems), gross euphotic-zone integrated $bSiO_2$ production rates are lower than major $bSiO_2$ producing regions (e.g. upwelling systems). However, when normalizing to the depth of the euphotic zone, the $bSiO_2$ production rates on the LS are like normalized rates in upwelling systems. We suggest local river-plume influenced hydrography concentrates diatom productivity within shallow euphotic zones, making production more accessible to higher trophic organisms. Comparison of rates between the LS and MB suggest that the fluvial nitrate within the LS stimulates $bSiO_2$ production above that in the MB, which has a smaller watershed and is less eutrophic (relatively). Beyond understanding the factors controlling regional $bSiO_2$ production, these data offer the most comprehensive Si-cycle baseline to date as the LS and MB will likely exchange freely in the mid to late century due to land subsidence of the Mississippi River delta and/or sea-level rise.

KEYWORDS

biogenic silica production, Gulf of Mexico, Louisiana Shelf, Mississippi Bight, eutrophication, diatom

Introduction

Diatoms play important roles in coastal biogeochemistry and often dominate the phytoplankton biomass and bloom productivity in these environments. Diatoms are unique in their obligate requirement for silicon, which is required in near unity to nitrogen under the many growth conditions among low- to high-latitude ecosystems (Brzezinski, 1985; Lomas et al., 2019). Widespread use of agricultural fertilizer has increased fluvial nitrogen loading in many watersheds and in some cases has resulted in a doubling of riverine nitrogen input to the coastal ocean (Cloern, 2001). In many eutrophied rivers for nitrogen, dissolved silicon ($Si(OH)_4$) has declined or remained stable, thereby lowering the Si:N ratio below diatoms' optimum (i.e. <1.0) potentially favoring diatoms blooms to deplete $Si(OH)_4$ before NO_3. The decline in $Si(OH)_4$ availability relative to nitrate and phosphate has been linked to shifts from diatom-dominated to flagellate-dominated ecosystems; this so called '$Si(OH)_4$ Paradigm' (Ragueneau et al., 2006) was first proposed for coastal systems by Officer and Ryther (1980) and has been evoked as a potential mechanism for changes in many systems (reviewed by Cloern (2001)). However, the linkage among significant Si:N perturbations and the changing role of diatoms is built largely on standing stock data (e.g. nutrients, phytoplankton abundance), rather than physiological rate data, as the latter data are absent in many systems. Furthermore, testing for an Si:N effect in these systems is challenging given the lack of baseline information prior to the nutrient perturbation.

In the Mississippi River (MR), which discharges onto the Louisiana Shelf (LS) in the northern Gulf of Mexico (nGoM), the annual average Si:N ratio declined from >3 in 1960 to ~1 in 1980. The change was driven by both increasing nitrate and decreasing $Si(OH)_4$ concentrations and has remained around the latter Si:N value to present day (Figure 1). The MR now exhibits strong seasonal oscillations between favorable (>1.0, late summer/autumn) and unfavorable (<1.0, spring) Si:N conditions for diatoms (Figure 1C). This unfavorable period corresponds to the annual peak in MR discharge and elevated primary production rates on the LS from nitrate loading (Lohrenz et al., 1997). The changes in the MR-derived nutrients in the late 20th century coincided with major ecosystem-wide changes in the nGoM, e.g. frequent and intense hypoxia events (Rabalais et al., 2007). On the LS, multiple species from the pennate diatom genera *Pseudo-nitzschia* numerically dominate the diatom assemblage during periods of high MR flow (Bargu et al., 2016). These results, combined with increasing *Pseudo-nitzschia* preserved in regional sediments during the late 20th century (Parsons et al., 2002) and the rise of more flagellate harmful algal species on the LS (Dortch et al., 1999), have led to the hypothesis that the Si:N changes in the MR watershed may have reduced the diatom contribution to food web processes in this system (Turner et al., 1998).

Biogenic silica ($bSiO_2$) production rates can serve as a proxy for diatom growth as silicon is used to produce their $bSiO_2$ shell. While recent reports have shown the importance of cyanobacteria and Rhizaria in $bSiO_2$ cycling, e.g. (Baines et al., 2012; Biard et al., 2018), diatom biomass is significantly higher on the LS than these other groups. The only published $bSiO_2$ production data in this area was

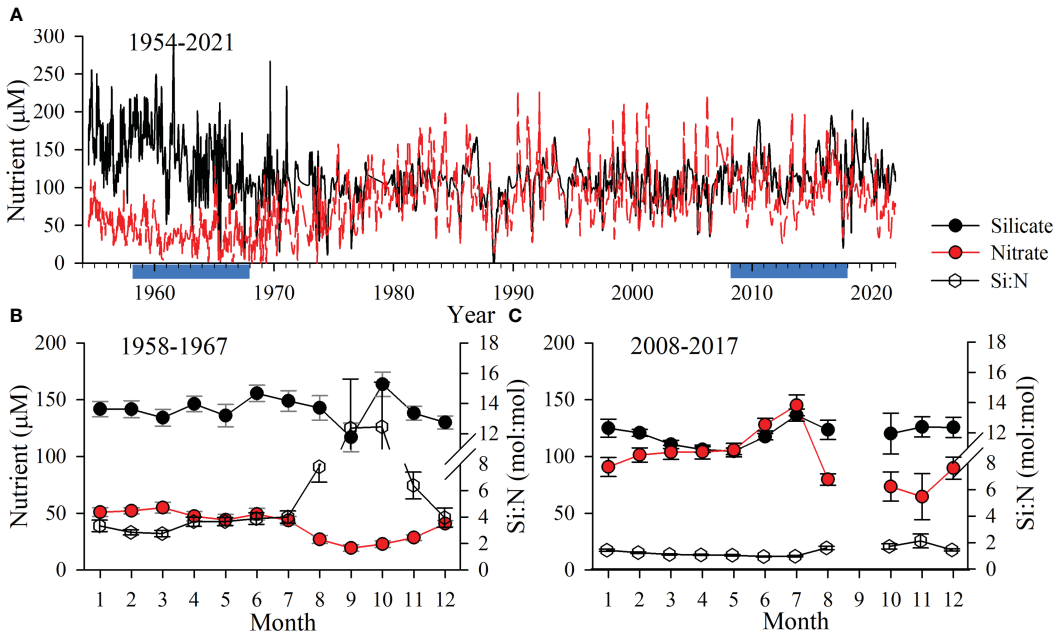

FIGURE 1
(A) Time series of Mississippi River silicate and nitrate at the United States Geological Survey Station 07373420 in St. Francisville, Louisiana, United States, from August 1954 through December 2021. **(B, C)** Comparison of the monthly average (± standard error) for each nutrient (left scale) and the silicate:nitrate (Si:N) molar ratio (right scale) among 10-year subsets (blue highlights in A) separated by 50 years: 1958 through 1967 **(B)** and 2008 through 2017 **(C)**.

acquired on the LS in the early 1990s (Nelson and Dortch, 1996), approximately a decade after the major MR watershed shift in nutrients stabilized, and this prior work only examined processes (e.g. kinetics of $Si(OH)_4$ uptake by diatoms) at a single depth. There are currently no available euphotic-zone profile data to determine whether diatom $Si(OH)_4$ consumption on the shelf may exceed the delivery of $Si(OH)_4$ from the MR or benthic flux sources, which (if found) would support the hypothesis that Si may exert a strong control over regional diatom productivity, e.g. Dale et al. (2007).

The Mississippi Bight (MB) is located to the east of the LS shelf and MR delta extending to Perdido Bay, Florida (Figure 2). The MB is a river-dominated system fed from the combined rivers of Mobile Bay (Alabama). Analysis of water oxygen isotopic signatures show that MR water did not dominate the freshwater loading to the MB during multiple years in mid 2010s, instead this was driven largely by the combined rivers from the northern domain, especially those discharging through Mobile Bay (Sanial et al., 2019). Mobile Bay has the fourth highest freshwater discharge rate in the United States (Stumpf et al., 1993) but nitrate concentrations rarely exceed 20 µM (Pennock et al., 1999). The MB is also highly productive, being the central habitat range for a variety of economically important fish and invertebrate fauna and is the eastern extension of the so called 'Fertile Fisheries Crescent' where, historically, ~70-80% of fisheries landings in the entire GoM occur (Gunter, 1963). Comparison of diatom processes within the water column of the LS and MB allows an assessment of similarities, i.e. both are river plume systems where the main distributaries are separated by ~200 km, and differences occurring due to the watershed sizes and the degree of nutrient loading and/or eutrophication.

Hydrographic processes in both the MB and LS have significantly changed in the last century. Since the 1950s, the river discharge increased 31% and 15% in the MR and Mobile Bay river system, respectively (Milliman et al., 2008), and this trend is expected to increase in the 21st century (Tao et al., 2014). Land subsidence rates in southeastern Louisiana are rapid (Kolker et al., 2011) and there will be pelagic connectivity between the MB and LS domains as the MR delta becomes submerged. Thus, baseline data on diatom biogeochemical processes are required to ground truth models attempting to predict how the MB and LS pelagic ecosystems will alter as their connectivity increases.

The overarching goal of this study was to evaluate whether $bSiO_2$ cycling rates in the LS have significantly changed in the last 30 years and test the hypothesis that $Si(OH)_4$ availability controls diatom productivity. Here, we evaluated seasonal variability between systems and establish baseline rates and stocks. The nGoM is a model region for river-dominated systems which have undergone significant anthropogenic perturbations. The $bSiO_2$ cycling processes in this region may be relevant to many low-latitude river-dominated regions that have undergone, or are presently experiencing, similar stressors.

Methods

Four cruises in the LS and MB were completed as part of the Coastal Louisiana Silicon Cycle (CLASiC) and Consortium for Coastal River-Dominated Ecosystems (CONCORDE) projects, respectively. These programs were independent and had different goals (Greer et al., 2018; Pickering et al., 2020), but similar silicon-cycling rate and ancillary measurements were obtained. The CLASiC cruises were conducted aboard the R/V *Pelican* during summer (27 August – 6 September 2016) and spring (4 – 13 May 2017), corresponding to the low and high-flow periods of the MR discharge onto the LS, respectively. The two CONCORDE cruises

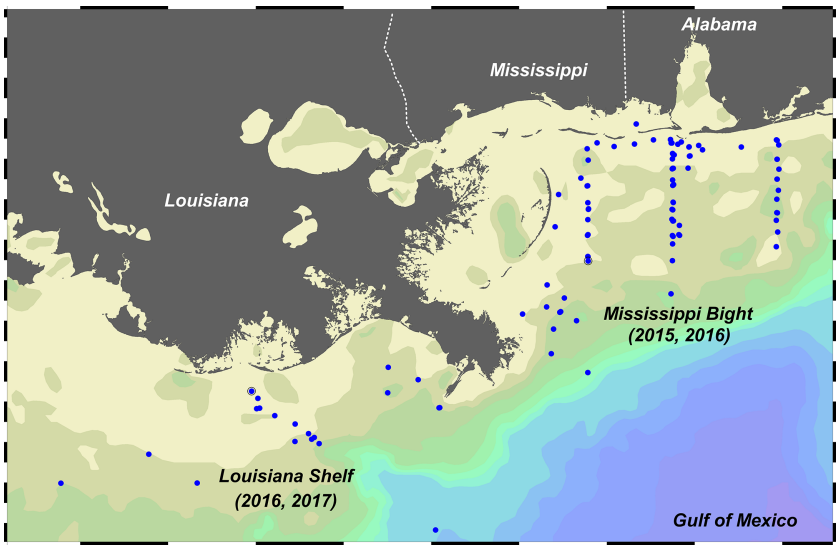

FIGURE 2
Station map for four cruises in the Louisiana Shelf (LS) and Mississippi Bight (MB). LS cruises were part of the Coastal Louisiana Silicon Cycling (CLASiC) project in August-September 2016 and May 2017 (Pickering et al., 2020, Ghaisas et al., 2021); MB cruises were part of the Consortium for Oil Spill Exposure Pathways in Coastal River-Dominated Ecosystems (CONCORDE) project in October-November 2015 and March-April 2016 (Dzwonkowski et al., 2017; Sanial et al., 2019). Map made using Ocean Data View (Schlitzer, 2016).

were conducted aboard the R/V *Point Sur* during autumn (28 October – 7 November 2015) and spring (29 March – 11 April 2016), where the spring cruise corresponded to the annual maximum discharge onto the MB from the Mobile Bay riverine complex and other local rivers.

Water column stations were sampled in salinity zones (CLASiC) and geographic corridors (CONCORDE). Given the dominance of the MR in surface hydrography on the LS, CLASiC cruise stations were targeted to river-influence zones operationally defined by a strong (salinity <25), moderate (salinity 25 – 30), or low riverine signal (salinity >30) in surface salinity. CONCORDE stations were aligned primarily among meridional transects in the west, middle, and east of the MB, with the autumn cruise sampling also in the southern zone near the eastward distributary of the MR and the spring cruise had some stations parallel to the barrier island coast of Alabama in the northern domain. All water column sampling was done using a 12-bottle rosette sampler equipped with 12 L Niskin bottles and a SeaBird SBE911 CTD with a Biospherical photosynthetically active radiation sensor and WET Labs C-Star transmissometer (instruments on both vessels). For CLASiC stations, CTD sampling was conducted ~1 hour after sunrise or in the late afternoon/early evening <2 hours prior to sunset. Samples were either selected at pre-determined depths (standing stocks) or specified light levels (for incubations) normalized to the irradiance available just below the surface (i.e. I_0). Specific light levels included 100% (just below surface), 50%, 20%, 5%, and 1% I_0. During most CONCORDE stations, sampling was done throughout the night and only surface samples were taken for incubation (i.e. no light depths). Select vertical profiles were conducted, and these hydrocasts were taken in the morning to target the defined light depths as during CLASiC. As in prior studies, e.g. (Lomas et al., 2009; Krause et al., 2021), Niskin samples were pooled into 10 L carboys (covered with opaque bags) and then subsampled for various measurements; the carboy was gently mixed during sampling to keep the contents in suspension.

Subsamples were collected for nutrients and particulate matter. 50 mL of seawater was immediately filtered using a 0.2 µm polycarbonate filter (CLASiC) or ~0.6 µm glass-fiber filter (CONCORDE) for nutrient analyses. Analyses were done as described previously (Dzwonkowski et al., 2017; Pickering et al., 2020) but are briefly discussed here. For $Si(OH)_4$, samples were analyzed using a manual colorimetric method at sea (CLASiC) or on frozen samples (CONCORDE), which were thawed at room temperature for sufficient time to allow Si polymers to break down prior to colorimetric analysis. Filtrate for all other nutrients was immediately frozen. Dissolved inorganic nitrogen (nitrate + nitrite, NO_3+NO_2; ammonium, NH_4) and dissolved soluble reactive phosphorus (SRP) were analyzed using a Skalar autoanalyzer. During CONCORDE, ~500 mL samples were filtered onto 1.2 µm polycarbonate filters for $bSiO_2$ and frozen. In the laboratory, samples were dried and run using a sodium hydroxide digestion (Krause et al., 2009). Samples were collected and stored similarly during CLASiC. However, given the quantity of lithogenic silica in the waters, time-course digestions in sodium carbonate were used. This method is like those used for quantifying $bSiO_2$ in sediments, e.g. Pickering et al. (2020), and can better constrain uncertainty among individual $bSiO_2$ and lithogenic sample pools. Although it is less sensitive, there is sufficient $bSiO_2$ in this system such that detection and quantitation are not issues. Other studies in coastal systems with high and variable lithogenic silica have used modified sodium hydroxide digestions, e.g. Ragueneau et al. (2005), however, we chose the time course to avoid using empirical ratio-based corrections for the lithogenic material.

Additional subsamples were collected to determine rates of $bSiO_2$ production (denoted as ρ). 125 mL or 250 mL polycarbonate bottles (depending on the station biomass) were filled to the brim and received 333 Bq of $^{32}Si(OH)_4$ (>20 kBq µg Si^{-1}). Bottles were immediately capped, gently inverted to mix the tracer, and placed into mesh bags made of neutral density screening to simulate the percent of incident irradiance (%I_0) at the depth of sample collection. The bottles were then incubated for 24 hours in a deck-board incubator cooled by continuously flowing surface seawater. Following incubations, samples were filtered onto 25 mm diameter and 1.2 µm pore size polycarbonate filters, which were then placed onto nylon disc planchettes to dry and covered with a mylar film (secured using a nylon ring). ^{32}Si activity was quantified using gas-flow proportional counting with a GM-25 multicounter (Risø National Laboratory, Technical University of Denmark) after aging the daughter isotope of ^{32}Si, ^{32}P, for seven half-lives (~4 months) to achieve secular equilibrium (Krause et al., 2011). Although some data from the middle MB corridor during autumn 2015 CONCORDE has been published (Dzwonkowski et al., 2017), the remaining data for this cruise, the spring 2016 CONCORDE cruise, and the two CLASiC cruises are original. Blanks were run on filtered seawater samples in which ^{32}Si was added, incubated, and filtered again. Due to the cost of ^{32}Si, only single replicates were done per sample point. Recent observations in the Bering and Chukchi Seas, both high diatom biomass systems like the nGoM, indicated that the coefficient of variation for replicate ^{32}Si data from the averaged 12% and did not change significantly between diatom bloom and non-bloom stations (Krause et al., 2021). Statistical analysis of trends in biomass-normalized $bSiO_2$ production among cruises were done using backward stepwise regression models in SigmaPlot software. Non-parametric comparisons of medians (Mann Whitney U Test) were used to evaluate differences in rates among prior studies and this one.

Results

Physical conditions

In the nGoM, atmospheric forcing (e.g. wind, precipitation) drives physical and biogeochemical variability in shelf waters. Dzwonkowski et al. (2017) observed that the induced storm surge following the passage of post-Hurricane Patricia (fall 2015) over the MB resulted in higher-than-normal and less variable salinity waters (ranging 32.1 to 35.6) drained from the regional estuaries. While most of the MB stations were surface-only, for two rate profiles at shallow stations (bottom depth 18 – 21 m), the irradiance rapidly attenuated and the euphotic zone depths ranged between 7 – 12 m.

During the spring MB cruise, temperatures were similarly constrained and ranged from 19.3 to 21.2°C. Due to the high discharge, as expected, surface salinity ranged from 17.9 to 33.5 and laterally increased away from Mobile Bay (Figure 3). The depth of the euphotic zone ranged from 4 – 27 m among five vertical profiles. The two shallowest euphotic zones were associated with the shallowest sites (8 and 12 m) and the euphotic zones were 16 – 27 m (27 – 36 m bottom depth) among the three other sites.

The LS physical conditions were similar to MB. Summertime LS surface temperatures were warmest among the four cruises, ranging from 29.0 to 30.3°C. Surface salinities during this cruise ranged from 16.7 to 33.9. All summer stations sampled were between the 20 and 50 m isobaths, and the euphotic zone depths ranged from 5 – 48 m; like the MB, the shallower euphotic zones on the LS were associated with the shallower stations. During the spring LS cruise, the surface temperatures were elevated compared to the spring MB cruise, ranging from 20.9 to 26.0, likely due to the May period LS cruise being later in spring (vs. late March – April for the MB cruise). The surface salinity range sampled was comparable but slightly narrower than the summer cruise, 19.6 to 31.6, although one station was sampled in Mississippi Canyon (~1000 m bottom depth, hereafter referred to as the "deep-water" site) and surface salinity

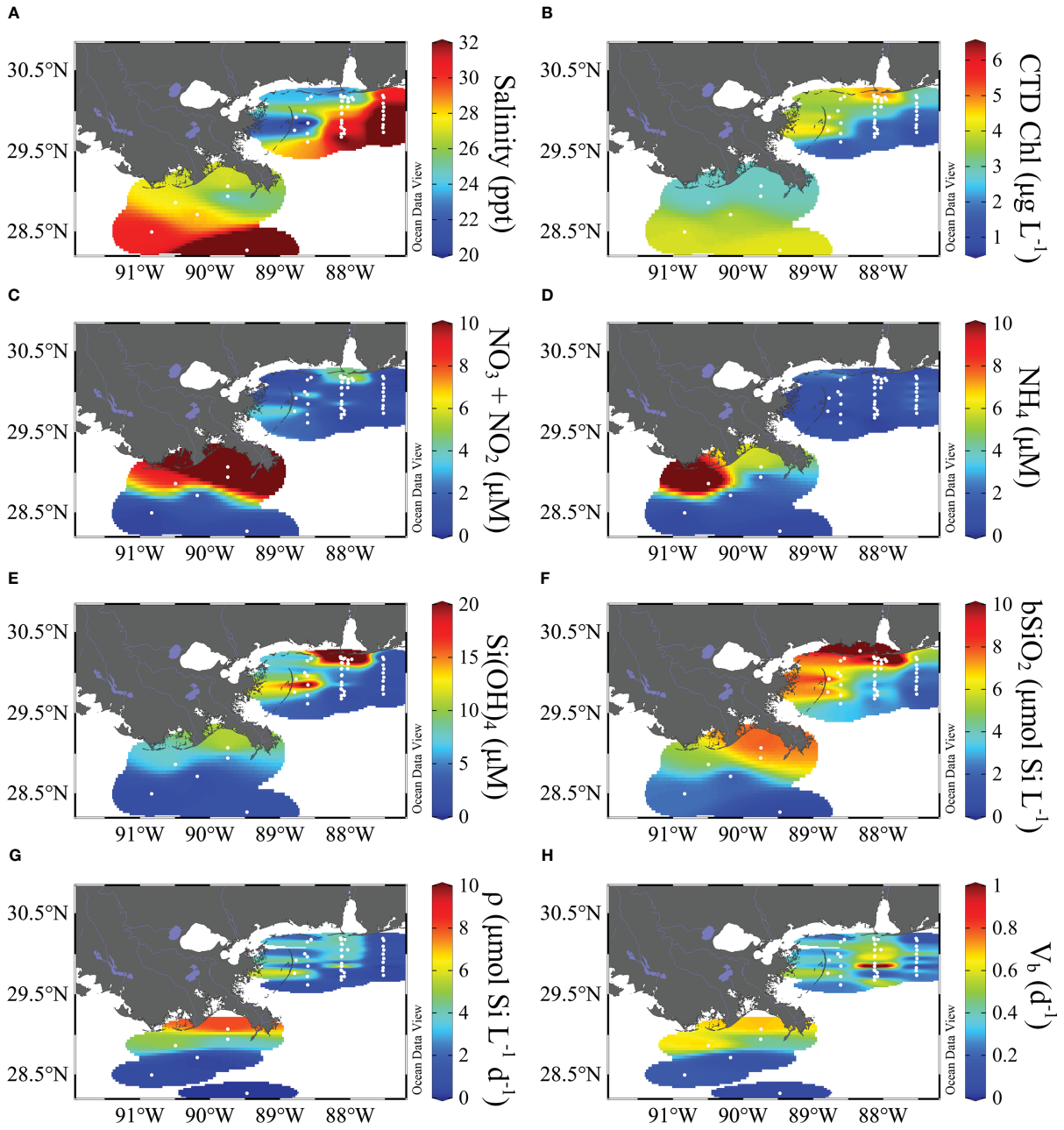

FIGURE 3
Surface properties for the spring cruises: LS during May 2017 and MB during March-April 2016. Properties include salinity **(A)**, CTD-fluorescence based chlorophyll **(B)**, nitrate+nitrite **(C)**, ammonium **(D)**, silicate **(E)**, biogenic silica standing stock **(F)**, production rate **(G)** and stock-normalized production rate **(H)**. Units are listed on the plot. Map made using Ocean Data View (Schlitzer, 2016).

was 36.3 —typical of deeper regional waters outside the direct freshwater influence. The spring-period LS euphotic zones were largely shallower than observed in summer, ranging from 7 – 19 m, and there was no clear relationship with bottom depth.

Dissolved nutrients

During autumn on the MB, dissolved nutrients showed typical ranges as observed in prior studies. NO_3+NO_2 and NH_4 concentrations in the surface averaged 0.46 µM (range: detection limit – 2.1) and 0.33 µM (range: detection limit – 1.3), respectively (Figure 4). SRP was lower and less variable, averaging 0.28 µM (range 0.15 – 0.42). $Si(OH)_4$ concentrations were an order of magnitude higher, averaging 3.51 µM (range: 1.31 – 10.2). The highest concentrations corresponded to surface stations on the southern MB shelf just offshore and eastward of the MR delta. Vertically, there were few differences among stations, unsurprising given the storm passage which thoroughly mixed the water column. During the spring, nutrients in the MB surface concentrations were higher and more variable (Figure 3). NO_3+NO_2 and NH_4 concentrations averaged 2.78 µM (range: detection limit – 13.1) and 0.95 µM (range: detection limit – 3.78), respectively (Figure 4). The average SRP concentration 0.39 µM (range: 0.03 – 3.1) was not as high as inorganic nitrogen forms; however, the dissolved N:P ratios were still below the canonical Redfield-Ketchum-Richards ratio (16:1). $Si(OH)_4$ was also higher than in autumn, averaging 9.33 µM (range 0.42 – 45.3, Figure 4). The highest concentrations for all nutrients were typically observed in the northern domain and a high station in the mid-shelf western domain (except for NH_4) just offshore of the Chandeleur Islands (barrier island chain that forms a western boundary for the MB, Figure 3).

While clear seasonal differences were observed on the LS, there was also a strong difference between nutrient magnitude in the MB and LS. During the LS summer, surface NO_3+NO_2 and NH_4 concentrations averaged 7.40 µM (range: 0.30 – 29.3) and 4.12 µM (range: 1.94 – 7.47), respectively (Figure 4). The average surface SRP was 0.64 µM (range: 0.25 – 2.25). $Si(OH)_4$ concentrations were higher than other nutrients, averaging 18.6 µM (range: 2.40 – 64.7). There was clear spatial variability among nutrients, with the highest concentrations in proximity to the MR outflow (see Dzwonkowski et al. (2018)). During spring, surface NO_3+NO_2 and NH_4 concentrations averaged 5.20 µM (range: 0.17 – 14.9) and 5.59 µM (range: 0.20 – 15.8), respectively (Figures 3, 4). The surface SRP also was lower and less variable, averaging 0.14 µM (range: 0.12 – 0.17). At the deep-water station, surface nutrients were significantly lower than inshore with NO_3+NO_2, NH_4, and SRP concentrations of 0.33, 0.34 and 0.18 µM, in that order (Figures 3, 4). Surface $Si(OH)_4$ concentrations during the spring averaged 4.51 µM (range: 0.17 – 10.4) for the inshore stations, while the surface concentration at the deep-water station was 1.78 µM (Figures 3, 4). There were strong spatial gradients associated with the river proximity, i.e. the highest

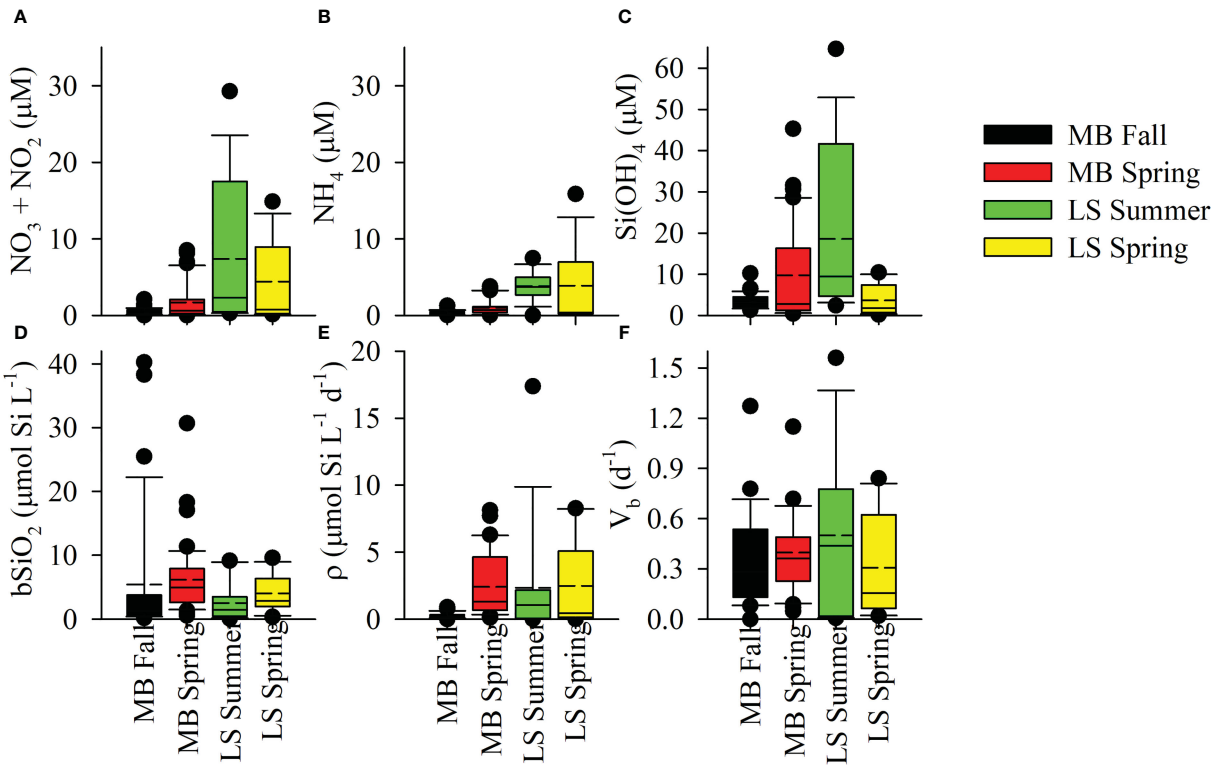

FIGURE 4
Surface box plots for nitrate+nitrite **(A)**, ammonium **(B)**, silicate **(C)**, biogenic silica standing stock **(D)**, production rate **(E)** and stock-normalized production rate **(F)** among all cruises. Box shows median (solid line) and average (dashed line), the box upper/lower boundaries denote the 25 and 75th percentiles with the whiskers denote the 10 and 90th percentiles.

concentrations observed near the river, except for NH_4 where the highest concentration observed in the surface was to the west and inshore (Figure 3).

Biogenic silica stock and production rates

$bSiO_2$ standing stocks in the MB and LS were high but variable. During the autumn MB cruise, surface $bSiO_2$ averaged 5.42 µmol Si L^{-1} (range: 0.16 – 40.3), while average $bSiO_2$ in the surface was ~20% higher in spring, 6.18 µmol Si L^{-1} with a lower range (0.55 – 30.7, Figure 4). On the LS, surface $bSiO_2$ were lower, averaging 2.53 µmol Si L^{-1} (range: 0.06 – 9.14) during the summer cruise. Surface $bSiO_2$ at the shelf stations were elevated during LS spring and averaged 4.42 µmol Si L^{-1} (range: 1.37 – 9.59, Figures 3, 4). At the deep-water station, surface $bSiO_2$ was lower (0.35 µmol Si L^{-1}), consistent with the lower observed nutrients (Figure 3). At the stations where $Si(OH)_4$ <1 µM, $bSiO_2$ was 2.6 – 7.9 times higher than $Si(OH)_4$, suggesting significant accumulation of diatom biomass. Vertically, $bSiO_2$ in the euphotic zone declined with depth on the MB, although there was considerable variation in the average for the base of the euphotic zone, consistent with the shallow water column depth sampled and therefore the proximity to the sediment/water interface and nepheloid layer (Figure 5). On the LS, $bSiO_2$ increased to a subsurface maximum in the mid-euphotic zone, with surface and deep average concentrations being similar (Figure 5). Between both regions, the average $bSiO_2$ among euphotic zone depths varied by less than a factor of two, much less than variability in rates of production (discussed below).

Despite the apparent difference in surface $bSiO_2$ between regions, there was less variation in the euphotic zone integrated stock. $\int bSiO_2$ in the two autumn MB profile stations were 6.17 and 29.0 mmol Si m^{-2}, this was lower than the $\int bSiO_2$ among the four spring MB profile stations which averaged 57.1 mmol Si m^{-2} (range: 46.7 – 70.1, Table 1). On the LS, $\int bSiO_2$ in the summer was similar to MB in the autumn, averaging 21.9 mmol Si m^{-2} (range: 3.85 – 48.9, Table 1). However, $\int bSiO_2$ on the LS during spring was nearly three-fold higher, averaging 64.1 mmol Si m^{-2} (range: 31.8 – 108.8). At the deep-water station, $\int bSiO_2$ was 18.7 mmol Si m^{-2} (Table 1).

The minor disparities in surface $bSiO_2$ between regions were not apparent in the rate of biogenic silica production, ρ, in the surface. During autumn (MB), ρ averaged 0.28 µmol Si L^{-1} d^{-1} (range: below detection – 0.89). In the MB spring, surface ρ increased by an order of magnitude compared to the autumn, averaging 2.41 µmol Si L^{-1} d^{-1} (range: 0.11 – 8.11, Figure 3). On the LS during summer, the average ρ in the surface, 2.34 µmol Si L^{-1} d^{-1}, and the range of ρ spanned over four orders of magnitude (range: below detection – 17.4, Figure 4). During spring, surface rates were similar, averaging 2.73 µmol Si L^{-1} d^{-1} (range: 0.06 – 8.26, Figure 3) on the shelf, with a low rate in the deep-water station (<0.01 µmol Si L^{-1} d^{-1}, Figure 3). Vertically, ρ declined with depth in the euphotic zone for both regions (Figure 5); however, there was a disparity at depth, as ρ in the mid euphotic zone on the LS was ~twice the rate at the same light depth on the MB. ∫ρ during the autumn MB cruise stations were 6.17 and 29.0 mmol Si m^{-2} d^{-1}, this was elevated in the MB during the spring where the average was 9.39 mmol Si m^{-2} d^{-1} (range: 4.86 – 15.3, Table 1). On the LS, ∫ρ in the summer and spring averaged 9.54 mmol Si m^{-2} d^{-1} (range: 0.27 – 30.8) and 27.0 mmol Si m^{-2} d^{-1} (range: 2.63 – 65.7), respectively. In the deep-water station, ∫ρ was 0.36 mmol Si m^{-2} d^{-1}.

$bSiO_2$ normalized ρ, V_b, suggest many zones had active diatom assemblages (Figure 5). During autumn on the MB, surface V_b averaged 0.36 d^{-1} (range: below detection to 1.27 d^{-1}), while in the spring, the average V_b was similar 0.40 d^{-1} (range: 0.05 to 1.27 d^{-1}).

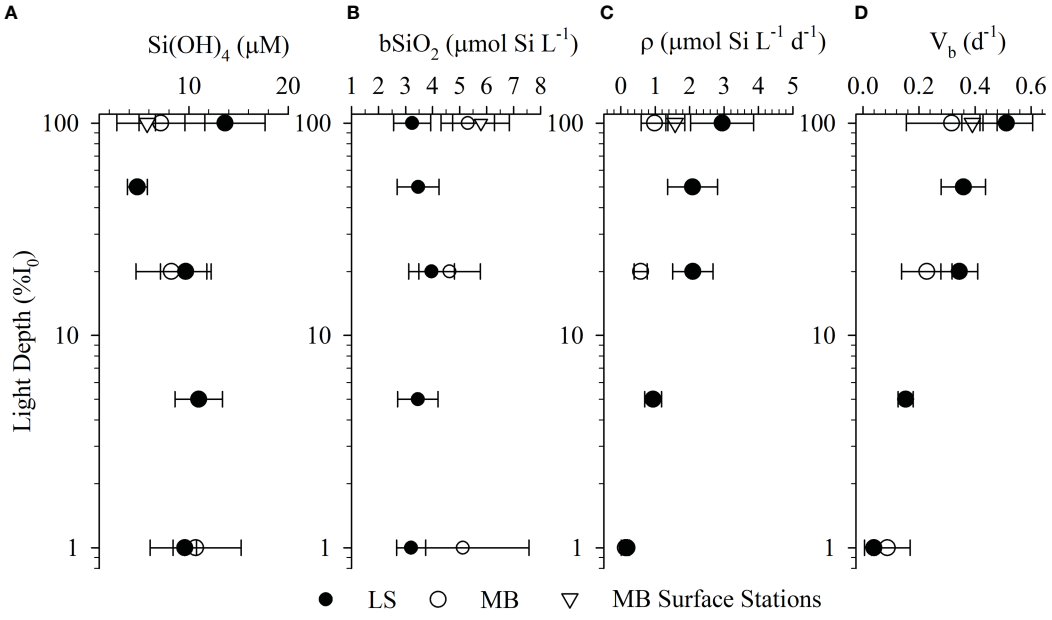

FIGURE 5
Average (± standard error) for silicate **(A)**, biogenic silica standing stock **(B)**, production rate **(C)**, and stock-normalized production rate **(D)** per irradiance depth (LS and MB) or surface-only stations (MB).

10.3389/fmars.2023.1162685

TABLE 1 Station locations and surface salinity, euphotic zone depth, and integrated $Si(OH)_4$, $bSiO_2$ and ρ among cruises.

Region/ Season	Lat. (N)	Long. (E)	Surface Sal	∫Z (m)	$\int Si(OH)_4$ (mmol m^{-2})	$\int bSiO_2$ (mmol m^{-2})	∫ρ (mmol m^{-2} d^{-1})
MB Autumn	29.85	-88.61	34.2	21	14.6	6.17	0.34
	30.13	-88.13	33.7	18	28.7	29.0	1.95
MB Spring	29.77	-88.09	29.3	25	21.1	70.1	5.34
	29.80	-88.13	29.7	27	85.2	50.8	4.86
	29.72	-88.09	30.0	16	69.3	46.7	15.3
	31.20	-88.14	26.2	9	122	60.8	12.1
LS Summer	28.87	-90.48	30.0	14	234	3.85	1.35
	28.87	-90.47	31.1	18	187	7.17	0.27
	28.87	-90.48	30.4	14	113	18.8	6.54
	28.87	-89.46	16.7	14	242	21.7	6.16
	29.01	-89.58	20.2	11	302	11.7	5.73
	29.01	-89.58	21.7	13	397	7.99	3.85
	28.64	-91.11	31.1	16	240	24.5	16.2
	28.45	-91.61	32.7	39	111	19.4	0.56
	28.50	-91.61	33.9	48	144	26.3	1.14
	28.70	-90.28	27.4	20	114	48.9	30.8
	28.72	-90.17	28.7	35	205	48.1	15.9
	28.87	-89.45	22.7	5	132	24.0	26.0
LS Spring	28.87	-90.50	27.6	11	89.7	57.7	26.2
	28.86	-90.50	31.2	11	51.4	66.1	28.1
	28.87	-90.49	27.0	7	68.9	36.8	39.8
	29.07	-89.75	27.5	9	106	71.1	38.4
	29.07	-89.75	26.3	11	116	86.5	54.9
	29.07	-89.75	29.0	10	50.4	80.6	15.5
	28.50	-90.83	30.5	11	18.8	31.8	5.85
	28.50	-90.83	30.9	16	16.0	44.2	2.63
	28.50	-90.83	31.6	16	13.6	45.4	9.78
	28.95	-89.75	24.1	13	85.9	80.2	31.4
	28.96	-89.75	24.4	11	47.5	109	21.5
	28.95	-89.75	19.6	12	106	89.6	65.7
	28.72	-90.18	28.5	19	54.6	34.6	10.6
	28.27	-89.48	36.3	56	100	18.7	0.36

Note, because we did not do profiles among all sites in the MB, stations below represent a subset of the stations visualized in Figure 2.

These average specific rates imply doubling times approximately 1.5 – 1.9 days. On the LS during summer, surface V_b exceeded the spring values in the MB, averaging 0.50 d^{-1} (range: <0.05 to 1.56 d^{-1}). The summer surface rate was also higher than the average V_b during the spring for the shelf stations, 0.33 d^{-1} (range: 0.02 to 0.84 d^{-1}). These LS rates imply doubling times between 1.4 – 2.1 days. At the deep-water station, V_b was low (0.03 d^{-1}) and suggests a doubling time of ~23 days. The similarity in V_b between regions also manifested in vertical trends, as V_b declined precipitously in the lower euphotic zone (Figure 5).

Statistical analysis on the drivers of V_b (to account for biomass differences) were done using surface data. During the autumn on the MB, backward stepwise regression model retained $Si(OH)_4$ and salinity as the best predictors of V_b (Table 2); however, in the spring, the NO_3+NO_2 alone was retained (Table 2). On the LS (excluding the deep-water site), the model retained $Si(OH)_4$ in

TABLE 2 Backwards stepwise regression analysis to explore drivers of V_b in the surface waters among stations and cruises.

Region	Season/Year	Retained parameters: coefficient ± SE	Adjusted R^2	F-value	P-value
MB	Autumn 2015	Constant: 11.7 ± 3.38 $Si(OH)_4$: -0.14 ± 0.07 Salinity: -0.31 ± 0.09	0.55	6.38	0.03
MB	Spring 2016	Constant: 0.21 ± 0.05 NO_3+NO_2: 0.14 ± 0.02	0.50	34.2	<0.01
LS	Summer 2016	Constant: 0.58 ± 0.16 $Si(OH)_4$: 0.05 ± 0.02 SRP: -1.42 ± 0.56	0.59	5.74	0.03
LS	Spring 2017	Constant: -1.14 ± 0.44 $Si(OH)_4$: 0.10 ± 0.02 NO_3+NO_2: -0.02 ± 0.01 Salinity: 0.04 ± 0.01	0.97	86.2	<0.01

Models started with all parameters and the most predictive were retained (coefficient shown). Also reported are the adjusted R^2 for the model and the associated F- and P-values from an Analysis of Variance.

both seasons, but in summer and spring, SRP and NO_3+NO_2 were also retained, respectively, along with salinity in the spring (Table 2).

Discussion

High silica production in the northern Gulf of Mexico: physics and allochthonous factors

River plumes are among the most highly productive ecosystems in the ocean. The nGoM shelf waters have been dubbed the 'Fertile Fisheries Crescent' (Gunter, 1963) due to the exceptional productivity of upper trophic level biomass. In many productive fisheries environments (e.g. Monterey Bay, Bering Sea), diatom production can be exceptional (Brzezinski et al., 2003; Krause et al., 2021). To our knowledge, this study reports the first ∫ρ rates within the euphotic zone for the nGoM. Despite the backdrop of a highly productive pelagic ecosystem, the measured ρ on the LS and MB are not among the highest in systems studied to date. Among a survey of 24 studies within many high and low productivity regions, the average ∫ρ rate on the LS shelf was among the upper 33% whereas MB is closer to the median (Figure 6A). ∫ρ in the highest productivity systems (e.g. coastal upwelling zones, Southern Ocean sectors) exceed averages of 50 mmol Si m^{-2} d^{-1}, whereas the average for the LS during spring was 25 mmol Si m^{-2} d^{-1} (Table 1) and for MB was 10 mmol Si m^{-2} d^{-1} (Table 1). While the spring cruises were in different years (2016, MB; 2017, LS), the spread of the ∫ρ and the consistently higher values quantified on the LS suggests this may be a consistent difference; we discuss the potential reason(s) for this below (final discussion section). However, the magnitude of diatom production, while enhanced relative to many other systems, is not so exceptionally high as to be a clear factor leading to the stimulation of fisheries production in this region. Therefore, we propose that the unique hydrographic factors working in this system, help to physically concentrate diatom biomass to make it more assessable to higher trophic organisms. Some potential mechanisms are explored below:

Given the river plume forcing, we posit that the high system productivity in the LS and MB can be partially explained by diatom productivity being highly accessible to higher trophic organisms. When normalizing the ∫ρ depth to the depth of the euphotic zone (i.e. mathematically equivalent to volumetric rates, e.g. μmol L^{-1} d^{-1} or mmol m^{-3} d^{-1}), the LS is the 5th highest, and the MB is in the upper 50% for ∫ρ among our survey (Figure 6B). The local river plume forcing facilitates water-column stability (stratification) and thereby allows phytoplankton to consume nutrients and avoid light limitation due to deep mixing. The degree of stratification in this system is extreme, as density differences between the surface and main pycnocline due to salinity are typically much higher (>>1 kg m^{-3}) than open ocean metrics used define mixed layers (e.g. >0.1 kg m^{-3} differences from the surface). Thus, residence in this stable water column facilitates phytoplankton consumption of nutrients to exhaustion —if other ecological or physical factors are favorable. Indeed, the lowest surface $Si(OH)_4$ observed during the LS spring bloom was 0.17 μM. This concentration is multiple factors lower than $Si(OH)_4$ observed (i.e. ~0.6 – 0.8 μM) in the low-diatom-biomass oligotrophic gyres (Brzezinski et al., 2011; Krause et al., 2017) and is similar to intense diatom blooms observed on the LS (Nelson and Dortch, 1996) or in productive upwelling systems (Nelson et al., 1981; Krause et al., 2015; Closset et al., 2021). We suggest that the LS and MB physics allow for diatom production to be more accessible to higher trophic organisms compared to other systems where the integrated productivity may be higher, but more diffusely distributed within the water column. This is consistent with ideas concerning the importance of spatial aggregations as predictors of higher trophic level variation, e.g. Benoit-Bird and McManus (2012), opposed to typical volumetric abundances. Specifically, the ideas that have emerged in the last decade are not that volume-based rates or standing stock matter for ecological productivity, but instead how aggregated and concentrated production is (or can be at times), as highly concentrated production can be more easily accessed by higher trophic levels.

Beyond basic river-plume stratification dynamics (discussed above), there is regional evidence that small scale and/or ephemeral physical mechanisms in the nGoM may also help efficiently funnel diatom productivity to higher trophic levels.

10.3389/fmars.2023.1162685

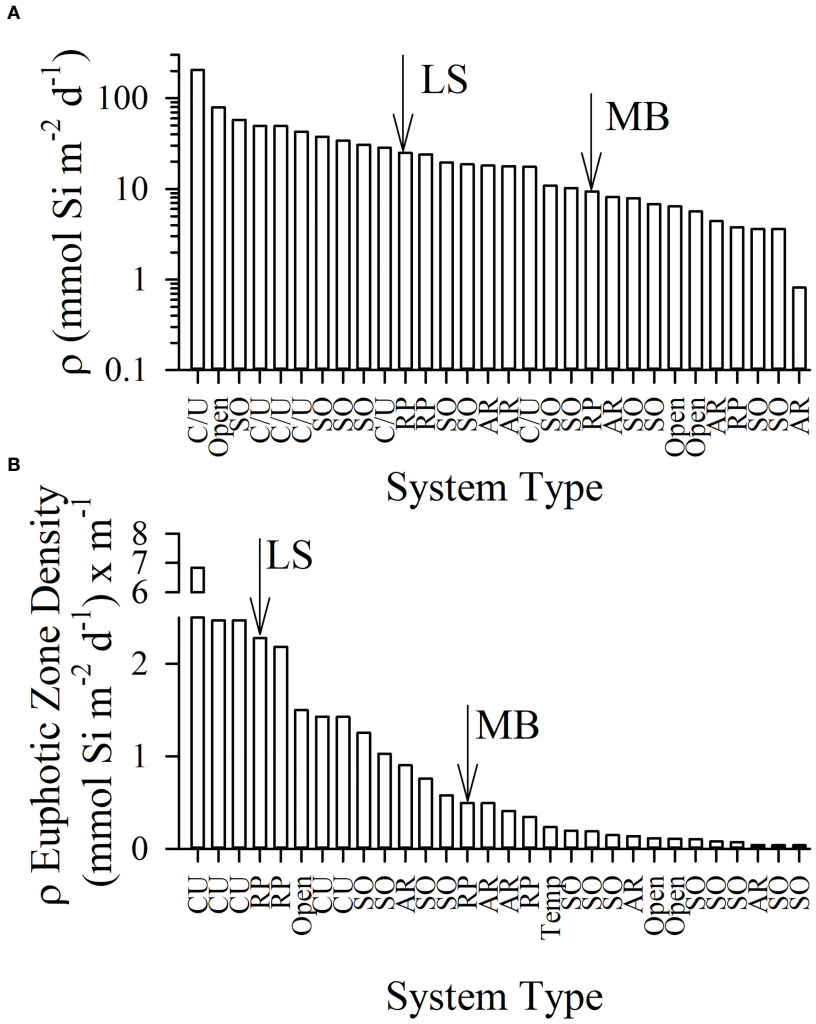

FIGURE 6
Survey of integrated euphotic zone biogenic silica production rate ranged from highest to lowest **(A)** among 24 studies and the euphotic-zone depth normalized production **(B)**, termed euphotic zone density (mathematically equivalent single-depth units) for the same studies arranged from high to low. Average values per study are reported from the literature including the following systems: coastal/upwelling (C/U), river plume (RP), open ocean (Open), Southern Ocean (SO), and the Arctic region (RU); studies from mid-ocean gyres (e.g. Hawaii Ocean Time-series, Bermuda Atlantic Time Series study) were omitted due to very low absolute and depth-normalized rates. The average LS and MB value are denoted by the arrows in each plot. Data and original studies are listed in Supplementary Table S1.

Using an *in situ* imaging system, Greer et al. (2020) observed a ~2.3 km (lateral extent) thin layer, dominated by the diatom *Odontella* sp., during July 2016 in the southwestern domain of the MB. *Odontella* species typically have large cell sizes compared to other diatom genera, especially slender pennate species which are abundant regionally (MacIntyre et al., 2011; Bargu et al., 2016). Greer et al. (2020) suggested the growth and grazing decoupling and motility (i.e. *Odontella* sp. is not a swimmer) in the thin layer were not major factors contributing to its formation. Specifically, *Odontella* sp. abundances outside of the thin layer were so low the disparity in abundances within and outside of the layer could not be solely from increased growth rates within the layer; therefore, these authors concluded diatom cells were concentrated by physical processes. Leveraging a high-resolution physical model, Greer et al. (2020) suggested the thin-layer feature was driven by surface convergence and vertical shear. Furthermore, their model outputs suggested that similar convergences occur frequently in the MB region and may contribute to efficient trophic transfer of phytoplankton organic matter to higher trophic levels. Such an idea is consistent with other studies in warm-water regions where standing stocks of phytoplankton may be relatively low but can be enhanced by similar physical mechanisms and fuel efficient passage of producer organic matter to higher trophic level organisms, e.g. Hawaii (McManus et al., 2012).

Despite the potential importance for thin layers regionally, it is unlikely that such dynamics were resolved in our study. Our vertical sampling was limited to four or five depths, which were predetermined based on the irradiance levels required for our deck board incubator. Consequently, it is unlikely that such thin-layer biomass would have been accurately captured in our rates. Specifically, the vertical orientation of the Niskin bottle would likely have sampled a component of such a layer (if any at all). However,

this may not matter when trying to quantify the regional ρ. Our bottle incubations clearly captured the vertical extent of euphotic-zone productivity (Figure 5). Such short-duration physical dynamics acting to concentrate (opposed to stimulate) diatom production within a vertical layer would not radically alter the total euphotic zone integrated production, but redistribute (i.e. concentrate) the biomass. Thus, these features may not affect total ρ or annual productivity but could be important to facilitate more efficient transfer of this material up the foodweb.

Comparison of ∫ρ rates with riverine $Si(OH)_4$ delivery show differences in the river effect between systems. Given our vertical sampling was confined to the euphotic zone, we consider stocks and rates in a euphotic-zone integrated context (e.g. one euphotic-zone box opposed to a two-box water column). In the MB, the delivery of riverine $Si(OH)_4$ to the CONCORDE sampling domain (area of the three corridors) would support ~33-40% of the ∫ρ (Table 3); the proportional importance decreases if the entire MB shelf area is considered (i.e. Si in discharged water would be spread over a larger area). This implies that other $Si(OH)_4$ sources are necessary to sustain the production rates of diatoms in the water column. Water-column recycling of $bSiO_2$ can be quantitatively important. Brzezinski et al. (2003) reported that even during blooms in productive systems (e.g. Monterey Bay), 10-20% of ∫ρ was supported by euphotic-zone $bSiO_2$ remineralization. Furthermore, the proportional support of ∫ρ from dissolution increases during non-bloom periods (e.g. 60-70% of ρ) or in regions with warmer water temperatures (e.g. ~30% in a Gulf Stream Warm Core Ring). Given surface temperatures in the MB were ~20°C and 24°C for the spring and autumn cruises, respectively, and the specific dissolution rate for $bSiO_2$ in slightly cooler (~15-20°C) subtropical waters was reported to be ~0.15 d^{-1} (Brzezinski and Nelson, 1989), such a dissolution rate applied to our measured $\int bSiO_2$ standing stock would be sufficient to meet 65-100% of the ∫ρ during the MB cruises (Table 1). Note, this would be an upper estimate if most of the $bSiO_2$ standing stock dissolves below the euphotic zone. Furthermore, benthic flux, while not reported for $Si(OH)_4$ in the MB is likely similar to that observed on the LS given the similarity in $bSiO_2$ content in sediments between these regions (Pickering et al., 2020; Kemp et al., 2021). Lehrter et al. (2012) reported benthic Si flux rates ranging from 0.3 – 4.4 mmol Si m^{-2} d^{-1} on the LS in spring and summer. This represents a major pool of usable Si but given the shallow euphotic zones and surface layers, such a pool may not be accessible to diatoms until tropical cyclones (e.g. summer) or cold fronts (e.g. autumn) break down this stratification and mix the water column. Taken together, the MB data suggest that over the entirety of the shelf, riverine Si and internal recycling may meet the Si demand for diatoms; however, within this broad area, there are ephemeral conditions where diatoms can exhaust Si faster than replenishment, as has been observed offshore of coastal Alabama in the northern domain of the MB, e.g. MacIntyre et al. (2011).

Unlike the delivery of $Si(OH)_4$ to the MB, the MR delivers an order of magnitude more Si to the LS where it is used in an area less than twice that considered for the MB (Table 3). During the summer and spring, the riverine flux averaged 62% and 92% of the measured ∫ρ. Thus, over the entirety of the shelf, the river flux combined with internal recycling of $bSiO_2$ (discussed above) should have been sufficient to meet the Si demand for diatoms. Furthermore, consistent with calculations by Lehrter et al. (2012), benthic flux of Si could also have been a significant source of Si to help diatom avoid limitation, especially for any diatom production occurring deeper than the main pycnocline. While many studies have suggested that Si limitation may be more prevalent now than before eutrophication (Turner et al., 1998), when considering bulk rates of delivery and shelf-wide production, any limitation by Si is not due to a lack of Si within the integrated system (i.e. upper water column over the shelf area) but must be due to the balance between diatom growth and the $Si(OH)_4$ supply to the euphotic zone. While the Turner et al. (1998) study (among others), inferred diatom Si limitation by nutrient ratios (i.e. Si depleted before N), there is more direct evidence showing that diatoms can be limited by $Si(OH)_4$ on the LS. Nelson and Dortch (1996) reported many instances where $Si(OH)_4$ in the upper water column was <1.5 μM in the summer and <0.4 μM in the spring. We did not observe such low concentrations during the summer, but during the spring on the LS six (of 14) stations had surface $Si(OH)_4$ <1 μM with the lowest concentration of 0.17 μM (Figure 3). Thus, both our study and Nelson and Dortch (1996) demonstrate diatoms can effectively exhaust $Si(OH)_4$ faster than local physical delivery (e.g. mixing) or remineralization scales in the euphotic zone, despite considerable pools of Si which are separated by relatively short vertical scales (e.g. <5 m) —especially compared to gradients in

TABLE 3 Comparison of riverine $Si(OH)_4$ flux relative to ∫ρ (e.g. Table 1) on the MB and LS during each cruise (error is standard deviation).

Region	Season/ Year	Cruise-period discharge (m^3 s^{-1})	Shelf Area (km^2)	Riverine $Si(OH)_4$ (mmol Si m^{-2} d^{-1})	∫ρ (mmol Si m^{-2} d^{-1})	Riverine $Si(OH)_4$ /∫ρ
MB	Autumn 2015	866 ± 365	9000	0.47 ± 0.35	1.15 ± 1.14	0.41 ± 0.51
	Spring 2016	3487 ± 1730	9000	2.49 ± 0.75	7.44 ± 5.22	0.33 ± 0.26
LS	Summer 2016	12987 ± 1259	16500	8.78 ± 1.16	9.54 ± 10.3	0.92 ± 1.01
	Spring 2017	25786 ± 5316	16500	15.7 ± 3.62	25.1 ± 19.7	0.62 ± 0.51

MB discharge data are from Mobile Bay were aggregated from United States Geological Survey stations 02428400 (Alabama River) and 02469761 (Tombigbee River); these two rivers represent ~90% of the Mobile Bay discharge and were corrected to account for this volume difference as in Dykstra and Dzwonkowski (2020). LS discharge data are from the Mississippi River at United States Geological Survey station 7374000. The MB and LS areas were estimated based on the main area encompassing the three CONCORDE meridional transects offshore of Mobile Bay (MB) and the Mississippi River plume affected area of the LS (Ebner, 2019) without affects from the Atchafalaya River. Riverine $Si(OH)_4$ for MB was estimated using the highest values quantified during CONCORDE and average values for months at the FOCAL Mobile Bay stations (Sutton et al., 2023) from 2008-2012.

deep-water systems. In the absence of exceptionally concentrated diatom production, which can deplete $Si(OH)_4$ to levels that likely limit diatom growth, e.g. Nelson and Dortch (1996) (and this study), it appears that most of the Si production on the shelf can be met by external Si delivered by the MR with the rest being met by internal recycling or benthic flux (after the exceptional water column stratification is broken down).

Biogenic silica production drivers

While many factors potentially affect the rate of biogenic silica production (i.e. V_b), our analysis focused on a common subset of parameters available for all cruises. The models all explain at least a majority of the variance (i.e. R^2 = 0.50 to 0.97), but only one explains nearly all the variance (i.e. LS Spring). Thus, for the other three cruises (LS Summer, MB cruises), there is a quantitatively significant portion of variance which cannot be explained by the variables considered. Despite this, the model results provide an empirical approach to evaluate the factors which best correlated to V_b during these cruises.

A significant number of studies reporting ρ are from systems with relatively invariant salinity. Even in coastal systems with such data, e.g. Bay of Brest (Beucher et al., 2004), salinity ranges are relatively minor (e.g. 32 – 36) compared to the nGoM. During our study, we observed considerable variability in surface salinity during spring (both regions, Figure 3) and summer (LS). For the MB, the effect of the estuarine condition differed between autumn and spring. The autumn cruise occurred after the passage of the remnants from Hurricane Patricia (Dzwonkowski et al., 2017); note, given the lack of historical data, we cannot disentangle the effect of any prior anthropogenic changes that may alter the response following the storm. The storm surge flooded the nGoM estuaries, and as the waters flowed back into the Gulf, the post-storm stratification led to increased rates of primary production, especially among larger cells (e.g. *Trichodesmium*, diatoms) within 15 km of the Mobile Bay outflow (Dzwonkowski et al., 2017). The regression model for these autumn 2015 data shows that the strongest predictors for V_b were salinity and $Si(OH)_4$ (Table 2). Both parameters had negative coefficients, which means they scaled in the same direction. $Si(OH)_4$ in the waters feeding MB (e.g. Mobile Bay) behaves semi-conservatively, especially compared to other dissolved nutrients, e.g. NO_3+NO_2, NH_4, SRP (Sutton et al., 2023), and thus we would expect $Si(OH)_4$ and salinity to be negatively correlated (i.e. higher $Si(OH)_4$ at lower salinities). Our model instead showed these parameters trended the same direction and V_b was highest when $Si(OH)_4$ and salinity were lower. Such a trend was likely driven by the receding storm surge. Thus, the importance of the salinity effect in this specific season was the ability for the low salinity water to stabilize the water column (which had been well mixed) post storm thereby allowing phytoplankton (e.g. diatoms) to grow; this is consistent with interpretations by Dzwonkowski et al. (2017). During spring in the MB, salinity was not a significant predictor, as V_b was positively associated with NO_3 +NO_2 (Table 2). Such a result is consistent with the differences in the Si:N ratio of waters feeding the MB and LS, where Si:N in the MB is high (>1) and optimal for diatoms compared to the LS (Figure 1, discussed below). In this case, the quantity of NO_3+NO_2 to the MB was the best predictor of the quantified diatom silica production rate, suggesting a potential stimulatory effect near the plume edge where nutrients are still elevated relative to the offshore waters.

Drivers on the LS differed from those on the MB. The loading of nutrients in the MR watershed increased both N and P in the river over time (Figure 1 for nitrate). Determining what nutrient may limit primary production for the community has important regional implications for management actions in the watershed. For instance, much of the regional regulatory effort to combat hypoxia on the LS focuses on the reduction of N in the river. But while N can limit primary productivity on the LS, e.g. Rabalais et al. (2002) and references therein, there are times when P can be limiting, e.g. Sylvan et al. (2006). The LS cruise effort was more focused on benthic-pelagic coupled processes vs. the cruises in the MB with more fine-scale spatial sampling; therefore, in the LS we have only ~25% of the spatial stations compared to the MB: although unlike the MB, we have full vertical profiles for each occupied station.

The backward stepwise regression model analysis identified that the strongest nutrient predictors for V_b during the summer and spring cruises were NO_3+NO_2 (spring, negative coefficient), SRP (summer, negative coefficient), silicate (both seasons, positive coefficient), and salinity (spring, positive coefficient). Thus, our data analysis suggests that diatom productivity (V_b) was responding more to NO_3+NO_2 in the spring and SRP in the summer, while there is a persistent underlying response to $Si(OH)_4$ in both seasons. The latter is expected as $Si(OH)_4$ affects both diatom growth rates and their rate of Si uptake (e.g. nutrient kinetics). The positive correlation between $Si(OH)_4$ and V_b in our statistical analysis infers some degree of kinetic limitation, i.e. $Si(OH)_4$ is suboptimal for uptake (V_b at ambient $Si(OH)_4$ < V_b at non-limiting $Si(OH)_4$) and under these conditions diatoms alter physiology to compensate (McNair et al., 2018). Such kinetic limitation is also consistent with previous LS data from the early 1990s (Nelson and Dortch, 1996).

Model results indicate that the sign of the model coefficients for NO_3+NO_2 in the spring and SRP in summer are negative. These data infer that V_b, a proxy for diatom growth, is stimulated at lower NO_3+NO_2 and SRP concentrations than the high-nutrient riverine endmember (if this were the case, then the model coefficient for both would be positive). This is consistent with both remote data and shipboard incubation work showing that primary production and phytoplankton biomass accumulation rates are not highest in the main part of the river discharge zone but downstream, likely due to improved light conditions (reduced turbidity) and stratification which facilitates growth (Lohrenz et al., 1997; Lehrter et al., 2009). Our project results highlight that $Si(OH)_4$ always plays a role in diatom Si uptake (and potentially becomes a growth-limiting factor when concentrations are very low, e.g. <1 μM), but typically diatom activity switches from being more correlated to NO_3+NO_2 in the spring and SRP in the summer. Such empirical connection of diatom activity to three different nutrients suggests modeling diatom growth in this region over time may be challenging. Identifying the underlying factors affecting these trends (e.g.

changes in diatom assemblage, direct evidence of nutrient limitation) should be a priority given diatoms critical role in system productivity.

Has diatom silica production changed due to eutrophication?

As discussed, there have been significant changes to $Si(OH)_4$ and NO_3 concentrations in the MR (Figure 1) which feeds the nGoM (Turner and Rabalais, 1991; Turner and Rabalais, 1994a; Turner and Rabalais, 1994b; Turner et al., 2008). These results compelled a United States Environmental Protection Agency Science Advisory Board (Dale et al., 2007) to recommend that:

". the potential for silicate limitation and its effects on phytoplankton production and composition on the Louisiana-Texas continental shelf should be explored when carrying out experiments on the importance of N and P as limiting factors and when considering nutrient management scenarios."

The relationship between eutrophication and diatom production could be evaluated by understanding how diatom production rates respond to eutrophied conditions. However, the lack of diatom-specific rate information, facilitated by using isotope-addition methods (e.g. ^{30}Si, ^{32}Si), has hindered understanding the quantity of production attributed to diatoms in this system. While our production rate data set lacks a robust baseline, i.e. one study reporting data on ρ during the early 1990s (Nelson and Dortch, 1996), the comparison between the LS and MB offers potential insight regarding how the system operates now and we can speculate whether this may have changed in the last half century.

Compared to a past study in the nGoM (Nelson and Dortch, 1996), we find no evidence that diatom growth (i.e. V_b is proxy) in the upper depths is significantly different. Working in the same region of the LS during the early 1990s, rates reported by Nelson and Dortch (1996) during the summer and spring fell within the range for our study on the LS during the same seasons (Figure 4) with no significant differences (Mann Whitney U Test (Summer, Spring), U = 25, 47, p = 0.29, 0.88), albeit these earlier data are less variable. Nelson and Dortch (1996) also observed a significant difference between LS rates during spring (lower) and summer (higher), such a trend was not resolved during this present study. With the caveat that Nelson and Dortch (1996) did not report vertically integrated rates, the comparison of our data with those in the early 1990s does not suggest any significant change to the specific rate of diatom $bSiO_2$ production.

Comparison of the ∫ρ data during spring between the MB and LS are consistent with a eutrophication effect suggested in previous studies. There is relatively low nitrate in the Mobile Bay waters, <20 μM (Pennock et al., 1999), compared to the >100 μM concentrations in the MR derived from eutrophication in the watershed (Figure 1). The high nitrate and relative lack of light limitation as the MR discharges onto a deeper continental shelf, potentially facilitates $Si(OH)_4$ uptake while waters are diluted on the LS (consistent with reported non-conservative behavior for $Si(OH)_4$). This situation (i.e. high NO_3+NO_2 and NO_3+NO_2>$Si(OH)_4$) does not appear to occur in the MB (consistent with reported conservative behavior for $Si(OH)_4$). During spring, the LS had higher surface concentrations and ranges for NO_3+NO_2 and NH_4 relative to those in the MB, but surface concentrations of $Si(OH)_4$ were higher in the MB than in LS (Figure 3). Such differences are consistent with the well-reported anthropogenic factors in the MR watershed compared to the MB watersheds. For example, the increased nitrogen has been linked to fertilizer use in the MR watershed (Turner et al., 1998). Whereas the reduced $Si(OH)_4$ over time has been attributed to factors like damming (e.g. $bSiO_2$ retained in reservoirs behind dams vs. being carried downstream and dissolving en route), as reported in the Black Sea (Humborg et al., 1997) and other systems (Humborg et al., 2000). In the MB, the watersheds which provide fluvial input onto the shelf ecosystem are much smaller, with comparatively less developed urban and agricultural regions, and have the opposite nutrient trends (i.e. relatively lower NO_3+NO_2 and higher $Si(OH)_4$) than the MR. Although urbanization is occurring within the MB watershed, the degree of eutrophication is much lower than for the MR (Pennock et al., 1999). Such watershed differences would be expected to affect diatom processes downstream in the coastal domain.

The integrated diatom productivity appears to be significantly higher in the LS compared to the MB during spring, the season we can compare directly. Despite comparable V_b in the MB surface waters, the average ∫ρ was 2.5x higher in the euphotic zone of the LS than the MB. This difference is stark considering the average euphotic zone depth on the LS in spring was ~12 m vs. ~19 m for the MB. While both euphotic zones are relatively shallow compared to deep-water systems, there is likely a vertical zone in both systems where cells switch from nutrient limitation (under high irradiance) to light limitation —sensu Dugdale (1967). Phytoplankton cells can compensate for the lower light by increasing their light harvesting capacity (e.g. increase pigment per cell); however, pigment complexes have higher N requirements relative to P (Geider et al., 1996). Thus, given that the integrated standing stock of NO_3+NO_2 on the LS in spring was double (~90 mmol m^{-2}) that in the euphotic zone of the MB (~45 mmol m^{-2}, data not shown), the additional NO_3+NO_2 may have helped diatoms in the lower euphotic zone avoid reducing growth rates due to rapidly attenuating light in the turbid waters. Hence, we posit that eutrophication sets a higher potential for diatom biomass due to higher total N to exploit (if sufficient Si is available) and increases the euphotic-zone ∫ρ via facilitating higher uptake rates at depth (Figure 5).

Due to lack of baseline data for the water column on the effect of eutrophication on diatom production, our interpretation that ρ on the LS has increased in response to eutrophication cannot be tested directly. However, we can glean insights from local sediment records or use experimental approaches (e.g. bioassays) in future studies. For example, on the LS, there has been an increased preservation of diatom valves (especially the genera *Pseudo-nitzschia* which can have toxic species) in sediments through the end of the 20th century (Parsons et al., 2002). On a similar timescale, albeit not directly synchronized with *Pseudo-nitzschia*, there have also been increases in sediment $bSiO_2$ (Turner et al., 2008). It is unknown if these trends have continued in the last two decades since these reports. The general trend of increased

$bSiO_2$ preservation in sediments after eutrophication, due to increased diatom ρ in the water column, has been observed in limnic systems (Schelske et al., 1987), suggesting some fundamental similarities in the responses of diatoms assemblages to eutrophication among environments. Given the lack of baseline data to assess the general trends in ρ during and before eutrophication in the 20th century, new methods (e.g. silicon stable isotopes) could be employed to fill these temporal gaps. Comparison of trends over time between the LS and MB sediments could provide a means to better understand whether eutrophication has changed diatom silica utilization and production regionally or if similar spatial differences observed in this study reflect general subregional differences driven by the size of the watersheds feeding each site.

Data availability statement

The datasets presented in this study can be found in online repositories. The names of the repository/repositories and accession number(s) can be found below: https://www.bco-dmo.org/project/712667, http://data.gulfresearchinitiative.org (doi: 10.7266/N78050N9), http://data.gulfresearchinitiative.org (doi: 10.7266/N70K2738).

Author contributions

All authors were involved in the collection of samples, sample analyses, archiving data, and assisted with editing the manuscript. The study was conceived by JK with input from KM. The data analysis and initial manuscript was done by JK. All authors contributed to the article and approved the submitted version.

Funding

The Louisiana Shelf work was funded by the United States National Science Foundation Chemical Oceanography (OCE-1558957 to JK and KM). The Mississippi Bight research was made possible by a grant from the Gulf of Mexico Research Initiative through the CONCORDE Consortium and ACER Consortium programs (both to JK). Data associated with this work are publicly available through the Biological & Chemical Oceanography Data Management Office (https://www.bco-dmo.org/project/712667) and Gulf of Mexico Research Initiative Information & Data Cooperative (GRIIDC) at http://data.gulfresearchinitiative.org (doi: 10.7266/N78050N9, 10.7266/N70K2738).

Acknowledgments

We dedicate this work to the memory of our friend and colleague, Sydney Acton; her technical efforts before, during, and after these four cruises was critical to their success. We also thank the captains, crew, and science parties aboard the R/V Point Sur and R/V Pelican (especially Kevin Martin, Allison Mojzis, Wokil Bam, Neha Ghaisas), Brian Dzwonkowski and Alan Shiller for helpful discussions, and John Perry, Eric Lachenmyer, Grant Lockridge, Yantzee Hintz, and Laura Linn for technical assistance.

Conflict of interest

The authors declare that the research was conducted in the absence of any commercial or financial relationships that could be construed as a potential conflict of interest.

Publisher's note

Supplementary material

The Supplementary Material for this article can be found online at: https://www.frontiersin.org/articles/10.3389/fmars.2023.1162685/full#supplementary-material

References

Baines, S. B., Twining, B. S., Brzezinski, M. A., Krause, J. W., Vogt, S., Assael, D., et al. (2012). Significant silicon accumulation by marine picocyanobacteria. *Nat. Geosci.* 5, 886–891. doi: 10.1038/ngeo1641

Bargu, S., Baustian, M. M., Rabalais, N. N., Del Rio, R., Von Korff, B., and Turner, R. E. (2016). Influence of the Mississippi river on pseudo-nitzschia spp. abundance and toxicity in Louisiana coastal waters. *Estuaries Coasts* 39, 1345–1356. doi: 10.1007/s12237-016-0088-y

Benoit-Bird, K. J., and McManus, M. A. (2012). Bottom-up regulation of a pelagic community through spatial aggregations. *Biol. Lett.* 8, 813–816. doi: 10.1098/rsbl.2012.0232

Beucher, C., Tréguer, P., Corvaisier, R., Hapette, A. M., and Elskens, M. (2004). Production and dissolution of biosilica, and changing microphytoplankton dominance in the bay of Brest (France). *Mar. Ecology-Progress Ser.* 267, 57–69. doi: 10.3354/meps267057

Biard, T., Krause, J. W., Stukel, M. R., and Ohman, M. D. (2018). The significance of giant phaeodarians (Rhizaria) to biogenic silica export in the California current ecosystem. *Global Biogeochemical Cycles* 32, 987–1004. doi: 10.1029/2018GB005877

Brzezinski, M. A. (1985). The Si:C:N ratio of marine diatoms: interspecific variability and the effect of some environmental variables. *J. Phycology* 21, 347–357. doi: 10.1111/j.0022-3646.1985.00347.x

Brzezinski, M. A., Jones, J. L., Bidle, K. D., and Azam, F. (2003). The balance between silica production and silica dissolution in the sea: insights from Monterey bay, California, applied to the global data set. *Limnology Oceanography* 48, 1846–1854. doi: 10.4319/lo.2003.48.5.1846

Brzezinski, M. A., Krause, J. W., Church, M. J., Karl, D. M., Li, B., Jones, J. L., et al. (2011). The annual silica cycle of the north pacific subtropical gyre. *Deep-Sea Res. I* 58, 988–1001. doi: 10.1016/j.dsr.2011.08.001

Brzezinski, M. A., and Nelson, D. M. (1989). Seasonal changes in the silicon cycle within a gulf stream warm-core ring. *Deep-Sea Res.* 36, 1009–1030. doi: 10.1016/0198-0149(89)90075-7

Cloern, J. E. (2001). Our evolving conceptual model of the coastal eutrophication problem. *Mar. Ecol. Prog. Ser.* 210, 223–253. doi: 10.3354/meps210223

Closset, I., Mc Nair, H. M., Brzezinski, M. A., Krause, J. W., Thamatrakoln, K., and Jones, J. L. (2021). Diatom response to alterations in upwelling and nutrient dynamics associated with climate forcing in the California current system. *Limnology Oceanography* 66, 1578-1593. doi: 10.1002/lno.11705

Dale, V., Bianchi, T., Blumberg, A., Boynton, W., Conley, D., Crumpton, W., et al. (2007). "Hypoxia in the northern gulf of Mexico: an update by the EPA science advisory board," in *EPA-SAB-08-003* (Washington, DC: EPA Science Advisory Board), 333 pp.

Dortch, Q., Parsons, M., Rabalais, N., and Turner, R. (1999). What is the threat of harmful algal blooms in Louisiana coastal waters. *Recent Res. Coast. Louisiana: Natural System Funct. Response to Hum. Influences* 230, 134-144.

Dugdale, R. C. (1967). Nutrient limitation in the sea: dynamics, identification, and significance. *Limnology Oceanography* 12, 685–695. doi: 10.4319/lo.1967.12.4.0685

Dykstra, S., and Dzwonkowski, B. (2020). The propagation of fluvial flood waves through a backwater-estuarine environment. *Water Resour. Res.* 56, e2019WR025743. doi: 10.1029/2019WR025743

Dzwonkowski, B., Fournier, S., Reager, J. T., Milroy, S., Park, K., Shiller, A. M., et al. (2018). Tracking sea surface salinity and dissolved oxygen on a river-influenced, seasonally stratified shelf, Mississippi bight, northern gulf of Mexico. *Continental Shelf Res.* 169, 25–33. doi: 10.1016/j.csr.2018.09.009

Dzwonkowski, B., Greer, A., Briseño-Avena, C., Krause, J., Soto, I., Hernandez, F. J., et al. (2017). Estuarine influence on biogeochemical properties of the Alabama shelf during the fall season. *Continental Shelf Res.* 140, 96–109. doi: 10.1016/j.csr.2017.05.001

Ebner, B. (2019). *Spatiotemporal variation of benthic silica fluxes in the NGOM shelf* (Louisiana State University: Masters).

Geider, R. J., MacIntyre, H. L., and Kana, T. M. (1996). A dynamic model of photoadaptation in phytoplankton. *Limnology Oceanography* 41, 1–15. doi: 10.4319/lo.1996.41.1.0001

Ghaisis, N. A., Maiti, K., and Roy, A. (2021). Iron-mediated organic matterpreservation in the Mississippi River influenced shelf sediments. *Journal ofGeophysical Research: Biogeosciences* 126, e2020JG006089. doi: 10.1029/2020JG006089

Greer, A. T., Boyette, A. D., Cruz, V. J., Cambazoglu, M. K., Dzwonkowski, B., Chiaverano, L. M., et al. (2020). Contrasting fine-scale distributional patterns of zooplankton driven by the formation of a diatom-dominated thin layer. *Limnology Oceanography* 65, 2236–2258. doi: 10.1002/lno.11450

Greer, A., Shiller, A., Hofmann, E., Wiggert, J., Warner, S., Parra, S., et al. (2018). Functioning of coastal river-dominated ecosystems and implications for oil spill response: from observations to mechanisms and models. *Oceanography* 31, 90–103. doi: 10.5670/oceanog.2018.302

Gunter, G. (1963). The fertile fisheries crescent. *Mississippi Acad. Sci. J.* 9, 286–290.

Humborg, C., Conley, D. J., Rahm, L., Wulff, F., Cociasu, A., and Ittekkot, V. (2000). Silicon retention in river basins: far-reaching effects on biogeochemistry and aquatic food webs in coastal marine environments. *Ambio* 29, 45–50. doi: 10.1579/0044-7447-29.1.45

Humborg, C., Ittekkot, V., Cociasu, A., and Vonbodungen, B. (1997). Effect of Danube river dam on black Sea biogeochemistry and ecosystem structure. *Nature* 386, 385–388. doi: 10.1038/386385a0

Kemp, E. J., Roseburrough, R. R., Elliott, E. A., and Krause, J. W. (2021). Spatial variability of sediment amorphous silica and its reactivity in a northern gulf of Mexico estuary and coastal zone. *Gulf Caribbean Res.* 32, SC6–SC11. doi: 10.18785/gcr.3201.14

Kolker, A. S., Allison, M. A., and Hameed, S. (2011). An evaluation of subsidence rates and sea-level variability in the northern gulf of Mexico. *Geophysical Res. Lett.* 38, L21404. doi: 10.1029/2011GL049458

Krause, J. W., Brzezinski, M. A., Baines, S. B., Collier, J. L., Twining, B. S., and Ohnemus, D. C. (2017). Picoplankton contribution to biogenic silica stocks and production rates in the Sargasso Sea. *Global Biogeochemical Cycles* 31, 762-774. doi: 10.1002/2017GB005619

Krause, J. W., Brzezinski, M. A., Goericke, R., Landry, M. R., Ohman, M. D., Stukel, M. R., et al. (2015). Variability in diatom contributions to biomass, organic matter production, and export across a frontal gradient in the California current ecosystem. *J. Geophysical Research: Oceans* 120, 1032–1047. doi: 10.1002/2014JC010472

Krause, J. W., Brzezinski, M. A., and Jones, J. L. (2011). Application of low level beta counting of 32Si for the measurement of silica production rates in aquatic environments. *Mar. Chem.* 127, 40–47. doi: 10.1016/j.marchem.2011.07.001

Krause, J. W., Lomas, M. W., and Danielson, S. (2021). Diatom growth, biogenic silica production, and grazing losses to microzooplankton during spring in the northern Bering and chukchi seas. *Deep-Sea Res. II* 191-192, 104950. doi: 10.1016/j.dsr2.2021.104950

Krause, J. W., Nelson, D. M., and Lomas, M. W. (2009). Biogeochemical responses to late-winter storms in the Sargasso Sea, II: increased rates of biogenic silica production and export. *Deep-Sea Res. I* 56, 861–874. doi: 10.1016/j.dsr.2009.01.002

Lehrter, J. C., Beddick, D. L.Jr., Devereux, R., Yates, D. F., and Murrell, M. C. (2012). Sediment-water fluxes of dissolved inorganic carbon, O2, nutrients, and N2 from the hypoxic region of the Louisiana continental shelf. *Biogeochemistry* 109, 233–252. doi: 10.1007/s10533-011-9623-x

Lehrter, J. C., Murrell, M. C., and Kurtz, J. C. (2009). Interactions between freshwater input, light, and phytoplankton dynamics on the Louisiana continental shelf. *Continental Shelf Res.* 29, 1861–1872. doi: 10.1016/j.csr.2009.07.001

Lohrenz, S. E., Fahnenstiel, G. L., Redalje, D. G., Lang, G. A., Chen, X., and Dagg, M. J. (1997). Variations in primary production of northern gulf of Mexico continental shelf waters linked to nutrient inputs from the Mississippi river. *Mar. Ecol. Prog. Ser.* 155, 45–54. doi: 10.3354/meps155045

Lomas, M. W., Baer, S. E., Acton, S., and Krause, J. W. (2019). Pumped up by the cold: elemental quotas and stoichiometry of polar diatoms. *Front. Mar. Sci.* 6, 286. doi: 10.3389/fmars.2019.00286

Lomas, M. W., Lipschultz, F., Nelson, D. M., Krause, J. W., and Bates, N. R. (2009). Biogeochemical responses to late-winter storms in the Sargasso Sea, I–pulses of primary and new production. *Deep-Sea Res. I* 56, 843–860. doi: 10.1016/j.dsr.2008.09.002

MacIntyre, H. L., Stutes, A. L., Smith, W. L., Dorsey, C. P., Abraham, A., and Dickey, R. W. (2011). Environmental correlates of community composition and toxicity during a bloom of pseudo-nitzschia spp. in the northern gulf of Mexico. *J. Plankton Res.* 33, 273–295. doi: 10.1093/plankt/fbq146

McManus, M. A., Sevadjian, J. C., Benoit-Bird, K. J., Cheriton, O. M., Timmerman, A. H., and Waluk, C. M. (2012). Observations of thin layers in coastal Hawaiian waters. *Estuaries coasts* 35, 1119–1127. doi: 10.1007/s12237-012-9497-8

McNair, H. M., Brzezinski, M. A., and Krause, J. W. (2018). Diatom populations in an upwelling environment decrease silica content to avoid growth limitation. *Environ. Microbiol.* 20, 4184–4193. doi: 10.1111/1462-2920.14431

Milliman, J. D., Farnsworth, K., Jones, P., Xu, K., and Smith, L. (2008). Climatic and anthropogenic factors affecting river discharge to the global ocean 1951–2000. *Global Planetary Change* 62, 187–194. doi: 10.1016/j.gloplacha.2008.03.001

Nelson, D. M., and Dortch, Q. (1996). Silicic acid depletion and silicon limitation in the plume of the Mississippi river: evidence from kinetic studies in spring and summer. *Mar. Ecology-Progress Ser.* 136, 163–178. doi: 10.3354/meps136163

Nelson, D. M., Goering, J. J., and Boisseau, D. W. (1981). "Consumption and regeneration of silicic acid in three coastal upwelling systems," in *Coastal upwelling*. Ed. F. A. Richards (Washington, D.C.: American Geophysical Union), 242–256.

Officer, C. B., and Ryther, J. H. (1980). The possible importance of silicon in marine eutrophication. *Mar. Ecol. Prog. Ser.* 3, 83–91. doi: 10.3354/meps003083

Parsons, M. L., Dortch, Q., and Turner, R. E. (2002). Sedimentological evidence of an increase in pseudo-nitzschia (Bacillariophyceae) abundance in response to coastal eutrophication. *Limnology Oceanography* 47, 551–558. doi: 10.4319/lo.2002.47.2.0551

Pennock, J. R., Boyer, J. N., Herrera-Silveira, J. R., Iverson, R. L., Whitledge, T. E., Mortazavi, B., et al. (1999). "Nutrient behavior and phytoplankton production in gulf of Mexico estuaries," in *Biogeochemistry of gulf of Mexico estuaries*. Eds. T. S. Bianchi, J. R. Pennock and R. R. Twiley (New York: John Wiley & Sons), 109–162.

Pickering, R. A., Cassarino, L., Hendry, K. R., Wang, X. L., Maiti, K., and Krause, J. W. (2020). Using stable isotopes to disentangle marine sedimentary signals in reactive silicon pools. *Geophysical Res. Letters* 47, e2020GL087877. doi: 10.1029/2020GL087877

Rabalais, N. N., Turner, R. E., Dortch, Q., Justic, D., Bierman, V. J., and Wiseman, W. J. (2002). "Nutrient-enhanced productivity in the northern gulf of Mexico: past, present and future," in *Nutrients and eutrophication in estuaries and coastal waters* (Dordrecht: Springer), 39–63.

Rabalais, N. N., Turner, R. E., Sen Gupta, B. K., Platon, E., and Parsons, M. L. (2007). Sediments tell the history of eutrophication and hypoxia in the northern gulf of Mexico. *Ecol. Appl.* 17, S129–S143. doi: 10.1890/06-0644.1

Ragueneau, O., Conley, D. J., Leynaert, A., Longphuirt, S. N., Slomp, C. P., Ittekkot, V., et al. (2006). "Responses of coastal ecosystems to anthropogenic perturbations of silicon cycling," in *The silicon cycle : human perturbations and impacts on aquatic systems*. Eds. V. Ittekkot, C. Unger, N. Humborg and An Tac (Scientific Committee on Problems of the Environment (SCOPE) Series 66), 197–213.

Ragueneau, O., Savoye, N., Del Amo, Y., Cotten, J., Tardiveau, B., and Leynaert, A. (2005). A new method for the measurement of biogenic silica in suspended matter of coastal waters: using Si: Al ratios to correct for the mineral interference. *Continental Shelf Res.* 25, 697–710. doi: 10.1016/j.csr.2004.09.017

Sanial, V., Shiller, A. M., Joung, D., and Ho, P. (2019). Extent of Mississippi river water in the Mississippi bight and Louisiana shelf based on water isotopes. *Estuarine Coast. Shelf Sci.* 226, 106196. doi: 10.1016/j.ecss.2019.04.030

Schelske, C. L., Conley, D. J., Stoermer, E. F., Newberry, T. L., and Campbell, C. (1987). "Biogenic silica and phosphorus accumulation in sediments as indices of eutrophication in the laurentian great lakes," in *Paleolimnology IV* (Dordrecht: Springer), 79–86.

Schlitzer, R. (2016). Ocean data view. Available at: https://odv.awi.ed.

Stumpf, R. P., Gelfenbaum, G., and Pennock, J. R. (1993). Nutrient flux and physical stability drive phytoplankton biomass variability along the Alabama shelf [Data set]. *Continental Shelf Res.* 13, 1281–1301. doi: 10.1016/0278-4343(93)90053-Z

Sutton, J. R., Dzwonkowski, B., Krause, J. W., Hernandez, F. J., and Graham, W. M. (2023). *Nutrient flux and physical stability drive phytoplankton biomass variability along the Alabama shelf [Data set]* (Dauphin Island Sea Lab, Dauphin Island, AL). doi: 10.57778/MCG4-F330

Sylvan, J. B., Dortch, Q., Nelson, D. M., Brown, A. F. M., Morrison, W., and Ammerman, J. W. (2006). Phosphorus limits phytoplankton growth on the Louisiana shelf during the period of hypoxia formation. *Environ. Sci. Technol.* 40, 7548–7553. doi: 10.1021/es061417t

Tao, B., Tian, H., Ren, W., Yang, J., Yang, Q., He, R., et al. (2014). Increasing Mississippi river discharge throughout the 21st century influenced by changes in climate, land use, and atmospheric CO2. *Geophysical Res. Lett.* 41, 4978–4986. doi: 10.1002/2014GL060361

Turner, R. E., Qureshi, N., Rabalais, N. N., Dortch, Q., Justic, D., Shaw, R. F., et al. (1998). Fluctuating silicate : nitrate ratios and coastal plankton food webs. *Proc. Natl. Acad. Sci. USA* 95, 13048–13051. doi: 10.1073/pnas.95.22.13048

Turner, R. E., and Rabalais, N. N. (1991). Changes in Mississippi river water-quality this century. *Bioscience* 41, 140–147. doi: 10.2307/1311453

Turner, R. E., and Rabalais, N. N. (1994a). "Changes in the Mississippi river nutrient supply and offshore silicate-based phytoplankton community responses," in *Changes in fluxes in estuaries: implications from science to management*. Eds. K. R. Dyer and R. J. Orth (Fredesnborg: Olsen & Olsen), 485.

Turner, R. E., and Rabalais, N. N. (1994b). Coastal eutrophication near the Mississippi river delta. *Nature* 368, 619–621. doi: 10.1038/368619a0

Turner, R. E., Rabalais, N. N., and Justic, D. (2008). Gulf of Mexico hypoxia: alternate states and a legacy. *Environ. Sci. Technol.* 42, 2323–2327. doi: 10.1021/es071617k

frontiers | Frontiers in Marine Science

TYPE Original Research
PUBLISHED 22 November 2023
DOI 10.3389/fmars.2023.1291294

OPEN ACCESS

EDITED BY
Lihua Ran,
Ministry of Natural Resources, China

REVIEWED BY
Haimanti Biswas,
Council of Scientific and Industrial Research (CSIR), India
Xin Lin,
Xiamen University, China

*CORRESPONDENCE
Kimberlee Thamatrakoln
thamat@marine.rutgers.edu

†PRESENT ADDRESSES
Michael A. Maniscalco,
Ocean Ecology Lab (Code 616), NASA Goddard Space Flight Center, Greenbelt, MD, United States;
Hydrosphere, Biosphere, Geophysics Support Group, Science Systems and Applications, Inc., Greenbelt, MD, United States

RECEIVED 08 September 2023
ACCEPTED 02 November 2023
PUBLISHED 22 November 2023

CITATION
Maniscalco MA, Brzezinski MA, Krause JW and Thamatrakoln K (2023) Decoupling silicon metabolism from carbon and nitrogen assimilation poises diatoms to exploit episodic nutrient pulses in a coastal upwelling system. *Front. Mar. Sci.* 10:1291294. doi: 10.3389/fmars.2023.1291294

Decoupling silicon metabolism from carbon and nitrogen assimilation poises diatoms to exploit episodic nutrient pulses in a coastal upwelling system

Michael A. Maniscalco[1†], Mark A. Brzezinski[1], Jeffrey W. Krause[2,3] and Kimberlee Thamatrakoln[4*]

[1]Marine Science Institute and The Department of Ecology, Evolution, and Marine Biology, University of California, Santa Barbara, CA, United States, [2]Dauphin Island Sea Lab, Dauphin Island, AL, United States, [3]Stokes School of Marine and Environmental Sciences, University of South Alabama, Mobile, AL, United States, [4]Department of Marine and Coastal Sciences, Rutgers, The State University of New Jersey, New Brunswick, NJ, United States

Diatoms serve as the major link between the marine carbon (C) and silicon (Si) biogeochemical cycles through their contributions to primary productivity and requirement for Si during cell wall formation. Although several culture-based studies have investigated the molecular response of diatoms to Si and nitrogen (N) starvation and replenishment, diatom silicon metabolism has been understudied in natural populations. A series of deckboard Si-amendment incubations were conducted using surface water collected in the California Upwelling Zone near Monterey Bay. Steep concentration gradients in macronutrients in the surface ocean coupled with substantial N and Si utilization led to communities with distinctly different macronutrient states: replete ('healthy'), low N ('N-stressed'), and low N and Si ('N- and Si-stressed'). Biogeochemical measurements of Si uptake combined with metatranscriptomic analysis of communities incubated with and without added Si were used to explore the underlying molecular response of diatom communities to different macronutrient availability. Metatranscriptomic analysis revealed that N-stressed communities exhibited dynamic shifts in N and C transcriptional patterns suggestive of compromised metabolism. Expression patterns in communities experiencing both N and Si stress imply that the presence of Si stress may partially ameliorate N stress and dampen the impact on organic matter metabolism. This response builds upon previous observations that the regulation of C and N metabolism is decoupled from Si limitation status, where Si stress allows the cell to optimize the metabolic machinery necessary to respond to episodic pulses of nutrients. Several well-characterized Si-metabolism associated genes were found to be poor molecular markers of Si physiological status; however, several uncharacterized Si-responsive genes were revealed to be potential indicators of Si stress or silica production.

KEYWORDS

diatom, biogenic silica production, metatranscriptomics, silicon metabolism, nitrogen assimilation, carbon metabolism, nutrient limitation, gene set analysis

Introduction

As silicifying photoautotrophs, diatoms serve as a critical link between ocean silicon (Si), nitrogen (N), and carbon (C) biogeochemical cycles. In productive coastal regimes, wind-driven upwelling events bring deep macronutrient-rich water to the surface, fueling >30% of annual productivity (Krause et al., 2013). In the coastal upwelling zone (CUZ) near Monterey Bay, strong late spring and summer upwelling can bring water to the surface with $Si(OH)_4$ and NO_3^- concentrations in excess of 25 μM in a ~1.2:1 ratio (Brzezinski et al., 1997). Diatoms can rapidly respond to the influx of nutrients and utilize $Si(OH)_4$ and NO_3^- in a 1:1 ratio (Brzezinski, 1985), implying that a diatom-dominated community in Monterey Bay could account for nearly all of the new production within the system. The similarity between the mean supply and utilization ratios suggests diatoms could simultaneously drawdown NO_3^- and $Si(OH)_4$ to low levels, setting up a potential scenario where diatom cells experience physiological stress related to the lack of both macronutrients. However, variations from the mean nutrient supply ratio, the amount of nitrogen regenerated in the system (Brzezinski et al., 1997), or the community nutrient consumption ratio can determine the ultimate limiting nutrient regime, which may have dramatically different impacts on cell physiology (De La Rocha and Passow, 2004; Brembu et al., 2017a; Smith et al., 2019) and bloom fate.

In response to low N availability that reduces the rate of N uptake, diatoms attempt to maintain growth by reducing cellular N quotas through decreased concentrations of chlorophyll, total protein, and other N-dependent biomolecules (Osborne and Geider, 1986; Liefer et al., 2019). This is driven by the down-regulation of genes involved in C metabolism and accompanied by a characteristic shift in the expression of N-assimilation genes (Bender et al., 2014; Smith et al., 2019). Low extracellular N availability can also lead to cellular amino acid and protein recycling (Falkowski et al., 1989; Alipanah et al., 2015) and up-regulation of the ornithine-urea cycle, which plays a key role in the redistribution of intracellular N (Allen et al., 2011). These strategies slow progression into total N starvation and cell cycle arrest, but progressively induces physiological stress that ultimately reduces growth. The loss of key metabolites in the process results in an extended lag phase upon N replenishment (De La Rocha and Passow, 2004; Hockin et al., 2012). In contrast, when diatoms are kinetically limited by low Si availability, a reduction in cellular Si quota is achieved by the production of less silicified cell walls, or frustules, allowing cells to maintain growth (Paasche, 1973; McNair et al., 2018a). Reductions in silica production could also reduce cellular N quota given the role of long-chain polyamines, derived from the urea cycle, in silicification (Kröger et al., 2000). Only when the limitation by Si exceeds the capacity of the cell to thin the frustule does growth limitation ensue; this can be due to low dissolved Si driven by bloom conditions or chronically low Si concentrations (e.g. open ocean). However, as Si is a structural component and not heavily utilized in vital intracellular machinery, Si limitation has less of an impact on C and N metabolism, thereby allowing diatoms to rapidly return to optimal growth rates upon Si replenishment (De La Rocha and Passow, 2004). Thus it has been suggested that Si limitation may be an evolutionary adaptation that allows diatoms to rapidly resume growth upon nutrient resupply (Flynn and Martin-Jézéquel, 2000; De La Rocha and Passow, 2004; Raven and Waite, 2004).

Unlike the well-characterized molecular response to N stress, the molecular response to Si stress is less defined, in part because of an incomplete understanding of the molecular mechanisms of silicification and the metabolic pathways impacted by Si stress. Numerous culture-based transcriptomic studies have explored the molecular response to Si starvation and replenishment (Mock et al., 2008; Sapriel et al., 2009; Shrestha et al., 2012; Smith et al., 2016; Brembu et al., 2017a), but the majority of genes identified in these studies encode for hypothetical or uncharacterized proteins. Proteomic-based studies confirm the role of numerous known and unknown proteins in Si metabolism, but also reveal the expression of proteins involved in cell cycle progression, amino acid synthesis, and cell wall synthesis (Du et al., 2014; Chen et al., 2018; Thangaraj et al., 2019). Among the known proteins are the silicon transporters (*SITs*), a family of membrane-bound proteins responsible for intracellular silicon uptake (Hildebrand et al., 1997; Hildebrand et al., 1998; Thamatrakoln and Hildebrand, 2007) when extracellular $Si(OH)_4$ concentrations are <20 μmol L^{-1} (Shrestha and Hildebrand, 2015; Knight et al., 2016); above that, passive uptake occurs with $Si(OH)_4$ freely diffusing across the cell membrane (Thamatrakoln and Hildebrand, 2008; Shrestha and Hildebrand, 2015). Other diatom-specific proteins directly involved in silica deposition (i.e. silica production) have also been characterized including silaffins (Kröger et al., 1999), silacidin (Wenzl et al., 2008), cingulins (Scheffel et al., 2011), silicalemma-associated proteins (Tesson et al., 2017), and silicanin-1 (Kotzsch et al., 2017).

Here we investigate the physiological impact of, and interplay between, N and Si stress of a diatom bloom near Monterey Bay, CA to understand how nutrient-limited communities respond when resupplied with episodic pulses of nutrients. To provide a molecular framework for the response to nutrient limitation, we used a combination of metatranscriptomic analyses and biogeochemical measurements to contextualize the resident diatom communities. We further evaluate the utility of diatom transcriptomic fingerprints in diagnosing N and Si stress.

Materials and methods

Environmental sample collection and experimental design

Incubation samples were collected during the "DYE labeling of diatoms" (DYEatom) cruise between 27 June and 05 July 2013 on board the R/V Point Sur (PS1312; 27 June-5 July 2013) off the California coast near Monterey Bay. Details about the cruise track and hydrodynamic conditions can be found elsewhere (Kranzler et al., 2019; Krause et al., 2020). Stations reflecting a progression of bloom states were initially identified using satellite derived ocean color and sea surface temperature (SST; MODIS Level-2 products, NASA), high frequency radar arrays (Kaplan and Largier, 2006);

Central and Northern California Ocean Observing System, www.cencoos.org), and the vessel's underway data acquisition and flow-through seawater systems to identify areas with high phytoplankton biomass. Stations were sampled just after local sunrise. Water was collected using a rosette containing twelve 10L Niskin bottles, Sea-Bird Electronics conductivity-temperature-depth sensor, Chelsea fluorometer, and photosynthetically active radiation (PAR) sensor from Bio-Spherical Instruments. Data from three stations, S2, S4 and S11 were analyzed for the present study.

The phytoplankton community response to silicic acid addition was investigated through a series of deckboard incubation experiments and a combination of biogeochemical measurements and metatranscriptome sequencing. Water was collected from a depth corresponding to 55% of the surface irradiance level (I_0) and transferred to replicate acid-washed polycarbonate bottles. Bottles were left unamended as control (Ctrl) or amended with 18 µmol L^{-1} $Si(OH)_4$ (+Si) and incubated in deckboard incubators shaded to 55% I_0 with window screening and cooled to *in situ* temperatures with flow-through surface seawater.

Silica production rate measurements

Community biogenic silica (bSi) production rates were measured using the radiotracer ^{32}Si. At the start of each incubation experiment a 250 mL polycarbonate bottle was filled to the brim with 304 mL of seawater, amended with 263 Bq of high-specific activity ^{32}Si (>40 kBq µg Si^{-1}), and incubated for 4, 12, and/or 24 h. At the termination of each incubation, samples were filtered onto 25 mm, 1.2-µm pore-size polycarbonate filters and processed for ^{32}Si activity using low-level gas-flow proportional counting (Krause et al., 2011). Volumetric Si production rates (ρ in µmol Si L^{-1} d^{-1}) were normalized to bulk bSi concentrations (µmol Si L^{-1}) to obtain specific silicic acid uptake rates (V_b, d^{-1}). Two methods were used to assess the degree that the ambient $Si(OH)_4$ concentration limited bSi production (i.e. Si uptake), both of which used the same ^{32}Si activity addition, incubation conditions, and processing as described above. The first method measured ^{32}Si uptake as a function of silicic acid concentration along an eight-point concentration gradient between 0-18 µmol L^{-1} $Si(OH)_4$, i.e. sample water was distributed into eight different bottles, and seven received added $Si(OH)_4$ (one remained at ambient) to create the gradient. The dependence of V_b on the substrate concentration conforms to a rectangular hyperbola described by the Michaelis-Menten equation:

$$V_b = V_{max} \times [Si(OH)_4] \times (K_s + [Si(OH)_4])^{-1} \quad (1)$$

where V_{max} is the maximum specific uptake rate and K_s is the half saturation constant. Data were fit to a non-linear curve using the self-starting Michaelis-Menten function (SSmicmen) from the R *stats* package v.3.6.2. The second method used bSi production rates measured at ambient $Si(OH)_4$ concentration and +18.0 µmol L^{-1} $Si(OH)_4$ to saturate Si uptake and approximate V_{max} and measure V_b in Eq. 1 (Brzezinski et al., 1997). Kinetic Si-limitation, or Si-stress, was defined as the ratio of Si production at ambient $Si(OH)_4$ concentration (V_{amb}) to the enhanced +18µmol L^{-1} $[Si(OH)_4]$ (V_{enh}), $V_{amb} : V_{enh}$ (Nelson et al., 2001).

$$Si\ stress = V_{amb} / V_{enh} \quad (2)$$

ere lower values correspond to greater stress. Based on the analytical error of the measurement, Si stress values >0.92 were considered within detection error and are not resolvable from a value of 1 which would indicate Si sufficiency (Krause et al., 2012).

For station S11, the end point of the kinetic incubation (4 h) differed from that of the incubation used for RNA extraction and sequencing (36 h). Thus, the initial conditions (e.g. bSi_0, $[Si(OH)_4]_0$, V_{max}, V_b, and K_s) were used to estimate the final specific uptake rate and Si stress. Eq. 1 was converted into Eqs. 3-4 to determine the bSi concentration (bSi_n) at the end of a given time-step (t_n, iteration number n). The bSi_n and $Si(OH)_4$ concentration after t_n ($[Si(OH)_4]_n$) were then used to calculate the specific uptake rate at the end of each time-step (1 min) and iterated for each time-step from 4 to 36 h (Eqs. 5-6).

$$bSi_n = bSi_0 \times e^{t_n \times V_b} \quad (3)$$

$$[Si(OH)_4]_n = [Si(OH)_4]_0 - (bSi_n - bSi_0) \quad (4)$$

$$V_n = V_{max} \times [Si(OH)_4]_0 \times (K_s + [Si(OH)_4]_n)^{-1} \quad (5)$$

$$V_n = ln\left((bSi_{n+1} + bSi_n) \times (bSi_n)^{-1}\right) \times t_{n+1}{}^{-1} \quad (6)$$

This simplified calculation assumes there was minimal dissolution of the bSi pool during the time-course of the incubation (i.e. gross production = net production), which is reasonable for this region where the average dissolution rate has been measured at ~0.05 d^{-1} (Brzezinski et al., 2003). Furthermore, although shifts in species composition can community alter V_{max} and K_s values, the incubations were short enough (12-36 h) that we assumed these values did not change.

Nutrient and particulate analyses

Seawater samples for dissolved nutrient analysis (nitrite + nitrate, orthophosphate and silicic acid) were syringe filtered through 0.6 µm-polycarbonate filters into polypropylene scintillation vials and immediately frozen at -20°C. Concentrations of NO_2^- + NO_3^-, and PO_4^{-3} were measured at the University of California, Santa Barbara Marine Science Institute using a Lachat Instruments QuikChem 8500 Series 2 (Parsons et al., 1984), while $Si(OH)_4$ was quantified using the ammonium molybdate colorimetric assay (Brzezinski and Nelson, 1995). For bSi samples, 600 mL of seawater was vacuum filtered onto 0.6-µm pore-size polycarbonate filters and digested shipboard using 0.2 N NaOH digestion in Teflon tubes (Krause et al., 2010). Final neutralized bSi digests were then quantified using similar colorimetric procedures as described for $Si(OH)_4$ samples (Krause et al., 2010). For chlorophyll measurements, samples were collected by filtration onto 0.45-µm pore-size HAWP cellulose filters (Millipore) and frozen at -20°C. Chlorophyll *a* was extracted with

90% acetone at -20˚C for 24 h using the acidification method and measured with the Turner Designs 10-AU fluorometer (Strickland and Parsons, 1972; Parsons et al., 1984).

Metatranscriptome analysis

Seawater samples for metatranscriptome analysis were collected by filtration at <5 psi onto 47 mm, 1.2 µm pore-size polycarbonate membranes, flash frozen in liquid N_2, and stored at -80°C. Total RNA was extracted from filters using the Trizol-RNeasy method with an additional bead beating step. In brief, filters were transferred to tubes containing RNase/DNase free 100 µm zirconia/silica beads with 1 mL of Trizol reagent, vortexed for 2 min, incubated at room temperature for 5 min, vortexed again for 2 min before following the standard Trizol RNA extraction protocol. The upper aqueous phase was transferred to a clean 1.5 mL tube with an equal volume of 70% alcohol, mixed, and added to QIAgen RNAeasy column. The standard RNeasy protocol with the optional on-column DNase treatment was followed.

RNA was quantified using a Qubit® RNA HS Assay, and RNA integrity was determined using the Agilent Bioanalyzer RNA 6000 Pico kit eukaryotic assay. Total RNA (500 ng) was used for library prep with Illumina TruSeq RNA Library Prep kit v2 with mRNA purified using Oligo-dT bead capture polyA tails. Library quality was assessed on an Agilent Bioanalyzer and quantified via Qubit before being pooled in equal quantities. The pooled libraries were sequenced at UC-Davis Genome Center on HiSeq 4000 in lanes of paired-end-150bp flow cell.

Primer and adapter sequences were removed from raw sequencing reads with trimmomatic v0.38 (Bolger et al., 2014). Paired-end reads were merged with interleave-reads.py from the khmer package v2.1.2 before removal of rRNA reads with sortmeRNA v2.0 utilizing the built in SILVA 16s, 18s, 23s, and 28s databases (Kopylova et al., 2012). Remaining reads were separated (using the deinterleave_fastq.sh https://gist.github.com/nathanhaigh/3521724) and assembled into contiguous sequences (contigs) with megahit v1.1.3 using 'meta-large' setting (Li et al., 2015). Open reading frames (ORFs) were predicted from assembled contigs using FragGeneScan v1.31 (Rho et al., 2010), and orfs shorter than 150 bp were removed. Reads counts for remaining orfs were estimated using salmon v0.6.0 `quant` quasi-mapping with seqBias and gcBias features.

Orfs were annotated based on best homology (lowest *E*-value) using BLASTP v.2.5.0+ with an *E*-value threshold of$<10^{-3}$. Taxonomic and functional annotations were assigned using the MarineRefII (roseobase.org/data), a custom databased maintained by the Moran Lab at the University of Georgia that includes sequences from PhyloDB v.1.076 which contains 24,509,327 peptides from 19,962 viral, 230 archaeal, 4,910 bacterial and 894 eukaryotic taxa, including peptides from KEGG, GenBank, JGI, ENSEMBL, CAMERA and 410 taxa from the Marine Microbial Eukaryotic Transcriptome Sequencing Project (MMETSP), as well as the associated KEGG functional and NCBI taxonomic annotations through a related SQL database. NCBI taxonomic annotations were further curated (Cohen et al., 2017); (https://github.com/marchettilab/metatranscriptomicsPipeline) to ensure the use of consistent taxonomic ranks. KEGG Ortholog (KO) classifications of diatom urea transporters, nitrite reductase, ammonium transporters were manually verified against known gene phylogenies and edited accordingly (Smith et al., 2019).

Silaffin-like genes were identified in *Pseudo-nitzschia multiseries* (CLN-47 v1) genome, as described previously (Scheffel et al., 2011), using an initial signal peptide screen of translated nucleotide sequences and subsequence sliding window search for amino acid (AA) sequences containing a 100-2000 long segment with ≥10% lysine and ≥18% serine residues. Full length *P. multiseries* putative silaffin amino acid sequences were subsequently screened for the presence the characteristic silaffin-like motifs using the FIMO program within the Multiple EM for Motif Elicitation (MEME suite v.5.4.1) motif scanning software package (Grant et al., 2011). Additional functional annotation was performed using BLASTP with the NCBI nr database (E-value$<10^{-10}$) and KEGG GhostKOALA (score<40). This process identified 157 putative unique *P. multiseries* silaffin-like genes (PNSLs) which were used with BLASTP+ v2.5.0 (E-value$<10^{-5}$) to identify homologous sequences within our metatranscriptome assembly. To identify the distribution of these genes in diatoms and other microalgae, BLASTP was used against a database containing the 67 translated transcriptomes from the MMETSP (Keeling et al., 2014). PNSLswith no significant hits (E-value$<10^{-10}$) to non-diatom genes were considered "diatom-specific".

For genes of interest that did not have an associated KO number, such as silicon transporters (SITs) and silicanin-1 (Sin-1), manual annotation was performed as previously described (Durkin et al., 2016; Brembu et al., 2017a; Kotzsch et al., 2017) using BLASTP+ v2.5.0 best hit with e-value cutoff of 10^{-5}. Putative SIT sequences were further classified to clade designations, using a maximum-likelihood tree constructed from a reference alignment (Durkin et al., 2016) with RAxML version 8.2.12 – PROTGAMMAWAGF substitution model and 100 bootstrap replicates (Stamatakis, 2014). A HMM-profile was constructed from the reference alignment (using hmmbuild 3.2.1) and used with hmmalign to align amino acid sequences corresponding to SIT orfs. Alignment and tree files were packaged using taxtastic v.0.8.3, and SIT orfs were placed on the reference tree using pplacer v.1.1.alpha19 with posterior probability calculated (Matsen et al., 2010). The most closely related reference sequence was assigned to each SIT orf using guppy v.1.1.alpha19 (Matsen et al., 2010).

Prior to differential abundance analysis, raw counts were aggregated within diatom genera by KO number. For genes lacking a KO number, e.g. *SITs*, ISIPs, Sin1, etc., aggregation was done based on gene assignment through KEGG annotation or BLASTX query of supplemental databases. Genus-specific aggregation of functionally annotated reads reduces redundancy and allows the use of tools originally designed for single organism RNAseq analysis (e.g. DESeq2, edgeR). This is necessary for microbial community transcriptomic analysis due to methodological and computational difficulties in resolving species-level, differential transcript abundance (Toseland et al., 2014; Alexander et al., 2015; Kopf et al., 2015; Cohen et al., 2017; Hu et al., 2018; Lampe et al., 2018; Cohen et al., 2021). However,

this approach does not resolve species-level contig abundance, nor does it *a priori* resolve clade-specific abundance patterns for genes that belong to multigene families. In the case of SITs, individual clades were identified through phylogenetic analysis as described above, and manually annotated to allow interrogation of SIT transcripts at the clade level. Additionally, annotations for urea transporters 1 and 2 were grouped together because of their close phylogenic relationship and shared abundance pattern in response to nitrogen supply (Smith et al., 2019). A similar approach for other multigene families, such as ammonium transporters and nitrate transporters, was not used because abundance of these genes in response to nitrogen supply does not appear to be clade-specific (Smith et al., 2019).

Metabolic pathway groupings

Genes indicative of nitrogen limitation were selected based on culture-based studies characterizing the response of the diatom *Phaeodactylum tricornutum* to depletion and replenishment of nitrate, nitrite, and ammonia (Smith et al., 2019). Using independent transcriptomic studies of Si-depleted and replenished *Thalassiosira pseudonana* cultures (Shrestha et al., 2012; Smith et al., 2016; Brembu et al., 2017a), we identified a subset of genes conserved across those studies in either their response to silicon starvation or association with silica production and denote these here as SiLA (Si-limitation associated) or SiPA (silica production associated), respectively. SiLA genes were identified as those with a >2-fold increase in transcript abundance >4 h-post Si-starvation and that did not increase expression in response to Si replenishment. Similarly, SiPA genes were identified as those with a >2-fold increase in transcript abundance >4 h-post Si replenishment and did not increase expression in response to Si starvation. The 2-fold threshold was used to provide confidence that the response would be robust while the response time of >4 h was chosen to exclude genes involved in the initial response to changes in $Si(OH)_4$ concentration and ensure that the change in expression was persistent. The rationale for this is that for the expression of a gene to be useful as a molecular marker in natural communities, it should be robust and persistent given that the biogeochemical history of a phytoplankton community is usually unknown prior to sampling. Putative *T. pseudonana* SiLA and SiPA genes were screened for RXL and KXXK silaffin motifs as described above. Gene annotations included for carbon metabolism included genes from *T. pseudonana* CCMP 133, *F. cylindrus* CP 1102, and *P. tricornutum* CCAP 1055 included in the KEGG modules: carbon fixation in photosynthetic organisms, photosynthesis, photosynthesis - antennae protein, as well as KEGG class-3 modules for ATP synthesis and carbon fixation. Genes annotated as carbonic anhydrase, DIC uptake, and flavodoxin were also included.

Statistical analysis

The normalization and differential abundance analysis of metatranscriptome data was analyzed within each taxonomic group using edgeR v.3.32.1 (Robinson et al., 2010). Significance between samples was determined using exactTest with tagwise dispersion and corrected for multiple testing with a significance threshold of FDR<0.05 (Benjamini and Hochberg, 1995). Significant differential abundance of genes related to carbon, nitrogen, and silicon metabolism was visualized through heatmaps. Differential enrichment of gene sets was assessed using mroast within the limma v.3.50.3 package with default settings (Wu et al., 2010) which assigns statistical significance to a set of genes within a metabolic pathway of interest and returns the number of genes detected (n), the percent of the gene set that was differentially expressed, and the p-value.

Principle component analysis was performed using the log-transformed normalized counts for the 2500 most variable genes and supplemental environmental data. PCA biplots were created with ggplot2 v.3.3.5 and factoextra v.1.0.7.

Data deposition

All cruise related data can be accessed through the Biological and Chemical Oceanography Data Management Office project number 550825 (https://www.bco-dmo.org/project/550825). All raw sequence data have been deposited in the NCBI sequence read archive and can be accessed under BioProject accession no. PRJNA790068 (BioSample accession nos SAMN11263639 and SAMN24193217-SAMN24193233). The assembled orfs and associated counts and annotation files used in this study can be found at Dryad.

Results

This study was part of the "DYE labeling of diatom silica" (DYEatom) cruise (PS1312; 27 June–05 July 2013) that set out to examine the response of diatom communities to a range of $Si(OH)_4$ concentrations within the CUZ (Kranzler et al., 2019; Krause et al., 2020). Upwelling favorable conditions near Monterey Bay over the 10 days prior to the start of the cruise, 10-21 June 2013, coincided with decreased SST (Krause et al., 2020). Satellite imagery depicted elevated (>5 μg L^{-1}) chlorophyll *a* (Chl *a*) concentration within and northwest of Monterey Bay throughout the duration of the study (Figure 1). *In situ* samples from three stations (S2, S4, and S11; Figure 1) indicated the presence of substantial diatom biomass within the phytoplankton community, with Chl *a* and bSi concentration to 8.74 - 11.84 μg L^{-1} and 5.3 - 6.7 μmol L^{-1}, respectively (Table 1).

Initial macronutrient concentrations varied among the three stations, with the highest concentrations of NO_3^- + NO_2^-, hereafter denoted NO_3^-, 8.79 μmol L^{-1}, and $Si(OH)_4$, 9.98 μmol L^{-1} at S2. In contrast, the initial NO_3^- concentrations at both S4 and S11 were sub-micromolar, 0.23 and 0.60 μmol L^{-1}, respectively, while $Si(OH)_4$ concentrations were slightly higher, 1.60 and 2.85 μmol L^{-1}, respectively. The excess $Si(OH)_4$ relative to NO_3^- at S2, ~1.14:1, is typical of the Monterey Bay regime (Brzezinski et al., 1997), while the higher ratios at S4 (6.83) and S11 (4.81) may be linked to N depletion prior to station occupation. To investigate the impact of low Si and/or N on diatom physiology, bottle incubations were set up at each

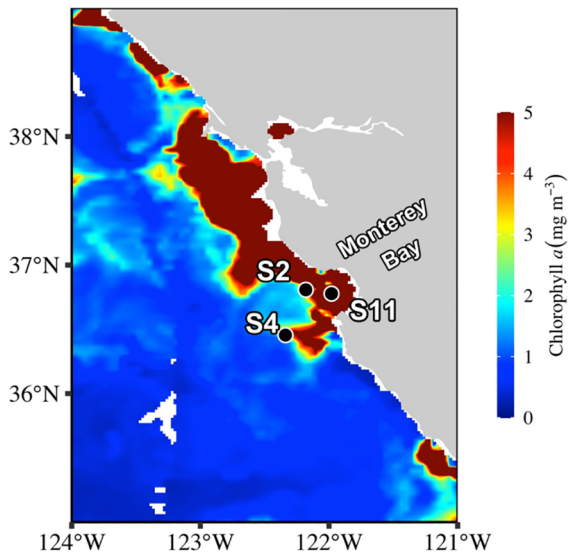

FIGURE 1
Sampling site locations overlayed on surface chlorophyll *a* concentrations from level-2 MODIS 8-day average from 2013, June 29 (https://giovanni.gsfc.nasa.gov/giovanni/).

station with unamended controls (Ctrl) and +18 µmol L^{-1} Si-amended (+Si) samples.

Characterization of macronutrient status

In the first 12 h of the deckboard incubations at S2 and S11, the specific rate of silicic acid uptake (V_b) in the Ctrl treatments were similar, 0.62 - 0.66 d^{-1}, and corresponded to a doubling of the initial bSi concentration in ~1.1 days. In contrast, V_b in the S4 Ctrl treatment was ~40% lower at 0.35 d^{-1} (Figure 2A). Rates measured over 24 h at S2 and S4, which both had high initial $Si(OH)_4$ concentrations (>5 µmol L^{-1}), were nearly identical to their respective 12 h measurements, indicating there was no diurnal pattern of Si uptake at these stations (Supplementary Table S1).

Kinetic limitation of Si uptake was assessed by the ratio of V_b in Ctrl (V_{amb}) to +Si treatments (V_{enh}), with values <0.3 indicative of severe Si limitation and values >0.7 indicative of no kinetic Si limitation (Nelson and Brzezinski, 1990; Krause et al., 2011). At S2, V_{amb} : V_{enh} was 0.95, indicating there was no Si stress during the 24 h incubation (Supplementary Table S2). In contrast, communities at S4 exhibited signs of increasing Si stress (V_{amb} : V_{enh} = 0.28) from 0-12 h, which intensified from 12 - 24 h when V_{amb} : V_{enh} decreased to 0.17 (Supplementary Table S2). At S11, the community started with minor kinetic Si limitation (V_{amb} : V_{enh} = 0.80 from 0-4 h), but became increasingly Si limited as V_{amb} : V_{enh} decreased to 0.47 between 4-12 h (Supplementary Table S2). Although Si uptake rates were not measured at the endpoint, 36 h, of the S11 incubation, the Michaelis-Menten based model utilizing the initial biogeochemical measurements and kinetic values (see Methods) predicted low final V_{amb}, 0.02, and severe Si stress (V_{amb} : V_{enh} = 0.03) for the Ctrl treatment (Supplementary Table S2).

In the absence of N uptake or NO_3^- concentration measurements at the end of each incubation, we used V_b (Eq.4) to estimate the amount of new bSi produced and, assuming a 1:1 ratio of N:Si uptake (Brzezinski, 1985), determined the likelihood of N-limitation in our incubations. At S2, 3.7 and 3.9 µmol L^{-1} of new bSi produced in Ctrl and +Si treatments, respectively would have only drawn down the initial $Si(OH)_4$ and NO_3^- to 6.19 and 5.3 µmol L^{-1}, which is not considered rate limiting (Figure 2B; White and Dugdale, 1997), and was unlikely to be yield limiting given the initial biomass. In contrast, at S4, the 1.2 and 5.3 µmol L^{-1} of new bSi produced in Ctrl and +Si treatments, respectively (Figure 2B), would have created a substantial debit against the initial 0.23 µmol L^{-1} of NO_3^- even without considering shifts in N:Si ratios of uptake of N by other taxa. Similarly, at S11, in Ctrl and +Si treatments, there was 2.0 and 3.9 µmol L^{-1} of new bSi produced, respectively, which would have created an associated N demand of 1.8 (Ctrl) and 2.5 µmol L^{-1} (+Si). Considering the initial NO_3^- concentration at S11 was 0.59 µmol L^{-1}, both treatments were likely deplete of NO_3^- by 36 h.

Taken together, we classified each station and treatment based on the likely nutrient-driven physiological state (Supplementary Figure 1). At S2, both Ctrl and +Si treatments were classified as replete, based on the lack of Si stress and the presence of ample NO_3^-. At S4 and S11, the +Si treatments were considered N stressed because the amount of NO_3^- required to support the amount of new bSi produced exceeded the initial NO_3^- concentration. In contrast, the Ctrl treatments at both S4 and S11 were considered stressed by both N and Si.

Phytoplankton community composition

The relative proportion of taxonomically annotated mRNA reads from the end of each incubation showed diatoms dominated >50% of the phytoplankton transcripts at S2 and S4, but accounted for a lower percentage of transcripts at S11. Dinoflagellates and other non-diatom eukaryotes accounted for

TABLE 1 Particulate biomass and macronutrient concentrations of initial water at each sampling site.

Station	Particulate biomass		Dissolved macronutrients		Incubation length (hours)
	bSi (µmol L^{-1})	Chl a (µg L^{-1})	$Si(OH)_4$ (µmol L^{-1})	N+N (µmol L^{-1})	
S2	5.28	8.74	9.98	8.79	24
S4	6.69	10.87	1.60	0.23	12
S11	5.56	11.83	2.85	0.59	36

10.3389/fmars.2023.1291294

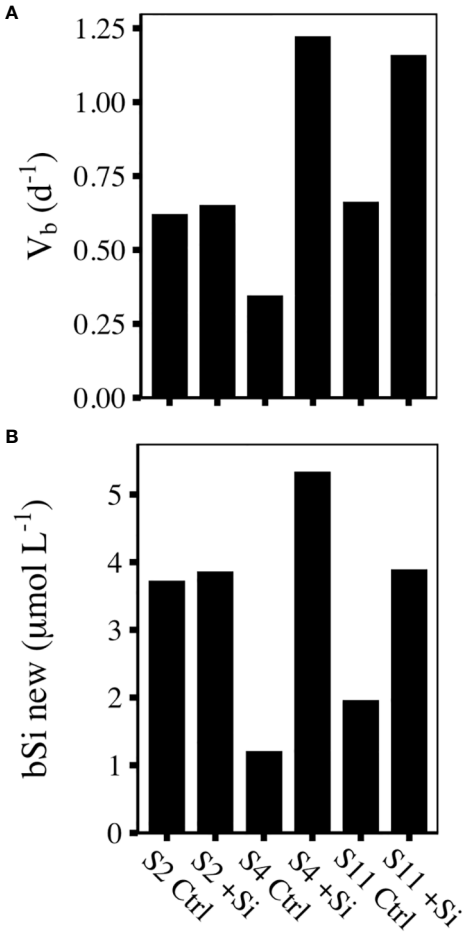

FIGURE 2
(A) Biomass specific Si uptake rates (d^{-1}) and **(B)** new bSi produced (µmol L^{-1}) over the first 12 h of control (Ctrl) and Si-amended (+Si) incubations at each sampling site.

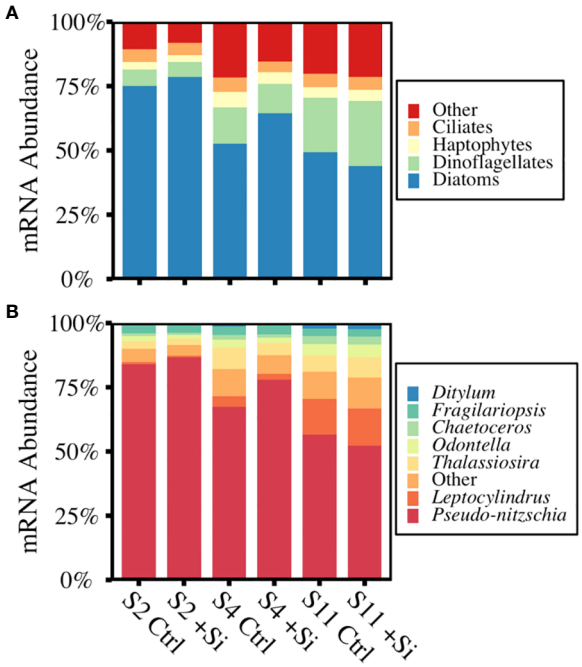

FIGURE 3
Percent annotated mRNA reads of the communities sampled at the end of each incubation across **(A)** the major phytoplankton groups and **(B)** diatom genera present. Data are the average of replicates (n=3).

the remaining 21 - 56% of annotated mRNA reads (Figure 3C). Among the diatoms, *Pseudo-nitzschia* transcripts made up the majority, 52 - 87%, with the next highest representation by *Leptocylindrus* and *Thalassiosira* (1 - 15%; Figure 3D). This supports a previous description of the initial phytoplankton community based on 18s rRNA that found diatoms made up 74 - 91% of the total reads, with >90% belonging to the genus *Pseudo-nitzschia* (Kranzler et al., 2019; Krause et al., 2020).

Nutrient-driven transcriptomic response

Comparative metatranscriptomic sequence analysis was used to assess the molecular response of the diatom community to the different nutrient scenarios at each station. Principle component analysis (PCA) of the transcriptomic profiles showed substantial separation of samples based on macronutrient status. PC1 accounted for 74% of the variance between samples and primarily separated the N-replete samples at S2 (Ctrl, +Si) from the N-deplete samples (+Si) and the N- and Si-deplete samples (Ctrl) from S4 and S11 (Figure 4). Furthermore, based on the loading of the biogeochemical supplemental variables, PC1 described the absence of NO_3^- and presence of Chl *a*, informed by the high cosine square values that represented the importance of the PC to a given observation. PC2 only represented 8% of the variance between samples and appeared to separate samples by geographic location. The substantial separation between N-deplete samples relative to the N-replete sample and the small degree of separation between Ctrl and +Si samples suggests that co-occurring Si stress did not add to the transcriptomic changes that were already occurring due to N stress.

To interrogate the transcriptomic response of the diatom community to the differing nutrient regimes, a focused rotation gene set testing (ROAST) approach (Wu et al., 2010) was used in combination with individual gene expression analysis. While gene-by-gene comparisons are useful for assessing the expression of key, rate-limiting steps within a metabolic pathway, a multivariate approach for gene set analysis (GSA) is considered more robust (Rahmatallah et al., 2014). The response to N stress was characterized by comparing the gene expression profiles between replete (Ctrl and +Si treatments at S2) to N deplete samples (+Si treatments at S4 and S11; Supplementary Figure 1). Expression profiles of samples that were both N and Si deplete (Ctrl treatment at S4 and S11) were compared to replete samples (Ctrl and +Si treatments at S2) to assess the response to co-occurring N and Si stress. Lacking samples that exclusively experienced Si stress, the response to Si stress was assessed by comparing samples that experienced both N and Si stress (Ctrl treatments at S4 and S11) to those that were solely N stressed (+Si treatments at S4 and S11; Supplementary Figure 1). These comparisons can potentially

10.3389/fmars.2023.1291294

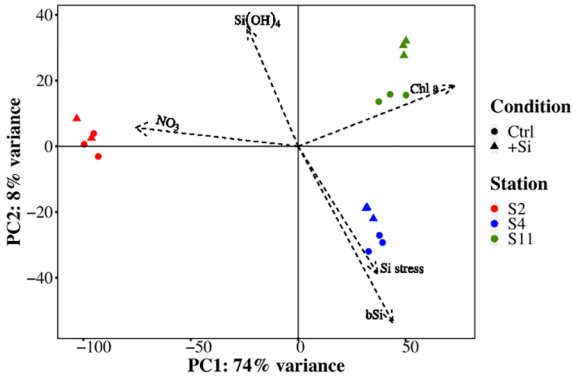

FIGURE 4
Principle component analysis biplot of gene transcript abundance (loading of principle components) and the relationship with treatment (shape), sampling site (color), and supplemental environmental variables.

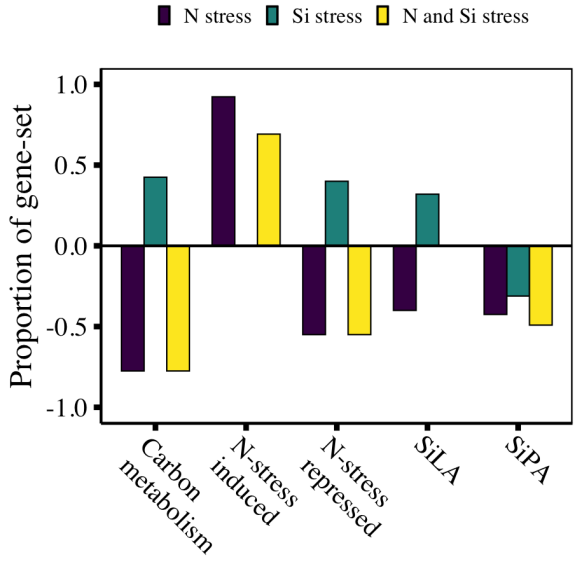

FIGURE 5
Gene set expression analysis showing the proportion of gene set for each metabolic pathway for *Pseudo-nitzschia* assemblages under N stress, Si stress, or N and Si stress. Summary statistics for GSA are provided in Supplementary Dataset 1.

disentangle the Si stress response from the shared response to N stress and identify changes in transcript abundance that explain the lower silica production rates in the communities experiencing co-occurring N and Si stress relative to those experiencing exclusively N stress. Furthermore, we aimed to identify transcriptomic changes that could be attributed to kinetic Si limitation and/or triggered by the interplay between Si and N stress. Given the dominance of *Pseudo-nitzschia* transcripts, the subsequent sections focus on this genus, but when available, leverage data from *Thalassiosira* and *Leptocylindrus* to highlight conserved responses.

Carbon metabolism

The GSA of carbon assimilation-related genes in *Pseudo-nitzschia*, which include genes related to the light harvesting complex (LHC), photosynthetic electron transport (pet), photosystem I (psa), photosystem II (psb), and glycolysis, revealed a significant proportion of the gene set had lower transcript abundance under N stress relative to replete conditions (n=40, 78% of gene set, FDR<0.001; Figure 5). Carbon assimilation gene sets in *Thalassiosira* and *Leptocylindrus* also decreased (*Thalassiosira*: n=56, 80% of gene set, FDR<0.001; *Leptocylindrus*: n=29, 55% of gene set, FDR<0.001; Supplementary Dataset 1). Compared to replete conditions, similar reductions were observed when both N and Si stress were present (n=40, 78% of gene set, FDR<0.001, Figure 5), but interestingly, when comparing N- and Si-stressed communities to N-stressed communities, Si stress appeared to up-regulate carbon assimilation relative to N stress (n=40, 43% of gene set, FDR<0.01, Figure 5). This was also apparent on an individual gene level where transcripts for some genes were less abundant under N stress, but more abundant under Si stress (FDR<0.05; Figure 6A). This included genes involved in the pentose phosphate pathway – PGK and PRK; glycolysis – TPI; the citric acid cycle – PEPC; and photosystem II – psb27, psb28, psbO, and psbU.

Nitrogen assimilation

The transcriptomic response to N availability consists of genes that are expected to increase in response to N limitation (N-stress induced) and those expected to decrease (N-stress repressed). Consistent with a culture study of *T. pseudonana* (Smith et al., 2019), N-stressed *Pseudo-nitzschia* was significantly enriched with N-stress induced genes (n=13, 92% of gene set, FDR<0.001, Figure 5). Of the N-stress repressed genes, 55% of the gene set was less abundant in N-stress compared to replete conditions (n=20, FDR<0.001, Figure 5). On an individual gene level, there was a small subset of genes typically repressed under N-limited conditions that were significantly (FDR<0.05) more abundant in our analysis – ferredoxin-independent nitrite reductase (nirB, 6.6-fold), nitrate reductase (NR, 3.9-fold) and acetylglutamate kinase (AGK, 4.5-fold; Figure 6B).

When N and Si stress co-occurred, GSA of N-stress induced and N-stress repressed gene sets recapitulated the pattern observed under N stress alone (Figure 5). However, similar to C assimilation, Si stress appeared to reverse the pattern of expression of N-stress repressed genes, enriching them on both a gene set (n=20, 40% of gene set, FDR<0.01, Figure 5) and individual gene level (Figure 6B). For example, transcripts for glutamine synthetase (GSII) and glutamate N-acetyltransferase (GACT), were more abundant under Si stress, and less abundant under N stress (Figure 6B). Si stress also appeared to reduce the transcript abundance of two urea cycle-related genes, proline dehydrogenase (PRODH, 1.8-fold) and urea transporters 1 and 2 (UT1_2, 3.0-fold; Figure 6C), neither of which were altered under N stress alone.

10.3389/fmars.2023.1291294

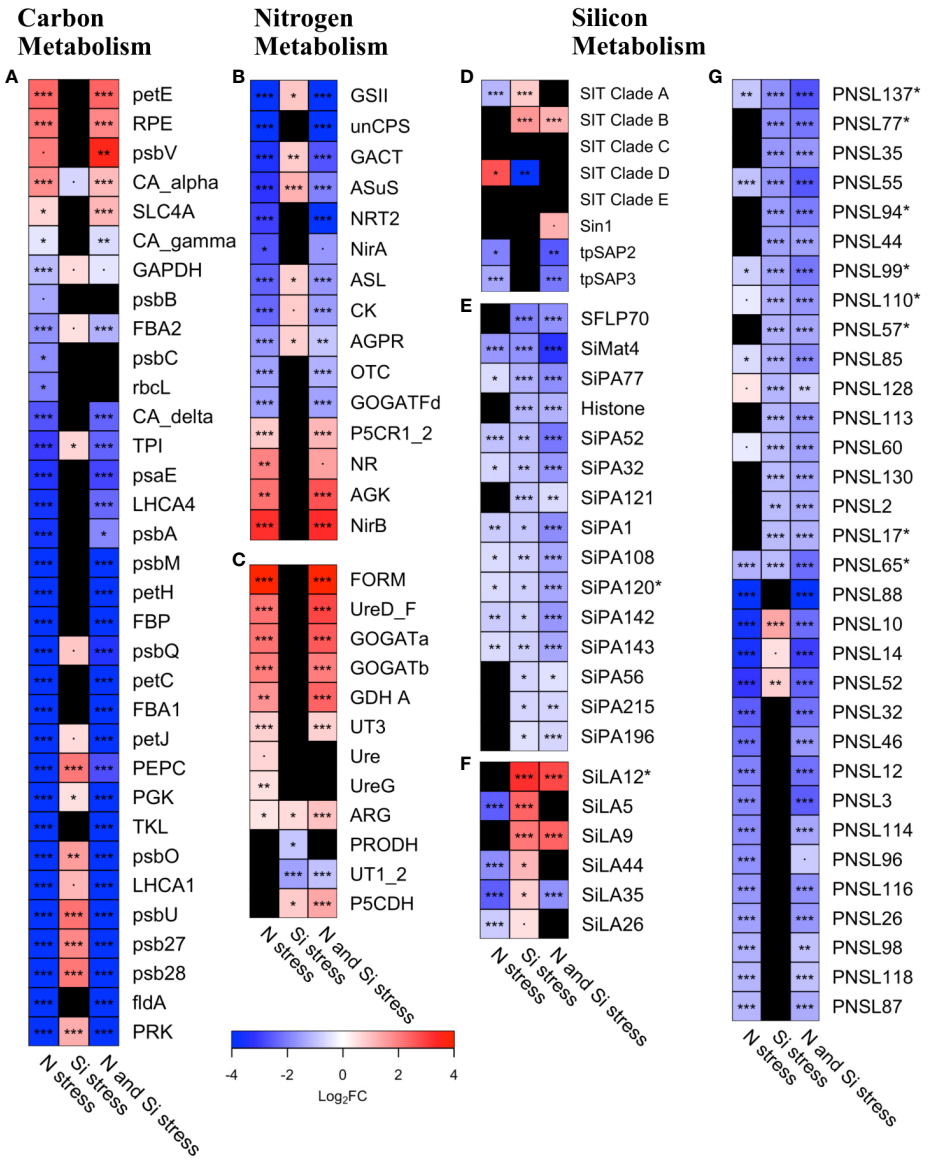

FIGURE 6
Heatmap of transcript abundance (log_2 fold-change) for *Pseudo-nitzschia* under Si, N, or N and Si stress for **(A)** carbon metabolism genes **(B)** genes expected to be repressed under N-stress (N-stress repressed), **(C)** genes expected to be induced under N-stress (N-stress induced), **(D)** silicon transporters, Sin-1, and tpSAPs, **(E)** silica-production associated (SiPA) genes, **(F)** Si-stress associated genes (SiLA), and **(G)** *Pseudo-nitzschia* silaffin like (PNSL) genes. Black boxes indicate genes that were not differentially abundant. Asterisks denote the false discovery rate (FDR):·< 0.1, *< 0.05, **< 0.01, ***< 0.001. Abbreviations are as follows A) Phosphoribulokinase (PRK), Flavodoxin (fldA), photosystem II 13kDa protein (psb28), photosystem II protein (psb27), photosystem II PsbU protein (psbU), light-harvesting complex I chlorophyll a/b binding protein 1 (LHCA1), photosystem II oxygen-evolving enhancer protein 1 (psbO), Transketolase (TKL), Phosphoglycerate kinase (PGK), Phosphoenolpyruvate carboxylase (PEPC), cytochrome c6 (petJ), photosystem II oxygen-evolving enhancer protein 3 (psbQ), Fructose bisphosphatase (FBP), ferredoxin–NADP+ reductase [EC:1.18.1.2] (petH), photosystem II PsbM protein (psbM), photosystem II P680 reaction center D1 protein [EC:1.10.3.9] (psbA), light-harvesting complex I chlorophyll a/b binding protein 4 (LHCA4), photosystem I subunit IV (psaE), Triose phosphate isomerase (TPI), Carbonic anhydrase_delta (CA_delta), Ribulose-1,5-Bisphosphate carboxylate, large subunit (rbcL), photosystem II CP43 chlorophyll apoprotein (psbC), FBA class 2 (Fructose-1, 6-bisphosphate aldolase, FBA2), photosystem II CP47 chlorophyll apoprotein (psbB), Glyceraldehyde-3-phosphate dehydrogenase (GAPDH), carbonic anhydrase_gamma (CA_gamma), solute carrier family 4 (anion exchange, SLC4A), carbonic anhydrase_alpha (CA_alpha), photosystem II cytochrome c550 (psbV), Ribulose-5-P (Ru-5-P) epimerase (RPE), plastocyanin (petE), Formamidase (FORM), Urea active transporter, mitochondrial (UT3), proline dehydrogenase (PRODH), Urease (Ure), mitochondria (GDH A), Urea transporter, extracellular (UT1_2), arginase (ARG), 1-pyrroline-5-carboxylate dehydrogenase (P5CDH), UreaseG (UreG), UreaseD_F (UreD_F), Cyanate lyase (CL), mitochondria (GOGATb), mitochondria (GOGATb); C) ornithine carbamoyl transferase, mitochondrial (OTC), Argininosuccinate synthase (ASuS), N-acetyl-gamma-glutamyl-phosphate reductase (AGPR), Glutamine synthetase, chloroplast (GSII), Carbamoyl phosphate synthase (ammonia, unCPS), pyrroline-5-carboxylate reductase (P5CR1_2), Glutamate synthase (ferredoxin), chloroplast (GOGATFd), Nitrate transporter (NRT2), Nitrate reductase (NADH) (NR), Carbamate kinase (CK), acetylglutamate kinase (AGK), Ferredoxin-Nitrite Reductase (NirA), glutamate N-acetyltransferase (GACT), Nitrite reductase (NADPH), chloroplast (NirB), Si matrix protein 4 (SiMat4), silicon transporter (SIT). Asterisks next to gene names denote those that are specific to diatoms. Summary statistics are provided in Supplementary Dataset 2.

Silicon metabolism-related genes

The impact of N and Si stress on Si metabolism was explored by examining changes in transcript abundance of individual genes with well-described roles in silicification. Transcripts of clades A and D SITs were both significantly differentially abundant under N stress with clade A SITs being 2.4-fold less abundant and clade D SITS being 5.3-fold more abundant compared to the replete condition (FDR<0.05; Figure 6D). In contrast, while Si stress led to a 1.7-fold increase in transcript abundance of clade A SITs and an 8-fold decrease in clade D SIT transcript abundance (FDR<0.05). These opposing impacts of N and Si stress on SIT transcript abundance manifested as no significant change in clades A and D transcript abundance under co-occurring N and Si stress (Figure 6D). In contrast, transcript abundance for clade B SITs were 3.2-fold elevated (FDR<0.001; Figure 6D).

There was no significant impact of any of the stress regimes on the transcript abundance of cingulins or silicidins, proteins in the silaffin-like family that play a role in silica polymerization. Transcripts for two silicalemma-associated proteins – tpSAP2 and tpSAP3 – were significantly less abundant under N stress (4.0- and 2.8-fold, respectively, FDR<0.05), as well as under combined N and Si stress (5.3- and 4.3-fold, respectively, FDR<0.05, Figure 6D). This appeared to be driven primarily by N stress as the abundance was not significantly different under Si stress (Figure 6D). Transcripts for Silicanin-1 (Sin-1) were 2.5-fold more abundant only under combined N and Si stress (FDR=0.05, Figure 6D). Although, silaffins directly facilitate the polymerization of silica in diatoms (Kröger et al., 2002), the gene sequences are not well-conserved, precluding the identification of them in metatranscriptomes through homology-based searches. Therefore, the *Pseudo-nitzschia* genome was screened using established guidelines (see Methods) to identify putative *Pseudo-nitzschia* silaffin like genes (PNSLs). Of the 157 candidates identified in the genome, 142 were detected across all of the metatranscriptomes (Supplementary Dataset 2). When bSi production was low, as was the case in samples with co-occurring N and Si stress (Supplementary Table S1), 45 of the 68 significantly differentially abundant PNSLs were lower when compared to replete conditions (1.5- to 8-fold, FDR<0.05, Figure 6G, Supplementary Dataset 2), consistent with their predicted role in silica production. Similarly, under Si stress, the majority of the >1.5-fold differentially expressed PNSLs were less abundant (21 out of 24, Figure 6G, Supplementary Dataset 2). There was a more even distribution of differentially abundant PNSLs (29 more abundant, 24 less abundant) when N-stressed samples were compared to replete samples, possibly related to the bSi production rates being similar in these conditions, or that some of the PNSL candidates identified *in silico* may not be true silaffins. In a more rigorous analysis, the 8 putative PNSL genes that are found only in diatoms were specifically assessed (Figure 6G). Intriguingly, all eight (PNSL17, PNSL57, PNSL65, PNSL77, PNSL94, PNSL99, PNSL110, PNSL137) were less abundant in the combined N- and Si-stressed samples when bSi production was low. Only two of these (PNSL65 and PNSL137) were also less abundant in N-stressed samples compare to replete, while the remaining six were unaffected by N-stress alone, highlighting that these six are strong candidates for a role in silica production.

To identify other potential silicification-related genes *a priori*, we leveraged multiple transcriptomic culture-based studies that investigated the response of diatoms to Si starvation and subsequent Si replenishment (Shrestha et al., 2012; Smith et al., 2016; Brembu et al., 2017a). Comparing these distinct datasets, a subset of 230 Si starvation and 48 Si replenishment genes were identified and termed Si-limitation associated (SiLA) and silica production associated (SiPA) genes, respectively (Supplementary Dataset 2). Although the majority of these genes are annotated as hypothetical proteins with no known function, their conserved expression profile across different studies suggests they play a role in some aspect of silicon metabolism. Of the 278 total genes identified, 25 SiLA and 106 SiPA genes were detected in *Pseudo-nitzschia*. GSA revealed that 40% and 42% of the SiLA and SiPA gene sets, respectively, were less abundant under N stress compared to replete conditions (FDR≤0.001; Figure 5). When N- and Si-stress co-occurred, 49% of the SiPA gene set was less abundant (n=106, FDR<0.001) than replete conditions, but there was no significant difference in transcript abundance of the SiLA gene set. Interestingly, when N- and Si-stressed samples were compared to N-stressed samples, the additional Si stress had minimal impact on SiLA and SiPA abundance. Only 32% of SiLA gene sets were more abundant (n=25, FDR<0.01) and 31% of SiPA gene sets were less abundant (n=106, FDR<0.01) in Si-stressed *Pseudo-nitzschia*.

On an individual gene level, there were 5 SiLA genes (SiLA5, SiLA9, SiLA12, SiLA35, SiLA44) that were significantly more abundant when Si stress was present (1.6-6.5 fold, FDR<0.05, Figure 6F). Two of these, SiLA9 and SiLA12, were among the most highly differentially abundant genes within the SiLA gene set and were also significantly more abundant when N and Si stress co-occurred (4.8- and 5.6-fold, respectively). Both were also unaffected by N stress alone, highlighting a potential role of these two genes in a response to Si stress. Both encode for hypothetical proteins, with SiLA12 being found only in diatoms.

Within the SiPA gene set, of the 15 genes that significantly differentially abundant in Si-stressed samples (1.5-4.3-fold), the majority of them (11) were less abundant compared to samples that were not Si stressed (Figure 6E). This is consistent with a role for SiPAs in bSi production as the rate of bSi production was low in the Si-stressed samples (Supplementary Table S1). Similarly, 68% of the differentially abundant SiPA genes (25 out of 37, 1.7-7.5-fold) were lower when N and Si stress co-occurred, where bSi production was also low, compared to replete. There were 28 SiPA genes with significantly different transcript abundances during N stress compared to replete, with 11 being more abundant (2.2-8.3-fold) and 17 being less abundant (1.5-5-fold; Figure 6E). Given that bSi production was high under both replete and N-stressed conditions (Supplementary Table S1), these particular SiPAs may be more representative of a response to N stress than an association with bSi production.

Discussion

Persistence and physiological status of Monterey Bay diatom blooms

Satellite imagery and biogeochemical stock measurements revealed a persistent phytoplankton bloom in and near Monterey

Bay during the study period dominated by the diatom *Pseudo-nitzschia*. Blooms of *Pseudo-nitzschia* were observed in the three years preceding this study (McCabe et al., 2016), making the Monterey Bay area a "hot spot" for this toxigenic diatom (Trainer et al., 2000; Trainer et al., 2012). The addition of Si in bottle incubations led to an increase in the specific rate of $Si(OH)_4$ uptake at 2 of the 3 stations (S4 and S11), despite low concentrations of NO_3^-. This may have been supported by regenerated sources of N, but may also be due to the plasticity of diatoms to repartition intracellular N and reduce cellular Si quotas when nutrients are growth limiting. It is reasonable to presume that co-addition of $Si(OH)_4$ and NO_3^- would have stimulated diatom bSi production even more. Regardless, increased Si uptake upon $Si(OH)_4$ addition demonstrates that the diatom communities at these stations were substrate-limited. Ambient Si uptake rates that were a low fraction of saturated rates ($V_{amb} : V_{max} < 0.3$) suggest the Si stress was severe and near the threshold (~0.25) used to infer when diatoms likely progress beyond kinetic Si limitation and into growth limitation (Martin-Jézéquel et al., 2000). The dramatically reduced bSi production rate in these samples is also consistent with Si-limited growth (Paasche, 1973; Brzezinski et al., 1990). However, sub-micromolar concentrations of NO_3^- suggests there was likely simultaneous N stress, even if the diatoms were utilizing Si:N in a ratio lower than the typical 1.1:1 when conditions are optimal (Brzezinski, 1985). Although not directly measured, organic nitrogen also appeared to be limiting given the increased abundance of transcripts for genes associated with the urea cycle. In contrast, station S2 had moderately high concentrations of both $Si(OH)_4$ and NO_3^- and an Si stress value of 0.95, indicating the diatom communities were unlikely to be stressed by Si or N. Taken together, we categorized our bottle treatments as nutrient replete (Ctrl and +Si at S2), N stressed (+Si at S4 and S11), or both N and Si stressed (Ctrl at S4 and S11) allowing us to evaluate the molecular response of *Pseudo-nitzschia* to each scenario.

The diatom community transcriptomic profile is driven more by N stress than Si stress

There was a far greater number of transcripts altered by N stress than Si stress in *Pseudo-nitzschia*. Transcriptomic profiles exhibited a large degree of separation along PC1 that explained ~75% of the variance and correlated with NO_3^- concentration (Figure 4). In contrast, there was only a modest separation between Si-replete and Si-stressed samples even at the two stations (S4 and S11) where $Si(OH)_4$ amendment showed a significant response by the diatom community. This was somewhat unexpected given culture studies have shown a clear transcriptomic response of diatoms to $Si(OH)_4$ availability (Shrestha et al., 2012; Smith et al., 2016; Brembu et al., 2017a). One explanation may be that because Si stress co-occurred with N stress, any additional impact on gene expression already imposed by N stress was minor. Given that stress induced by either low N or Si can result in slowed growth and cell cycle arrest (Olson and Chisholm, 1986; Vaulot et al., 1987; Brzezinski et al., 1990; Du et al., 2014), there may be a general macronutrient stress response that minimizes any additive response when both nutrients are limiting. Alternatively, as silicon is primarily required for cell wall synthesis, there may be only a small fraction of genes that are specific to silicon metabolism.

Si stress dampens the molecular response to N stress

A gene set analysis approach to elucidate changes in key metabolic pathways (Figure 7) was used to attribute changes in cellular physiology to specific nutrient stress responses. As changing nutrient concentrations can have a complex and cascading impact on genome-wide transcription and physiology (Smith et al., 2019), interpretation of metatranscriptomic data is still dependent on, and in some cases lacking, a strong foundation of how transcript abundance should be *expected* to change under individual and multi-stressor environmental conditions (e.g. macronutrients, vitamins, trace metals, temperature, diurnal rhythm). Even individual genes that are strong transcriptomic markers of a seemingly single process may be unreliable in a mixed community exposed to a multitude of varying environmental conditions. For example the diatom iron-starvation-induced-protein 2A and ferritin, both of which have been used as indicators of Fe limitation, are also strongly modulated by N availability, likely because both of these limitation scenarios impact photosynthetic processes (Bender et al., 2014; Marchetti et al., 2017). Another example where cross-talk between metabolic pathways can complicate interpretation is in the case of phosphorus limitation where the expression pattern of two "highly nitrate sensitive" genes – nitrate reductase and glutamine synthetase (Smith et al., 2019) – is also regulated by phosphorus availability (Helliwell et al., 2021). With an increase in available reference genomes and transcriptomes, extensive mapping of metabolic pathways (Armbrust et al., 2004; Bowler et al., 2008; Keeling et al., 2014; Tully et al., 2018), and the increasing availability of culture-based, genome-wide expression data under numerous conditions (Thamatrakoln et al., 2012; Nymark et al., 2013; Alipanah et al., 2015; Brembu et al., 2017b; a; Smith et al., 2019; Moreno et al., 2020), analysis of larger gene sets of metabolic processes provides a more robust and reliable method to infer cellular physiology (Rahmatallah et al., 2014).

The transcriptomic changes driven by N stress resulted in substantial decreases in the expression of genes involved in carbon metabolism and those expected to decrease in response to N stress (e.g. N-stress repressed), consistent with changes observed in culture studies (Bender et al., 2014; Smith et al., 2019). Similar decreases were observed when both N- and Si- stress co-occurred. However, in Si-stressed *Pseudo-nitzschia*, 43% and 40% of the carbon assimilation and N-stress repressed gene sets increased, respectively, reversing the decreases observed in samples were N-alone or N- and Si-stressed. This reversal of expression was even more apparent on an individual gene level. For example, where genes associated with photosystem II (e.g psbU, psb27, and psb28) were ~15-fold less abundant under N stress, the same genes were only 10-11-fold less abundant under N- and Si-stress, offset by the

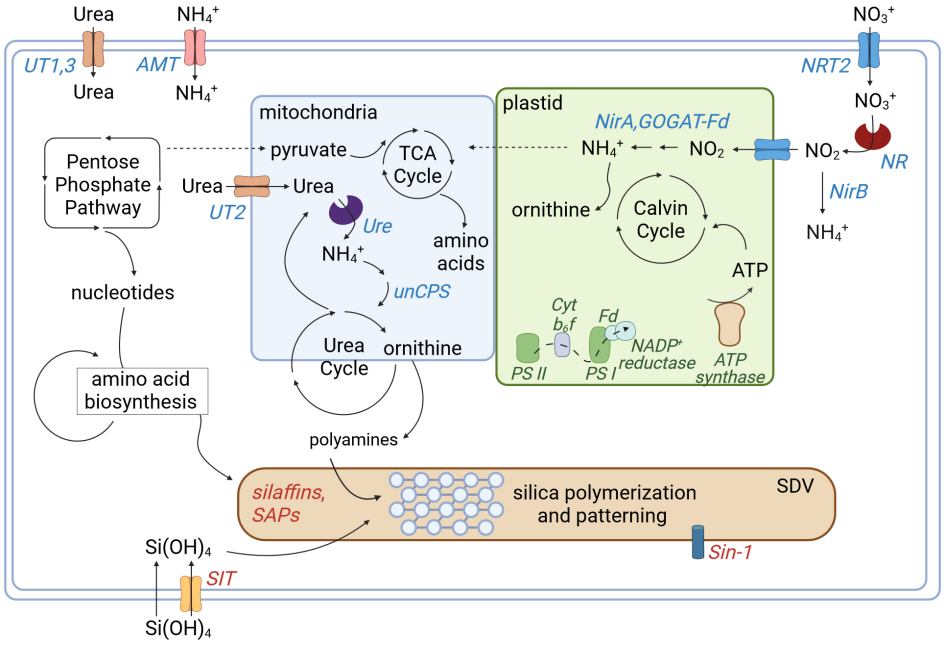

FIGURE 7
Simplified schematic depicting cellular nitrogen, carbon, and silicon metabolism. Genes associated with proteins involved in nitrogen metabolism are shown in blue, carbon in green and silicon in red with arrows depicting the general movement of molecules. The SDV denotes the silica deposition vesicle where silica polymerization and patterning of the frustule occurs. Abbreviations are listed in Figure 6. Created with BioRender.com.

~4-fold increase in abundance observed when Si stress was present. Furthermore, there was a decrease in the abundance of genes associated with the urea cycle (UT1_2, PRODH) under Si stress. Given that polyamines, produced by the urea cycle, are required for silica precipitation and pattern formation (Kröger et al., 2000), decreased expression of these genes may reflect a reduction in the cellular N demand. Taken together, we posit that growth-limiting concentrations of Si insulate *Pseudo-nitzschia* from further impact imposed by low concentrations of N, rather than low Si and N acting synergistically and intensifying cellular physiological stress. Such a response is consistent with Liebig's Law of the Minimum that states growth is ultimately controlled by a single macronutrient (Liebig, 1840; Rhee, 1978).

Si limitation as an ecological advantage

De La Rocha and Passow (2004) proposed that Si limitation of diatoms confers an ecological advantage by slowing growth through limitation of cell wall synthesis such that diatoms are able to maintain key cellular constituents (e.g. proteins and chlorophyll) that allow them to more rapidly respond to episodic nutrient injection events, such as those that occur during upwelling. If the cell division rate of diatoms is set by the speed at which the silicified cell wall can be produced, carbon and nitrogen metabolism may become insulated from the nutrient regulating growth (i.e. Si) and can adjust independently beyond the adjustments necessary to accommodate slower growth imposed by Si limitation. While physiological adjustments in response to low levels of non-growth-limiting macronutrients are possible, such responses may be independent of the response to Si, which is largely confined to cell wall formation. This would explain how Si-starved diatoms maintain near Redfield C:N ratios and the capacity to rapidly recover upon Si replenishment (De La Rocha and Passow, 2004). Although we did not sample diatom assemblages that were solely Si limited, our data illustrates relatively minimal impact of additional Si stress on N-stressed diatom assemblages. Although we cannot discern how much of the N-stress response would have occurred under Si stress alone, it is clear that the addition of Si stress dampened the cellular impact of N stress, corroborating previous work that demonstrated the efficiency of Si-limited diatoms to recover upon Si replenishment (Flynn and Martin-Jézéquel, 2000; De La Rocha and Passow, 2004).

Potential transcriptomic markers of bSi production or Si stress

Despite the numerous studies exploring the molecular regulation of silicon metabolism in diatoms (Mock et al., 2008; Shrestha et al., 2012; Smith et al., 2016; Brembu et al., 2017a), we still lack a comprehensive molecular framework for silicification. Therefore, using a holistic, *a priori* approach, we leveraged culture-based transcriptomic studies to identify a putative subset of SiLA and SiPA genes. GSA revealed that neither of these gene sets had a particularly strong transcriptomic response to Si stress with only ~30% of the gene sets being differentially expressed compared to non Si-stress conditions. In addition, transcript abundance of

several SiPA genes appeared more affected by N depletion rather than exclusive Si stress. This does not exclude the possibility that these genes are directly involved in silicification, but rather the lack of response to Si may be due to feedbacks between slower growth under N stress that demand a reduction in the rate of cell wall formation (Harrison et al., 1977).

Given that a large proportion of both SiLA and SiPA gene sets are hypothetical or proteins with unknown function, many of them may not be specifically involved in silicon metabolism, but rather play a general role in growth, cell cycle progression, or the cytoskeleton. It might also be because the gene sets were derived from *T. pseudonana* and, given the striking lack of shared genes among relatively closely related diatom species (Bowler, 2008), may simply not have homologs in *Pseudo-nitzschia*, which was the focus of our analysis here. However, the low proportion of differentially abundant transcripts of genes involved with carbon metabolism and nitrogen assimilation supports the notion that additional Si stress had a relatively minor effect on the already N-stressed community. It is also possible that although *Pseudo-nitzschia* was numerically dominant, it may not have been responsible for the equivalent proportion of the community silica production or may not have experienced the bulk of the measured Si stress. Indeed, taxon-specific differences in silica production have been observed in mixed communities and relatively minor constituents of the community can be the major contributors (McNair et al., 2018a; McNair et al., 2018b).

Although powerful in contextualizing the physiological state of cells to changing environmental conditions, gene set analysis is most powerful when applied to well-characterized and well-defined metabolic pathways, which is not the case for silicon metabolism. Until there is a more comprehensive understanding of the molecular framework for silicification, our ability to harness the growing number of marine metagenomic and metatranscriptomic sequence data from individual researchers, as well as large collaborative projects such as EXPORTS (Siegel et al., 2016), BIOS-SCOPE, BioGEOTRACES (Biller et al., 2018), Global Ocean Sampling (Rusch et al., 2007), Tara Oceans (Bork et al., 2015), and Bio-GO-SHIP (Larkin et al., 2021) for understanding diatom community responses to Si availability is limited. With an interest in linking cellular metabolism with ocean processes, we aimed to test the relationship of putative silicification-related gene expression with biogeochemical stocks and rate measurements.

Through an *in silico* screen of the *P. multiseries* genome, 8 diatom-specific PNSL genes were identified in our metatranscriptomes. Intriguingly all 8 were less abundant in samples where the rate of bSi production was low, consistent with the role of silaffins in silica production (Kröger et al., 1999). While these may be candidate gene markers for silica production, poor sequence conservation among silaffin genes across species may preclude their use beyond communities dominated by *Pseudo-nitzschia* (Poulsen and Kröger, 2004). In contrast, high sequence conservation among genes encoding for *SITs* make SIT expression an attractive potential marker of silicon uptake or low $Si(OH)_4$ concentrations given that *SITs* are primarily responsible for $Si(OH)_4$ uptake at <20 μmol L^{-1} $Si(OH)_4$ concentrations (Thamatrakoln and Hildebrand, 2007; Shrestha and Hildebrand, 2015). Si-stressed communities had significantly higher abundance of clade B SITs in *Pseudo-nitzschia* compared to non-Si stressed communities, consistent with findings in laboratory cultures (Durkin et al., 2012). However, N stress alone also altered SIT transcript abundance, decreasing clade A SIT abundance and increasing clade D SIT abundance. When Si stress co-occurred with N stress, transcript abundance of clade A and D SITs was unaffected. Taken together with previous findings that all clades of SIT genes increased in response to Fe limitation (Maniscalco et al., 2022), these data suggest SIT transcript abundance should not be used as a field marker for Si uptake or production, nor should it be used as a molecular proxy for Si limitation, as previously done (Zielinski et al., 2016), given the variable response of different clades to different nutrient stressors. It is possible that *SIT* protein expression might be a more reliable proxy for Si status in natural communities, given the disconnect between SIT transcript and protein abundance (Thamatrakoln and Hildebrand, 2007), but this would require further investigation. While other genes with documented roles in silicon metabolism were detected in our metatranscriptome data (e.g. cingulin, Sin-1, tpSAP2, and tpSAP3), none of them were differentially impacted by Si stress or had expression patterns consistent with a role in bSi production. Furthermore, we did not find any differentially expressed genes that were shared across the three transcriptionally dominant diatoms (*Pseudo-nitzschia, Thalasssioria*, and *Leptocylindrus*). This might be due to there not being enough reads associated with *Thalassiosira* and *Leptocylindrus* to resolve their response, but could also underscore taxon-specific differences that has been observed from both a silica production perspective (McNair et al., 2018a; b) and a transcriptomic perspective (Durkin et al., 2012). While genes that are diatom-specific have potential to be used collectively to characterize Si stress in diatom communities, a more comprehensive understanding beyond SITs and silaffin-like proteins of the molecular regulation of silicification is needed.

Interestingly, a few putative SiLA and SiPA genes emerged as potentially useful markers of silicon metabolism. SiLA9 and SiLA12 both encode hypothetical proteins in *T. pseudonana* (Thaps_25507 and Thapss_3250, respectively) with SiLA12 being found exclusively in diatoms. Both of these genes were more abundant when $Si(OH)_4$ concentrations were kinetically limiting and neither were differentially abundant under N stress alone, making them potentially specific to kinetic Si limitation. Six SiPA genes (SiPA16, SiPA32, SiPA41, SiPA52, SiPA77, SiPA167) were less abundant when bSi production was low making them potential candidates as molecular markers silica production. However, SiPA52, a PT-repeat protein (Thaps_12192) and SiPA41, a silica matrix protein, SiMat4 (Thaps_25912; Kotzsch et al., 2016) were also less abundant in N-stressed assemblages. Given that producing the siliceous diatom frustule is intimately linked to cell growth and division, these particular genes might be related to a generalized response to macronutrient-limited growth. Likewise, SiPA32 (Thaps_8522), a ribonucleoside-diphosphate reductase and, SiPA167, histone H1, may be more related to DNA synthesis and nucleosome stability, respectively. SiPA41 (Thaps_4922), a subtilisin-like serine protease, is also unlikely to be specific to silica production. SiPA16 (Thaps_24597), however, encodes a protein belonging to the

silaffin-like family (SFLP70; Scheffel et al., 2011), making it a strong potential marker of bSi production.

Conclusions

Through manipulative incubation experiments of a natural diatom bloom near Monterey Bay, CA, this study investigated the diatom response to N stress and co-occurring N and Si stress. Biogeochemical measurements of silica production and bulk macronutrient concentrations was used to diagnose Si and N stress along with analysis of the diatom community response using metatranscriptomics. Compared to N stress alone, combined N- and Si- stress did not lead to a substantial additive response on a transcriptomic level, implying a shared molecular response to these two stressors. Furthermore, the addition of Si stress to N-stressed communities appeared to reverse the transcriptional expression pattern of key genes involved in carbon metabolism and nitrogen assimilation, indicating a decoupling of Si and organic matter metabolism under these conditions. These findings that Si stress can dampen the impact of N limitation adds to previous ideas that Si limitation may potentially be advantageous given observations that Si-stressed diatoms recover faster than those experiencing other forms of macronutrient limitation (Flynn and Martin-Jézéquel, 2000; De La Rocha and Passow, 2004; Raven and Waite, 2004). Our results point to an additional advantage of Si stress in lessening the overall impact of other nutrient stressors in episodic environments where multiple nutrients can be simultaneously depleted. This added benefit broadens the adaptive advantages of Si stress and helps explain the prevalence of Si limitation across the global ocean including in coastal systems (Nelson and Dortch, 1996; Brzezinski and Phillips, 1997; Krause et al., 2015), high latitudes (Nelson et al., 2001; Krause et al., 2018), and deep water upwelling regions (Brzezinski et al., 2008). To the extent that the degree of Si stress in these systems limits growth diatoms that become Si limited prior to the onset of N stress will be better poised to rapidly capitalize on nutrient pulses.

We found that genes with well-characterized roles in silicon metabolism – SITs, cingulins, SAPs, and Sin-1 – do not appear to have a specific or consistent correlation with silica production or silicon stress, making them unreliable molecular markers of these processes. While *Pseudo-nitzschia* silaffin-like genes did appear to correlate with high silica production, lack of sequence similarity across species and taxon-specific differences in silica production may limit their utility in mixed diatom communities. Two potential markers of kinetic Si limitation and one for silica production were identified, making them ideal candidates for further study of their role in silicon metabolism.

Data availability statement

The datasets presented in this study can be found in online repositories. The names of the repository/repositories and accession number(s) can be found in the article/Supplementary Material.

Author contributions

MM: Formal Analysis, Investigation, Software, Validation, Visualization, Writing – original draft, Writing – review & editing, Data curation, Methodology, Project administration. MB: Funding acquisition, Resources, Supervision, Validation, Writing – review & editing, Conceptualization, Data curation, Investigation, Methodology, Project administration, Visualization. JK: Funding acquisition, Resources, Writing – review & editing, Investigation, Project administration, Visualization. KT: Conceptualization, Funding acquisition, Investigation, Methodology, Resources, Supervision, Validation, Writing – review & editing, Project administration, Visualization.

Funding

The author(s) declare financial support was received for the research, authorship, and/or publication of this article. We acknowledge funding from the National Science Foundation (OCE-1334387 to MB, OCE-1333929 and OCE-2049386 to KT, OCE-1155663 to JK). Computing resources were administered by the Center for Scientific Computing (CSC) with funds from the National Science Foundation (CNS-1725797). The CSC is supported by the California NanoSystems Institute and the Materials Research Science and Engineering Center (MRSEC; NSF DMR 1720256) at UC Santa Barbara.

Acknowledgments

We thank the captain and crew of R/V Point Sur. We also like to thank Janice Jones, Eric Lachenmyer, Heather McNair, Israel Marquez for assistance during the cruise.

Conflict of interest

The authors declare that the research was conducted in the absence of any commercial or financial relationships that could be construed as a potential conflict of interest.

Publisher's note

Supplementary material

The Supplementary Material for this article can be found online at: https://www.frontiersin.org/articles/10.3389/fmars.2023.1291294/full#supplementary-material

References

Alexander, H., Rouco, M., Haley, S. T., Wilson, S. T., Karl, D. M., and Dyhrman, S. T. (2015). Functional group-specific traits drive phytoplankton dynamics in the oligotrophic ocean. *Proc. Natl. Acad. Sci. U.S.A.* 112, E5972–E5979. doi: 10.1073/pnas.1518165112

Alipanah, L., Rohloff, J., Winge, P., Bones, A. M., and Brembu, T. (2015). Whole-cell response to nitrogen deprivation in the diatom *Phaeodactylum tricornutum*. *J. Exp. Bot.* 66, 6281–6296. doi: 10.1093/jxb/erv340

Allen, A. E., Dupont, C. L., Oborník, M., Horák, A., Nunes-Nesi, A., McCrow, J. P., et al. (2011). Evolution and metabolic significance of the urea cycle in photosynthetic diatoms. *Nature* 473, 203–207. doi: 10.1038/nature10074

Armbrust, V. E., Berges, J. A., Bowler, C., Green, B. R., Martinez, D., Putnam, N. H., et al. (2004). The genome of the diatom *Thalassiosira Pseudonana*: Ecology, evolution, and metabolism. *Science (1979)* 306, 79–86. doi: 10.1126/science.1101156

Bender, S. J., Durkin, C. A., Berthiaume, C. T., Morales, R. L., and Armbrust, V. E. (2014). Transcriptional responses of three model diatoms to nitrate limitation of growth. *Front. Mar. Sci.* 1. doi: 10.3389/fmars.2014.00003

Benjamini, Y., and Hochberg, Y. (1995). Controlling the false discovery rate: a practical and powerful approach to multiple testing. *J R Stat Soc Series B Stat Methodol* 57, 289–300. doi: 10.1111/j.2517-6161.1995.tb02031.x

Biller, S. J., Berube, P. M., Dooley, K., Williams, M., Satinsky, B. M., Hackl, T., et al. (2018). Marine microbial metagenomes sampled across space and time. *Sci. Data* 5, 1 5: 1–1 5: 7. doi: 10.1038/sdata.2018.176

Bolger, A. M., Lohse, M., and Usadel, B. (2014). Trimmomatic: A flexible trimmer for Illumina sequence data. *Bioinformatics* 30, 2114–2120. doi: 10.1093/bioinformatics/btu170

Bork, P., Bowler, C., de Vargas, C., Gorsky, G., Karsenti, E., and Wincker, P. (2015). Tara Oceans studies plankton at Planetary scale. *Science (1979)* 348, 873. doi: 10.1126/science.aac5605

Bowler, C. (2008). Genomics and evolution of microbial eukaryotes. *J. Phycol.* 44, 1625–1627. doi: 10.1111/j.1529-8817.2008.00613.x

Bowler, C., Allen, A. E., Badger, J. H., Grimwood, J., Jabbari, K., Kuo, A., et al. (2008). The *Phaeodactylum* genome reveals the evolutionary history of diatom genomes. *Nature* 456, 239–244. doi: 10.1038/nature07410

Brembu, T., Chauton, M. S., Winge, P., Bones, A. M., and Vadstein, O. (2017a). Dynamic responses to silicon in *Thalasiossira pseudonana* - Identification, characterisation and classification of signature genes and their corresponding protein motifs. *Sci. Rep.* 7, 4865. doi: 10.1038/s41598-017-04921-0

Brembu, T., Mühlroth, A., Alipanah, L., and Bones, A. M. (2017b). The effects of phosphorus limitation on carbon metabolism in diatoms. *Philos. Trans. R. Soc. B.: Biol. Sci.* 372, 20160406. doi: 10.1098/rstb.2016.0406

Brzezinski, M. A. (1985). The Si:C:N ratio of marine diatoms: interspecific variability and the effect of some environmental variables. *J. Phycol.* 21, 347–357. doi: 10.1111/j.0022-3646.1985.00347.x

Brzezinski, M. A., Dumousseaud, C., Krause, J. W., Measures, C. I., and Nelson, D. M. (2008). Iron and silicic acid concentrations together regulate Si uptake in the equatorial Pacific Ocean. *Limnol. Oceanogr.* 53, 875–889. doi: 10.4319/lo.2008.53.3.0875

Brzezinski, M. A., Jones, J. L., Bidle, K. D., and Azam, F. (2003). The balance between silica production and silica dissolution in the sea: Insights from Monterey Bay, California, applied to the global data set. *Limnol. Oceanography* 5 (48), 1846–1854. doi: 10.4319/lo.2003.48.5.1846

Brzezinski, M. A., and Nelson, D. M. (1995). The annual silica cycle in the Sargasso Sea near Bermuda. *Deep-Sea Res. Part I* 42, 1215–1237. doi: 10.1016/0967-0637(95)93592-3

Brzezinski, M. A., Olson, R., and Chisholm, S. S. W. (1990). Silicon availability and cell-cycle progression in marine diatoms. *Mar. Ecol. Prog. Ser.* 67, 83–96. doi: 10.3354/meps067083

Brzezinski, M. A., and Phillips, D. R. (1997). Evaluation of 32Si as a tracer for measuring silica production rates in marine waters. *Limnol. Oceanogr.* 42, 856–865. doi: 10.4319/lo.1997.42.5.0856

Brzezinski, M. A., Phillips, D. R., Chavez, F. P., Friederich, G. E., and Dugdale, R. C. (1997). Silica production in the Monterey, California, upwelling system. *Limnol. Oceanogr.* 42, 1694–1705. doi: 10.4319/lo.1997.42.8.1694

Chen, X. H., Li, Y. Y., Zhang, H., Liu, J. L., Xie, Z. X., Lin, L., et al. (2018). Quantitative proteomics reveals common and specific responses of a marine diatom *Thalassiosira pseudonana* to different macronutrient deficiencies. *Front. Microbiol.* 9. doi: 10.3389/fmicb.2018.02761

Cohen, N. R., Ellis, K. A., Lampe, R. H., McNair, H. M., Twining, B. S., Maldonado, M. T., et al. (2017). Diatom transcriptional and physiological responses to changes in iron bioavailability across ocean provinces. *Front. Mar. Sci.* 4, 1–20. doi: 10.3389/fmars.2017.00360

Cohen, N. R., McIlvin, M. R., Moran, D. M., Held, N. A., Saunders, J. K., Hawco, N. J., et al. (2021). Dinoflagellates alter their carbon and nutrient metabolic strategies across environmental gradients in the central Pacific Ocean. *Nat. Microbiol.* 6, 173–186. doi: 10.1038/s41564-020-00814-7

De La Rocha, C. L., and Passow, U. (2004). Recovery of Thalassiosira weissflogii from nitrogen and silicon starvation. *Limnol. Oceanogr.* 49, 245–255. doi: 10.4319/lo.2004.49.1.0245

Du, C., Liang, J. R., Chen, D. D., Xu, B., Zhuo, W. H., Gao, Y. H., et al. (2014). ITRAQ-based proteomic analysis of the metabolism mechanism associated with silicon response in the marine diatom *Thalassiosira pseudonana*. *J. Proteome Res.* 13, 720–734. doi: 10.1021/pr400803w

Durkin, C. A., Koester, J. A., Bender, S. J., and Armbrust, V. E. (2016). The evolution of silicon transporters in diatoms. *J. Phycol.* 52, 716–731. doi: 10.1111/jpy.12441

Durkin, C. A., Marchetti, A., Bender, S. J., Truong, T., Morales, R. L., Mock, T., et al. (2012). Frustule-related gene transcription and the influence of diatom community composition on silica precipitation in an iron-limited environment. *Limnol. Oceanogr.* 57, 1619–1633. doi: 10.4319/lo.2012.57.6.1619

Falkowski, P. G., Sukenik, A., and Herzig, R. (1989). Nitrogen limitation in isochrysis galbana (Haptophyceae). Ii. Relative abundance of chloroplast proteins. *J. Phycol.* 25, 471–478. doi: 10.1111/j.1529-8817.1989.tb00252.x

Flynn, K. J., and Martin-Jézéquel, V. (2000). Modeling Si–N-limited growth of diatoms. *J. Plankton Res.* 22, 447–472. doi: 10.1093/plankt/22.3.447

Grant, C. E., Bailey, T. L., and Noble, W. S. (2011). FIMO: scanning for occurrences of a given motif. *Bioinformatics* 27, 1017–1018. doi: 10.1093/BIOINFORMATICS/BTR064

Harrison, P. J., Conway, H. L., Holmes, R., and Davis, C. (1977). Marine diatoms grown in chemostats under silicate or ammonium limitation. III. Chaetoceros debilis, Skeletonema costatum, and *Thalassiosira gravida**. *Mar. Biol.* 43, 19–31. doi: 10.1007/BF00392568

Helliwell, K. E., Harrison, E. L., Christie-Oleza, J. A., Rees, A. P., Kleiner, F. H., Gaikwad, T., et al. (2021). A novel ca2+ Signaling pathway coordinates environmental phosphorus sensing and nitrogen metabolism in marine diatoms. *Curr. Biol.* 31, 978–989.e4. doi: 10.1016/J.CUB.2020.11.073

Hildebrand, M., Dahlin, K., and Volcani, B. E. (1998). Characterization of a silicon transporter gene family in Cylindrotheca fusiformis: Sequences, expression analysis, and identification of homologs in other diatoms. *Mol. Gen. Genet.* 260, 480–486. doi: 10.1007/S004380050920/METRICS

Hildebrand, M., Volcani, B. E., Gassmann, W., and Schroeder, J. I. (1997). A gene family of silicon transporters. *Nature* 385, 6618 385: 688–689. doi: 10.1038/385688b0

Hockin, N. L., Mock, T., Mulholland, F., Kopriva, S., and Malin, G. (2012). The response of diatom central carbon metabolism to nitrogen starvation is different from that of green algae and higher plants. *Plant Physiol.* 158, 299–312. doi: 10.1104/pp.111.184333

Hu, S. K., Liu, Z., Alexander, H., Campbell, V., Connell, P. E., Dyhrman, S. T., et al. (2018). Shifting metabolic priorities among key protistan taxa within and below the euphotic zone. *Environ. Microbiol.* 20, 2865–2879. doi: 10.1111/1462-2920.14259

Kaplan, D. M., and Largier, J. L. (2006). HF radar-derived origin and destination of surface waters off Bodega Bay, California. *Deep-Sea Res. Part II* 25–26, 2906–2930. doi: 10.1016/J.DSR2.2006.07.012

Keeling, P. J., Burki, F., Wilcox, H. M., Allam, B., Allen, E. E., Amaral-Zettler, L. A., et al. (2014). The marine microbial eukaryote transcriptome sequencing project (MMETSP): illuminating the functional diversity of eukaryotic life in the oceans through transcriptome sequencing. *PloS Biol.* 12, e1001889. doi: 10.1371/journal.pbio.1001889

Knight, M. J., Senior, L., Nancolas, B., Ratcliffe, S., and Curnow, P. (2016). Direct evidence of the molecular basis for biological silicon transport. *Nat. Commun.* 7, 1–11. doi: 10.1038/ncomms11926

Kopf, A., Kostadinov, I., Wichels, A., Quast, C., and Glöckner, F. O. (2015). Metatranscriptome of marine bacterioplankton during winter time in the North Sea assessed by total RNA sequencing. *Mar. Genomics* 19, 45–46. doi: 10.1016/j.margen.2014.11.001

Kopylova, E., Noé, L., and Touzet, H. (2012). SortMeRNA: Fast and accurate filtering of ribosomal RNAs in metatranscriptomic data. *Bioinformatics* 28, 3211–3217. doi: 10.1093/bioinformatics/bts611

Kotzsch, A., Gröger, P., Pawolski, D., Bomans, P. H. H., Sommerdijk, N. A. J. M., Schlierf, M., et al. (2017). Silicanin-1 is a conserved diatom membrane protein involved in silica biomineralization. *BMC Biol.* 15, 9–11. doi: 10.1186/s12915-017-0400-8

Kotzsch, A., Pawolski, D., Milentyev, A., Shevchenko, A. A., Scheffel, A., Poulsen, N., et al. (2016). Biochemical composition and assembly of biosilica-associated insoluble organic matrices from the diatom *Thalassiosira pseudonana*. *J. Biol. Chem.* 291, 4982–4997. doi: 10.1074/jbc.M115.706440

Kranzler, C. F., Krause, J. W., Brzezinski, M. A., Edwards, B. R., Biggs, W. P., Maniscalco, M., et al. (2019). Silicon limitation facilitates virus infection and mortality of marine diatoms. *Nat. Microbiol.* 4, 1790–1797. doi: 10.1038/s41564-019-0502-x

Krause, J. W., Brzezinski, M. A., and Jones, J. L. (2011). Application of low-level beta counting of 32Si for the measurement of silica production rates in aquatic environments. *Mar. Chem.* 127, 40–47. doi: 10.1016/j.marchem.2011.07.001

Krause, J. W., Brzezinski, M. A., Landry, M. R., Baines, S. B., Nelson, D. M., Selph, K. E., et al. (2010). The effects of biogenic silica detritus, zooplankton grazing, and diatom size structure on silicon cycling in the euphotic zone of the eastern equatorial Pacific. *Limnol. Oceanogr.* 55, 2608–2622. doi: 10.4319/lo.2010.55.6.2608

Krause, J. W., Brzezinski, M. A., Largier, J. L., McNair, H. M., Maniscalco, M., Bidle, K. D., et al. (2020). The interaction of physical and biological factors drives phytoplankton spatial distribution in the northern California Current. *Limnol. Oceanogr.* 65, 1974–1989. doi: 10.1002/lno.11431

Krause, J. W., Brzezinski, M. A., Siegel, D. A., and Thunell, R. C. (2013). Biogenic silica standing stock and export in the Santa Barbara Channel ecosystem. *J. Geophys Res. Oceans* 118, 736–749. doi: 10.1029/2012JC008070

Krause, J. W., Brzezinski, M. A., Villareal, T. A., and Wilson, C. (2012). Increased kinetic efficiency for silicic acid uptake as a driver of summer diatom blooms in the North Pacific subtropical gyre. *Limnol. Oceanogr.* 57, 1084–1098. doi: 10.4319/lo.2012.57.4.1084

Krause, J. W., Duarte, C. M., Marquez, I. A., Assmy, P., Fernández-Méndez, M., Wiedmann, I., et al. (2018). Biogenic silica production and diatom dynamics in the Svalbard region during spring. *Biogeosciences* 15, 6503–6517. doi: 10.5194/BG-15-6503-2018

Krause, J. W., Stukel, M. R., Taylor, A. G., Taniguchi, D. A. A., De Verneil, A., and Landry, M. R. (2015). Net biogenic silica production and the contribution of diatoms to new production and organic matter export in the Costa Rica Dome ecosystem. *J. Plankton Res.* 38, 216–229. doi: 10.1093/plankt/fbv077

Kröger, N., Deutzmann, R., Bergsdorf, C., and Sumper, M. (2000). Species-specific polyamines from diatoms control silica morphology. *Proc. Natl. Acad. Sci. U.S.A.* 97, 14133–14138. doi: 10.1073/pnas.260496497

Kröger, N., Deutzmann, R., and Sumper, M. (1999). Polycationic peptides from diatom biosilica that direct silica nanosphere formation. *Science (1979)* 286, 1129–1132. doi: 10.1126/science.286.5442.1129

Kröger, N., Lorenz, S., Brunner, E., and Sumper, M. (2002). Self-assembly of highly phosphorylated silaffins and their function in biosilica morphogenesis. *Science* (1979) 298, 584–586. doi: 10.1126/science.1076221

Lampe, R. H., Mann, E. L., Cohen, N. R., Till, C. P., Thamatrakoln, K., Brzezinski, M. A., et al. (2018). Different iron storage strategies among bloom-forming diatoms. *Proc. Natl. Acad. Sci.* 115, E12275–E12284. doi: 10.1073/pnas.1805243115

Larkin, A. A., Garcia, C. A., Garcia, N., Brock, M. L., Lee, J. A., Ustick, L. J., et al. (2021). High spatial resolution global ocean metagenomes from Bio-GO-SHIP repeat hydrography transects. *Sci. Data* 8, 1 8, 1–6. doi: 10.1038/s41597-021-00889-9

Li, D., Liu, C. M., Luo, R., Sadakane, K., and Lam, T. W. (2015). MEGAHIT: An ultra-fast single-node solution for large and complex metagenomics assembly via succinct de Bruijn graph. *Bioinformatics* 31, 1674–1676. doi: 10.1093/bioinformatics/btv033

Liebig, J. (1840). *Die organische Chemie in ihrer Anwendung auf Agricultur und Physiologie* (Braunschweig, Germany: Friedrich Vieweg und Sohn Publishing Company). doi: 10.5962/bhl.title.42117

Liefer, J. D., Garg, A., Fyfe, M. H., Irwin, A. J., Benner, I., Brown, C. M., et al. (2019). The macromolecular basis of phytoplankton C:N:P under nitrogen starvation. *Front. Microbiol.* 10. doi: 10.3389/fmicb.2019.00763

Maniscalco, M. A., Brzezinski, M. A., Lampe, R. H., Cohen, N. R., McNair, H. M., Ellis, K. A., et al. (2022). Diminished carbon and nitrate assimilation drive changes in diatom elemental stoichiometry independent of silicification in an iron-limited assemblage. *ISME Commun.* 2, 1 2: 1–10. doi: 10.1038/s43705-022-00136-1

Marchetti, A., Moreno, C. M., Cohen, N. R., Oleinikov, I., deLong, K., Twining, B. S., et al. (2017). Development of a molecular-based index for assessing iron status in bloom-forming pennate diatoms. *J. Phycol.* 53, 820–832. doi: 10.1111/jpy.12539

Martin-Jézéquel, V., Hildebrand, M., and Brzezinski, M. A. (2000). Silicon metabolism in diatoms: Implications for growth. *J. Phycol.* 36, 821–840. doi: 10.1046/j.1529-8817.2000.00019.x

Matsen, F. A., Kodner, R. B., and Armbrust, V. E. (2010). pplacer: linear time maximum-likelihood and Bayesian phylogenetic placement of sequences onto a fixed reference tree. *BMC Bioinf.* 11, 538. doi: 10.1186/1471-2105-11-538

McCabe, R. M., Hickey, B. M., Kudela, R. M., Lefebvre, K. A., Adams, N. G., Bill, B. D., et al. (2016). An unprecedented coastwide toxic algal bloom linked to anomalous ocean conditions. *Geophys Res. Lett.* 43, 10,366–10,376. doi: 10.1002/2016GL070023

McNair, H. M., Brzezinski, M. A., and Krause, J. W. (2018a). Diatom populations in an upwelling environment decrease silica content to avoid growth limitation. *Environ. Microbiol.* 20, 4184–4193. doi: 10.1111/1462-2920.14431

McNair, H. M., Brzezinski, M. A., Till, C. P., and Krause, J. W. (2018b). Taxon-specific contributions to silica production in natural diatom assemblages. *Limnol. Oceanogr.* 63, 1056–1075. doi: 10.1002/lno.10754

Mock, T., Samanta, M. P., Iverson, V., Berthiaume, C., Robison, M., Holtermann, K., et al. (2008). Whole-genome expression profiling of the marine diatom *Thalassiosira pseudonana* identifies genes involved in silicon bioprocesses. *Proc. Natl. Acad. Sci. U.S.A.* 105, 1579–1584. doi: 10.1073/pnas.0707946105

Moreno, C. M., Gong, W., Cohen, N. R., DeLong, K., and Marchetti, A. (2020). Interactive effects of iron and light limitation on the molecular physiology of the Southern Ocean diatom Fragilariopsis kerguelensis. *Limnol. Oceanogr.* 65, 1511–1531. doi: 10.1002/lno.11404

Nelson, D., and Brzezinski, M. A. (1990). Kinetics of silicic acid uptake by natural diatom assemblages in two Gulf Stream warm-core rings. *Mar. Ecol. Prog. Ser.* 62, 283–292. doi: 10.3354/meps062283

Nelson, D. M., Brzezinski, M. A., Sigmon, D. E., and Franck, V. M. (2001). A seasonal progression of Si limitation in the Pacific sector of the Southern Ocean. *Deep Sea Res. 2 Top. Stud. Oceanogr.* 48, 3973–3995. doi: 10.1016/S0967-0645(01)00076-5

Nelson, D. M., and Dortch, Q. (1996). Silicic acid depletion and silicon limitation in the plume of the Mississippi River: evidence from kinetic studies in spring and summer. *Mar. Ecol. Prog. Ser.* 136, 163–178. doi: 10.3354/meps136163

Nymark, M., Valle, K. C., Hancke, K., Winge, P., Andresen, K., Johnsen, G., et al. (2013). Molecular and photosynthetic responses to prolonged darkness and subsequent acclimation to re-illumination in the diatom *phaeodactylum tricornutum*. *PloS One* 8, e7743. doi: 10.1371/journal.pone.0058722

Olson, R. J., and Chisholm, S. W. (1986). Effects of light and nitrogen limitation on the cell cycle of the dinoflagellate Amphidinium carteri. *J. Plankton Res.* 8, 785–793. doi: 10.1093/PLANKT/8.4.785

Osborne, B. A., and Geider, R. J. (1986). Effect of nitrate-nitrogen limitation on photosynthesis of the diatom *Phaeodactylum tricornutum* Bohlin (Bacillariophyceae). *Plant Cell Environ.* 9, 617–625. doi: 10.1111/J.1365-3040.1986.TB01619.X

Paasche, E. (1973). Silicon and the ecology of marine plankton diatoms. I. *Thalassiosira pseudonana* (Cyclotella nana) grown in a chemostat with silicate as limiting nutrient. *Mar. Biol.* 19, 117–126. doi: 10.1007/BF00353582

Parsons, T. R., Maita, Y., and Lalli, C. M. (1984). *A manual of chemical and biological methods for seawater analysis* (Elmsford, New York: Pergamon Press).

Poulsen, N., and Kröger, N. (2004). Silica morphogenesis by alternative processing of silaffins in the diatom *Thalassiosira pseudonana*. *J. Biol. Chem.* 279, 42993–42999. doi: 10.1074/jbc.M407734200

Rahmatallah, Y., Emmert-Streib, F., and Glazko, G. (2014). Comparative evaluation of gene set analysis approaches for RNA-Seq data. *BMC Bioinf.* 15, 1–15. doi: 10.1186/S12859-014-0397-8/FIGURES/5

Raven, J. A., and Waite, A. M. (2004). The evolution of silicification in diatoms: inescapable sinking and sinking as escape? *New Phytol.* 162, 45–61. doi: 10.1111/J.1469-8137.2004.01022.X

Rhee, G.-Y. (1978). Effects of N:P atomic ratios and nitrate limitation on algal growth, cell composition, and nitrate uptake 1. *Limnol. Oceanogr.* 23, 10–25. doi: 10.4319/LO.1978.23.1.0010

Rho, M., Tang, H., and Ye, Y. (2010). FragGeneScan: Predicting genes in short and error-prone reads. *Nucleic Acids Res.* 38, 1–12. doi: 10.1093/nar/gkq747

Robinson, M. D., McCarthy, D. J., and Smyth, G. K. (2010). edgeR: a Bioconductor package for differential expression analysis of digital gene expression data. *Bioinformatics* 26, 139–140. doi: 10.1093/bioinformatics/btp616

Rusch, D. B., Halpern, A. L., Sutton, G., Heidelberg, K. B., Williamson, S., Yooseph, S., et al. (2007). The sorcerer II global ocean sampling expedition: northwest atlantic through eastern tropical pacific. *PloS Biol.* 5, e77. doi: 10.1371/JOURNAL.PBIO.0050077

Sapriel, G., Quinet, M., Heijde, M., Jourdren, L., Tanty, V., Luo, G., et al. (2009). Genome-wide transcriptome analyses of silicon metabolism in *Phaeodactylum tricornutum* reveal the multilevel regulation of silicic acid transporters. *PloS One* 4, e7458. doi: 10.1371/journal.pone.0007458

Scheffel, A., Poulsen, N., Shian, S., and Kröger, N. (2011). Nanopatterned protein microrings from a diatom that direct silica morphogenesis. *Proc. Natl. Acad. Sci.* 108, 3175–3180. doi: 10.1073/pnas.1012842108

Shrestha, R. P., and Hildebrand, M. (2015). Evidence for a regulatory role of diatom silicon transporters in cellular silicon responses. *Eukaryot. Cell* 14, 29. doi: 10.1128/EC.00209-14

Shrestha, R. P., Tesson, B., Norden-Krichmar, T., Federowicz, S., Hildebrand, M., and Allen, A. E. (2012). Whole transcriptome analysis of the silicon response of the diatom *Thalassiosira pseudonana*. *BMC Genomics* 13, 1. doi: 10.1186/1471-2164-13-499

Siegel, D. A., Buesseler, K. O., Behrenfeld, M. J., Benitez-Nelson, C. R., Boss, E., Brzezinski, M. A., et al. (2016). Prediction of the export and fate of global ocean net primary production: The exports science plan. *Front. Mar. Sci.* 3, 22. doi: 10.3389/FMARS.2016.00022/BIBTEX

Smith, S. R., Dupont, C. L., McCarthy, J. K., Broddrick, J. T., Oborník, M., Horák, A., et al. (2019). Evolution and regulation of nitrogen flux through compartmentalized metabolic networks in a marine diatom. *Nat. Commun.* 10, 4552. doi: 10.1038/s41467-019-12407-y

Smith, S. R., Glé, C., Abbriano, R. M., Traller, J. C., Davis, A. K., Trentacoste, E., et al. (2016). Transcript level coordination of carbon pathways during silicon starvation-induced lipid accumulation in the diatom *Thalassiosira pseudonana*. *New Phytol.* 210, 890–904. doi: 10.1111/nph.13843

Stamatakis, A. (2014). RAxML version 8: A tool for phylogenetic analysis and post-analysis of large phylogenies. *Bioinformatics* 30, 1312–1313. doi: 10.1093/bioinformatics/btu033

Strickland, J. D. H., and Parsons, T. R. (1972). *Practical handbook of seawater analysis 2nd edition*. Ottawa, Canada: Fisheries Research Board of Canada. doi: 10.25607/OBP-1791

Tesson, B., Lerch, S. J. L., and Hildebrand, M. (2017). Characterization of a new protein family associated with the silica deposition vesicle membrane enables genetic manipulation of diatom silica. *Sci. Rep.* 7, 1–13. doi: 10.1038/s41598-017-13613-8

Thamatrakoln, K., and Hildebrand, M. (2007). Analysis of *Thalassiosira pseudonana* silicon transporters indicates distinct regulatory levels and transport activity through the cell cycle. *Eukaryot. Cell* 6, 271–279. doi: 10.1128/EC.00235-06

Thamatrakoln, K., and Hildebrand, M. (2008). Silicon uptake in diatoms revisited: A model for saturable and nonsaturable uptake kinetics and the role of silicon transporters. *Plant Physiol.* 146, 1397–1407. doi: 10.1104/pp.107.107094

Thamatrakoln, K., Korenovska, O., Niheu, A. K., and Bidle, K. D. (2012). Whole-genome expression analysis reveals a role for death-related genes in stress acclimation of the diatom *Thalassiosira pseudonana*. *Environ. Microbiol.* 14, 67–81. doi: 10.1111/j.1462-2920.2011.02468.x

Thangaraj, S., Shang, X., Sun, J., and Liu, H. (2019). Quantitative Proteomic Analysis Reveals Novel Insights into Intracellular Silicate Stress-Responsive Mechanisms in the Diatom *Skeletonema dohrnii*. *Int. J. Mol. Sci. Article* 20, 2540. doi: 10.3390/ijms20102540

Toseland, A., Moxon, S., Mock, T., and Moulton, V. (2014). Metatranscriptomes from diverse microbial communities: Assessment of data reduction techniques for rigorous annotation. *BMC Genomics* 15, 1–7. doi: 10.1186/1471-2164-15-901

Trainer, V. L., Adams, N. G., Bill, B. D., Stehr, C. M., Wekell, J. C., Moeller, P., et al. (2000). Domoic acid production near California coastal upwelling zones, June 1998. *Limnol. Oceanogr.* 45, 1818–1833. doi: 10.4319/LO.2000.45.8.1818

Trainer, V. L., Bates, S. S., Lundholm, N., Thessen, A. E., Cochlan, W. P., Adams, N. G., et al. (2012). *Pseudo-nitzschia* physiological ecology, phylogeny, toxicity, monitoring and impacts on ecosystem health. *Harmful Algae* 14, 271–300. doi: 10.1016/J.HAL.2011.10.025

Tully, B. J., Graham, E. D., and Heidelberg, J. F. (2018). The reconstruction of 2,631 draft metagenome-assembled genomes from the global oceans. *Sci. Data* 5, 1 5: 1–1 5: 8. doi: 10.1038/sdata.2017.203

Vaulot, D., Merkel, S., Olson, R. J., and Chilsholm, S. W. (1987). Cell-cycle response to nutrient starvation in two phytoplankton species, *Thalassiosira weissflogii* and *Hymenomonas carterae*. *Mar. Biol.* 630, 625–630. doi: 10.1007/BF00393106

Wenzl, S., Hett, R., Richthammer, P., and Sumper, M. (2008). Silacidins: Highly acidic phosphopeptides from diatom shells assist in silica precipitation in *vitro*. *Angewandte Chem. - Int. Ed.* 47, 1729–1732. doi: 10.1002/anie.200704994

White, K. K., and Dugdale, R. C. (1997). Silicate and nitrate uptake in the Monterey Bay upwelling system. *Cont. Shelf. Res.* 17, 455–472. doi: 10.1016/S0278-4343(96)00042-8

Wu, D., Lim, E., Vaillant, F., Asselin-Labat, M. L., Visvader, J. E., and Smyth, G. K. (2010). ROAST: rotation gene set tests for complex microarray experiments. *Bioinformatics* 26, 2176–2182. doi: 10.1093/BIOINFORMATICS/BTQ401

Zielinski, B. L., Allen, A. E., Carpenter, E. J., Coles, V. J., Crump, B. C., Doherty, M., et al. (2016). Patterns of transcript abundance of eukaryotic biogeochemically-relevant genes in the Amazon river plume. *PloS One* 11, 1–20. doi: 10.1371/journal.pone.0160929

frontiers | Frontiers in Marine Science

TYPE Original Research
PUBLISHED 22 December 2023
DOI 10.3389/fmars.2023.1269142

OPEN ACCESS

EDITED BY
Eric 'Pieter Achterberg,
GEOMAR Helmholtz Center for Ocean Research Kiel, Germany

REVIEWED BY
Xiangbin Ran,
Ministry of Natural Resources, China
Shuijing Zhai,
Fujian Normal University, China

*CORRESPONDENCE
Mélanie Raimonet
melanie.raimonet@univ-brest.fr

RECEIVED 29 July 2023
ACCEPTED 20 November 2023
PUBLISHED 22 December 2023

CITATION
Raimonet M, Ragueneau O, Soetaert K, Khalil K, Leynaert A, Michaud E, Moriceau B, Rabouille C and Memery L (2023) Benthic contribution to seasonal silica budgets in two macrotidal estuaries in North-Western France. *Front. Mar. Sci.* 10:1269142. doi: 10.3389/fmars.2023.1269142

Benthic contribution to seasonal silica budgets in two macrotidal estuaries in North-Western France

Mélanie Raimonet [1,2]*, Olivier Ragueneau [1,2], Karline Soetaert [3], Karima Khalil [4], Aude Leynaert [1], Emma Michaud [1], Brivaela Moriceau [1], Christophe Rabouille [5] and Laurent Memery [1]

[1]CNRS, Univ Brest, IRD, Ifremer, LEMAR, IUEM, Plouzane, France, [2]LTSER, Zone Atelier Brest Iroise, Plouzane, France, [3]Department Estuarine and Delta Systems, Netherlands Institute for Sea Research, Yerseke, Netherlands, [4]Ecole Supérieure de Technologie d'Essaouira, Université Cadi Ayyad, Essaouira, Morocco, [5]Laboratoire des Sciences du Climat et de l'Environnement, UMR 1572, Gif sur Yvette, France

The paper aims to build seasonal silica budgets in two macrotidal estuaries, the Elorn and Aulne estuaries of the Bay of Brest (North-Western France), based on modeling and measurements, in order to increase our understanding of the silica (Si) cycle at land-sea interfaces. A diagenetic model was developed to quantify benthic Si fluxes, e.g. $aSiO_2$ deposition fluxes that are difficult to assess through direct measurements. Sediment cores were also seasonally sampled at six stations to provide data essential to parametrize and validate the model. Vertical profiles of porosity, burrowing depth, biodiffusive coefficients, concentrations of amorphous silica ($aSiO_2$) and silicic acid ($Si(OH)_4$ and the proportion of reactive $aSiO_2$ were measured. The results show that sites sampled along the Elorn and Aulne estuaries constitute significant net Si deposition areas (1-4.5 mmol Si m^{-2} d^{-1}), particularly in the upstream during winter and in midstream and downstream during summer. Year round, reprecipitation is negligible (< 3%) while burial accounts for the retention of ~ 30-80% of deposited $aSiO_2$. In winter, burial dominates the benthic Si budget. As surface-integrated benthic Si fluxes are low compared to riverine $aSiO_2$ fluxes, the Si export to coastal waters is high (93%) during winter. In contrast, in summer, burial accounts for 38% of river Si fluxes, and $Si(OH)_4$ flux from the sediment is high as a result of enhanced benthic recycling and bioirrigation. Internal estuarine processes, e.g., benthic and pelagic primary production, dissolution and benthic Si fluxes, surpass river fluxes in magnitude during summer. Overall, we conclude that the Elorn and Aulne macrotidal estuaries are efficient filters of Si, retaining about 4-38% of river Si fluxes, and even 6-67% when accounting for retention in intertidal marshes, but with massive exports occurring during winter floods.

KEYWORDS

silica cycle, estuary, diagenetic modeling, bioturbation, benthic-pelagic coupling

1 Introduction

In aquatic ecosystems, silicon (Si) is an essential element for the growth of diatoms, which account for up to 75% of the coastal primary production (Nelson et al., 1995) and which play an essential role in the oceanic carbon biological pump (Buesseler, 1998; Ragueneau et al., 2006; Tréguer et al., 2018). The inputs of reactive Si to coastal and oceanic waters are mainly transported by rivers (Tréguer et al., 2021), essentially in the dissolved form, i.e. silicic acid $Si(OH)_4$ (Dürr et al., 2011), but with a non-negligible contribution in particulate form, i.e. amorphous silica ($aSiO_2$), as phytoliths and products of riverine primary production (Conley, 1997; Farmer et al., 2005). These inputs are mostly natural but, in the last few decades, anthropogenic activities leading to eutrophication (Conley et al., 1993; Garnier et al., 2021), river damming (Humborg et al., 1997; Maavara et al., 2020) or the proliferation of invasive species related to globalization of maritime transport (Ragueneau et al., 2005a) have strongly disturbed the transit of Si from land to coastal waters, most often decreasing it strongly. The synergistic decrease of Si river loads and the enhanced nitrogen and phosphorus run-off due to agriculture, industry and urbanization, have decreased the ratios of Si over nitrogen and phosphorus in coastal waters (Garnier et al., 2010; Maavara et al., 2020). This has led to Si limitation of primary production and shifts from diatom to dinoflagellate-dominated phytoplankton communities that are potentially toxic to consumers, in many coastal ecosystems around the world (Officer and Ryther, 1980; Garnier et al., 2010), and could be associated with an increase in diatom toxicity (e.g. *Pseudo-nitzschia fraudulenta*; Tatters et al., 2012).

At the land-sea interface, estuaries constitute potentially efficient filters for nitrogen (~22%), phosphorus (~24%) and carbon (~60%) (Laruelle, 2009; Regnier et al., 2013). While data are quite abundant for nitrogen or phosphorus, datasets for Si are very sparse or based on punctual field work (Ragueneau et al., 2010; Dürr et al., 2011; Mangalaa et al., 2017), despite the importance of this element for coastal and oceanic ecological and biogeochemical processes, tightly coupled to the carbon cycle through silicified organisms e.g. diatoms, plants, sponges, radiolarians (Tréguer, 2002; Tréguer et al., 2021). Estuaries are characterized by high primary production often dominated by diatoms (Ragueneau et al., 2002b; Roubeix et al., 2008b; Wallington et al., 2023), and high $aSiO_2$ dissolution resulting from high bacterial biomass and increased salinity (Roubeix et al., 2008a; Loucaides et al., 2010). The distribution of diatom production and degradation in estuarine waters emerges by a complex balance between light and nutrients for production (DeMaster et al., 1983; Zhang et al., 2020) and between temperature, salinity, and bacterial activity for degradation (Ragueneau et al., 2002b; Roubeix et al., 2008a). However the estuarine filter capacity is strongly linked to the benthic ecosystem through $aSiO_2$ deposition, recycling and/or storage (Carbonnel et al., 2009; Rebreanu, 2009) and through $Si(OH)_4$ reprecipitation (Michalopoulos and Aller, 2004; Ehlert et al., 2016). Finally, tidal saltmarshes can constitute transient sources of $Si(OH)_4$, especially during summer (Struyf et al., 2006) and increase the residence time of Si in estuaries (Carey and Fulweiler, 2014).

Although the benthic Si cycle is often neglected in estuaries because of lower benthic fluxes than river fluxes (Arndt et al., 2009), benthic Si fluxes can become significant, especially during summer, due to the reduced river discharges (Anderson, 1986), higher dissolution rates (Yamada and D'Elia, 1984; Rebreanu, 2009) or enhanced bioirrigation activities (Green et al., 2004). Especially during summer, benthic $Si(OH)_4$ fluxes can slightly enhance (Arndt and Regnier, 2007) or even sustain pelagic primary production (Ragueneau et al., 2002a). The interactions between benthic and pelagic ecosystems are even stronger along estuaries because of water column shallowness (Sundbäck et al., 2003), resuspension processes induced by a strong hydrodynamic regime from tidal to seasonal scales (Gehlen and Van Raaphorst, 2002; Welsby et al., 2016), lateral loads from large intertidal areas (Sun et al., 1994; Struyf et al., 2006; Wallington et al., 2023), and climate change (Fulweiler and Nixon, 2009) or the presence of benthic suspension feeders (Cloern, 1982; Ragueneau et al., 2002a).

Estuaries are indeed highly dynamic and complex zones submitted to intense and interacting physical, biological and biogeochemical processes leading to strong spatial and temporal gradients at various scales e.g. upstream-downstream gradient, cross-section, vertical, tidal or seasonal variations (Pritchard, 1967; Cloern et al., 2017), and modified by anthropogenic activities (Nichols et al., 1986). Studying estuaries requires modeling and/or large datasets to document these gradients. Different approaches have been used to build Si budgets and estimate the filtering and retention capacities of aquatic systems from rivers to coastal waters (Ragueneau et al., 2005a; Soetaert et al., 2006; Arndt et al., 2009; Laruelle, 2009; Wallington et al., 2023). The most common methods are mixing diagrams, box models, or dynamic reactive-transport models of the pelagic ecosystem (Peterson, 1979; Anderson, 1986; Soetaert et al., 2006; Arndt et al., 2007; Testa and Kemp, 2008; Arndt et al., 2009; Carbonnel et al., 2009). Mixing diagrams are useful for determining the gains and losses along salinity gradients, assuming a steady state river flow (Anderson, 1986; Ragueneau et al., 2002b). Contrary to mixing diagrams, box models account for internal estuarine processes (Ragueneau et al., 2005a; Carbonnel et al., 2009). Reactive-transport models are useful for representing coupled physical and biological processes with strong spatial and temporal variations (Arndt and Regnier, 2007), and for highlighting the potentially erroneous interpretations that may result from mixing diagrams when transient river flows are not considered (Regnier et al., 1998; Arndt et al., 2009).

In general, estimates of benthic retention are performed through indirect methods by determining differences between pelagic input and output fluxes (Carbonnel et al., 2009), by subtracting benthic fluxes (Ragueneau et al., 2005a), or through analytical modeling (Arndt and Regnier, 2007): however, such estimates neglect or simplify the vertical discretization of benthic fluxes, and do not take into account the non-local bioirrigation processes. Even if calibration and data from the literature is often used to calibrate and/or validate models, the acquisition of extensive datasets is essential to better constrain the model and reduce uncertainties. If the quantification of $Si(OH)_4$ and $aSiO_2$ contents is an essential requirement, better constraints could be obtained by

10.3389/fmars.2023.1269142

complementary experiments on major processes in order to quantify the seasonality of pelagic $aSiO_2$ production, the proportion of highly reactive $aSiO_2$, or bioturbation coefficients.

The aim of this study is to investigate the seasonality of the main processes involved in the benthic Si cycle along the estuaries of the two main rivers (Elorn, Aulne) that extend to the Bay of Brest. The methodology involves diagenetic modeling coupled to measurements. After the seasonal characterization of deposition fluxes along the estuaries, the main processes (e.g. diffusion fluxes at the sediment-water interface, bioirrigation, reprecipitation, burial) involved in the benthic Si cycle of estuarine muddy sediments are quantified. Finally, the retention of Si through benthic estuarine processes is estimated and compared to river fluxes and pelagic processes (e.g. production).

2 Material and methods

2.1 Model description

The diagenetic Si model was modified from Khalil et al. (2007) and implemented in the R software (http://cran.r-project.org). A short description of equations, processes and parameters is given below.

The general equation of the reactive-transport model affecting solids and solutes (Eq. 1) represent diffusive and advective transport (first and second terms, respectively) and reactive processes (third term):

$$\frac{\partial \xi C_i}{\partial t} = -\frac{\partial}{\partial z}\left(-\xi D \frac{\partial C_i}{\partial z}\right) - \frac{\partial}{\partial z}(\xi w C_i) + \Sigma \xi R \quad (1)$$

All fluxes are in mmol m^{-3} d^{-1} and are detailed below.

The originality of the work of Khalil et al. (2007) is to implement two variables of $aSiO_2$ with different reactivity. The model has thus three sets of variables: less reactive $aSiO_2$ concentrations (C_{aSiS}, µmol l^{-1}), highly reactive $aSiO_2$ concentrations (C_{aSiF}, µmol l^{-1}) and dissolved $Si(OH)_4$ concentrations (C_{dSi}, µmol l^{-1}) implemented in Eqs. 2, 3, 4 and 5.

The transport of the two solid fractions - less and highly reactive $aSiO_2$ - is controlled by the biodiffusion rates (D_b, m^2 d^{-1}) linked to sediment mixing by benthic organisms, and by the advection rates (w, m d^{-1}) linked to the accumulation of newly deposited particles and steady-state compaction.

$$\frac{\partial (1-\phi) C_{aSiS}}{\partial t} = -\frac{\partial}{\partial z}\left(-(1-\phi) D_b \frac{\partial C_{aSiS}}{\partial z} + w(1-\phi) C_{aSiS}\right) - (1-\phi) R_{dissS} \quad (2)$$

$$\frac{\partial (1-\phi) C_{aSiF}}{\partial t} = -\frac{\partial}{\partial z}\left(-(1-\phi) D_b \frac{\partial C_{aSiF}}{\partial z} + w(1-\phi) C_{aSiF}\right) - (1-\phi) R_{dissF} \quad (3)$$

The biodiffusion rate is depth-dependent and calculated at each depth as follows:

$$For\ z \le z_b,\ D_b(z) = D_{b0}$$

$$For\ z > z_b,\ D_b(z) = D_{b0} exp(-(z - z_b) \times coeff_b)$$

where D_{b0} is the surface biodiffusion coefficient (m^2 d^{-1}), z_b is the biodiffusion depth for solids (m) and $coeff_b$ is the exponential decrease constant for biodiffusion (m).

The $aSiO_2$ dissolution term (R_{dissS} or R_{dissF}; Eqs. 4 and 5) is parametrized by different dissolution rates (k_{aSiS} and k_{aSiF}, d^{-1}, dependent on *in situ* temperature and salinity) and equilibrium concentrations (C_{dSieqS} and C_{dSieqF}, µmol l^{-1}) for each $aSiO_2$ phase.

$$R_{dissS} = k_{aSiS}\ C_{aSiS}\left(1 - \frac{C_{dSi}}{C_{dSieqS}}\right) \quad (4)$$

$$R_{dissF} = k_{aSiF}\ C_{aSiF}\left(1 - \frac{C_{dSi}}{C_{dSieqF}}\right) \quad (5)$$

Note that the porosity ϕ is depth-dependent and defined at each depth as follows:

$$\phi(z) = (\phi_0 - \phi_\infty) \exp(-z \times coef_\phi) + \phi_\infty$$

Where ϕ_0 is the porosity at sediment-water interface, ϕ_∞ the asymptotic porosity and z_{por} the exponential decrease constant for porosity.

The reactive-transport of solutes - $Si(OH)_4$ (noted dSi in equations) - is modified from Khalil et al. (2007) and described in Eq. 6. Advection is neglected because of the dominance of the diffusive process (Peclet number >> 1; McManus et al., 1995). The processes of molecular diffusion, dissolution ($R_{diss} = R_{dissF} + R_{dissS}$) and reprecipitation ($R_{precip} = K_p\ (C_{dSi} - C_{dSieqp})$) are kept as described by Khalil et al. (2007). Secondly, a bioirrigation process (R_{irr}) is added to take into account the transport of $Si(OH)_4$ with solutes by bioturbation activities.

$$\frac{\partial \phi C_{dSi}}{\partial t} = -\frac{\partial}{\partial z}\left(-\phi D_{dSi} \frac{\partial C_{dSi}}{\partial z}\right) + \phi R_{diss} - \phi R_{precip} - \phi R_{irr} \quad (6)$$

Bioirrigation is represented with a non-local term described in Eq. 7 for depth $z \le z_{irr}$ (Emerson et al., 1984; Boudreau, 1994).

$$R_{irr} = \alpha\ (C_{dSi} - C_{dSi0}) \quad (7)$$

The bioirrigation rate parameter α (d^{-1}) is constant over the bioirrigation depth (m) and exponentially decreases below that depth. C_{dSi0} is the concentration of $Si(OH)_4$ at the sediment-water interface (z=0).

At the sediment-water interface (z=0), diffusive fluxes of $Si(OH)_4$ are prescribed by Fick's first law of diffusion (Eq. 8).

$$F_{dSi0} = -\phi_0\ D_{dSi0} \frac{\partial C_{dSi}}{\partial z} \quad (8)$$

Where D_{dSi0} is the diffusion coefficient for $Si(OH)_4$ (m^2 d^{-1}) and $\frac{\partial C_{dSi}}{\partial z}$ is the concentration gradient of $Si(OH)_4$ (mmol m^{-3} m^{-1}) at sediment-water interface.

The upper boundary of the solid fraction is prescribed as a net deposition flux (including resuspension and benthic primary production). At the lower boundary, zero-gradients are imposed for both solid and solute fractions.

The model is solved to steady-state, using methods implemented in R-package rootSolve (Soetaert, 2009). Mass balance is calculated in order to ensure the internal validity of the mathematical steady-state solution. At all times, the difference between the deposition flux of $aSiO_2$ and the sum of benthic fluxes of $Si(OH)_4$, burial and reprecipitation fluxes of $aSiO_2$ was < 10^{-12}.

2.2 Study site and sampling design

2.2.1 Study area

This study was conducted in the Elorn and Aulne estuaries, linking the Elorn and Aulne rivers with the Bay of Brest in northwestern France (Figure 1). The Elorn and Aulne rivers bring 85% of fresh water to the Bay of Brest - a macrotidal semi-enclosed coastal embayment subject to intense water exchanges with the Iroise Sea (semi-diurnal tidal amplitude of 4 m, 7.5 m during spring tides). The Elorn Estuary is ~ 15 km long, straight and directly exposed to marine hydrodynamics, while the Aulne Estuary is longer (~ 35 km), meandering and more protected by the Bay of Brest. The oceanic climate leads to high precipitation associated to frequent storms in winter compared to summer, thus modifying river flow. We sampled the two estuarine areas in February, April, August and November 2008 and February, May, July and October/November 2009. Except for the vertical $aSiO_2$ profiles measured in February, April and November 2008 and the proportion of highly reactive aSiO2 in sediments measured in February 2008, all the results presented here were obtained from the sampling performed in 2009.

The wind speed, the precipitation and the river flow were all higher during winter and fall than in spring and summer (Figures 2A–C). Note that a winter storm occurred just before sampling in February leading to strong winds (up to 15 kt) and high precipitation (> 25 mm d^{-1}). In winter, Elorn and Aulne River flows increased to 30 and 130 m^3 s^{-1}, respectively, during initial sampling in February, and decreased by a factor > 2 by the end of the sampling period (Figure 2C). The Aulne River flow was higher than the Elorn River flow by a factor of ~ 5 during winter, but was similar or occasionally lower than the Elorn River flow during summer. Water temperature ranged from 7.4-8.2 in winter to 16.7-19.7 in summer, and salinity varied between 0-8.7 to 20-34.2 from upper to lower estuarine stations depending on season (Table 1).

2.2.2 Surface water sampling

Surface water was sampled from salinity 0 to 35 at intervals of 5 from the center of the estuary aboard the *R/V Hésione*. Surface water was collected with a Niskin bottle, immediately stored in dark bottles in an icebox and brought back to the laboratory. Water was filtered on a polycarbonate membrane (0.6 µm pore size, 47 mm diameter) for $aSiO_2$ and $Si(OH)_4$ analyses, and on Whatman® GF/F precombusted filters (0.7 µm pore size, 47 mm diameter) for pigments analyses - e.g., chlorophyll a (Chl *a*) and phaeopigments (Phae). Polycarbonate membranes were oven-dried during 48 h and filters were stored at - 20°C until analyses. Filtered water was stored in vials at 4°C until $Si(OH)_4$ analyses.

2.2.3 Sediment and porewater sampling

Benthic sampling was performed at three stations located from upstream to downstream of Elorn (E1, E2, E3) and Aulne (A1, A2, A3) estuaries, at salinity of about ~ 0, ~ 10-20 and ~ 30 (Figure 1; Table 1). Sampling was done aboard the *R/V Hésione* at mid-tide, between the channel and the border, in subtidal sediments, based on a high spatial and temporal variability study (Raimonet et al., 2013b). A gravity corer (UWITEC®) was used to sample plexiglass cores (9.5 cm diameter × 60 cm long). Corer weight was adjusted to allow ~ 30 cm penetration into the sediment with minimal disturbance of the sediment-water interface. Geochemical measurements were done from triplicate sediment cores which were immediately sliced at 0.5 cm intervals in the first 2 cm, at 1 cm

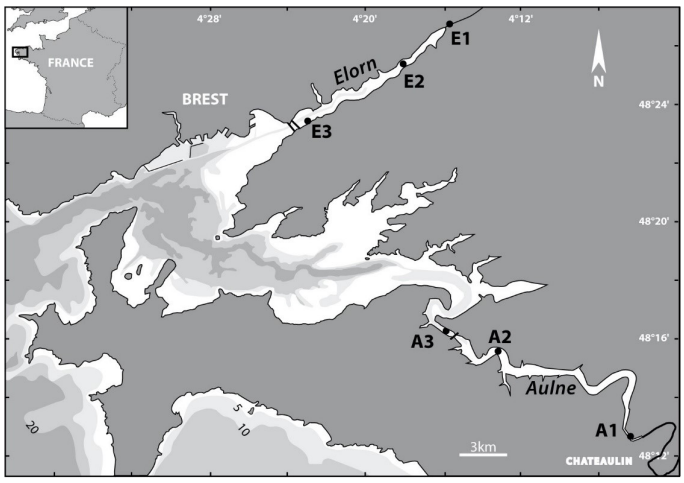

FIGURE 1
Location of benthic sampling sites along the Elorn (E1, E2, E3) and Aulne (A1, A2, A3) estuaries.

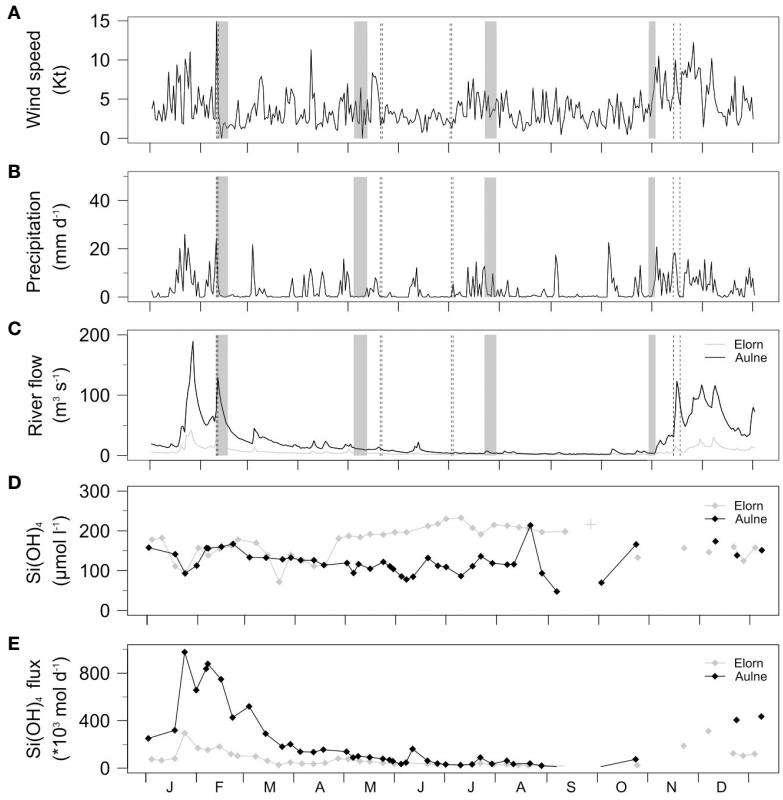

FIGURE 2
(A) Wind speed (Kt) at 10 m above the surface and **(B)** precipitations (mm d^{-1}) measured at Lanvéoc Meteo Station (Source: Meteo France). **(C)** River flow (m^3 s^{-1}) at Landerneau and 43 km upstream Chateaulin (Source: Banque Hydro). **(D)** Weekly $Si(OH)_4$ concentrations (µmol l^{-1}) at Landerneau and Chateaulin river outfalls (Source: Ecoflux). **(E)** $Si(OH)_4$ fluxes (*1000 mol d^{-1}) obtained by multiplying riverine concentrations with river flow. Pelagic and benthic sampling periods are indicated by black dashed lines and grey areas, respectively.

intervals for 2-4 cm, at 2 cm intervals for 4-12 cm, and at 4 cm intervals for 12-20 cm. Sediment sections were put in sealed 50-ml centrifugate tubes containing Vectaspin 20 filters (0.45 µm pore size, Whatman®) according to Andrieux-Loyer et al. (2008). Interstitial waters were extracted by centrifuging at 3500 rpm for 10 min (twice) at cooled temperature and acidified to pH = 2. An aliquot was preserved at 4°C for $Si(OH)_4$ analyses. Centrifuged sediments were freeze-dried for 48 h, put at 60°C to ensure complete sediment dryness and powdered for further analyses of $aSiO_2$ in the solid fraction. Subcores of 2.8 cm internal diameter were frozen with liquid nitrogen and stored at – 80°C until pigment analyses (Ni Longphuirt et al., 2006).

2.2.4 Sediment biodiffusion experiments

To measure the sediment biodiffusion rates, we used the method which consists of the vertical profile analysis of inert and fluorescent tracer introduced artificially (e.g., luminophores; Duport et al., 2006; Oleszczuk et al., 2019). Three additional sediment cores (Ø: 9.5 cm; sediment height: 30 cm; overlying water height: 40 cm) were therefore sampled at each station for these bioturbation experiments. The whole set of sediment cores was kept in controlled laboratory conditions, which mimicked the natural conditions for the estuarine temperatures and salinities (Table 1). After three days of stabilization in the controlled conditions, 3 g of luminophores (60–90 µm diameter) were homogeneously added to the overlying water and gradually spread on the sediment surface of each core without disturbing the resident infauna. Overlying water was renewed every four days with bottom water coming from each station. Cores were aerated by bubbling to keep the overlying water saturated with oxygen. Sediment cores were incubated in those conditions for 10 days, which is the minimum time to enable the characterization of the different transport modes (François et al., 1997). After this time of incubation in stable conditions, the surface water was carefully removed and cores were sliced horizontally in 0.5 cm layers from 0 to 2 cm depth, and in 1 cm layers between 2 and 10 cm depth. Each sediment layer was directly frozen to be analyzed later at the laboratory.

2.3 Field and laboratory measurements

Vertical profiles of sediment porosity: Sediment porosity in each sediment slide over depth was obtained after drying wet sediment of known volume for 5 days, after which the loss of weight was determined (Berner, 1980). This data was used to fit vertical porosity decreasing profiles.

Pelagic and benthic $aSiO_2$ contents: Pelagic $aSiO_2$ concentrations were determined using the sequential alkaline digestion method of Ragueneau et al. (2005b) and benthic $aSiO_2$ contents were

10.3389/fmars.2023.1269142

TABLE 1 Environmental parameters (temperature T, salinity S, depth D, river flow Q, tidal coefficient, $Si(OH)_4$ concentrations at the sediment-water interface C_{dSi0}) at each station and season during benthic sampling.

Station	T	S	D	Q	Tidal coefficient	C_{dSi0}
	°C	–	m	$m^3\ s^{-1}$	–	$\mu mol\ l^{-1}$
February 2009						
E1	8	0	1	18.5	108	115
E2	7.6	17.5	2	15.7	106	72
E3	8.2	29	3.5	14.5	98	25
A1	7.7	0	2.5	64.6	85	95
A2	7.4	13.7	3	54.1	70	78
A3	8	20	1.75	49.7	54	51
May 2009						
E1	12.3	0	1	4.69	51	148
E2	13.4	21.7	1.5	4.33	56	51
E3	12.8	33.5	6	4.24	64	5
A1	14.4	0	2	10.4	83	120
A2	14	22.5	3	9.95	85	44
A3	13.5	24.6	2	10.7	77	31
July 2009						
E1	16.7	0	0.5	2.79	88	100
E2	16.7	12.2	1	2.48	94	101
E3	17.7	33.5	6	1.77	102	6
A1	19.7	0	0.5	4.24	103	100
A2	19.5	27.5	1.5	5.01	105	70
A3	19.1	30.9	3	3.59	95	20
October 2009						
E1	15	0.8	0.5	1.45	38	120
E2	15.1	29.6	1.2	1.45	38	30
E3	15.3	34.2	8	1.42	49	10
A1	14.2	8.7	1	3.67	61	110
A2	15.5	29.9	1	3.47	72	28
A3	15	33	2.5	4.91	81	16

The tidal coefficient is a dimensionless number calculated from the tidal range, which characterizes the size of the tide on a scale from 20 to 120 (source: French Navy Hydrographic and Oceanographic Service).

quantified as in DeMaster (1981). Both methods allow to correct amorphous silica concentrations from lithogenic silica interference which is essential in environments rich in aluminosilicates - e.g. estuaries. Benthic $aSiO_2$ concentrations are expressed as % to refer to % g gDW^{-1}.

As $aSiO_2$ concentrations can vary from values less than 1% to more than 50% depending on study sites, we used $aSiO_2$ profiles measured in 2008 and surface $aSiO_2$ concentrations in 2009 to constrain modelled $aSiO_2$ profiles at each station. These profiles were used to estimate the range of $aSiO_2$ contents (± 1-3%) rather than to represent the fine scale vertical discontinuities (that cannot be captured by steady-state modeling). As no $aSiO_2$ profile was available for July, an annually averaged $aSiO_2$ profile of February, April and November was calculated for each station.

Vertical profiles of $Si(OH)_4$ concentrations: $Si(OH)_4$ concentrations in porewaters of each sediment slice were measured with an Auto Analyser III (Bran+Luebbe®) using the method of Tréguer and Le Corre (1975). The triplicate $Si(OH)_4$ profiles measured at each station and season in 2009 were averaged and used for fitting.

Chl a and Phae concentrations: were performed on surface water samples by using the SOMLIT protocol (http://somlit.epoc.u-

bordeaux1.fr) and on surface sediment (0.5 cm) by using a method adapted from Lorenzen (1966) and Riaux-Gobin and Klein (1993). For surface sediment, 10 ml of 90% acetone was added to each sample that was stored in the dark under constant agitation at 4°C for approximately 18 h. Chl *a* and Phae were respectively measured in the supernatant before and after acidification with a KONTRON fluorimeter (Kontron Instruments).

Proportion of highly reactive $aSiO_2$ in sediments: Dissolution experiments were carried out on 3 sediment layers (0-1, 2-3 and 6-7 cm), at all stations sampled in February 2008. The temporal increase of $Si(OH)_4$ concentrations was monitored during 21 days in batches containing the sediments and artificial seawater close to the measured *in situ* conditions: *in situ* salinity, pH of 8, constant temperature and in the dark to avoid any production of biogenic silica due to benthic organisms. The concentrations were normalized to the initial introduced Si concentrations in order to determine the dissolution rates of highly and less reactive $aSiO_2$ phases (the first and second slope of the curve). The proportion of highly reactive $aSiO_2$ was determined by statistical inverse modeling (Model 2 described in Moriceau et al., 2009). Note that we used the proportion of highly reactive $aSiO_2$ but not the dissolution rates to constrain the benthic Si model. Indeed, discrepancies between predicted and measured dissolution rates are expected in response to 1) the high detrital-to-amorphous opal ratio in our sediments (> 30%; Ragueneau and Tréguer, 1994), which increases aluminium concentrations and decreases the dissolution rate and solubility (Dixit et al., 2001); 2) the transport of fresh $aSiO_2$ to deep sediment layers by nonlocal bioturbation (Gallinari et al., 2008); 3) the absence of feedback between reprecipitation and dissolution in the model formulation (Khalil et al., 2007); 4) the cleaning of $aSiO_2$ particles from their alumino-silicate coating at the beginning of batch experiments (Khalil et al., 2007); and 5) agitation during experiments, which increases dissolution rates compared to stationary sediments (Fabre et al., 2019).

Biodiffusion coefficients: Luminophores were visualized and counted at each sediment layer by image processing (Michaud, 2006). The vertical profiles of luminophores were adjusted to a reaction diffusion type model in order to quantify biological sediment transport (Duport et al., 2006; Oleszczuk et al., 2019) and more specifically the biodiffusion-like transport coefficient (*Db*; $m^2\ d^{-1}$). The best fit between the observed and modelled tracer distribution is estimated by the least-squares method and produces the best *Db* coefficients. Sediment biodiffusion rates and depths were quantified at each station in February, July and October.

2.4 Model parameters

As detailed above, the model contains a large number of parameters that could potentially lead to multiple solutions. In order to reduce uncertainties and ensure the uniqueness of the solution calculated by the model, the strategy was to constrain parameter values with a high number of direct observations and experimental data obtained in this study, as done in (Khalil et al., 2007). All model parameters were determined from measurements and/or inverse modeling and summarized in Tables 1, 2.

Direct observations: Temperature T, salinity S and $Si(OH)_4$ concentrations in overlying water C_{dSi0} were determined from direct measurements and summarized in Table 1. Parameters ϕ_0, ϕ_∞ and $coef_\phi$ were adjusted to fit vertical porosity profile measurements (Table 2).

Assumptions based on experimental data and other measurements (Table 2): Most parameters were obtained from measurements detailed in sections 2.2 and 2.3. The biodiffusion rates D_{b0} and depths z_b were determined from ex situ experiments. Equilibrium concentrations for the two phases were assumed to be identical and equal to deep asymptotic $Si(OH)_4$ concentrations obtained from vertical profiles of $Si(OH)_4$. Based on the dissolution experiments, the proportion of highly reactive $aSiO_2$ in the deposition flux was set to 0.5 as a compromise between the low values ~ 0.3-0.5 - resulting from statistical inverse modeling of dissolution experiments performed on sediments collected in February 2008 (with the model 2 of Moriceau et al., 2009) - and the generally higher values ~ 0.5-0.9 from Khalil et al. (2007). The bioirrigation depths z_{irr} were visually adjusted to the vertically constant portions of $Si(OH)_4$ profiles where fauna was observed. Accumulation rates w were estimated from radionuclide measurements (~ 0.005 cm d^{-1}; Khalil et al., 2018). Reprecipitation rates K_p were set in the range 10^{-5}-10^{-4} d^{-1} because of the high detrital sediment content known to enhance reprecipitation rates (Khalil et al., 2007).

Inverse modeling (Table 2): was performed to estimate the values of undetermined parameters by using the package FME (Soetaert and Petzoldt, 2010). The non-linear fitting procedure using the Levenberg-Marquardt algorithm aims to minimize the sum of squared residuals of model outputs ($aSiO_2$ and $Si(OH)_4$ profiles) versus data and reproduce the curvature of these profiles. The following parameters were estimated: $aSiO_2$ deposition flux, dissolution rates of highly and less reactive $aSiO_2$ and non-local bioirrigation rate. When necessary, final adjustments were performed on the proportion of highly reactive $aSiO_2$ and reprecipitation rates. During the fitting process, upper and lower bounds in the range of expected likely values were imposed for each fitted parameter.

2.5 Benthic budgets

Model outputs (deposition fluxes of less and highly reactive $aSiO_2$, benthic fluxes of $Si(OH)_4$ including diffusion and bioirrigation, burial fluxes, reprecipitation fluxes) were used to build benthic Si budgets and to estimate the seasonal and spatial variation of fluxes at each station of the two estuaries (in mmol $m^{-2}\ d^{-1}$).

2.6 Seasonal and annual Si retention in estuaries

Fluxes of the benthic Si budgets were then extrapolated to the entire surface of each estuary and compared to river Si fluxes and pelagic production. All fluxes are presented in a conceptual scheme (Figure 3).

10.3389/fmars.2023.1269142

TABLE 2 Measured and fitted parameters used in the model for each station and season.

Parameter	Unit	Station						Source
		E1	E2	E3	A1	A2	A3	
February								
ϕ_0	–	0.76	0.84	0.84	0.85	0.86	0.87	obs
ϕ_∞	–	0.73	0.76	0.68	0.76	0.76	0.78	obs
$coef_\phi$	cm^{-1}	0.25	0.25	0.25	0.25	0.25	0.25	obs
D_{b0}	$cm^2\ h^{-1}$	5.71E-05	9.70E-05	6.85E-05	2.85E-06	2.28E-06	3.20E-05	obs
$coef_b$	cm^{-1}	1	1	1	1	1	1	obs
z_b	cm	7.5	7.5	5	0	1.5	2	obs
C_{dSieqF}	$\mu mol\ l^{-1}$	260	325	330	505	400	400	obs
C_{dSieqS}	$\mu mol\ l^{-1}$	260	325	330	505	400	440	obs
w	$cm\ h^{-1}$	2.00E-04	2.00E-04	2.00E-04	2.00E-04	2.00E-04	2.00E-04	obs
p_{aSiF}		0.5	0.5	0.5	0.5	0.5	0.5	obs/fitted
z_{irr}	cm	8	12	15	0	0	10	obs/fitted
α		3.60E-02	1.80E-03	8.64E-04	0.00E+00	0.00E+00	1.15E-03	obs/fitted
K_{aSiF}	h^{-1}	3.46E-05	4.00E-05	2.00E-05	2.08E-04	4.00E-04	2.50E-05	fitted
K_{aSiS}	h^{-1}	3.46E-08	8.33E-06	5.00E-06	1.04E-06	4.17E-07	2.08E-06	fitted
K_p	$\mu mol\ l^{-1}$	1.00E-04	1.00E-07	1.00E-04	1.00E-06	1.00E-03	0.000001	fitted
C_{dSieqP}	$\mu mol\ l^{-1}$	100	200	200	200	200	200	fitted
May								
ϕ_0	–	0.89	0.87	0.85	0.92	0.86	0.91	obs
ϕ_∞	–	0.81	0.74	0.72	0.81	0.62	0.79	obs
$coef_\phi$	cm^{-1}	0.81	0.25	0.27	0.13	0.12	0.86	obs
D_{b0}	$cm^2\ h^{-1}$	9.13E-05	1.35E-04	1.06E-04	5.71E-07	2.28E-06	3.20E-05	obs
$coef_b$	cm^{-1}	1	1	1	1	1	1	obs
z_b	cm	11.25	11.25	7	0.25	2.5	3.25	obs
C_{dSieqF}	$\mu mol\ l^{-1}$	200	300	300	425	365	470	obs
C_{dSieqS}	$\mu mol\ l^{-1}$	200	380	300	425	365	470	obs
w	$cm\ h^{-1}$	2.00E-04	2.00E-04	2.00E-04	2.00E-04	2.00E-04	2.00E-04	obs
p_{aSiF}		0.5	0.5	0.5	0.5	0.5	0.5	obs/fitted
z_{irr}	cm	11	8	11	0	0	7	obs/fitted
α		3.60E-02	7.20E-03	3.60E-02	0.00E+00	0.00E+00	4.32E-02	obs/fitted
K_{aSiF}	h^{-1}	4.17E-04	3.00E-05	5.00E-05	5.00E-05	2.00E-05	3.00E-05	fitted
K_{aSiS}	h^{-1}	4.17E-06	5.00E-07	1.39E-06	5.00E-07	4.17E-07	2.00E-06	fitted
K_p	$\mu mol\ l^{-1}$	1.00E-04	1.00E-05	1.00E-07	1.00E-06	1.00E-03	1.00E-06	fitted
C_{dSieqP}	$\mu mol\ l^{-1}$	200	200	200	200	200	200	fitted
July								
ϕ_0	–	0.88	0.88	0.81	0.93	0.75	0.81	obs
ϕ_∞	–	0.77	0.77	0.72	0.85	0.72	0.75	obs
$coef_\phi$	cm^{-1}	0.16	0.54	0.56	0.25	0.25	0.25	obs

(Continued)

10.3389/fmars.2023.1269142

TABLE 2 Continued

Parameter	Unit	Station						Source
		E1	E2	E3	A1	A2	A3	
D_{b0}	$cm^2\ h^{-1}$	1.26E-04	1.71E-04	1.43E-04	5.71E-07	1.71E-06	1.71E-06	obs
$coef_b$	cm^{-1}	2	2	2	2	2	2	obs
z_b	cm	15	15	9	0.5	3.5	3.5	obs
C_{dSieqF}	$\mu mol\ l^{-1}$	290	275	400	325	260	520	obs
C_{dSieqS}	$\mu mol\ l^{-1}$	290	275	400	325	260	520	obs
w	$cm\ h^{-1}$	2.00E-04	2.00E-04	2.00E-04	2.00E-04	2.00E-04	2.00E-04	obs
p_{aSiF}		0.5	0.5	0.5	0.5	0.5	0.5	obs/fitted
z_{irr}	cm	13	11	8	0	4	7	obs/fitted
α		7.20E-03	1.08E-02	7.20E-03	0.00E+00	6.48E-03	6.12E-03	obs/fitted
K_{aSiF}	h^{-1}	1.00E-04	3.00E-05	6.00E-05	4.00E-05	2.00E-05	4.00E-05	fitted
K_{aSiS}	h^{-1}	2.08E-07	4.17E-06	1.04E-06	1.00E-06	2.08E-06	2.00E-08	fitted
K_p	$\mu mol\ l^{-1}$	5.00E-04	1.00E-06	1.00E-07	1.00E-07	1.00E-05	1.00E-07	fitted
C_{dSieqp}	$\mu mol\ l^{-1}$	200	200	200	200	200	200	fitted
October								
ϕ_0	–	0.90	0.87	0.77	0.90	0.80	0.94	obs
ϕ_∞	–	0.72	0.72	0.72	0.83	0.72	0.79	obs
$coef_\phi$	cm^{-1}	0.18	0.28	0.25	0.10	0.10	1.17	obs
D_{b0}	$cm^2\ h^{-1}$	9.13E-05	1.35E-04	1.06E-04	5.71E-07	2.28E-06	3.20E-05	obs
$coef_b$	cm^{-1}	2	2	2	2	2	2	obs
z_b	cm	11.25	11.25	7	0.25	2.5	3.25	obs
C_{dSieqF}	$\mu mol\ l^{-1}$	320	300	425	250	285	420	obs
C_{dSieqS}	$\mu mol\ l^{-1}$	320	300	425	250	285	420	obs
w	$cm\ h^{-1}$	2.00E-04	2.00E-04	2.00E-04	2.00E-04	2.00E-04	2.00E-04	obs
p_{aSiF}		0.5	0.5	0.5	0.5	0.5	0.5	obs/fitted
z_{irr}	cm	19	12	6	0	5	8	obs/fitted
α		6.12E-03	6.12E-03	8.00E-03	0.00E+00	9.00E-03	1.80E-03	obs/fitted
K_{aSiF}	h^{-1}	2.00E-05	3.00E-05	2.00E-05	2.00E-05	1.07E-05	2.00E-05	fitted
K_{aSiS}	h^{-1}	2.08E-07	4.17E-06	1.00E-06	8.33E-07	2.08E-07	1.00E-06	fitted
K_p	$\mu mol\ l^{-1}$	2.00E-04	1.00E-05	1.00E-05	1.00E-05	1.00E-05	1.00E-07	fitted
C_{dSieqp}	$\mu mol\ l^{-1}$	200	200	200	200	200	200	fitted

River Si fluxes were determined as the sum of $Si(OH)_4$ and $aSiO_2$ fluxes. $Si(OH)_4$ fluxes were estimated as the product of weekly $Si(OH)_4$ concentrations (from the citizen-science network ECOFLUX; Abbott et al., 2018) by weekly river flow (from Banque Hydro) at the outlet of Elorn and Aulne rivers. $aSiO_2$ fluxes were estimated as the product of seasonal $aSiO_2$ concentrations (this study) by the same weekly river flow. Weekly fluxes were summed to obtain seasonal and annual fluxes.

Deposition, burial and benthic $Si(OH)_4$ fluxes were estimated by multiplying modelled fluxes at the 3 stations of the 2 estuaries (section 2.5) by the estuary surface of each estuarine section in order to estimate the retention of Si in the estuaries (in kmol) at the seasonal and annual scales. The surface of spatial integration for the 3 stations in each estuary was determined using a GIS-based approach (Khalil et al., 2018).

Burial fluxes in tidal saltmarshes were estimated for saltmarshes invaded and non-invaded by *Spartina alterniflora* in the Elorn estuary (Querné, 2011). The ratio of intertidal burial over subtidal burial was calculated for the Elorn estuary (0.69) and used to estimate intertidal burial in the Aulne estuary.

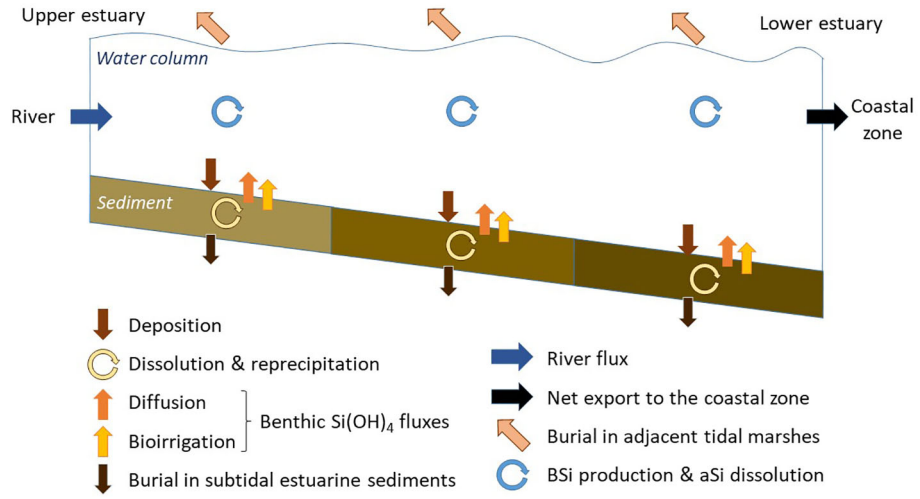

FIGURE 3
Conceptual scheme presenting fluxes of the Si budget along the estuary. The size of arrows is not proportional to quantified fluxes.

Export was the difference between river fluxes and burial (in subtidal sediments and in intertidal saltmarches).

Pelagic primary production was estimated as the sum of pelagic production rates (measured in this study at salinity 0, 5, 10, 15, 20, 25 and 30) vertically integrated on the seven estuarine boxes in each estuary for each season. Incubations were performed at *in situ* conditions (temperature, attenuated light) for 24h with ^{14}C tracer following the method of Le Bouteiller et al. (2003). The range of pelagic BSi production rates was estimated by multiplying carbon primary production rates by the Si:C factor of 0.03 and 0.13. The factor 0.13 is characteristic of 100% diatoms and preservation, while 0.03 is used to consider that only 25% is related to diatoms and/or preserved. The volume of spatial integration was described with a power function (Eq. 9; Soetaert et al., 2006) and validated with morphological observations (Bassoulet, 1979; Google Map©; this study).

$$x = x_{riv} + (x_{riv} - x_{sea})\frac{x^a}{x^a + (ks_a)^a} \quad (9)$$

with x is the estuary volume. x_{riv} and x_{sea} are the values at the freshwater and marine water end-members of the estuary, respectively. The exponent *a* regulates the steepness of the relationship.

3 Results

3.1 $Si(OH)_4$, $aSiO_2$ and Chl *a* in estuarine waters

Temporal changes of $Si(OH)_4$ loads at the freshwater end-member

The $Si(OH)_4$ concentrations at the freshwater end-member (station E1 and A1) were similar in Elorn and Aulne from December to April (140 ± 29 and 140 ± 22 µmol l^{-1}, respectively), but were higher in Elorn from May to September (203 ± 15 and 108 ± 31 µmol l^{-1}, respectively; Figure 2D).

The $Si(OH)_4$ fluxes at the freshwater end-member were higher 1) in winter when the river flow increased, and 2) in the Aulne River from December to April (42 ± 30 t d^{-1} for the Aulne River, versus 7 ± 5 t d^{-1} for the Elorn River; Figure 2E). The fluxes were lower and more similar from May to October (5 ± 4 t d^{-1} in the Aulne River versus 2 ± 1 t d^{-1} in the Elorn River), but they were occasionally higher at the mouth of the Elorn River in July and October (Figure 2E). The relative contribution of the Aulne River to the $Si(OH)_4$ fluxes in the Bay of Brest ranged from a minimum of 40% in summer to a maximum of 80% in winter.

Seasonal distributions of $Si(OH)_4$, $aSiO_2$, and Chl a concentrations along the estuaries

The $Si(OH)_4$ concentrations behaved almost conservatively and continuously decreased along the salinity gradients of both the Elorn and Aulne estuaries at all seasons except July (Figure 4A). In the Elorn Estuary, the $Si(OH)_4$ concentrations were similar at these three seasons. In the Aulne Estuary, the $Si(OH)_4$ concentrations at the freshwater end-member decreased from fall/winter to spring/summer, leading to seasonal variations of the slope. In summer, the curve was no longer conservative, which suggested $Si(OH)_4$ consumption in both estuaries. Note that the $Si(OH)_4$ (and $aSiO_2$; Figure 4B) concentrations at the freshwater end-member in the Elorn Estuary were lower than at salinity 5 in February. This non conservative profile resulted probably from the transient increase of river flow (Figure 2C) as explained by Regnier et al. (1998).

In both estuaries, the $aSiO_2$ concentrations decreased with increasing salinity at all seasons, except July (Figure 4B). In the Aulne Estuary, a steep decrease of $aSiO_2$ concentrations occurred between salinity 0 and 5. The highest $aSiO_2$ concentrations were observed in July and reached a maximum at the salinity range of 5-15 (data not available for the Elorn Estuary).

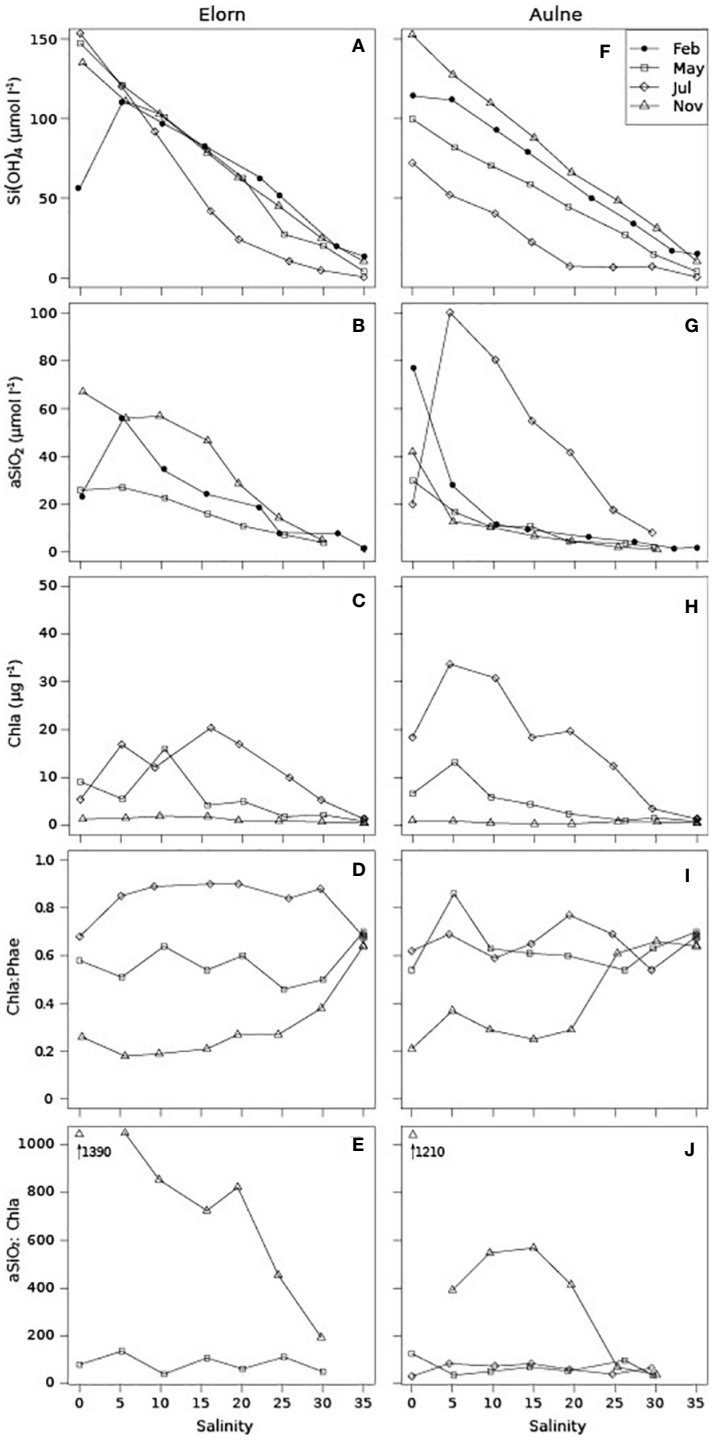

FIGURE 4
Pelagic $Si(OH)_4$, $aSiO_2$ and Chl *a* concentrations, Chl *a*: (Chl *a*+Phea) ratios, and $aSiO_2$: Chl *a* ratios, along the Elorn Estuary **(A–E)** and the Aulne Estuary **(F–J)**, in February, May, July and November 2009.

In spring and summer, maximal concentrations of Chl *a* were generally observed between salinity 5 and 20, as observed for $aSiO_2$ concentrations in July. In November, Chl *a* concentrations were low and constant with salinity, which completely differed from the high and decreasing $aSiO_2$ concentrations. In both estuaries, the Chl *a*: (Chl *a*+Phae) ratios were higher in spring/summer than in winter and reached an annually constant marine end-member ratio in the range 0.6-0.7 (Figure 4D). The $aSiO_2$:Chl *a* ratios were low in spring/summer and very high in winter, especially in upper estuaries (Figure 4E).

3.2 Surface sediments $aSiO_2$ and Chl *a* along estuaries

The $aSiO_2$ concentrations were in the range 0.5-3% in the surface sediments (Figure 5A). At each season, they decreased from upstream to downstream in the Elorn Estuary, and they were minimal at the intermediate station in the Aulne Estuary (Figure 5A). At all stations, surface Chl *a* concentrations increased from February to July, and then decreased in November (Figure 5B). The Chl *a*:(Chl *a*+Phae) ratios were always > 0.4 (Figure 5C). The $aSiO_2$:Chl *a* ratios decreased from February to July regardless of station, and from upstream to downstream in winter (Figure 5D).

3.3 Benthic Si cycle along estuaries: data and modeling

Observed and simulated $aSiO_2$ and $Si(OH)_4$ profiles

The observed $aSiO_2$ profiles were vertically constant with small discontinuities along the sediment cores. The model represented well the range of $aSiO_2$ concentrations but failed to reproduce the small vertical heterogeneities. Although variable between stations, $Si(OH)_4$ concentrations in general increased with depth (Figure 6; black circles). A regular hyperbolic profile, commonly observed in stable or oceanic sediments, was observed at station A1, while stations E1, E2, E3, and A3 showed concentrations that became stable over the first centimeters (of variable thickness) which then increased again at greater depths. In general the model provided a good fit to the observed $Si(OH)_4$ trends, with the exception of the subsurface maxima of $Si(OH)_4$ concentrations observed at station A2 in February and May (Figure 6).

Estimated and calibrated parameters

The biodiffusion rates of sediments (obtained from core incubations with luminophores) increased from February to July (Table 2). These rates were higher in the Elorn (1-4 10^{-7} m^2 d^{-1}) than in the Aulne Estuary (< 1 10^{-7} m^2 d^{-1}), and they were almost null at stations A1 and A2. The bioirrigation rates varied relatively similarly to biodiffusion rates (Table 2). The calibrated dissolution rates of the less reactive $aSiO_2$ were in the range 10^{-5}- 2 10^{-4} d^{-1} (Table 2). The lowest rates were observed at stations E1 and A2. The calibrated dissolution rates of the highly reactive $aSiO_2$ were in the range 10^{-3}- 2 10^{-2} d^{-1} (Table 2), and generally increased from February to July or October; however, at stations A1 and A2, the highest rates were found in February. Reprecipitation rates generally varied between 10^{-5} and 10^{-4} d^{-1}.

Simulated fluxes

The simulated deposition fluxes of $aSiO_2$ were in the range 2-4.5 mmol m^{-2} d^{-1}, regardless of season and station (Figure 7A). In both estuaries, maximal deposition fluxes were observed upstream of the estuaries in winter, and midstream/downstream during other seasons. The burial fluxes of the less and highly reactive $aSiO_2$ were 25-80% of the deposition flux of $aSiO_2$ (Figures 7B, C, 8). In the Elorn Estuary and at station A3, the proportion of burial decreased from winter to summer. This decrease was due to an increase of sediment-water $Si(OH)_4$ effluxes by diffusion and non-

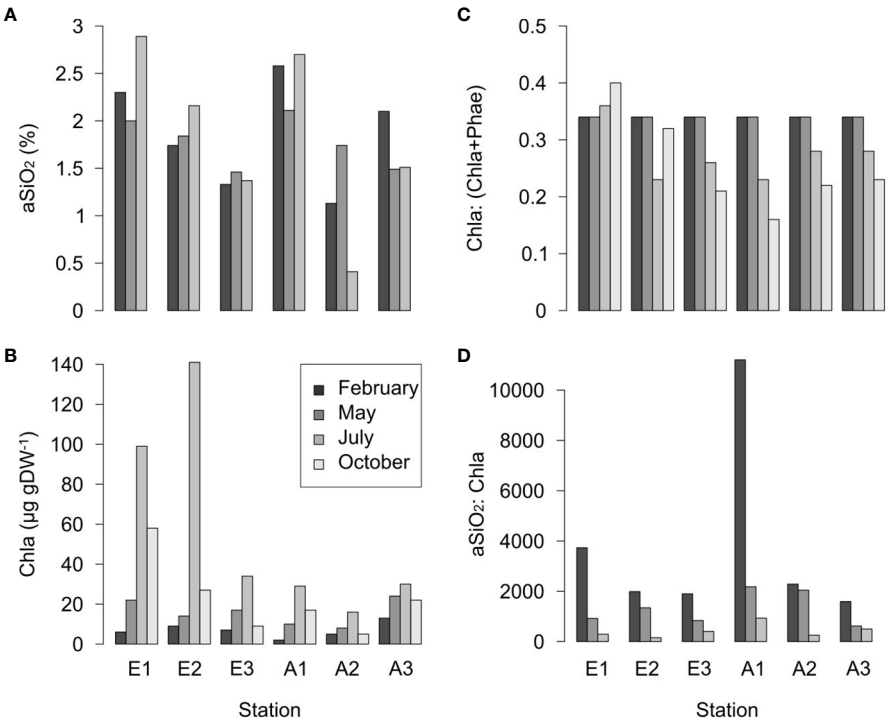

FIGURE 5
(A) $aSiO_2$ content (%), **(B)** Chl *a* concentrations (µg l^{-1}), **(C)** Chl *a*: (Chl *a*+Phea) and **(D)** $aSiO_2$: Chl *a* ratios measured at each season (February, May, July, October 2009) in superficial sediments at the stations 1, 2 and 3 (n = 3) of the Elorn and Aulne estuaries.

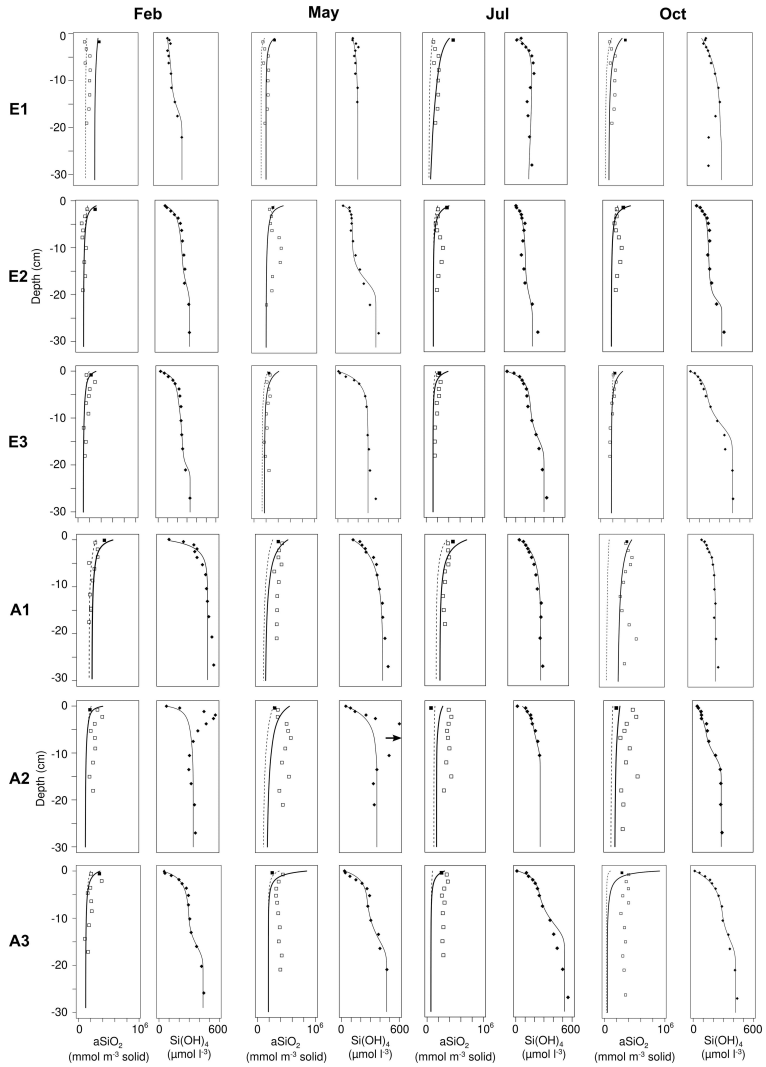

FIGURE 6
$Si(OH)_4$ and $aSiO_2$ concentrations in benthic sediments at each station (1, 2, 3) of Elorn and Aulne estuaries in February, May, July and October 2009. Both data from 2008 (cross) and 2009 (points) and model outputs (lines) are represented. For $aSiO_2$, the continuous line represents the total concentration while the dashed line represents the less reactive fraction.

local bioirrigation, with a generally higher contribution of bioirrigation (Figures 7E, F). The decrease of burial fluxes in summer is not observed at stations A1 and A2, where bioirrigation is low. Reprecipitation fluxes were generally < 5% regardless of station and season (Figures 7D, 8).

3.4 Seasonal and annual Si retention in Elorn and Aulne estuaries

The Aulne river-estuary had a larger contribution than the Elorn river-estuary to all fluxes because of the larger size of its watershed and estuary. The Table 3 summarizes the estuarine Si budget and retention for the Elorn, Aulne and the two estuaries, at seasonal and annual scales.

As previously observed (Figure 2E), total Si river fluxes are two to three orders of magnitude higher in winter (134074 kmol per season) than in summer (8417 kmol per season). The Si loads are dominated by $Si(OH)_4$ in both estuaries (64 to 90% from winter to summer). Compared to the Elorn river, the Aulne river brings 66 to 90% of river Si fluxes to the Bay of Brest from summer to winter.

Deposition fluxes are similar for all seasons (8570-10784 kmol per season) but strongly vary from 6% of river loads in winter to more than 100% during summer.

Recycling leads to benthic fluxes of $Si(OH)_4$ ranging from 3585 kmol in winter to 6409 kmol in summer. Bioirrigation accounts for 46% of benthic fluxes (15-68%), with stronger bioirrigation in the Elorn estuary (64-68%) than in the Aulne estuary (15-34%). During summer, benthic recycling (6409 kmol) provides a quantity of $Si(OH)_4$ close to river fluxes (7348 kmol $Si(OH)_4$; 87% of 8417 kmol total Si).

The reprecipitation flux is low and negligible with 168 kmol per year for the two rivers.

Burial in subtidal sediments accounts for 10-39% of river Si loads in the Elorn estuary and 3-38% in the Aulne estuary, from

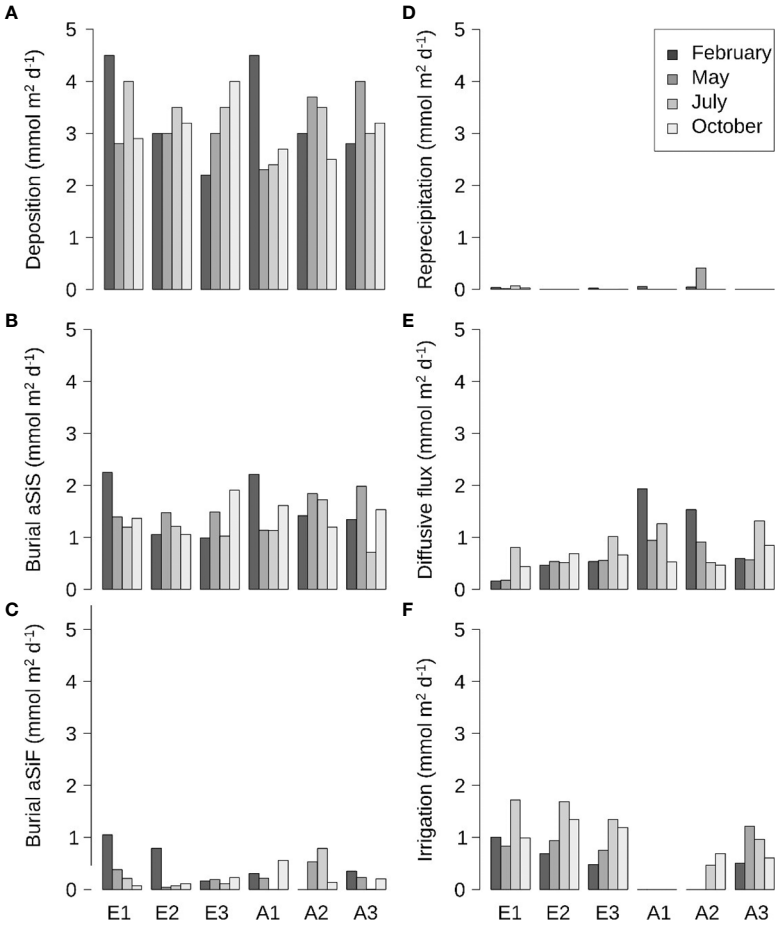

FIGURE 7
Benthic Si budget: **(A)** deposition flux of $aSiO_2$, **(B)** burial flux of less reactive $aSiO_2$, **(C)** burial flux of highly reactive $aSiO_2$, **(D)** reprecipitation flux, **(E)** benthic diffusive flux of $Si(OH)_4$, and **(F)** non-local bioirrigation flux, for stations E1, E2, E3, A1, A2 and A3 at all seasons.

winter to summer. Burial in tidal marshes is estimated to ~2/3 of subtidal burial (based on data on the Elorn estuary; Querné, 2011). Including burial in tidal marshes leads to an estimated burial of 17-41% of river Si loads in the Elorn estuary and 16-64% in the Aulne estuary.

Finally, export is high during winter and fall (125 649 kmol; 93% of river flux; 51% of annual export flux), but lower during summer (2 779 kmol; 33% of river flux; 1% of annual export flux).

4 Discussion

4.1 Seasonality of $aSiO_2$ deposition and quality along Elorn and Aulne estuaries

In this study, steady-state diagenetic modeling is used to quantify the averaged benthic processes at seasonal scale along two estuaries. Modeling is particularly efficient for determining the deposition fluxes, which otherwise are very difficult to assess by direct measurements (Ridd et al., 2001). Regardless of the station and season, the deposition fluxes in the Elorn and Aulne estuaries (2-4.5 mmol m^{-2} d^{-1}; Figure 7A) are in the same order of magnitude than in the seaward Bay of Brest (0.6-3 mmol m^{-2} d^{-1}; Ragueneau et al., 2005a). These high deposition fluxes are consistent with the high accumulation rates measured through radionuclide measurements that constrain the model (Khalil et al., 2018). High deposition and accumulation of $aSiO_2$ are generally observed seaward in large rivers (e.g., the Amazon, Congo, and Yangtze rivers; DeMaster et al., 1985; Shiller, 1996; Raimonet et al., 2015) that have high river flow rates. In contrast, in our study, the $aSiO_2$ deposition fluxes are high in the estuary due to lower river flow rate and the semi-enclosed shape of the system. These deposition fluxes calculated in the macrotidal Aulne and Elorn estuaries are in the range of values determined for the macrotidal Scheldt river and estuary: from ~0.028-0.034 mmol m^{-2} d^{-1} in subtidal sediments in the Scheldt river (Carbonnel et al., 2009), to ~1.6 mmol m^{-2} d^{-1} in marsh sediments in the Scheldt estuary (Struyf et al., 2006) and a maximum of 8 mmol m^{-2} d^{-1} in subtidal sediments in the Scheldt river/estuary (Arndt and Regnier, 2007).

In this study, maximal deposition fluxes are observed upstream of the estuaries during winter, which is mostly related to higher $aSiO_2$ river concentrations and fluxes. High $aSiO_2$ concentrations and fluxes brought to the estuary are related to enhanced soil weathering and river flows (Figure 2C), as previously reported by

10.3389/fmars.2023.1269142

TABLE 3 River Si fluxes compared to deposition, benthic fluxes including bioirrigation, reprecipitation, subtidal and tidal marsh burial, and export (kmol per year and per season) for the Elorn and Aulne estuaries.

	Total Elorn+Aulne					Elorn					Aulne				
	Annual	Winter	Spring	Summer	Autumn	Annual	Winter	Spring	Summer	Autumn	Annual	Winter	Spring	Summer	Autumn
River flux	277321	134074	24262	8417	110568	35239	13349	5163	2855	13872	242081	120724	19099	5562	96696
including $Si(OH)_4$ flux	80%	75%	83%	87%	75%	83%	85%	86%	90%	69%	77%	64%	80%	85%	81%
Deposition	38944	8570	10784	9622	9967	11973	2311	2808	3303	3551	26971	6259	7976	6319	6416
Benthic fluxes	19135	3585	4586	6409	4555	6207	990	1259	2194	1764	12929	2595	3328	4215	2791
including bioirrigation	46%	40%	45%	49%	50%	66%	64%	68%	67%	66%	25%	15%	23%	30%	34%
Reprecipitation	168	40	120	3	5	24	16	1	2	4	144	24	119	1	1
Subtidal burial	19639	4944	6078	3210	5407	5742	1304	1548	1107	1783	13897	3639	4530	2104	3625
Tidal marsh burial	*13473*	*3481*	*4092*	*2428*	*3471*	3939	*985*	*985*	*985*	*985*	*9534*	*2496*	*3108*	*1443*	*2486*
Export	*244209*	*125649*	*14092*	*2779*	*101689*	*25558*	*11060*	*2630*	*764*	*11105*	*218650*	*114588*	*11462*	*2015*	*90585*

Smis et al. (2011). These winter deposition fluxes are associated with detrital $aSiO_2$, as shown by high $aSiO_2$:Chl *a* and low Chl *a*:(Chl *a* +Phae) benthic ratios (Figure 5).

Deposition is observed more downstream and all along the estuary in spring and summer. The matter deposited then is also more reactive because of a higher contribution of riverine and estuarine, pelagic and benthic, primary production, stimulated by increasing light and temperature, often observed in estuaries (Heip et al., 1995).

The increase in river primary production (either benthic and/or pelagic) is highlighted by a decrease in $Si(OH)_4$ concentrations (consumption) and an increase in Chl *a* concentrations at the freshwater end-members from winter to summer (Figures 2, 4). This riverine material generally settles before salinity 5 (Anderson, 1986) and fuels deposition in the upper estuary.

The contribution of estuarine pelagic primary production to $aSiO_2$ deposition in the two estuaries is highlighted by an increase in Chl *a* and $aSiO_2$ concentrations in the water column at salinity 5-20, and decreasing $aSiO_2$: Chl *a* ratios (Figures 4, 5), as well as production estimates along estuaries (estimated to be 57-225 10^3 mol d^{-1} from incubations performed in this study). Benthic primary production (subtidal or intertidal by lateral transport) are suggested by the Chl *a* concentrations in surface sediments at stations E1 and E2 that are 4-15 times higher than in Aulne Estuary in summer, whereas Chl *a* concentrations in the water column are similar in both estuaries. This pelagic and benthic production must have settled inside the estuary depending on tidal range and river flow.

The relatively low increase of deposition fluxes during summer compared to winter (Figure 7A), as well as lower benthic than pelagic Chl *a*:(Chl *a*+Phae) ratios in summer (Figures 4D, 5C), also suggest the enhancement of pelagic dissolution in summer; dissolution increases the degradation state of deposited $aSiO_2$ and decreases the quantity of $aSiO_2$ at the sediment-water interface. Pelagic dissolution has been estimated to account for ~ 50% of pelagic $aSiO_2$ production in the Bay of Brest (Beucher et al., 2004) and > 80% in estuaries reaching the Chesapeake Bay (Anderson, 1986), and is expected to be enhanced by bacterial degradation in estuaries (Roubeix et al., 2008a). Moreover, the constant benthic Chl *a*:(Chl *a*+Phae) ratios observed from winter to spring, which decrease during the summer and co-occur with the highest pelagic ratios, suggests enhanced benthic macrofauna grazing (Cariou-Le Gall and Blanchard, 1995), alterations caused by light (Nelson, 1993) and redox conditions (Sun et al., 1993). All of these results confirm the estimation of 50% highly reactive $aSiO_2$ calculated through an inverse statistical method (Moriceau et al., 2009) and used in our diagenetic model of benthic Si cycle.

4.2 Seasonal benthic Si budgets along estuaries

As suggested in the previous section, deposition fluxes are tightly related to seasonal changes of river fluxes, detrital loads, benthic and pelagic primary production, and/or lateral transport. Once $aSiO_2$ is deposited at the sediment-water interface, benthic

processes lead either to the return of Si to the water column through dissolution and/or bioirrigation, or to its sequestration in sediments through burial and/or reprecipitation.

The formation of $Si(OH)_4$ through benthic recycling is known to potentially suffer reverse weathering in benthic sediments (Michalopoulos and Aller, 2004). Indeed, very high reprecipitation has even been reported in high-detrital sediments of the subtropical Amazon delta, in which ~ 90% of initial benthic $aSiO_2$ has been converted to clay (Michalopoulos and Aller, 2004), or in the Mississippi River Delta, where it accounts for ~ 40% of Si storage (Presti and Michalopoulos, 2008) or in the Barentz Sea (37% at station B13; Ward et al., 2022). In our study, the reprecipitation processes are limited, and reprecipitation fluxes estimated by the model are < 5% of deposition fluxes regardless of station (Figure 8). This is consistent with the values found in the Scheldt Estuary (Rebreanu, 2009). Laboratory experiments are however needed to confirm our model estimates.

The high burial fluxes determined in this study may be linked to 1) high deposition fluxes related to high $aSiO_2$ fluxes coming from rivers (high concentrations during high river flow; Figures 2C, 4B), 2) high detrital and aluminium contents, which increase $aSiO_2$ preservation (Van Cappellen et al., 2002), 3) the macrotidal regime and associated resuspension events, which increase recycling in the water column (Gehlen and Van Raaphorst, 2002), which decreases $aSiO_2$ reactivity, and 4) bioturbation and more specifically sediment mixing, which increases the transfer of newly settled $aSiO_2$ deeper in the sediment and increases its preservation, as observed in organic matter (Aller and Mackin, 1984). Such high burial rates have already been observed in highly accumulating zones, e.g., Antarctic sediments in which one third of $aSiO_2$ deposited accumulates in sediments (Pondaven et al., 2000; DeMaster, 2002). On the contrary, estuaries of large rivers (e.g., Amazon, Congo) have low retention due to export to the coastal margins where deposition and accumulation take place (Michalopoulos and Aller, 2004; Dürr et al., 2011; Raimonet et al., 2015).

In summer, the estimated fluxes are similar to those observed within the Bay of Brest during the productive period, where burial fluxes were estimated to be ~ 32% (Ragueneau et al., 2005a). However, distinct processes cause these similar proportions. In the Bay of Brest, the absence of total recycling is explained by the presence of an invasive filter feeder species, *Crepidula fornicata*, that increases $aSiO_2$ preservation in sediments through 1) its incorporation in feces covered by organic matter, and 2) the presence of aluminium-rich sediments (Ragueneau et al., 2005a). In the Elorn and Aulne estuaries, invasive species are absent at the sediment-water interface, and the high burial fluxes are instead explained by the enhanced preservation due to high aluminium and detrital contents (Van Cappellen et al., 2002), high deposition rates (Aller and Mackin, 1984; Conley and Johnstone, 1995), and burrowing depth reaching more than 20 cm in depth.

During the productive period, particularly during summer, the increased proportion of $Si(OH)_4$ fluxes associated to dissolution and bioirrigation (> 60%; Figure 8) compared to burial fluxes is explained by the enhancement of dissolution rates by temperature (Kamatani, 1982; Ragueneau et al., 2002a) as well as deposition of more reactive (autochthonous) material, and bioirrigation (Green et al., 2004).

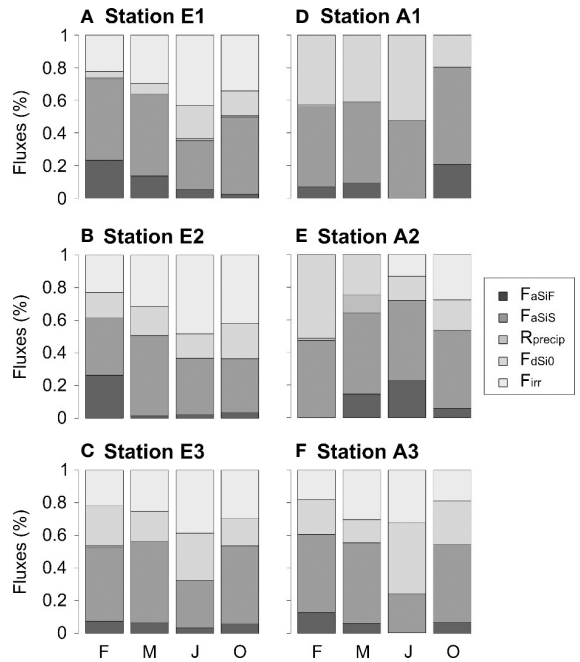

FIGURE 8
Benthic Si budget: proportion of each flux in February, May, July and October (noted F, M, J and O, respectively), for **(A)** station E1, **(B)** station E2, **(C)** station E3, **(D)** station A1, **(E)** station A2 and **(F)** station A3.

4.3 Seasonal contribution of benthic silica cycle to the estuarine filter

First, our study confirms the importance to include $aSiO_2$ when investigating Si retention in estuaries (Carbonnel et al., 2013) or building global silica budgets (Tréguer et al., 2021).

Regardless of the method used, estuarine budgets do not generally explicitly account for the benthic ecosystem in estuaries, due to the assumed small contribution of benthic fluxes compared to that of river fluxes (Arndt et al., 2009). However, benthic sediments may be subject to non-local transport associated with bioirrigation, which is known to strongly increase benthic $Si(OH)_4$ fluxes at the sediment-water interface (Marinelli, 1992; Forja and Gómez-Parra, 1998), and this is also observed in our study (~50%). Although Arndt and Regnier (2007) have recently analytically resolved benthic processes in a reactive-transport silica model which couples benthic and pelagic processes, methods used to estimate estuarine Si budgets do not vertically resolve the nonlocal benthic processes, e.g., bioirrigation. Contrary to reactive-transport modeling of water column processes, which provides high spatio-temporal resolution, the goal of the present study is to precisely investigate benthic processes in Elorn and Aulne estuary sediments in order to build Si budgets. Our results show the usefulness to incorporate irrigation effects in reactive-transport modeling along estuaries.

During winter floods, the high river flows increase the $aSiO_2$ and $Si(OH)_4$ river fluxes to both estuaries as well as the export to the coastal waters (Table 3). This transient and high export of particulate matter, mostly detritic (see section 4.1), has previously been observed in this ecosystem for organic matter (Savoye, 2001). The increase in river flow also decreases the contribution of benthic $Si(OH)_4$ fluxes (2.7%), $aSiO_2$ burial (3.7%) and $aSiO_2$ deposition fluxes (6.4%) compared to $aSiO_2$ river fluxes. These results confirm that generally low benthic-pelagic coupling occurs during high river flow conditions (Eyre and Ferguson, 2006).

From winter to summer, the drop in the river flow reduces $aSiO_2$ and $Si(OH)_4$ fluxes and increases water residence times throughout the estuary. The $aSiO_2$ deposition becomes higher than river fluxes (Table 3), which highlights that other sources become significant in fueling the sediment-water interface: not only river loads, but also pelagic primary production in the estuary, lateral transport from intertidal sediments or from mixing of marine waters.

First, the $aSiO_2$ deposition fluxes are enhanced by the increase in pelagic primary production in summer. This is highlighted by the high Chl *a* concentrations measured in May and even more in July (from 6 to 35 $\mu g\ l^{-1}$ along the salinity gradient; Figure 4C). Note that these concentrations are higher than those in the Bay of Brest (generally < 10 $\mu g\ l^{-1}$ even during blooms, except a maximum of 21 $\mu g\ l^{-1}$ observed in 1981; Chauvaud et al., 2000), and that even higher concentrations have already been measured in these estuaries during summer (88 and 46 $\mu g\ l^{-1}$; Savoye, 2001). In this study, the extrapolation of the pelagic primary production measurements in the Aulne Estuary allows us to roughly estimate a total pelagic primary production of ~ 57-225 10^3 mol d^{-1}. This estimate is slightly lower than the production of 448 10^3 mol d^{-1} estimated in the Bay of Brest (Ragueneau et al., 2002a). However, this estimation is close to the deposition flux (107 10^3 mol d^{-1}; Table 3), which consequently appears to be related to pelagic production. Since dissolution also occurs in estuarine waters (accounting for 20-80% of pelagic $aSiO_2$ recycling; DeMaster et al., 1983; Ragueneau et al., 2002b; Beucher et al., 2004), it follows that other sources must also contribute to the deposition flux of $aSiO_2$. This exercise highlights the importance of directly quantifying the pelagic silica dissolution rates in estuaries to better constrain their budgets. In the Bay of Brest, pelagic dissolution rates were shown to recycle ~ 50% of $aSiO_2$ production annually (Beucher et al., 2004), but these rates could be even higher throughout estuaries because of enhanced $aSiO_2$ dissolution by bacterial degradation of organic coatings (Roubeix et al., 2008a).

As suggested in section 4.1., other possible sources of deposited $aSiO_2$ are benthic primary production, lateral resuspension and redistribution of particles from tidal mudflats and small water outlets. The high deposition fluxes of estuarine materials are particularly highlighted by benthic Chl *a* concentrations (140 $\mu g\ gDW^{-1}$; Figure 5B) that are much higher than those already reported in the Bay of Brest (Ragueneau et al., 1994; Sagan and Thouzeau, 1998; Ni Longphuirt et al., 2006). Such high Chl *a* (or fucoxantin) concentrations have previously been reported to mirror the higher pelagic and benthic production taken place in estuaries, the lateral resuspension and redistribution of particles, with the higher deposition rates related to a shallower water column (Sun et al., 1994; Mangalaa et al., 2017; Wallington et al., 2023). Marine loads might be low due to the absence of a connection between estuarine and coastal waters observed in the Elorn and Aulne estuaries (Savoye, 2001), except in the downstream parts of these estuaries where marine materials are more significant (Khalil et al., 2013). Marine $aSiO_2$ loads can however be much higher in some estuaries; for instance, it reaches 25% in the Scheldt estuary (Carbonnel et al., 2013).

The relative contribution of benthic $Si(OH)_4$ fluxes compared to river fluxes is consequently enhanced (Figure 8), which highlights the important role of benthic recycling to the pelagic ecosystem, especially in summer. Even if benthic fluxes are generally lower compared to river fluxes in large estuaries (Arndt et al., 2009), their contribution can become significant in small and shallow estuaries (Anderson, 1986), such as in the Elorn and Aulne, as well as during the low-flow season (this study). The contribution of benthic fluxes to the pelagic ecosystem in summer is higher in the Aulne than in the Elorn Estuary, not just due to the lower river flow, but also due to the higher benthic surface of the Aulne Estuary and its meandering shape (Raimonet et al., 2013a).

Finally, this work bring new data on Si retention in small macrotidal estuaries, at seasonal and annual scales. While retention is ≤ 5% of river Si flux in winter, it increases to 38% in summer, and even 67% when accounting for burial in intertidal mudflats (Table 3). The annual burial of Si in the Elorn and Aulne estuaries is estimated to be 7% in subtidal sediments, and 12% when accounting for intertidal mudflat burial. These estimates are similar for the two estuaries, but lower than a ten times bigger estuary, the Scheldt estuary, where annual retention of $Si(OH)_4$ and $aSiO_2$ are estimated to attain 28% and 64%, respectively (Carbonnel et al., 2013). Such difference is expected because of (1) higher water residence time in the Scheldt estuary, which increases retention and limits flushing, and (2) intense dredging activity, which reduce sediment export to the coastal zone (Carbonnel et al., 2013). In this study, we gathered and measured a large number of data to better constrain and limit uncertainties on our estimates. Our values could however be refined, e.g. by coupling our results with a hydro-sedimentary model e.g. Grasso et al. (2018) in order to quantify retention at a fine spatial and temporal scale. This could help in quantifying the spatial heterogeneity and the transient regime of erosion and export of estuarine sediments.

5 Conclusions

Diagenetic modeling accounting for two reactive $aSiO_2$ phases, as well as reprecipitation and bioirrigation processes, is a useful tool for determining benthic Si fluxes, e.g., deposition fluxes that are difficult to measure *in situ* in estuaries. The Elorn and Aulne tidal estuaries are characterized by high deposition and burial fluxes throughout the year, indicating the high potential retention in these estuaries. Benthic recycling increases from winter to summer. A representation of bioirrigation appears necessary in such bioirrigated estuarine sediments in order to account for the doubling of benthic fluxes at the sediment-water interface.

Reprecipitation is expected to be insignificant in the Elorn and Aulne estuaries, but this result should be confirmed through laboratory experiments. An investigation into the sediment dynamics in these estuaries and the importance of mudflats in estuarine retention would be of interest. In this study, the functioning of small and shallow tidal estuaries (Elorn and Aulne) is shown to be dominated by river inputs and export during high river flow conditions, and by estuarine internal recycling during summer. The application of a transport-reaction model accounting for benthic-pelagic coupling appears useful for quantifying the spatio-temporal variations of the benthic Si cycle (and carbon, nitrogen, and phosphorus cycles) along estuaries, and for investigating the impact of small scale variations (biological and physical processes) on the general functioning of the ecosystem.

Data availability statement

The raw data supporting the conclusions of this article will be made available by the authors upon request to interested researchers.

Ethics statement

The manuscript presents research on animals that do not require ethical approval for their study.

Author contributions

MR: Conceptualization, Data curation, Formal analysis, Investigation, Methodology, Project administration, Software, Validation, Visualization, Writing – original draft, Writing – review & editing. OR: Conceptualization, Funding acquisition, Investigation, Methodology, Project administration, Resources, Validation, Writing – review & editing. KS: Conceptualization, Resources, Writing – review & editing, Methodology, Software, Validation. KK: Writing – review & editing, Data curation. AL: Data curation, Writing – review & editing, Investigation, Methodology. EM: Data curation, Investigation, Methodology, Writing – review & editing. BM: Data curation, Investigation, Methodology, Writing – review & editing. CR: Investigation, Writing – review & editing. LM: Writing – review & editing, Conceptualization, Funding acquisition, Resources.

Funding

The author(s) declare financial support was received for the research, authorship, and/or publication of this article. This work was supported by the French National Program for Coastal Environment (PNEC-EC2CO), and the salaries of MR and EM were funded by the Ministère de l'Enseignement Supérieur et de la Recherche and the Conseil général du Finistère, respectively. Publication fees were partly funded by the Agence Nationale de la Recherche (ANR-23-CE03-0004-01).

Acknowledgments

We gratefully thank all the participants of the project, including the R/V *Côtes de la Manche* crew, Manon Le Goff, Bruno Bombled, Agnès Youenou, Françoise Andrieux-Loyer, Xavier Philippon, Florian Caradec for their valuable help for cores sampling and processing, Marie Czamanski, Solène Mineau, Tualenn Le Roch and Rudolph Corvaisier for their contribution to $aSiO_2$ measurements, Erwan Amice and Robert Marc for their helpfull assistance on board the *Hésione* (IUEM), Francois Maguer, Stéphane L'Helguen, Claire Labry, Daniel Delmas for surface water sampling, the ECOFLUX network (IUEM/Conseil Général du Finistère) for river flux data. For the purpose of Open Access, a CC-BY public copyright license has been applied by the authors to the present document and will be applied to all subsequent versions up to the Author Accepted Manuscript arising from this submission.

Conflict of interest

The authors declare that the research was conducted in the absence of any commercial or financial relationships that could be construed as a potential conflict of interest.

Publisher's note

References

Abbott, B. W., Moatar, F., Gauthier, O., Fovet, O., Antoine, V., and Ragueneau, O. (2018). Trends and seasonality of river nutrients in agricultural catchments: 18years of weekly citizen science in France. *Sci. Total Environ.* 624, 845–858. doi: 10.1016/j.scitotenv.2017.12.176

Aller, R. C., and Mackin, J. E. (1984). Preservation of reactive organic matter in marine sediments. *Earth Planetary Sci. Lett.* 70, 260–266. doi: 10.1016/0012-821X(84)90010-4

Anderson, G. F. (1986). Silica, diatoms and a freshwater productivity maximum in Atlantic Coastal Plain estuaries, Chesapeake Bay. *Estuarine Coast. Shelf Sci.* 22, 183–197. doi: 10.1016/0272-7714(86)90112-5

Andrieux-Loyer, F., Philippon, X., Bally, G., Kérouel, R., Youenou, A., and Le Grand, J. (2008). Phosphorus dynamics and bioavailability in sediments of the penzé Estuary (NW France): in relation to annual P-fluxes and occurrences of alexandrium minutum. *Biogeochemistry* 88, 213–231. doi: 10.1007/s10533-008-9199-2

Arndt, S., and Regnier, P. (2007). A model for the benthic-pelagic coupling of silica in estuarine ecosystems: sensitivity analysis and system scale simulation. *Biogeosciences* 4, 331–352. doi: 10.5194/bg-4-331-2007

Arndt, S., Regnier, P., and Vanderborght, J.-P. (2009). Seasonally-resolved nutrient export fluxes and filtering capacities in a macrotidal estuary. *J. Mar. Syst.* 78, 42–58. doi: 10.1016/j.jmarsys.2009.02.008

Arndt, S., Vanderborght, J.-P., and Regnier, P. (2007). Diatom growth response to physical forcing in a macrotidal estuary: Coupling hydrodynamics, sediment transport, and biogeochemistry. *J. Geophys. Res.: Oceans* 112. doi: 10.1029/2006JC003581

Bassoulet, P. (1979). *Etude de la dynamique des sédiments en suspension dans l'estuaire de l'Aulne (rade de Brest)*. (Brest, France: Université de Bretagne Occidentale).

Berner, R. A. (1980). *Early Diagenesis: A Theoretical Approach* (Princeton, New Jersey: Princeton University Press). doi: 10.1515/9780691209401

Beucher, C., Tréguer, P., Corvaisier, R., Hapette, A. M., and Elskens, M. (2004). Production and dissolution of biosilica, and changing microphytoplankton dominance in the Bay of Brest (France). *Mar. Ecol. Prog. Ser.* 267, 57–69. doi: 10.3354/meps267057

Boudreau, B. P. (1994). *Diagenetic models and their implementation. Modelling transport and reactions in aquatic sediments* (Berlin: Sringer).

Buesseler, K. O. (1998). The decoupling of production and particulate export in the surface ocean. *Global Biogeochemical Cycles* 12, 297–310. doi: 10.1029/97GB03366

Carbonnel, V., Lionard, M., Muylaert, K., and Chou, L. (2009). Dynamics of dissolved and biogenic silica in the freshwater reaches of a macrotidal estuary (The Scheldt, Belgium). *Biogeochemistry* 96, 49–72. doi: 10.1007/s10533-009-9344-6

Carbonnel, V., Vanderborght, J.-P., and Chou, L. (2013). *Silica Mass-Balance and Retention in the Riverine and Estuarine Scheldt Tidal System (Belgium/The Netherlands)*. Available at: http://agris.fao.org/agris-search/search.do?recordID=US201400145698 (Accessed December 23, 2016).

Carey, J. C., and Fulweiler, R. W. (2014). Salt marsh tidal exchange increases residence time of silica in estuaries. *Limnology Oceanography* 59, 1203–1212. doi: 10.4319/lo.2014.59.4.1203

Cariou-Le Gall, V., and Blanchard, G. F. (1995). Monthly HPLC measurements of pigment concentration from an intertidal muddy sediment of marennes-oléron bay, france. *Mar. Ecol. Prog. Ser.* 121, 171–179. doi: 10.3354/meps121171

Chauvaud, L., Jean, F., Ragueneau, O., and Thouzeau, G. (2000). Long-term variation of the bay of brest ecosystem: benthic-pelagic coupling revisited. *Mar. Ecol. Prog. Ser.* 200, 35–48. doi: 10.3354/meps200035

Cloern, J. E. (1982). Does the benthos control phytoplankton biomass in South San Francisco Bay? *Mar. Ecol. Prog. Ser.* 9, 191–202. doi: 10.3354/meps009191

Cloern, J. E., Jassby, A. D., Schraga, T. S., Nejad, E., and Martin, C. (2017). Ecosystem variability along the estuarine salinity gradient: Examples from long-term study of San Francisco Bay. *Limnology Oceanography* 62, S272–S291. doi: 10.1002/lno.10537

Conley, D. J. (1997). Riverine contribution of biogenic silica to the oceanic silica budget. *Limnology Oceanography* 42, 774–777. doi: 10.4319/lo.1997.42.4.0774

Conley, D. J., and Johnstone, R. (1995). Biogeochemistry of N, P and Si in Baltic Sea sediments: response to a simulated deposition of a spring diatom bloom. *Mar. Ecol. Prog. Ser.* 122, 265–276. doi: 10.3354/meps122265

Conley, D. J., Schelske, C. L., and Stoermer, E. F. (1993). Modification of the biogeochemical cycle of silica with eutrophication. *Mar. Ecol. Prog. Ser.* 101, 179–192. doi: 10.3354/meps101179

DeMaster, D. J. (1981). The supply and accumulation of silica in the marine environment. *Geochimica Cosmochimica Acta* 45, 1715–1732. doi: 10.1016/0016-7037(81)90006-5

DeMaster, D. J. (2002). The accumulation and cycling of biogenic silica in the Southern Ocean: revisiting the marine silica budget. *Deep Sea Res. Part II: Topical Stud. Oceanography* 49, 3155–3167. doi: 10.1016/S0967-0645(02)00076-0

DeMaster, D. J., Knapp, G. B., and Nittrouer, C. A. (1983). Biological uptake and accumulation of silica on the Amazon continental shelf. *Geochimica Cosmochimica Acta* 47, 1713–1723. doi: 10.1016/0016-7037(83)90021-2

DeMaster, D. J., McKee, B. A., Nittrouer, C. A., Jiangchu, Q., and Guodong, C. (1985). Rates of sediment accumulation and particle reworking based on radiochemical measurements from continental shelf deposits in the East China Sea. *Continental Shelf Res.* 4, 143–158. doi: 10.1016/0278-4343(85)90026-3

Dixit, S., Van Cappellen, P., and van Bennekom, A. J. (2001). Processes controlling solubility of biogenic silica and pore water build-up of silicic acid in marine sediments. *Mar. Chem.* 73, 333–352. doi: 10.1016/S0304-4203(00)00118-3

Duport, E., Stora, G., Tremblay, P., and Gilbert, F. (2006). Effects of population density on the sediment mixing induced by the gallery-diffusor Hediste (Nereis) diversicolor O.F. Mülle. *J. Exp. Mar. Biol. Ecol.* 336, 33–41. doi: 10.1016/j.jembe.2006.04.005

Dürr, H., Meybeck, M., Hartmann, J., Laruelle, G. g., and Roubeix, V. (2011). Global spatial distribution of natural riverine silica inputs to the coastal zone. *Biogeosciences* 8, 597–620. doi: 10.5194/bg-8-597-2011

Ehlert, C., Doering, K., Wallmann, K., Scholz, F., Sommer, S., Grasse, P., et al. (2016). Stable silicon isotope signatures of marine pore waters – Biogenic opal dissolution versus authigenic clay mineral formation. *Geochimica Cosmochimica Acta* 191, 102–117. doi: 10.1016/j.gca.2016.07.022

Emerson, S., Jahnke, R., and Heggie, D. (1984). Sediment-water exchange in shallow water estuarine sediments. *J. Mar. Res.* 42, 709–730. doi: 10.1357/002224084788505942

Eyre, B. D., and Ferguson, A. J. P. (2006). Impact of a flood event on benthic and pelagic coupling in a sub-tropical east Australian estuary (Brunswick). *Estuarine Coast. Shelf Sci.* 66, 111–122. doi: 10.1016/j.ecss.2005.08.008

Fabre, S., Jeandel, C., Zambardi, T., Roustan, M., and Almar, R. (2019). An overlooked silica source of the modern oceans: are sandy beaches the key? *Front. Earth Sci.* 7. doi: 10.3389/feart.2019.00231

Farmer, V. C., Delbos, E., and Miller, J. D. (2005). The role of phytolith formation and dissolution in controlling concentrations of silica in soil solutions and streams. *Geoderma* 127, 71–79. doi: 10.1016/j.geoderma.2004.11.014

Forja, J. M., and Gómez-Parra, A. (1998). Measuring nutrient fluxes across the sediment-water interface using benthic chambers. *Mar. Ecol. Prog. Ser.* 164, 95–105. doi: 10.3354/meps164095

François, F., Poggiale, J.-C., Durbec, J.-P., and Stora, G. (1997). A new approach for the modelling of sediment reworking induced by a macrobenthic community. *Acta Biotheoretica* 45, 295–319. doi: 10.1023/A:1000636109604

Fulweiler, R. W., and Nixon, S. W. (2009). "Responses of benthic-pelagic coupling to climate change in a temperate estuary," in *Eutrophication in Coastal Ecosystems: Towards better understanding and management strategies Selected Papers from the Second International Symposium on Research and Management of Eutrophication in Coastal Ecosystems, 20–23 June 2006, Nyborg, Denmark*. Eds. J. H. Andersen and D. J. Conley (Dordrecht: Springer Netherlands), 147–156. doi: 10.1007/978-90-481-3385-7_13

Gallinari, M., Ragueneau, O., DeMaster, D. J., Hartnett, H., Rickert, D., and Thomas, C. (2008). Influence of seasonal phytodetritus deposition on biogenic silica dissolution in marine sediments–potential effects on preservation. *Deep Sea Res. Part II: Topical Stud. Oceanography* 55, 2451–2464. doi: 10.1016/j.dsr2.2008.06.005

Garnier, J., Beusen, A., Thieu, V., Billen, G., and Bouwman, L. (2010). N:P:Si nutrient export ratios and ecological consequences in coastal seas evaluated by the ICEP approach. *Global Biogeochemical Cycles* 24, GB0A05. doi: 10.1029/2009GB003583

Garnier, J., Billen, G., Lassaletta, L., Vigiak, O., Nikolaidis, N. P., and Grizzetti, B. (2021). Hydromorphology of coastal zone and structure of watershed agro-food system are main determinants of coastal eutrophication. *Environ. Res. Lett.* 16, 023005. doi: 10.1088/1748-9326/abc777

Gehlen, M., and Van Raaphorst, W. (2002). The role of adsorption–desorption surface reactions in controlling interstitial Si(OH)4 concentrations and enhancing Si (OH)4 turn-over in shallow shelf seas. *Continental Shelf Res.* 22, 1529–1547. doi: 10.1016/S0278-4343(02)00016-X

Grasso, F., Verney, R., Le Hir, P., Thouvenin, B., Schulz, E., Kervella, Y., et al. (2018). Suspended sediment dynamics in the macrotidal seine estuary (France): 1. Numerical modeling of turbidity maximum dynamics. *J. Geophysical Research: Oceans* 123, 558–577. doi: 10.1002/2017JC013185

Green, M. A., Gulnick, J. D., Dowse, N., and Chapman, P. (2004). Spatiotemporal patterns of carbon remineralization and bio-irrigation in sediments of Casco Bay Estuary, Gulf of Maine. *Limnology Oceanography* 49, 396–407. doi: 10.4319/lo.2004.49.2.0396

Heip, C. H. R., Goosen, N. K., Herman, P. M. J., Kromkamp, J., Middelburg, J. J., and Soetaert, K. (1995). Production and consumption of biological particles in temperate tidal estuaries. In: *Oceanography and marine Biology: An Annual Review*. Available at: https://www.vliz.be/nl/open-marien-archief?module=ref&refid=8311&printversion=1&dropIMIStitle=1 (Accessed March 28, 2022).

Humborg, C., Ittekkot, V., Cociasu, A., and Bodungen, B. v (1997). Effect of Danube River dam on Black Sea biogeochemistry and ecosystem structure. *Nature* 386, 385–388. doi: 10.1038/386385a0

Kamatani, A. (1982). Dissolution rates of silica from diatoms decomposing at various temperatures. *Mar. Biol.* 68, 91–96. doi: 10.1007/BF00393146

Khalil, K., Laverman, A. M., Raimonet, M., and Rabouille, C. (2018). Importance of nitrate reduction in benthic carbon mineralization in two eutrophic estuaries: Modeling, observations and laboratory experiments. *Mar. Chem.* 199, 24–36. doi: 10.1016/j.marchem.2018.01.004

Khalil, K., Rabouille, C., Gallinari, M., Soetaert, K., Demaster, D. J., and Ragueneau, O. (2007). Constraining biogenic silica dissolution in marine sediments: A comparison between diagenetic models and experimental dissolution rates. *Mar. Chem.* 106, 223–238. doi: 10.1016/j.marchem.2006.12.004

Khalil, K., Raimonet, M., Laverman, A. M., Yan, C., Andrieux-Loyer, F., Viollier, E., et al. (2013). Spatial and temporal variability of sediment organic matter recycling in two temperate eutrophicated estuaries. *Aquat. Geochemistry* 19, 517–542. doi: 10.1007/s10498-013-9213-8

Laruelle, G. G. (2009). *Quantifying nutrient cycling and retention in coastal waters at the global scale*. Available at: http://dspace.library.uu.nl/handle/1874/35870 (Accessed January 2, 2017).

Le Bouteiller, A., Leynaert, A., Landry, M. R., Le Borgne, R., Neveux, J., Rodier, M., et al. (2003). Primary production, new production, and growth rate in the equatorial Pacific: Changes from mesotrophic to oligotrophic regime. *J. Geophys. Res.* 108. doi: 10.1029/2001JC000914

Lorenzen, C. J. (1966). A method for the continuous measurement of in *vivo* chlorophyll concentration. *Deep Sea Res. Oceanographic Abstracts* 13, 223–227. doi: 10.1016/0011-7471(66)91102-8

Loucaides, S., Michalopoulos, P., Presti, M., Koning, E., Behrends, T., and Van Cappellen, P. (2010). Seawater-mediated interactions between diatomaceous silica and terrigenous sediments: Results from long-term incubation experiments. *Chem. Geology* 270, 68–79. doi: 10.1016/j.chemgeo.2009.11.006

Maavara, T., Akbarzadeh, Z., and Van Cappellen, P. (2020). Global dam-driven changes to riverine N:P:Si ratios delivered to the coastal ocean. *Geophysical Res. Lett.* 47, e2020GL088288. doi: 10.1029/2020GL088288

Mangalaa, K. R., Cardinal, D., Brajard, J., Rao, D. B., Sarma, N. S., Djouraev, I., et al. (2017). Silicon cycle in Indian estuaries and its control by biogeochemical and anthropogenic processes. *Continental Shelf Res.* 148, 64–88. doi: 10.1016/j.csr.2017.08.011

Marinelli, R. L. (1992). Effects of polychaetes on silicate dynamics and fluxes in sediments: Importance of species, animal activity and polychaete effects on benthic diatoms. *J. Mar. Res.* 50, 745–779. doi: 10.1357/002224092784797566

McManus, J., Hammond, D. E., Berelson, W. M., Kilgore, T. E., Demaster, D. J., Ragueneau, O. G., et al. (1995). Early diagenesis of biogenic opal: Dissolution rates, kinetics, and paleoceanographic implications. *Deep Sea Res. Part II: Topical Stud. Oceanography* 42, 871–903. doi: 10.1016/0967-0645(95)00035-O

Michalopoulos, P., and Aller, R. C. (2004). Early diagenesis of biogenic silica in the Amazon delta: alteration, authigenic clay formation, and storage. *Geochimica Cosmochimica Acta* 68, 1061–1085. doi: 10.1016/j.gca.2003.07.018

Michaud, E. (2006). *Rôle de la diversité fonctionnelle de la communauté à macoma balthica (Estuaire du saint-laurent, québec, canada) sur les flux biogéochimiques à l'interface eau-sèdiment et sur le mélange particulaire*. Available at: http://www.theses.fr/2006AIX22056.

Moriceau, B., Goutx, M., Guigue, C., Lee, C., Armstrong, R., Duflos, M., et al. (2009). Si–C interactions during degradation of the diatom Skeletonema marinoi. *Deep Sea Res. Part II: Topical Stud. Oceanography* 56, 1381–1395. doi: 10.1016/j.dsr2.2008.11.026

Nelson, D. M., Tréguer, P., Brzezinski, M. A., Leynaert, A., and Quéguiner, B. (1995). Production and dissolution of biogenic silica in the ocean: Revised global estimates, comparison with regional data and relationship to biogenic sedimentation. *Global Biogeochemical Cycles* 9, 359–372. doi: 10.1029/95GB01070

Nelson, J. R. (1993). Rates and possible mechanism of light-dependent degradation of pigments in detritus derived from phytoplankton. *J. Mar. Res.* 51, 155–179. doi: 10.1357/0022240933223837

Nichols, F. H., Cloern, J. E., Luoma, S. N., and Peterson, D. H. (1986). The modification of an estuary. *Science* 231, 567–573. doi: 10.1126/science.231.4738.567

Ni Longphuirt, S. N., Leynaert, A., Guarini, J., Chauvaud, L., Claquin, P., Herlory, O., et al. (2006). Discovery of microphytobenthos migration in the subtidal zone. *Mar. Ecol. Prog. Ser.* 328, 143–154. doi: 10.3354/meps328143

Officer, C. B., and Ryther, J. H. (1980). The possible importance of silicon in marine eutrophication. *Mar. Ecol. Prog. Ser.* 3, 83–91. doi: 10.3354/meps003083

Oleszczuk, B., Michaud, E., Morata, N., Renaud, P. E., and Kędra, M. (2019). Benthic macrofaunal bioturbation activities from shelf to deep basin in spring to summer transition in the Arctic Ocean. *Mar. Environ. Res.* 150, 104746. doi: 10.1016/j.marenvres.2019.06.008

Peterson, D. H. (1979). Sources and sinks of biologically reactive oxygen, carbon, nitrogen, and silica in northern San Francisco Bay. *Estuar. Res.*, 153–187.

Pondaven, P., Ragueneau, O., Tréguer, P., Hauvespre, A., Dezileau, L., and Reyss, J. L. (2000). Resolving the 'opal paradox' in the southern ocean. *Nature* 405, 168–172. doi: 10.1038/35012046

Presti, M., and Michalopoulos, P. (2008). Estimating the contribution of the authigenic mineral component to the long-term reactive silica accumulation on the western shelf of the Mississippi River Delta. *Continental Shelf Res.* 28, 823–838. doi: 10.1016/j.csr.2007.12.015

Pritchard, D. W. (1967). *What is an estuary: Physical Viewpoint* (American Association for the Advancement of Science). Available at: https://tamug-ir.tdl.org/handle/1969.3/24383 (Accessed March 29, 2022).

Querné, J. (2011). *Invasion de Spartina alterniflora dans les marais de la rade de Brest. Comportement invasif et impact sur le cycle biog\textbackslash'eochimique du silicium*. Available at: http://scholar.google.fr/scholar?q=related:OBhHKBbubiUJ:scholar.google.com/&hl=fr&as_sdt=0,5 (Accessed May 8, 2012).

Ragueneau, O., Chauvaud, L., Leynaert, A., Thouzeau, G., Paulet, Y.-M., Bonnet, S., et al. (2002a). Direct evidence of a biologically active coastal silicate pump: Ecological implications. *Limnology Oceanography* 47, 1849–1854. doi: 10.4319/lo.2002.47.6.1849

Ragueneau, O., Chauvaud, L., Moriceau, B., Leynaert, A., Thouzeau, G., Donval, A., et al. (2005a). Biodeposition by an Invasive suspension feeder impacts the biogeochemical cycle of si in a coastal ecosystem (Bay of brest, France). *Biogeochemistry* 75, 19–41. doi: 10.1007/s10533-004-5677-3

Ragueneau, O., Conley, D. J., DeMaster, D. J., Dürr, H. H., and Dittert, N. (2010). Biogeochemical Transformations of Silicon Along the Land–Ocean Continuum and Implications for the Global Carbon Cycle1. In: *Carbon and nutrient fluxes in continental margins* (Springer). Available at: http://link.springer.com/chapter/10.1007/978-3-540-92735-8_10 (Accessed April 10, 2015).

Ragueneau, O., De Blas Varela, E., Tréguer, P., Quéguiner, B., and Del Amo, Y. (1994). Phytoplankton dynamics in relation to the biogeochemical cycle of silicon in a coastal ecosystem of western Europe. *Mar. Ecol. Prog. Ser.* 106, 157–172. doi: 10.3354/meps106157

Ragueneau, O., Lancelot, C., Egorov, V., Vervlimmeren, J., Cociasu, A., Déliat, G., et al. (2002b). Biogeochemical transformations of inorganic nutrients in the mixing zone between the danube river and the North-western Black Sea. *Estuarine Coast. Shelf Sci.* 54, 321–336. doi: 10.1006/ecss.2000.0650

Ragueneau, O., Savoye, N., Del Amo, Y., Cotten, J., Tardiveau, B., and Leynaert, A. (2005b). A new method for the measurement of biogenic silica in suspended matter of coastal waters: using Si:Al ratios to correct for the mineral interference. *Continental Shelf Res.* 25, 697–710. doi: 10.1016/j.csr.2004.09.017

Ragueneau, O., Schultes, S., Bidle, K., Claquin, P., and Moriceau, B. (2006). Si and C interactions in the world ocean: Importance of ecological processes and implications for the role of diatoms in the biological pump. *Global Biogeochemical Cycles* 20. doi: 10.1029/2006GB002688

Ragueneau, O., and Tréguer, P. (1994). Determination of biogenic silica in coastal waters: applicability and limits of the alkaline digestion method. *Mar. Chem.* 45, 43–51. doi: 10.1016/0304-4203(94)90090-6

Raimonet, M., Andrieux-Loyer, F., Ragueneau, O., Michaud, E., Kérouel, R., Philippon, X., et al. (2013a). Strong gradient of benthic biogeochemical processes along a macrotidal temperate estuary: focus on P and Si cycles. *Biogeochemistry* 10. doi: 10.1007/s10533-013-9843-3

Raimonet, M., Ragueneau, O., Andrieux-Loyer, F., Philippon, X., Kerouel, R., Le Goff, M., et al. (2013b). Spatio-temporal variability in benthic silica cycling in two macrotidal estuaries: Causes and consequences for local to global studies. *Estuarine Coast. Shelf Sci.* 119, 31–43. doi: 10.1016/j.ecss.2012.12.008

Raimonet, M., Ragueneau, O., Jacques, V., Corvaisier, R., Moriceau, B., Khripounoff, A., et al. (2015). Rapid transport and high accumulation of amorphous silica in the Congo deep-sea fan: A preliminary budget. *J. Mar. Syst.* 141, 71–79. doi: 10.1016/j.jmarsys.2014.07.010

Rebreanu, L. (2009). *Study of the Si biogeochemical cycle in the sediments of the Scheldt continuum, Belgium/The Netherlands*. Available at: http://hdl.handle.net/2013/ (Accessed March 28, 2022).

Regnier, P., Friedlingstein, P., Ciais, P., Mackenzie, F. T., Gruber, N., Janssens, I. A., et al. (2013). Anthropogenic perturbation of the carbon fluxes from land to ocean. *Nat. Geosci.* 6, 597–607. doi: 10.1038/ngeo1830

Regnier, P., Mouchet, A., Wollast, R., and Ronday, F. (1998). A discussion of methods for estimating residual fluxes in strong tidal estuaries. *Continental Shelf Res.* 18, 1543–1571. doi: 10.1016/S0278-4343(98)00071-5

Riaux-Gobin, C., and Klein, B. (1993). "Microphytobenthic Biomass Measurement Using HPLC and Conventional Pigment Analysis," in *Handbook of Methods in Aquatic Microbial Ecology* (Boca Raton, London, New York, Washington DC: CRC Press).

Ridd, P., Day, G., Thomas, S., Harradence, J., Fox, D., Bunt, J., et al. (2001). Measurement of Sediment deposition rates using an optical backscatter sensor. *Estuarine Coast. Shelf Sci.* 52, 155–163. doi: 10.1006/ecss.2000.0635

Roubeix, V., Becquevort, S., and Lancelot, C. (2008a). Influence of bacteria and salinity on diatom biogenic silica dissolution in estuarine systems. *Biogeochemistry* 88, 47–62. doi: 10.1007/s10533-008-9193-8

Roubeix, V., Rousseau, V., and Lancelot, C. (2008b). Diatom succession and silicon removal from freshwater in estuarine mixing zones: From experiment to modelling. *Estuarine Coast. Shelf Sci.* 78, 14–26. doi: 10.1016/j.ecss.2007.11.007

Sagan, G., and Thouzeau, G. (1998). Microphytobenthic biomass in the Bay of Brest and the western English Channel. *Oceanologica Acta* 5, 677–694. doi: 10.1016/S0399-1784(99)80024-3

Savoye, N. (2001). *Origine et transfert de la matière organique particulaire dans les écosystèmes littoraux macrotidaux*. (Brest, France: Université de Bretagne Occidentale).

Shiller, A. M. (1996). The effect of recycling traps and upwelling on estuarine chemical flux estimates. *Geochimica Cosmochimica Acta* 60, 3177–3185. doi: 10.1016/0016-7037(96)00159-7

Smis, A., Van Damme, S., Struyf, E., Clymans, W., Van Wesemael, B., Frot, E., et al. (2011). A trade-off between dissolved and amorphous silica transport during peak flow events (Scheldt river basin, Belgium): impacts of precipitation intensity on terrestrial Si dynamics in strongly cultivated catchments. *Biogeochemistry* 106, 475–487. doi: 10.1007/s10533-010-9527-1

Soetaert, K. (2009). *rootSolve: Nonlinear root finding, equilibrium and steady-state analysis of ordinary differential equations*. Available at: https://cran.r-project.org/package=rootSolve.

Soetaert, K., and Petzoldt, T. (2010). Inverse modelling, sensitivity and monte carlo analysis in r using package FME. *J. Stat. Softw.* 33, 1–28. doi: 10.18637/jss.v033.i03

Soetaert, K., Middelburg, J. J., Heip, C., Meire, P., Van Damme, S., and Maris, T. (2006). Long-term change in dissolved inorganic nutrients in the heterotrophic Scheldt estuary (Belgium, The Netherlands). *Limnology Oceanography* 51, 409–423. doi: 10.4319/lo.2006.51.1_part_2.0409

Struyf, E., Dausse, A., Van Damme, S., Bal, K., Gribsholt, B., Boschker, H. T. S., et al. (2006). Tidal marshes and biogenic silica recycling at the land-sea interface. *Limnology Oceanography* 51, 838–846. doi: 10.4319/lo.2006.51.2.0838

Sun, M.-Y., Aller, R. C., and Lee, C. (1994). Spatial and temporal distributions of sedimentary chloropigments as indicators of benthic processes in Long Island Sound. *J. Mar. Res.* 52, 149–176. doi: 10.1357/0022240943076768

Sun, M.-Y., Lee, C., and Aller, R. C. (1993). Anoxic and oxic degradation of 14C-labeled chloropigments and a 14C-labeled diatom in long island sound sediments. *Limnology Oceanography* 38, 1438–1451. doi: 10.4319/lo.1993.38.7.1438

Sundbäck, K., Miles, A., Hulth, S., Pihl, L., Engström, P., Selander, E., et al. (2003). Importance of benthic nutrient regeneration during initiation of macroalgal blooms in shallow bays. *Mar. Ecol. Prog. Ser.* 246, 115–126. doi: 10.3354/meps246115

Tatters, A. O., Fu, F.-X., and Hutchins, D. A. (2012). High CO2 and silicate limitation synergistically increase the toxicity of pseudo-nitzschia fraudulenta. *PloS One* 7, e32116. doi: 10.1371/journal.pone.0032116

Testa, J. M., and Kemp, W. M. (2008). Variability of biogeochemical processes and physical transport in a partially stratified estuary: a box-modeling analysis. *Mar. Ecol. Prog. Ser.* 356, 63–79. doi: 10.3354/meps07264

Tréguer, P. (2002). Silica and the cycle of carbon in the ocean. *Comptes Rendus Geosci.* 334, 3–11. doi: 10.1016/S1631-0713(02)01680-2

Tréguer, P., Bowler, C., Moriceau, B., Dutkiewicz, S., Gehlen, M., Aumont, O., et al. (2018). Influence of diatom diversity on the ocean biological carbon pump. *Nat. Geosci.* 11, 27–37. doi: 10.1038/s41561-017-0028-x

Tréguer, P., and Le Corre, P. (1975). *Manuel d'analyse des sels nutritifs dans l'eau de mer: utilisation de l'auto-analyseur Technicon II* (Rapport de l'Universite de Bretagne Occidentale, Brest). Available at: https://ci.nii.ac.jp/naid/10012431976/ (Accessed March 28, 2022).

Tréguer, P. J., Sutton, J. N., Brzezinski, M., Charette, M. A., Devries, T., Dutkiewicz, S., et al. (2021). Reviews and syntheses: The biogeochemical cycle of silicon in the modern ocean. *Biogeosciences* 18, 1269–1289. doi: 10.5194/bg-18-1269-2021

Van Cappellen, P., Dixit, S., and van Beusekom, J. (2002). Biogenic silica dissolution in the oceans: Reconciling experimental and field-based dissolution rates. *Global Biogeochemical Cycles* 16, 1075. doi: 10.1029/2001GB001431

Wallington, H., Hendry, K., Perkins, R., Yallop, M., and Arndt, S. (2023). Benthic diatoms modify riverine silicon export to a marine zone in a hypertidal estuarine environment. *Biogeochemistry* 162, 177–200. doi: 10.1007/s10533-022-00997-7

Ward, J. P., Hendry, K. R., Arndt, S., Faust, J. C., Freitas, F. S., Henley, S. F., et al. (2022). Benthic silicon cycling in the Arctic Barents Sea: a reaction–transport model study. *Biogeosciences* 19, 3445–3467. doi: 10.5194/bg-19-3445-2022

Welsby, H. J., Hendry, K. R., and Perkins, R. G. (2016). The role of benthic biofilm production in the mediation of silicon cycling in the Severn Estuary, UK. *Estuarine Coast. Shelf Sci.* 176, 124–134. doi: 10.1016/j.ecss.2016.04.008

Yamada, S. S., and D'Elia, C. F. (1984). Silicic acid regeneration from estuarine sediment cores. *Mar. Ecol. Prog. Ser.* 18, 113–118. doi: 10.3354/meps018113

Zhang, Z., Cao, Z., Grasse, P., Dai, M., Gao, L., Kuhnert, H., et al. (2020). Dissolved silicon isotope dynamics in large river estuaries. *Geochimica Cosmochimica Acta* 273, 367–382. doi: 10.1016/j.gca.2020.01.028

frontiers | Frontiers in Marine Science

TYPE Original Research
PUBLISHED 02 July 2024
DOI 10.3389/fmars.2024.1331333

OPEN ACCESS

EDITED BY
Hongbin Liu,
Hong Kong University of Science and Technology, Hong Kong SAR, China

REVIEWED BY
Alessandra Norici,
Marche Polytechnic University, Italy
Jun Sun,
China University of Geosciences, China

*CORRESPONDENCE
Aurélie Godrant
liligodrant@gmail.com
Brivaela Moriceau
brivaela.moriceau@univ-brest.fr

RECEIVED 31 October 2023
ACCEPTED 28 May 2024
PUBLISHED 02 July 2024

CITATION
Godrant A, Leynaert A and Moriceau B (2024) A study of the influence of iron, phosphate, and silicate in Si uptake by two *Synechococcus* strains. *Front. Mar. Sci.* 11:1331333. doi: 10.3389/fmars.2024.1331333

A study of the influence of iron, phosphate, and silicate in Si uptake by two *Synechococcus* strains

Aurélie Godrant[1,2*], Aude Leynaert[2] and Brivaela Moriceau[2*]

[1]AlgaeNutri, Brest, France, [2]Univ Brest, CNRS, IRD, Ifremer, LEMAR, Plouzane, France

We investigated the influence of iron (Fe), phosphate (PO_4), and silicic acid [$Si(OH)_4$] concentrations on Si uptake rate by two strains of *Synechococcus*. Growth rates, cellular biogenic silica (bSi), and silicon uptake rates were measured and compared. Both strains showed significant Si cellular contents varying from 0.04 47 fmol cell^{-1} to a maximum of 47 fmol cell^{-1}, confirming that the presence of Si in *Synechococcus* is a common feature of the genus but with strain specificity. Maximum Si cell contents were measured when Fe and P co-limited RCC 2380 growth (47 fmol Si cell^{-1}) and under -Fe-Si limitations (6.6 fmol Si cell^{-1}) for the second strain RCC 1084. Unambiguously, all conditions involving P limitations induced an increase in the Si uptake by the two *Synechococcus*. Moreover, RCC 1084 showed a relationship between Si cellular quota and growth rate. However, both strains also showed a clear impact of Fe concentrations on their Si uptake: Si quotas increased 1) under Fe limitation even without P co-limitation and 2) under simple Fe limitation for RCC 1084 and with Si co-limitations for RCC 2380. Both strains exhibited a behavior that has never been seen before with changing $Si(OH)_4$: concentrations of 150 µM of $Si(OH)_4$ negatively impacted RCC 2380 growth over 10 generations. Conversely, RCC 1084 was limited when $Si(OH)_4$ concentrations dropped to 20 µmol L^{-1}. Maximum *Synechococcus* Si uptake rates normalized to the organisms' size (7.46 fmol µm^{-3} day^{-1}) are comparable to those measured for diatoms and rhizarians. From our data, and using all the data available on *Synechococcus* Si content and Si uptake rates, their average concentrations for each Longhurst province, and existing descriptions of the dominant nutrient limitations and *Synechococcus* strain specificity, we estimated at the global scale that the annual bSi stock contained in *Synechococcus* is 0.87 ± 0.61 Tmol Si, i.e., around a quarter of the bSi stock due to diatoms. We also estimated that the global Si production due to *Synechococcus* could average 38 ± 27 Tmol Si year^{-1}, which is roughly 17% of the total global annual Si production.

KEYWORDS

iron, phosphorus, silicon, *Synechococcus*, Si uptake, global Si budget

Introduction

The ocean is an important climate regulator, absorbing about one quarter of anthropogenic carbon (C) through its physical and biological pumps. The biological carbon pump (BCP) intensity depends on several complex processes that challenge our capacity to quantify its impact (Siegel et al., 2023). Among these difficulties, we may cite the understanding of the contribution of the different groups of organisms (Benedetti et al., 2023). Diatoms are well-known actors of the BCP due to their diversity, size, and capacity to dominate high-latitude ecosystems: their heavy frustule of biogenic silica that ballasts them and their capacity to aggregate, two characteristics that increase their sinking toward deep layers (Tréguer et al., 2018). It appears that high-latitude ecosystems dominated by diatoms are efficient at exporting C, but the proportion of this exported C reaching sequestration depth, i.e., the transfer efficiency, is low. Conversely, large oligotrophic zones do not export much C to the top of the mesopelagic layer but are efficient at transferring it to sequestration depth (Henson et al., 2012). Moreover, small cells such as cyanobacteria may also be important contributors to the C export (Richardson and Jackson, 2007; De Martini and Neuer, 2016). Through their domination in oligotrophic waters, a large part of the ocean, models estimate that pico-phytoplankton may contribute for 46% of the C export (Letscher et al., 2023). One of these groups, *Synechococcus*, contributes to the total primary production as high as 30% in the subtropical North Atlantic (Duhamel et al., 2019) or 25% in Costa Rica upwelling (Muñoz-Marín et al., 2020), and their global contribution has been estimated using niche model to be 16.7% (Flombaum et al., 2013). Indeed, *Synechococcus* have a wide repartition zone and a small seasonality (Visintini and Flombaum, 2022). These traits may be attributed to high adaptability in order to grow at low nutrient concentrations, use mixotrophy, or change their pigment content (Flombaum et al., 2013; Grébert et al., 2018; Muñoz-Marín et al., 2020; Visintini et al., 2021; Visintini and Flombaum, 2022). Surprising most of the scientific community, *Synechococcus* has been found to accumulate Si at a level that cellular ratios of Si/S and Si/P approach those detected in diatoms from the same environment (Baines et al., 2012; Ohnemus et al., 2016; Wei et al., 2022; Churakova et al., 2023). Until now, the scientific community has been unable to identify physiological mechanisms requiring the assimilation of dissolved Si (Brzezinski et al., 2017) and, thus, to understand the implication of this accumulation on the processes driving the oceanic C and silicon cycles. While poorly constrained models predict that climate change may increase the global abundances of *Synechococcus* at the expense of diatoms, they will be favored by three main impacts: ocean acidification, warming waters, and decrease of nutrients (Marinov et al., 2013; Dutkiewicz et al., 2015; MaChado et al., 2019; Flombaum and Martiny, 2021). However, due to the lack of data and comprehensive processes, none of these models consider the implication of *Synechococcus* accumulating Si. Moreover, considering the predicted increase of nutrient limitation, one has to comprehend the *Synechococcus* Si uptake under different limitations. Previous study showed the implications of P in the Si absorption process by *Synechococcus*: Si uptake rates were inhibited after addition of PO_4 in the medium of laboratory cultures (Brzezinski et al., 2017), suggesting that Si would be transported by P transporters instead of P. However, this study also showed that addition of a mix of vitamins and metals in this culture increased the specific uptake rate of Si compared to control. Both these results, and unpublished data that we collected in our laboratory with *Synechococcus* cultures, lead us thinking that Fe plays an important role in Si uptake by these cyanobacteria.

Due to its extremely low concentration, iron (Fe) limits phytoplankton productivity in ~30% of the world's oceans, in the high-nutrient low-chlorophyll waters (Moore et al., 2013). Cyanobacteria have been proposed to possess a high cellular growth requirement for Fe as a vestige of the high availability of Fe in the ancient ocean: Brand's (1991) hypothesis was based on the much higher subsistence Fe/P requirements in six coastal and oceanic *Synechococcus* strains whose growth has been reduced to zero by Fe limitation in comparison to subsistence Fe/P values of eukaryotic algae. There is no evidence for potential direct effect on cyanobacterial growth due to interactions between Fe and P concentrations in the environment, but, as Fe is an important controlling factor for phytoplankton growth, it has a feedback effect on the P demand and potentially on Si absorption.

In the present study, we propose to examine the uptake of Si by two *Synechococcus* strains under various $Si(OH)_4$, PO_4, and Fe conditions to help understand the processes involved, the *Synechococcus* contribution to the global Si oceanic cycle and whether *Synechococcus* may be or become a competitor of diatoms for Si resources.

Materials and methods

Cultures

Two strains of *Synechococcus* were studied: *Synechococcus* RCC2380 (ROS8604 Syn Clonal) from the Roscoff Estacade from France (48.732001, −3.982762), and RCC1084 (WH5701) from the Long Island Sound in USA (41.074403, −73.071732). These strains were sampled in coastal areas, but they belong to two clades that are more widely distributed: the RCC2380 belongs to the clade I that is widely represented worldwide from the Arctic to the Antarctic and in the westerlies domains, and RCC1084 belongs to the clade 5.2 that is a more coastal *Synechococcus* also observed in the Antarctic ocean (Doré et al., 2022 and 2023).

Semi-continuous batch cultures were maintained in an incubator at 22°C under 12-h/12-h light/dark cycle with a light intensity of 100 µEinstein m^{-2} s^{-1}, in order to keep cultures in the exponential growth phase. Cultures were maintained in acid washed polycarbonate flasks, in a variation of the Aquil medium (Price et al., 1989) containing EDTA (5 µmol/L; Table 1). Various concentrations of Fe, $Si(OH)_4$, and PO_4 were tested as indicated in Table 2. Like for every semi-continuous culturing system, macronutrient concentrations were high compared to environmental conditions, to compensate for the lack of renewal in the system compared to *in situ* and due to the cell concentration in our cultures that were much higher than in the ocean. It is a well-known method that using higher nutrient concentrations in semi-continuous cultures helps keeping good ratios between micronutrient concentrations and control the limitations. Limitations were evidenced through a decrease of the growth rates (Figure 1).

All conditions were adapted for eight generations and maintained between 2 and 8 months. Each experiment was done on at least four

10.3389/fmars.2024.1331333

TABLE 1 Aquil medium recipe for salt and nutrients, according to Price et al. (1989), EDTA is used at a final concentration of 5 µmol/L to stabilize metal concentrations.

	Final concentration (mol/L)
Synthetic oceanic water	
NaCl	4.20×10^{-1}
KBr	8.40×10^{-4}
Na_2SO_4	2.88×10^{-2}
$NaHCO_3$	2.38×10^{-3}
KCl	9.39×10^{-3}
H_3BO_3	4.85×10^{-4}
NaF	7.14×10^{-5}
$MgCl_2$, $6H_2O$	5.46×10^{-2}
CaCl2, $2H_2O$	1.05×10^{-2}
SrCl2, $6H_2O$	6.38×10^{-5}
Nutrients	
NaH_2PO_4, $2H_2O$	2.00×10^{-5}
$NaNO_3$	8.84×10^{-4}
$Na2SiO_3$, $9H_2O$	1.50×10^{-4}
Trace metals	
$ZnSO_4$, $7H_2O$	4.00×10^{-9}
$MnCl_2$, $4H_2O$	2.30×10^{-8}
$CoCl_2$, $6H_2O$	2.50×10^{-9}
$CuSO_4$, $5H_2O$	9.97×10^{-10}
Na_2MoO_4, $2H_2O$	1.00×10^{-7}
Na_2SeO_3	1.00×10^{-8}
$KCr(SO_4)_2$, $12H_2O$	1.00×10^{-8}
Na_3O_4V	1.00×10^{-8}
$FeCl_3$, $6H_2O$	1.00×10^{-7}

TABLE 2 Concentrations of PO_4, $Si(OH)_4$, and Fe in Aquil for the different conditions studied in the present study.

Name	PO4 (mol/L)	Si(OH)4 (mol/L)	Fe (mol/L)
Control	2.00×10^{-5}	1.50×10^{-4}	1.00×10^{-7}
-Fe	2.00×10^{-5}	1.50×10^{-4}	1.00×10^{-8}
-P	2.00×10^{-6}	1.50×10^{-4}	1.00×10^{-7}
-Si	2.00×10^{-5}	2.00×10^{-5}	1.00×10^{-7}
-Fe-P	2.00×10^{-6}	1.50×10^{-4}	1.00×10^{-8}
-Fe-Si	2.00×10^{-5}	2.00×10^{-5}	1.00×10^{-8}
-Si-P	2.00×10^{-6}	2.00×10^{-5}	1.00×10^{-7}
-Si–Fe	2.00×10^{-5}	2.00×10^{-5}	1.00×10^{-9}

culture replicates. Flow cytometry was used to count the cells and check their physiological stability by following the relative size (FSC), relative complexity (SSC), and fluorescence (yellow and red fluorescence) every 3 days. Experiments and analyses were only done when the parameters stayed within 90% of their optimum value and at the exponential phase. Growth curves and rates were determined every three days from these counts.

For a more fluid reading, we indicated in the rest of the text the PO_4 and $Si(OH)_4$ medium concentrations as follows: "P" and "Si."

Si-cellular quotas

Hereafter, Si-cellular quotas are understood as being the total amount of Si coming from the cells (including particulate and soluble Si). Si-cellular quotas were measured on 10 mL to 15 mL of cultures that were filtered on 0.4-µm pores polycarbonate filters. Filters were rinsed with synthetic oceanic water (SOW) (Price et al., 1989) to wash away adsorbed $Si(OH)_4$ and placed in 15-mL tubes for drying at 60°C in an oven. Cells were digested in NaOH (0.2 mol/L) at 90°C in a water bath for 4 h (Moriceau et al., 2007). After cooling, the digestates were acidified with HCl (1 mol L^{-1}), and the tubes were centrifuged at

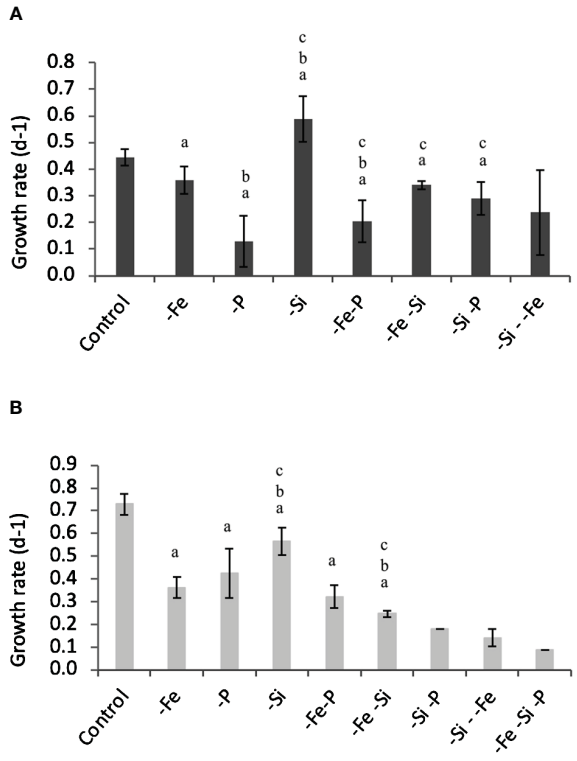

FIGURE 1
Specific growth rates of cultures RCC 2380 **(A)** and RCC 1084 **(B)** exposed to different concentrations of Fe, PO_4, and $Si(OH)_4$. Error bars represent standard deviations. Tamhane test with $p < 0.05$ was indicated in the graph with "a" for treatments significantly different from control, with "b" for treatments significantly different from -Fe, and with "c" for treatments significantly different from -P. For RCC 2380 treatment -Si–Fe and for RCC 1084 treatments -Si-P, -Si–Fe and -Fe-Si-P, too few data were obtained and statistical analyses were not possible.

3,000 rpm for 5 min. The supernatant was analyzed for silicates by colorimetry using an AutoAnalyzer (Bran and Luebbe Technicon Autoanalyzer, accuracy of 0.1%) according to the protocol optimized by Aminot and Kérouel (Aminot and Kérouel, 2007).

Rate of Si uptake

Biogenic Si uptake rates (ρSi) were measured by the ^{32}Si method (Tréguer et al., 1991; Leynaert et al., 1996). Culture flasks of 15 mL to 20 mL were spiked with 650 Bq of radiolabeled ^{32}Si-silicic acid solution with a specific activity of 18.5 kBq µg Si^{-1}, resulting in an increase in silicic acid concentration no greater than 0.1 µmol L^{-1}. Samples were then incubated in the laboratory for 24 h. After incubation, samples were filtered onto 0.6-µm Nucleopore polycarbonate filters and rinsed twice with filtered seawater to wash away non-particulate ^{32}Si. Each filter was then placed in a 20-mL polypropylene scintillation vial. The activity of ^{32}Si in the samples was determined 12 months later, allowing ^{32}Si and its daughter isotope ^{32}P to return to secular equilibrium. Samples were assayed using a scintillation counter Wallac Model 1414. The silicic acid uptake rate (ρ_{Si}, in µmol L^{-1} h^{-1}) was calculated as follows:

$$\rho_{Si} = \frac{A_f}{A_i} \times [Si(OH)_4] \times \frac{1}{\Delta t}$$

where $[Si(OH)_4]$ is the silicic acid concentration of the sample (µmol L^{-1}); A_i and A_f are the initial and final activities of the sample (cpm), respectively; and Δt is the incubation time (in hours). Triplicate 60-min counts were performed on each sample. Counting precision (95% confidence interval) was< ± 5%. The background for the ^{32}Si radioactive activity counting was 8 cpm. Samples for which the measured activity was less than three times the background were considered to lack Si uptake.

Statistical analysis

Statistical analyses were conducted on the growth rates and the Si-cellular quotas using one-way ANOVA. When ANOVA showed significance, we applied a *post-hoc* Tamhane test adapted to unequal variance to determine which of the treatment pairs are significantly different (Figures 1, 2).

For the analysis of the results displayed in Figures 3A, 4C, we conducted linear regressions and obtained the Pearson's correlation coefficients for each of them with $p< 0.05$.

Results

Effect of Fe, PO_4, and $Si(OH)_4$ concentrations on specific growth rates

We obtained growth rates for the two strains for each culturing condition described in Table 2. Results are indicated in Figures 1A, B. Firstly, the decrease in P and/or Fe concentrations in the culture media induced significant lower growth rates for both RCC 2380 and RCC 1084. When P concentration decreased from 20 µmol L^{-1} to 2 µmol L^{-1}, the growth rate was reduced from 0.44 day^{-1} to 0.1 day^{-1} for RCC 2380 and from 0.73 day^{-1} to 0.4 day^{-1} for RCC 1084. When Fe concentration was lowered from 100 nmol L^{-1} to 10 nmol L^{-1}, the growth rate significantly decreased for both RCC 2380 and RCC 1084 from 0.44 day^{-1} to 0.36 day^{-1} and from 0.73 day^{-1} to 0.36 day^{-1}, respectively. When $Si(OH)_4$ concentration decreased from 150 µmol L^{-1} to 20 µmol L^{-1}, RCC 2380 growth rate increased from 0.44 day^{-1} to 0.59 day^{-1}, whereas RCC 1084 growth rate decreased from 0.73 day^{-1} to 0.57 day^{-1}. Secondly, the maximum decrease in RCC 2380's growth rate was achieved when only P concentration was lowered. None of the additional limitations showed any further reduction in growth rate, even when co-limited with P (-Fe-P and -Si-P). In contrast, RCC 1084 growth rates were systematically more impacted when more than one nutrient was limiting, with values lower than 0.3 day^{-1} and down to 0.1 day^{-1} when Fe, Si, and P concentrations were simultaneously reduced in the culture media. However, the growth rate decrease observed for -Fe-P co-limitation was not significantly different from those measured for Fe and P simple limitation.

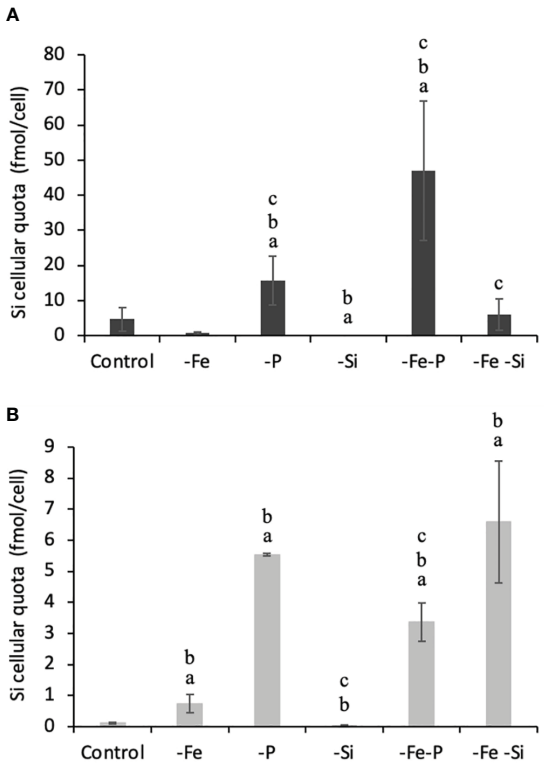

FIGURE 2
Biogenic silica cell content varying with culturing conditions for RCC 2380 **(A)** and RCC 1084 **(B)**. Error bars represent standard deviations. $p< 0.05$, significantly different from control marked with a "a," test significantly different from -Fe marked with a "b," and significantly different from -P marked with a "c.".

Effect of $Si(OH)_4$, Fe, and PO_4 concentrations on Si cellular quotas

The two strains were examined for their Si quotas as a function of nutrients variations as described in the method. Figure 2

10.3389/fmars.2024.1331333

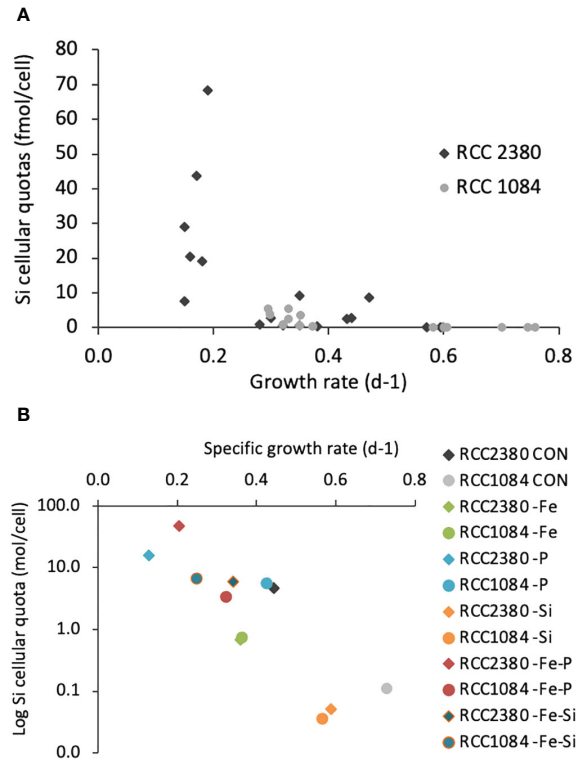

FIGURE 3
Si cellular quotas as a function of specific growth rates of RCC 2380 and RCC 1084 in all various media conditions. All data are indicated in **(A)**, and average results for each medium condition are indicated in **(B)**.

represents cellular Si quotas for the two strains, with variable P, Fe, and Si concentrations. RCC 2380 had Si quotas ranging from 0.05 fmol cell^{-1} to 47 fmol cell^{-1}, whereas RCC 1084, starting from a similar value of 0.04, only reached maximum Si quotas of 6.6 fmol cell^{-1}: RCC 2380 had a maximum Si quota seven times higher than that of RCC 1084. In our conditions, the maxima were reached for the -Fe-P conditions for RCC 2380.

Considering simple and co-limitation of P, both -P and -P-Fe significantly increased bSi as they were multiplied by 3 to 50 for both strains compared to controls. P limitation strongly increased Si quotas, an effect that is enhanced for Fe co-limitation in RCC 2380.

When Fe concentration was reduced from 100 nmol L^{-1} to 10 nmol L^{-1}, both strains exhibited opposite trends for simple Fe limitation: RCC 2380 decreased its Si content from 4.74 fmol cell^{-1} to 0.69 fmol cell^{-1}, whereas RCC 1084 increased it from 0.11 fmol cell^{-1} to 0.73 fmol cell^{-1}. For both strains, adding P to Fe limitation enhanced Si quotas compared to both control and -Fe. Moreover, -Fe-Si exhibited higher Si quotas than -Si for RCC 1084.

When $Si(OH)_4$ concentration was reduced from 150 µmol/L to 20 µmol/L, Si quota slightly decreased for RCC 1084 from 0.11 fmol cell^{-1} to 0.04 fmol cell^{-1}, whereas it decreased by two orders of magnitude for RCC 2380: from 4.74 fmol cell^{-1} to 0.05 fmol cell^{-1}. However, as described earlier, when both Fe and Si were reduced, the two strains increased their Si quota compared to -Si: from 0.05 fmol cell^{-1} to 5.98 fmol cell^{-1} for RCC 2380 and from 0.04 fmol cell^{-1} to 6.59 fmol/cell^{-1} for RCC 1084.

We investigated the relationship between growth rates and Si-cellular quotas for both strains, and the results are presented in Figure 3. Linear regressions give an r-value of −0.60 for RCC 2380 and −0.71 for RCC 1084 ($p< 0.05$), which means that the correlation between Si-cellular quotas and growth rates is negative (bSi decreases when growth rate increases) and that it is stronger for RCC 1084 than for RCC 2380. However, the coefficients being not very high, they show that the correlation between bSi and growth rates is not very strong.

Displaying the average value of each condition in Figure 3B, this indicates the differences between the two strains: the correlation between growth rate and Si-cellular quotas was extremely similar for the two strains only for -Si and -Fe conditions. All other conditions were very different.

Si uptake rates

The Si uptake rates were measured as indicated in the method for the control, -Fe, -P, -Si, and -P-Fe conditions for both strains and -Fe-Si for RCC 2380 (Figure 4).

Si uptake rates of RCC 2380 (Figures 4A1, A2) varied between 0.01 fmol cell^{-1} day^{-1} for -Si and 21.4 fmol cell^{-1} day^{-1} for -Fe-P. Meanwhile, for RCC 1084 (Figures 4B1, B2), it varied between 0.002 fmol cell^{-1} day^{-1} for -Si and 2 fmol cell^{-1} day^{-1} for -P. As a global observation, RCC 1084 Si uptake rates were one order of magnitude lower than RCC 2380, as for the Si quotas. In general, we observe that the variations between conditions have similar trends than the Si quotas: linear regression gave an r-value of 0.99 ($p< 0.05$), which shows a very good correlation between Si-cellular quotas and Si uptake rates (Figure 4C).

Considering variations in Si uptake rates with varying Si medium conditions, RCC 2380 control exhibited a rate of 0.92 and fmol cell^{-1} day^{-1}, but it was close to the detection limit for the -Si and -Si -Fe conditions with rates of 0.010 fmol cell^{-1} day^{-1} and 0.007 fmol cell^{-1} day^{-1}, respectively. For RCC 1084, both the control and the -Si condition were close to the limit of detection with rates of 0.020 fmol cell^{-1} day^{-1} and 0.002 fmol cell^{-1} day^{-1}, respectively.

For both strains, Si uptake rates were higher for all the -P simple and co-limitations compared to control. We can see differences between RCC 2380 and RCC 1084 for -Fe limitations: RCC 2380 -Fe uptake rate decreased compared to the control; -Fe-P was higher than the control and even higher than the -P condition; whereas, for RCC 1084, -Fe and -Fe-P conditions showed both higher Si uptake rates than the control.

These data represent specific uptake rates between 0.0003 h^{-1} and 0.0195 h^{-1}, which we can compare with the rates of 0.007 h^{-1} to 0.101 h^{-1} found in previous study (Brzezinski et al., 2017).

Discussion

Regulation of *Synechococcus* Si uptake by dissolved Fe, Si, and P concentrations

In the present study, we analyzed how the capacity to uptake Si of two strains of the genus *Synechococcus* from two distinct clades

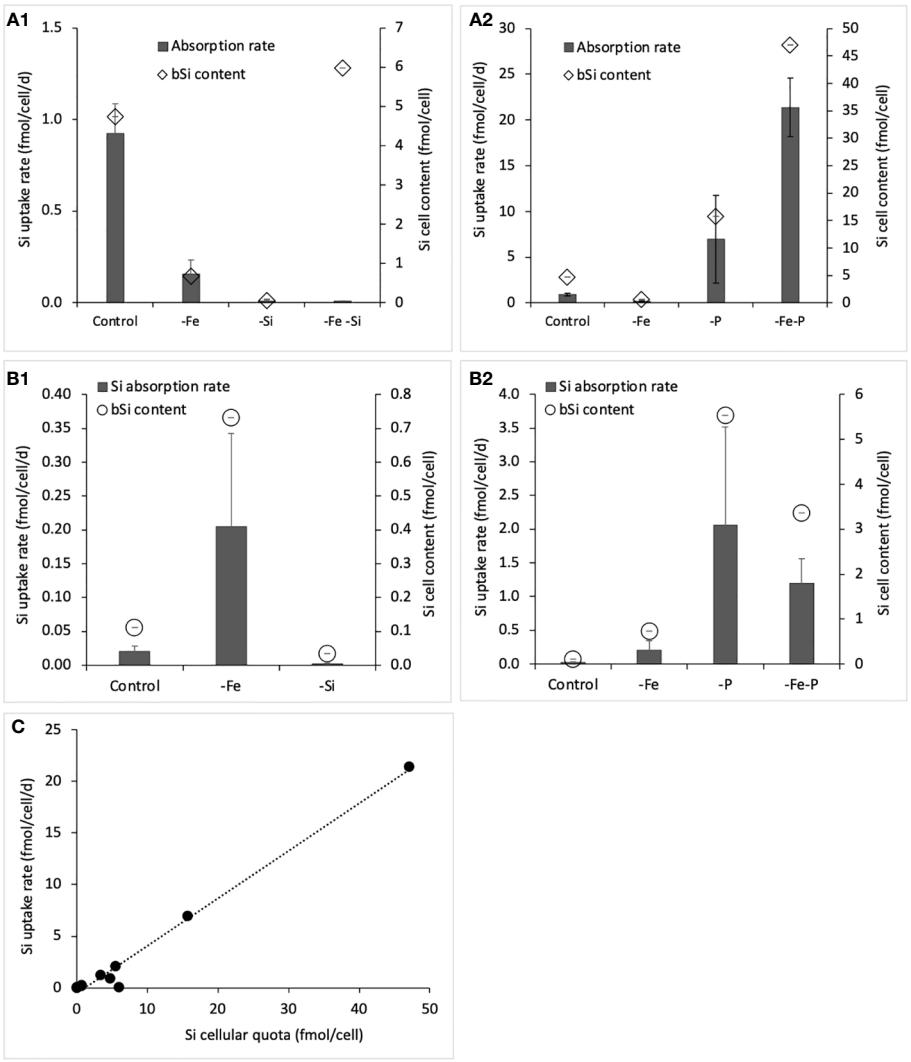

FIGURE 4
Silicic acid uptake rates and Si cellular quotas (bSi) for **(A1)**: RCC 2380 cultured in control conditions vs. Fe simple limitations, low silicic acid concentration, Fe limitations combined to low silicic acid concentrations; **(A2)** RCC 2380 cultured under no limitations vs. Fe and P simple and co-limitations; **(B1)** RCC 1084 cultured under no limitations vs. Fe and Si simple limitations; **(B2)** RCC 1084 cultured under no limitations vs. Fe and P simple and co-limitations. Panel **(C)** compares Si cellular quotas and Si uptake rates for both strains.

(RCC2380, clade I and RCC1084, clade 5.2) may be modified by changing Fe, P, and Si concentrations. Observations of Si accumulation inside *Synechococcus* cells are challenging and must be conducted under strict control of the pH. We took care to maintain pH, i.e., remaining< 8.3 and Si uptake rate obtained in our study were truly biotic processes and not abiotic Si precipitation (Nelson et al., 1984). We undertook our experiments using the Aquil medium, allowing us to control every single nutrient, metal, and vitamin and to provide stable conditions. Nutrient limitations were established by the decrease in the growth rate measured for RCC 2380 and RCC 1084. With this definition in mind, all conditions where growth rate decreased (stable over 10 generations) implied an efficient limitation.

For RCC 2380, the decrease in growth rate between -Si and control suggested a toxic effect of $Si(OH)_4$ on *Synechococcus* growth. The fact that $Si(OH)_4$ concentrations modified the growth rates of both strains is surprising given that *Synechococcus* is known to lack an obligate need for silicon (Brzezinski et al., 2017) and seems insensitive to potential toxic effects of high $Si(OH)_4$ concentrations (Tostevin et al., 2021). However, considering 1) the lower RCC 2380 growth rates in all conditions compared to -Si and especially the increase in growth rate for -Si compared to the control and for -Si-P compared to -P and 2) taking into account that, for RCC 1084, all the conditions, including -Si, have lower growth rates than the control, suggest strain-dependent toxicity effect of high $Si(OH)_4$ concentrations. Our two strains are coastal and used to meet large variations in $Si(OH)_4$ concentrations. Indeed, RCC 2380 is from the Manche, whereas RCC 1084 is from Long Island Sound a semi-enclosed Bay in the USA. By comparison, the strain from the study by Tostevin is pelagic and comes from the Caribbean Sea. At the Roscoff site, $Si(OH)_4$ reaches a maximum of 6 µmol L^{-1} in winter and a minimum of 1.5 µmol L^{-1} in June (Sournia and Birrien, 1995;

Cariou et al., 2004). The ecosystem encounters silicate limitation with respect to nitrate during winter and spring (DIN: DSi< 1) and nitrate limitation during summer. In long Island Sound, $Si(OH)_4$ varies annually from 40 µmol L^{-1} to 1.6 µmol L^{-1} in spring and summer (Gobler et al., 2006; George et al., 2015), and phytoplankton is Si limited with respect to N in summer. In our study, $Si(OH)_4$ concentrations had a strain-specific impact on *Synechococcus* growth rate. RCC 2380 was negatively affected by the highest $Si(OH)_4$ concentrations, and its growth rate significantly increased when $Si(OH)_4$ concentrations decreased from 150 µmol L^{-1} to 20 µmol L^{-1}. This trend can be seen comparing four culturing conditions: control vs. -Si and -P vs. -P-Si. On the contrary, RCC 1084 growth rate significantly decreased when $Si(OH)_4$ concentration was reduced, as seen comparing control vs. -Si, -P vs. -P-Si, and also -Fe vs. -Fe-Si.

Brzezinski and collaborators (2017) also studied the growth rates of six *Synechococcus* clones (including the WH5701 = RCC 1084 in the present study), under varying $Si(OH)_4$ medium concentrations of 1 µmol L^{-1}, 60 µmol L^{-1}, or 120 µmol L^{-1}, and found no significant differences in their growth rates. Our cultures were maintained in a completely synthetic and controlled Aquil medium containing PO_3 (20 µmol L^{-1}) and Fe (100 nmol L^{-1}), whereas Brzezinski's cultures were maintained in a medium made of aged 0.2-µm filtered surface Sargasso Sea water with f/2 medium constituents and containing added PO_3 (36 µmol L^{-1}) and Fe (11.7 µmol L^{-1}). Differences in growth rates between our study and Brzezinski et al. (2017) might stem from medium differences and more specifically metals concentrations. Our study highlights the potential role of metal and, specifically, Fe concentrations on Si uptake by *Synechococcus*. Moreover, these results indicate strain-dependent discrepancies.

The range of Si uptake rates obtained in our study (0.04 fmol Si $cell^{-1}$ to 47 fmol Si $cell^{-1}$ and 0.003 fmol μm^{-2} to 4 fmol μm^{-2}) confirms those measured during field observations from the equatorial Pacific, the Sargasso Sea, and laboratory experiments (0.0006 fmol Si $cell^{-1}$ to 4.7 fmol Si $cell^{-1}$; Baines et al., 2012; Ohnemus et al., 2016; Brzezinski et al., 2017, 2018; Krause et al., 2017; Wei et al., 2022). *Synechococcus* cells contain significant but variable amounts of Si, with cellular Si quotas staying low compared to the most studied silicifiers, i.e., diatoms, cultivated in different nutrients' availability (20 pmol Si $cell^{-1}$ to 225 pmol Si $cell^{-1}$; Martin-Jézéquel et al., 2000; Marchetti and Harrison, 2007; Boutorh et al., 2016). Si cellular quota in our laboratory was more stable than in field samples, where Si per cell could vary at least by an order of magnitude among cells from a single sample. However, many strains coexist *in situ*, and we observed large strain-specific responses to nutrient conditions, probably due to their high capacity to adapt to their environment.

The first hypothesis proposed to explain the mechanisms of Si accumulation by *Synechococcus* (Brzezinski et al., 2017) suggested two possibilities: 1) a lack of selectivity in the transport of PO_4 through the cell membrane, leading to $Si(OH)_4$ molecules being transported instead of PO_4 inside the cell and 2) passive diffusion of $Si(OH)_4$ into the cell, with both mechanisms being enhanced by decreased growth rates, allowing more $Si(OH)_4$ accumulation inside the cells.

A global analysis of RCC 1084 suggests that most limitations, except -Si, simultaneously decreased cell growth and increased Si cell content supporting Brzezinski's hypothesis. Indeed, for RCC 1084, Figure 3 shows that Si cellular quota is dependent upon growth rate with a R^2 of 0.65. However, such a growth effect is not clear for RCC 2380 with a R^2 of only 0.29. PO_4 concentration and Si:P ratio appear to be determinant parameters for Si uptake by *Synechococcus*, as suggested by Brzezinski's study. Additionally, our results indicate the involvement of Fe in Si uptake by some strains of *Synechococcus*. For *Synechococcus*, -Fe-Si induced a higher Si quota than -Si and -Fe alone despite higher growth rate for RCC 2380. The interaction between P and Fe metabolisms and Si accumulation in *Synechococcus* is evident, suggesting a complex role of Fe in Si uptake, possibly, but not exclusively, through implications of Fe in the PO_4 transporters, albeit differently between strains. The significantly higher Si quotas of cells grown under -Fe-Si compared to -Fe, challenge the theory of passive silicon diffusion through cell membranes, especially considering RCC 2380.

In their study, Marron et al. (2016) suggested that the SIT-L in *Synechococcus* may be to avoid $Si(OH)_4$ toxicity in ancient oceans, potentially implying that Si cellular quotas may be more controlled in organisms that have the presence of this Si transporter. RCC 2380 and RCC 1084 are positioned at the two extreme opposite ends of the phylogenetic tree drawn by Doré and collaborators (Doré et al., 2020), suggesting different evolutionary histories and adaptations. RCC 1084 likely appeared much earlier than RCC 2380, possibly before 878 My ago (Doré et al., 2020), when Si concentration in the world oceans was above 1 mol L^{-1}. We do not have the timing for RCC 2380 occurrence, but it appeared much later than 250 My ago, when Si in the ocean waters started to significantly decrease (Marron et al., 2016). The relatively low gene fixation rate observed by Doré et al. (2020) implies that flexible genes that are fixed within a clade (i.e., clade-specific genes) were gained tens of millions of years ago and thus might be more reflective of past selective forces than of recent adaptation to newly colonized niches. We could not find such SIT-L genes in the published genomes of RCC 2380 and RCC1084, and further exploration is needed.

Another hypothesis from Tang et al. (2014) suggests that silicon may accumulate and precipitate on the cell membrane of dead *Synechococcus*. If we consider that the growth rate may be an indicator of the number of dead *Synechococcus* in the culture, then, indeed, low growth rates may involve more dead cells and following the Tang's hypothesis, more silicon accumulating on the membrane of the cells. However, our study showed that growth conditions modified Si content without affecting growth rate, indicating a more complex relationship. For example, -Fe and -Fe-P conditions for RCC 2380 and -Fe, -P, and -Fe-P conditions for RCC 1084 led to similar growth rate but different Si cellular quotas and Si uptake rates.

Overall, our study sheds light on the regulation of Si uptake in *Synechococcus*, emphasizing the importance of Fe, Si, and P concentrations and highlighting strain-specific responses, which contribute to our understanding of the ecological roles of these microorganisms in the oceanic ecosystem. However, the mechanisms explaining these links still need further exploration.

In comparison, the metabolic response of diatoms to Fe limitation is also species specific (Cohen et al., 2017), leading to different consequences for Si accumulation with increasing silicification and frustule mechanical strength for some species (Wilken et al., 2011), no change of Si cellular quotas (Brzezinski et al., 2011) or decreasing silicification in others (Boutorh et al., 2014; Lasbleiz et al., 2014). Although Fe may be involved in Si homeostasis in diatoms (Petrucciani et al., 2022), the link between Fe availability and diatom Si metabolism remains misunderstood despite the fact that diatoms are the most studied silicified marine organisms.

Si uptake rates measured in our study are surprisingly comparable to those measured for diatoms and rhizarians, which play an important role in the Si cycle (Biard et al., 2018; Llopis Monferrer et al., 2020; Tréguer et al., 2021). In our study, Si uptake rates varied from 0.01 to 21 fmol cell^{-1} day^{-1}. By comparison, diatoms have Si uptake rates ranging from 1 to 21,000 fmol cell^{-1} day^{-1}, and rhizarians from 170,000 to 2,000,000 fmol cell^{-1} day^{-1} (Figure 5). Normalizing adsorption rates to biovolume shows similar Si uptake rates between the three silicifiers: 7.46 fmol µm^{-3} day^{-1} for rhizarians, 82.03 fmol µm^{-3} day^{-1} for diatoms, and 55.7 fmol µm^{-3} day^{-1} for *Synechococcus*. In the world ocean, diatoms uptake varies from 0.14 in the North Atlantic Tropical Gyre (Poulton et al., 2006; Tréguer et al., 2021) to a maximum of 202 mmol Si m^{-2} day^{-1} in the upwelling of California (Brzezinski et al., 1997; Tréguer et al., 2021). With a global average cell concentrations of 4 × 10^4 cells mL^{-1} and an average depth of 80 m (Visintini and Flombaum, 2022) cyanobacteria may uptake up to 22 mmol m^{-2} day^{-1} under P limitation and 68 mmol m^{-2} day^{-1} under P and Fe co-limitation. This renders *Synechococcus* real competitors of diatoms for $Si(OH)_4$ resource in the environment especially in zones encountering P and Fe limitations. Whereas P mostly is a secondary limiting nutrient and -P-Fe co-limited zones are scarce in the global ocean, Fe limitation concerns almost a third of the world ocean (Browning and Moore, 2023).

In conclusion, our study highlights the complex interplay between Fe, P, and Si concentrations in regulating Si uptake by *Synechococcus*, with strain-specific responses indicating the need for further research to elucidate the underlying mechanisms and ecological implications.

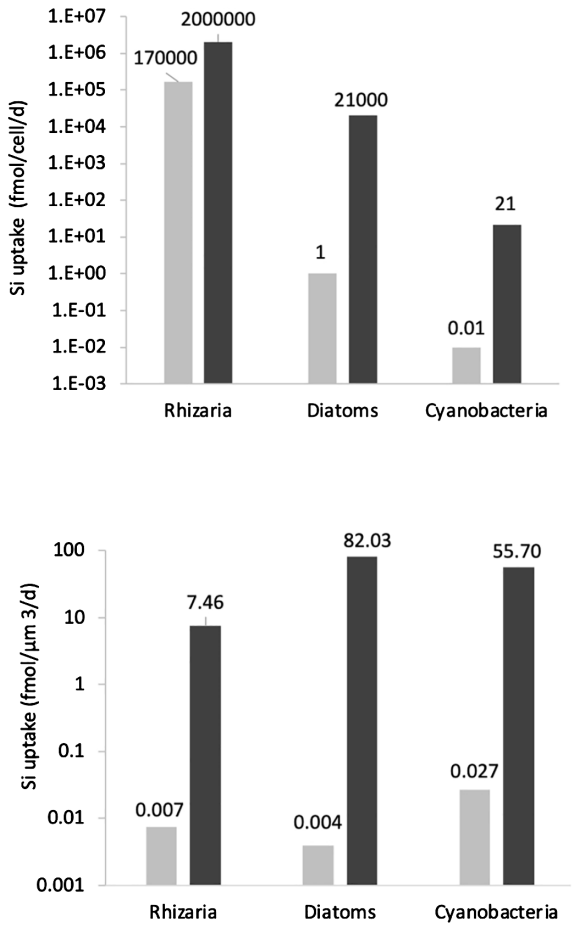

FIGURE 5
Global comparison of Si uptake rates between Rhizarians (Llopis Monferrer, 2020), Diatoms (Llopis Monferrer, 2020), and Cyanobacteria (present study). The first panel represents the Si uptake in fmol/cell/day, whereas, for the second panel, data were corrected with cell volumes and are presented in fmol/µm^3/day. Light gray bars represent the minimum values, and dark gray bars represent the maximum values found.

Meanings for the environment

Synechococcus dominate in oligotrophic waters. Meanwhile, their abundance is quite constant everywhere and throughout the year varying around 4×10^4 cells mL^{-1} with a global yearly abundance between 6.1 and 6.9×10^{26} cells (Visintini et al., 2021; Visintini and Flombaum, 2022). At the global scale, their seasonal variability is 15% (Visintini and Flombaum, 2022), and their concentration increases with temperature (Li, 1998). Spatially, their abundance is maximum in the westerlies winds domain and the trade winds domain defined by Longhurst (Longhurst et al., 1995) with a light decrease in cell abundance around 30° N and S and a minimum in the polar systems (Visintini et al., 2021; Visintini and Flombaum, 2022). The study by Baines and coworkers (2012) revealed for the first time that *Synechococcus* cells may contain Si in non-negligible amount, opening an interesting question on their potential contribution to the Si cycle. However, small diatoms of size similar to that of *Synechococcus* grow in similar locations than *Synechococcus* (Leblanc et al., 2018), which create difficulties to measure *in situ* the *Synechococcus* contribution to Si production, underlying the need to use process studies to evaluate their importance in the dynamics of the Si cycle.

Using a method similar to Tréguer et al. (2021), we estimated *Synechococcus*' global contribution to the Si cycle (Supplementary Materials). The annual average of the bSi standing stock related to *Synechococcus* is 0.87 ± 0.61 Tmol Si. To estimate the variability, we used the maximum standard deviation found in our experimental estimation of the Si quotas, which is smaller than *in situ* variability between cells that may be from different clades and reach more than 200% (Baines et al., 2012; Wei et al., 2022). Moreover, we could not consider seasonal variations of the clade dominance that seems to emerge from the different studies described in Table 3. This estimate is about an order of magnitude higher than the 0.05–0.09 Tmol-Si estimated from *in situ* data and Si/C quotas by Wei et al. (2022). By mean of comparison, rhizarians' Si standing stocks have been estimated to range from 0.08 to 5.25 Tmol Si by Biard et al. (2018) and between 0.07 and 0.72 Tmol Si by Llopis Monferrer et al. (2020) using a global ocean surface area of 328,106 km^2. Diatoms stay the main contributors of the pelagic stocks with 2–4 Tmol of Si (Leblanc et al., 2012). *Synechococcus* may contribute up to 20% of the total bSi pelagic stocks estimated here as the sum of the Si stocks constituted by the three silicifiers mentioned above.

In the revised Si budget made by Tréguer and co-workers, the annual production of biogenic silica at the global scale is 255 ± 52 Tmol $year^{-1}$, with most attributed to diatoms. However, in some region of the ocean (oligotrophic gyres), the contribution of the< 3-µm-size fraction, where *Synechococcus* fall, may reach up to 55% of the Si production (Krause et al., 2017). This production has been attributed to *Synechococcus* by the authors, but this is debated in Leblanc et al. (2018) as nano-diatoms may also be responsible for part of the Si production by small size organisms. On the other side, Wei and collaborators estimated the global annual Si production in the surface ocean due to picocyanobacteria would reach 45% (Wei et al., 2023). Si production is generally measured *in situ* on pelagic communities belonging to the > 0.45–0.6µm size fraction. With cell diameter varying between 0.8 µm and 3 µm and length above 1 µm, we may consider that *Synechococcus* contribution is included in the global Si budget. With this consideration in mind, the global annual Si production of 38 ± 27 Tmol Si $year^{-1}$ calculated in this study corresponds to a contribution of 17% of the total Si production. Acknowledging the high uncertainty, it is interesting to note that this is not so far from the 16.7% contribution to the C production estimated from niche model by Flombaum and collaborators (2013). This contribution shows strong spatial disparities, with a global 93% of the Si production attributed to *Synechococcus* in the Westerlies winds but only 10% in trade winds domain. Surprisingly, their contribution to the Southern Ocean may reach half of the Si production, most probably due here to the high cell abundance found by Visintini' study in the SANT and SSTC regions together with Fe limitations. Please note that, in this Southern region, the cellular Si quotas used to calculate the contribution of *Synechococcus* were not from our study. Despite uncertainties and strain differences in Si metabolisms, *Synechococcus*' contribution to the Si cycle, especially in oceanic regions like the westerlies or the Southern Ocean, is significant. With predicted increases of *Synechococcus* growth in future oceans, their role as actor in the Si cycle deserves to be taken into consideration with an urgent need to understand the mechanisms at stake.

Conclusions

The mechanisms governing Si accumulation in *Synechococcus* are complex and strain-specific, extending beyond the previously suggested factors of non-specific PO_4 transporters, $Si(OH)_4$ diffusion, and growth effects. Our study reveals that *Synechoccocus* Si metabolism is strain specific and that 1) Fe is involved in Si cellular accumulation but Fe limitation consequences on Si quotas are strain specific; 2) our *Synechococcus* strains revealed to be sensitive to Si $(OH)_4$ concentrations in their environment with opposite results, with one of them being negatively affected and the other one being positively affected by high $Si(OH)_4$ concentrations; and 3) Si cellular accumulation can increase or decrease even when $Si(OH)_4$ concentration in the medium decreases. Neither RCC 2380 nor RCC 1084 genomes contain identified SIT-L genes that could explain Si uptake by *Synechococcus*, underscoring the need for further laboratory experiments to explore additional nutrients and genetic factors influencing Si uptake. Not only the physiological mechanisms but also the consequences of this misunderstanding capacity of *Synechococcus* to accumulate Si need to be comprehended if we want to better predict the future of the Si cycle and of the BCP.

Overall, our study suggests a complex interplay between nutrient availability, particularly P and Fe, and Si uptake in *Synechococcus*, with strain-specific responses and potential ecological implications for nutrient cycling in the ocean.

Several questions remain unanswered, including the implications of *Synechococcus* Si accumulation for sinking and export, trophic interactions, and competition with diatoms. Future research perspectives may involve studying a larger

TABLE 3 *Synechococcus* contribution to the Si global oceanic cycle: review of the Supplementary Materials.

	Synechoccocus							Diatoms	Global Si cycle			Rhizarians	
	Average *Synechococcus* abundance		Ocean surface	Qsi	bSi	PbSi		bSi stocks	Surface used for diatom calculation	PbSi		bSi	PbSi
	10^4 cells/mL	10^{24} cells	10^6 km^2	fmol Si/cell	10^{10} mol Si	10^{12} mol an^{-1}	mol m^{-2} an^{-1}	mol Si	10^6 km^2	10^{12} mol an^{-1}	mol m^{-2} an^{-1}	mol Si	mol an^{-1}
Coastal	2.26	67.81	34.35	1.14	3.99	3.27	0.10		37	138.04	3.73		
Westerlies winds domain	2.51	248.89	132.97	3.18	81.59	38.02	0.29		129.9	29.65	0.23		
Trade winds domain	2.72	580.79	139.90	3.18	6.74	5.02	0.04		139.9	50.42	0.36		
Polar	0.63	9.26	20.78	3.19	3.06	1.50	0.07		53.98	66.83	1.24		
Global Ocean	2.27	648.43	328.00		95.38	47.80	0.15	2–4 × 10^{12}	360.78	284.93	0.79	0.66–7.22 × 10^{11}	2–58 × 10^{12}
Total Arctique	0.30	0.40	1.66		0.00	0.00	0.00		14	1.42	0.10		
Total Atlantique	2.20	151.12	74.15		15.92	15.48	0.21		86	21.50	0.25		
Total Océan Indien	2.88	107.81	45.38		0.74	0.27	0.01		54	37.19	0.69		
Total Pacifique	2.43	313.33	148.92		20.86	15.18	0.10		134	145.74	1.09		
Total Antarctique	1.26	75.78	57.89		57.85	16.87	0.29		73	42.76	0.59		
Global Ocean	1.81	648.43	328.00		95.37	47.80	0.15	2–4 × 10^{12}	361	248.61	0.69	0.66–7.22 × 10^{11}	2–58 × 10^{12}

For the purpose of comparison, data for diatoms and rhizarians are also provided in the table. Diatoms' bSi standing stock is sourced from Leblanc et al. (2018), whereas data on total Si production are obtained from Tréguer et al. (2021). Data for rhizarians are sourced from Llopis Monferrer et al. (2020).

10.3389/fmars.2024.1331333

number of *Synechococcus* strains coming from various clades to elucidate global physiological characteristics and specific habitat preferences.

Data availability statement

The original contributions presented in the study are included in the article/Supplementary Material. Further inquiries can be directed to the corresponding authors.

Author contributions

AG: Conceptualization, Formal analysis, Funding acquisition, Investigation, Methodology, Validation, Writing – original draft, Writing – review & editing. AL: Formal analysis, Methodology, Writing – original draft, Writing – review & editing. BM: Conceptualization, Formal analysis, Funding acquisition, Investigation, Methodology, Writing – original draft, Writing – review & editing.

Funding

The author(s) declare financial support was received for the research, authorship, and/or publication of this article. This work has been funded by ANR BIOPSIS project, grant ANR-16-CE-0002–01 of the French Agence Nationale de la Recherche. This work was partially supported by ISblue project, Interdisciplinary graduate school for the blue planet (ANR-17-EURE-0015) and co-funded by a grant from the French government under the program "Investissements d'Avenir" embedded in France 2030.

Acknowledgments

The authors gratefully acknowledge the technical support of M. Le Goff(1) and M. Gallinari(1) through the analytical platform PACHIDERM.

Conflict of interest

Author AG was employed by the company AlgaeNutri.

The remaining authors declare that the research was conducted in the absence of any commercial or financial relationships that could be construed as a potential conflict of interest.

Publisher's note

Supplementary material

The Supplementary Material for this article can be found online at: https://www.frontiersin.org/articles/10.3389/fmars.2024.1331333/full#supplementary-material

SUPPLEMENTARY TABLE 1

Synechococcus contribution to the global Si cycle. The contribution of *Synechococcus* to the annual stocks of bSi was estimated for each of the Longhurst provinces using (1) the *Synechococcus* concentration found in the dataset made available by Visintini et al. (2021), (2) the main *Synechococcus* clade of the different oceanic areas (Zwirglmaier et al., 2008; Tai and Palenik, 2009; Huang et al., 2012; Sohm et al., 2016; Grébert et al., 2018; Doré et al., 2020; Wang et al., 2022; Wei et al., 2022), and (3) the *in situ* and clade specific laboratory measurements of Si *Synechococcus* cellular quotas from this study but also to our acknowledge, those from all other existing studies (Baines et al., 2012; Ohnemus et al., 2016; Brzezinski et al., 2017; Krause et al., 2017; Wei et al., 2022). For the first time in a budget, we also integrated the impact of P and Fe limitations. To do so we assigned a limitation to each Longhurst provinces using Browning and Moore (2023). We used the Si quotas corresponding to the P and Fe limitations when our clades were dominating the corresponding zone, and data measured *in situ* when possible. When no *in-situ* data are available we used the Si content measured for the main clade of the zone without taking into account the limitations. For Si production rates we used our measurements which considers the main nutrient limitations describe by Browning and Moore. When our clades were not one of the main *Synechococcus* observed in the Longhurst area, i.e., mainly in Trade winds domain, we used an average value of the rates measured in our study under the limitation describe by Browning and Moore. This hypothesis may give a good idea of the Si production because production rates were not so much clade specific and resemble the two existing other studies (Brzezinski et al., 2017; Krause et al., 2017).
Description of the different data used to estimate the global contribution to the Si cycle: stocks and production. The exponent indicates the origin of the data from literature while the ** Denotes when the data are issued from this study. * Is used when the definition of the headers is provided below the table. Qsi* (fmol/cell) is the Si quota used in the calculation, estimated as describe above. VSi* (d^{-1}): is the Si uptake used to calculate the global Si production due to *Synechococcus*. estimated as described above. bSi stocks resulting from the equation: bSi = [Syn] * productive depth * surface of the Longhurst region * Qsi With [Syn] the average cell concentration estimated from Visintini et al. (2021). PbSi* is the bSi production due to *Synechococcus*. Calculated using the duration of the productive period (t_{pp}: 9 months (Visintini and Flombaum, 2022), except for polar seas where we used 3.5 months as for diatoms in Tréguer et al. (2021)). PbSi = bSi * VSi *t_{pp}/12 a- Brzezinski et al., 2017; b- Doré et al., 2020; c- Grébert et al., 2022; d- Huang et al., 2012; e- Ohnemus et al., 2016; f-Sohm et al., 2016; g- Tai and Palenik, 2009; h- Tang et al., 2014; i- Wang et al., 2022; j- Wei et al., 2022; k- Zwirglmaier et al., 2007, 2008; L- Robicheau et al., 2022; m- Visintini et al., 2021; Visintini and Flombaum, 2022; n- Browning and Moore, 2023; o- Longhurst et al., 1995.

References

Aminot, A., and Kérouel, R. (2007). *Dosage automatique des nutriments dans les eaux marines* (Ifremer), 187.

Baines, S. B., Twining, B. S., Brzezinski, M. A., Krause, J. W., Vogt, S., Assael, D., et al. (2012). Significant silicon accumulation by marine picocyanobacteria. *Nat. Geosci.* 5, 886–891. doi: 10.1038/ngeo1641

Benedetti, F., Gruber, N., and Vogt, M. (2023). Global gradients in species richness of marine plankton functional groups. *J. Plankton Res.* 45 (6), 832–852. doi: 10.1093/plankt/fbad044

Biard, T., Krause, J. W., Stukel, M. R., and Ohman, M. D. (2018). The significance of giant phaeodarians (Rhizaria) to biogenic silica export in the california current ecosystem. *Glob. Biogeochem. Cycles* 32, 987–1004. doi: 10.1029/2018GB005877

Boutorh, J., Cheize, M., Planquette, H., Shelley, R., Lacan, F., Heimbürger, L. E., et al. (2014). III. 5. Trace elements and their isotopes. *CRUISE REPORT* 67.

Boutorh, J., Moriceau, B., Gallinari, M., Ragueneau, O., and Bucciarelli, E. (2016). Effect of trace metal-limited growth on the postmortem dissolution of the marine diatom Pseudo-nitzschia delicatissima: micronutrient-limited diatom dissolution. *Glob. Biogeochem. Cycles* 30, 57–69. doi: 10.1002/2015GB005088

Brand, L. E. (1991). Minimum iron requirements of marine phytoplankton and the implications for the biogeochemical control of new production. *Limnol. Oceanogr.* 36, 1756–1771. doi: 10.4319/lo.1991.36.8.1756

Browning, T. J., and Moore, C. M. (2023). Global analysis of ocean phytoplankton nutrient limitation reveals high prevalence of co-limitation. *Nat. Commun.* 14 (1), 5014. doi: 10.1038/s41467-023-40774-0

Brzezinski, M. A., Alldredge, A. L., and O'Bryan, L. M. (1997). Silica cycling within marine snow. *Limnol. Oceanogr.* 42, 1706–1713. doi: 10.4319/lo.1997.42.8.1706

Brzezinski, M. A., Baines, S. B., Balch, W. M., Beucher, C. P., Chai, F., Dugdale, R. C., et al. (2011). Co-limitation of diatoms by iron and silicic acid in the equatorial pacific. *Deep Sea Res. Part II: Topical Stud. Oceanography* 58 (3-4), 493–511. doi: 10.1016/j.dsr2.2010.08.005

Brzezinski, M. A., Krause, J. W., Baines, S. B., Collier, J. L., Ohnemus, D. C., and Twining, B. S. (2017). Patterns and regulation of silicon accumulation in *Synechococcus* spp. *J. Phycol* 53, 746–761. doi: 10.1111/jpy.12545

Cariou, T., Macé, E., and Morin, P. (2004). *La série océanographique littorale Estacade de l'Observatoire Océanologique de Roscoff: résultats des observations 1985 – 2002*. Available online at: https://www.researchgate.net/publication/299430343_La_serie_oceanographique_littorale_Estacade_de_l'Observatoire_Oceanologique_de_Roscoff_resultats_des_observations_1985_-_2002.

Churakova, Y., Aguilera, A., Charalampous, E., Conley, D. J., Lundin, D., Pinhassi, J., et al. (2023). Biogenic silica accumulation in picoeukaryotes: Novel players in the marine silica cycle. *Environ. Microbiol. Rep.* 15, 282–290. doi: 10.1111/1758-2229.13144

Cohen, N. R., Ellis, K. A., Lampe, R. H., McNair, H., Twining, B. S., Maldonado, M. T., et al. (2017). Diatom transcriptional and physiological responses to changes in iron bioavailability across ocean provinces. *Front. Mar. Sci.* 4. doi: 10.3389/fmars.2017.00360

De Martini, F., and Neuer, S. (2016). From grazer control to carbon export: contrasting the role of synechococcus and prochlorococcus in the sargasso sea. *Am. Geophysical Union* 2016, B31A–B302.

Doré, H., Farrant, G. ,. K., Guyet, U., Haguait, J., Humily, F., Ratin, M., et al. (2020). Evolutionary mechanisms of long-term genome diversification associated with niche partitioning in marine picocyanobacteria. *Front. Microbiol.* 11, 23. doi: 10.3389/fmicb.2020.567431

Doré, H., Guyet, U., Leconte, J., Farrant, G. K., Alric, B., and Garczarek, L. (2023). Differential global distribution of marine picocyanobacteria gene clusters reveals distinct niche-related adaptive strategies. *ISME J.* 17 (5), 720–732. doi: 10.1038/s41396-023-01386-0

Doré, H., Leconte, J., Guyet, U., Breton, S., Farrant, G. K., Demory, D., et al. (2022). Global phylogeography of marine synechococcus in coastal areas reveals strong community shifts. *Msystems* 7 (6), e00656–e00622. doi: 10.1128/msystems.00656-22

Duhamel, S., Kim, E., Sprung, B., and Anderson, O. R. (2019). Small pigmented eukaryotes play a major role in carbon cycling in the P-depleted western subtropical North Atlantic, which may be supported by mixotrophy. *Limnol. Oceanogr.* 64, 2424–2440. doi: 10.1002/lno.11193

Dutkiewicz, S., Morris, J. J., Follows, M. J., Scott, J., Levitan, O., Dyhrman, S. T., et al. (2015). Impact of ocean acidification on the structure of future phytoplankton communities. *Nat. Clim. Change* 5, 1002–1006. doi: 10.1038/nclimate2722

Flombaum, P., Gallegos, J. L., Gordillo, R. A., Rincón, J., Zabala, L. L., Jiao, N., et al. (2013). Present and future global distributions of the marine Cyanobacteria *Prochlorococcus* and *Synechococcus*. *Proc. Natl. Acad. Sci.* 110, 9824–9829. doi: 10.1073/pnas.1307701110

Flombaum, P., and Martiny, A. C. (2021). Diverse but uncertain responses of picophytoplankton lineages to future climate change. *Limnol. Oceanogr.* 66, 4171–4181. doi: 10.1002/lno.11951

George, J. A., Lonsdale, D. J., Merlo, L. R., and Gobler, C. J. (2015). The interactive roles of temperature, nutrients, and zooplankton grazing in controlling the winter-spring phytoplankton bloom in a temperate, coastal ecosystem, Long Island Sound: Long Island Sound winter-spring bloom. *Limnol. Oceanogr.* 60, 110–126. doi: 10.1002/lno.10020

Gobler, C. J., Buck, N. J., Sieracki, M. E., and Sañudo-Wilhelmy, S. A. (2006). Nitrogen and silicon limitation of phytoplankton communities across an urban estuary: The East River-Long Island Sound system. *Est. Coast. Sh. Sci.* 68, 127–138. doi: 10.1016/j.ecss.2006.02.001

Grébert, T., Doré, H., Partensky, F., Farrant, G. K., Boss, E. S., Picheral, M., et al. (2018). Light color acclimation is a key process in the global ocean distribution of *Synechococcus* cyanobacteria. *Proc. Natl. Acad. Sci.* 115, E2010–E2019. doi: 10.1073/pnas.1717069115

Henson, S. A., Sanders, R., and Madsen, E. (2012). Global patterns in efficiency of particulate organic carbon export and transfer to the deep ocean: export and transfer efficiency. *Glob. Biogeochem. Cycles* 26, GB1028. doi: 10.1029/2011GB004099

Huang, S., Wilhelm, S. W., Harvey, H. R., Taylor, K., Jiao, N., and Chen, F. (2012). Novel lineages of *Prochlorococcus* and *Synechococcus* in the global oceans. *ISME J.* 6, 285–297. doi: 10.1038/ismej.2011.106

Krause, J. W., Brzezinski, M. A., Baines, S. B., Collier, J. L., Twining, B. S., and Ohnemus, D. C. (2017). Picoplankton contribution to biogenic silica stocks and production rates in the Sargasso Sea. *Glob. Biogeochem. Cycles* 31, 762–774. doi: 10.1002/2017GB005619

Lasbleiz, M., Leblanc, K., Blain, S., Ras, J., Cornet-Barthaux, V., Hélias Nunige, S., et al. (2014). Pigments, elemental composition (C, N, P, and Si), and stoichiometry of particulate matter in the naturally iron fertilized region of Kerguelen in the Southern Ocean. *Biogeosciences* 11, 5931–5955. doi: 10.5194/bg-11-5931-2014

Leblanc, K., Arístegui, J., Armand, L., Assmy, P., Beker, B., Bode, A., et al. (2012). A global diatom database–abundance, biovolume and biomass in the world ocean. *Earth Syst. Sci. Data* 4 (1), 149–165. doi: 10.5194/essd-4-149-2012

Leblanc, K., Cornet, V., Rimmelin-Maury, P., Grosso, O., Hélias-Nunige, S., Brunet, C., et al. (2018). Silicon cycle in the tropical South Pacific: contribution to the global Si cycle and evidence for an active pico-sized siliceous plankton. *Biogeosciences* 15, 5595–5620. doi: 10.5194/bg-15-5595-2018

Letscher, R. T., Moore, J. K., Martiny, A. C., and Lomas, M. W. (2023). Biodiversity and stoichiometric plasticity increase pico-phytoplankton contributions to marine net primary productivity and the biological pump. *Glob. Biogeochem. Cycles* 37, e2023GB007756. doi: 10.1029/2023GB007756

Leynaert, A., Tréguer, P., Nelson, D. M., and Del Amo, Y. (1996). "32Si as a tracer of biogenic silica production: methodological improvements," in *Integrated marine system analysis. european network for integrated marine system analysis. FWO vlaanderen: minutes of the first network meeting (Brugge, 29.02.96-02.03.96)*. Ed. J. Baeyens, et al, 29–35.

Li, W. K. W. (1998). Annual average abundance of heterotrophic bacteria and *Synechococcus* in surface ocean waters. *Limnol. Oceanogr.* 43, 1746–1753. doi: 10.4319/lo.1998.43.7.1746

Llopis Monferrer, N. L. (2020). Unveiling the role of Rhizaria in the silicon cycle. Université de Bretagne occidentale - Brest. English. ⟨NNT: 2020BRES0041⟩.

Llopis Monferrer, N., Boltovskoy, D., Tréguer, P., Sandin, M. M., Not, F., and Leynaert, A. (2020). Estimating biogenic silica production of rhizaria in the global ocean. *Glob. Biogeochem. Cycles* 34, e2019GB006286. doi: 10.1029/2019GB006286

Longhurst, A., Sathyendranath, S., Platt, T., and Caverhill, C. (1995). An estimate of global primary production in the ocean from satellite radiometer data. *J. Plankton Res.* 17, 1245–1271. doi: 10.1093/plankt/17.6.1245

MaChado, K. B., Vieira, L. C. G., and Nabout, J. C. (2019). Predicting the dynamics of taxonomic and functional phytoplankton compositions in different global warming scenarios. *Hydrobiologia* 830, 115–134. doi: 10.1007/s10750-018-3858-7

Marchetti, A., and Harrison, P. J. (2007). Coupled changes in the cell morphology and the elemental (C, N, and Si) composition of the pennate diatom *Pseudo-nitzschia* due to iron deficiency. *Limnol. Oceanogr.* 52, 2270–2284. doi: 10.4319/lo.2007.52.5.2270

Marinov, I., Doney, S. C., Lima, I. D., Lindsay, K., Moore, J. K., and Mahowald, N. (2013). North-South asymmetry in the modeled phytoplankton community response to climate change over the 21st century. *Glob. Biogeochem. Cycles* 27, 1274–1290. doi: 10.1002/2013GB004599

Marron, A. O., Ratcliffe, S., Wheeler, G. L., Goldstein, R. E., King, N., Not, F., et al. (2016). The evolution of silicon transport in eukaryotes. *Mol. Biol. Evol.* 33, 3226–3248. doi: 10.1093/molbev/msw209

Martin-Jézéquel, V., Hildebrand, M., and Brzezinski, M. A. (2000). Silicon metabolism in diatoms: implications for growth. *J. Phycol.* 36, 821–840. doi: 10.1046/j.1529-8817.2000.00019.x

Moore, C. M., Mills, M. M., Arrigo, K. R., Berman-Frank, I., Bopp, L., Boyd, P. W., et al. (2013). Processes and patterns of oceanic nutrient limitation. *Nat. Geosci.* 6, 701–710. doi: 10.1038/ngeo1765

Moriceau, B., Garvey, M., Ragueneau, O., and Passow, U. (2007). Evidence for reduced biogenic silica dissolution rates in diatom aggregates. *Mar. Ecol. Prog. Ser.* 333, 129–142. doi: 10.3354/meps333129

Muñoz-Marín, M. C., Gómez-Baena, G., López-Lozano, A., Moreno-Cabezuelo, J. A., Díez, J., and García-Fernández, J. M. (2020). Mixotrophy in marine picocyanobacteria: use of organic compounds by *Prochlorococcus* and *Synechococcus*. *ISME J.* 14, 1065–1073. doi: 10.1038/s41396-020-0603-9

Nelson, D. M., Riedel, G. F., Millan-Nunez, R., and Lara-Lara, J. R. (1984). Silicon uptake by algae with no known Si requirement. I. True cellular uptake and pH-induced precipitation by *phaeodactylum tricornutum* (bacillariophyceae) and *platymonas* sp.(prasinophyceae) 1. *J. Phycol.* 20, 141–147. doi: 10.1111/j.0022-3646.1984.00141.x

Ohnemus, D. C., Krause, J. W., Brzezinskid, M. A., Colliere, J. L., Baines, S. B., and Twining, B. S. (2018). The chemical form of silicon in marine *Synechococcus*. *Mar.Chem.* 206, 44–51. doi: 10.1016/j.marchem.2018.08.004

Ohnemus, D. C., Rauschenberg, S., Krause, J. W., Brzezinski, M. A., Collier, J. L., Geraci-Yee, S., et al. (2016). Silicon content of individual cells of *Synechococcus* from the North Atlantic Ocean. *Mar. Chem.* 187, 16–24. doi: 10.1016/j.marchem.2016.10.003

Petrucciani, A., Knoll, A. H., and Norici, A. (2022). Si Decline and diatom evolution: Insights from physiological experiments. *Front. Mar. Sci.* 9, 924452. doi: 10.3389/fmars.2022.924452

Poulton, A. J., Sanders, R., Holligan, P. M., Stinchcombe, M. C., Adey, T. R., Brown, L., et al. (2006). Phytoplankton mineralization in the tropical and subtropical Atlantic Ocean. *Glob. Biogeochem. Cycles* 20 (4). doi: 10.1029/2006GB002712

Price, N. M., Harrison, G. I., Hering, J. G., Hudson, R. J., Nirel, P. M. V., Palenik, B., et al. (1989). Preparation and chemistry of the artificial algal culture medium Aquil. *Biol. Oceanogr.* 6, 443–461. doi: 10.1080/01965581.1988.10749544

Richardson, T. L., and Jackson, G. A. (2007). Small phytoplankton and carbon export from the surface ocean. *Science* 315, 838–840. doi: 10.1126/science.1133471

Robicheau, B. M., Tolman, J., Bertrand, E. M., and LaRoche, J. (2022). Highly-resolved interannual phytoplankton community dynamics of the coastal northwest atlantic. *ISME Commun.* 2 (1), 38.

Siegel, D. A., DeVries, T., Cetinić, I., and Bisson, K. M. (2023). Quantifying the ocean's biological pump and its carbon cycle impacts on global scales. *Annu. Rev. Mar. Sci.* 15, 329–356. doi: 10.1146/annurev-marine-040722-115226

Sohm, J. A., Ahlgren, N. A., Thomson, Z. J., Williams, C., Moffett, J. W., Saito, M. A., et al. (2016). Co-occurring synechococcus ecotypes occupy four major oceanic regimes defined by temperature, macronutrients and iron. *ISME J.* 10 (2), 333–345. doi: 10.1038/ismej.2015.115

Sournia, A., and Birrien, J. L. (1995). La série océanographique côtière de Roscoff (Manche occidentale) de 1985 à 1992. *Cahiers Biologie Mar.* 36, 1–8.

Tai, V., and Palenik, B. (2009). Temporal variation of *Synechococcus* clades at a coastal Pacific Ocean monitoring site. *ISME J.* 3, 903–915. doi: 10.1038/ismej.2009.35

Tang, T., Kisslinger, K., and Lee, C. (2014). Silicate deposition during decomposition of cyanobacteria may promote export of picophytoplankton to the deep ocean. *Nat. Commun.* 5 (1), 4143. doi: 10.1038/ncomms5143

Tostevin, R., Snow, J. T., Zhang, Q., Tosca, N. J., and Rickaby, R. E. M. (2021). The influence of elevated SiO_2(aq) on intracellular silica uptake and microbial metabolism. *Geobiology* 19, 421–433. doi: 10.1111/gbi.12442

Tréguer, P., Bowler, C., Moriceau, B., Dutkiewicz, S., Gehlen, M., Aumont, O., et al. (2018). Influence of diatom diversity on the ocean biological carbon pump. *Nat. Geosci.* 11, 27–37. doi: 10.1038/s41561-017-0028-x

Tréguer, P., Lindner, L., van Bennekom, A. J., Leynaert, A., Panouse, M., and Jacques, G. (1991). Production of biogenic silica in the weddell-scotia seas measured with 32Si. *Limnol. Oceanogr.* 36 (6), 1217–1227. doi: 10.4319/lo.1991.36.6.1217

Tréguer, P. J., Sutton, J. N., Brzezinski, M., Charette, M. A., Devries, T., Dutkiewicz, S., et al. (2021). Reviews and syntheses: the biogeochemical cycle of silicon in the modern ocean. *Biogeosciences* 18 (4), 1269–1289. doi: 10.5194/bg-2020–274

Visintini, N., and Flombaum, P. (2022). Picophytoplankton phenology in the global ocean assessed by quantitative niche models. *Mar. Biol.* 169 (7), 93. doi: 10.1007/s00227-022-04080-5

Visintini, N., Martiny, A. C., and Flombaum, P. (2021). *Prochlorococcus*, *Synechococcus*, and picoeukaryotic phytoplankton abundances in the global ocean. *Limnol. Oceanogr. Lett.* 6, 207–215. doi: 10.1002/lol2.10188

Wang, T., Chen, X., Li, J., and Qin, S. (2022). Distribution and phenogenetic diversity of synechococcus in the bohai sea, china. *J. Oceanology Limnology* 40 (2), 592–604.

Wei, Y., Qu, K., Cui, Z., and Sun, J. (2023). Picocyanobacteria–a non-negligible group for the export of biomineral silica to ocean depth. *J. Environ. Manage.* 342, 118313. doi: 10.1016/j.jenvman.2023.118313

Wei, Y., Sun, J., Li, L., and Cui, Z. (2022). *Synechococcus* silicon accumulation in oligotrophic oceans. *Limnol. Oceanogr.* 67, 552–566. doi: 10.1002/lno.12015

Wilken, S., Hoffmann, B., Hersch, N., Kirchgessner, N., Dieluweit, S., Rubner, W., et al. (2011). Diatom frustules show increased mechanical strength and altered valve morphology under iron limitation. *Limnol. Oceanogr.* 56, 1399–1410. doi: 10.4319/lo.2011.56.4.1399

Zwirglmaier, K., Jardillier, L., Ostrowski, M., Mazard, S., Garczarek, L., Vaulot, D., et al. (2008). Global phylogeography of marine synechococcus and prochlorococcus reveals a distinct partitioning of lineages among oceanic biomes. *Environ. Microbiol.* 10 (1), 147–161. doi: 10.1111/j.1462-2920.2007.01440.x

Frontiers in Marine Science

Explores ocean-based solutions for emerging global challenges

The third most-cited marine and freshwater biology journal, advancing our understanding of marine systems and addressing global challenges including overfishing, pollution, and climate change.

Discover the latest Research Topics

See more →

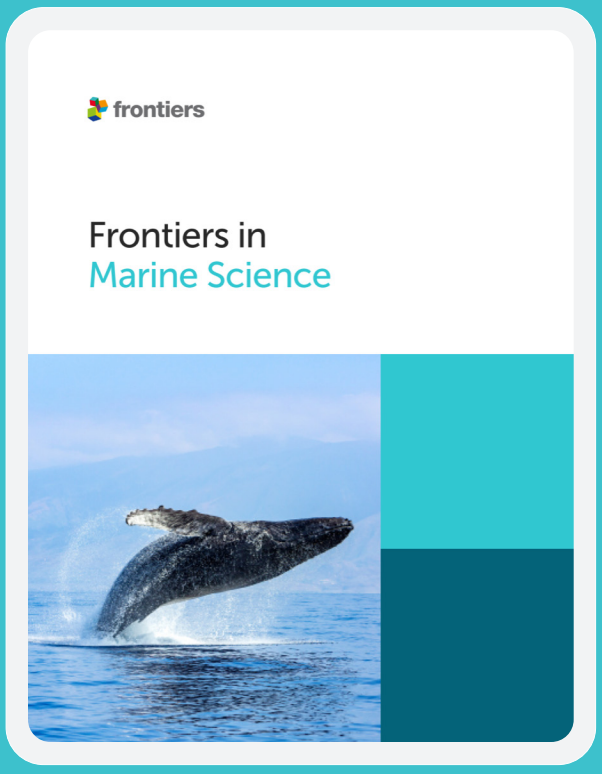

Frontiers

Avenue du Tribunal-Fédéral 34
1005 Lausanne, Switzerland
frontiersin.org

Contact us

+41 (0)21 510 17 00
frontiersin.org/about/contact